AGARD-CP-570

AGARD

ADVISORY GROUP FOR AEROSPACE RESEARCH & DEVELOPMENT
7 RUE ANCELLE, 92200 NEUILLY-SUR-SEINE, FRANCE

AGARD CONFERENCE PROCEEDINGS 570

Aerodynamics of Store Integration and Separation

(l'Aérodynamique de l'intégration et du largage des charges externes)

Papers presented and discussions recorded at the 76th Fluid Dynamics Panel Symposium held in Ankara, Turkey, 24-27 April 1995.

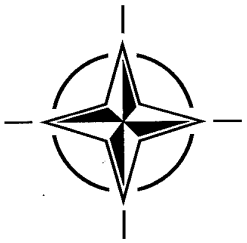

NORTH ATLANTIC TREATY ORGANIZATION

Published February 1996

Distribution and Availability on Back Cover

DISCLAIMER NOTICE

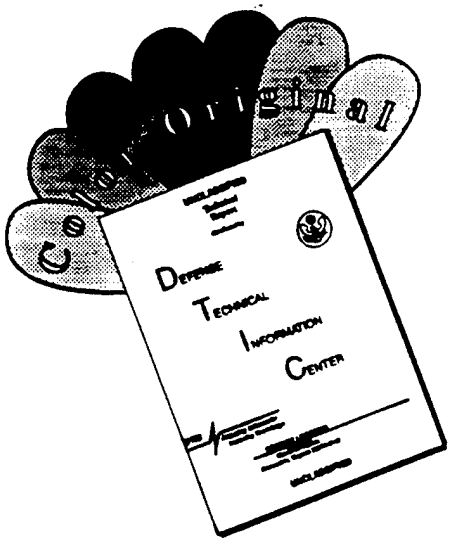

THIS DOCUMENT IS BEST QUALITY AVAILABLE. THE COPY FURNISHED TO DTIC CONTAINED A SIGNIFICANT NUMBER OF COLOR PAGES WHICH DO NOT REPRODUCE LEGIBLY ON BLACK AND WHITE MICROFICHE.

DISCLAIMER NOTICE

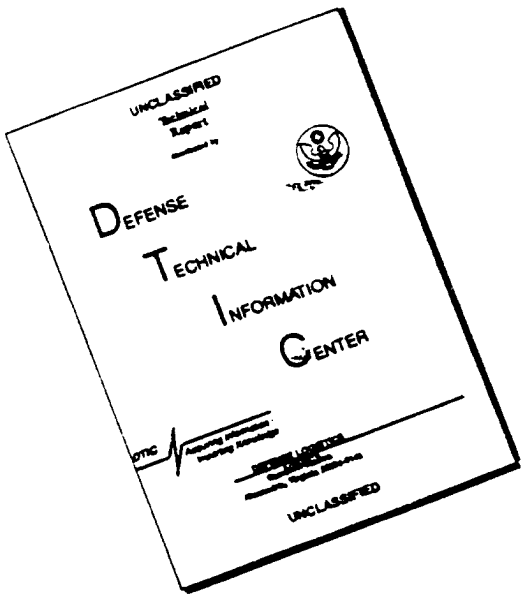

THIS DOCUMENT IS BEST QUALITY AVAILABLE. THE COPY FURNISHED TO DTIC CONTAINED A SIGNIFICANT NUMBER OF PAGES WHICH DO NOT REPRODUCE LEGIBLY.

AGARD-CP-570

AGARD

ADVISORY GROUP FOR AEROSPACE RESEARCH & DEVELOPMENT
7 RUE ANCELLE, 92200 NEUILLY-SUR-SEINE, FRANCE

AGARD CONFERENCE PROCEEDINGS 570

Aerodynamics of Store Integration and Separation

(l'Aérodynamique de l'intégration et du largage des charges externes)

Papers presented and discussions recorded at the 76th Fluid Dynamics Panel Symposium held in Ankara, Turkey, 24-27 April 1995.

North Atlantic Treaty Organization
Organisation du Traité de l'Atlantique Nord

The Mission of AGARD

According to its Charter, the mission of AGARD is to bring together the leading personalities of the NATO nations in the fields of science and technology relating to aerospace for the following purposes:

- Recommending effective ways for the member nations to use their research and development capabilities for the common benefit of the NATO community;
- Providing scientific and technical advice and assistance to the Military Committee in the field of aerospace research and development (with particular regard to its military application);
- Continuously stimulating advances in the aerospace sciences relevant to strengthening the common defence posture;
- Improving the co-operation among member nations in aerospace research and development;
- Exchange of scientific and technical information;
- Providing assistance to member nations for the purpose of increasing their scientific and technical potential;
- Rendering scientific and technical assistance, as requested, to other NATO bodies and to member nations in connection with research and development problems in the aerospace field.

The highest authority within AGARD is the National Delegates Board consisting of officially appointed senior representatives from each member nation. The mission of AGARD is carried out through the Panels which are composed of experts appointed by the National Delegates, the Consultant and Exchange Programme and the Aerospace Applications Studies Programme. The results of AGARD work are reported to the member nations and the NATO Authorities through the AGARD series of publications of which this is one.

Participation in AGARD activities is by invitation only and is normally limited to citizens of the NATO nations.

Published February 1996

ISBN 92-836-0022-3

Printed by Canada Communication Group
45 Sacré-Cœur Blvd., Hull (Québec), Canada K1A 0S7

Aerodynamics of Store Integration and Separation

(AGARD CP-570)

Executive Summary

Airframe/store capability is of major importance to the aircraft and weapon designer. Weapon system capability and aircraft performance are directly affected by the problems associated with store integration and separation. Improved weapon integration can improve the air vehicle effectiveness by orders of magnitude. The aerodynamic problems associated with the carriage of stores and their release from military aircraft are numerous and very complex, making this a most difficult task for the aircraft designer. Improvements in the integration process can lead to significant reductions in the air vehicle development costs.

The aim of this symposium was to bring together engineers in the fields of theoretical and experimental aerodynamics, as applied to the store integration problem, to review and discuss the state of the art in the prediction, methodology and experimental techniques currently being developed and applied to the aerodynamics of store carriage and release, and to assess new design concepts. The program included 35 papers from North America and Western Europe and was organized in 6 technical sessions.

The previous AGARD conference on this subject was held in the mid 1980's and significant progress has been made since then in the design and integration of modern weapons. At that time, the principle of an integrated weapon system design was only just being accepted into practice. The weapon design/clearance process was largely experimental based with theoretical methods only just being accepted as part of the process. A recommendation from this Symposium was that integrated weapon systems be pursued more vigorously.

Although significant limitations remain, the symposium demonstrated that considerable progress has been made in the decade since the previous symposium on this subject. The topics covered demonstrated that the principle of integration has been widely accepted and that the design of the stores is considered as an integral part of the aircraft. Improvements in the development and application of Computational Fluid Dynamics to the design of Weapon Systems were demonstrated and it was shown that the limiting factor was available computing power.

The importance of both experimental and semi-empirical techniques was emphasized and it was demonstrated that the use of theory and experiment in combination leads to a design and clearance tool box of high integrity. The symposium provided a unique forum for publicizing new developments and an appreciation of the importance of the constraints imposed on weapon carriage concepts by aircraft signature requirements.

Overall, the conference was very successful, as attested to by the high attendance figures and lively discussion at the conclusion. Several areas that require emphasis in future research and development programs were identified and an excellent exchange of ideas/experiences occurred.

C.D.S. Clarkson
Programme Committee Chairman

L'aérodynamique de l'intégration et du largage des charges externes
(AGARD CP-570)

Synthèse

La capacité du couple cellule/charges externes est d'une importance capitale pour le concepteur d'aéronefs et de systèmes d'armes. Les performances d'un aéronef, tout comme la capacité d'un système d'armes, sont directement influencées par les problèmes associés à l'intégration et au largage des charges externes. L'efficacité globale des véhicules aériens peut être améliorée de façon exponentielle par une meilleure intégration des systèmes d'armes. Les problèmes aérodynamiques associés à l'emport des charges externes et à leur largage à partir d'aéronefs militaires sont nombreux et très complexes, et présentent des difficultés particulières pour le concepteur. Les améliorations des techniques d'intégration pourraient permettre des économies considérables au niveau des coûts de développement des véhicules aériens.

Le symposium a eu pour objectif de rassembler des ingénieurs travaillant dans le domaine de l'aérodynamique théorique et expérimentale dans la mesure où cette dernière s'applique au problème d'intégration, de définir et de discuter de l'état actuel des connaissances technologiques dans le domaine de la prévision, la méthodologie et les techniques expérimentales en cours de développement, en vue de leur application à l'aérodynamique de l'emport et du largage des charges externes, et d'évaluer les nouveaux concepts de construction. Le programme comportait 35 communications présentées par des auteurs originaires de l'Amérique du Nord et de l'Europe occidentale, organisé en six sessions:

La précédente conférence AGARD sur ce sujet a été organisée pendant les années 80 et depuis lors, des progrès considérables ont été réalisés dans le domaine de la conception et de l'intégration des systèmes d'armes modernes. A l'époque, le principe de la conception intégrée des systèmes d'armes était loin d'être universellement accepté. La procédure de conception/homologation reposait largement sur des bases expérimentales, les méthodes théoriques ne faisant qu'à peine partie de la pratique à suivre. L'une des recommandations du symposium a été de poursuivre plus activement la question des systèmes d'armes intégrés.

S'il existe encore des limitations non négligeables dans ce domaine, le symposium a mis en évidence les progrès considérables qui ont été réalisés au cours de la décennie qui sépare le présent symposium du précédent sur le même sujet. Les sujets abordés témoignent de l'acceptation généralisée du principe d'intégration. A l'évidence, la conception des charges externes peut désormais être considérée comme faisant partie intégrante de la conception globale de l'aéronef. La démonstration a été faite de certaines améliorations en ce qui concerne le développement et l'application de l'aérodynamique numérique à la conception des systèmes d'armes et il a été constaté que la puissance de calcul disponible demeure le facteur limitatif dans ce domaine.

L'importance des techniques expérimentales et semi-empiriques a été soulignée et il a été démontré que l'emploi combiné de la théorie et de l'expérimentation débouche sur une «boîte à outils» de conception et d'homologation de grande fiabilité. Le symposium a servi d'unique occasion pour l'annonce des derniers développements et a permis une appréciation de l'importance des contraintes imposées aux concepts de l'emport des armes en raison des considérations de signature radar.

Généralement la conférence a été très réussie, comme en témoigne le nombre élevé de participants et le caractère animé des discussions qui ont précédé la clôture. La conférence a pu identifier un certain nombre de domaines dans l'élaboration de futurs programmes de recherche et développement, qui méritent une attention particulière. Le symposium a également permis de nombreux échanges d'idées et d'expériences.

Contents

SESSION VI: DESIGN AND INTEGRATION OF AIRFRAME/STORES
THIS SESSION IS CLASSIFIED "CONFIDENTIAL"
Chairman: P.W. Sacher

† Contribution from FVP
* Published in the Classified Supplement CP-570(S)

Fluid Dynamics Panel

Recent Publications of the Fluid Dynamics Panel

AGARDOGRAPHS (AG)

Computational Aerodynamics Based on the Euler Equations
AGARD AG-325, September 1994

Scale Effects on Aircraft and Weapon Aerodynamics
AGARD AG-323, July 1994

Design and Testing of High-Performance Parachutes
AGARD AG-319, November 1991

Experimental Techniques in the Field of Low Density Aerodynamics
AGARD AG-318 (E), April 1991

Techniques expérimentales liées à l'aérodynamique à basse densité
AGARD AG-318 (FR), April 1990

A Survey of Measurements and Measuring Techniques in Rapidly Distorted Compressible Turbulent Boundary Layers
AGARD AG-315, May 1989

Reynolds Number Effects in Transonic Flows
AGARD AG-303, December 1988

REPORTS (R)

Parallel Computing in CFD
AGARD R-807, Special Course Notes, October 1995

Optimum Design Methods for Aerodynamics
AGARD R-803, Special Course Notes, November 1994

Missile Aerodynamics
AGARD R-804, Special Course Notes, May 1994

Progress in Transition Modelling
AGARD R-793, Special Course Notes, April 1994

Shock-Wave/Boundary-Layer Interactions in Supersonic and Hypersonic Flows
AGARD R-792, Special Course Notes, August 1993

Unstructured Grid Methods for Advection Dominated Flows
AGARD R-787, Special Course Notes, May 1992

Skin Friction Drag Reduction
AGARD R-786, Special Course Notes, March 1992

Engineering Methods in Aerodynamic Analysis and Design of Aircraft
AGARD R-783, Special Course Notes, January 1992

Aircraft Dynamics at High Angles of Attack: Experiments and Modelling
AGARD R-776, Special Course Notes, March 1991

ADVISORY REPORTS (AR)

Aerodynamics of 3-D Aircraft Afterbodies
AGARD AR-318, Report of WG17, September 1995

A Selection of Experimental Test Cases for the Validation of CFD Codes
AGARD AR-303, Vols. I and II, Report of WG-14, August 1994

Quality Assessment for Wind Tunnel Testing
AGARD AR-304, Report of WG-15, July 1994

Air Intakes of High Speed Vehicles
AGARD AR-270, Report of WG13, September 1991

Appraisal of the Suitability of Turbulence Models in Flow Calculations
AGARD AR-291, Technical Status Review, July 1991

Rotary-Balance Testing for Aircraft Dynamics
AGARD AR-265, Report of WG11, December 1990

Calculation of 3D Separated Turbulent Flows in Boundary Layer Limit
AGARD AR-255, Report of WG10, May 1990

Adaptive Wind Tunnel Walls: Technology and Applications
AGARD AR-269, Report of WG12, April 1990

CONFERENCE PROCEEDINGS (CP)

Aerodynamics and Aeroacoustics of Rotorcraft
AGARD CP-552, August 1995

Application of Direct and Large Eddy Simulation to Transition and Turbulence
AGARD CP-551, December 1994

Wall Interference, Support Interference and Flow Field Measurements
AGARD CP-535, July 1994

Computational and Experimental Assessment of Jets in Cross Flow
AGARD CP-534, November 1993

High-Lift System Aerodynamics
AGARD CP-515, September 1993

Theoretical and Experimental Methods in Hypersonic Flows
AGARD CP-514, April 1993

Aerodynamic Engine/Airframe Integration for High Performance Aircraft and Missiles
AGARD CP-498, September 1992

Effects of Adverse Weather on Aerodynamics
AGARD CP-496, December 1991

Manoeuvring Aerodynamics
AGARD CP-497, November 1991

Vortex Flow Aerodynamics
AGARD CP-494, July 1991

Missile Aerodynamics
AGARD CP-493, October 1990

Aerodynamics of Combat Aircraft Controls and of Ground Effects
AGARD CP-465, April 1990

Computational Methods for Aerodynamic Design (Inverse) and Optimization
AGARD CP-463, March 1990

Applications of Mesh Generation to Complex 3-D Configurations
AGARD CP-464, March 1990

Fluid Dynamics of Three-Dimensional Turbulent Shear Flows and Transition
AGARD CP-438, April 1989

Validation of Computational Fluid Dynamics
AGARD CP-437, December 1988

Aerodynamic Data Accuracy and Quality: Requirements and Capabilities in Wind Tunnel Testing
AGARD CP-429, July 1988

Aerodynamics of Hypersonic Lifting Vehicles
AGARD CP-428, November 1987

Aerodynamic and Related Hydrodynamic Studies Using Water Facilities
AGARD CP-413, June 1987

Applications of Computational Fluid Dynamics in Aeronautics
AGARD CP-412, November 1986

AERODYNAMICS OF STORE INTEGRATION AND SEPARATION

Technical Evaluation Report

Cliff Bore

Research & Innovation

41 Kelvedon Close, Kingston upon Thames, KT2 5LF, UK

1.0 SUMMARY

This TER sets the achievements of the symposium in the perspective of concepts of ***airforce value*** that were agreed by the AGARD Working Group which reported in 1977. This started the push towards designing stores and aircraft with full allowance for their strong mutual interactions: a process now known as ***integration***.

Reduction of installed store drag, and assessment of the effects of drag on ***range, warload,*** and ***vulnerability due to reduced agility*** were barely considered, so further action on ***drag and its effects*** should be worthwhile.

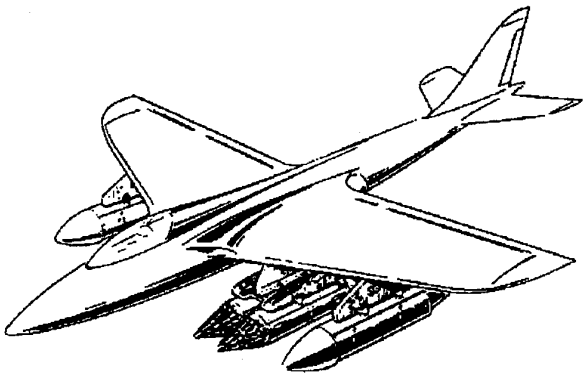

FIGURE 1 WHY SHOULD AERODYNAMIC CLEANLINESS STOP AT THE PYLON?

Broadly, the papers divided into two main groups: (1) the experienced and competent "engineering" groups who gave state-of-the-art reviews of their latest improvements in techniques, and (2) a range of approaches to using Computational Fluid Dynamics (CFD), stimulating searches for faster forms of space lattices and solvers to predict ***strong aerodynamic disturbances*** with less time and computer use. A small but informative third category (3) illuminated yet more complex store interactions for future fighters, such as computer-stability systems for unstable fighters, aircraft flexibility and buffet, ERUs, and low observability.

As result of integration techniques, catastrophic separations of stores have been eliminated. Good progress is being made in CFD, but good experiments remain their final test. "Engineers need plenty of tools in the toolbox, and good tools should not be discarded simply because colourful new tools are being developed."

2.0 INTRODUCTION

An important part of an evaluation report is to re-examine our basic objectives, so that we can see how progress measures up to the aims. Then we can consider how more progress yet may achieved. As it is 10 years since the previous symposium, let us recall the beginning of the Fluid Dynamics Panel' s adoption of this topic, about 21 years ago.

After finding that the aerodynamic drag of a typical array of under-wing stores, with excrescences everywhere, could far exceed the total drag of the clean aircraft, I pressed the question: ***"Why should aerodynamic cleanliness stop at the pylons?"***

At the time, the attitude was that aerodynamically dirty stores were standard things that a fighter was required to carry. The assumption was that stores are meant to be destroyed when released, so they had to be cheap (and by implication, nasty!). That did not stand up to examination,

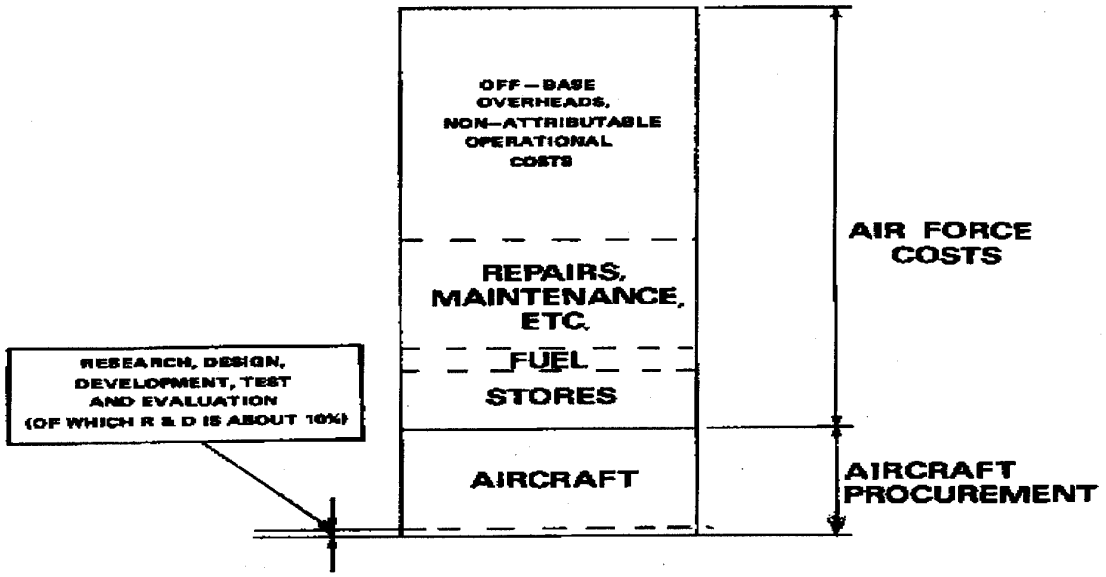

FIGURE 2 APPROXIMATE LIFE—CYCLE COSTS OF C.A.S AIRFORCE

at least for "dumb" stores, for in total they cost only roughly half as much as the aircraft, which in turn cost around 20% of the life-time cost of a typical airforce (figure 2), whereas excessively draggy stores could reduce the operational value of an airforce by far more than half (for those sorties), through their effects on range, area coverage, and extra vulnerability of the aircraft when loaded.

Figure 2 shows that the R&D costs for a typical airforce are around only 0.1% of the lifetime costs. So "economising" by eliminating R&D might save 0.1% of the lifetime costs, while of course ensuring that the airforce will be ineffective! ***A less value-effective way of "saving money" than cutting out the "thinking" is inconceivable.*** Similar arguments apply to other industrial situations, but of course with different proportions, and it depends on ***whose costs!***

That was only the start of the thinking, for in some cases, stores may fly so wildly when jettisoned that they may damage or destroy the aircraft. If stores could be so wildly disturbed when released, what sort of target-destroying probability did the airforce possess after all the expense, effort and risks of flying to the target?

Some 20 years ago, it was proposed that the Panel should study this in a co-ordinated manner, and a 7-nation Working Group, with co-operation of FMP and SMP, worked for two and a half years to produce Reference **A**. It reported on ***drag, flying qualities of the aircraft, airload prediction, store separation, structural integrity, performance and manoeuvrability.***

We concluded that by considering all such aspects of aircraft and store together, and standardisation within NATO, it was possible to more than double the overall value of NATO airforces.

2.1 Formulas for Airforce Value

In order to assess changes in airforce value, I constructed simple equations for lifetime airforce value. The basic equation states that the value is proportional to the **W**arload carried **(W)**, the **A**vailability of the aircraft in wartime **(A)**, and the target **K**illing effectiveness **(K)**. Thus:

Value (V)

$$V = W\ A\ C\ K \quad \ldots\ldots\ldots\ldots 1$$

where **C** is the constant of proportionality, assumed to be not less than the overall lifetime cost.

Further equations were devised (ref.A) to show the dependence of the factors **W, A, K** on performance parameters. Such equations show how the lifetime value of an airforce depends sensitively upon performance improvements, most of them strongly influenced by store installation improvements. From a national point of view, ***any group that improves one of these factors by 1% contributes that increase in a large lifetime value. Increasing value has far more leverage than reducing costs.***

The technological community tends to concentrate properly upon new technological areas according to the practical benefits sought, but decisions on less technical matters or policy, such as reducing excrescence drag on existing stores, tend to be actioned (or not!) by official admin departments. Unfortunately, sometimes they choose the path of ***reducing cost***, and thus fail to ***increase value,*** so some orders may be needed? For example, why shouldn't the most rugged excrescences on draggy stores be replaced by low-drag modifications, unless it can be demonstrated that the discounted cost will exceed a substantial fraction of the value benefit: say (25 %?).

3.0 HOW MUCH OF THE AIMS ADDRESSED?

The ***drag-reduction*** objective (in the context of improving range, area coverage, performance, and reducing vulnerability due to lower drag) was barely discussed, but related topics of ***drag prediction***, and ***aerodynamics of cavities*** intended to convey stores, were major topics.

The topics covered demonstrate that the principle of ***integration*** has been widely accepted, where the term is interpreted broadly, to mean ***considering the design of the stores as an integral part of the loaded aircraft.***

Requirements for store release are now much more stringent than when we started, for it is no longer enough for an airforce to conclude its flight trials happily merely because none of the releases damaged or destroyed aircraft (though that is enough for empty fuel tanks or rocket pods). It is now recognised that a ***high probability of hitting targets*** is essential. Indeed, experience such as in Libya, the Gulf War and the Balkans indicates that the requirements of accuracy need to be more stringent yet, for it is now necessary to have **a *low probability of missing targets,*** since killing innocent people nearby is counterproductive!

3.1 THEME OF THIS SYMPOSIUM

"The topic of airframe/store compatibility is of major importance to both the aircraft and weapon designer. The aerodynamics problems associated with the carriage of stores and the release from military aircraft are numerous and very complex, making this a most difficult task for today's aerodynamicist. The scene is ever changing with novel design concepts being researched and implemented. The aim of this symposium is to review the state-of-the-art in the prediction methodology and experimental techniques currently being developed and applied to the aerodynamics of store carriage and release, and to assess design concepts."

4.0 REVIEW OF PAPERS, Session by Session

4.1 Keynote Paper :

Deslandes gave a masterly review (1) of strategies for modelling aerodynamic intereferences. As the rigid- body dynamics of the store takes only 5% of the time, it is the aerodynamics that takes most effort. It is ***strong aerodynamic disturbances,*** such as shocks, vortices, jets and B.L. separations that cause most of the trouble, so any method that fails to model these will fail to head-off trouble, eventually. He divided the strategies into *pseudo unsteady, *unsteady.

The pseudo-unsteady strategy uses stored data on both aircraft flow-field and store, and allows for store motion by its effects on local crossflow incidence angles. This approach is economical of time and effort, but may sometimes miss details of the mutual interference. Two-sting survey methods in wind tunnels remain essential, and panel methods remain as useful tools for estimating flow-fields, though needing empirical knowledge of strong disturbances to be added-in.

The unsteady strategy represents the airflow more elaborately, - and with more cost! Now *(10 years after Carrol Dougherty reviewed Chimera at Athens)* the Chimera system of overlapping body-linked grids has become very popular. Euler methods can give useful and economical insights into compressible flow fields, while to compute viscous effects, Navier-Stokes solvers need to be used, with more substantial costs and time delays. With continuing development, it is expected that such solvers will cost less time and money.

4.2 Computational Fluid Dynamics (CFD)

Simpson (2) reviewed 10 years of CFD work for stores clearance at Wright Labs, Eglin. They concluded that CFD is not entirely accurate, but neither are wind-tunnel techniques, and a judicious mix of both can give good overall understanding. Impressive computations were shown, for quite complex store clearances.

Gillyboeuf (3) showed trials of new Chimera approaches. They concluded that for bodies in close contact, their "mixed" mehod looks promising. They intend to go on to a full Chimera scheme.

Jeune and Mansuy (4) reviewed the state of the art at Matra, including their engineering methods. They concluded that Chimera methods need to be less time-consuming and costly.

In discussion, it was remarked that Chimera is, in principle, well-suited to "catastrophic" store interactions. Computations need to be better for low-inertia stores, because they are disturbed much more.

Blaylock (5) reviewed DRA`s FAME method of using overlapping grids, showing some impressive-looking results from an Euler solver. They had not made comparisons with Chimera. They are developing a N-S solver.

In discussions, it was noted that although flow-solvers give impressive-looking colour contours, ***experimental comparisons are essential to validate computations.***

Sellars (6) presented a comparison of four Euler codes, tested on circular and square-with-rounded-corner section bodies up to 20 degrees. They found that the computed separations near the corners varied with grid size.

Discussion of the significance of the "artificial dissipation" term in the Euler solver argued that ***if this introduces some allowance for viscosity, surely it should be possible to work out an effective Reynolds number for the computations?***

Gulcat and Aslan (7) had made a promising start on N-S solvers (but for low Mach numbers), using techniques aimed at reducing computer memory needed.

4.3 Engineering Methods

Broadly, "engineering methods" piece together systematic experimental data, and flow-field surveys (wind tunnel or computed), to construct a wide range of aircraft/store configurations.

McDougall and Press (8) updated latest developments of the NUFA empirical program, which has been extended and validated over the years. It now allows for up to 5 sets of lifting surfaces, with incidences (variable along the missile length) up to 90 degrees, to M=5. It has been coupled into various trajectory suites.

Chen and Liu (9) used piecewise doublet singularity methods to model store releases, using a high-order panel method.

Experienced engineers felt that for incidences above 10 degrees, it would be essential to insert crossflow drags, and that it was unlikely that strong disturbances would be modelled reliably.

A Nielsen team (10) gave a competent review of their methods, emphasising the importance of strong disturbances. They allow for fin stall, and track vortices. Computation of shocks is not so rigorous, because of using panel methods for flowfields.

A Nielsen team (11) outlined the elaborate computational methods used to ensure safe release of the massive Pegasus air-launched space booster. They found that it was difficult to produce repeatable agreement between prediction and flight, but they were able to assure safe releases.

4.4 Experimental Techniques

Captive trajectory rigs are a well-established technique, but of course there are new facilities being established.

Lombardi and Johnston (12) showed 6-degrees-of- freedom tests, using a separate drive for each D.O.F. Although they distinguished between "position" and "velocity" modes, both modes were "quasi steady", for the moving mode took 10 minutes.

The ONERA team (13) had just tested their fine new facility at M=0.95 in the sonic tunnel. It has a large-scale system for moving a store on a simulated trajectory. As results from the S1 and S2 tunnels and flight test were similar, they are satisfied.

Bettridge and Sheard (14) described techniques for the ***Accelerated Model Rig***, using ***light model scaling.*** Their new semi-conductor strain-gauge balances, insensitive to temperature, look very promising for small store balances, and for cryogenic tunnels. They expect to have 5mm balances by the end of 1995. They also outlined the fine technology that went into their AMR facility, with miniature ERUs and actuators for free drops in the wind tunnel, tracked by 2,000 frames/s cine. Free drops tests have been checked against flight test, including the exceptionally sensitive case of a fuel tank collision. ***"Comparisons between tunnel and flight have been invariably favourable".***

Thain (15) described a bold new installation for the NRC, which features the Optotrack store-tracking system, using 2 cameras with CCD retinas, and IREDS target markers, on store and aircraft. This enables them to track the store relative to the aircraft despite flexibilities.

Piperni and Stokoe (16) had used a transonic small-perturbation (t.s.p.) program from the US Navy, to investigate store interferences. Although their comparisons with wind-tunnel tests produced "similar trends", they concluded that tunnel tests would still be necessary. In discussion, it was opined that this type of problem is mathematically ill-conditioned, and consequently unreliable.

Donaldson (17) described improvements in flight test techniques for store release trajectories, notably the VISTA sytem for tracking the store released in flight, by superimposing computer-generated images over the photographed real position. As this is very time consuming, a much faster process is being developed.

4.5 Cavity Aspects

Tracey and Richards (18) showed impressive results of N-S solutions for flows in rectangular cavities. They found that the 3D implicit code was needed for better agreement with experiment. Fast Fourier transforms of the frequency contents of oscillations agreed well with experiment. They intend to incorporate a higher-order turbulence model.

Zhang (19) showed analysis of unsteady supersonic flows over single and double cavities, which illuminated the the way that turbulent flows cause oscillating shock waves, and interact with downstream cavities.

Suhs (20) showed results of an implicit N-S method used for a fairly complex weapons bay with a store, validated against wind-tunnel tests on a well-instrumented model. An impressive video of the calculated vortices was shown. Good agreement was obtained between calculated and experimental sound pressure levels in the bay.

Ross showed experimental results (21) for various arrays of stores in cavities. They found that ***with shallow cavities, stores could experience strong "suck-in" forces.*** Angled rear-end walls made improvements to the recirculating flows in the cavities,- reducing noise levels by 6dB. They extended Rossiter`s correlation of sound pressure levels in cavities to length/depth ratio of 13.

This experimental investigation investigated a wider range of configurations than CFD could accomplish for given effort, and it stimulated questions on likely effects of open cavity doors, and effects of transverse frames (to mount stores) on recirculating flows.

Suhs gave a clear and wide-ranging historical perspective (22) on techniques for safe store release, and ballistic accuracy, including techniques such as free-drop, captive store trajectory, grid loads, flow fields, and CFD.

4.6 Airframe/ Store Integration

Allen and Hulme`s paper (23) illuminated complexities of interactions between store effects and the stability of aircraft control systems for unstable fighters. It indicated that flight control systems may have to be adjusted for different store arrays.

Yalcinel showed results (24) of calculations which traced the way that vortex elements shed into the wake during manoeuvres caused the wake to roll-up in highly convoluted forms.

As their computation was a vortex grid panel method, only attached flow was modelled, but it is known that some forms of aerodynamic unsteadiness are due to unsteady wakes rolling-up close to the aircraft, so this approach gives food for thought on wake-induced unsteadiness.

Meijer and Cunningham (25) deduced unsteady airloads on an aircraft by measuring the unsteady pressures on the stalling surfaces, and integrating these to find the unsteady forces as forced flutter *(and buffet?)*. They got reasonable agreements between calculations and test.

4.7 Design and Integration of Airframe/Stores

Moretti (BAe) gave a competent review (26) showing many practical and complicated problems of "store" release on real aircraft, including the notable example of ejection of a canopy and an ejector seat.

STARS is their computer assembly of many engineering methods (and Euler to model flow-fields) to feed out store trajectories. NUFA (8) can be coupled into this. It was shown that fuel sloshing (in jettisoned fuel tanks) can be important.

Dunkley (28) illuminated the magnitude and effects of the initial jolt from the apparently small bits of equipment known as Ejector Release Unit (ERU).

Nangia (29) discussed the effects of nearby vectored jets upon adjacent stores if jettisoned, showing that they may greatly affect the store trajectory.

Jechura (30) outlined computation of the unsteady flow-field under a B-1B wind-tunnel model, using Chimera with XAIR flow solver (Euler or N-S). This predicted surface pressures, and the order of magnitude of bay turbulence,- but for better results, the approaching boundary layer should no longer be assumed "thin" in the N-S computations.

The Dassault team described their development and use of an industrial store release computation (31). This is based upon fully automated unstructured triangular grids for each different store position (1 minute each grid), using an Euler solver. It is capable of modelling intake and exhaust flows. Impressive video of store trajectory calculations was shown, showing "reasonable" agreement with experiment. This was for a gentle trajectory, calculated for quasi-steady conditions. They aim to get calculations in a day. They said it is possible to take crossflow motion into account (though they had not yet done it), and they aim to homogenize grids, and use parallel computation.

Richardt showed impressive Euler trajectory calculations (32) of Apache release under realistic conditions. The code has corrections for crossflow drag in it (one must not, of course, confuse attitude with angle of attack). These showed that it was necessary to impose non- symmetric ERU impulse on this store in order to avoid a dangerous trajectory.

Sheard gave a clear presentation (33) of CFD for stores clearance, concentrating on "realism within days". Panel methods need empirical corrections for crossflow, as a collision on Buccaneer showed that panel methods were unrealistic without them. Engineers with plenty of physical insight can use consistent methods and get quick responses, but fast Euler and N-S are sought.

Howell gave a clear presentation (34) on store separation techniques for the F-22,- an aircraft with large arrays of both internal and external stores. An interesting observation was the effect s of oblique shocks (such as from the air intake) potentially deflecting a missile, unless it "punches through" the shock. Impressive results were shown of N-S calculations of a tumbling fuel tank. Free drops of a 600 gall fuel tank were done using heavy model scaling: a fallacious system! A specially written paper on model scaling (ref.B) has been sent.

Hatch gave a clear paper (35) illuminating considerations of store carriage for low "observability". He correctly posed the relative advantages and disadvantages of internal store carriage. One slide showed that a single iron bomb has an RCS signature an order of magnitude greater than a low-observable aircraft configuration: food for thought to those contemplating external carriage! On the other hand, big internal store bays may severely reduce combat performance for a given engine.

5.0 CONCLUDING DISCUSSIONS

In contrast with the previous symposium, this conference demonstrated that the principle of total aircraft/store integration has been widely accepted, and significant improvements in design capabilities (both experimental and theoretical) have been achieved. In particular, as a result of developments in integration techniques, catastrophic separations of stores have been eliminated. Much remains to be done, however.

It was generally agreed that experimental work remains essential: CFD developments will increase understanding, and reduce timescales and computer costs, but ***tests remain the final check on computations, no matter how impressive the colour videos of Euler computations look.***

"Engineers need plenty of tools in the toolbox, and well-tested tools should not be discarded simply because some colourful new tools are being developed".

On CFD techniques, structured grids seem more favoured than unstructured grids, though to this reviewer it seems likely that the ultimate discrimination will not be made by comparing Euler calculations, for ***it is the viscous effects sought by N-S solvers that require fine-mesh grids placed strategically to capture the high-shear layers where strong disturbances arise.***

Deslandes concluded that ***automated grid generation needs to be adopted generally, and that Chimera schemes are very promising for the potentially dangerous, and therefore more important cases, and these should be extendable to N-S solvers.***

6.0 REFERENCES

(A) C L Bore (Ed), **Drag and other aerodynamic effects of external stores. AGARD-AR-107, 1977**

(B) C L Bore, **Scaling rules for free-drop stores trajectories: light/heavy model rules revisited. Research & Innovation R&I-Aero-111, June 1995.**

Other references are numbered as in contents list.

LIST OF CONTENTS

realsitic conditions with the DASA store separation program SSP94.

33) S R Sheard, Aero. Technology, BAe Brough, UK. **The application of CFD methods for stores carriage and release.**

34) G A Howell, Lockheed Fort Worth, Texas, US. **Store separation test and analysis techniques employed on the F-22 program.**

35) T J Hatch, BAe Military Aircraft Division, Warton, UK.: **Carriage of external stores for low observability.**

Strategies for Modelling Aerodynamic Interference during Store Separation

Dr. R. Deslandes

Daimler-Benz Aerospace AG, Military Aircraft Division, LME12
D-81663 München, Germany

Summary

All contributions dealing with the modelling of aerodynamic interference of store separation can be catalogued according to their strategies. In the following it will be shown, that the great number of available solutions can be reduced to only two categories denominated here Pseudo-Unsteady and Unsteady Strategies.

Pseudo Unsteady Strategies are the most common solutions applied to industrial projects. There three powerful variants are identified as Decay Factorization, Flow Angularity and Iterative Techniques. This last subcategory provides the link between pseudo and real unsteady approaches, which are divided into two main groups of strategies, assigned to Global Solutions and Grid-Overlapping Techniques.

In addition to this catalogue, the common computational fluid dynamical tools of store separation are outlined respective to their physical relevance and their numerical complexity.

Finally an example based on consideration of three strategies, in use at Daimler-Benz Aerospace AG (DASA) will be demonstrated.

Objective

The analysis of the separation behaviour of a store represents one of the most outstanding task throughout all engineering efforts associated to the operational role equipment of a fighter aircraft. The demand for a perfect weapon performance in order to achieve a high degree of target accuracy, requires a predictable, repeatable, controllable and reliable separation behaviour. Pragmatically considered, this ambitious scope also requires a realistic physical understanding and accurate description of a dynamical event with a duration of hardly more than one second, as shown in fig. 1. Within this short period of time strong aerodynamic interactions may occur between the aircraft and the released or jettisoned store, depending on the flight conditions. In certain cases unfavourable release disturbances may cause some risks for collisions or may completely degrade the release accuracy of the weapon and end up with an operational loss.

Since more than 50 years, this task is treated extensively with all kinds of methodologies. Most of the early approaches were restricted to three degrees of freedom and formulated for two dimensional solutions only. These limitations were mainly imposed by the lack of powerful computing machines, able to solve the complex mathematic systems of partial differential equations associated to the task.

Nowadays we are facing to bundles of promising codes, operating with more or less different strategies. Therefore the scope of this contribution will be an attempt to illuminate these typical modelling strategies starting up with almost basical theories up to state of the art CFD-approaches without wasting efforts on cumbersome algebraics.

Design Drivers

Therefore let us consider the typical concept of such separation codes or programmes. As shown in fig. 2 the core of these software packages consists of two major engineering parts associated to the description of flight mechanics and aerodynamics. For one separation sequence, both tasks are computed consecutively within a time cycle in the magnitude of some milliseconds. Hereby, flight mechanics for store separation can be considered as a solved item. So in a standard code, the motion of the separating bodies is represented in all six degrees of freedom, whereby rotation is formulated in terms of quaternions [1], in order to conserve all the coupled non-linearities of the system.

In contrast to this, the aerodynamic part is still a prosperous field for engineering efforts. In general, the computer spends only 5% of its performance evaluating the flight mechanics and all other special effects such as an autopilot control, but shares approximately 95% uniquely for calculation of aerodynamics and interactions.
As soon as either a weapon, pod or tank starts to move relative to the carrier, aerodynamic loads become a dominant factor in their equations of motion. In general the leading parts for forces and moments can be assigned to following important contributions:

- basic aerodynamics of the store
- distortion of the local flow around the aircraft and other stores in terms of up-, side- and down-wash.
- reciprocal effects
- higher order flow phenomena such as compressibility, vortex systems, viscosity effects and interactions, thermodynamics of plume and engine flows.
- aircraft maneouvres during separation

Paper presented at the AGARD FDP Symposium on "Aerodynamics of Store Integration and Separation", held in Ankara, Turkey from 24-27 April 1995, and published in CP-570.

- store velocities and rates
- unsteadiness of all contributions and of additional terms such as shock reflections, engine operation, control surface deployements and deflections.

The first four categories above are associated to pure fluid dynamical effects, whereas the last three affect a-priori the time dependent boundary conditions varying along the trajectory.

The mathematical complexity of the aerodynamical approach is an important factor which not only determines the computing power requirement, but also the turn around time for one complete trajectory.

Assuming a typical workstation performance of 30 Mflops, one trajectory with a duration of one second real time, might be computed over a period from 2 minutes up to 2 days or even more elapsed time, depending on the strategy selected.

Fast strategies allow extensive work on multiparametrical studies of the separation process within the complete aircraft envelope, but request an higher amount in verification work. Therefore such strategies must be extensively supported by experimental work and also have to provide sufficient possibilities for the implementation of corrective upgrades.

Strategies involving complex CFD-solutions with a high level of confidence, are slow and expensive, but once qualified, request a minimum amount of experimental certification and validation. Especially considering an appropriate flight test programme, considerable cost savings can be performed by downsizing flight test hours and trials by selecting a more expensive simulation strategy. This fact justifies nowadays even the use of NS-codes as demonstrated in the work of [2].

A strategy should be adapted to the targets of each appropriate task. Only the fact, that an emergency jettison analysis for a heavy store ejection requires a less accurate modelling as an autopilot optimization study for a rail launched missile, may already provide two completely different strategy concepts.

Finally a strategy should be universally formulated in order to ensure a broad variety of applications.

It's portability depends on the followed methodology and on the validity or restrictions of the tools applied. If, for instance experimentally based, an application to other shapes or types of stores and aircraft is not possible without complementary measurements. Theoretical tools may be more flexible as far as adaption is concerned, but can be limited within their prediction range.

The best strategy would be to use an universal tool enabling the perfect modeling of all these contributions at the same time. However, without any exaggeration, such an approach will be hardly available within the next ten years.

Therefore it is necessary to develop suitable strategies according to the methodology available and well balanced against all the engineering aspects involved in the overall process called store separation.

Basic Strategies

Currently used modelling strategies can be classified into two basic categories:

- pseudo unsteady strategies
- unsteady strategies.

Pseudo unsteady strategies are using stored data for the representation of basic aerodynamics of the store as well as for the reproduction of interference effects. Such data libraries may be derived from the wind tunnel or may be preprocessed with an appropriate theoretical method. Interference and basic aerodynamics are considered as quasi-steady effects. However, taking into account the unsteady represented motions of store and aircraft, these preprocessed data can be linearly corrected by introducing time dependent orientational increments. Such strategies are very popular, because they enable the use of complex tools without providing excessive computing time for one trajectory.

Unsteady strategies request physically unsteady formulations and the use of time accurate solvers. In such a strategy the time behaviour of the fluid dynamic computation become the driving parameter, whereas the first category was governed by the flight mechanical motion. Unsteady solutions are useful in order to investigate time dependent phenomena especially in cases of heavy release disturbances, such as separation of internally carried stores, separation in presence of heavy shocks and in viscous formulations.

Pseudo Unsteady Strategies

Because of its universality this category of strategies is very popular in industrial applications. Three different variants can be distinguished here:

- Decay Factorization Schemes
- Flow Angularity Techiques
- Iterative Techniques.

Decay Factorization provides a very fast solution for modelling the aerodynamic interactions during a separation sequence. It requests two basic data sets which describe the carriage loads, when the store is attached to the aircraft and it's freeflight aerodynamics. Assigning the differences between both data to aerodynamic interactions, a decay-function is used in order to control the intensity of the interactions in dependency of the relative distance between aircraft and separating store. The most simplified function is a linear decay-function, whereby the decay distance must be approximated by experience or specified by read-across. This strongly pragmatic strategy is very cheap and common in use at early stages of industrial projects. For more accurate investigations it has to be refined by a complementary strategy. The preprocessed data are preferably taken from wind tunnel tests

if available, but can be adequately assessed with a reliable theoretical approach. In the last case, additive corrections for drag and viscous non-linearities at high angles of attack are strongly recommended.

A further Pseudo-Unsteady strategy is the so-called Flow Angularity Technique. The preprocessed data required here consist of basic aerodynamics of the store and a library with the distortions of the flow around the aircraft. Both can be taken from experiments or evaluated theoretically. The Flow Angularity Technique reproduces the interference as an additional contribution to the angle of attack of the separating store. This additive term is locally varying and therefore provides an angular distribution along the store. In this approach rotational terms, implemented by the aircraft or the store maneouvres, are expressed as additional contributions to the local flow distortions. Here the basic aerodynamic properties of the store are represented by sectionally decomposed coefficients of the forces and moments. Flow Angularity Techniques are quite similar to Influence Function Methods, where the total interference loads are built up by influence coefficients and flow angularities such as described in [13]. Within a Flow Angularity Technique, reciprocal interferences between store and aircraft are not implecitely represented. Therefore these results can considerably be improved in combination with a Decay Factorisation scheme, where such effects are sufficiently represented.

Iterative Techniques have been basically developed in combination with captive trajectory applications or double-action-sting systems. The basic conception consists in a stepwise treatment of the trajectory as sketched in fig. 3. An initial predictor-step leads to the first store position. In a second step, the loads for this fictive store position are computed and the trajetory is re-iterated in a corrector-step, by using the now known evolution of the loads between both positions. These iteration-cycles are repeated till the separation process is considered terminated. In the case that the trajectory loads are interpolated from an experimental loads-survey, we obtain a typical CTS-strategy. If the aerodynamic interferences are step-by-step evaluated by theoretical tools, two other basic versions of this strategy are obtained:

- Global Remeshing
- Grid Overlapping Techniques

Global Remeshing is common with Potential Theoretical Solutions of surface-oriented codes but also opens a wide field of applications for the much more accurate Euler and NS-solutions. This strategy is suitable for unstructured-grid-approaches such as [14], however, applications with structured monoblocks have also been realized in combination with Zonal Decomposition concepts, in which the representation of the aircraft geometry is confined to only those parts directly exposed to the separating store [10]. A typical remeshing situation is shown in fig. 4, where a crew-escape-module separation has been modelled by Zonal Decomposition. Such an approach requires considerable efforts in order to reorganize the structure of the meshes after each incremental step.

In contrast to this, Grid Overlapping Techniques offer a much more efficient solution of the aerodynamic task. Instead of remeshing one global mesh around store and aircraft, both geometries are modelled in two separate meshes. As shown in fig. 5 the aircraft governs the overall space-grid structure, which wraps completely around store and the anticipated trajectory corridor. After each trajectory step, the mesh of the store must be translated and rotated according to the relative motion with respect to the aircraft. Fig. 6 compares the meshsize as requested for freeflight aerodynamic computations with one reduced for an overlapping grid application. As far as the number of cells is concerned, a downsizing factor of 5 can be assumed between both meshes. In addition to the smaller meshsize, remeshing work is also not necessary. Therefore, a Grid Overlapping Technique allows much faster solutions as Global Remeshing.

Unsteady Strategies

Similar to the above, Unsteady Strategies can be subdivided into two categories assigned to:

- Global Solutions
- Dynamically Overlapping Grids

Although identical in the basic conception, the unsteady treatment of the physical parameter time provides here a fundamental difference.

In a pseudo-unsteady strategy, the time step is set in relation with typical flight mechanical events such as the velocity or rates of the store, or with the autopilot frequency. In general, such time-steps are in the order of a millisecond, and are externally specified.

In contrast to this, an unsteady strategy is always internally clocked according to stability conditions implemented by the numerical robustness of the solving algorithm. A typical flux splitting algorithm for Euler Equations provides for instance time steps about 10^{-5} seconds, using an implicit formulation. For a trajectory of one second elapsed time as described at the beginning, nearly 10^5 cycles have to be achieved. In this case Turn-around-time peaks up to several days in a Global Solution and about 20 hours for a "Chimera Code"-strategy using dynamically overlapping grids. Such "Chimera-Codes" therefore are becoming more and more popular as a standard industrial application, whereas Global Solutions are only recommended for solvers with a low level of mathematical complexity.

Useful Methodologies and Tools

As discussed above, most Pseudo-Unsteady Strategies can be supported by appropriate experiments as well as by theoretical approaches. Unsteady Strategies however, remain a unique field of application for computational fluid dynamics.

Reviewing some publications on store separation aerodynamics from the last two decades, a great preference for theoretical solutions can also be found. Nevertheless two useful experimental contributions shall be here outlined as essential strategical tools:

- installed load measurements for the determination of carriage and tip-off loads

- double-sting-systems for systematical flowfield surveys and interference load analysis in the vicinity of the carrier aircraft.

Typical test arrangements are shown in fig. 7 where installed and end-of-stroke missile loads are investigated and fig. 8 for a typical two sting system, here configured for an interference load investigation with a multiple carriage configuration.

In contrast to this, there is a broad variety of methodologies, theories and codes successfully operating since years in the store separation business. Some typical descriptions are referred to in [2] to [11].

In fig. 9 the most important applications have been systematically classified, according to topics such as numerical complexity, geometrical representativity, and predictive confidence with respect to the aerodynamic task of store separation.

The first three methods can be assigned to typical surface-oriented potential theoretical solutions whereas the last three ones represent typical space-oriented solutions.

The numbers in the CPU-column indicates how much computing time is needed for the evaluation of one snapshot, expressed in multiple of the fastest solution. This weighting factor can also be considered as representative value for the required main memory dimension of the respective application.

In Singularity Techniques, which are the most fundamental applications of the potential theory, aircraft and store geometries must be idealized to regular bodies. As shown in fig. 10, a three dimensional problem must be decomposed into characteristic parts representing body/wing thickness and lifting surfaces.

Planar and Higher Order panel geometries are much more realistic. Examples for these typical applications are shown in fig. 11 and 12. The level of confidence of these three methods strongly depends on the experience and skill of the operator. Therefore it is strongly recommended to consider experimental verification steps in such applications, which allow to tune or refine all especially treated boundary conditions.

Transonic Small Pertubation methods provide an interim step between the fully linearized potential theory and the highly nonlinear Euler and NS-solutions. The representation of propagating disturbances between two bodies is here superior to the surface oriented discontinuity effects in Panel Methods, but also smoothed out by the linearization.

Depending on the availability of powerful mesh generators, Euler Solutions can provide a very good 3D modelling capability. Such results are not much dependent on the skill or experience of a potential user and provide a high level of accuracy. Euler solutions require very fast processors and preferably such ones which enable either vectorizing or parallel processing. Inspite of rather expensive computing costs, their popularity especially for store separation application is considerably increasing, due to the high level of confidence they provide. Fig. 13 shows a fighter aircraft surface topology used at DASA in order to generate a H^3-type mesh with approximately $3 \cdot 10^5$ cells.

In contrast to this, NS-Solutions require much more refinements as far as cell sizes are concerned. For a comparable aircraft geometry as shown in fig. 13, more than 10^6 cells would be necessary at a minimum, in order to provide space areas with NS-quality. Inspite of their very good predictive properties, and the completeness of their formulation, NS-solutions are actually not very common in store separation work.

This fact hopefully will change after some more years of progresses to be performed in the field of computing speed and turbulence modelling.

Applied Strategies

In order to visualize the universality of the above classifications, a typical industrial application achieved at Daimler Benz Aerospace AG (DASA) is outlined in the following.

This example deals with an investigation of multiparametrical aerodynamic interferences during store separation. The selected configuration is shown in fig. 14, and consists of a GE/IDS-TORNADO with two cruise missiles in two different operational modes. The left missile is committed to launch and has already an opened intake and a running engine, whereas the right one is still asleep and remains on the aircraft in the carriage position.

The correct representation of such complex flow properties within a unique mathematical formulation is only feasible at the highest level of complexity. Therefore, an implicit flux-splitting Euler Solver was selected and linked into a grid overlapping scheme. On top of this, a strategy based on a combination of Decay Factorization and Flow Angularity Techniques served as predictor-step for positioning the stores into the flowfield of the aircraft. The above combination results into a typical iterative technique, as previously described and classified in the group of Pseudo-Unsteady Strategies.

The objectives of this complex application were focussed on three different topics. First of all, installed loads were generated for the missile, taking into account the running engine, i.e. intake flow and jet flow properties in the environment of the underfuselage configuration. The second target was to refine the decay-funtion respective to the nontrivial interference situation with a second store on-board. Finally some unsteady effects occuring during the separatiion sequence had to be validated for a nontrivial case where damping terms, control surfaces deflections and asymmetrical aircraft manoeuvre effects at a high transonic speed in sealevel were involved.

The grid topologies are shown in fig. 15 for a fictive twin-carriage position. The finite volume dimensions in the subgrids are much finer than in the aircraft mesh. 20000 cells where used for the aircraft, whereas each store is represented by a monoblock with 38 000 finite volumes. Using a Global Remeshing Strategy for the same case would have required more than 10^6 finite volumes, and an unaccaptable computing performance.

Using the grids shown in fig.15, each corrector step could be achieved within 4 hours, whereby the resulting trajectory already converged after the first two predictor/corrector cycles. The final result is shown in fig. 16. After launch the missile is stabilized into a horizontal cruise attitude, whereby the bank and roll-rate of the aircraft are completely levelled out. The total physical elapsed time for the event shown in fig. 16 is about 0.9 seconds.

Fig. 17 shows the pressure distribution plotted as isobar-fields over the surfaces of the aircraft and the stores installed and separating. Red spots indicate high pressures and blue ones low pressurized zones. The third missile position at the bottom of fig. 17 is already outside of the interference field of the carriage configuration. The decay-function was linearized between installed position on the two first corrector steps.

Fig. 18 shows the plume of the missile at the end of the first corrector step. The red zone indicates here temperatures of approximately 250° C. The plume doesn't affect the aircraft surfaces and can be considered as non-critical.

Finally fig. 19 and fig. 20 are showing the characteristics of interactions occuring at the first two positions, again expressed in terms of isobar fields. In contrast to fig. 17, an additional plane has now been considered, which allows a better judgement of the propagation of the interactions in the flow fields.

In the present case, the aerodynamic release disturbances were balanced by an active autopilot, and therefore the effect of release disturbance remains low. This is the reason why the iterative strategy was so well conditioned. In other cases, where autopilot activity is suppressed and especially in such cases where the store attains high angles of attack and rates, more than 6 corrector steps are necessary to satisfy convergency.

Concluding Remarks

Summarizing the above, the essential message of this contribution consists in the proposed identification catalogue for common store separation strategies.

It shall also provide ideas how to shape a new version according to a special problem or to tune and refine an already available strategy.

As far as future trends are concerned, Pseudo-Unsteady Strategies will remain the dominant group of standard applications, whereas Unsteady Strategies combined with Euler Solutions on Overlapping Grids will be favorized for validation of standard applications and for non-trivial separation cases.

References

[1] T.E. Surber

On the use of Quaternions to Describe the Angular Orientation of Space Vehicles

Journal of Aerospace Sciences Vol. 28 No 1, January 1961.

[2] Joseph L. Steger

Chimera Simulation of Viscous and Vortical Flows about Aircraft

IBM CFD Short courses Monterey California April 1991

[3] W. Lorentz Meyer

Drei- und Sechskomponentenmessungen an einem Behältermodell mit und ohne Flügelattrappe im Transsonik Kanal der AVA

69A07/1969

[4] Fernandes F.D.

Theoretical Prediction of Interference Loading on Aircraft-Stores
Part I - Subsonic Speeds

NASA-CR-112065-1 (1972)

[5] Goodwin F.K./Nielsen J.N./Dillenius M.F.E.

A Method for Predicting Three-Degree-of-Freedom-Store Separation Trajectories at Speeds Up to the Critical Speed

AFFDL-TR-71-81 (1974)

[6] R. Deslandes

Theoretische Bestimmung der Trajektorien abgehender Flugkörper von Kampfflugzeugen

MBB/UFE/1361/1978

[7] A. Cenko

PAN AIR Applications to Complex Configurations AIAA-33-0007/Reno 1983

[8] C.D.S. Clarkson

Prediction of Store Carriage/Release Behaviour using CFD (or HOM)

ISBN 0903409631/Bath UK 1990

[9] J. Steger; F.C. Dougherty; J.A. Benek

A Flexible Grid Embedding Technique with Application to the Euler Equations

AIAA 83-1944/1984

[10] R. Deslandes

Zonal Decomposition, an Advanced Concept for Euler Codes to Predict Carriage Loads on Non-Trivial External Store Configurations

MBB/LKE121-S-Pub/215/1985

[11] T.L. Donegan and J.H. Fox

Analysis of Store Trajectories from Tactical Aircraft Proceeding of the 8th JOCG Aircraft Stores Compatibility Symposium 1990

[12] L. Fornasier

HISSS - A Higher Order Panel Method for Subsonic and Supersonic Attached Flow about Arbitrary Configurations

Third GAMM Seminar Kiel, January 1987

[13] A. Cenko, J. Waskiewicz

Recent Improvements in Prediction Techniques for Supersonic Weapon Separation

Journal of Aircraft Vol. 20, No. 8 / August 1983

[14] S. Barbero

Store Release in Heavily Disturbed Aircraft Flowfield, a Case for Accurate Euler Solvers

Proceeding of: Recent Development and Application in CFD Royel Aircraft Establishment / Bristol 1993

[15] H. Richardt

Evaluation of the Apache Separation Behaviour under Realistic Conditions with the DASA Store Separation Program (SSP 94)

76th FDP Symposium on Aerodynamics of Store Integration and Separation, Ankara 1995

[16] R. Deslandes

A Grid Overlapping Technique with Smart Monoblocks for Unsteady, Time Accurate Euler Solutions, Applied to Store Separation Problems.

32nd AIAA Aerospace Sciences Meeting, Reno 1994

Figures

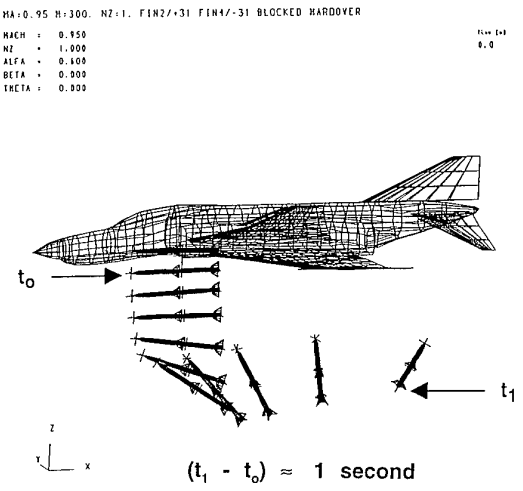

Fig. 1 Duration of a Separation Sequence

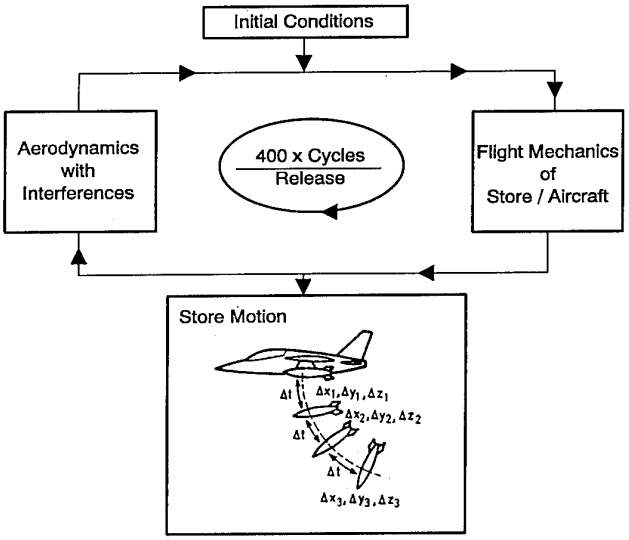

Fig. 2 Code Conception

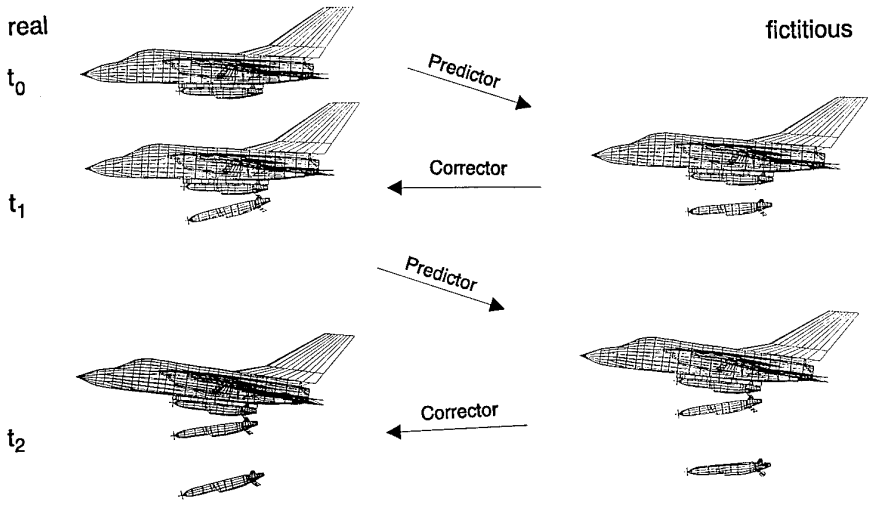

Fig. 3 Iterative Strategy Concept

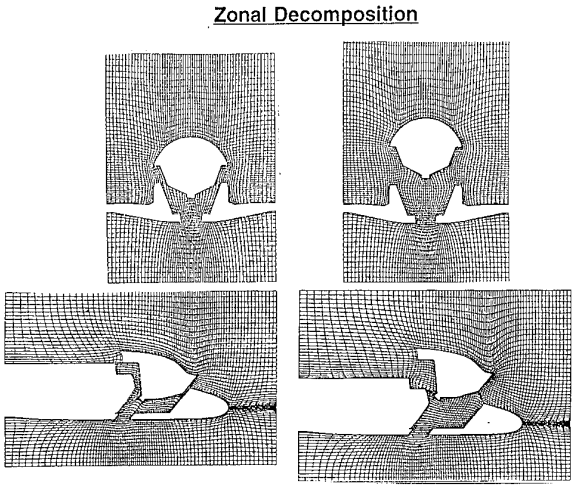

Fig. 4 Iterative Global Remeshing

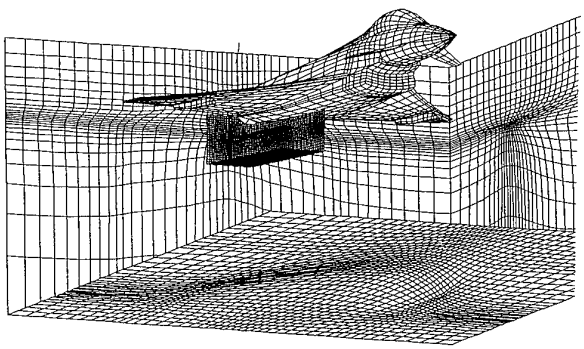

Fig. 5 Iterative Grid Overlapping

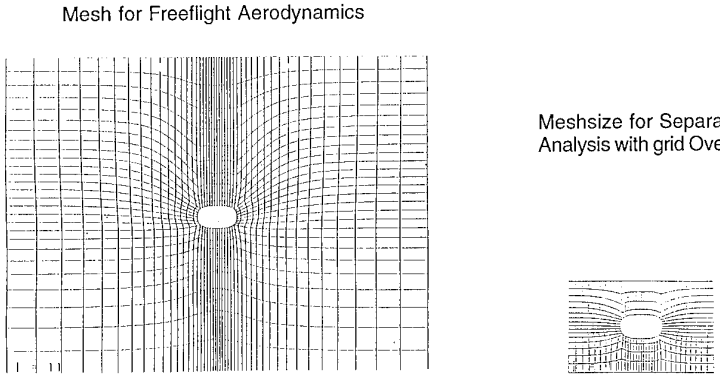

Fig. 6 Downsizing for Grid Overlapping

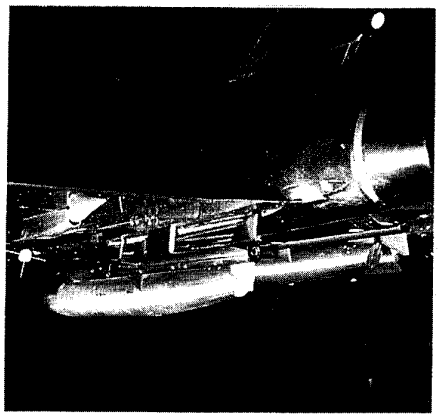

Fig. 7 Installed / End-of-Stroke Measurements

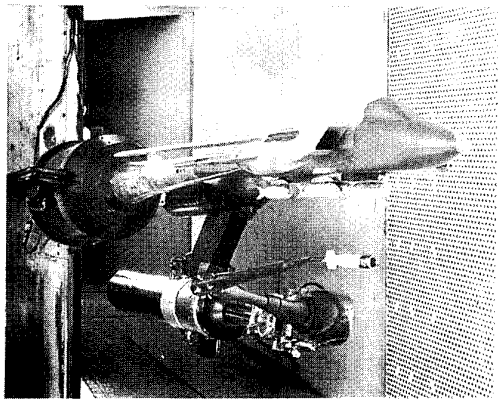

Fig. 8 Typical Multiple Sting System

Method/Theory	CPU	model geometry	basic aerodynamics	Distortions	Reciprocal	Shocks	Vortex	Viscosity
Singularity Techniques (Lifting line/Lifting surface	1	simplified 3D Resol.	needs upgrade	qualitative	weak	special treatment	special singul.	ad on correction
Planar Panel Methods	10^2	smoothed 3D Resol.	needs upgrade	acceptable	weak	restricted to < 1	special treatment	add on correction
Higher Order Panel Formulations	10^3	smoothed 3D Resol.	needs upgrade	acceptable	weak	linearized	special treatment	add on correction
Transonic Small Pertubation Methods	10^4	smoothed 3D Resol.	upgrade recommended	linearized	linearized	weak	special treatment	add on correction
Euler Solutions	10^5	3D Resol.	good	good	good	good	good	add on correction
NS-Solutions	$x{\cdot}10^6$	full 3D Resol.	good	good	good	good	good	included

Fig. 9 Theoretical Tools

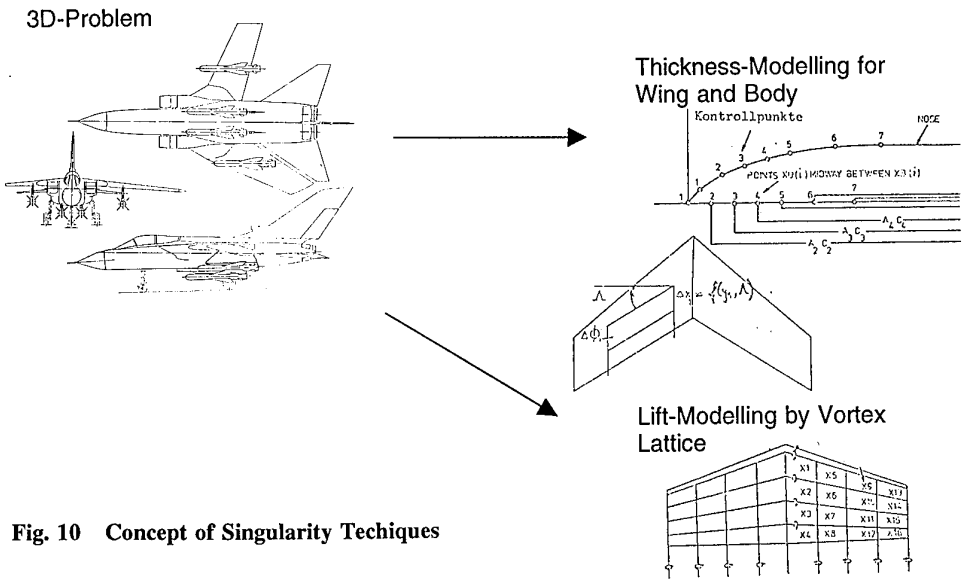

Fig. 10 Concept of Singularity Techiques

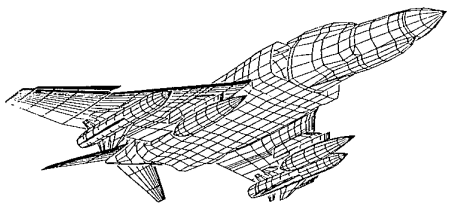

Fig. 11 Resolution of a Planar Panel Method

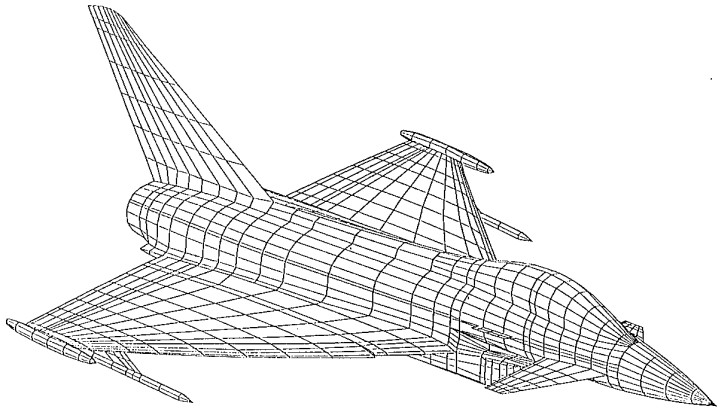

Fig. 12 Higher Order Panel-Geometry

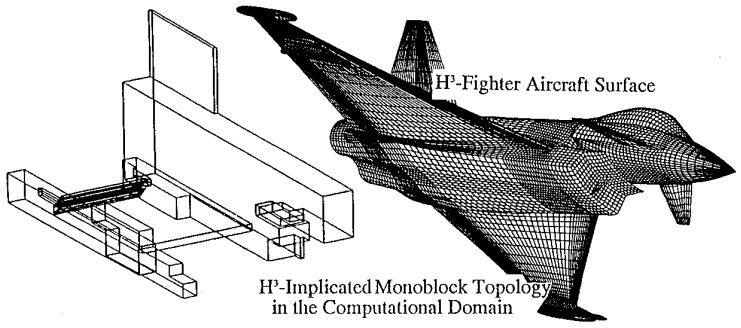

Fig. 13 Monoblocked Surface for a H^3-Euler Mesh

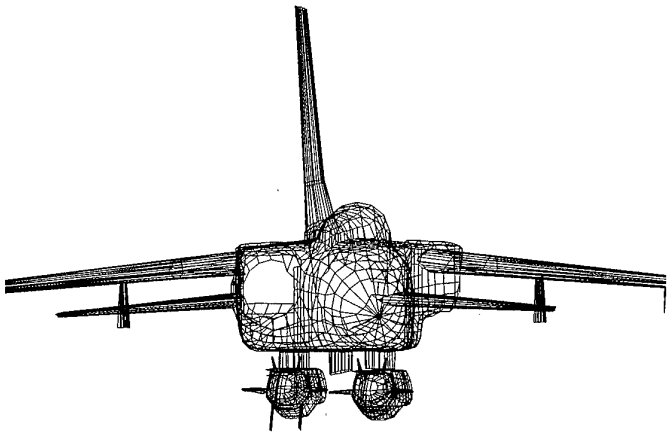

Fig. 14 Demo-Configuration: TORNADO with 2 Cruise Missiles

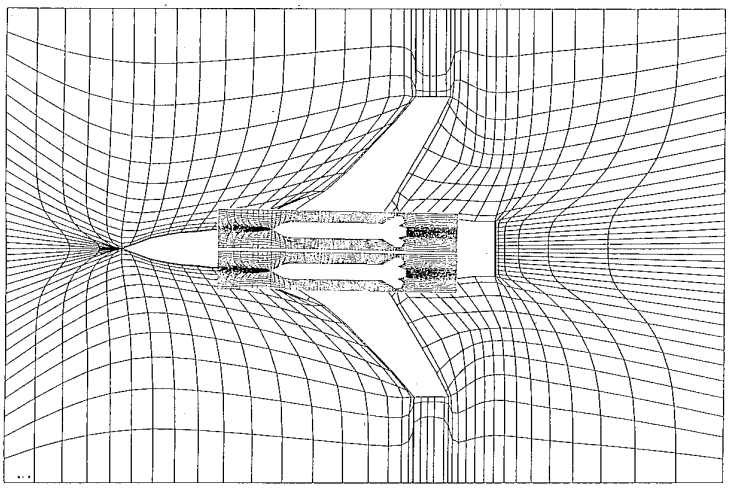

Fig. 15 TORNADO Grid Topology with Two Overlapping Missile-Grids

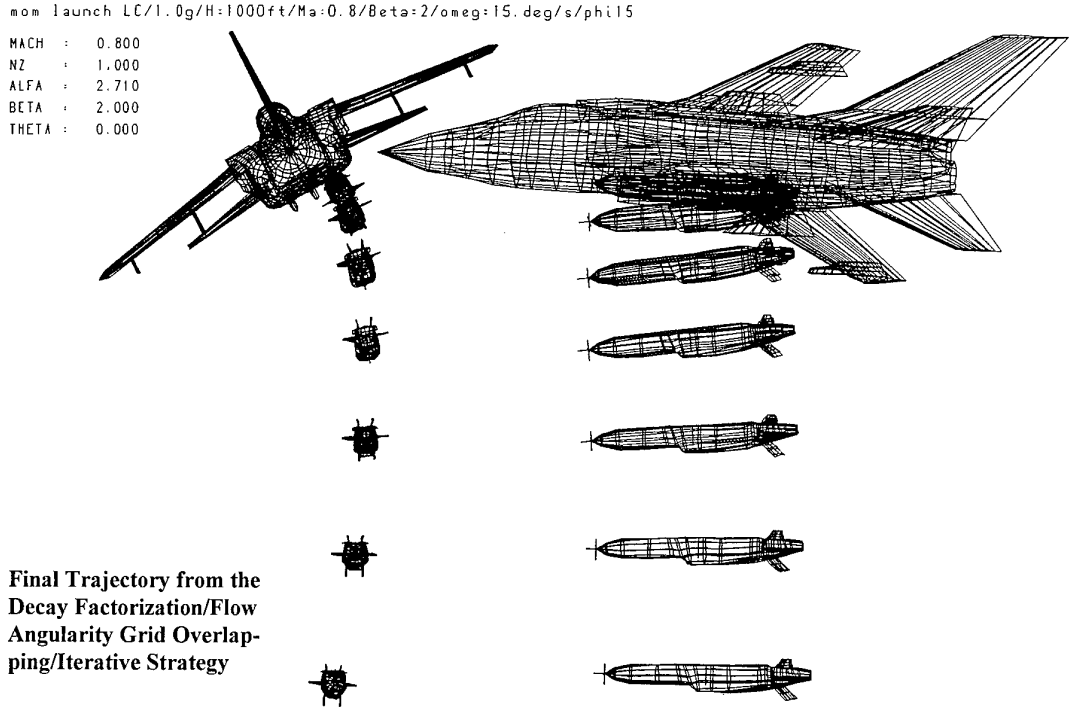

Fig. 16 Final Trajectory from the Decay Factorization/Flow Angularity Grid Overlapping/Iterative Strategy

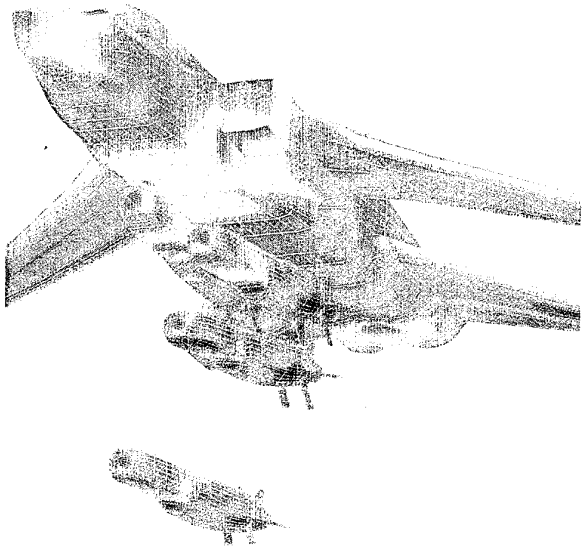

Fig. 17 Euler based Loads ($-C_p$) for the Corrector Steps

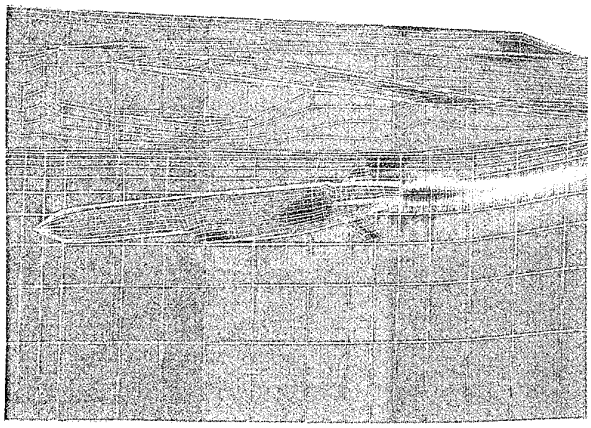

Fig. 18 Plume/Aircraft Interaction in Terms of Isotherms

Fig. 19 Flowfield Isobars View from Starboard

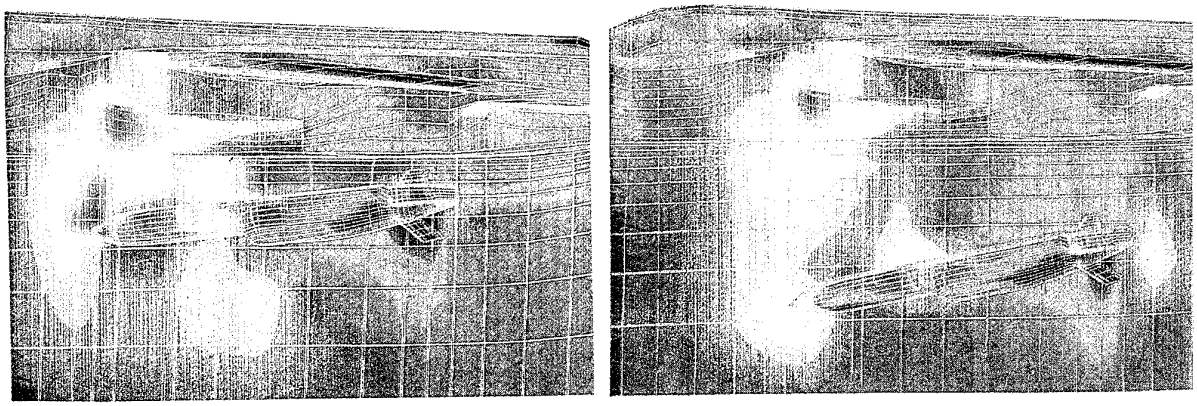

Fig. 20 Flowfield Isobars View from Port

PRACTICAL USE OF COMPUTATIONAL FLUID DYNAMICS IN STORES CLEARANCES

L. Bruce Simpson
Weapon Flight Mechanics Division
Wright Laboratory, Armament Directorate
101 West Eglin Boulevard
Eglin AFB FL 32542-6810
USA

SUMMARY

A description in the use of Computional Fluid Dynamics (CFD) for Stores clearance analysis is provided. CFD provides an accurate assessment of both steady and unsteady aerodynamics needed for stores clearance analysis. CFD is used for store carriage loads and separation analysis. Results are shown for both types of analysis and conclusions are drawn regarding the future trend of CFD for stores clearance.

1.0 INTRODUCTION

Computational Fluid Dynamics (CFD) has evolved into a powerful analysis tool for the prediction of aerodynamics for weapons carriage and release from modern aircraft. Weapons are currently carried and deployed almost exclusively in the transonic flow regime. Transonic flows (with embedded shocks) are intrinsically nonlinear in nature and therefore are the most difficult to predict. Historically, stores clearance analysis has relied almost exclusively on wind tunnel test data for aerodynamic predictions (Ref. 1). Data which is very expensive and time consuming to obtain and is not without its own set of short comings. For example, the weapon separation event is a time dependent event requiring the relative motion between multiple bodies and unsteady transonic aerodynamics. Due to testing limitations wind tunnels simulate the weapon separation event in a quasi-steady mode. That is the store aerodynamic loading is measured, the forces and moments are applied to a 6-DOF simulation to predict the next position of the store and new set of aerodynamic forces and moments are measured. The system is considered quasi-steady since the angle-of-attack of the store is adjusted to partially account for the vertical velocity of the store. CFD has the benefit of being able to accurately simulate the entire time dependent problem including the unsteady transonic aerodynamics.

CFD provides a method for determining the interference aerodynamics between aircraft and stores. Due to the highly non-linear aspects of the aerodynamics and the fact that aerodynamics is a critical aspect of stores clearance analysis (Fig. 1), CFD has become a critical store clearance tool. Definition of the interference aerodynamics and the surrounding flowfield is of extreme importance.

Computational Fluid Dynamics provides many advantages over other prediction methods and over wind tunnel testing. CFD with current numerical algorithms such as Total Variations Diminishing (TVD) are quite capable of accurately modeling nonlinear flows. They are capable of modeling the viscous effects for weapon separation and provide a reasonable estimate for aerodynamics up to moderate angles-of-attack ($\leq$ 10 degs). CFD also provides the user with a wealth of information regarding the flow field surrounding the aircraft/weapon combination. Data which is very useful to the designer as well as the flight clearance analysis engineer. For example, with current flow visualization techniques one might observe an otherwise unnoticed potential problem such as a shock impingement on a critical component of the store or aircraft. A problem which could go completely unobserved during a wind tunnel test only to cause problems during the flight test portion of the flight clearance process. However, for every advantage there are similar disadvantages. An example is once wind tunnel testing is underway it is very easy to collect force and moment store loads data for many different flight conditions. Large matrixes of Mach, altitude, AOA, Side-slip angle are obtained without a great increase in time or cost. This is not true for CFD analysis. While CFD provides a wealth of information about the local flow field each new data point of the matrix (Mach, altitude, AOA, and Side-slip angle) require a new CFD solution. Therefore, to complete a similar test matrix would be very expensive and time consuming. For these reasons CFD has become a very important tool for store clearances analysis but has not and is not expected to become a replacement for wind tunnel and flight testing.

Paper presented at the AGARD FDP Symposium on "Aerodynamics of Store Integration and Separation", held in Ankara, Turkey from 24-27 April 1995, and published in CP-570.

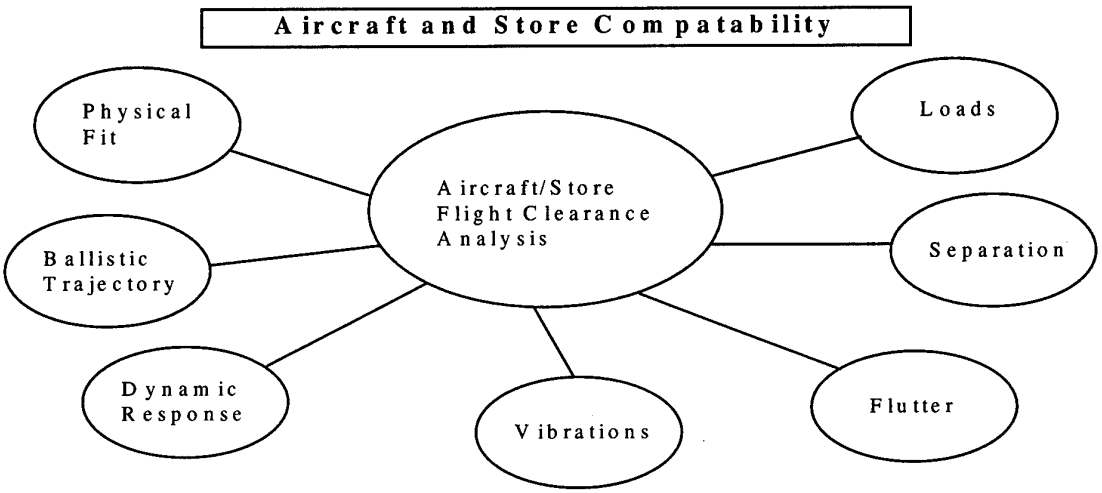

Figure 1. Aerodynamic Needs for Store Clearance Analysis

The development of CFD as a software tool is only a portion of the total store clearance solution. Without the significant advances of computer processor capabilities for both Cray type supercomputers and very powerful graphic workstations, CFD would still be only a distant hope for the current stores clearance analyst.

2.0 CFD TECHNIQUES

2.1 Grid Generation. Grid generation for the complex configurations of aircraft and multiple stores presents significant and time consuming problems. Two seemingly quite different techniques for discretizing the flowfield for complex geometrics have been developed. They are referred to as structured and unstructured grids.

Unstructured grids are composed of triangles in 2-D and tetrahedron in 3-D and have no preferred coordinate directions in the grid structure. Structured grids are made up of rectangles in 2-D and quadrilaterals in 3-D with a preferred coordinate direction in the grid structure. Very efficient unstructured grid generation codes have been developed but due to the slower development for unstructured grid flow solvers in compressible aerodynamics, these techniques have not readily found their way into the stores clearance arena. A set of papers addressing the pros and cons for structured and unstructured grids for store separation analysis is included in Refs. 3-8.

Structured grids have become the current technique of choice for stores clearance analysis. A domain decomposition technique (Ref. 9) referred to as Chimera is often used by stores clearance engineers at Arnold Engineering Development Center. The Chimera scheme allows for grids to be developed surrounding each individual component of the configuration independently. For example, a simple grid surrounding a store is independent of another simple grid surrounding the wing (Fig. 2). The two grids are then placed in the proper location relative to one another with the store grid being entirely embedded within the wing grid. Linkages are determined to provide intergrid communication during flow solutions. This scheme provides not only very efficient techniques for simplifying grid generation, but also provides a unique capability for relative motion between the store grid and the wing grid without requiring grid stretching or regeneration.

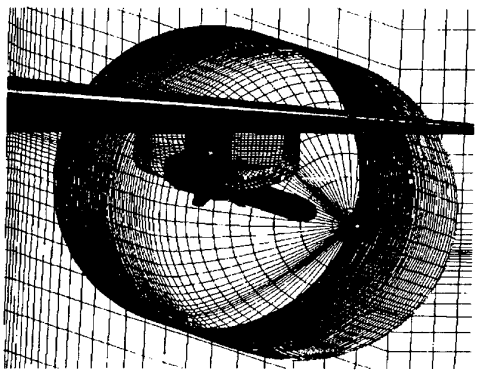

Figure 2. Wing-pylon-finned store overlap grids.

Another domain decomposition technique referred to as blocked grids also allows for the configuration to be subdivided and grids placed in subdomain regions. However, blocked grids require point and preferability slope continuity at block interfaces (Fig. 3). Blocked grids do not allow for the easy manipulation of relative motions between grids but do, because of the contiguous nature of the subregions, allow for very efficient and accurate flow solutions across blocked boundaries.

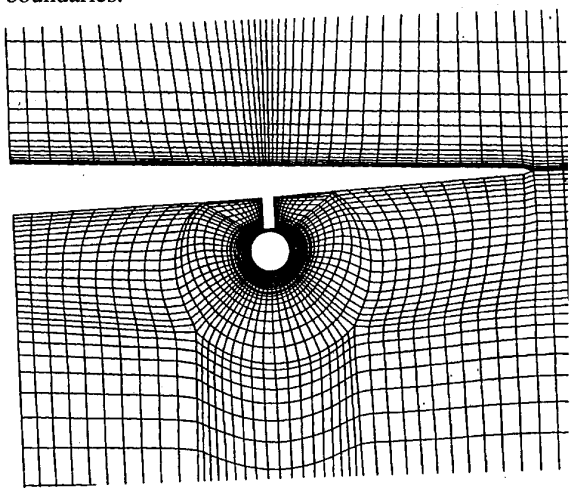

Figure 3. Blocked Wing/Pylon Store Grid System.

Perhaps the best possible solution for stores clearance analysis is a combination of blocked and overlapped grids. Thus taking advantage of both techniques' advantages and minimizing the disadvantage. This combination of techniques has recently been applied to stores clearance analysis at Eglin AFB. The remainder of this paper will discuss this method and its uses for stores clearance activities by USAF. Blocked grids are used to provide efficient and accurate flow solutions for a finned store (Fig. 4). Note the blocked grid structure between the store fins. This entire blocked grid is then embedded inside a set of grids; one surrounding the pylon and another surrounding the wing. This technique provides several advantages: (1) Reduces the overlapped grid points, thereby reducing the severity of grid-to-grid boundary communications, (2) Provides for an excellent method to allow relative motion between the store and the wing/pylon combination, (3) Enables the clearance engineer to build a library of grid files that allow for different aircraft/pylon/ weapon loadouts to be built up very quickly and easily.

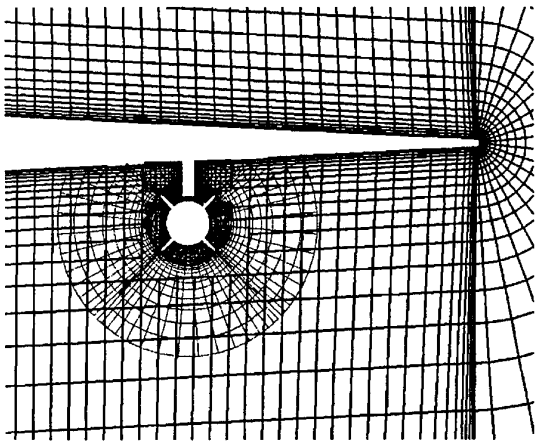

Figure 4. Wing/Pylon Grid System with Finned Store Embedded.

2.2 Flow Solver. While many flow solver algorithms have been developed and used over the years for store clearance analysis, the basic framework for the solver has remained the same for the past 7-8 years. The solvers are based on an implicit, finite volume, upwind scheme based on Roe's approximate Riemann Solver (Ref. 10). The basic formulation is based on obtaining the first-order portion of the flux from Roe's Riemann Solver. The higher-order contributions are based on Osher and Chakravarthy (Ref. 11). The algorithm has been documented by Whitfield et al. in Ref. 12. This algorithm is described in such a manner to be applied to the Euler Eqs. This is not considered a severe restriction since a large portion of the store clearance work is, by necessity, at low to moderate angles-of-attack and is therefore by its very nature, not a viscous dominated flow. However, for those instances when viscous effects are important, (i.e., high angle-of-attack or weapons bay carriage/separation) a Navier-Stokes solver has been developed (Ref. 13 and 14).

2.3 Stores Clearance Code. A CFD code for predicting compressible aerodynamics for stores carriage and separation analysis has been developed by Belk (Ref.15). The code referred to as BEGGER code is based on the use of combinations of blocked and overlapped grids and contains a flow solution algorithm based on Roe's Reimann Solver. The code was designed with the stores clearance analyst in mind. Inputs from the user are minimized for a complex configuration such as an F-15, and an AGM-130 weapon. The code automatically determines all intergrid connectivity and regions of one overlapped grid which is inside a solid body of another grid.

These inputs can, in other overlapped grid codes, require thousands of lines of input to correctly annotate all necessary intergrid communications. BEGGER requires, as inputs, only: (1) Good Grids, (2) Physical Boundary Conditions (i.e., no slip), (3) Flow Solver Parameters (i.e., CFL number, Mach number, angle-of-attack, etc.), and (4) Specification of Required Outputs. Without this capability, it is not practical for the stores clearance analyst to use CFD as a tool. Prior to this development, the CFD portion for clearance analysis was performed by a CFD specialist and the solution then passed to the clearance analyst.

3.0 RESULTS

The practical use of CFD for stores clearance analysis is presented below in several examples.

3.1 F-16/Finned Store Verification (Ref. 16).
Verification of the accuracy of aerodynamic data provided by CFD is of obvious concern since flight safety issues are involved. This example was a test case to present the accuracy of CFD to predict the flow field surrounding a configuration, surface pressured distribution, and the force and moment coefficients acting on the bodies. The configuration consisted of an F-16 with 370-gallon fuel tanks on stations 4 and 6 and a generic finned store (2000 lb class weapon) on stations 3 or 7. The configuration is shown in Fig. 5. The configuration was tested in the 4-T wind tunnel at Arnold Engineering and Development Center (AEDC) for the store on station 3 in a carriage only mode. The finned store was a metric body with pressure taps along the body and over the fins. Pressure measurements were obtained every 10 degrees circumferentially around the body and at 8 different span locations on the fins. (Fig. 6.)
The CFD solutions used 23 overlapped grids and approximately 3.1 million grid points to model the configuration. Wind tunnel data and CFD calculations were compared for a typical carriage condition for the F-16 and a 2000 lb class weapon at Mach 0.95 and 4 degrees angle-of-attack. Fig. 7 shows the surface pressure contour maps for the finned store. The surface contours are color coded to match the CFD solutions. The pressure port colors are coded to match the wind tunnel data. Figs. 8 and 9 show a good comparison with CFD pressure distributions and wind tunnel data, with the exception of the Euler calculations over predicting the expansions as one would expect near the flow separation regions around fin trailing edges and store boattail regions. However, Figs. 10 and 11 show fair agreement between the CFD solutions and wind tunnel integrated force and moment data. The data shows CFD easily predicting forces to within engineering requirements but with slightly larger than hoped for errors in predicting the aerodynamic moments. In either case, most CFD solutions are within acceptable error bounds for comparisons wind tunnel data.

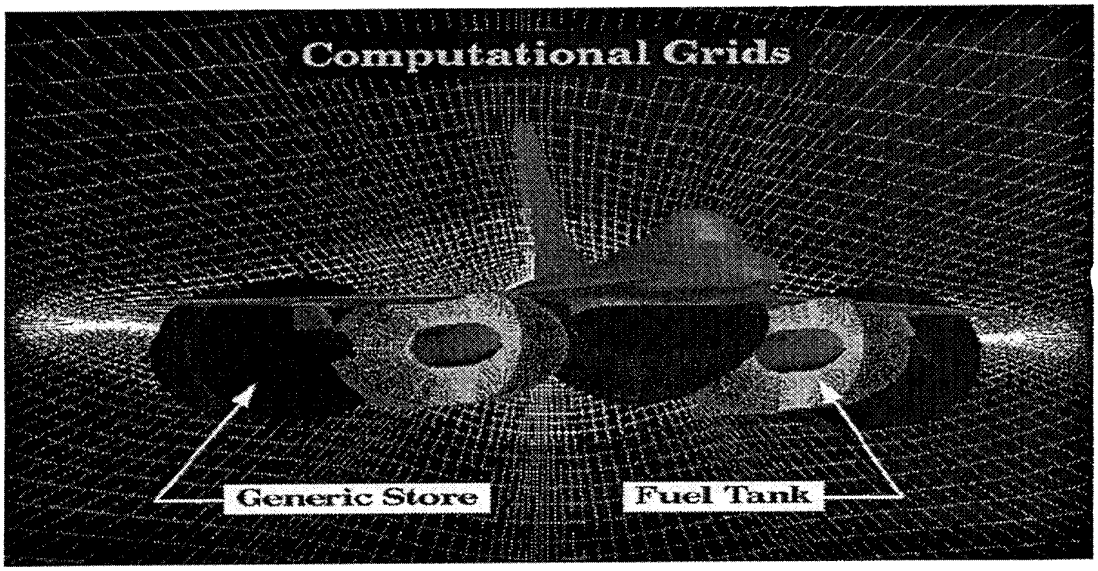

Figure 5. Embedded Grid System for F-16.

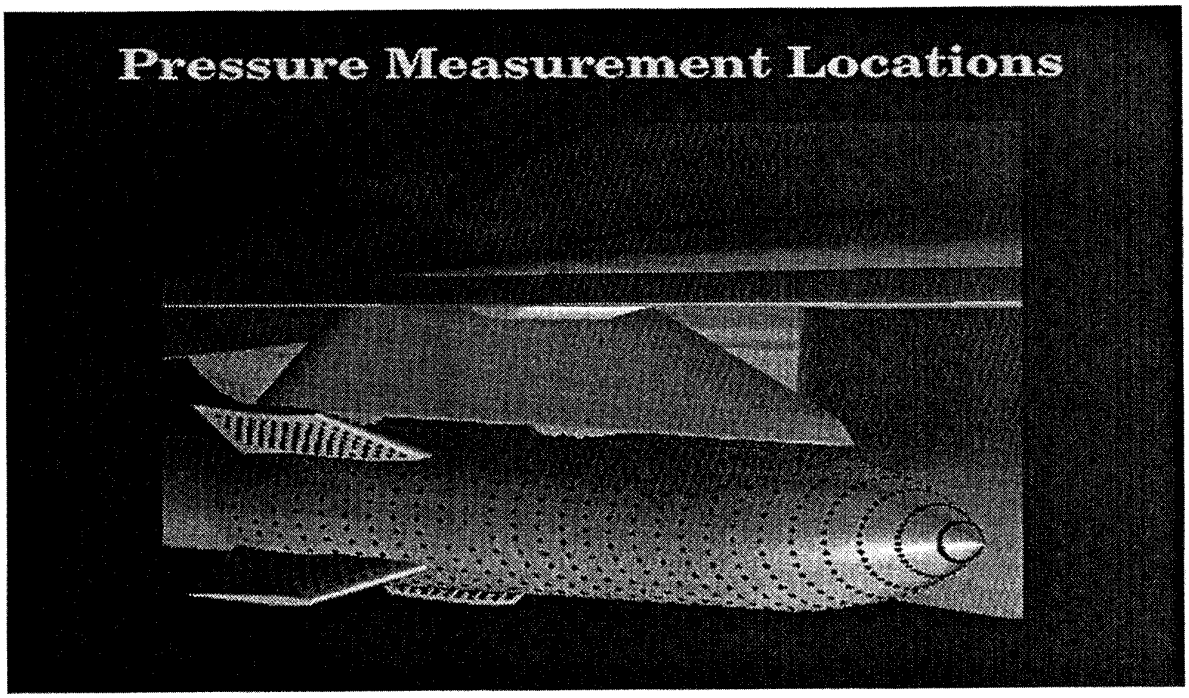

Figure 6. Pressure Measurement Locations for Wind Tunnel Test.

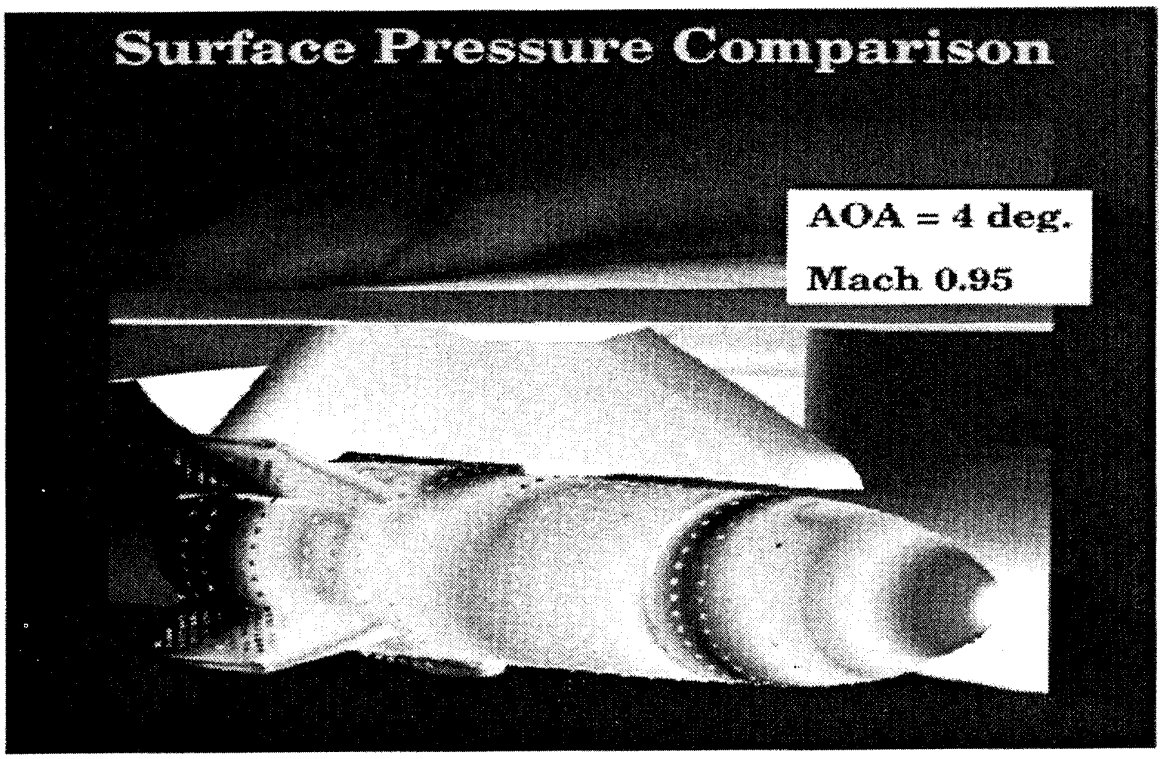

Figure 7. Surface Pressure Contours for Store.

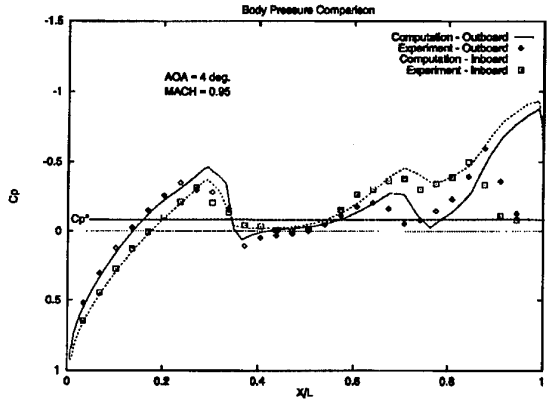

Figure 8. Surface Pressure Comparisons (Inboard and Outboard)

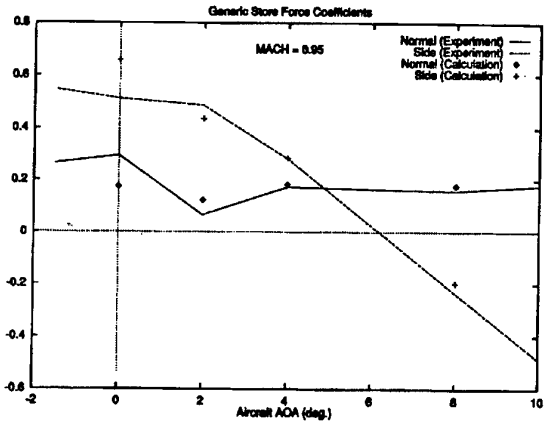

Figure 10. Store Force Coefficients

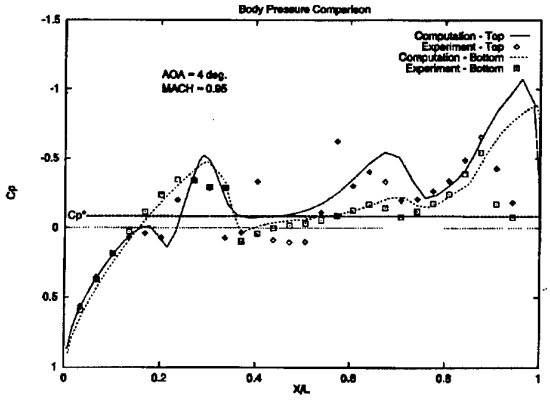

Figure 9. Surface Pressure Comparisons (Top and Bottom)

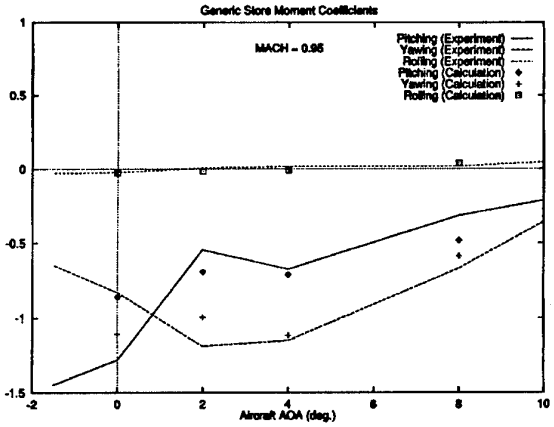

Figure 11. Store Moment Coefficients

3.2 Pressure Port Analysis. (Ref. 17).

One of the great benefits of CFD as applied to stores clearance is to provide data on incremental changes to a configuration. Often times, the use of CFD to predict the actual aerodynamic coefficients such as lift coefficient or pitching moment are suspect due to questions about grid sizes, turbulence models, simplifications to a configuration, and many other possible questions. However, CFD has been shown to be extremely capable of predicting increments to aerodynamic coefficients. This capability has been demonstrated several times including analyzing wing attachment modifications for a missile, removal of a spacer between a bomb unit and a solid rocket motor, and a review of the effects of a battery firing device (BFD) pack and a lanyard guide (Ref. 17) to the localized flow and the pressure measured at a nearby pressurt port. See Fig. 12. The canard controlled munition was modeled using a four-block C-O grid scheme, with one block between each canard. The (BFD) was modeled with an O-H grid embedded in the overall four-block grid for the nose section of the munition. And the lanyard guide was modeled using a C-H grid embedded in the four-block grid. The battery firing device grid is shown in Fig. 12. The use of the BEGGER flow solver to easily allow the insertion of a small device such as the BFD into a previously built grid system was a major contribution to the success of the analysis. The inclusion of the BFD and lanyard grid required only a few man-hours. Building a new grid for the munition and the BFD/lanyard combination would have required many man-weeks. The BEGGER flowsolver was used to develop 33 separate solutions, varying Mach numbers, angle-of-attack, roll angle, and fin deflection angles. The entire analysis was completed in less than three weeks. These results could not have been obtained without the user friendly environment of the BEGGER flow solver.

3.3 F-16 and ECM Pod Carriage Analysis.

An example of a carriage configuration for the F-16 is shown in Fig. 13. This configuration consisted of an F-16 with 370 gal fuel tank on station 4, an ECM pod on station 3, and an AIM-9 missile on station 2. The wing-tips for this case were clean. The flight clearance questions centered around the ECM pod and questions about its own structural integrity to withstand the rigors of high-g flight on the F-16 wing. This particular areo shell was not designed for carriage on the F-16. The loads engineer, in order to provide a proper flight clearance analysis, needed for some information regarding the aerodynamic load distribution along the pod body. This load distribution was then used as inputs to store loads code to compute the total loads (aerodynamic and inertial) distribution which was then used to provide a critical path structural analysis. The structural analysis searched for insufficient safety margins in the stress levels computed in the body. The CFD code was used to provide the aerodynamic pressure distribution for the configuration at several Mach numbers and angles-of-attack. The surface pressure contour map in Fig. 13. Shows the pressure contours for Mach 0.95 and zero

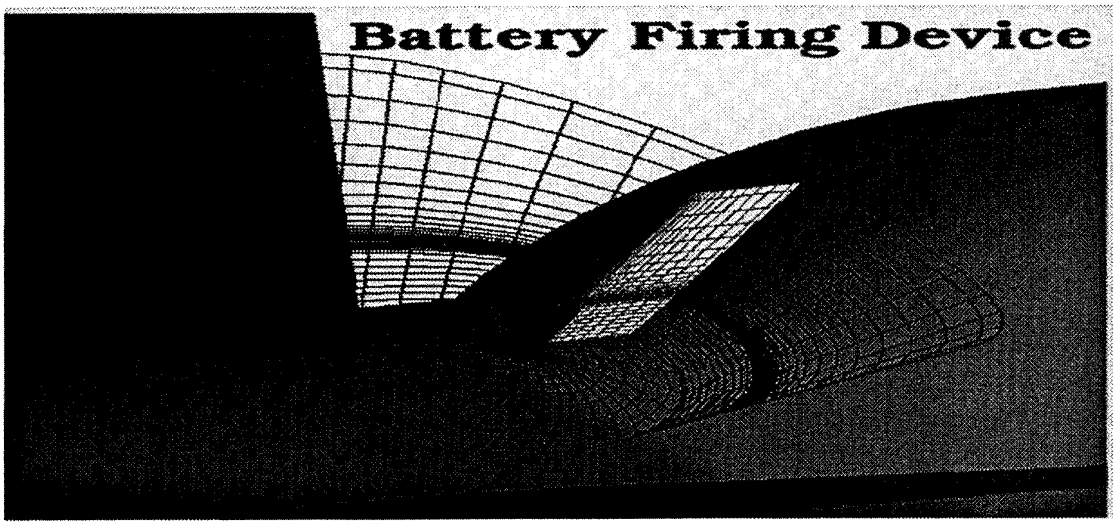

Figure 12. Battery Firing Device Grid Embedded in Blocked Grid.

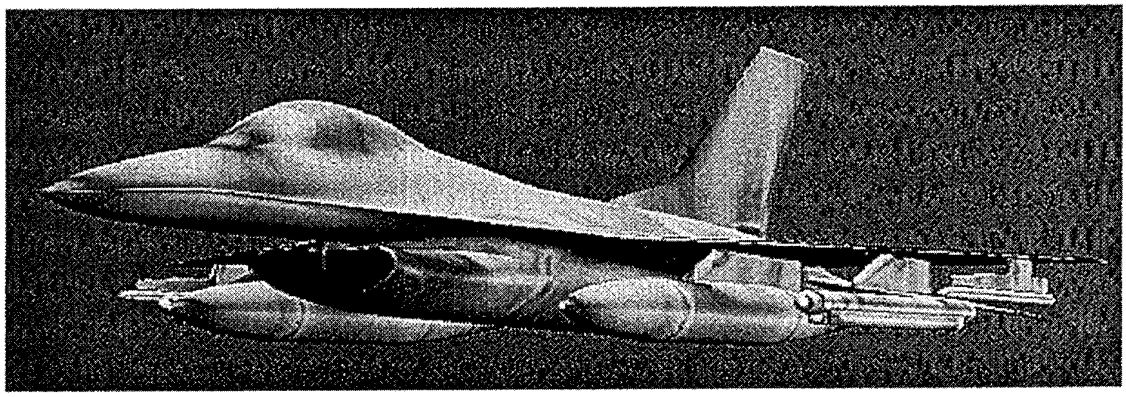

Figure 13. F-16/ECM POD Pressure Contours

degree angle-of-attack. This configuration was cleared for flight without any additional wind tunnel test data.

3.4 F-15 and AGM-130 Store Separation.

Often times the most time consuming and expensive store clearance analysis to be performed is that for store separation. The development of overlapped grid technology and the dramatic improvement of high-speed computers in the past few years now make CFD a practical tool for store separation. Figure 14 describes the general steps involved in a CFD based store separation analysis (Ref.18). After the overlapped grid interconnectivity is determined (Step 1), the flow solver is turned on to obtain steady-state solution for the carriage conditions (Step 2). The flow solver is integrated with a 6-DOF simulation code to model store dynamics. The aerodynamic forces and moments computed for store carriage are used along with ejector forces and moments as inputs to the 6-DOF code to compute a new store location (Step 3).

The CFD code updates its time by $t = t_0 + ndt$ where n is the step counter and determines new intergrid connectivity (Step 4). The flow solver then updates the flow solution including all the unsteady aerodynamic terms (Step 5). If the target location or step count number has been reached, the solution then stops or it returns to Step 3 and a new store location is computed by the 6-DOF and the process repeats.

The process has recently been applied to the F-15 and AGM-130 separation analysis shown in Fig. 15. This configuration was wind tunnel tested and analyzed prior to flight test. The CFD solutions were obtained post flight test to determine if CFD could capture the rather severe rolling and pitching motion observed in flight test. The results of the analysis show that CFD does, indeed, capture the majority of these severe motions upon separation. This case was used as an example to demonstrate the robustness of CFD for store separation analysis.

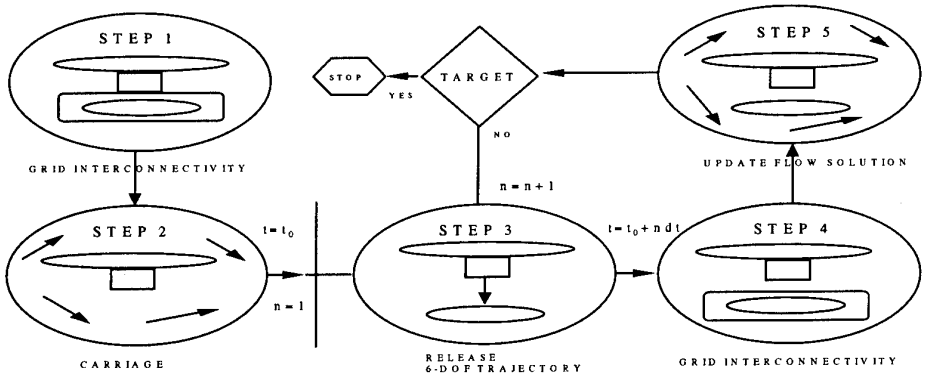

Figure 14. Store Separation Process (Ref. 18)

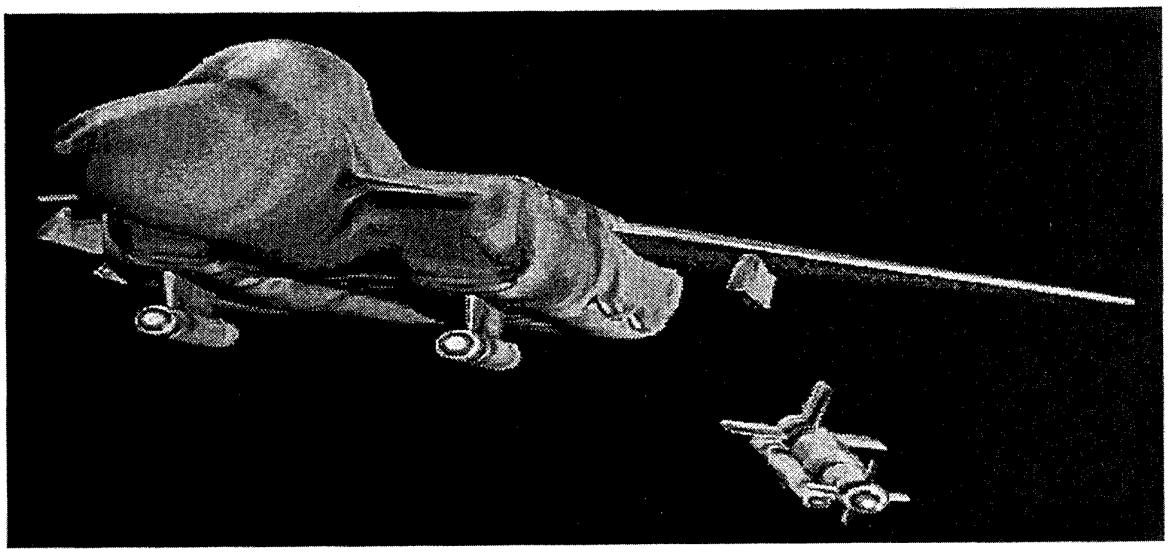

Figure 15. F-15 and AGM-130 Separation.

4.0 CONCLUSIONS

CFD has been developing over the past decade until it is now a major player in stores clearance analysis. It is used on a daily basis for analyzing incremental changes to know configurations. It is also used regularly for carriage analysis where it provides to the loads engineer, the installed distributed aerodynamics for the configuration. This data is then used to obtain total loads and then provide structural analysis of critical paths for store or aircraft structural integrity. Finally, CFD is becoming a common player in the store separation problems. Here, CFD codes are coupled with 6-DOF simulations for store dynamics and the combination provides unsteady separation analysis. Unsteady in the terms of including all the unsteady aerodynamics of the problem. In the future, as computing power continues to increase and flow solvers improve, CFD will become the major provider of unsteady aerodynamics for flutter and dynamic response analysis. Indeed, CFD will provide the aerodynamics for all the phases of store clearance analysis (Fig. 1) and provide that data based on first principles and in a timely and affordable manner.

5.0 ACKNOWLEDGEMENTS

The author wishes to express his sincere thanks to all the contributing scientists for their help and support and to Ms. Cherry Filer for the preparation of this paper.

6.0 REFERENCES

1. Korn, Stephen C.; Mathews, Charles B.; and Pinney, Charles W., "Store Separation", AGARD Conference Proceedings No. CP270,1982.

2. Meakin, R., "Computations of the Unsteady Flow About A Generic Wing/Pylon/Finned Store Configuration", AIAA paper - 92-4568, Aug 92.

3. Lijewski, L.and Suhs, N., "Chimera-Eagle Store Separation", AIAA paper - 92-4569, Aug 92.

4. Jordan, J., "Computational Investigation of Predicted Store Loads in Mutual Interference Flowfields", AIAA paper - 92-4570, Aug 92.

5. Baysal, O. and Newman, J. III, "Transonic Solutions of A Wing/Pylon/Finned Store Using Hybrid Domain Decomposition", AIAA paper - 92-4571, Aug 92.

6. Parikh, P.; Pirzaheh, S.; and Frink, N., "Unstructured Grid Solutions to Wing/Pylon/Store Configurations Using VGRID3D/USM3D", AIAA paper - 92-4572, Aug 92.

7. Tu, Y.; Noack, R.; and Bishop, D., "Three-Dimensional Euler Solutions on Wing-Pylon-Store Configuration With Unstructured Tetrahedrel Meshes", AIAA paper - 92-4574, Aug 92.

8. Kennon, S.; Meyering, J.; Berry, C.; and Oden, J;, "Geometry-Based Delaunay Tetrahedralization and Mesh Movement Strategies for Multibody CFD", AIAA paper - 92-4575, Aug 92.

9. Benek, J.A.; Steger, J.L.; and Dougherty, F.C., "A Flexible Grid Embedding Technique With Applications To The Euler Equations", AIAA paper - 83-1944, Jun 83.

10. Roe, P.L., "Approximate Riemann Solvers, Parameter Vector, and Difference Schemes", Journal of Computational Physics, Vol. 43, 1981, pp. 357-372.

11. Osher, S. and Chakravarthy, S.R., "Very High Order Accurate TVD Schemes", ICASE Report No. 84-44, Sep 84.

12. Whitfield, D.L., Janus, J.M., and Simpson, L.B., "Implicit Finite Volume High Resolution Wave-Split Scheme for Solving the Unsteady Three-Dimensional Euler and Navier-Stokes Equations on Stationary or Dynamic Grids", Engineering and Industrial Research Station Report MSSU-EIRS-ASE-88-2, Mississippi State university, Mississippi State MS, Feb 88.

13. Gatlin, B., "An Implicit, Upwind Method for Obtaining Symbiotic Solutions to the Thin-Layer Navier-Stokes Equations", Ph.D. Dissertation, Mississippi State University, Aug 87.

14. Simpson, L.B. and Whitfield, D.L., "Flux-Difference Split Algorithm for Unsteady Thin-Layer Navier-Stokes Solutions", AIAA Journal, Vol. 30,No. 4, Apr 92, pp. 914-922.

15. Belk, Dave M., "The Role of Overset Grids in the Development of the General Purpose CFD Code", To be presented at Workshop on Surface Modeling, Grid Generation, and Related Issues in CFD Solutions, May 95.

16. Riner, William C.; Jolly, Bruce a.; Prewitt, Nathan C.; and Brock, Jim, "Verification of Transonic Euler Solutions of an F-16 Aircraft with Stores Using a Chimera Grid Scheme", presented at AIAA 2nd Overset Composite Grid and Solution Technology Symposium, Oct 94.

17. Jolly, Bruce A.; Brock, Jim; and Coleman, Larry, "GBU-28 Pressure Port Analysis", presented at AIAA 2nd Overset Composite Grid and Solution Technology Symposium, Oct 94.

18. Lijewski, L.E. and Suhs, N.E., "Time-Accurate Computational Fluid Dynamics Approach to Transonic Store Separation Trajectory Prediction", AIAA Journal of Aircraft, Vol. 31, No. 4, pp.886-891.

UNE NOUVELLE MÉTHODE CHIMÈRE POUR LE CALCUL DE MISSILES EN POSITION D'EMPORT

J.-P. Gillybœuf *
AEROSPATIALE-MISSILES
Annexe des Gâtines
91370 Verrières-le-Buisson
France

RÉSUMÉ

Le principe des méthodes d'incidence locale utilisées à AEROSPATIALE-MISSILES pour les études de largage est présenté. Leurs limites sont mises en évidence. Pour cette raison, elles sont complétées par des simulations numériques de l'écoulement autour de la configuration avion-missile qui reposent sur la résolution des équations d'Euler. La principale difficulté d'un calcul de ce genre est de créer les maillages. La technique chimère est utilisée pour la contourner. Le principe de la première méthode qui fut développée, appelée Méthode Chimère par Recouvrement (MCR), est rappelé. Elle s'inspire très largement de celle présentée par Benek et al.. Elle a été utilisée pour simuler le largage d'un missile ASMP sous un Mirage 2000. Cependant, des problèmes apparaissent lorsque le missile est en position d'emport ou très proche de l'avion. C'est pourquoi une nouvelle méthode, appelée Méthode Chimère par Troncature (MCT), est développée. Son principe est exposé, avec le souci de préciser ce qui la distingue de la MCR. Elle a également des inconvénients. Une troisième méthode, appelée Méthode Chimère Mixte (MCM), est créée. Elle mélange la MCR et la MCT, de façon à ne conserver de chacune de ces méthodes que ses avantages. La MCT est validée sur un cas 2D. L'étude d'une configuration 3D, qui peut représenter un missile en position d'emport, montre que la MCM donne des résultats bien meilleurs que ceux obtenus avec la MCR.

1. INTRODUCTION

1.1. Rappels sur les techniques de calcul simples utilisées pour les études de largage

Parmi les méthodes utilisées à AEROSPATIALE-MISSILES pour prédire les phénomènes aérodynamiques qui apparaissent au cours du largage d'un missile sous un avion de combat, seules celles qui reposent sur une approche quasi-stationnaire et ne sont pas purement expérimentales sont présentées dans cet article. Leur principe est le suivant : à chaque position du missile, on détermine par un calcul stationnaire les efforts qu'il subit et on en déduit son déplacement.

On peut ne calculer les efforts que pour les positions du missile rencontrées au cours de la trajectoire (approche trajectographique). On peut également les déterminer pour un certain nombre de positions qui couvrent l'espace que balaie le missile sous l'avion ; les efforts que le missile subit pendant sa trajectoire sont alors obtenus par interpolation dans cette base de données (approche grille). Par rapport à l'approche trajectographique, l'approche grille a l'inconvénient d'introduire, par l'interpolation, une source d'erreur supplémentaire. Son avantage est de permettre d'étudier de très nombreuses trajectoires et de faire des études de sensibilité (modification du calage du missile, des forces d'éjection, des moments d'inertie, etc.) à un coût beaucoup plus faible. Elle est couramment utilisée à AEROSPATIALE-MISSILES.

Les méthodes d'incidence locale ont été les premières employées pour obtenir les efforts dans le cadre de cette approche (fig. 1). Nous présentons leur principe dans le paragraphe suivant.

1.2. Principe des méthodes d'incidence locale

Soit C un coefficient aérodynamique. Une méthode d'incidence locale peut être décomposée en 7 étapes :

(1) On simule numériquement l'écoulement autour de l'avion seul dans les conditions du largage, en résolvant les équations du potentiel ou les équations d'Euler (idem pour (2)). On en déduit les valeurs extrêmes du Mach, de l'incidence et du dérapage locaux rencontrées sous l'avion. On vérifie que les angles locaux sont suffisamment faibles pour que les formules linéaires utilisées en (6) soient valides.

(2) On simule numériquement l'écoulement autour du missile seul pour différents Mach M_k choisis à l'intérieur de l'intervalle déterminé en (1). Pour chaque M_k, on fait les calculs suivants : $\alpha \neq 0$ et $\beta = 0$, $\alpha = 0$ et $\beta \neq 0$, et éventuellement $\alpha = 0$ et $\beta = 0$.

(3) On décompose le missile en éléments E^j. Pour chaque M_k, le premier et le deuxième calculs permettent d'obtenir $C^j_\alpha(M_k)$ et $C^j_\beta(M_k)$, dérivées par rapport à α et β de la valeur locale du coefficient C sur E^j ; le dernier calcul donne, lorsque c'est nécessaire, $C^j_0(M_k)$ (valeur locale du coefficient à incidence et dérapage nuls).

(4) On note G^j le centre de gravité de E^j. Le Mach, l'incidence et le dérapage locaux en G^j, notés respectivement M^j, α^j, et β^j, sont obtenus soit directement par le calcul, soit par interpolation dans le champ de l'avion.

(5) On peut calculer la valeur locale du coefficient C à incidence et dérapage nuls en G^j, ainsi que ses dérivées par rapport à α et β en interpolant dans les valeurs calculées au (3) :

$$\widetilde{C}^j_0(M^j) = \sum_k a_k C^j_0(M_k),$$

$$\widetilde{C}^j_\alpha(M^j) = \sum_k a_k C^j_\alpha(M_k),$$

$$\widetilde{C}^j_\beta(M^j) = \sum_k a_k C^j_\beta(M_k),$$

* Doctorant à l'ONERA

Paper presented at the AGARD FDP Symposium on "Aerodynamics of Store Integration and Separation", held in Ankara, Turkey from 24-27 April 1995, and published in CP-570.

où les a_k sont des coefficients d'interpolation.

(6) On déduit de (5) la valeur du coefficient en G^j en utilisant la formule linéaire :

$$C^j\left(M^j,\alpha^j,\beta^j\right) = \widetilde{C}_0^j\left(M^j\right) + \alpha^j\,\widetilde{C}_\alpha^j\left(M^j\right) + \beta^j\,\widetilde{C}_\beta^j\left(M^j\right).$$

(7) Le coefficient sur le missile en présence de l'avion est donné par :

$$C_{missile} = \sum_j k^j\, C^j\left(M^j,\alpha^j,\beta^j\right),$$

où les k^j sont des coefficients de correction qui tiennent compte des conditions locales de l'écoulement.

Deux méthodes d'incidence locale peuvent être utilisées. La première consiste à décomposer la surface du missile en panneaux ; C représente alors le coefficient de pression. La seconde revient à découper le missile en tranches ; C correspond alors aux coefficients de force.

Les deux méthodes ne représentent cependant pas tous les phénomènes physiques. C'est pourquoi, dans la pratique, nous soustrayons à la valeur des efforts qu'elles fournissent celle des efforts sur le missile seul. Cette valeur est obtenue par un calcul numérique semblable à celui de l'étape (2) ; le Mach est égal à celui de l'avion, les angles sont ceux du missile sous l'avion. On obtient ainsi une estimation de l'influence de l'avion sur la charge, que l'on ajoute à la valeur des efforts sur le missile que donne l'expérience (approche incrémentale).

Dans la deuxième partie, nous allons voir que les méthodes d'incidence locale sont limitées.

2. UTILISATION DE LA TECHNIQUE CHIMÈRE POUR LES ÉTUDES DE LARGAGE

2.1. Limites des méthodes d'incidence locale et avantages de la technique chimère

Les méthodes d'incidence locale ont l'avantage d'être rapides. Leur validité est cependant limitée lorsque le régime est transsonique ou lorsque les interactions entre le missile et l'avion sont fortes. Il est donc nécessaire de les compléter par des simulations numériques de l'écoulement autour de la configuration avion-missile.

La variété des configurations étudiées nous conduit à résoudre les équations d'Euler et de Navier-Stokes. Les méthodes multidomaine classiques utilisées à cette fin ne sont pas adaptées aux études de largage car elles nécessitent de créer un maillage volumique pour chaque position du missile. Avec les outils actuellement disponibles, cette tâche est longue. C'est pourquoi nous nous sommes intéressés à la technique chimère. Son principe consiste en effet à reporter sur les schémas numériques une partie des difficultés liées à la réalisation des maillages.

La technique chimère permet de créer un maillage pour chacun des éléments d'une configuration. Ces maillages sont ensuite assemblés, en se recouvrant mutuellement, pour former le maillage global. Ils peuvent être réalisés indépendamment les uns des autres. Il est possible d'en déplacer certains par rapport aux autres. Cet avantage rend la technique chimère particulièrement bien adaptée aux études de largage de missiles.

La principale difficulté pour les techniques multidomaine est de faire passer l'information d'un domaine vers un autre. La technique chimère, qui appartient à cette famille, utilise pour cela ce que nous appelons une condition d'influence (CDI). Les méthodes chimère qui sont présentées dans cet article correspondent à autant de façons de faire communiquer les domaines entre eux, i.e. à autant de CDI différentes.

Nous présentons dans le paragraphe suivant la première méthode chimère que nous avons développée.

2.2. La Méthode Chimère par Recouvrement

La première méthode fut développée en coopération avec l'ONERA. Elle s'inspire largement de celle que présentent Benek et al. [1]. Elle est appelée Méthode Chimère par Recouvrement (MCR) [2]. Nous nous appuyons sur la figure 2 pour illustrer notre propos. Elle représente un missile sous un avion. Le maillage de chacun des deux objets est composé de plusieurs domaines, notés $\mathcal{D}_1$ pour l'avion et $\mathcal{D}_2$ pour le missile.

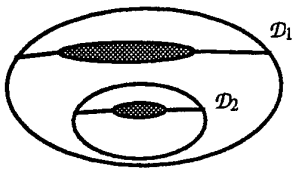

Fig. 2 - Missile sous un avion.

La présence du missile dans le maillage de l'avion oblige à faire un trou dans ce dernier. Les points de $\mathcal{D}_1$ situés dans ce trou sont appelés points masqués et sont exclus du calcul. Autour du trou, on définit des points interpolés. La valeur du champ en ces points est interpolée dans $\mathcal{D}_2$. L'information passe ainsi de $\mathcal{D}_2$ vers $\mathcal{D}_1$ par ce que nous appelons une condition d'influence (CDI).

La mise en oeuvre de la MCR peut être décomposée en deux parties. Premièrement, on écrit un pré-processeur qui détermine les données chimère (points masqués ; points interpolés et données d'interpolation qui leur sont associées). La plupart des problèmes sont de nature géométrique. Certains sont délicats à résoudre (exemple : un point est-il situé à l'intérieur d'un corps solide ?). Deuxièmement, on modifie le schéma numérique afin de tenir compte de l'existence des points masqués et des points interpolés et d'utiliser les données que fournit le pré-processeur.

La MCR a été introduite dans le code FLU3M, que l'ONERA a développé en coopération avec AEROSPATIALE [3]. Elle peut être employée pour résoudre les équations d'Euler ou de Navier-Stokes. Elle a été utilisée en Euler pour étudier le largage d'un missile ASMP sous un avion de combat Mirage 2000, pour différentes positions du missile [2] (fig. 3). Nous avons pu vérifier sur cet exemple que le prix à payer pour reporter sur les schémas numériques une partie des difficultés liées à la réalisation des maillages est faible en comparaison du coût d'un calcul stationnaire.

Nous allons voir cependant dans la troisième partie que la MCR n'est pas adaptée au cas où le missile est en position

d'emport ou très proche de l'avion. Cela nous a conduit à développer de nouvelles méthodes chimère.

3. NOUVELLES MÉTHODES CHIMÈRE

3.1. Limites de la Méthode Chimère par Recouvrement

Nous reprenons sur la figure 4 l'exemple de la figure 2. Considérons le point A. La valeur du champ en A est interpolée à partir des valeurs aux points M_j, qui forment ce que nous appelons la molécule d'interpolation de A, notée $\mathcal{M}_A$.

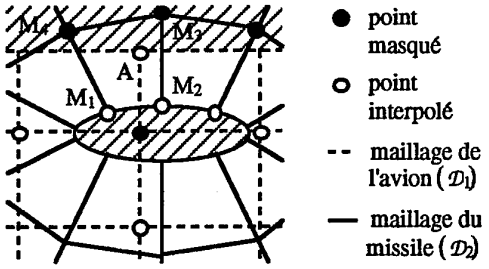

Fig. 4 - Limites de la MCR.

On dit que A est orphelin parce que $\mathcal{M}_A$ contient des points masqués (M_3 et M_4). La valeur du champ en ces points n'a pas de signification physique puisqu'ils sont exclus du calcul. Il faut donc les faire disparaître de $\mathcal{M}_A$. Le traitement que nous proposons est destiné uniquement à faire tenir les calculs. Il n'est pas précis. Nous notons c_j le coefficient d'interpolation associé a M_j. Les nouveaux coefficients sont définis par :

$$c_1' = c_1 + \frac{c_3 + c_4}{2},\ c_2' = c_2 + \frac{c_3 + c_4}{2},\ c_3' = 0 \text{ et } c_4' = 0.$$

On dit également que A est dégénéré parce que $\mathcal{M}_A$ contient des points qui sont eux-mêmes interpolés dans $\mathcal{D}_1$ (M_1 et M_2). Cela signifie que l'information fait la navette entre $\mathcal{D}_1$ et $\mathcal{D}_2$. La vitesse de convergence et la précision des résultats peuvent ainsi être dégradées.

Ces deux problèmes apparaissent lorsque le missile et l'avion sont proches l'un de l'autre, et tout particulièrement lorsqu'ils sont en contact. Il est possible de les contourner en créant ou en modifiant les maillages de façon qu'il n'y en ait qu'un seul qui fasse un trou dans l'autre (fig. 5).

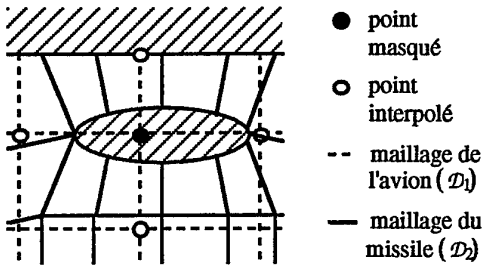

Fig. 5 - Contournement des difficultés liées à la MCR.

Cependant, ce n'est pas toujours facile ni commode. C'est pourquoi nous avons développé une nouvelle méthode chimère, dont nous exposons le principe dans le paragraphe suivant.

3.2. La Méthode Chimère par Troncature

La Méthode Chimère par Troncature (MCT) consiste à calculer les points situés autour des trous au lieu de les interpoler. Cela revient à définir une nouvelle CDI. Nous allons la présenter à partir de l'exemple de la figure 6, qui représente un corps solide superposé à un maillage.

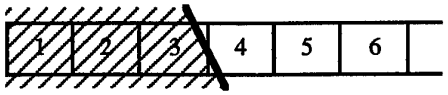

Fig. 6 - Corps solide superposé à un maillage.

Si on utilise la MCR, les points 1 à 3 sont masqués, les points 4 et 5 sont interpolés dans un autre maillage et le schéma numérique du second ordre en espace calcule le point 6 (fig. 7).

Fig. 7 - Principe de la MCR.

Si on utilise la MCT, les points 1 et 2 sont toujours masqués. Le schéma calcule les points 3 à 6 (fig. 8). Il faut pour cela prendre en compte certaines modifications aux points 3 et 4, appelés points coupés.

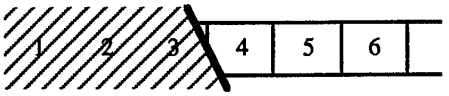

Fig. 8 - Principe de la MCT.

La figure 9 représente la cellule de contrôle d'un point coupé. La face 1 est dite masquée. Les faces 2 et 4 sont dites coupées. On définit une face solide, qui porte le numéro 5.

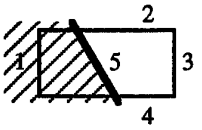

Fig. 9 - Cellule de contrôle d'un point coupé.

La mise en oeuvre de la MCT peut être décomposée de la même façon que celle de la MCR. Les données chimère sont les suivantes : points masqués ; points coupés et volume de leur cellule ; faces masquées ; faces coupées et leur vecteur normal ; vecteur normal aux faces solides et point coupé auquel elles sont associées. L'écriture du pré-processeur fait apparaître de nouveaux problèmes géométriques (exemple : intersection entre une cellule et un corps solide). Nous faisons quelques simplifications (voir fig. 10).

Fig. 10 - Simplifications géométriques.

La MCT a été introduite dans le code FLU3M. Ce dernier repose sur une approche de type volumes finis. L'utilisation de la technique MUSCL permet d'obtenir une précision du deuxième ordre en espace. Nous ne nous intéressons qu'aux fluides non visqueux. Nous allons présenter les modifications à apporter au schéma numérique pour tenir compte de l'existence des points coupés. On change la valeur du volume de la cellule de contrôle de ces points et de la normale aux faces coupées. On annule les pentes dont le calcul fait intervenir un point masqué et le flux à travers les faces masquées. Enfin on calcule un flux supplémentaire à travers les faces solides, appelé flux de paroi, pour représenter le corps solide.

Il existe de nombreuses façons de calculer le flux de paroi. Nous exposons la plus simple, qui a servi pour faire les calculs présentés au §4. Soit P un point coupé. Nous notons C le centre de la face solide qui lui est associée (fig. 11). En tout point d'une paroi, la vitesse est tangentielle à celle-ci. En conséquence, nous définissons le flux de paroi par $(0, p(C)\ \vec{n}, 0)^t$, où p(C) est une valeur de la pression au point C. On pose : p(C) = p(P).

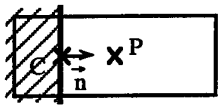

Fig. 11 - Flux de paroi.

Nous allons voir dans le paragraphe suivant que l'utilisation de la MCT pose des problèmes, ce qui rend nécessaire le développement d'une troisième méthode chimère.

3.3. La Méthode Chimère Mixte

Le principal inconvénient de la MCR est qu'elle n'est pas adaptée aux cas des corps en contact ou proches l'un de l'autre. La MCT a trois inconvénients. Tout d'abord, elle ne respecte pas la géométrie exacte des corps (voir fig. 10). Ensuite elle peut transformer un maillage initialement régulier en maillage très irrégulier. Nous voyons par exemple sur la figure 8 que le volume du point 3 devient très inférieur à celui du point 4. Cela peut poser des problèmes de stabilité. Enfin, la MCT ne permet pas de traiter le cas où une cellule de contrôle est décomposée en parties disjointes (fig. 12). Ce cas se produit fréquemment, par exemple au bord de fuite d'une aile.

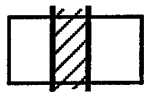

Fig. 12 - Cellule de contrôle décomposée en deux parties disjointes.

Seul le troisième inconvénient est rédhibitoire. Cela nous a conduit à construire une nouvelle méthode, appelée Méthode Chimère Mixte (MCM), i.e. une nouvelle CDI. C'est un mélange de la MCR et de la MCT. Le principe est simple : on utilise la MCT localement, dans les régions où les corps solides sont en contact ou proches l'un de l'autre ; partout ailleurs, on utilise la MCR. Comme les données chimère ne sont pas les mêmes pour ces deux méthodes, on introduit une région de transition (fig. 13). En construisant la MCM, nous avons essayé de combiner les avantages de la MCR et de la MCT. Il est important de remarquer que nous n'avons pas éliminé les deux premiers inconvénients de la MCT.

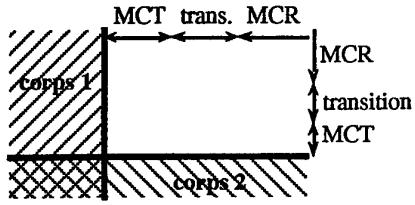

Fig. 13 - Principe de la MCM.

La mise en oeuvre de la MCM peut être décomposée de la même façon que celle des deux premières méthodes. Le pré-processeur applique la MCT dans tout l'espace. Les données ainsi obtenues sont ensuite :

- conservées dans les régions où les corps solides sont en contact ou proches l'un de l'autre ;
- modifiées dans la région de transition de façon à être compatibles à la fois avec la MCT et la MCR ;
- transformées partout ailleurs, de façon à correspondre à celles qu'utilise la MCR.

On définit par exemple dans la région de transition des points qui sont à la fois coupés (MCT) et interpolés (MCR). L'écriture du pré-processeur ne fait apparaître aucun problème géométrique nouveau.

L'introduction de la MCM dans le code FLU3M ne nécessite aucune modification supplémentaire. En effet, les données chimère soit correspondent à la MCR ou à la MCT, soit sont compatibles avec ces deux méthodes.

3.4. La Condition de Raccord Multiple

Nous reprenons l'exemple de la figure 2. Les points de la frontière extérieure de $\mathcal{D}_2$ sont appelés points de raccord. On leur applique une condition aux limites qui utilise une valeur du champ interpolée dans $\mathcal{D}_1$. L'information passe ainsi de $\mathcal{D}_1$ vers $\mathcal{D}_2$ par ce que nous appelons une condition de raccord multiple (CRM).

La CRM ne constitue pas l'essence de la technique chimère. Il s'agit toutefois d'une condition aux limites qui doit être disponible pour que l'on puisse faire des calculs avec cette technique. C'est pour cette raison que nous la présentons.

Soit $\mathcal{F}$ une frontière de maillage (fig. 14).

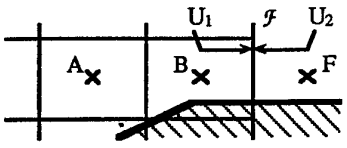

Fig. 14 - Principe de toute condition aux limites.

Nous notons B un point de calcul situé sur $\mathcal{F}$, F un point fictif associé à B, et I l'interface située entre B et F. Le vecteur d'état est noté U.

Nous rappelons que le code FLU3M utilise la technique MUSCL, i.e. la notion de pente, pour obtenir une précision du deuxième ordre en espace. Le principe de toute condition aux limites est le suivant :

(1) On définit U(F), ce qui permet de calculer la valeur de la pente au point B. On peut alors calculer la valeur du flux entre A et B, ainsi que celle de l'état à gauche de I, notée U_1.

(2) On définit la valeur de l'état à droite de I, notée U_2. Les valeurs U_1 et U_2 permettent, par application du schéma numérique, de calculer celle du flux à travers I, notée f.

(3) On modifie éventuellement la valeur de f.

Soit C le centre et S_j les sommets de I (fig. 15).

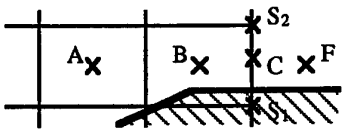

Fig. 15 - Principe de la CRM.

Le principe de la CRM est le suivant :

(0) On calcule U(C), soit directement par interpolation dans un autre maillage, soit en posant :

$$U(C) = \frac{1}{2}[U(S_1) + U(S_2)],$$

où les valeurs de $U(S_j)$ sont elles-mêmes interpolées.

(1) On calcule U(F) à partir de U(C). Il y a de nombreuses façons de le faire. Nous choisissons de poser : U(F) = U(C).

(2) On pose : $U_2 = U(C)$.

(3) On ne modifie pas f.

Ainsi écrite, la CRM est compatible avec toutes les méthodes chimère. On remarquera par exemple sur la figure 15 que C a été déplacé du fait qu'un corps solide recouvre $\mathcal{F}$. Cela rend la CRM compatible avec la MCT et la MCM.

4. VALIDATION DE LA MCT ET DE LA MCM

Les écoulements étudiés sont stationnaires. Nous résolvons les équations d'Euler.

4.1. Cas 2D : profil Naca0012 sous paroi

Objectif.
Valider la MCT.

Configuration.
Profil Naca0012 placé sous une paroi horizontale, à une distance égale à une corde.

Caractéristiques de l'écoulement.
M = 0,8 et $\alpha = 0°$.

Calculs.
(1) Calcul qui n'utilise pas la technique chimère (maillage représenté sur la figure 16).
(2) Calcul qui utilise la MCT. Volontairement, nous n'utilisons qu'un seul maillage (fig. 17).

Convergence.
Le calcul (1) a été fait avec une valeur du CFL égale à 30. Pour le calcul (2), nous avons été obligé de commencer à CFL = 2. Nous sommes passé à CFL = 3 après 560 itérations.

Résultats.
La figure 18 représente les lignes iso-Mach dans le champ de l'écoulement pour les calculs (1) et (2). Les deux calculs donnent des résultats identiques, sauf dans la région située autour du profil. En particulier, la position des chocs est la même.

Interprétation.
L'utilisation de la MCT crée des irrégularités dans le maillage. Nous avons calculé que le rapport entre les volumes de la plus grosse et de la plus petite cellule de contrôle est de l'ordre de 10^7. Cela explique pourquoi nous rencontrons sur cet exemple les problèmes évoqués au §3.3. Pour améliorer la stabilité des calculs, on peut associer une petite cellule à une cellule voisine, ou faire plusieurs itérations sur les petites cellules pour chaque itération d'ensemble.
La MCT permet d'obtenir des résultats de bonne qualité pour le corps auquel le maillage est adapté (en l'occurrence la paroi). Nous faisons remarquer que la taille, dans la direction longitudinale, des cellules situées près de la paroi est 2 fois plus importante pour (2) que pour (1). Pour le profil, les résultats sont moins bons. Cela peut venir soit du calcul du flux de paroi, qu'il est possible d'améliorer, soit du manque de précision du maillage au bord d'attaque (voir la figure 17).

4.2. Cas 3D : aile-mat-bidon

Objectif.
Comparer la MCR et la MCM sur un cas qui comporte des corps solides en contact.

Configuration.
Bidon attaché sous une aile par un mat. Un maillage a été créé pour chacun des trois corps. Nous avons représenté sur la figure 19 les maillages surfaciques. Elle permet de voir que les corps solides sont en contact.

Caractéristiques de l'écoulement.
M = 0,82 et $\alpha = 0°$ (pour l'aile).

Essais et calculs.
Pour l'aile seule (configuration I), nous disposons des résultats suivants :
(1) essais en soufflerie [4] ;
(2) calcul multidomaine classique [2].
Pour la configuration aile-mat-bidon (II), nous disposons des résultats suivants :
(3) essais en soufflerie [4] ;
(4) calcul qui utilise la MCR ;
(5) calcul qui utilise la MCM.
Nous n'avons pas pu faire de calcul avec la MCT parce que nous obtenions des cellules de contrôle décomposées en parties disjointes.

Données chimère.
La détermination des données chimère n'a pas posé de problème. Elle a nécessité, pour les calculs (4) et (5), des temps CPU comparables. Ceux-ci sont équivalents à une dizaine d'itérations d'un calcul implicite. Ils sont donc négligeables devant le temps CPU nécessaire pour faire converger un calcul stationnaire.

Convergence.
Pour le calcul (4), nous avons fait 1000 itérations avec un schéma implicite à CFL = 5. Pour le calcul (5), nous avons été obligé d'abaisser la valeur du CFL à 3. Pour atteindre la convergence, 1350 itérations on été nécessaires.

Résultats.
Nous notons C_p le coefficient de pression sur la paroi de l'aile. Nous avons retenu deux des sections de mesure choisies pour les essais (fig. 20). Les distributions de $C_p^{II,exp}$, $C_p^{II,MCR}$ et $C_p^{II,MCM}$ (configuration II : aile-mat-bidon) dans les sections 4 et 5 sont représentées sur les figures 21 et 22. Il y a des écarts entre les calculs et les essais. Ceux-ci sont cependant moins importants pour le calcul (5) que pour le calcul (4).
La figure 23 représente la distribution d'une grandeur notée ΔC_p, qui permet de connaître l'influence sur l'aile du mat et du bidon et est définie par :

$$\Delta C_p^{exp} = C_p^{I,exp} - C_p^{II,exp},$$
$$\Delta C_p^{MCR} = C_p^{I,calcul} - C_p^{II,MCR},$$
$$\Delta C_p^{MCM} = C_p^{I,calcul} - C_p^{II,MCM}.$$

Les courbes qui décrivent les distributions de ΔC_p^{exp} et ΔC_p^{MCM} sont très proches l'une de l'autre. La variable ΔC_p^{MCR} reste voisine de zéro, sauf au bord d'attaque de l'aile.

Interprétation.
Les écarts observés entre les essais et les calculs sur les figures 21 et 22 (variables C_p) sont dus au fait que la simulation numérique ne prend pas en compte les effets visqueux. Cela explique pourquoi, à l'extrados de l'aile, où la présence du mat et du bidon ne modifie pas l'écoulement, les résultats que donnent les calculs sont différents des résultats expérimentaux. La comparaison entre le calcul (2) et les essais (1) confirme cette analyse [2].
Pour cette raison, nous préférons étudier les variables ΔC_p. Elles permettent de connaître l'influence du mat et du bidon sur l'aile. Les essais montrent que celle-ci se traduit par une baisse de la pression à l'intrados (fig. 23). Comme la pression à l'extrados n'est pas changée, la portance de l'aile est diminuée. On ne retrouve pas ce phénomène avec le calcul (4). Tout ce passe comme si l'aile ne voyait pas le mat et le bidon. La seule explication que nous ayons trouvée à cela est la présence de très nombreux points orphelins et dégénérés. L'utilisation de la MCM améliore beaucoup les résultats. Les calculs (2) et (5) permettent de prédire correctement l'interaction entre les différents corps.

5. CONCLUSION

La validité des méthodes d'incidence locale est limitée dans l'étude des séparations d'une part lorsque le régime est transsonique, d'autre part lorsque les interactions entre le missile et l'avion sont fortes. C'est pourquoi il est nécessaire de les compléter par des simulations numériques de l'écoulement autour de la configuration avion-missile. Celles-ci sont réalisées sur des maillages structurés à l'aide de la technique chimère. La première méthode chimère développée pour les études de largage n'est pas adaptée au cas où le missile est en position d'emport ou très proche de l'avion. Les calculs effectués sur la configuration aile-mat-bidon le montrent. Une deuxième méthode est développée dans le but de pouvoir simuler ce genre de configuration. Elle donne de bons résultats en 2D, près du corps auquel le maillage est adapté ; autour de l'autre corps, qui ne possède pas de maillage, les résultats sont moins bons. Cet inconvénient n'est pas rédhibitoire pour une étude de largage, puisque chacun des deux corps a son propre maillage. L'exemple de la configuration aile-mat-bidon montre cependant que la deuxième méthode ne peut pas être utilisée seule lorsque la définition géométrique des corps est complexe. On se heurte en effet à la présence de cellules de contrôle décomposées en parties disjointes, qu'il est très difficile de prendre en compte. Cet exemple justifie le développement d'une troisième méthode. Celle-ci donne de meilleurs résultats que la première sur la configuration aile-mat-bidon. Combinée avec un calcul classique de l'écoulement autour de l'aile seule, elle permet de prédire correctement les interactions entre les trois corps. Ainsi, pour les études de largage, une approche incrémentale peut utiliser la technique chimère lorsque le missile est en position d'emport ou proche de l'avion.

REMERCIEMENTS

Le Ministère français de la Défense nationale (STPA) a financé cette étude, dans le cadre d'une coopération avec l'ONERA et MATRA DEFENSE.

Je remercie Philippe Mortel pour les renseignements qu'il m'a donnés sur le principe et l'utilisation des méthodes d'incidence locale.

RÉFÉRENCES

1. Benek, J. A., s, J. L., Dougherty, F. C., Buning, P. G., "Chimera : a Grid-Embedding Technique", AEDC-TR-85-64, pp. 1-125, April 1986.

2. Gillybœuf, J.-P., Mansuy, P., Pavsic, S., "Two New Chimera Methods : Application to Missile Separation", AIAA 95-0353, pp. 1-10, January 1995.

3. Guillen, P., Dormieux, M., "Design of a 3-D Multidomain Euler Code", Computational Mechanics Institute, Super computing in Fluid Flows, Boston, 1989.

4. Molinaro, R., "Essai d'une demi-voilure du Mirage F1 avec charge à l'échelle 1/4 dans la soufflerie S2MA", ONERA, Procès-verbal n° 010/3064 RYG, février 1982.

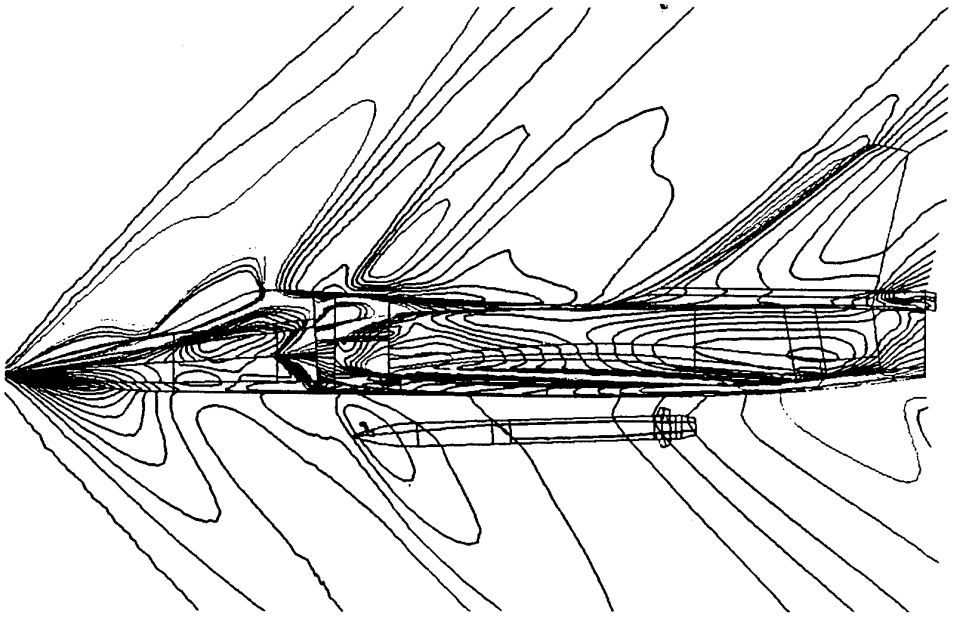

Fig. 1 - ASMP sous Mirage 2000 - Méthode d'incidence locale.

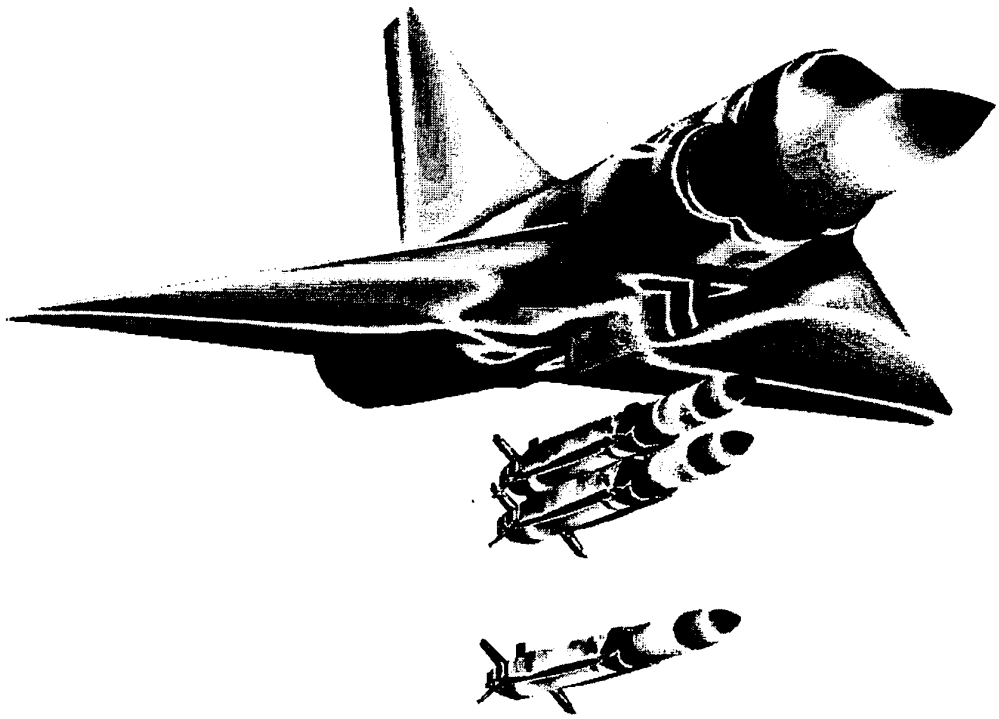

Fig. 3 - ASMP sous Mirage 2000 - Calcul chimère (MCR).

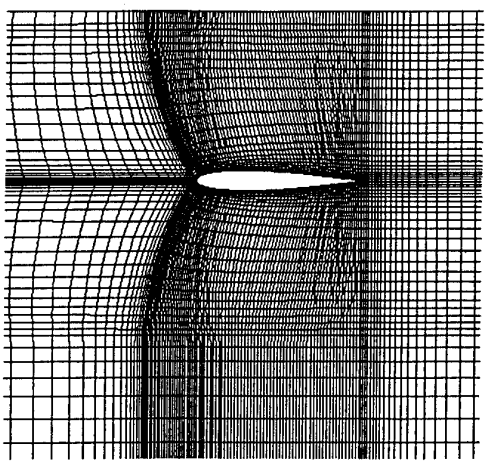

Fig. 16 - Naca0012 sous paroi - Maillage en H.

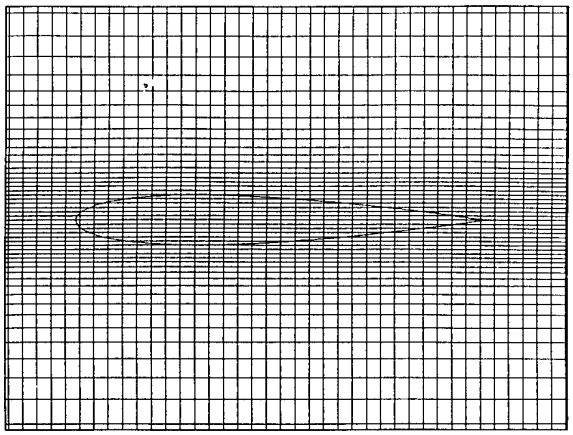

Fig. 17 - Naca0012 sous paroi - Maillage de la paroi et contour du profil.

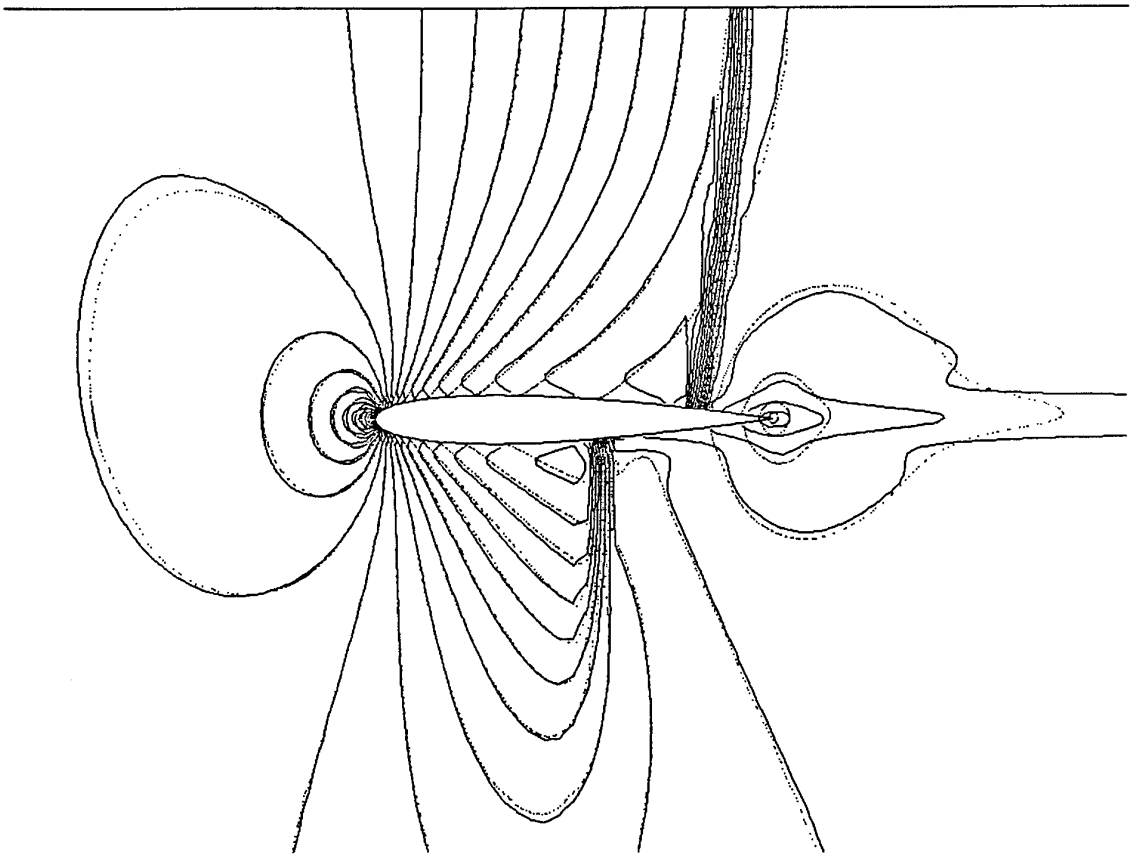

Fig. 18 - Naca0012 sous paroi - M = 0,8 - $\alpha = 0°$ - Lignes iso-Mach. Les lignes en pointillés correspondent au calcul de référence, les lignes pleines au calcul utilisant la MCT.

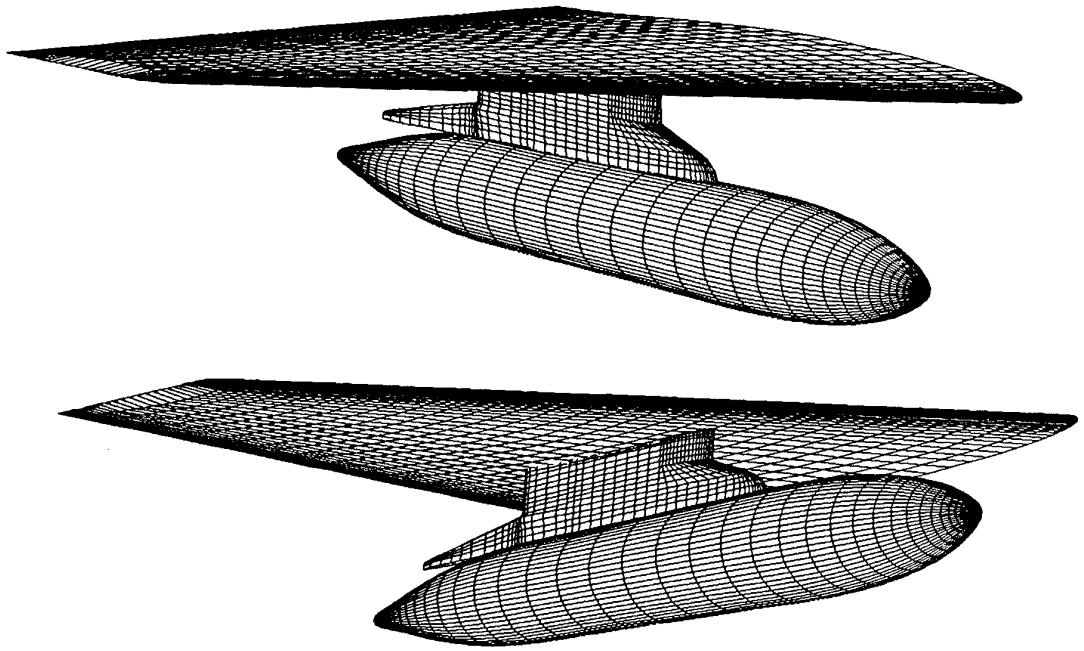

Fig. 19 - Aile-mat-bidon - Maillages surfaciques.

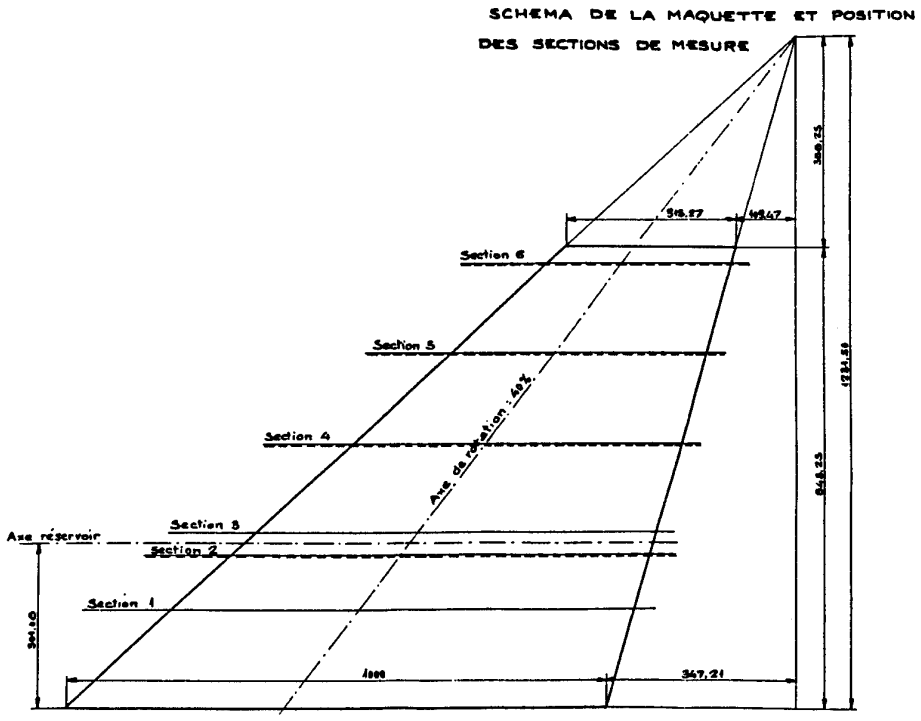

Fig. 20 - Aile-mat-bidon - Position des sections de mesure.

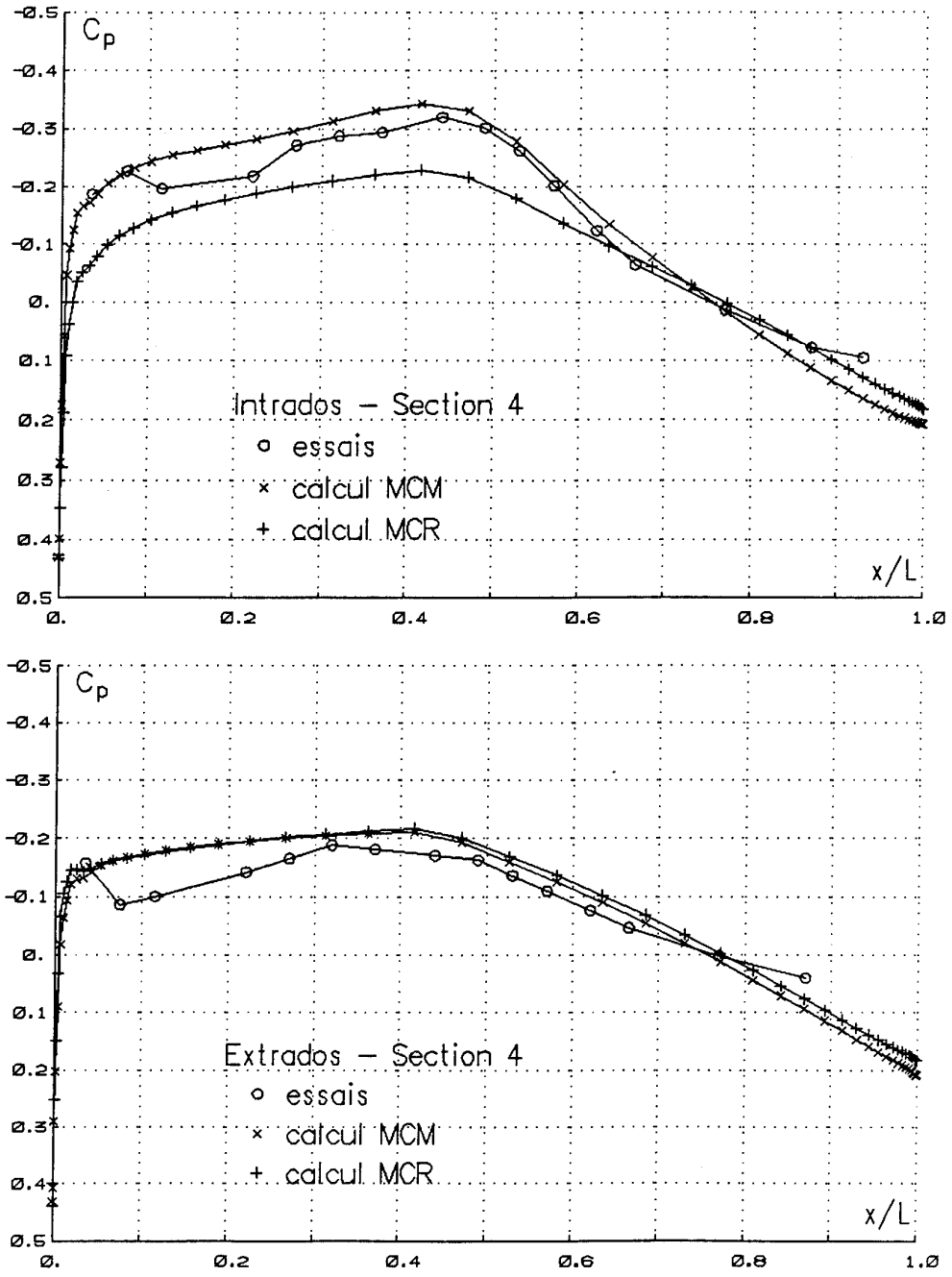

Figure 21 - Aile-mat-bidon - M = 0,82 - α = 0° - Distribution de C_p sur l'aile. Comparaison des résultats expérimentaux avec les résultats chimère.

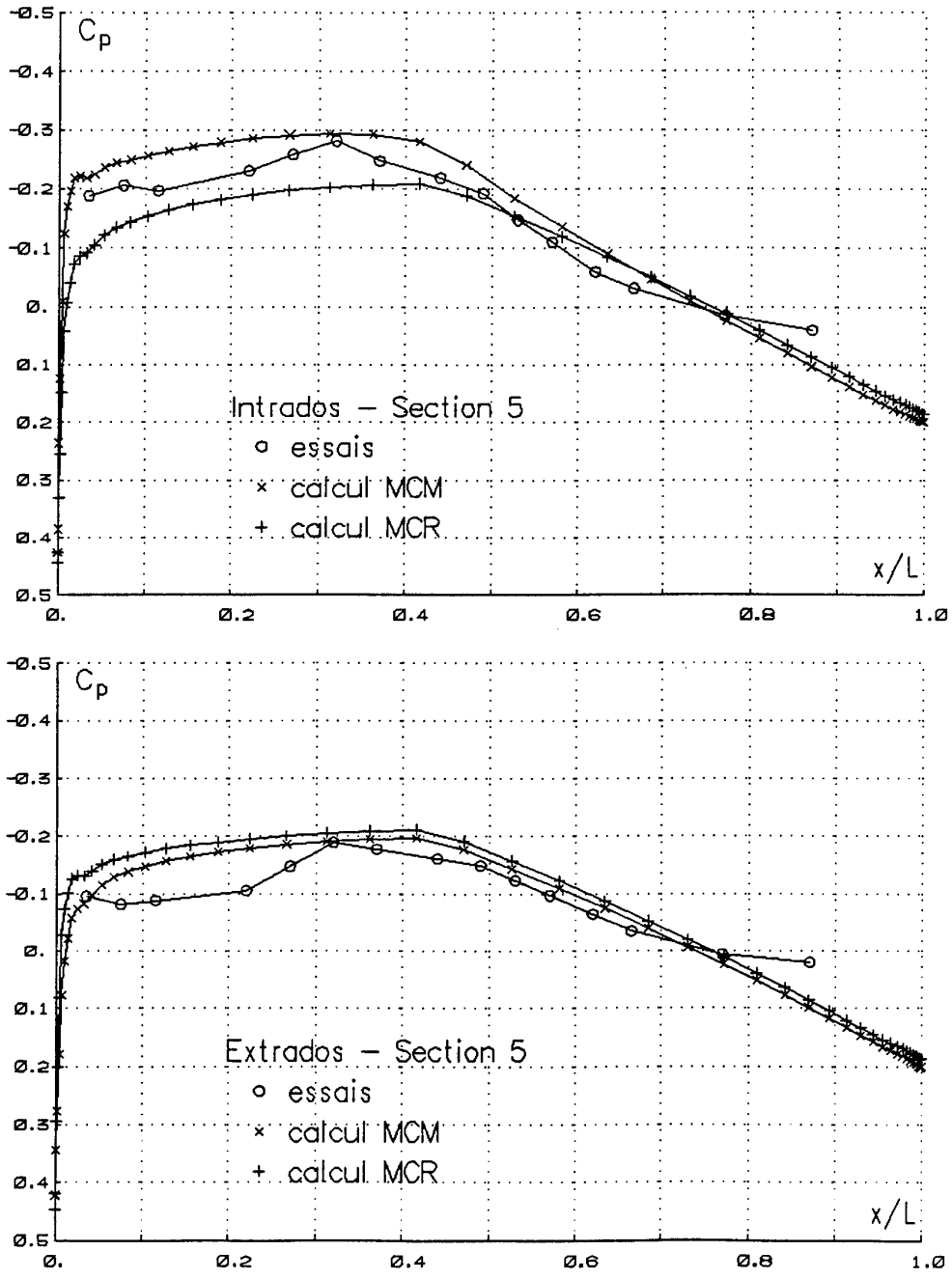

Figure 22 - Aile-mat-bidon - M = 0,82 - α = 0° - Distribution de C_p sur l'aile. Comparaison des résultats expérimentaux avec les résultats chimère.

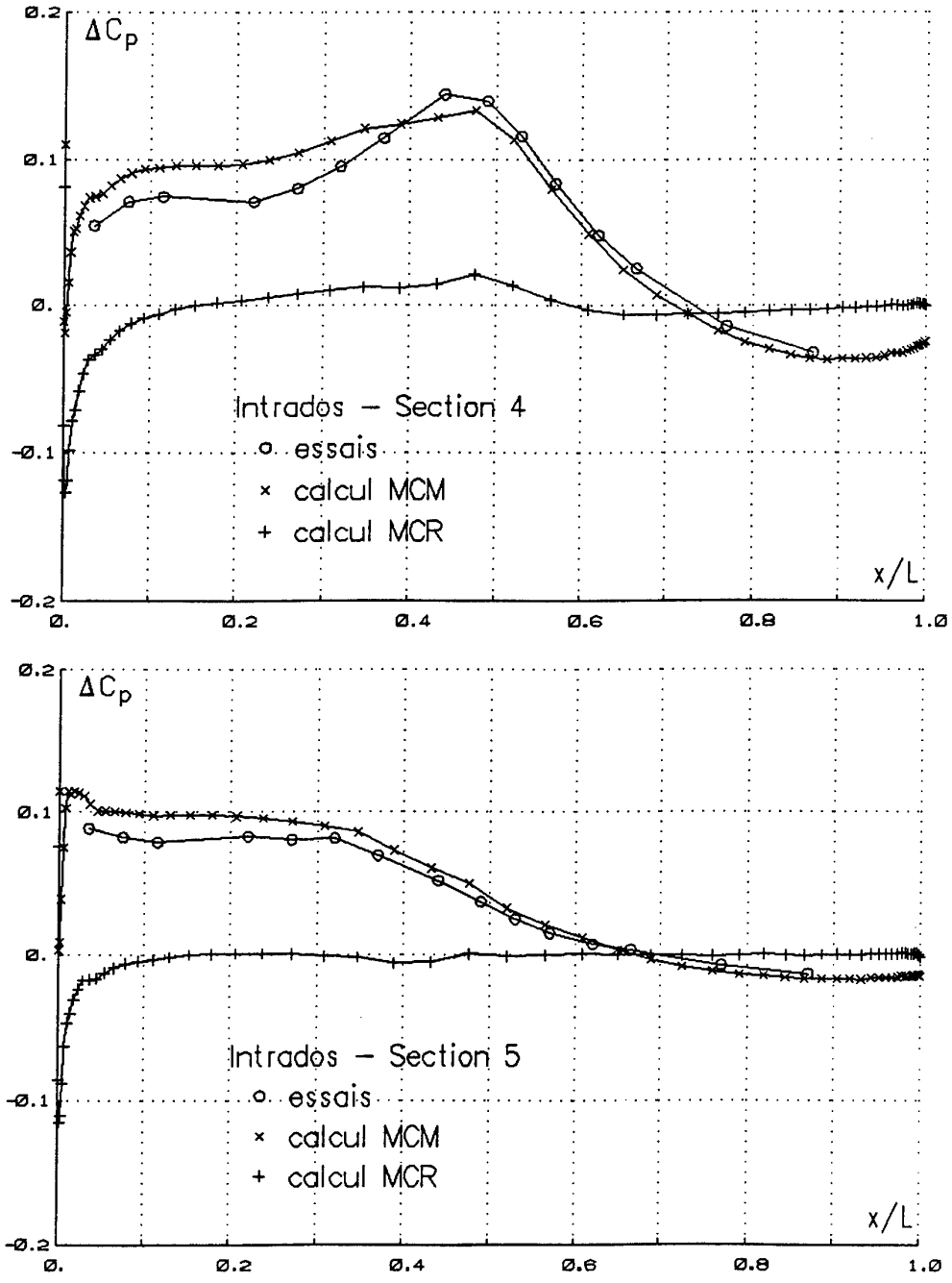

Figure 23 - Aile-mat-bidon - M = 0,82 - $\alpha = 0°$ - Distribution de ΔC_p sur l'aile. Comparaison des résultats expérimentaux avec les résultats chimère.

Méthodes pour la prédiction des séparations de charges : Etat de l'art à MATRA DEFENSE

C. Jeune
P. Mansuy
E. Ribadeau Dumas
M. Brédif
MATRA DÉFENSE
37, avenue Louis Bréguet - B.P. n° 1
78146 Vélizy-Villacoublay Cédex
France

SUMMARY

Ejection as a firing mode for new missiles developed by MATRA DEFENSE created a need for new developments in the simulation of the store aerodynamic behaviour during the separation phase.

We present here four methods used in the separation predictions, on one hand methods based on an experimental approach in wind tunnel : captive trajectories and grids, and on the other hand computational methods : "local flow incidence" method and Chimera method.

RESUME

Le mode de tir en éjection pour les nouveaux missiles développés à MATRA DÉFENSE a suscité des développements nouveaux pour simuler leur comportement aérodynamique au cours de la séparation.

Nous présentons ici quatre méthodes utilisées dans la prédiction des séparations, d'une part des méthodes basées sur une approche expérimentale : trajectoires captives et grilles, d'autre part des méthodes numériques : méthode "incidence locale" et méthode Chimère.

LISTE DES SYMBOLES

(x, y, z) : système d'axes lié au missile
(X, Y, Z) : système d'axes lié à l'avion
XR, YR, ZR : coordonnées relatives de la charge par rapport à l'avion, l'origine est fixée à l'emport, en mètre
ψR, θR, ϕR : angles d'Euler pour passer des axes avion aux axes missile, ou attitudes relatives de la charge/avion, en degré

Coefficients aérodynamiques de la charge (pour un missile cruciforme les axes y et z appartiennent à chacun des plans de voilure :

Cy : coefficient d'effort latéral
CN : coefficient de force normale
Cl : coefficient de moment de roulis
Cm : coefficient de moment de tangage
Cn : coefficient de moment de lacet
M : nombre de Mach de l'avion
α : incidence de l'avion (°)
Z : altitude de vol, en ft

1. INTRODUCTION

L'étude et le développement d'un missile air-air ou air-sol font de plus en plus appel aux simulations informatiques au détriment des essais en vol. Ceux-ci existent toujours mais leur nombre est réduit pour des raisons de coût liées à la complexité croissante des matériels à tester.

L'adaptation du missile à différents porteurs et la mise au point de la séparation n'échappent pas à cette règle.

Dans ce domaine, MATRA DÉFENSE bénéficie d'une longue expérience de missile air-air tirés sur rail, pour lesquels des essais en soufflerie préliminaires et des simulations permettaient de guider les essais en vol couvrant tout le domaine de tir.

Aujourd'hui, un nouveau mode de tir est utilisé pour les deux missiles MICA et APACHE : l'éjection contrôlée par le pilote du missile. Par rapport à un tir sur rail, les études liées à une éjection sont notablement plus complexes en raison du plus grand nombre de paramètres à gérer lié à la configuration de l'avion (proximité des réservoirs éventuels), la présence de l'éjecteur, la durée de la séparation avant l'allumage du propulseur (cas du MICA), le pilotage du missile à proximité de l'avion avec les contraintes de sécurité.

Pour appréhender le problème, on peut distinguer trois types d'études :

- étude de l'emport
- étude de la phase extraction / éjection
- étude de la trajectoire du missile libre, piloté ou non

Paper presented at the AGARD FDP Symposium on "Aerodynamics of Store Integration and Separation", held in Ankara, Turkey from 24-27 April 1995, and published in CP-570.

pour lesquelles il est nécessaire de connaître l'aérodynamique de la charge en présence de l'avion, fournie par trois sources de résultats :

- la soufflerie
- les essais en vol
- la simulation numérique

La soufflerie est la première source de résultats, utilisée dans les trois types d'études. Les essais en vol permettent de valider la mise en oeuvre globale de l'éjection et donc la prise en compte correcte des perturbations aérodynamiques. Ceux-ci sont ainsi exploités pour restituer au mieux l'environnement aérodynamique de la charge, ce qui permet de valider les modèles basés sur la soufflerie, ou ceux basés sur la simulation numérique. Celle-ci a en effet été largement développée suivant deux approches parallèles de complexité croissante :

- méthode "incidences locales".
- méthode "CHIMERE"

Nous présentons dans la suite les différentes méthodes de simulation de l'aérodynamique d'une charge en présence de l'avion tireur, méthodes qui, pour la plupart, permettent le calcul de trajectoire complète du missile en éjection.

Après une description de ces méthodes, plus détaillée pour les méthodes numériques, on présente un bilan des avantages et inconvénients de chacune d'elles.

Dans un troisième chapitre, on propose une illustration et une comparaison de ces méthodes par des résultats concernant les études de l'éjection du MICA sous le Mirage 2000-5.

2. DESCRIPTION DES DIFFERENTES METHODES

2.1. Trajectoires captives en soufflerie

La trajectoire est obtenue pas à pas en intégrant les équations de la mécanique du vol où les efforts et moments aérodynamiques sont issus des *pesées* de la maquette de la charge, en présence de la maquette de l'avion.

On peut distinguer deux types de simulations :

- simulation de charge "inerte" ou de maquette de missile propulsée ou non
- simulation d'un missile piloté.

Dans le second cas, l'échelle de la maquette ($\simeq$ 1/15e) interdit de simuler le braquage des gouvernes. L'efficacité des gouvernes doit donc être simulée par logiciel en intégrant tout ou partie du modèle aérodynamique du missile, en plus du modèle de pilotage, au logiciel de mécanique du vol pilotant les mouvements de la maquette. Ces ajouts peuvent nécessiter des aménagements des moyens informatiques en soufflerie, et aussi augmenter les temps d'essais.

2.2. Méthode de type grilles

Dans ce cas, la soufflerie est utilisée pour constituer une base de données permettant de calculer les coefficients aérodynamiques de la charge en fonction de ses attitudes et positions sous l'avion. Ce calcul est ainsi le résultat de l'interpolation sur 6 paramètres minimum : (XR, YR, ZR), positions relatives de la charge/avion, (ψR, θR, ϕR) angles d'Euler permettant de passer du repère avion au repère charge, ou attitudes relatives.

En soufflerie, les mesures peuvent être obtenues en réalisant des grilles élémentaires suivant l'un des 6 paramètres X, Y, Z, ou ϕ, θ, ψ, ou par une collection de points répartis dans le volume supposé contenir toutes les trajectoires de séparation.

Avant de pouvoir être associées à un logiciel de mécanique du vol pour le calcul des trajectoires, ces mesures doivent être soigneusement traitées pour pouvoir réaliser l'interpolation sur les 6 paramètres, et éventuellement des extrapolations en limite du domaine couvert par la soufflerie. Ce dernier point est résolu à MATRA DÉFENSE en utilisant dans la base de données non pas les données brutes de soufflerie, mais les *écarts* entre les coefficients mesurés sous l'avion et ceux en champ libre. Les résultats champ libre peuvent être mesurés lors des mêmes essais, ou provenir d'essais antérieurs de la charge seule, ou être fournis par le modèle aérodynamique de la charge, ce qui offre le plus de souplesse pour le calcul des écarts. Il suffit alors d'annuler les écarts *à l'extérieur* du domaine couvert par la soufflerie pour calculer de façon continue des trajectoires complètes de séparation.

Les coefficients aérodynamiques utilisés dans ces simulations sont donc la *somme* des coefficients fournis par le modèle champ libre de la charge et des écarts interpolés dans la base de données issue des grilles de soufflerie.

Méthode d'interpolation dans les grilles

La méthode utilisée sépare les paramètres en deux séries :

- les paramètres spatiaux : XR, YR et ZR
- les angles d'Euler : ψR, θR, ϕR

Pour les paramètres spatiaux, on se ramène au cas élémentaire d'un maillage parallélépipédique, en construisant un tel maillage qui englobe le domaine couvert par les mesures, et en projetant les données dessus, cf. figure n° 1-b. Pour les grilles obtenues en supersonique, un traitement particulier est prévu pour respecter les forts gradients induits par la traversée des *chocs* issus de l'intrados de l'avion (nez, entrée d'air, bidon ventral, ...).

Etant donnée l'orientation *oblique* de ceux-ci par rapport aux directions de projection, Y ou Z du maillage, on essaie d'effectuer l'interpolation suivant une direction perpendiculaire à la direction du choc. Le nombre de points du maillage dans les directions Y et Z est également augmenté.

Avant de réaliser l'interpolation en X, Y, Z, l'interpolation en ψ, θ, ϕ est réalisée aux 8 sommets de la cellule contenant la position de la charge. A cet effet, on construit en chaque point X, Y, Z du maillage une "fonction" des 3 angles d'Euler qui dépend du nombre de triplets (ψ, θ, ϕ) disponibles en ce point. Le nombre minimum est 4, le nombre moyen est de l'ordre de 6, et le nombre maximum peut dépasser 30 dans les cas où les mesures ont été réalisées par des variations continues de ϕ, θ ou ψ.

Dans le cas du MICA par exemple, les mesures en soufflerie ont évolué vers des acquisitions avec une variation continue de X, à différentes positions (Y, Z) prédéfinies et pour une série de 7 triplets (ψ, θ, ϕ) encadrant les attitudes du missile en emport :

- la richesse des points en X permet de restituer les maxima rencontrés à la traversée des chocs, en supersonique,
- le nombre plus restreint de triplets (ψ, θ, ϕ) suppose que l'on peut interpoler suivant chaque angle indépendamment des deux autres. Cette simplification est néanmoins corrigée dans le cas d'un missile cruciforme par les considérations de symétrie : dans un système d'axes fixes les coefficients aérodynamiques du missile sont *inchangés* par une rotation en ϕ d'angle $k\frac{\pi}{2}$, k = 1, 2, 3, ...

Pour les coefficients d'efforts Cy et CN en axes missile, on peut ainsi proposer une modélisation en ϕ du type :

$$Cy = A3 \sin 3\phi + B3 \cos 3\phi + A5 \sin 5\phi + B5 \cos 5\phi$$

$$CN = -B3 \sin 3\phi + A3 \cos 3\phi - B5 \sin 5\phi + A5 \cos 5\phi$$

pour laquelle il suffit de connaître 2 positions différentes en ϕ, $\phi 1$ et $\phi 2$ tels que $|\phi 1 - \phi 2| < 90°$, pour calculer les 4 coefficients A3, B3, A5 et B5.

La même formulation est utilisée pour les coefficients de moment Cm et Cn.

2.3. Méthode numérique Euler + "incidences locales"

2.3.1. Description générale

C'est une méthode originale développée à MATRA DÉFENSE depuis quelques années et largement utilisée dans les études de séparation du MICA sous le Mirage 2000-5. Elle est basée sur la mise au point d'un modèle aérodynamique du missile qui prend en compte des vitesses non uniformes le long de son axe pour restituer les coefficients aérodynamiques de celui-ci dans le champ perturbé de l'avion.

En séparant le calcul des perturbations de vitesses dues à l'avion de celui des coefficients aérodynamiques de la charge en présence de celui-ci, on simplifie le problème en *négligeant* les interactions mutuelles entre la charge et l'avion.

On verra que cette hypothèse n'est pas trop pénalisante dans le cas de missile de faible encombrement comme le MICA dès que le missile s'est quelque peu séparé de l'avion.

Le champ de perturbations dû à l'avion est décrit par les 3 composantes de la vitesse locale et la densité de l'air (u, v, w, ρ), issus d'un calcul numérique mettant en oeuvre le code Aérolog (réf. 4) développé à MATRA DÉFENSE dans sa version Euler et un maillage de l'avion sans la charge.

On peut faire un parallèle avec la simulation en soufflerie en comparant le moyen d'essais : soufflerie + maquette avion à la simulation numérique Euler, et la pesée de la maquette à la mise en oeuvre du modèle "champ perturbé" qui, comme la pesée, permet de restituer les coefficients aérodynamiques de la charge.

Pour le calcul des trajectoires, la procédure ressemble à celle décrite précédemment, en remplaçant le modèle aérodynamique "champ libre" par le nouveau modèle appelé modèle "champ perturbé", et les grilles de soufflerie par la grille de vitesse Euler. On peut noter que l'interpolation dans la grille de vitesse Euler est considérablement allégée par rapport à celle mise en oeuvre précédemment puisqu'il n'y a que les 3 coordonnées spatiales (X, Y, Z) de la charge à considérer.

Cette interpolation est par ailleurs simplifiée par l'utilisation d'une grille cartésienne en X Y Z à pas constant, identique dans les 3 directions. Les étapes du calcul se résument donc suivant le processus suivant :

- calcul Euler du champ complet autour de l'avion avec les éventuelles charges fixes type bidon (s). On porte un soin particulier au maillage de *l'intrados* où va évoluer le missile éjecté.
- projection des résultats du calcul Euler sur une grille cartésienne (parallélépipède parallèle aux axes avion), dont le volume englobe toutes les trajectoires de séparation, cf. figures n° 3-a et 3-b.
- simulations en *boucles fermées* : calcul de trajectoires avec un logiciel de mécanique du vol, intégrant éventuellement le pilotage du missile,
  ou simulations en *boucles ouvertes* : on impose dans ce cas la trajectoire et les attitudes du missile pour restituer un tir, effectuer des comparaisons avec des mesures en soufflerie, ou bien analyser des points particuliers. La figure 4-b présente des calculs en boucle ouverte sous forme d'écart entre le coefficient Cm en champ perturbé et le Cm en champ libre, dans le plan d'éjection. Les incidences locales sont visualisées sur la figure 4-a.

2.3.2. Description du modèle aérodynamique "champ perturbé"

Le but d'un tel modèle est de pouvoir restituer l'évolution des coefficients aérodynamiques de la charge en fonction des perturbations de vitesse induites par l'avion, et également représenter le plus fidèlement l'aérodynamique en champ libre puisqu'il remplace le modèle "champ libre" dans les simulations.

Un tel modèle a été mis au point pour le missile air-air MICA développé à MATRA DÉFENSE.

La base de départ est le modèle aérodynamique champ libre du missile, dans lequel le calcul des efforts est décomposé suivant des tronçons ou des éléments spécifiques du missile.

On distingue à cet effet :

- l'ogive et le tronçon cylindrique en avant des ailes
- le tronçon portant les ailes
- les 4 gouvernes modélisées séparément

Sur chacun des tronçons, une loi de répartition de la portance suivant x a été définie. Cette loi de répartition est issue des théories simplifiées type "théorie des corps élancés" et de l'expérience acquise sur les configurations de missile à ailes longues développées à MATRA DÉFENSE. Pour chacune des gouvernes, on utilise le concept d'incidence équivalente pour calculer la portance et prendre en compte simultanément l'écoulement potentiel, les interactions liées au sillage tourbillonnaire des ailes, et les interactions dues aux gouvernes voisines.

Intégration de la portance :

La formulation utilisée pour l'intégration de la portance qui prend en compte les variations de l'incidence locale est du type :

$$(1)\quad CN = \int_0^L \alpha(x) \cdot \frac{dCN\alpha(x)}{dx} \cdot dx + \int_0^L CN\alpha(x) \cdot \frac{d\alpha(x)}{dx} \cdot dx$$

dans laquelle :

$\alpha(x)$ est fournie par le champ de vitesse

$$(\alpha = \text{atg}(\frac{w}{u}))$$

$\frac{dCN\alpha(x)}{dx}$ traduit la loi de répartition de portance ; cette loi est approximée par des fonctions linéaires par morceaux, sauf pour l'ogive

$$CN\alpha(x) = \int_0^x \frac{dCN\alpha(x)}{dx}\, dx$$

$\frac{d\alpha(x)}{dx}$ est fournie aussi par le champ de vitesse, à partir de $\alpha(x)$.

Ceci peut aussi être écrit dans le plan (x, y) en remplaçant CN par - Cy et α par $\beta = \text{atg}\frac{v}{u}$. Le calcul des coefficients de moment Cm et Cn s'en déduit immédiatement en ajoutant le terme (x - xg) sous chaque signe $\int$.

La formulation (1) est dérivée de l'expression $CN = \int_0^L \frac{dCN}{dx}.dx$ dans laquelle $CN = CN\alpha \,.\, \alpha$ qui suppose une variation linéaire du Cz avec α.

Lorsque ce n'est pas le cas, on écrit le CN sous la forme :

$CN = CNo + CN\alpha\,(\alpha o)\,.\,(\alpha - \alpha o)$

en linéarisant celui-ci autour de l'incidence αo, qui sera l'incidence *moyenne* vue par le tronçon ou l'élément de missile sur lequel on effectue l'intégration.

2.4. Méthode Chimère : principe

Pour accéder à une meilleure précision, notamment dans le champ très proche de l'avion, il est indispensable de prendre en compte les intéractions entre la charge et le porteur. C'est ce que permettent les méthodes Chimère.

Un maillage spécifique est créé pour chaque objet impliqué dans la simulation. Chaque maillage - construit indépendamment des autres et une fois pour toutes - est ainsi parfaitement adapté au corps auquel il est rattaché. En raison de la position arbitraire des corps en présence - et donc des maillages correspondants - certains noeuds d'une grille peuvent se trouver dans des régions solides d'autres grilles (points solides). Par conséquent, ils ne doivent pas être pris en compte lors du calcul de l'écoulement. Ainsi, la technique Chimère introduit, dans le domaine global de calcul, des "trous" et des frontières artificielles autour de ces "trous".

Les communications entre maillages s'effectuent par l'intermédiaire des frontières artificielles (appelées aussi zones d'interpolation), où les valeurs idoines sont interpolées d'un maillage dans l'autre.

Le pré-processeur Chimère détermine la nature de chaque point du domaine global de calcul. On distingue trois types de points :

- les points masqués : ils n'ont pas de signification physique et sont ignorés par le solveur aérodynamique,
- les points interpolés : les grandeurs physiques en ces points ne peuvent pas être calculées par le solveur aérodynamique car leur molécule numérique contient un point masqué (nous appelons molécule numérique du point M l'ensemble des points qui intervient dans le calcul de l'état en M par le schéma numérique)[1] ; ces grandeurs sont interpolées à partir d'un autre maillage ; les points interpolés forment les zones d'interpolation,
- les points discrétisés : les grandeurs physiques y sont calculées classiquement par le solveur aérodynamique.

Il est ensuite nécessaire de modifier le solveur aérodynamique pour tenir compte de l'existence des différents types de points.

La méthode à partition (MAP), développée par MATRA DÉFENSE dans le cadre d'une collaboration avec l'ONERA et L'AÉROSPATIALE MISSILE financée par le STPA/EG, est basée sur les travaux de Chesshire et Henshaw (Réf. 1). Dans cette approche, on "empile" les maillages suivant un ordre arbitraire.

Tous les points d'un maillage qui se trouvent "sous" un maillage supérieur sont masqués (points cachés), ce qui permet d'obtenir une partition mathématique (aux bandes d'interpolation près) de l'espace de discrétisation. Ainsi, les points masqués sont les points solides et les points cachés. L'opérateur ne doit spécifier que l'ordre d'empilement des différents maillages. Cet ordre est indifférent en général, sauf dans le cas de solides en contact.

Le pré-processeur Chimère - entièrement automatique - a été développé et validé pour les maillages tridimensionnels structurés, multiblocs et en nombre quelconque. Il est indépendant du solveur Euler et ne doit en connaître que la taille de la molécule schéma, qui influe sur la définition des zones d'interpolation.

Tout en s'attachant à la grande généralité et à la robustesse des algorithmes, de nombreux heuristiques - pour accélérer notamment la recherche des points solides et des points interpolés - ont été développés, permettant d'aboutir à des temps de

1. La molécule numérique dépend du schéma

calcul des maillages Chimère, acceptables dans le cadre d'une utilisation industrielle (Réf. 3).

Typiquement, le temps d'éxécution du pré-processeur Chimère pour un groupe de maillages donné correspond à environ la durée de cinq itérations explicites du solveur Euler sur ces maillages, sachant qu'un calcul convergé nécessite de 2 000 à 5 000 itérations. Le solveur utilisé est le code Aérolog (réf. 4) dans sa version résolvant les équations d'Euler. Il s'agit d'un code tridimensionnel, multibloc, structuré, basé sur le schéma de Lax-Wendroff

La méthode a fait l'objet de plusieurs séries de validations, d'abord sur des cas académiques (bidon sous une aile de chasseur), puis sur des cas industriels (réf. 2, 3). Elle est désormais utilisée de façon industrielle, dans le cadre de développements de missiles. Cependant, dans l'état actuel d'avancement du pré-processeur Chimère, on ne peut calculer que des points de grilles. Aussi, les travaux se poursuivent, afin de permettre de simuler des trajectoires, incluant la mécanique du vol et un éventuel pilote du missile.

3. AVANTAGES ET INCONVENIENTS DE CHACUNE DES METHODES

3.1. Trajectoires captives en soufflerie comparées aux grilles

L'avantage par rapport aux grilles est de fournir un résultat immédiat.

Il y a ensuite une meilleure précision des coefficients aérodynamiques dans la mesure où il n'y a pas d'interpolation.

Pour les grilles, le principal avantage est de pouvoir s'intégrer au modèle de simulation complet du missile et de permettre de simuler un *nombre non limité* de trajectoires pour :

- optimiser les paramètres de pilotage
- étudier des cas de panne
- étudier la sensibilité aux conditions initiales

Les inconvénients des trajectoires captives sont à l'opposé des avantages cités pour les grilles du fait du nombre forcément limité des simulations en soufflerie. On peut ajouter également parfois *l'interruption* précoce des trajectoires à cause des *limitations* en débattement du dispositif d'essai. Cette limitation interdit assez souvent de s'assurer complètement de la sécurité d'un tir du fait que la trajectoire s'interrompt à une distance proche de l'avion.

Pour les grilles, l'inconvénient majeur reste lié au volume important de mesures à effectuer alourdissant les essais en soufflerie. La précision dans l'interpolation étant directement issue du pas des mesures, il faut trouver un compromis, pour chaque cas de charge, entre un volume de grilles raisonnable et la précision finale requise pour le calcul des perturbations aérodynamiques.

Enfin, pour ces deux méthodes liées à une approche expérimentale, le dernier inconvénient demeure le coût des essais en soufflerie :

- proportionnel au nombre de trajectoires captives
- proportionnel au volume de grilles : coût initial élevé mais indépendant du nombre de trajectoires simulées par la suite

3.2. Méthode "incidences locales" : avantages et inconvénients

L'avantage de cette méthode est sa grande souplesse d'emploi comparable à l'utilisation des grilles dans les modèles de simulations complets du missile, avec en plus beaucoup moins de lourdeur du fait de l'absence d'essais volumineux à réaliser et à traiter. On rappelle régalement qu'au cours d'une trajectoire, il n'y a qu'une interpolation en X, Y, Z à faire dans la grille de vitesses du champ Euler.

Un autre avantage, sur le plan de la modélisation, est la prise en compte exacte des *vitesses relatives* de la charge par rapport à l'avion. On sait que cela est impossible en soufflerie avec une trajectoire captive et également avec la méthode des grilles.

Toujours sur le plan de la modélisation, dans le cas où l'on calcule des trajectoires pilotées, on peut prétendre simuler avec plus de précision l'efficacité des gouvernes par rapport à l'approche expérimentale, du fait de la connaissance de l'incidence locale et de la pression dynamique locale au niveau de celles-là. Ces effets peuvent être significatifs en supersonique ou à grande incidence.

Un dernier avantage - et non le moindre - est le faible coût global car un seul calcul de champ de vitesses peut servir à l'étude de différentes positions d'emport (positions fuselages avant et arrière du MICA sous Mirage 2000-5, par exemple) et également différents types de charge.

Enfin, le calcul Euler de ces champs de vitesse peut permettre d'étudier la sensibilité à des paramètres non accessibles en soufflerie ou non

retenus du fait du coût des essais, comme le dérapage de l'avion ou le braquage de ses gouvernes.

En regard de ces nombreux avantages, il faut garder à l'esprit l'inconvénient majeur lié à la simplification du problème au travers de la non prise en compte de l'interaction mutuelle charge - avion. Le calcul est donc moins précis près de l'avion, l'erreur dépendant fortement de la taille relative de la charge par rapport à l'avion. C'est pour cela que cette méthode est essentiellement prévue pour des petites charges comme le missile MICA. Cependant, pour ce dernier, si l'erreur de modélisation du champ est moindre du fait de sa petite taille, celle-ci rend difficile la restitution du moment de roulis du missile dont l'envergure est de l'ordre de grandeur du pas du maillage.

Le dernier inconvénient que l'on peut citer pourrait être la mise au point du modèle champ perturbé, suivant le type de charges à modéliser et la plus ou moins grande connaissance préalable de ses caractéristiques aérodynamiques détaillées. En complément de la modélisation des caractéristiques en champ libre, on peut utiliser l'aide du numérique (code Euler) pour modéliser les répartitions d'effort. On peut également vérifier assez facilement l'effet d'un champ "uniformément perturbé" en imposant dans le calcul Euler une vitesse de tangage au missile.

3.3. Méthode Chimère : avantages et inconvénients

Ici encore, l'avantage principal de la méthode Chimère réside en sa grande souplesse d'emploi et sa rapidité de mise en oeuvre. Elle permet ainsi d'appréhender les problèmes liés à l'emport et au largage d'un missile, très tôt dans son développement et avant même que sa géométrie ne soit définitivement figée. Par ailleurs, elle permet d'explorer des régimes parfois difficilement accessibles à la mesure de soufflerie (séparation de charge en régime transsonique, par exemple) ou de simuler des positions relatives irréalisables expérimentalement, en raison des limites techniques imposées par les montages des maquettes (assiette relative importante de la charge, etc.). Dans un avenir proche, il sera également possible de tenir compte de la vitesse relative du missile par rapport à l'avion. Enfin, il est facile de simuler n'importe quel missile sous n'importe quel avion, dès lors que l'on possède un maillage de chacun.

Par ailleurs, la méthode Chimère ne nécessite l'élaboration d'aucun modèle aérodynamique du missile, mais la précision de ses résultats est directement liée à celle du calcul Euler. Par conséquent, il peut être nécessaire de recaler les coefficients du missile calculés dans le champ perturbé de l'avion, par un calcul en champ libre et de ne considérer ainsi que des différentiels de coefficients. Les résultats Chimère présentés dans le paragraphe 4 sont bruts : ils n'ont pas été recalés de la sorte.

On notera que les Chimères permettent aussi de calculer des géométries complexes en simplifiant considérablement la tâche de maillage.

Cependant, l'inconvénient actuel majeur de la méthode reste son coût, directement lié au grand nombre de points composant les maillages résultants. Comme on l'a vu, en effet, la réalisation du maillage Chimère ne réclame que peu de temps, mais la durée du calcul Euler lui-même est directement proportionnelle au nombre de points de maillage et peut donc rapidement devenir prohibitive. Un maillage classique (d'un missile ou d'un avion), compte de l'ordre de 300 000 points : le maillage Chimère d'un missile sous avion comprend donc de l'ordre de 600 000 points. De plus, il faut généralement simuler de nombreuses positions relatives, d'où une inflation des coûts de calcul. Pour que son utilisation devienne plus courante, il convient donc de développer des techniques appropriées permettant d'abaisser les temps de calcul Euler.

4. ILLUSTRATION DE CES METHODES : EJECTION DU MICA SOUS MIRAGE 2000-5

4.1. Difficultés et cadre de l'étude

La difficulté principale provenait du nombre de configurations d'emport à traiter :

- positions avant et arrière sous le fuselage
- emport de bidon (s) : avion lisse / 1 bidon / 3 bidons

et de l'étendue du domaine de tir en Mach et incidence de l'avion, incluant un large domaine allant du subsonique ∧ supersonique (jusqu'à Mach 1.8) et des incidences de 20°.

Par ailleurs, le domaine transsonique compris entre Mach 1 et Mach 1.4 est peu accessible en soufflerie, à cause des fortes interactions liées au dispositif réalisant les trajectoires captives ou les grilles (soufflerie S2 de l'ONERA). Les méthodes à base de simulations numériques, essentiellement la méthode champ Euler + "incidences locales", ont donc été utilisées *en complément* des méthodes à base expérimentale lorsque ce fut nécessaire.

4.2. Efforts en emport : comparaison vol - soufflerie

Des mesures d'efforts sur une maquette ont été réalisées en vol d'emport sous le Mirage 2000. La maquette est instrumentée pour mesurer tous les efforts aux niveaux des points d'attache avant et arrière. L'exploitation de ces mesures permet de restituer les efforts a*érodynamiques* vus par la maquette en emport, une fois retranchés les efforts massiques, et de les comparer avec ceux déduits des mesures en soufflerie au cours des trajectoires captives ou des grilles.

Les figures n° 7-b et c présentent l'effort latéral Fy, perpendiculaire au plan d'éjection, et le moment de roulis Mx autour de l'axe x du missile, au cours d'un vol où le nombre de Mach de l'avion est compris entre 0.5 et 1.5 (cf. figure 7-a), comparés aux mêmes efforts calculés avec les coefficients aérodynamiques mesurés en soufflerie et la pression dynamique rencontrée au cours du vol.

Le niveau des efforts vus en vol est très proche de ceux déduits des mesures de soufflerie en subsonique et transsonique et s'éloigne localement pour les nombres de Mach les plus élevés. L' écart constaté ici peut avoir de multiples causes et en premier lieu la difficulté de bien restituer les efforts aérodynamiques à partir d'une maquette dimensionnée pour mesurer des efforts beaucoup plus importants dans les cas de charge maximale en emport avec de fortes manoeuves de l'avion.

4.3. Restitution d'un tir de maquette

Pour valider le comportement de l'éjecteur et la bonne connaissance des perturbations aérodynamiques, de nombreux tirs de maquettes, non propulsées mais représentatives du missile (centrage, masse, inertie, aérodynamique), ont été effectués à partir des points latéraux fuselage du Mirage 2000-5.

Nous présentons les résultats d'un tir effectué à Mach 1.5 avec une incidence de 5.4° et un facteur de charge supérieur à 4, à partir du point arrière en présence d'un bidon ventral sous le fuselage.

4.3.1. Restitution en boucle ouverte

Les capteurs embarqués dans la maquette permettent de restituer la trajectoire de celle-ci en intégrant les mesures, ainsi que les forces et les moments aérodynamiques vus par l'engin en vol libre.

Ces forces et moments sont traduits en coefficients aérodynamiques qui sont comparés aux coefficients fournis par les différentes méthodes exposées précédemment en imposant la trajectoire et les attitudes restituées :

- méthode Chimère
- méthode "incidences locales"
- méthode des grilles

Ces comparaisons sont fournies sur les figures n° 8-a à 8-e, tous les coefficients étant tracés en fonction de la position relative ZR jusqu'à une distance de 14 m.

Pour la méthode Chimère, seuls quelques points près de l'avion sont calculés. Le maillage global utilisé pour ces calculs est constitué de quatre maillages différents (figure 5-a) : un pour l'avion, un pour le bidon, un pour le pylône et un pour le MICA (figure 5-b). Il comprend 660 000 points au total. Le temps CPU que nécessite le calcul Euler pour chaque position s'élève à environ 40 h sur une machine à 10 M flops (la construction de maillage Chimère ne réclamant que quelques minutes). Les résultats sont très proches de ceux du vol, mis à part le dernier point pour le Cl.

Les figures 6-a et 6-b représentent les répartitions de pression sur les différents corps en présence. On y distingue nettement les interactions entre le bidon et l'avion, le pylône et l'avion et - sur la figure 6-b - l'influence du champ ainsi perturbé sur le missile.

Pour les grilles et les incidences locales, les résultats sont confondus au-delà de 12 m car ils sont fournis par le modèle champ libre, et c'est presque le cas à partir de 9 m.

Globalement, les résultats de la méthode incidences locales sont plus proches du vol que ceux issus des grilles de soufflerie, ceci étant principalement dû à l'absence de mesures en soufflerie autour de l'incidence du tir et au recours à une *interpolation* entre deux grilles, l'une obtenue à $\alpha = 0.5°$ et l'autre à $\alpha = 10°$. Ces deux grilles sont illustrées sur les figures 2-a et 2-b, où sont présentés les écarts en Cm entre les mesures et le modèle champ libre. Les résultats de la méthode "incidences locales", au contraire, sont issus d'un champ de vitesse calculé à l'incidence du tir, $\alpha = 5.4°$.

En écoulement supersonique, l'inclinaison des ondes de choc par *rapport à l'avion* change avec l'incidence ce qui déplace les phénomènes liés à la traversée de ces chocs induisant de fortes variations sur les coefficients de moment.

Ceci peut expliquer l'écart important sur l'un des coefficients de moment, Cm, constaté pour $1.5 \leq Zr \leq 3$ m entre le vol et les grilles. En revanche, pour le coefficient Cn les résultats issus des grilles se superposent parfaitement avec le vol près de l'avion jusqu'à ZR = 3 m.

Enfin, les écarts apparaissant sur les coefficients de force Cy et CN loin de l'avion ne sont pas significatifs de la précision du modèle champ libre du missile, mais plutôt de l'imprécision de la restitution de ce type de tir où, d'une part, la précision des mesures se dégrade en fonction du temps et où, d'autre part, on n'a pas tenu compte d'un vent éventuel qui peut modifier les conditions aérodynamiques de l'engin dès lors que celui-ci n'est plus aligné avec l'avion.

4.3.2. Restitution en boucle fermée

On calcule dans ce cas la trajectoire de vol libre du missile avec les conditions initiales réelles du tir, soit avec la méthode incidences locales, soit avec la méthode des grilles. Les résultats sont comparés avec la trajectoire du vol sur les figures n° 8-f et 8-g.

La trajectoire du centre de gravité est bien restituée avec les deux méthodes, de façon plus précise pour YR avec les incidences locales.

5. CONCLUSION

Nous avons présenté plusieurs méthodes permettant l'étude et la prédiction des séparations de charges, à travers différentes voies pour simuler l'aérodynamique de celles-là dans le champ perturbé de l'avion.

Ces méthodes ont été validées et utilisées avec succès pour l'étude de l'éjection du MICA sous le Mirage 2000- 5.

La contribution de la méthode Chimère a été plus modeste du fait de son existence plus récente et des évolutions (en cours) pour permettre de simuler des trajectoires mais elle est appelée à jouer un rôle de plus en plus important, surtout pour l'étude de largage de charges volumineuses où les interactions entre l'avion et celles-ci sont très significatives. Cependant, une réduction drastique de son coût reste indispensable si l'on veut pouvoir l'utiliser de façon intensive.

Le besoin en simulations globales du missile est en effet de plus en plus important surtout dans le cas de l'éjection d'un missile piloté, pour valider le pilotage dans tout le domaine de tir et sa robustesse par rapport aux perturbations connues et par rapport aux dispersions sur le mouvement du missile à la séparation (en sortie de l'éjecteur).

L'idéal serait donc un outil de simulation rapide (peu cher) et assez souple pour être intégré au modèle complet du missile ce qui conduit à envisager de "combiner" l'emploi de la méthode "incidences locales" avec des résultats complémentaires près de l'avion pour en améliorer la précision. Ces résultats seraient fournis par la soufflerie ou la méthode Chimère. Une première étape dans ce processus est déjà effective puisque les résultats de soufflerie en emport et à la séparation ont été systématiquement employés pour calculer les conditions initiales des trajectoires libres du missile avec la méthode "incidences locales", dans les études de séparation du MICA.

En conclusion, l'expérience actuelle confirme le besoin et l'intérêt de continuer à développer des outils numériques performants pour les études aérodynamiques de séparation, *en complément* des outils expérimentaux plus traditionnels comme la soufflerie, ou des essais en vol en nombre limité.

Références :

[1] Chesshire, G., Henshaw, W.D., Composite overlapping meshess for the solution of partial differential equations, J.C.P., vol ; 90, pp. 1-64, 1990.

[2] Gillyboeuf, J.P., Mansuy, P., Pavsic, S., Two new Chimera methods : application to missile separation, AIAA 95-0353, 1995.

[3] Mansuy, P., Etude de la simulation numérique de la séparation de charges externes sur un avion de combat, Rapport final du contrat ONERA 22.356/SAT.2.Cch, novembre 1993.

[4] Borel, C., Brédif, M., High performance Parallelized implicit Euler solver for the analysis of unsteady aerodynamic flows, Proceedings of the First European Computational Fluids Dybamics Conference, pp, 1069-1072, 1992.

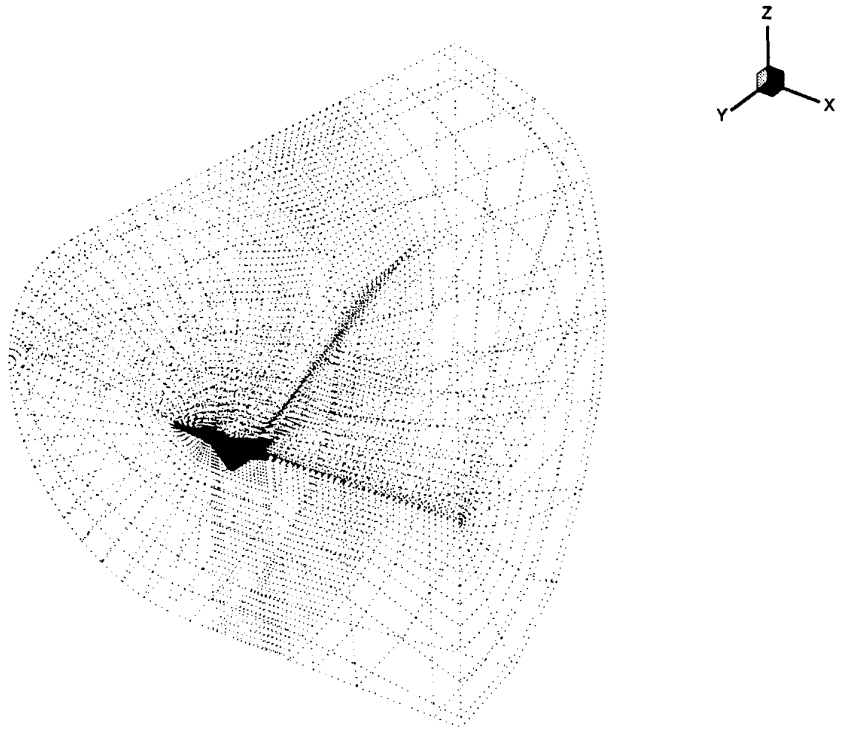

Figure 1a : Maillage du domaine de calcul EULER autour du MIRAGE 2000.

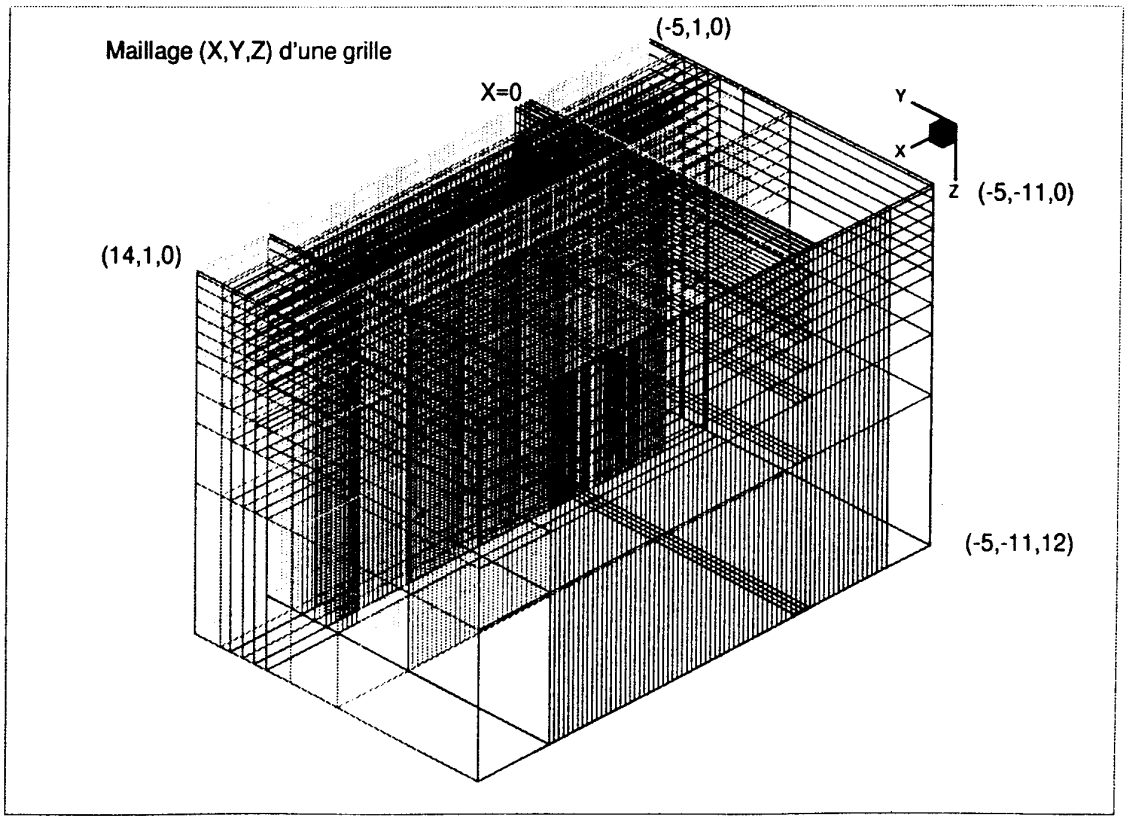

Figure 1b : Maillage cartésien utilisé pour projeter les résultats de soufflerie.

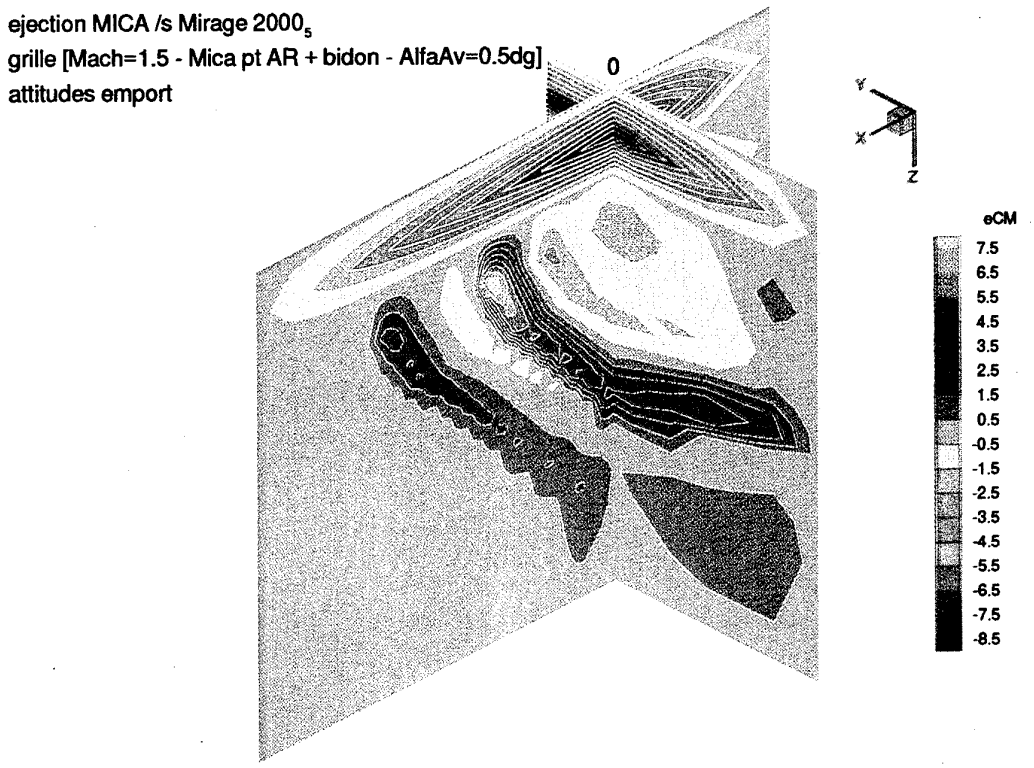

Figure 2a : Grilles de soufflerie : iso-ΔCm du MICA dans deux plans de maillage ($\alpha = 0^o$)

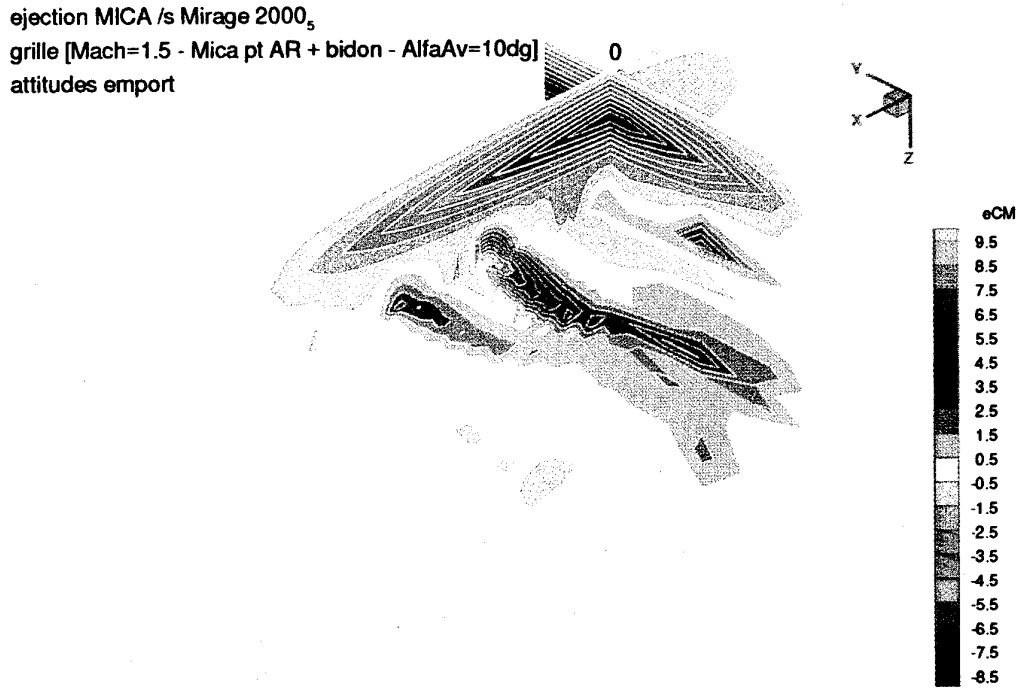

Figure 2b : Grilles de soufflerie : iso-ΔCm du MICA dans deux plans de maillage ($\alpha = 10^o$).
ΔCm = Cm (mesuré) - Cm (champ libre)

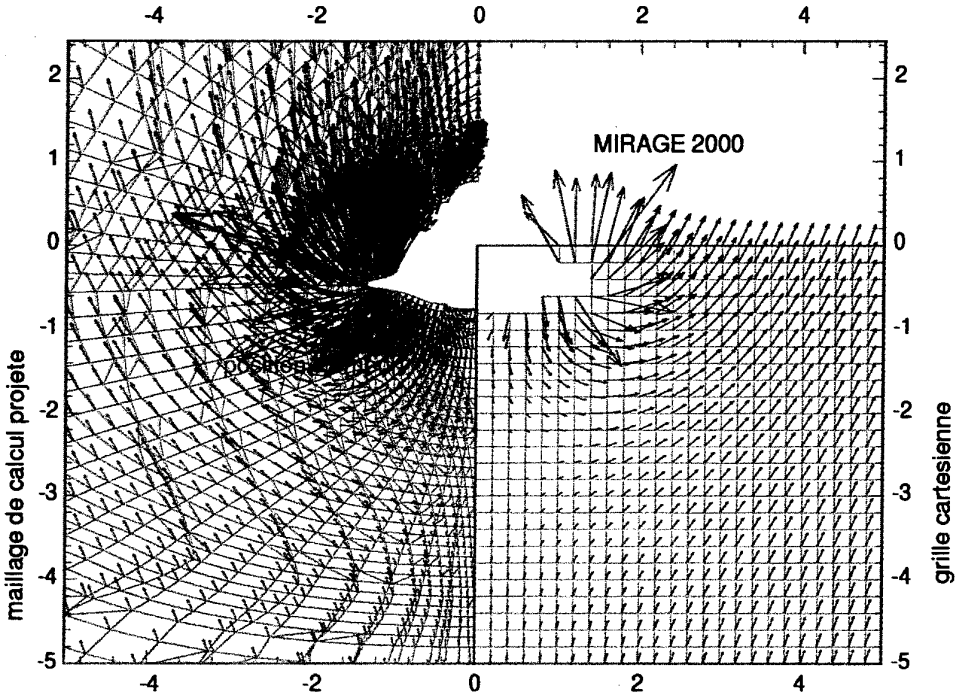

Figure 3a : Interpolation du champ de vitesse Euler du maillage physique sur la grille cartésienne.
(Vue du maillage dans un plan YZ)

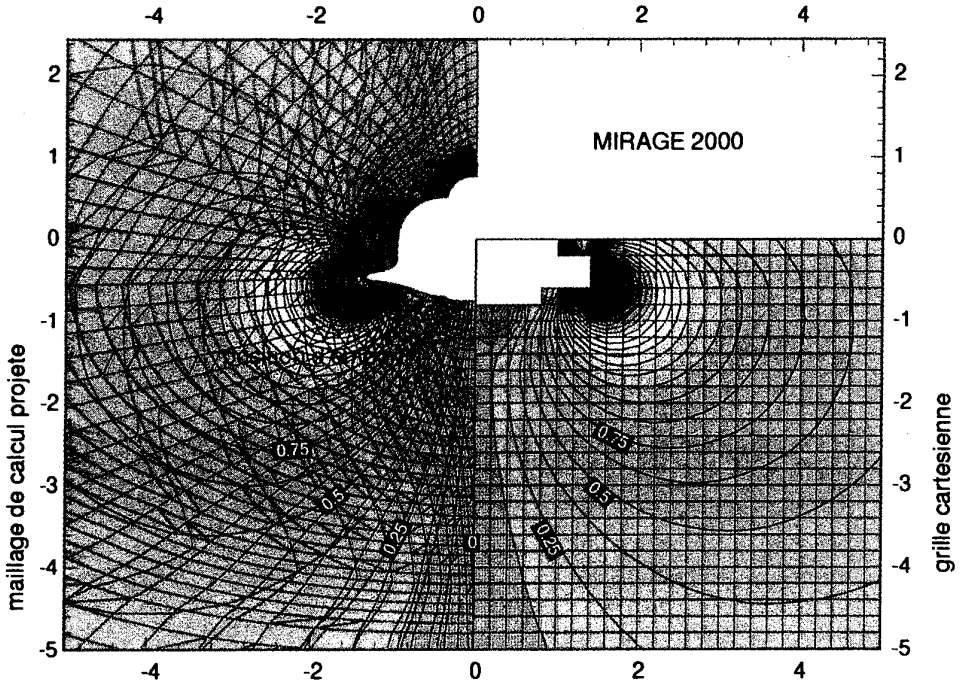

Figure 3b : Angle de dérapage de la vitesse de perturbation .

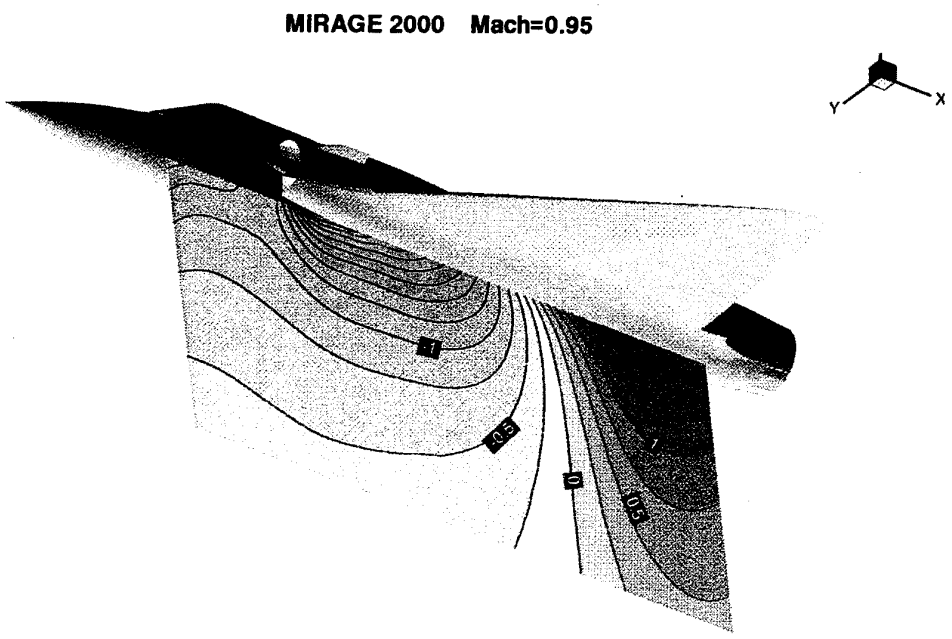

Figure 4a : Incidences locales : iso-α dans le plan d'éjection du missile.

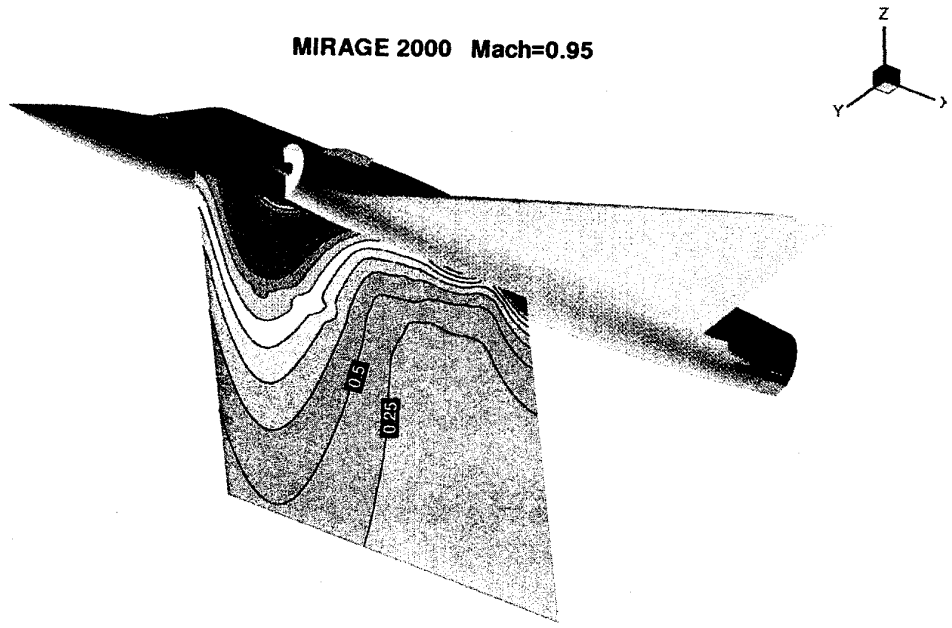

Figure 4b : Incidences locales : niveaux de perturbation en moment dans le plan d'éjection du missile.

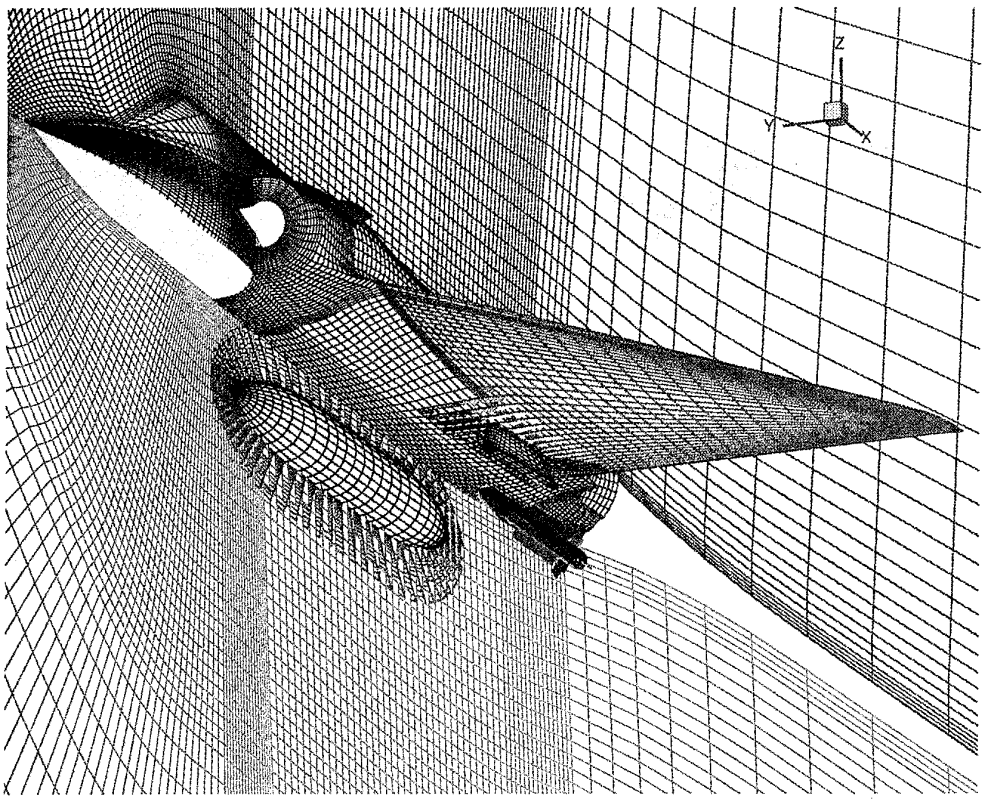

Figure 5a : Maillage chimère composé de quatre maillages distincts : MIRAGE2000, MICA, bidon, pylone.

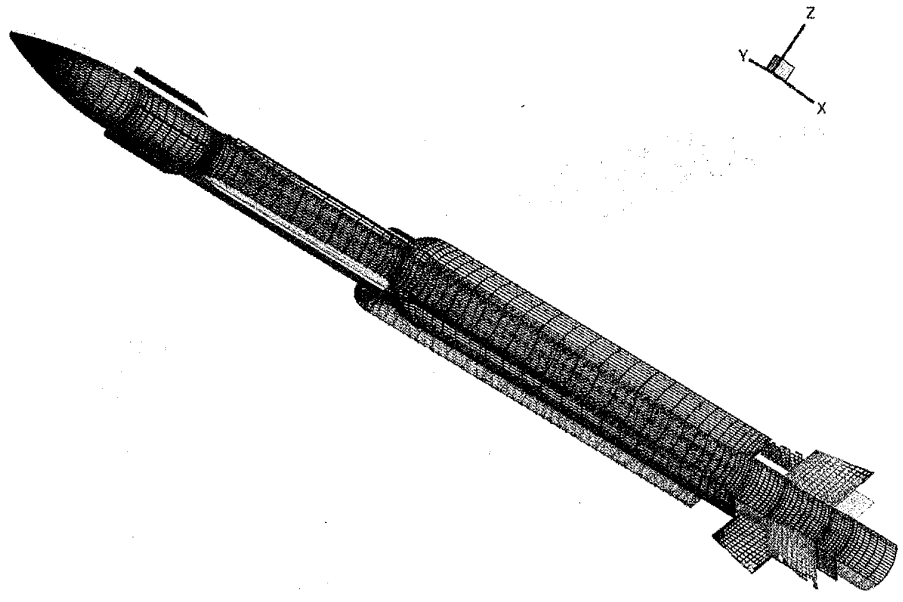

Figure 5b : Maillage du MICA utilisé notamment dans les calculs chimère.

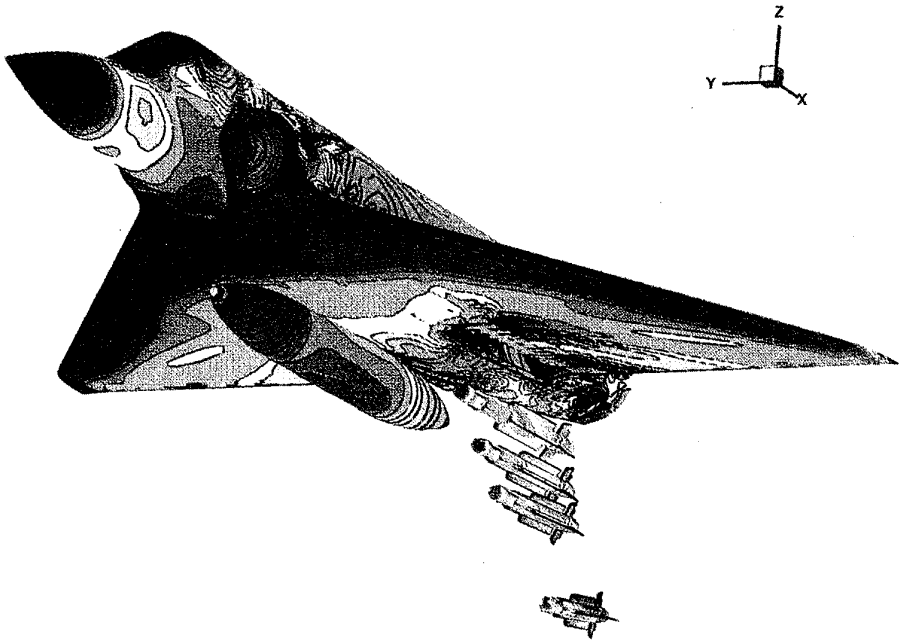

Figure 6a : Calcul chimère : résultat pour quatre positions relatives MICA / MIRAGE 2000.

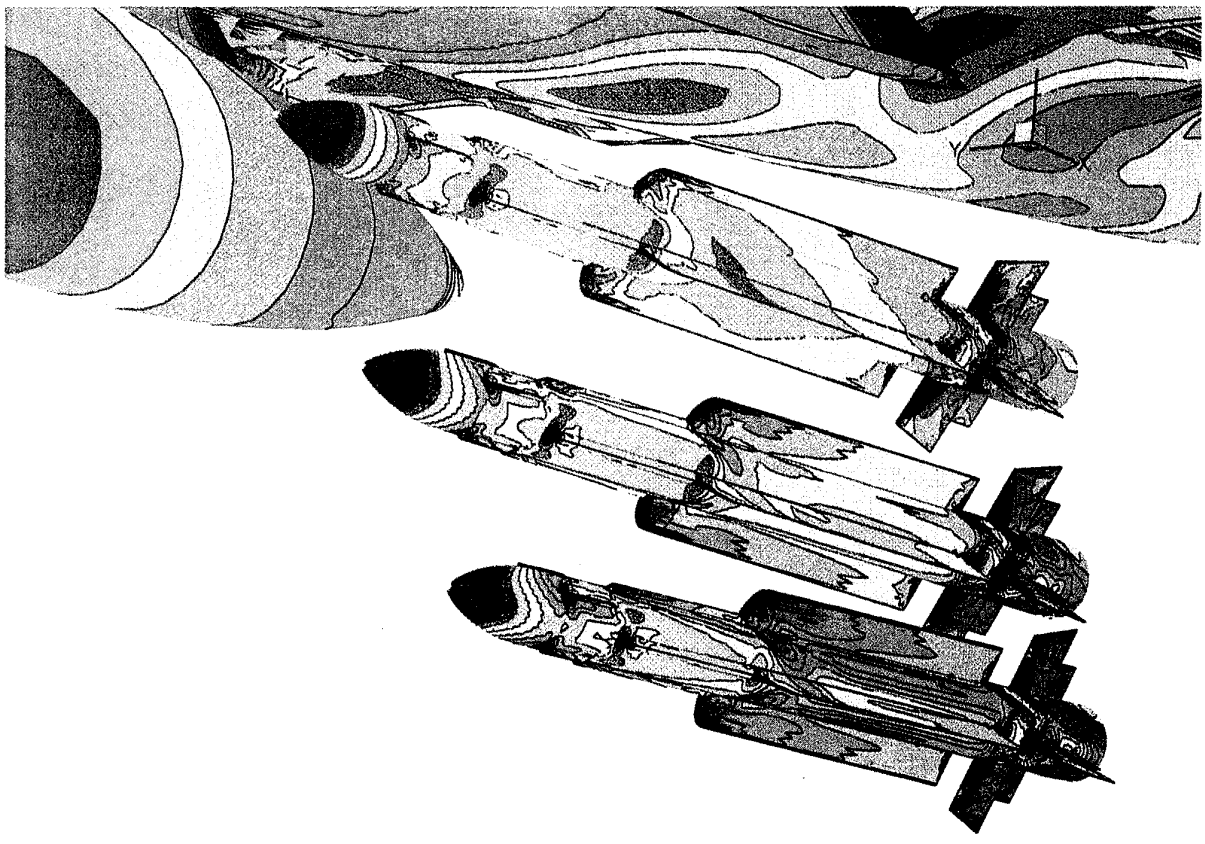

Figure 6b : Calcul chimère : détail de la répartition de pression sur le MICA pour trois positions relatives.

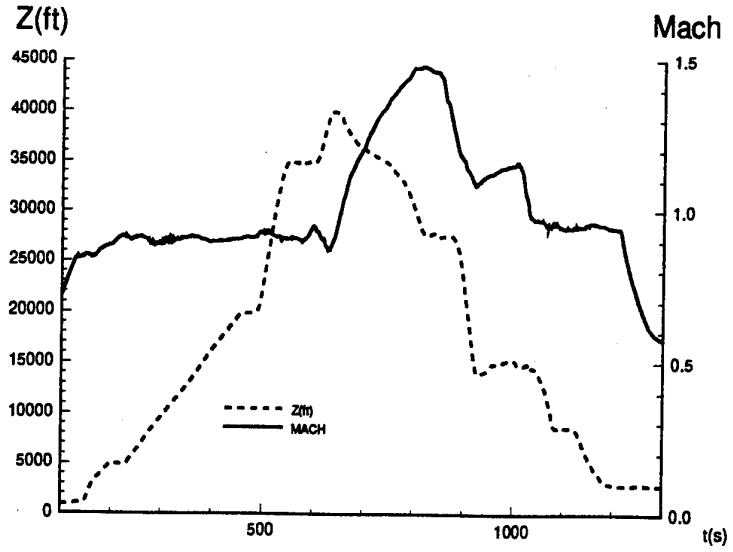

Figure 7a : profil du vol.

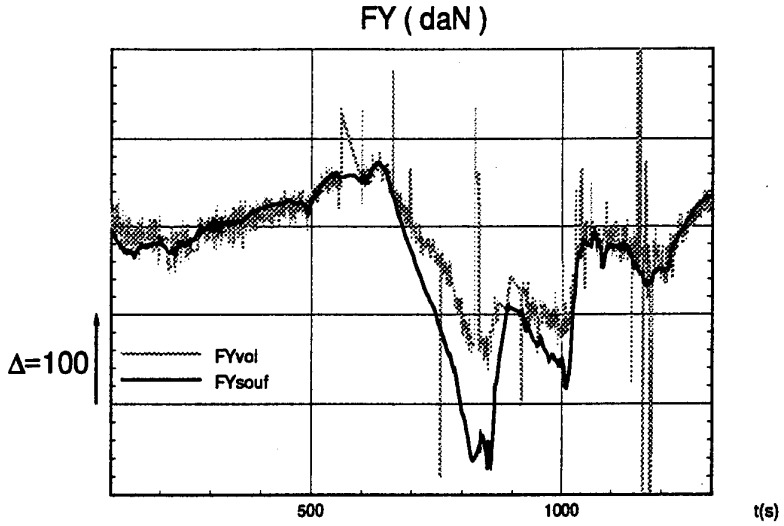

Figure 7b

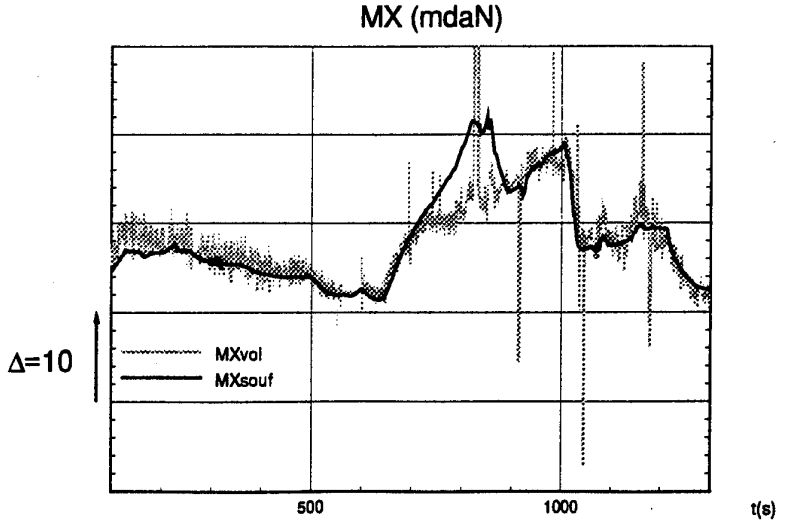

Figure 7c

Figures 7b à 7c : Efforts sur le MICA en emport.

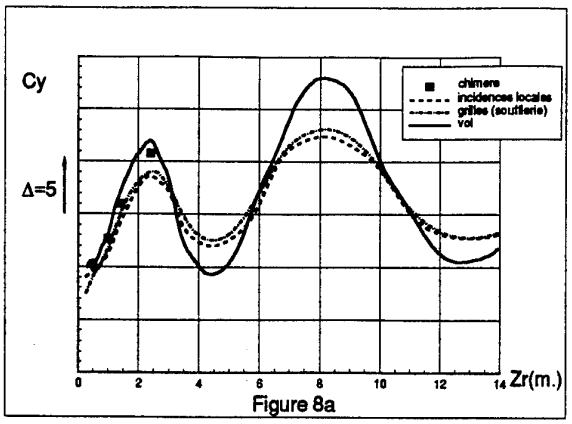

Figure 8a

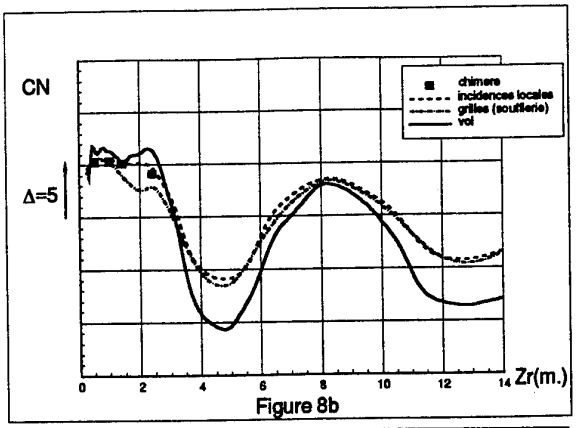

Figure 8b

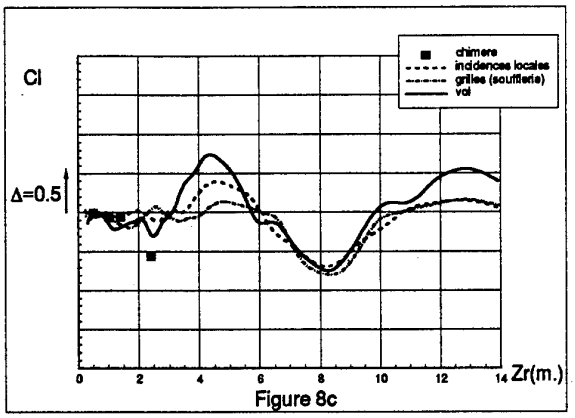

Figure 8c

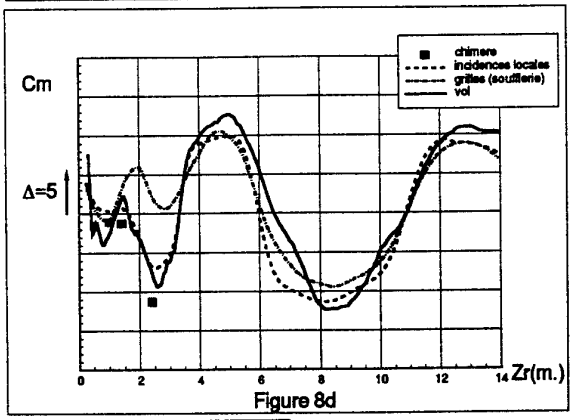

Figure 8d

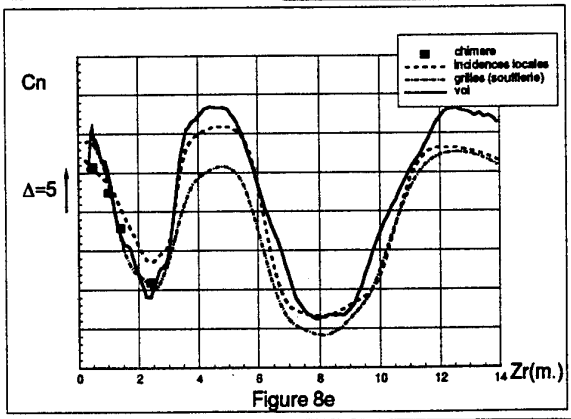

Figure 8e

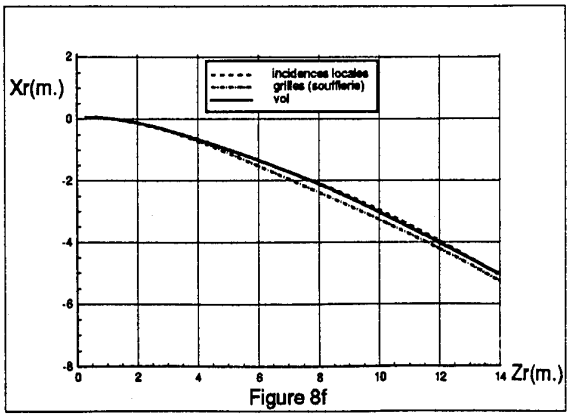

Figure 8f

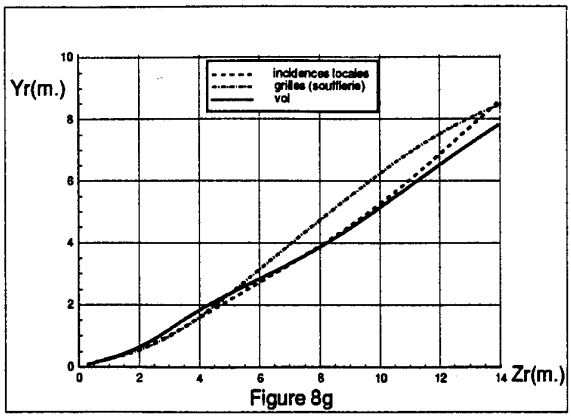

Figure 8g

Figures 8a à 8e : Coefficients aérodynamiques du MICA restitués en boucle ouverte.

Figures 8f et 8g : trajectoire calculée en boucle fermée.

Theoretical Prediction of Store Release Trajectory using the FAME Method

T A Blaylock
Low Speed and Basic Aerodynamics Dept.
Aircraft Sector
Defence Research Agency
Farnborough GU14 6TD
United Kingdom

ABSTRACT

A method is described for generating surface and field meshes around complex configurations. The method, known as FAME (Feature-Associated Mesh Embedding) combines a high degree of automation and ease of use with precise control over mesh quality. The extension of the method to deal with configurations with components in relative motion is described. Euler flow results, at a transonic Mach number and at two different angles of incidence, are presented for a store released from a cluster of three beneath a wing.

1 INTRODUCTION

Theoretical prediction methods for store release trajectory currently in routine use are singularity based methods such as RAENEAR and TSPARV(Refs [1] and [2]). Such methods suffer from limited accuracy, especially at high subsonic speeds, so there is a requirement for methods which solve the Euler or Navier-Stokes equations, necessitating the generation of a computational field mesh.

The generation of a good quality computational mesh for a complex configuration with fixed stores is itself a difficult exercise, requiring considerable user expertise and/or many man-weeks to obtain meshes of even modest quality. Allowing relative movement of parts of the configuration adds a further level of complication.

The use of conventional structured-mesh methods on a configuration with closely-coupled stores is difficult and error prone. Furthermore, allowing a store to move requires remeshing after each movement. The cost of this can be prohibitive.

Unstructured-mesh methods are relatively easy to use but mesh quality is not easily controllable and accuracy may fall short of requirements. More seriously, the use of inviscid flow solvers results in errors in forces, moments and velocities and hence the trajectory of a released store so the ultimate goal is a prediction method for viscous flows. Unstructured meshes are a poor choice for resolving thin shear layers.

The FAME method uses a composite, overlapping approach to mesh generation. It employs structured curvilinear surface-aligned meshes of limited field extent adjacent to solid surfaces and close to the far field boundary. All these meshes overlie a rectangular background mesh that covers the whole field and whose density varies across the field through embedding. Communication of flow data takes place between meshes where they overlap. The use of overlapping meshes effectively enables one to decouple the computational mesh for the fixed part of a configuration from the mesh for the moving part (subsequently referred to as the store). This enables the existing Euler flow solver to be used with the minimum of modification. In addition, the surface-aligned meshes for the store simply undergo rigid-body motion. Any remeshing which is required takes place locally on the rectangular background mesh and takes place to ensure that compatibility of mesh density is preserved at overlap.

The use of structured meshes close to solid surfaces also enables the straightforward incorporation of a Navier-Stokes flow algorithm: this work is in the initial development phase.

A brief description of the FAME method for fixed meshes is given in Section 2. Section 3 contains a description of the extension of FAME to moving mesh problems and a description of the process of performing a store trajectory calculation. Some results and conclusions are presented in Sections 4 and 5.

The work described here has been supported jointly by DTI(FG11K064) and MOD(AS011B12).

2 THE FAME METHOD FOR FIXED MESHES

2.1 Mesh generation

Only a brief description of the FAME method is given here. For a fuller description the reader is referred to Refs [3] and [4].

Curvilinear surface-aligned meshes are employed in regions of the field adjacent to solid surfaces and close to the far-field boundary. All these meshes overlie a rectangular background mesh that covers the whole field and whose density varies through embedding. Each curvilinear mesh is associated with and is aligned locally to one or more elementary geometric features of the configuration. Geometric features are of three types: a surface, a line of intersection of two surfaces (this includes a line in a single surface across which the surface normal is discontinuous - e.g. a wing trailing edge), and the point of intersection of three surfaces. Most configurations can be decomposed into a set of such elementary features. From a distribution of mesh points on each geometric surface, meshes are generated in the field (but with limited field extent) by simple algebraic means. The topology of each mesh is automatically determined by the geometric feature or features with which it is aligned. Features and their associated meshes fit naturally into a hierarchy, which is described in Ref [4].

With all the curvilinear meshes in place and with correct communication lines established, the background rectangular mesh which will subsequently be referred to as the type-0 mesh (see Ref [3]) is generated. This takes place automatically by successive local refinement by a factor of two in each coordinate direction until the density of the background mesh is similar (within a factor of two)

to the density of the curvilinear meshes where they overlap. The type-0 mesh consists of 'blocks' of nxnxn cells (where n is usually 4) so that all cells are cubes.

Fig 1 shows a close-up of the nose region of a body with its associated curvilinear mesh and the background mesh in the region of the body. Blocks of fine mesh are generated at the nose where the curvilinear mesh is finest. The change in type-0 mesh density is apparent as we move away from the solid surface.

For the purposes of this paper, only a subset of the range of mesh topologies in the FAME mesh hierarchy will be illustrated. Fig 2 shows selected coordinate surfaces of curvilinear meshes on a BL755 bomb together with sections through the rectangular background mesh. The bomb consists of five components: the body and four fins. Applying the FAME strategy, each of these components has its own mesh. For the body a simple mesh of O-O topology, known as a type-1 mesh, is used. The mesh extends only a few intervals into the field since its task is to facilitate the implementation of the solid surface boundary condition. Mesh quality, and hence flow solution quality, is compromised if a mesh is constrained to be aligned to several components of a configuration. Here it can be seen that the type-1 mesh has been generated without concession to the presence of the fins. For each fin a mesh of H-H topology, known as a type-1.5 mesh, is generated. The H-H topology gives good quality meshes on fins with sharp edges. Each type-1.5 mesh is also aligned to parts of the bomb body. This alignment ensures that the fin-fuselage junction region has a suitable mesh. Each type-1.5 mesh needs to extend only a few intervals into the field. The physical extent of the meshes into the field is a function of surface mesh density. However, some concession to the presence of other meshes is required where the type-1 and type-1.5 meshes overlap and here it is necessary to control the extent of the meshes so that compatibility of mesh density is achieved.

2.2 Inter-mesh communication

The embedding process automatically establishes the correct communication between the background mesh and all the curvilinear meshes that overlie it. Referring again to Fig 1, all type-0 points which lie within the curvilinear coordinate surface two cells in from the outer boundary are flagged to indicate that no flow data are held there. Points adjacent to these are flagged so that flow data are obtained by interpolation from the curvilinear mesh. The density of the mesh is automatically determined so that such points lie within a cell of the curvilinear mesh, thus guaranteeing that interpolation is always possible. Fig 2 serves to illustrate the other types of inter-mesh communication which take place, as it shows a close-up of the fin-body junction region. The type-1 and type-1.5 meshes overlap forward and rearward of each fin, and above and below each fin. The overlap regions allow flow data to be interpolated between meshes. Since the mesh communication is a two way process minimisation of the interpolation error is achieved by ensuring that both meshes have similar point densities where they overlap.

Points on the type-1 mesh having an incomplete stencil obtain data from the overlying type-1.5 mesh. All the curvilinear surface-aligned meshes have incomplete computational stencils at their outer boundary. These points obtain flow data by interpolation from the highest available mesh in the hierarchy. In this case the type-1 mesh obtains some outer boundary data from the type-1.5 meshes and some from the type-0 mesh, whilst the type-1.5 meshes obtain some outer boundary data from the type-1 mesh and some from the type-0 mesh.

2.3 The Euler flow algorithm

The Euler equations are solved in quasi-linear form. The formulation of the algorithm, Ref [5], has the following set of dependent variables: A, u, v, w and S, where A is a function of the speed of sound, c, given by $A=2c/(\gamma-1)$, γ is the ratio of specific heats, S is entropy and u, v and w are the velocity components in the x, y and z directions respectively. At present, the formulation is restricted to homentropic flow. The equations are discretised using the Split Coefficient Matrix method, Ref [6]. The equations are solved using Euler explicit time stepping. The formulation is upwind and the use of first-order differences leads to a compact stencil with robust treatment at the boundaries. The far field boundary conditions are implemented trivially by specifying all undisturbed stream quantities on the boundary, and allowing the upwind algorithm to select those that it needs according to the sign of each wave speed. Internal boundary conditions (between meshes) are treated similarly in that all flow quantities are interpolated from one mesh to another, thus leaving the algorithm to make its own selection. The procedure for solid-surface conditions is more complex but is still consistent with local wave propagation arguments. Second-order spatial accuracy in the steady-state is achieved by the use of a defect-correction scheme.

A more detailed description of the flow algorithm is given in Ref [4].

3 EXTENSION OF FAME TO MOVING MESHES

3.1 Mesh generation

Meshing and remeshing of components in relative motion is achieved efficiently by splitting the initial generation of the type-0 background mesh into two stages. At the first stage, which is performed only once for an entire trajectory calculation, blocks of finer mesh are generated to achieve comparability of mesh density to the fixed curvilinear meshes. At the second stage blocks of finer mesh are generated in response to the moving store meshes. Figs 3 and 4 illustrate the two stages. They show a cluster of three BL755 bombs located beneath a wing. In Fig 3, finer blocks have been generated in response to the wing and the two upper bombs. In Fig 4 additional type-0 blocks have been generated in response to the lower bomb. In Fig 5 the lower bomb has moved. The additional type-0 blocks (Fig 4) have been removed and the second stage has been repeated in response to the new position of the bomb.

3.2 The Flow algorithm for moving meshes

As explained in Section 2.2, at each iteration of the flow solver flow variables are updated on the outer boundary of a surface aligned mesh by interpolation. For a moving mesh, where this interpolation takes place from the type-0 mesh (which is fixed), the Cartesian velocity components of each outer boundary mesh point are simply subtracted from the interpolated values. In this way we obtain convergence to a quasi-steady solution in which account is taken of the instantaneous velocity of the store.

3.3 Calculation of the store trajectory

The trajectory of the released store is calculated using a program which is based on a grid loads method (Ref [7]). In the original program, the store motion is calculated by numerically integrating a particular formulation of the rigid body equations. Aerodynamic effects are incorporated by interpolating on appropriately prescribed data grids.

Here, as described above, a quasi-steady flow solution is obtained for the current instantaneous position and velocity of the store. Aerodynamic forces and moments are obtained by integrating over the surface of the store. The trajectory code uses these, together with the inertial characteristics of the store, to calculate the position, orientation and velocity (linear and angular) of the released store after a prescribed time. Using this information:

(i) the position of each store mesh point is calculated and used in the next pass through the mesh generation program;
(ii) the velocity of each outer boundary mesh point of the store is calculated and used in the next pass through the flow solver;
(iii) the current store position and velocity are used, together with aerodynamic forces calculated in the next pass through the flow solver, as input for the next pass through the trajectory program.

The entire process is summarised in the flow chart, Fig 6.

4 RESULTS

Results obtained on the test configuration are for a free stream Mach number of 0.85 at angles of incidence of 0.0° and 8.0°.

For the zero incidence case, Figs 7, 8 and 9 show shaded pressure contours on two planes, one of constant x and the other the vertical plane through the nose and tail of the released store. In Fig 7 the lower store is in its initial unreleased position. The position of the nose stagnation point and the strength of the lower shock indicate that the onset flow has been diverted by the presence of the wing and the other stores, effectively setting the lower store at negative incidence. The lift force generated is small and negative. The increased suction on the lower surface near the nose, coupled with the large region of high suction on the upper surface near the tail, give the store a nose-down attitude on release. After 0.05 seconds, Fig 8, the nose-down attitude is apparent. After 0.15 seconds, Fig 9, the nose- down attitude is more pronounced. The shock below the nose has increased in strength and there is still a fairly large region of high suction above the tail region. The pitching moment continues to increase in magnitude.

At 8.0° incidence, prior to release, Fig 10, the lower store is now effectively at small positive incidence to the onset flow. The pitching moment is still nose down, but much smaller in magnitude. The lift force generated is now positive, C_Z=0.018. 0.1 seconds after release, Fig 11, the store has risen slightly and has pitched nose down. The effective incidence has decreased by about 0.8°, the calculated lift has decreased, C_Z=0.007, and the pitching moment has increased in magnitude. After 0.15 seconds, Fig 12, while the centre of mass of the store has risen a little, the nose has tilted down another 9°. The large decrease in effective incidence gives rise to a stronger lower nose shock, while the region of high suction above the tail is still present. The calculated lift force is now negative, C_Z=-0.008 and the store is starting to drop away. The store is also moving to starboard and backwards and has yawed about 5° from its initial position. After 0.2 seconds, Fig 13, the store attitude is now about 18° from its initial position. The down-force on the store continues to increase but the pitching moment is now positive. In Fig 14 we see that after 0.25 seconds the store continues to pitch nose-down: the effect of the positive pitching moment has been merely to decrease the angular velocity of the store. Another view of the store, not shown here, indicates that the fins are passing dangerously close to those of the inboard upper store. After 0.3 seconds, Fig 15, the fins have cleared the upper store. The pitching moment is still increasing but recovery from the nose-down attitude remains slow.

5 CONCLUSIONS

The extension of the FAME system to the treatment of components of a complex configuration in relative motion is still at an early stage of development but the capability of the method has been adequately demonstrated here. It has been possible to obtain quasi-steady flow solutions with a minimum of modification to a conventional Euler solver. To establish confidence, initial evaluation of the method will involve its application to standard test cases so that results can be compared with those of existing methods.

The incorporation of a Navier-Stokes flow algorithm (which will ultimately be time-accurate) is currently under way. This will enable more accurate computation of the forces and moments acting on a released store. Some meaningful comparison can then be made with experimental results from the limited number of test cases available.

The moving mesh capability can be extended to flow-feature-aligned meshes, thus providing the mechanism for efficient 'directional' mesh refinement that is so difficult to achieve with most mesh generation or adaptation methods.

REFERENCES

[1] M.B.Wood, 'RAENEAR Users Guide', DRA AP6/2/92, WAIS Note 241, April 1992.

[2] J.A.H.Petrie, 'Running the B.Ae. Brough Trajectory System - TSPARV', B.Ae. Brough Note YAD 5115, December 1985.

[3] C.M.Albone, 'Embedded Meshes of Controllable Quality Synthesised from Elementary Geometric Features', AIAA Paper No.92-0662, 1992.

[4] T.A.Blaylock, S.H.Onslow, and C.M.Albone, 'Mesh Generation and Flow Solution for Complex Configurations Using the FAME System', Recent Developments and Applications in Aeronautical CFD, Royal Aeronautical Society, 1993.

[5] C.M.Albone, Private Communication.

[6] S.R.Chakravarthy, D.A.Anderson and M.D.Salas, 'The split-coefficient matrix method for hyberbolic systems of gas-dynamics equations.' AIAA Paper 80-0268, 1980.

[7] G.Robinson, 'A Grid Trajectory Simulation Program.' DRA Report, unpublished.

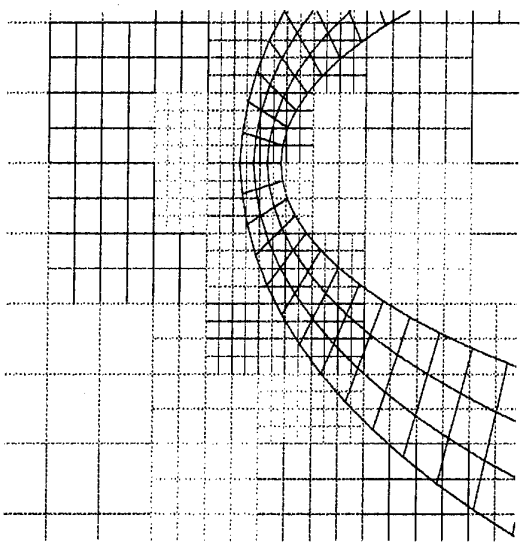

Figure 1. Type–1 and type–0 meshes

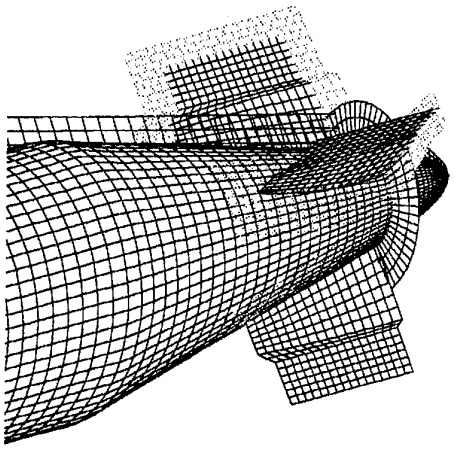

Figure 2. Selected coordinate surfaces of type–1 and type–1.5 meshes showing overlap.

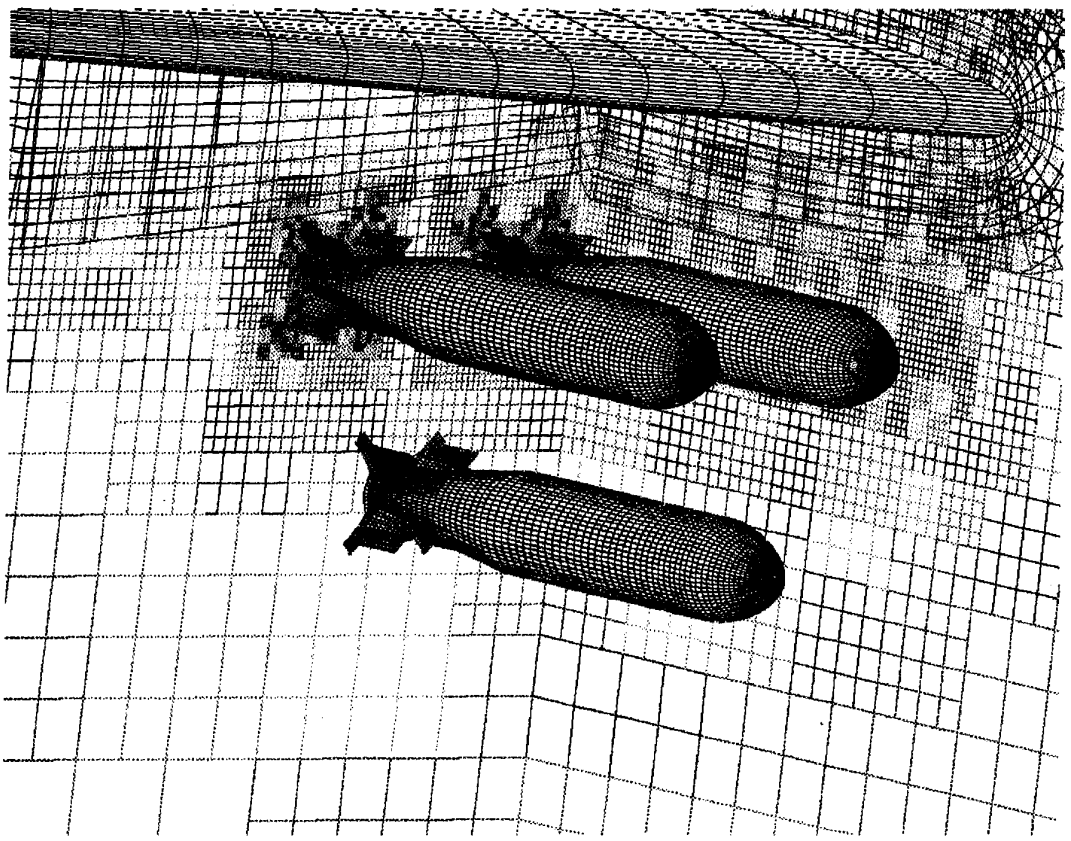

Figure 3. Type–0 blocks generated in response to the fixed meshes of the configuration (wing and upper stores).

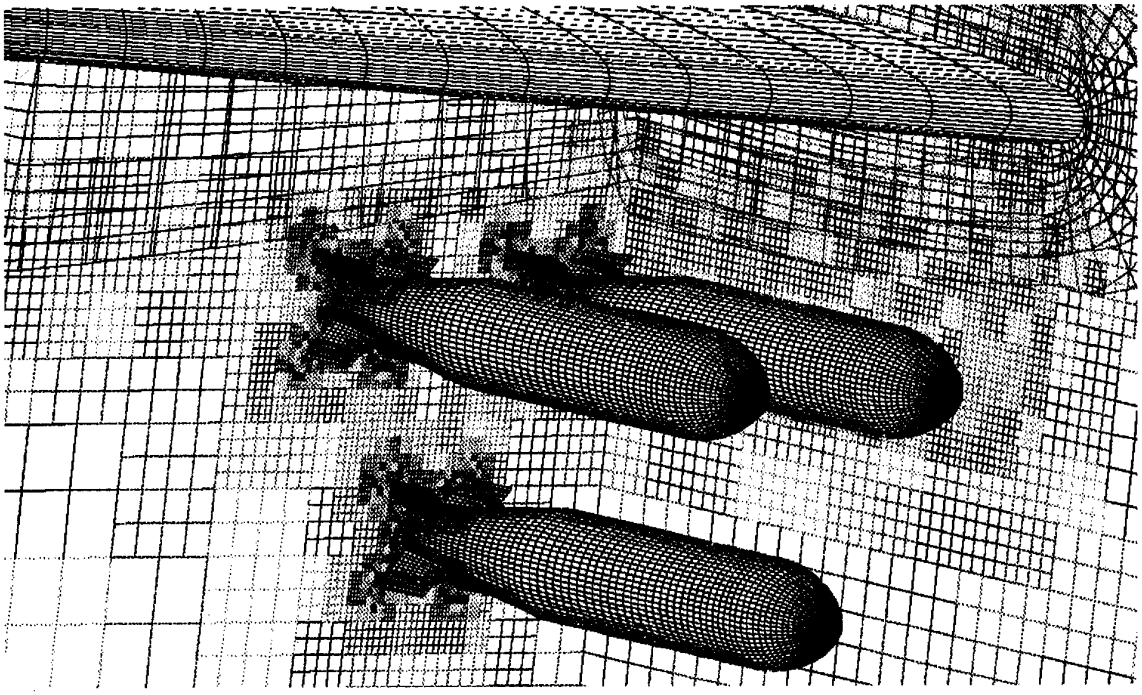

Figure 4. Type–0 blocks generated in response to both fixed and moving components of the configuration.

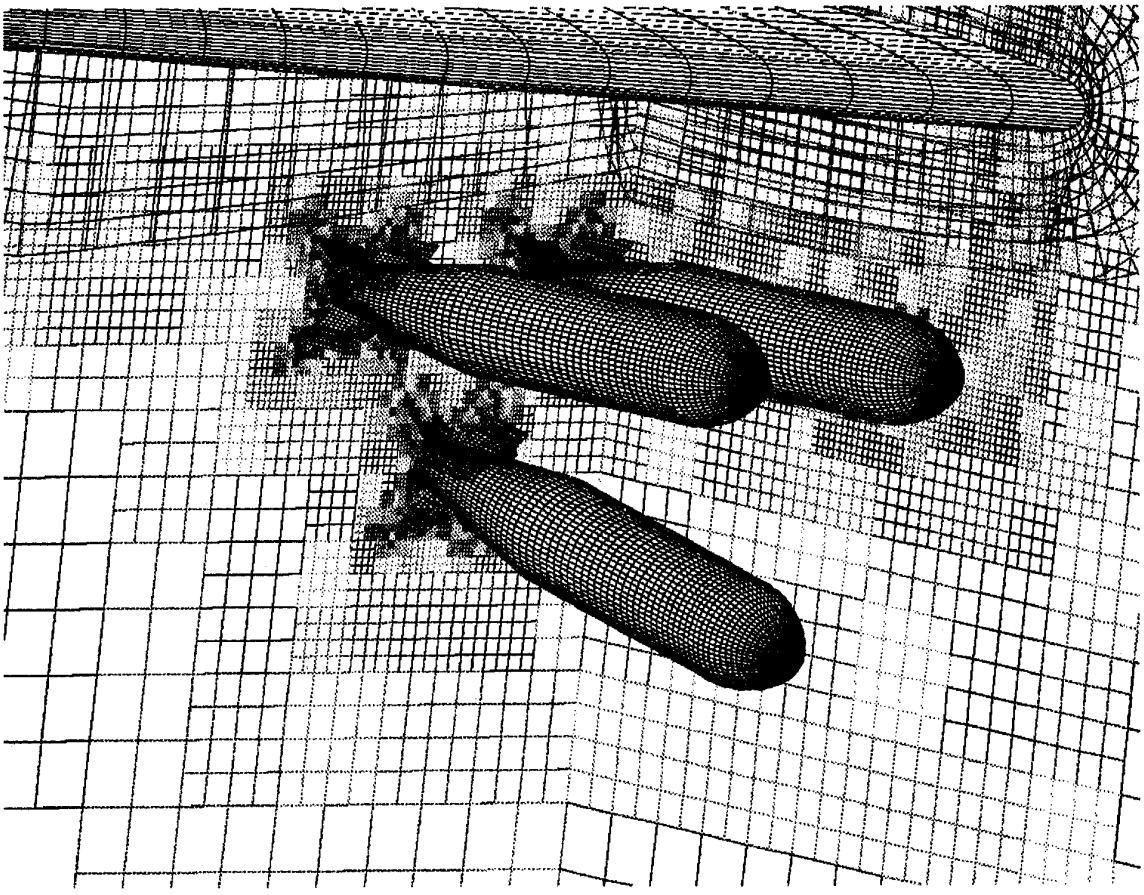

Figure 5. Type–0 blocks generated in response to the new position of the released store.

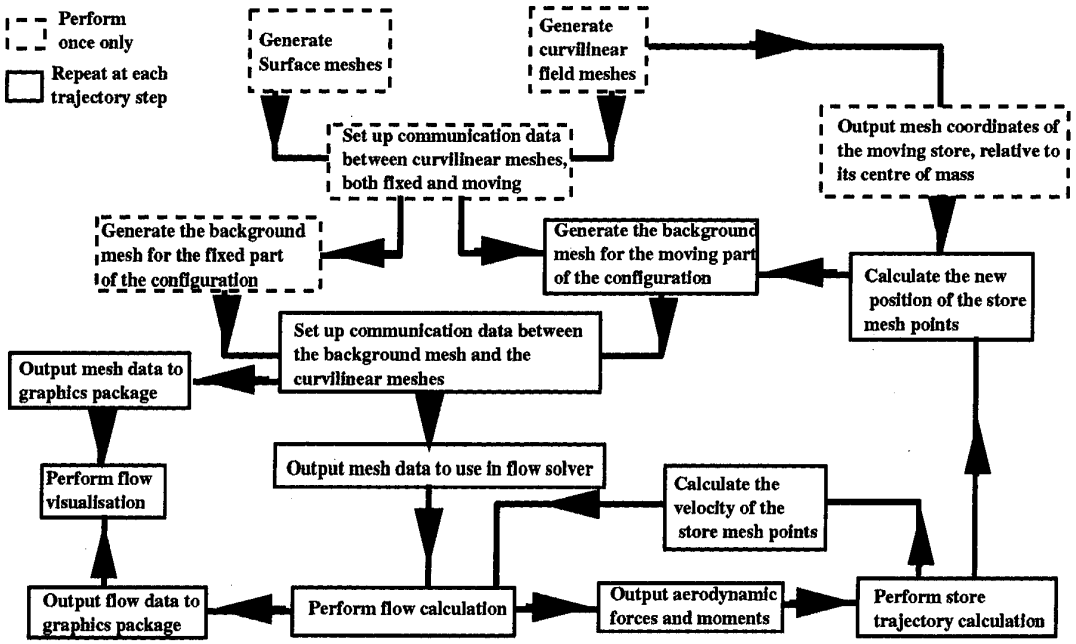

Figure 6. A flowchart of the complete store trajectory simulation process.

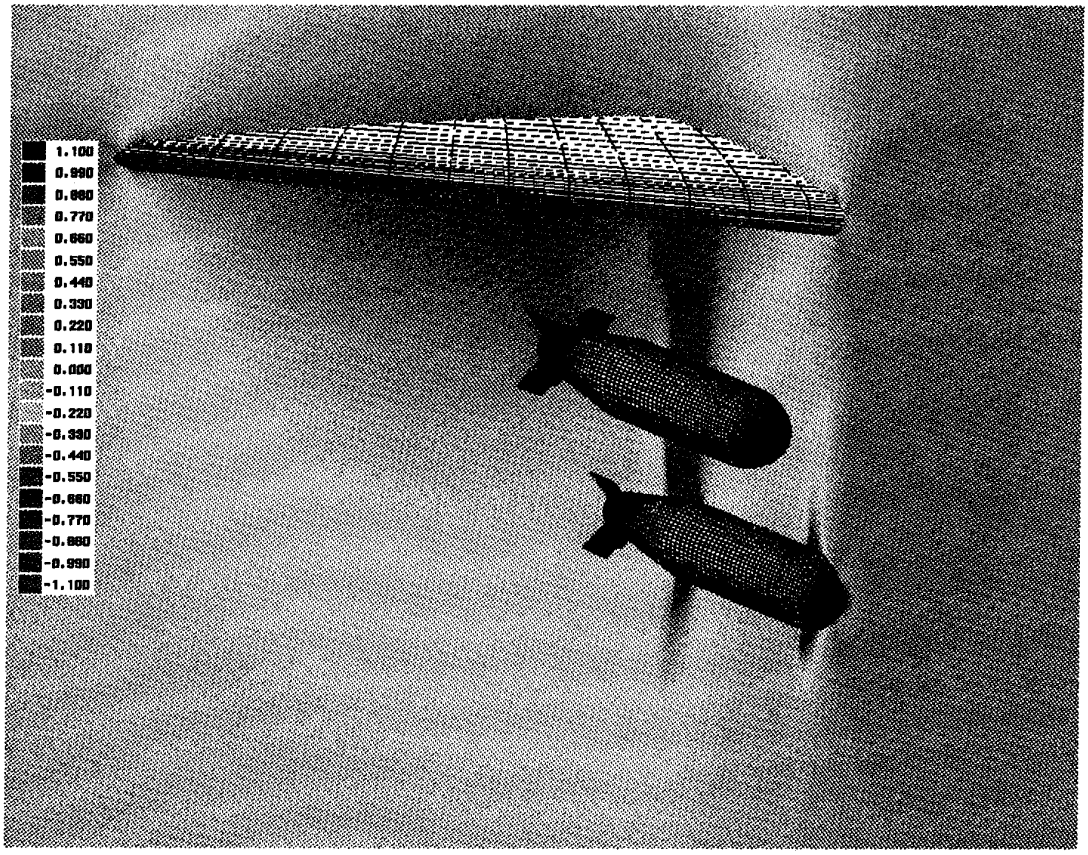

Figure 7. Pressure contours on the vertical plane through the nose and tail of the lower store, and on the plane x=1. M_∞=0.85, α=0.0°.

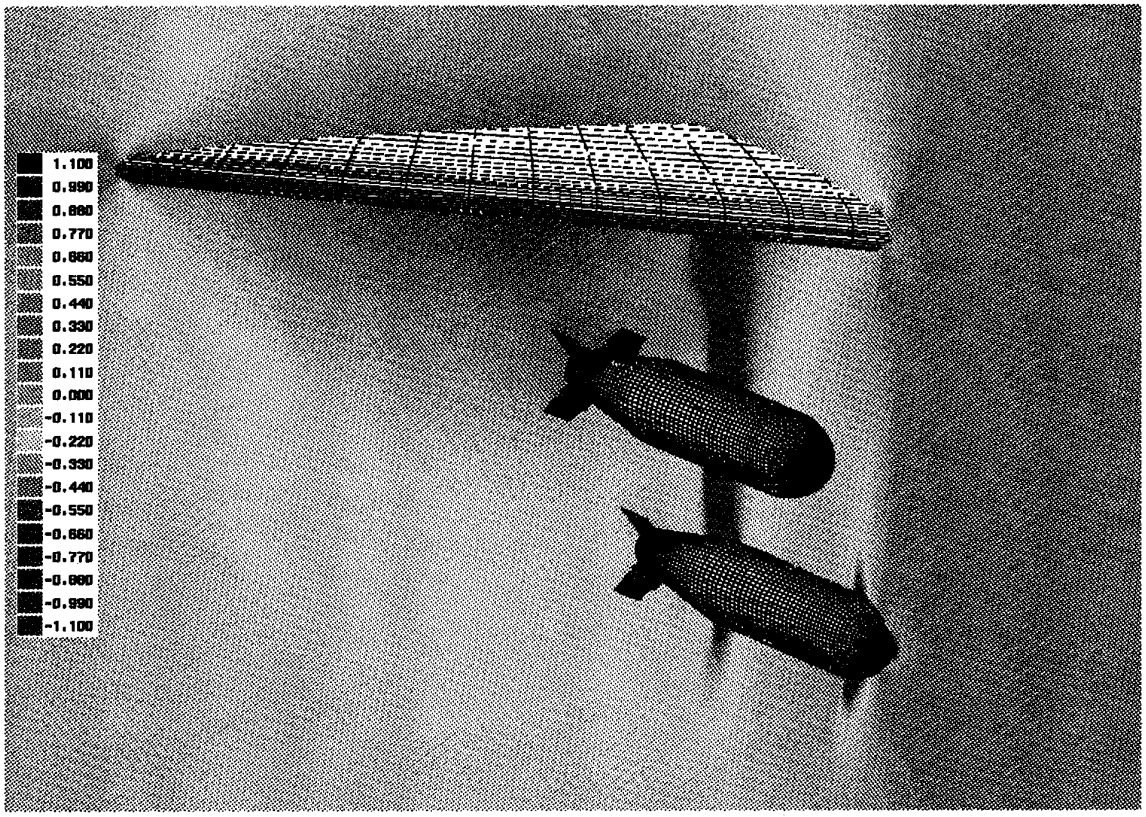

Figure 8. Pressure contours on the vertical plane through the nose and tail of the lower store, and on the plane x=1 (0.05 seconds after release). M_∞=0.85, α=0.0°

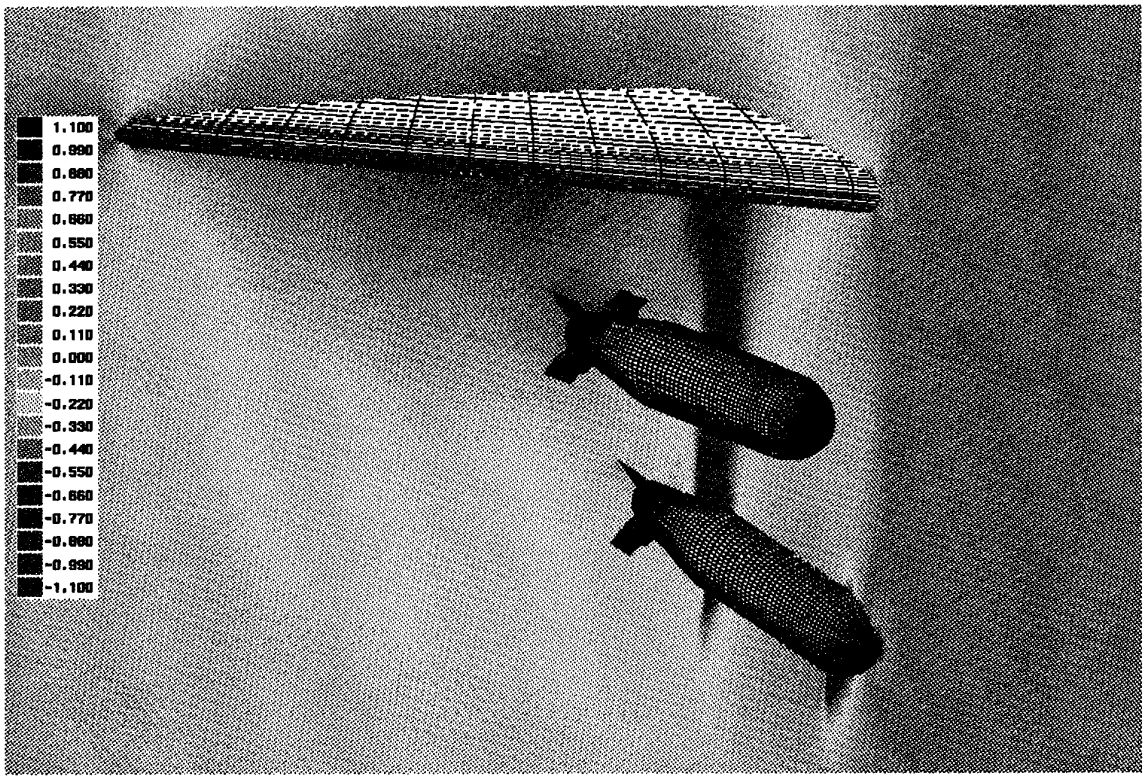

Figure 9. Pressure contours on the vertical plane through the nose and tail of the lower store, and on the plane x=1 (0.15 seconds after release). M_∞=0.85, α=0.0°

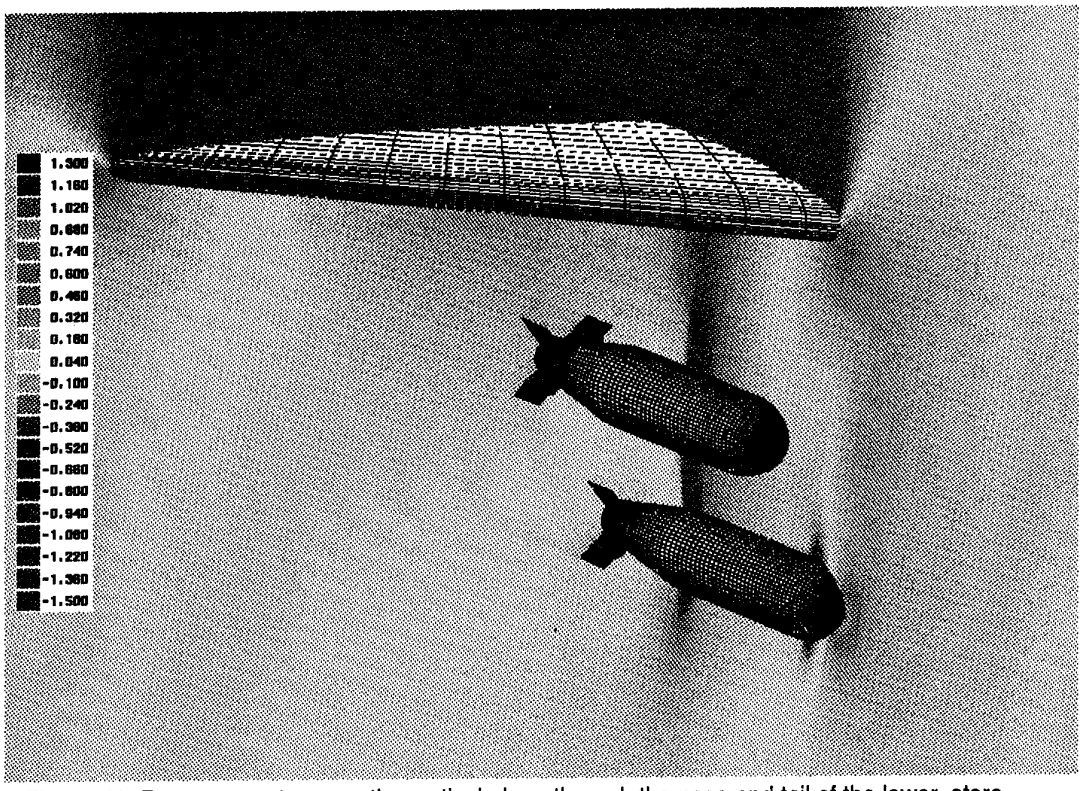

Figure 10. Pressure contours on the vertical plane through the nose and tail of the lower store, and on the plane x=1 (prior to release). M_∞=0.85, α=8.0°

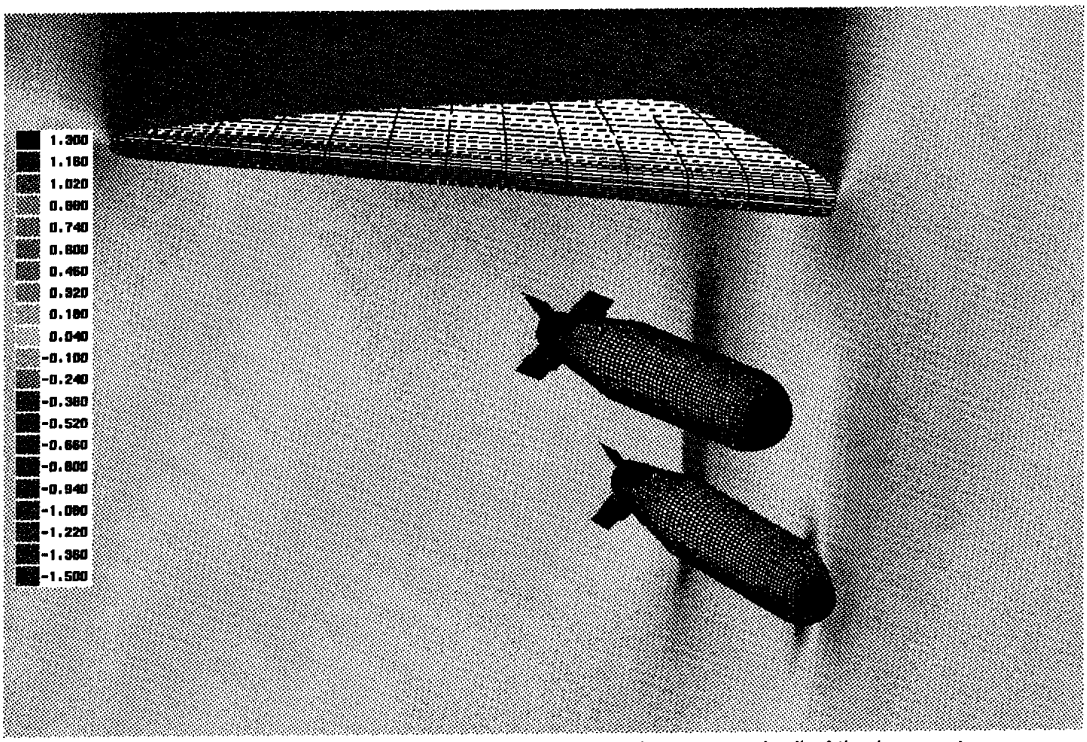

Figure 11. Pressure contours on the vertical plane through the nose and tail of the lower store, and on the plane x=1 (0.1 seconds after release). M_∞=0.85, α=8.0°

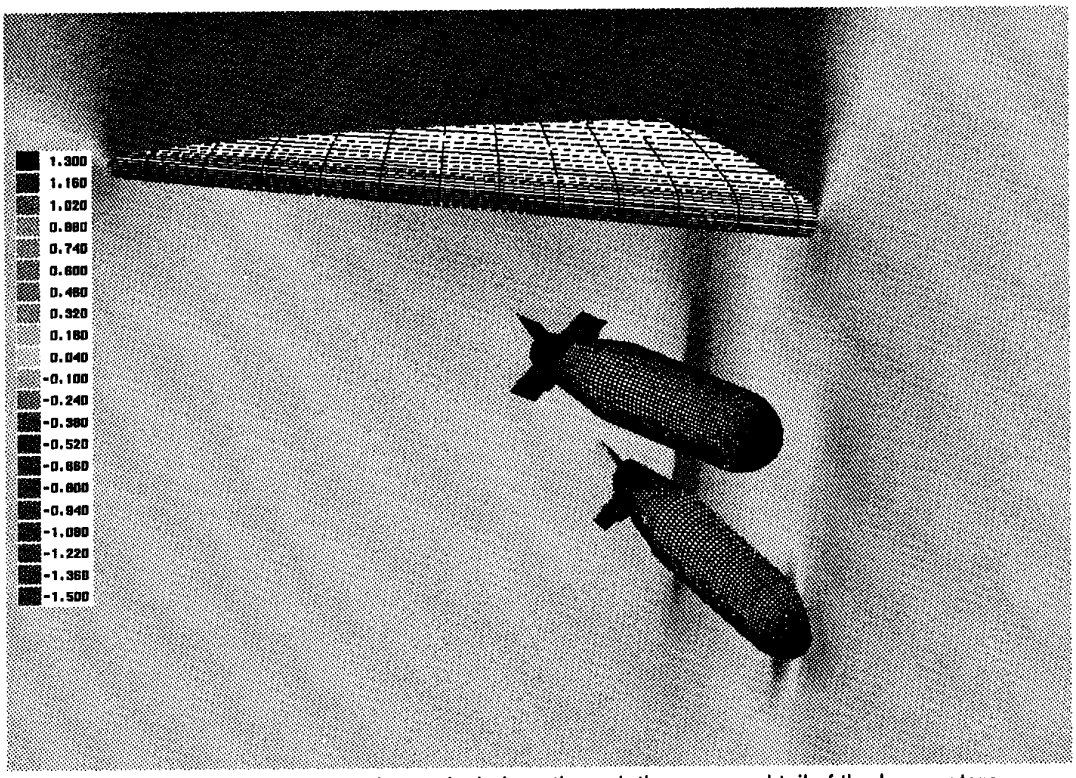

Figure 12. Pressure contours on the vertical plane through the nose and tail of the lower store, and on the plane x=1 (0.15 seconds after release). M_∞=0.85, α=8.0°

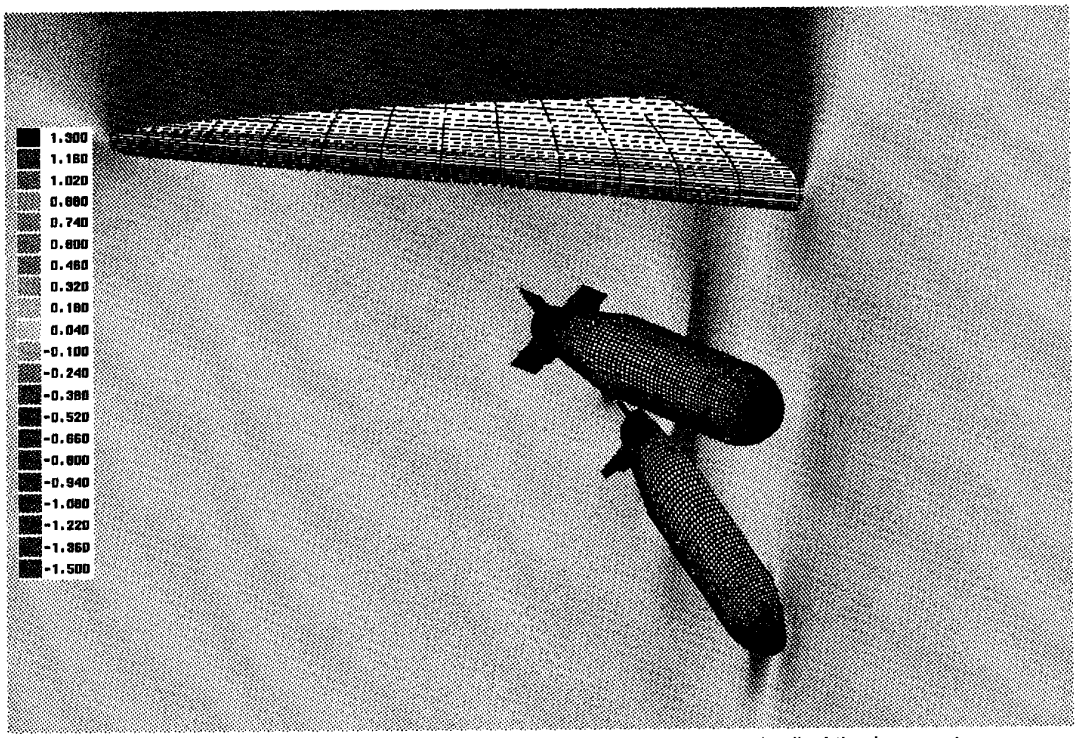

Figure 13. Pressure contours on the vertical plane through the nose and tail of the lower store, and on the plane x=1 (0.2 seconds after release). M_∞=0.85, α=8.0°

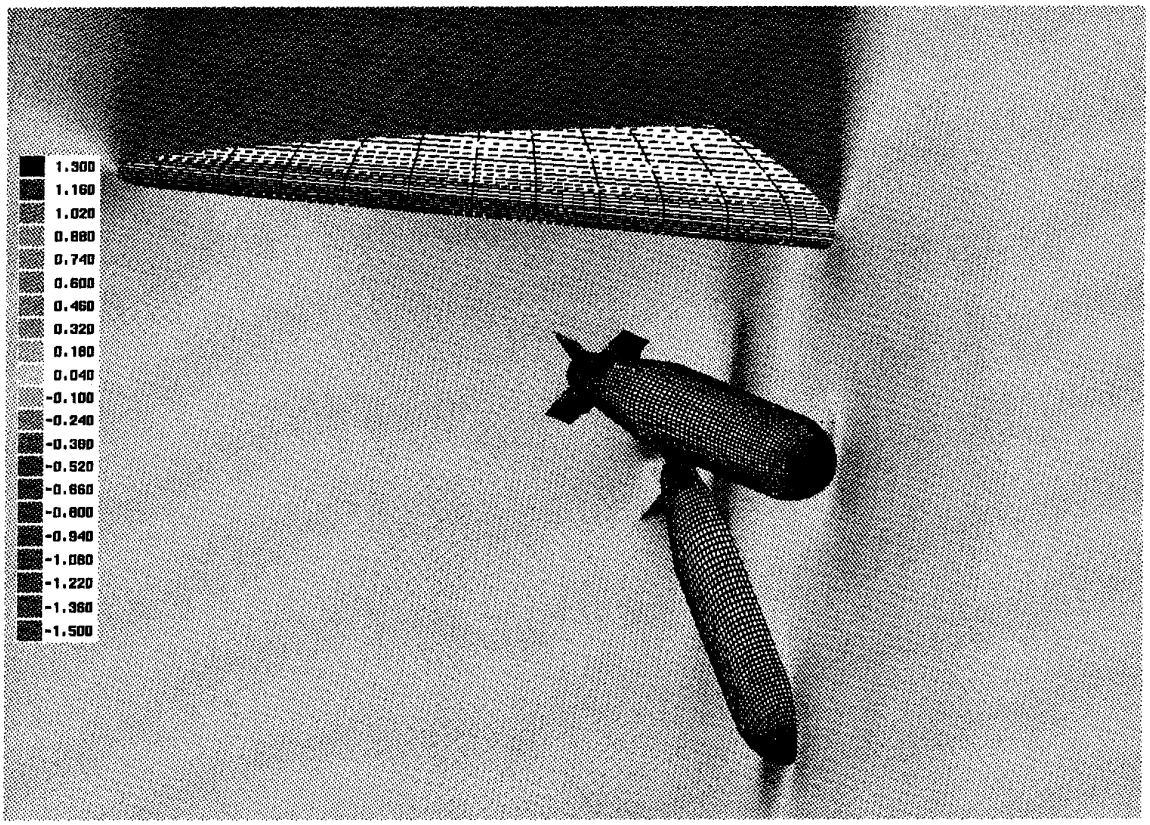

Figure 14. Pressure contours on the vertical plane through the nose and tail of the lower store, and on the plane x=1 (0.25 seconds after release). M_∞=0.85, α=8.0°

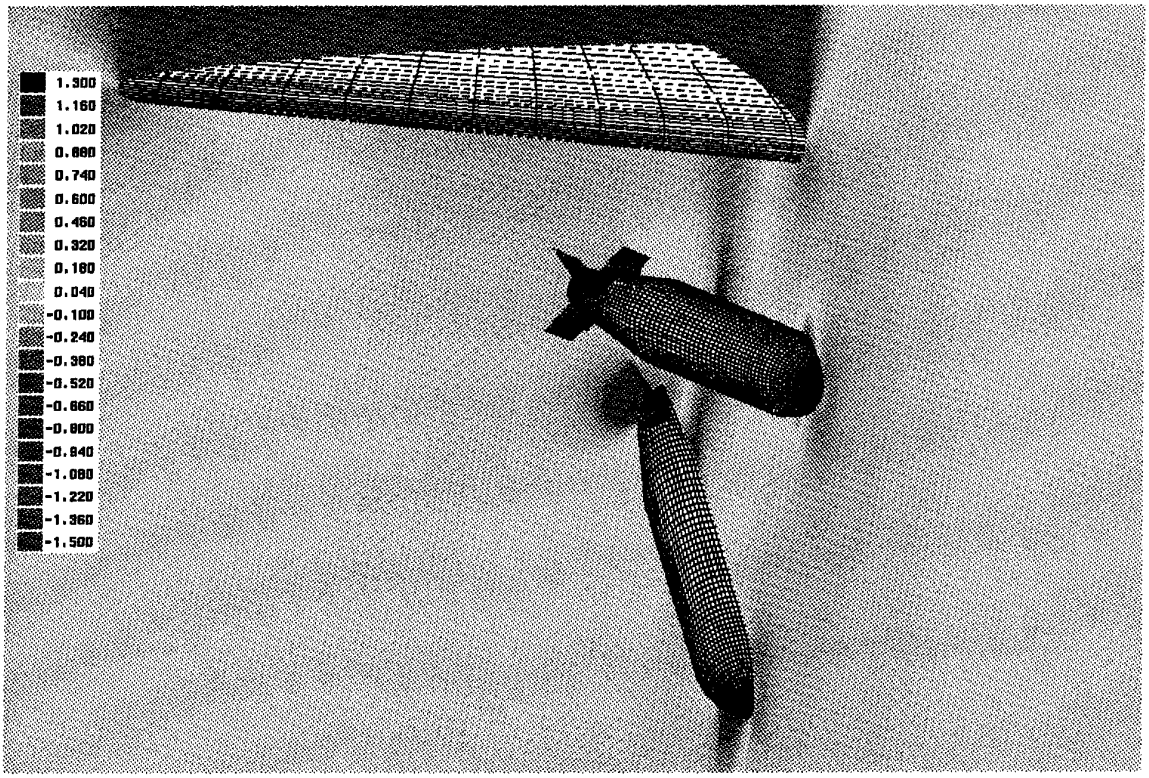

Figure 15. Pressure contours on the vertical plane through the nose and tail of the lower store, and on the plane x=1 (0.3 seconds after release). M_∞=0.85, α=8.0°

AN EVALUATION OF ADVANCED CFD CODES FOR STORES AT INCIDENCE

N. D. SELLARS, I. M. HALL
Aerospace Engineering Department
Victoria University Of Manchester
Manchester, M13 9PL
England.

SUMMARY

Computer codes solving the Euler Equations have been used to calculate the flow around a series of non-circular store bodies at transonic Mach numbers. Where possible Navier-Stokes solutions have been compared with these results. Four different cross-sections have been considered which are formed by gradually transforming a square into a circle by rounding the corners. Each of the stores has a tangent ogive nose. Both the full three dimensional solutions around these stores and the two dimensional crossflow solutions have been investigated.

The particular interest has been in the capability of Euler codes to predict crossflow separation. The results obtained show that for some cases, Euler codes can provide an inexpensive alternative to Navier-Stokes codes for use as an initial design tool.

LIST OF SYMBOLS

E	total energy per unit volume.
F	flux vector.
G	flux vector.
H	total enthalpy.
p	pressure.
q	heat transfer.
$\underline{S}$	surface vector.
t	time.
U	conservative vector.
u	x component of velocity.
v	y component of velocity.
x,y	Cartesian co-ordinates.
α	stores incidence.
α^I	Runge-Kutta coefficient.
ρ	density.
ϕ	store roll angle.
τ	stress tensor.
Ω	cell area.
^{n}	time step reference.
^{t}	matrix transpose.
$_{i,j}$	grid reference.
$_k$	cell side reference.

1. INTRODUCTION

Since the solution of the three-dimensional Navier-Stokes equations is relatively expensive this investigation was undertaken to ascertain whether useful results could be obtained using Euler codes, at least in the initial design stages. The assessment was made by comparison of the results obtained using Euler codes with experiment and where possible with Navier-Stokes results.

For the purpose of this investigation a series of isolated stores was chosen for which experimental results were available. Although this series of bodies is extremely simple, it was thought that the information gained on the capability of the Euler equations for use with isolated bodies could readily be extended for installed stores and stores with fins.

The cross-sections of these stores are illustrated in Figure 1 and are formed by gradually rounding the corners of a square. The ratios of the corner radius to body diameter were 0.5, 0.2, 0.1 and 0.0 with the two extremes being a circle and square respectively. Each store has a tangent ogive nose of slenderness ratio 2 and the overall body has a slenderness ratio of 8. These stores will be designated A-D with the latter having the square cross-section.

This particular series of stores has received attention in the past by Daniel, Yechout and Zollars (1) for low Mach numbers. A large number of wind tunnel tests on these same geometries for both subsonic and transonic Mach numbers has been carried out by British Aerospace, Military Aircraft Division. It has been possible to compare the CFD results with this large database of force and pressure data.

The use of stores with square cross-sections is of interest due to the possible improvements in packing and deployment of submunitions. In addition the side force generated when such a store is rolled allows the possibility of bank-to-turn control of missiles. However, the use of stores with

Paper presented at the AGARD FDP Symposium on "Aerodynamics of Store Integration and Separation", held in Ankara, Turkey from 24-27 April 1995, and published in CP-570.

fully square cross-sections has proved impracticable because of aerodynamic instability caused by sensitivity of the leeside vortices to roll angle. The use of squares modified by rounded corners has therefore been studied in an attempt to combat this instability problem whilst maintaining the obvious military advantages.

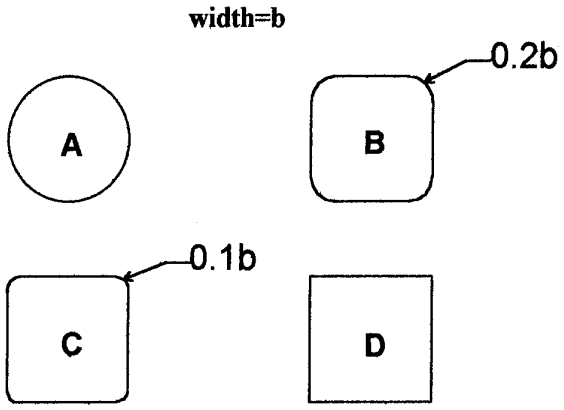

Figure 1: Store Cross-Sections

In the future, the conclusions gained from this research may be applicable to faceted bodies. These bodies are currently receiving interest due to their low Radar cross-section.

Euler codes have been used by several authors to study flows involving separation. The majority of this work has been directed towards the case of leading edge vortices on swept, sharp leading edge wings, as for example in the work of Murman and Rizzi (2). However, the flow about rounded leading edge wings has also been considered by Kandil and Chuang (3). The calculation of the flow about a supersonic tactical missile using four different Euler codes has been performed by Priolo and Wardlaw (4). They found quite good agreement with experimental results for this particular configuration.

In each of the above investigations it has been shown that separation can be predicted using Euler codes (with certain limitations). The authors' have attributed this to the artificial dissipation which is necessary within the codes.

The CFD evaluation was split into two distinct areas;

- a calculation of three dimensional solutions for the full stores geometries
- a two dimensional investigation into the differences found between Euler and Navier-Stokes codes for the solution about the store cross-sections.

The calculation of the three dimensional flow around the stores was performed using four CFD codes available within British Aerospace; namely, MGAERO, FLITE3D, MULTIBLOCK and RAMPANT that are described below in Section 4.

A two dimensional investigation was undertaken to further investigate the phenomenon of Euler separation. This was due to the large amount of time required to obtain three dimensional solutions and the obvious complexity in analysing the solutions.

This two dimensional investigation was originally used to examine the effects of varying artificial dissipation within an Euler code. Later however, time dependent Euler and Navier-Stokes solutions were calculated and compared. The conclusions gained from these comparisons can be extended (at least in principle) to the separated flow over missiles by using the crossflow theory originally proposed by Allen (5).

2. WIND TUNNEL DATA

Wind tunnel tests on the afore mentioned stores have been carried out for incidences up to 20° at Mach Numbers of 0.2 and 0.6-0.95, by British Aerospace, Military Aircraft Division. In addition stores B-D were tested for a number of roll orientations. The Reynolds number for the transonic tests was approximately 0.6×10^6.

This particular incidence range and Reynolds number should result in a fully turbulent boundary layer separation, as shown by the graph of critical Reynolds number boundaries for slender axi-symmetric bodies in Figure 2, due to Poll (6). Nevertheless, a transition band was still affixed near the nose of the stores to ensure a fully turbulent flow before separation

As the incidence range tested was less than twice the nose angle, the leeside vortices were expected to be steady and symmetrical. This assumption is supported by the lack of side force and yawing moment for the unrolled stores.

L-Laminar T-Transitional FT-Fully Turbulent

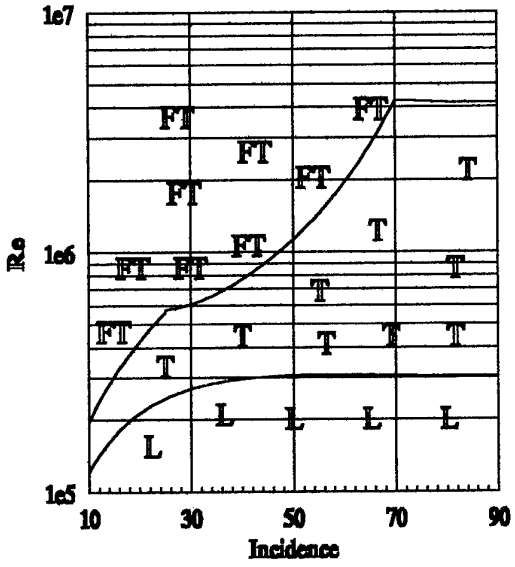

Figure 2: Critical Reynolds Number Boundaries

3. THEORY

3.1 Governing Equations

The Euler equations for two dimensional, compressible, time dependent flow are shown in Equation 1, using standard notation,

$$\frac{\partial U}{\partial t}+\frac{\partial F}{\partial x}+\frac{\partial G}{\partial y}=0 \qquad \textbf{(Eq.1)}$$

where,

$$U=\begin{pmatrix}\rho\\ \rho u\\ \rho v\\ \rho E\end{pmatrix} \quad F=\begin{pmatrix}\rho u\\ \rho u^2+p\\ \rho uv\\ \rho uH\end{pmatrix} \quad G=\begin{pmatrix}\rho v\\ \rho uv\\ \rho v^2+p\\ \rho vH\end{pmatrix}$$

The Navier Stokes equations for two dimensional, compressible, time dependent flow are shown in Equation 2.

$$\frac{\partial U}{\partial t}+\frac{\partial F}{\partial x}+\frac{\partial G}{\partial y}-\frac{\partial^2 F^v}{\partial x^2}-\frac{\partial^2 G^v}{\partial y^2}=0 \qquad \textbf{(Eq.2)}$$

where F^v and G^v are vectors containing the viscous terms,

$$F^v=\begin{pmatrix}0\\ \tau_{xx}\\ \tau_{xy}\\ u\tau_{xx}+v\tau_{xy}-q_x\end{pmatrix}$$

$$G^v=\begin{pmatrix}0\\ \tau_{xy}\\ \tau_{yy}\\ u\tau_{xy}+v\tau_{yy}-q_y\end{pmatrix}$$

3.2 Finite Volume Method

There are three standard approaches to solving the Euler and Navier-Stokes equations using discretization; Finite Difference, Finite Volume and Finite Element. Only Finite Volume methods were used in the current research.

The Finite Volume method uses the Euler equations written in integral form.

$$\frac{\partial}{\partial t}\iint_{\Omega} U d\Omega+\oint_{s}\{F\ G\}^t\cdot d\underline{S}=0 \qquad \textbf{(Eq.3)}$$

This can be discretized over a grid to give the equation,

$$\frac{\partial}{\partial t}(U_J\ \Omega_J)+\sum_{SIDES}(\{F\ G\}^t\cdot d\underline{S})=0 \qquad \textbf{(Eq.4)}$$

which can be computed by,

$$\frac{d}{dt}(U\Omega)_{i\,j}+\sum_{SIDES}(F_k\,\Delta y_k-G_k\,\Delta x_k)=0 \qquad \textbf{(Eq.5)}$$

This formula is applicable for any kind of grid whether it be made up of triangles, quadrilaterals or any other polygon.

The three dimensional analogy of this equation is given in reference (7).

There are many ways in which this equation can be solved numerically. Only one such method will be described here as it was the basis of all the codes used in the investigation except RAMPANT.

3.4 The Jameson Method

The Jameson method (8) solves Equation 5 using a Runge-Kutta scheme. A general 5-stage Runge-Kutta scheme is shown in Equation 6,

$$\begin{aligned} U^0 &= U^n \\ U^1 &= U^n - \alpha^1 \Delta t\, PU^0 \\ U^2 &= U^n - \alpha^2 \Delta t\, PU^1 \\ U^3 &= U^n - \alpha^3 \Delta t\, PU^2 \\ U^4 &= U^n - \alpha^4 \Delta t\, PU^3 \\ U^{n+1} &= U^n - \Delta t\, PU^4 \end{aligned} \qquad \textbf{(Eq.6)}$$

where the term PU is the second term of Equation 5 plus an artificial dissipation term, DU, defined below, both divided by area. The artificial dissipation term is required in order to provide numerical stability.

3.5 Artificial Dissipation

In the numerical solution of the Euler equations (and quite often the Navier-Stokes equations) it is necessary to add an artificial dissipation term. This term is required to make the numerical method stable after the partial differential equations have been discretized.

This artificial dissipation term may either be implicitly present within the numerical method or, as in the case of the Jameson method, be added explicitly.

The artificial dissipation term added to the Jameson method takes the form of a blend of second and fourth differences of the conservative vector. It should be noted that these terms do not represent true second and fourth derivatives as they have not been divided by the required length scales.

Equation 7 shows the form of the artificial dissipation used in the Jameson method.

$$\begin{aligned} DU &= D_x U + D_y U \\ D_x U &= d_{i+1/2,j} - d_{i-1/2,j} \\ D_y U &= d_{i,j+1/2} - d_{i,j-1/2} \end{aligned} \qquad \textbf{(Eq.7)}$$

A typical term of Equation 7 is given in Equation 8.

$$d_{1+1/2,j}U = \frac{\Omega_{i+1/2,j}}{\Delta t}\left\{\varepsilon^{(2)}_{i+1/2,j}(U_{i+1,j} - U_{i,j}) - \varepsilon^{(4)}_{i+1/2,j}(U_{i+2,j} - 3U_{i+1,j} + 3U_{i,j} - U_{i-1,j})\right\} \qquad \textbf{(Eq.8)}$$

where $\varepsilon^{(2)}$ is a pressure sensor term given by,

$$\varepsilon^{(2)}_{i+1/2,j} = k^{(2)} \max(\upsilon_{i+1,j}, \upsilon_{i,j})$$

where,

$$\upsilon_{i,j} = \frac{\left|P_{i+1,j} - 2P_{i,j} + P_{i-1,j}\right|}{P_{i+1,j} + 2P_{i,j} + P_{i-1,j}}$$

and $\varepsilon^{(4)}$ is given by,

$$\varepsilon^{(4)}_{i+1/2,j} = \max(0, k^{(4)} - \varepsilon^{(2)}_{i+1/2,j})$$

Typically $k^{(2)}$ and $k^{(4)}$ take the values 0.25, 0.004.

Other types of sensor have been used instead of the pressure sensor but these will not be described in the present paper.

By using this form of coefficients for the difference terms, the second difference term is only added in regions of high pressure gradient, in particular near shock waves in order to prevent large oscillations. The fourth difference term is likewise only added in regions of smooth flow to provide a level of 'background' dissipation.

The important feature in the current investigation is that these dissipation terms are similar to the viscous terms within the Navier-Stokes equations. Of course, it should not be expected that they will have the same effect. However, in some situations, for example where a shock wave occurs, or in regions of sharp changes in geometry, these terms can alter the Euler equations sufficiently to produce results similar to solutions of the Navier-Stokes at least for the purpose of engineering calculations.

4. DESCRIPTION OF CFD CODES[1]

MGAERO: This is a commercially available Euler code supplied by Analytical Method Inc. (9). The code uses Cartesian non-aligned grids that span the

[1] It should be noted that some of the codes described have since been updated and the current versions may use different methods.

computational domain. Important regions requiring greater resolution are defined using embedded grids. These embedded grids are then used to implement a multigrid solver in order to enhance convergence. The solution method is based on the Jameson Method described in Section 3.5.

FLITE3D: This is a British Aerospace Euler code based on the unstructured code developed at the University of Swansea (10). The grid is made up from tetrahedra produced with an advancing front grid generator. The flow solver is based on the Jameson method.

MULTIBLOCK: This is a British Aerospace Euler code that uses structured, body fitting grids. The computational domain is spanned by using a series of separate blocks of structured grids that allow complex geometries to be considered. The flow solver is based on the Jameson method.

RAMPANT: This is a commercially available Euler/Navier-Stokes code produced by Fluent Inc. (11). The code uses an unstructured tetrahedral grid (although structured grids can be used), combined with a solver that is based on a flux difference splitting algorithm. The solver makes use of multigrid to improve convergence and grid adaptation to improve the resolution of flow features. The Navier-Stokes code can be used for laminar and turbulent flows with a choice of k-ε and RNG turbulence models.

5. RESULTS

5.1 Evaluation Of 3D Codes

5.1.1 Grid Definition

Each of the codes described in Section 4 use a different approach to grid generation. It is therefore difficult to compare directly the various grid densities used. However, the following list gives an indication of the total number of grid cells used in each case,

- MGAERO: total number of cells ~400000.
- FLITE3D: ~400000 tetrahedral elements.
- MULTIBLOCK: ~100000 cells.
- RAMPANT: ~100000 tetrahedral elements.

MULTIBLOCK did not require as many cells as either MGAERO or FLITE3D in order to adequately define the geometry, but the number of cells that could be used for the RAMPANT grid was limited by the memory of the computer being used. The grid used for RAMPANT was therefore relatively coarse.

Figure 3 shows the unstructured surface mesh for the nose of Store A obtained using FLITE3D.

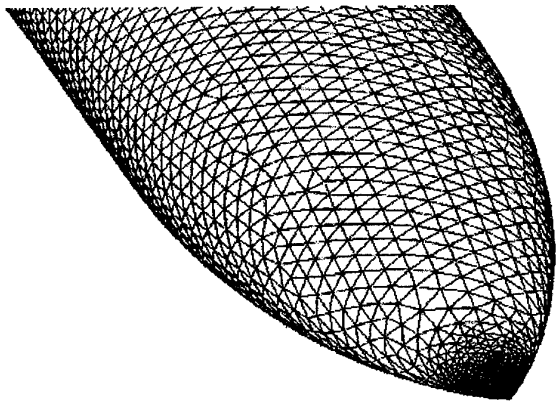

Figure 3: FLITE3D Unstructured Surface Grid

5.1.2 Results

The evaluation concentrated on obtaining Euler solutions for M=0.9, α=20°. In each case the surface pressure coefficient contours and normal force and pitching moment coefficients have been obtained. An example of contours of surface pressure coefficient, obtained using MGAERO for Stores A and D are shown in Figures 4 and 5. Both solutions show a large suction peak on the nose. This is consistent with inviscid slender body theory which predicts that an increase in cross-sectional area produces a lifting force, as originally shown by Munk (12). In each of the present transonic cases this suction peak is terminated by a shock wave.

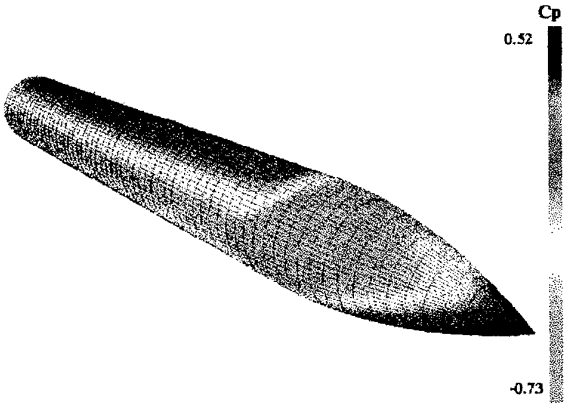

Figure 4: Surface Cp From MGAERO, Store A, M=0.9, α=20°

The crossflow velocity vectors and pressure contours for Store A at 5 diameters from the nose are shown in Figure 6. This shows that the flow is still attached, and that the pressures on the upper and lower surfaces of the body are approximately

equal. This solution resembles an two dimensional inviscid solution.

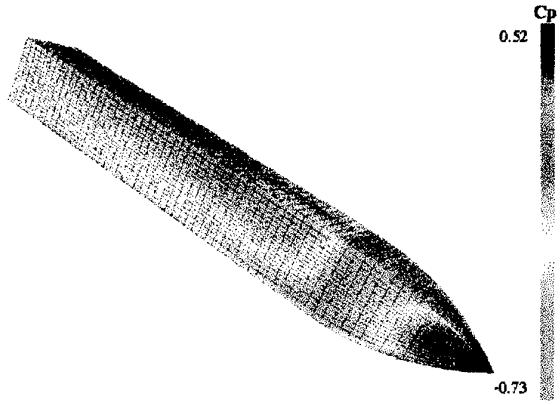

Figure 5: Surface Cp From MGAERO, Store D, M=0.9, α=20°

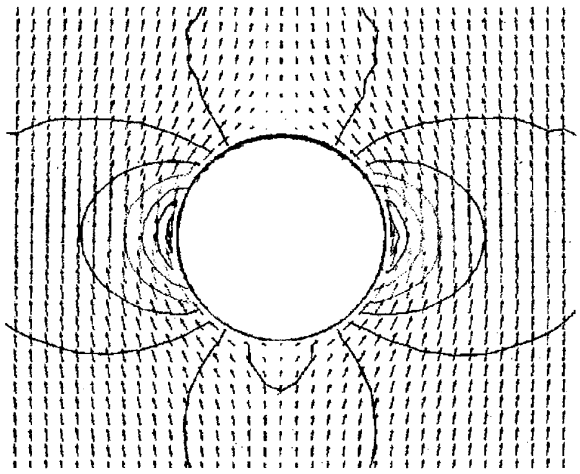

Figure 6: Store A Crossflow Velocity Vectors and Pressure Contours

The flow about Store D does not resemble an inviscid solution. Figure 7 shows that the flow has separated and that the pressure on the upper surface of the body is less than that on the lower surface thus producing a lift.

The crossflow for stores B and C also exhibit separation although in the case of store B the vortices are quite weak.

Each of the four codes evaluated produced similar results, with two main differences. Firstly, a coarser circumferential grid, for example as used by RAMPANT, produced a smaller pressure recovery on the leeside of the body thus producing a larger overall normal force, as described later. Secondly the codes making use of quadrilateral cells (MGAERO and MULTIBLOCK) predicted much larger vortices emanating from the lower corners of Store D. These however, seemed to have little effect on the leeside vortices.

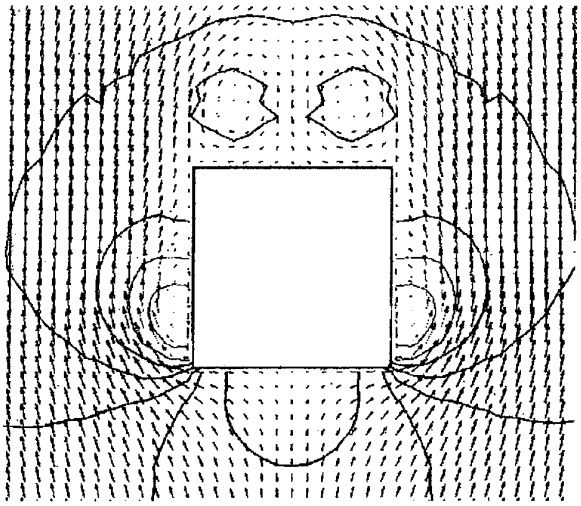

Figure 7: Store D Crossflow Velocity Vectors and Pressure Contours

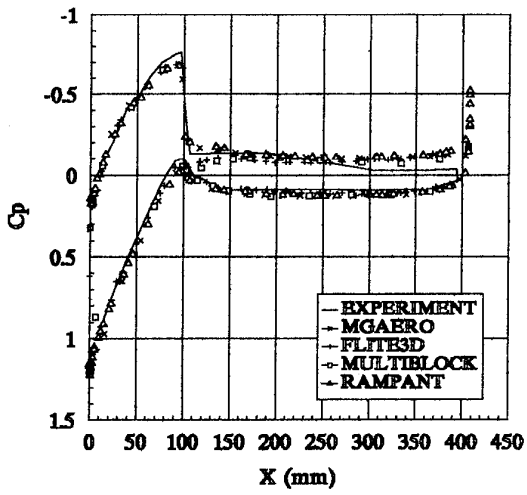

Figure 8: Store D Centre Line Pressure Coefficients Compared With Experiment.

The centre line pressure coefficient obtained for Store D, from each of the four codes, are compared with experiment in Figure 8. It can be seen that the predicted lower surface pressures are all very similar and compare closely with experiment. The predicted upper surface pressures vary between the codes, especially after the shock wave. In this region it can be seen that MULTIBLOCK and FLITE3D produce an overshoot in the pressures,

whereas RAMPANT and MGAERO underpredict the pressure jump.

All of the codes give similar results but begin to diverge from the experimental data towards the rear of the body, although it should be noted that there were few pressure tappings in this region.

The normal forces calculated for the four stores by the codes are compared with the wind tunnel data in Figure 9-12.

It can be seen that all of the codes under predict the normal force for Store A, although RAMPANT produces a close approximation. However, all the codes failed to predict separation for this store and it is thought that the unexpectedly high value of normal force predicted by RAMPANT is due to the coarse grid that was used. This agrees with part of the two dimensional investigation that showed that using a coarse grid around a circular cylinder produces a poor pressure recovery on the leeside. This was attributed to the artificial dissipation within the code. The normal force predicted by the other three codes is close to that predicted by slender body theory.

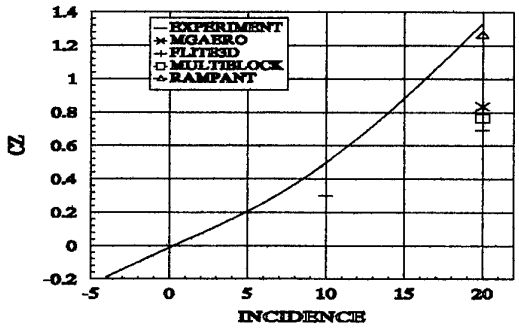

Figure 9: Predicted Normal Force For Store A

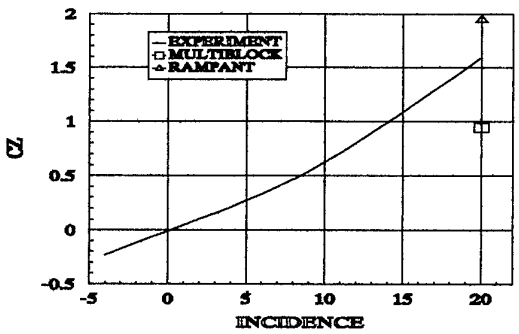

Figure 10: Predicted Normal Force For Store B

Only two of the codes were used to provide solutions for Store B and it can be seen that these provided widely varying normal forces. This difference can probably be attributed to grid definition. The unstructured grid used with RAMPANT did not provide a good definition of the corner radius, whereas the structured grid used with MULTIBLOCK actually clustered grid points in this region.

The normal forces predicted for Store C show an equally large variation of values. FLITE3D and MGAERO do however provide a good prediction of the normal force compared with experiment.

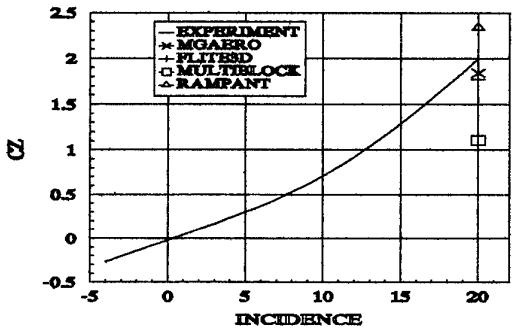

Figure 11: Predicted Normal Force For Store C

The normal forces predicted for Store D are much closer to one another and all provide a reasonably good agreement with experiment.

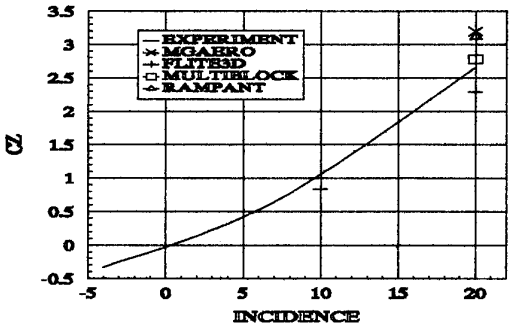

Figure 12: Predicted Normal Force For Store D

The predicted pitching moments show a smaller variation and for all the stores show reasonable agreement with experiment. This is due to the position of the moment reference point which is half way along the length of the constant area section. As can be deduced from Figure 8 the cross flow force is approximately constant along this section so that the nose section provides the majority of the

pitching moment. At the nose section the crossflow lift component can be predicted using slender body theory which is essentially the inviscid theory used in the codes.

The results at the other Mach numbers which were investigated provided similar conclusions. This is not surprising as in the wind tunnel tests the forces and moments showed little dependence on Mach number. It is not until higher incidences are reached where the crossflow Mach number becomes transonic that any major effects would become apparent.

An attempt was made at producing a Navier-Stokes solution for Store D using RAMPANT. However, currently it has not been possible to secure time on a suitable computer so that the required increase in grid points can be achieved. It has therefore only been possible to produce a solution on the same grid as used in the Euler solution and hence the boundary layer was not adequately resolved. The subsequent force on the body was almost exactly that found from the Euler calculation.

5.2 Investigation Of 2D Flow

In order to more fully investigate the observations made from the three dimensional results a two dimensional investigation was performed. This investigation looked at such factors as the effect of grid resolution and artificial dissipation on the solutions of the flow around the store cross-sections.

It was found that at sub-critical Mach numbers an Euler code did not predict separation for the circular cylinder. Figure 13 shows the streamlines for such a calculation at M=0.2 performed on a very fine grid suitable for Navier-Stokes solutions. It can be seen that the streamlines are symmetrical and that no wake exists. However, if the grid was made significantly coarser a wake began to form and a drag was predicted on the body. Nevertheless the solution remained attached.

It was found that increasing the freestream Mach number into the transonic regime produces shock induced separation around the circular cylinder. Figure 14 shows such the solution calculated after a non-dimensional time, t^*, of 3 for an impulsively started cylinder. The time is non-dimensionalized using the freestream velocity and store diameter. In crossflow theory this non-dimensionalization corresponds to a distance along the store and in this particular case for 20° incidence, the equivalent position for $t^*=3$ is eight store diameters from the nose.

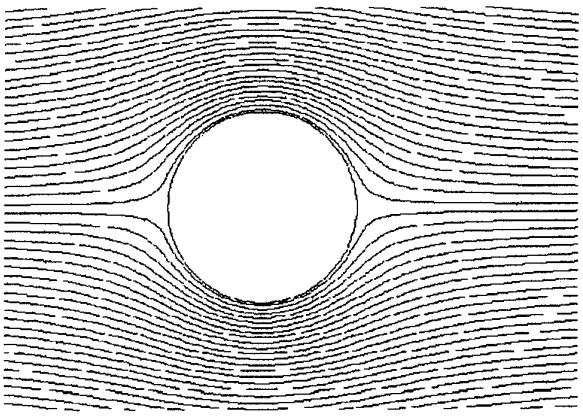

Figure 13: Euler Solution At M=0.2

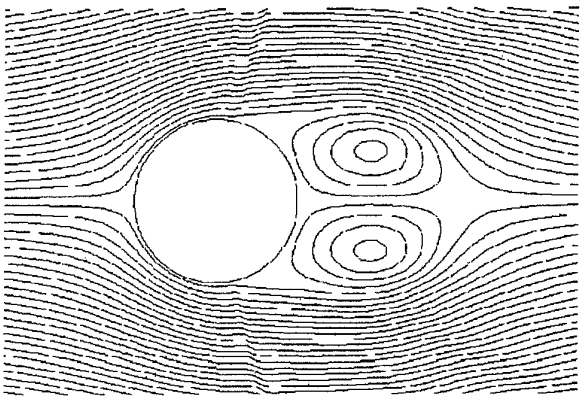

Figure 14: Euler Solution At M=0.6

A Navier-Stokes result for the same conditions with $Re=10^4$ is shown in Figure 15 and it can be seen that the primary vortices are similar in size and shape. The Navier-Stokes result does however show secondary separation near the body that the Euler code is obviously unable to predict.

A simple comparison of these two corresponding solutions shows that the Euler solution has a primary vortex strength (quantified using the total pressure loss) 10% less than the Navier-Stokes solution and a drag 20% less. Of course such a simple comparison is fairly limited, and to draw a significant conclusion, solutions for a number of other Reynolds numbers need to be examined.

The Euler solutions obtained for a square cylinder show that separation is predicted throughout the Mach number regime. For example, Figure 16 shows the flow for an impulsively started cylinder at $t^*=3$ and M=0.2.

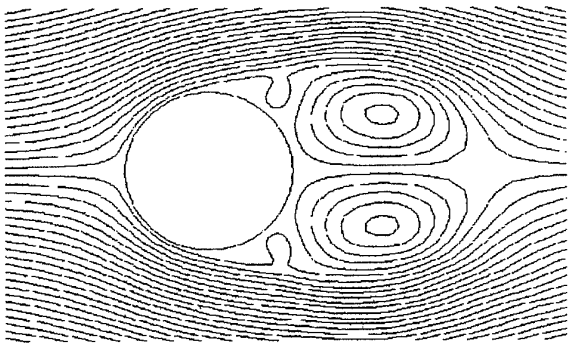

Figure 15: Navier-Stokes Solution At M=0.6

The flow solutions for this body, with sharp corners, show little variation with grid definition, although from the evaluation of the three dimensional codes it is thought that using an unstructured triangular mesh could affect the prediction of the lateral vortices.

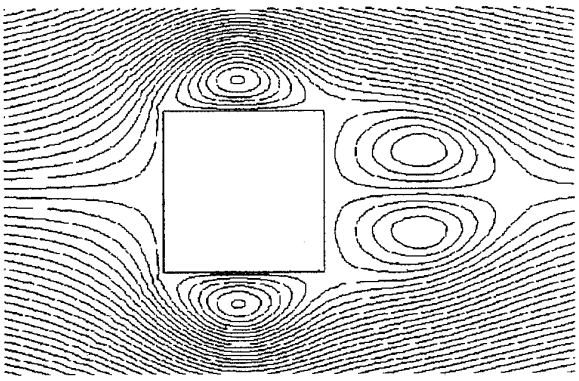

Figure 16: Euler Solution At M=0.2

Euler calculation for the modified square cylinders has shown that the results are sensitive to the grid density at subsonic Mach numbers, but less so at transonic Mach numbers. For subsonic Mach numbers, the use of a coarse grid results in flow separation, whereas a finer grid maintains attached flow for a greater distance.

6. CONCLUSIONS

Euler solutions for a series of non-circular stores have been calculated using four CFD codes available within British Aerospace. The results have shown that for the fully circular body the solution resembles that expected from slender body theory. However, for the fully square body a reasonable engineering type solution has been obtained where separation from the salient edges is predicted. The solutions for the modified square bodies have also shown that Euler methods can predict separation from rounded corners although the separation point cannot be relied upon.

The results obtained do show that the solutions obtained are sensitive to grid definition. This is not really surprising as the artificial dissipation within the method is fourth order in space (except near a shock wave) and should therefore tend towards zero as the grid size reduces. This is illustrated by the larger than expected normal force obtained from RAMPANT for the circular body, where the artificial dissipation has been large enough (due to the coarse grid used) to affect the leeside pressure recovery. The solutions for the square body show the least sensitivity to grid resolution because the separation is fixed by the sharp corners. This observation is in accordance with research into the use of Euler codes for sharp leading edge delta wings.

In order to more fully evaluate the use of Euler codes solutions were obtained for the crossflow around the bodies using both Euler and Navier-Stokes codes. The Euler solutions show the dependence of the flow solution on grid resolution. In addition, they have shown that separation can be predicted if it is induced by a shock wave.

In each of the solutions where separation is fixed the vortices predicted closely resemble the vortices predicted using Navier-Stokes methods. Therefore, if a wing and pylon were included in the analysis it is reasonable to assume that this situation would not change and that an engineering solution for store integration would be obtained at a much reduced cost from that obtained using Navier-Stokes.

In conclusion, the Euler solutions have shown that an Euler code can be expected to produce a good engineering solution only if the flow is relatively free of Reynolds number effects. So if the flow separation is fixed either by the geometry or by a shock wave and is not affected greatly by the condition of the boundary layer, a reasonable engineering solution may be obtained. Otherwise a Navier-Stokes solution will have to be attempted

(assuming suitable computer power is available) because the Euler result will be unreliable even if it manages to predict separation.

7. ACKNOWLEDGEMENTS

This research has been jointly funded by the Engineering and Physical Sciences Research Council under their CASE award scheme and by British Aerospace, Military Aircraft Division under their University Centre of Excellence scheme.

8. REFERENCES

1. Daniel, D.C., Yechout, T.R., Zollars, G.J., "Experimental Aerodynamic Characteristics of Missiles with Square Cross Sections", J.Spacecraft, 19, 2, Mar-Apr 1982, pp167-172.
2. Murman, E.M., Rizzi, A., "Applications of Euler Equations to Sharp Edge Delta Wings With Leading Edge Vortices", AGARD CP-412, 1986, Paper 15.
3. Kandil, O.A., Chuang, A.H., "Influence of Numerical Dissipation on Computational Euler Equations for Vortex Dominated Flows", AIAA J., 25, 11, Nov 1987, pp1426-1434.
4. Priolo, F.J., Wardlaw, A.B., "A Comparison of Inviscid Computational Methods for Supersonic Tactical Missiles", AIAA 87-0113, 1987.
5. Allen, H.J., "Estimation of the Forces and Moments Acting on Inclined Bodies of Revolution of High Fineness Ratio", NACA RM-A9I26, 1949.
6. Poll, D.I.A., "Some Effects of Boundary Layer Transition on Slender Axi-symmetric Bodies at Incidence in Incompressible Flow", AGARD CP-336, 1982, Paper 13.
7. Hirsch, C., "Numerical Computation of Internal and External Flows: Volume 1; Fundamentals of Numerical Discretization", Wiley, 1989, (ISBN 0-471-92385-0), pp256-260.
8. Jameson, A., Schmidt, W., Turkel, E., "Numerical Solution of the Euler Equations by Finite Volume Methods using Runge-Kutta Time Stepping Schemes", AIAA 81-1259, 1981.
9. Tidd, D.M., Strash, D.J., Epstein, B., Luntz, A., Nachshon, A., Rubin, T., "Multigrid Euler Calculations Over Complete Aircraft", J.Aircraft, 29, 6, Nov-Dec 1992, pp1080-1085.
10. Peraire, K., Morgan, K., Peiro, J., "Unstructured Finite Element Mesh Generation and Adaptive Procedures for CFD", AGARD CP-464, 1989, Paper 18.
11. "Rampant User Guide", Fluent Europe Inc.
12. Munk, M.M., "Aerodynamic Forces on Airship Hulls", NACA Rept.184, 1923.

AERODYNAMICS OF FUSELAGE AND STORE-CARRIAGE INTERACTION USING CFD

Ülgen Gülçat, A. Rüstem Aslan and Aydın Mısırlıoğlu
Faculty of Aeronautics and Astronautics
ITU, 80626, Maslak, Istanbul, Turkey

SUMMARY

Store-carriage, pylon, fuselage interaction problem for modelling part of a fuselage of a fighter aircraft in low Mach number flight is studied by solving the full Navier-Stokes Equations numerically. A Finite Element Method (FEM) with an explicit time marching scheme is used for the solution. An artificial viscosity, equivalent of streamwise upwinding, is implemented while obtaining the velocity field. The pressure field is determined via an auxiliary potential function obtained with an accelerated iterative solution of Poissons' equation. Comparison of the pressure distributions and aerodynamic force coefficients obtained by the code for various test cases has validated the code. Therefore the code is utilized for more complex flow predictions.

1. INTRODUCTION

During ninetees the easy accessibilty of high speed computational tools enabled the researchers in CFD to obtain numerical solutions of full Navier-Stokes Equations for investigations of general viscous flows involving arbitrary shapes. Because of complexity of the flow around multibodies, the analysis of this type of flow for the prediction of aerodynamic performance requires extensive use of CFD tools. In order to improve the aerodynamic performance of the whole configuration various parametric studies concerning the geometry and the flight conditions are required.

In the present work, incompressible viscous flow about a store-carriage, pylons and fuselage are studied solving the full Navier-Stokes Equations numerically. A Finite Element Method (FEM) with an explicit time marching scheme is used for the solution[1]. Element by element (E-B-E) technique is employed in order to ease the memory requirements needed by the storage of the stiffness matrix of FEM[2]. Since the scheme is time accurate, the transient nature of the flow field is properly predicted. For the subsonic flight case to be investigated the flow is turbulent and the Baldwin-Lomax turbulence model[3](a two-layer algebraic eddy viscosity model) for three-dimensional flows is used[4].

For the calibration of the code, two-dimensional cavity problem is solved. The comparison[5] with the existing literature[6] is satisfactory even for a coarse grid. Extension to three dimensional cavity problem also agrees well with the existing solutions in related literature[5]. A turbulent flow of Re=83000 in a straight duct is also computed and compared succesfully with data given elsewhere[4]. To test the capabilities of the code a Re=2000000 flow past a swept bump is computed. Satisfactory results are obtained for prediction of lift and drag.

In this paper two cases are considered: 1) Re=5000, Re=27000, Re=134000 and Re=10^6 flow about an external carriage configuration, and 2) Re=27000 and Re=134000 flow about a generic carriage, pylon, fuselage configuration.

The velocity and pressure distrubitions for zero degree angle of attack are presented in the results section. The drag and lift coefficients for each case and effect of fuselage and pylons on these values are discussed.
All the computations are performed on a personal computer equipped with a i860 Number Smasher board with 32 Mbytes of memory.

2. FORMULATION

2.1 Governing Equations

The Reynolds averaged Navier-Stokes and the continuity equations for the unsteady, incom-

Paper presented at the AGARD FDP Symposium on "Aerodynamics of Store Integration and Separation", held in Ankara, Turkey from 24-27 April 1995, and published in CP-570.

pressible flow of a viscous fluid, in the absence of body forces are:

$$\frac{\partial V_i}{\partial t} + V_j \frac{\partial V_i}{\partial X_j} =$$

$$-\frac{\partial p}{\partial X_i} + \frac{1}{Re}\frac{\partial}{\partial X_j}\left[\mu_{ef}\left(\frac{\partial V_i}{\partial X_j} + \frac{\partial V_j}{\partial X_i}\right)\right] \quad (1)$$

$$\frac{\partial V_i}{\partial X_i} = 0 \qquad (i,j = 1,2,3) \quad (2)$$

The equations are written using the indicial notation. The summation convention is employed on repeated indices from 1 to 3, as indicated. The variables are non-dimensionalized using a reference velocity and a characteristic length, as usual. Re is the Reynolds number, $Re = Ul/\nu$ where U is the reference velocity, l is the characteristic length and ν is the kinematic viscosity of the fluid. $\mu_{ef} = 1 + \mu_t$ is the effective viscosity coefficient which includes the turbulent viscosity coefficient μ_t. V_i (i=1,2,3)
corresponds to the Cartesian velocity components u,v, and w while X_i (i=1,2,3) denotes the corresponding Cartesian coordinates x,y, and z. Pressure is symbolized with p and the time is with t.

For a well posed problem, the governing equations are complemented with the following initial (t=0)

$$V_i(X_i,0) = V_i^o(X_i) \text{ and } p(X_i,0) = p^o(X_i) \quad (3)$$

and boundary conditions which have to be specified on related surfaces:

$$V_i = G_i \quad \text{and} \quad -pn_i + \frac{1}{Re}\frac{\partial V_i}{\partial n} = F_i \quad (4)$$

where G_i and F_i are prescribed boundary values, n_i are the direction cosines of unit vector normal to the boundary and ∂n is normal derivative.

2.2 Fractional Step Method

The governing equations are integrated in time using the fractional step method introduced by Mizukami and Tsuchiya[1], which constitutes a time marching scheme based on Helmholtz decomposition. A potential function with a single degree of freedom at each node is introduced and a Poisson equation for the potential is directly discretized. Details of the formulation which is modified for turbulent flow can be found in [2,4]. Using a forward difference operator for the time derivative in equation (1) and letting V_i^m and p^m be solutions at the known time level m, the fractional step velocities are defined as

$$V_i^{m+1/2} = V_i^m + \Delta t\left\{-\frac{\partial p^m}{\partial X_i} + \right. \quad (5)$$
$$\left.\frac{1}{Re}\frac{\partial}{\partial X_j}\left[\mu_{ef}^m\left(\frac{\partial V_i^m}{\partial X_j} + \frac{\partial V_j^m}{\partial X_i}\right)\right] - V_j^m\frac{\partial V_i^m}{\partial X_j}\right\}$$

Following additional equations complete the formulation[4,5].

$$V_i^{m+1} = V_i^{m+1/2} + \frac{\partial \phi}{\partial X_i} \quad (6)$$

$$\frac{\partial^2 \phi}{\partial X_i \partial X_i} = -\frac{\partial V_i}{\partial X_i}^{m+1/2} \quad (7)$$

$$p^{m+1} = p^m - \frac{\phi}{\Delta t} \quad (8)$$

where ϕ is the auxiliary potential function. The Fractional Step algorithm is constructed as follows:

1) calculate $V_i^{m+1/2}$ from equation (5)
2) solve equation (7) for ϕ
3) calculate V_i^{m+1} form equation (6)
4) calculate p^{m+1} from equation (8)

For the solution of equation (7), Element By Element (E-B-E) technique[2] is employed as explained in secton 2.4.

An artificial viscosity, equivalent of streamwise upwinding[7], is implemented while obtaining the velocity field. The following term is added to the right hand side of equation (1).

$$\frac{\partial}{\partial X_j}\left[k_j\left(\frac{\partial V_i^m}{\partial X_j}\right)\right]$$

Note that there is no summation for k_j which are the artificial viscosity coefficients defined in Appendix of reference [7].

Prior to computations, the integral finite element equations of (5) to (8), must be obtained.

2.3 Galerkin Method

Because of the dissipative character of the

Navier-Stokes equations[8] the Galerkin method is considered as the most convenient tool for formulating complex flows which involve high Reynolds Numbers and strong separation. In the present work 8-node isoparametric brick elements and trilinear interpolation functions for the velocity and the auxiliary potential are used. The pressure is defined at the centroid of each element. Application of the conventional Galerkin integral[8] to equations 5 to 8 and the boundary conditions (4) gives integral finite element formulations for one brick element[1,4]. Element mass matrix which appears in the finite element formulation is lumped. In contrast to the potential and velocity, pressure values are interpolated using piecewise constant functions at each element. The equation (8) thus becomes

$$P_e^{m+1} = P_e^m - \frac{\phi_e}{\Delta t} \tag{9}$$

where element potential ϕ_e is defined as

$$\phi_e = \frac{1}{vol(\Omega_e)} \int_{\Omega_e} N_i \, \phi_i \, d\Omega_e \tag{10}$$

where Ω is the flow region to be solved and Γ is the boundary of Ω. In addition to the boundary conditions given in equation (4) the following conditions for ϕ should also be imposed on the required section of the boundary Γ:

$$\phi = 0 \quad or \quad \frac{\partial \phi}{\partial n} = 0 \tag{11}$$

Conditions (4) are adopted as follows:

$$n_l \cdot V_l^{m+1} = n_l \cdot V_l^{m+1/2} \quad and \quad p^{m+1} = p^m \tag{12}$$

2.4 E-B-E Iteration Procedure

For the solution of equation (7), Element By Element (E-B-E) technique[2] is employed in order to ease the memory requirements needed by the storage of the stiffness matrix of FEM. The iterative solution is fully vectorized.

The matrix form of equation (7) is

$$S\phi = F \tag{13}$$

where S is the stiffness matrix, ϕ is the auxiliary potential and F is the right hand side of equation (7). The F values are indicative of compressibility for the fractional step velocity field and they are small in magnitude. Therefore, the F values are scaled with the square of the time step to increase accuracy. These scaling reduces the number of iterations by almost 50%.

$$F = F/(\Delta t)^2 \tag{14}$$

For further reduction in iteration the following is defined as preconditioner:

$$W_{ii} = \Sigma_e S_{ii}^e \tag{15}$$

Thus ϕ and equation (7) can be written as

$$\phi = W^{-1/2}\bar{\phi} \tag{16}$$

$$W^{-1/2} S \, W^{-1/2}\bar{\phi} = W^{-1/2} F \tag{17}$$

As a result, the diagonal elements of preconditioned stiffness matrix become unity. Thus the final form of equation (17) reads

$$\bar{S}\bar{\phi} = \bar{F} \tag{18}$$

Equation (18) is solved with conjugate gradient method developed for symmetric matrices. The iteration starts using the following initial values.

$$\begin{aligned} \text{choose:} \quad & \bar{\phi}^o = 0 \\ \text{residue:} \quad & r^o = \bar{F} - \bar{S}\bar{\phi}^o = \bar{F} \\ \text{define:} \quad & P^o = r^o \end{aligned}$$

Following initialization, a line search is performed to update solution and residue;

$$\begin{aligned} \text{set:} \quad & \lambda_m = (r^m . r^m)/(\bar{S}P^m . r^m) \\ \text{solution:} \quad & \bar{\phi}^{m+1} = \bar{\phi}^m + \lambda_m P^m \\ \text{residue:} \quad & r^{m+1} = r^m - \lambda_m \bar{S} P^m \end{aligned}$$

At the end of each iteration the norm of residue is checked for convergence

$$||r^{m+1}||/||r^o|| < 10^{-4} \tag{19}$$

Following this, a new conjugate search direction is obtained as,

$$\begin{aligned} \text{set:} \quad & \alpha_m = (r^{m+1} . r^{m+1})/(r^m . r^m) \\ \text{find:} \quad & P^{m+1} = r^{m+1} + \alpha_m P_m \end{aligned}$$

If the convergence is satisfied

$$\phi = W^{-1/2}\bar{\phi} \tag{20}$$

The ϕ values are rescaled with the square of the time step to obtain the final ϕ distribution.

$$\phi = \phi * (\Delta t)^2 \tag{21}$$

2.5 Vectorization of E-B-E Formulation

The iterative procedure described above as E-B-E formulation requires assembly of contributions coming from each element. In order to utilize the full vectorization in computation at each iteration, the assembly process is performed block by block. For this purpose, the whole domain is divided into blocks each containing 128 (vector size) elements. Then, for the evaluation of the right hand sides the multiplication of the element matrices with vectors of known quantities are performed in a single block. With this, in vector operations maximum benefit from vectorization is achieved.

If 'nblock' is the number of blocks, 'ns'=128, is the vector length and if in the inner DO LOOPS the data transfer from global to local and from local to global nodes are made with pointers, then the assembly algoritm reads,

```
do block i = 1, nblock
  do elem = 1, ns
   evaluate right hand sides
   locally at an element and
   store in arrays of length ns
  enddo
  do elem =1,ns
   accumulate globally
   on the right hand side
   at the node level
  enddo
enddo
```

2.6 Turbulence Model

The Baldwin-Lomax turbulence model[3] extended to three-dimensions [4] is utilized. The y^+ values, for the first point adjacent to the wall, vary between 5 and 55 ($y^+ = U^* n/\nu$ where U^* is the friction velocity and n is the normal distance to wall). The points of the profiles used in determining YMAX, FMAX values of the model are the rays perpendicular to the wall. For the wake region, however, aft portion of the axis of the body is considered as the wall. Then the profiles are determined accordingly.

3. RESULTS AND DISCUSSION

For various Reynolds numbers based on the carriage length (L=2144mm), the flow field both laminar and turbulent are predicted with the method described. For the present, for the flow about the carriage-pylon-fuselage interaction, the laminar flow is studied. The fuselage geometry is similar to that of the F-5 fighter aircraft[9]. The turbulent flow results about the carriage alone is compared with the experimental data[10].

Figure 1 shows the grid used for the laminar flow studies about the carriage alone. The carriage geometry is defined in reference[10]. The number of grid points is 38067 forming 33352 elements. The same grid is used for Reynolds numbers of 5000, 27000 and 134000.

Shown in figure 2 is the grid utilized for the turbulent flow study where the Reynolds number is 10^6. The number of grid points is 16596 forming 14042 elements. The minimum normal distance to wall is 0.008L.

The grid used for the laminar flow studies about the carriage-pylon-fuselage interaction is seen in figure 3. The number of grid points is 49691 forming 43552 elements. The same grid is used for Reynolds numbers of 27000 and 134000.

The complex nature of the flow field is clearly depicted in Figure 4, wherein the velocity vector field on the symmetry plane including the major part of the carriage, pylons and the bottom surface of the fuselage are shown. The main flow is from left to right and is laminar with the Reynolds number of 134 000. The recirculating regions at the step and at the wake, and the quiscent nature of the flow in between the pylons are readily visible. Associated pressure distribution on the symmetry plane is given with Figure 5.

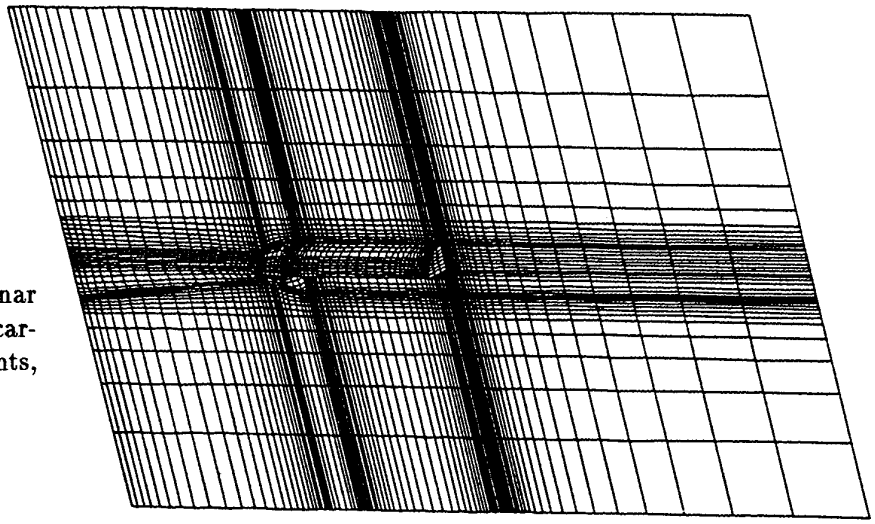

Fig.1 Grid used for laminar flow studies about the carriage alone. 38067 grid points, 33352 elements.

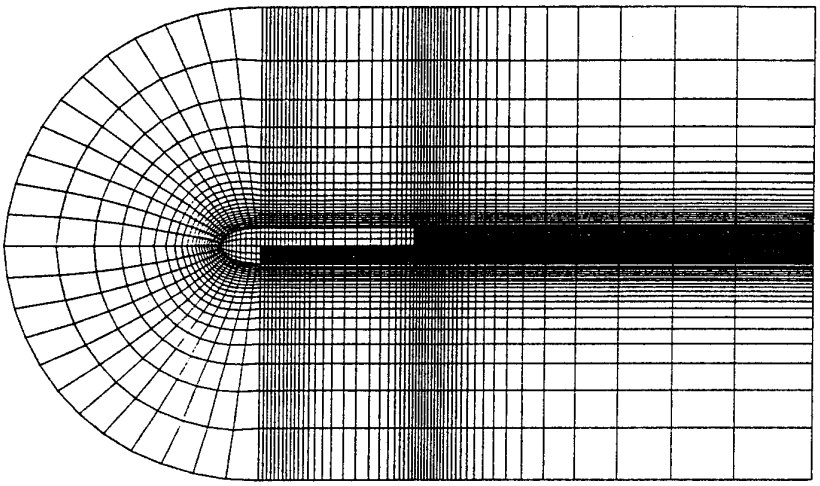

Fig.2 Grid used for turbulent flow studies about the carriage alone. 16596 grid points, 14042 elements.

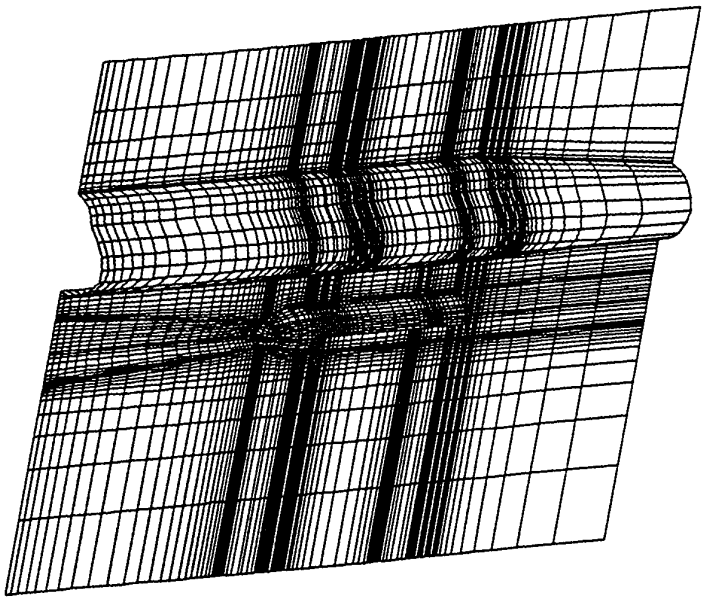

Fig.3 Symmetry plane grid for carriage-pylon-fuselage interaction. 49691 grid points, 43552 elements.

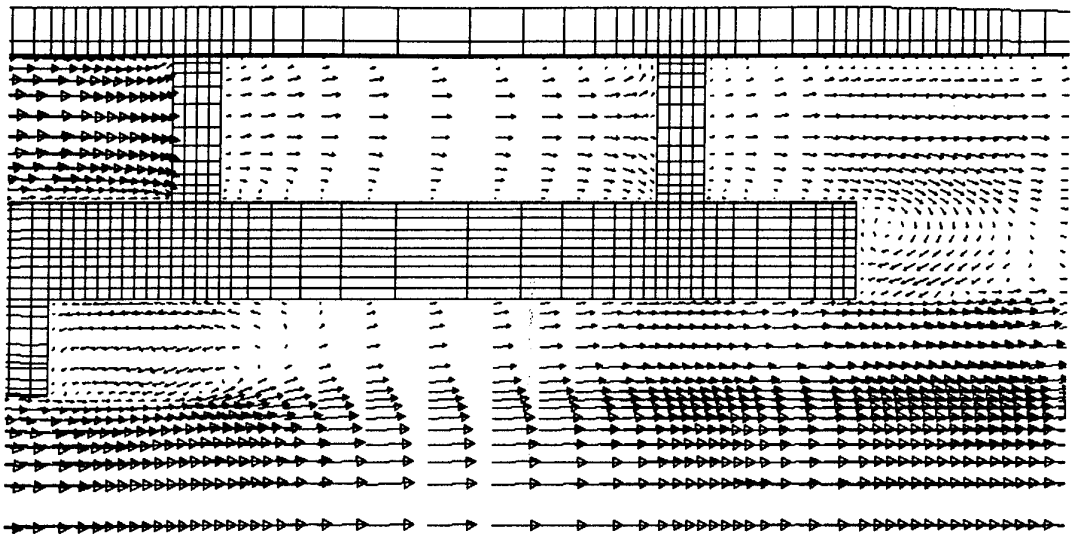

Fig.4 Velocity vectors at the symmetry plane, Re=134000.

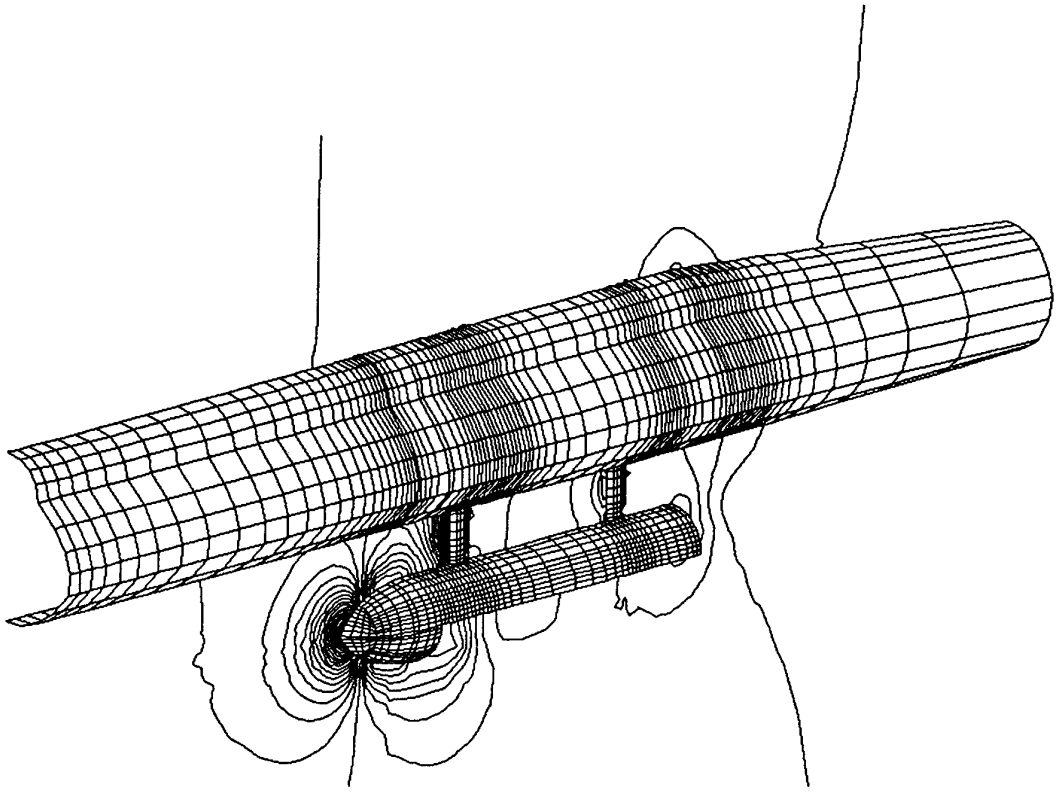

Fig.5 Pressure isolines at the symmetry plane, $(C_p)_{max}$= 1, $(C_p)_{min}$= −0.6, ΔC_p = 0.04, Re=134000.

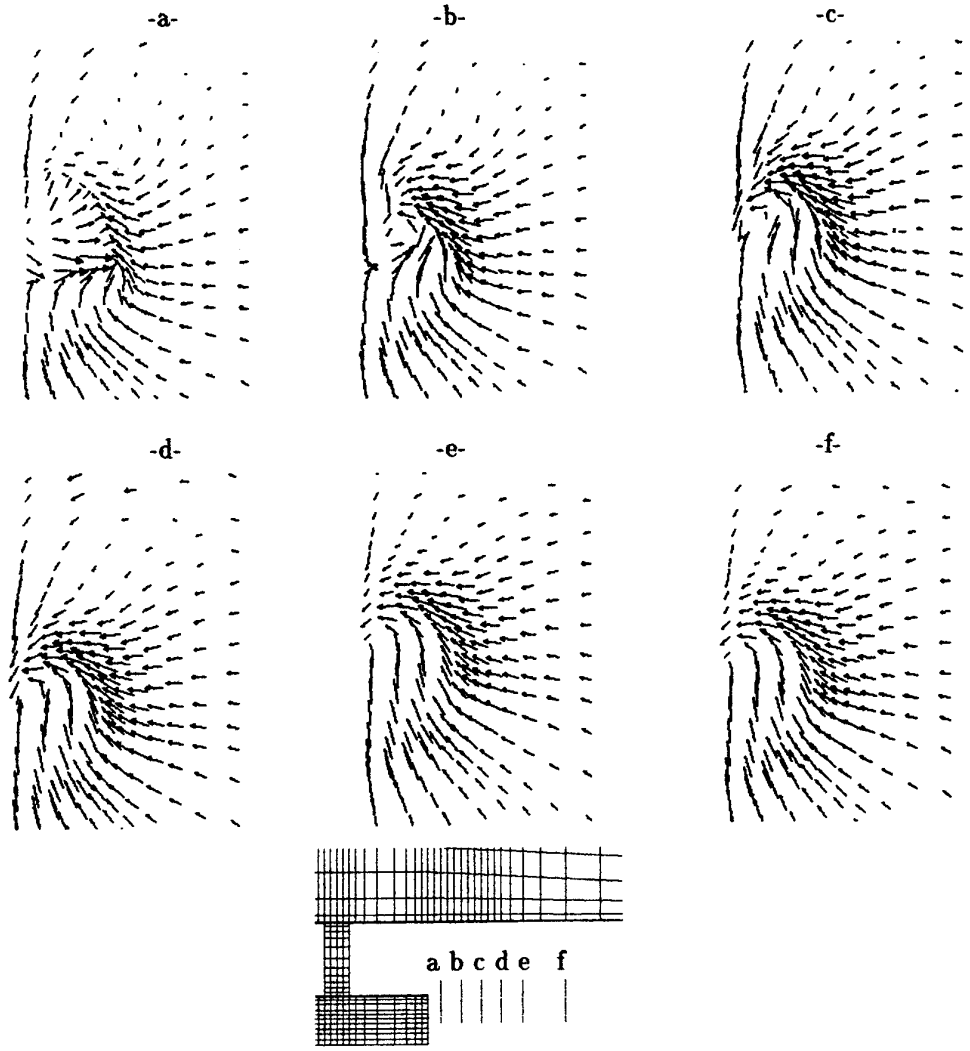

Fig.6 Cross-flow on various planes in near weak. a at 0.14 x/D, b at 0.34, c at 0.53, d at 0.74, e at 0.96 and f at 1.4 (D=400mm is the diameter of the carriage), $V_{max}/V_\infty = 0.1$.

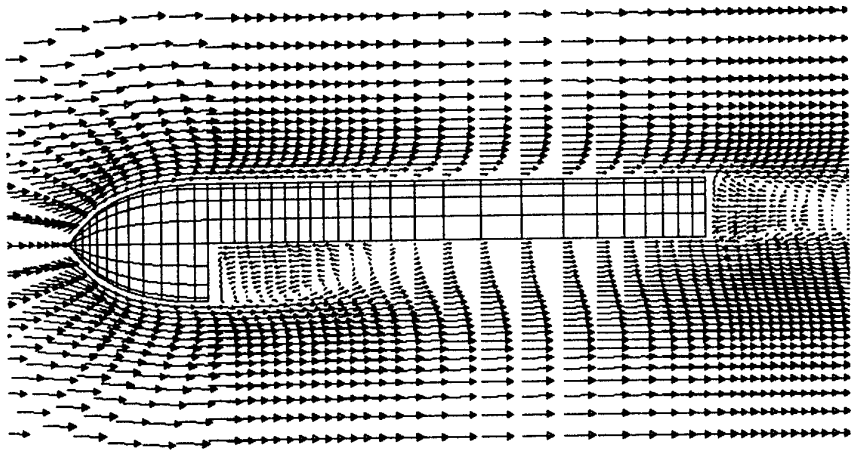

Fig.7 Velocity vectors at the symmetryplane of the carriage, Re=10^6

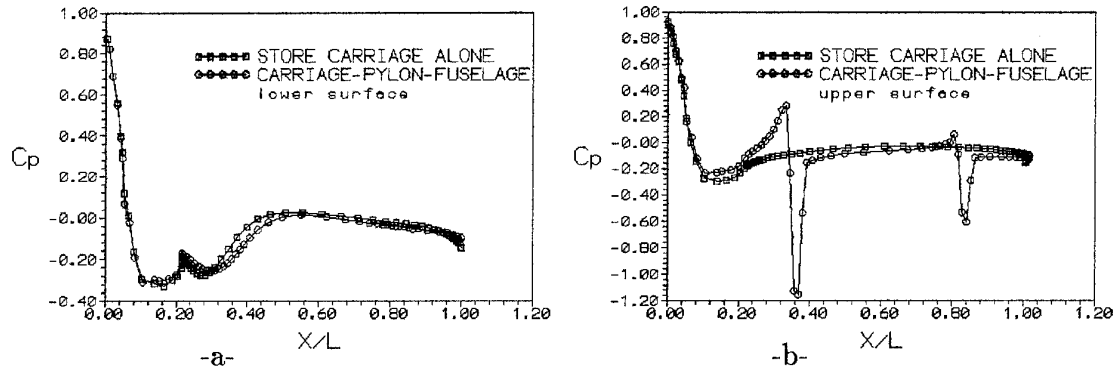

Fig.8 Surface pressure coefficient distrubition on the symmetry plane, Re=134000.

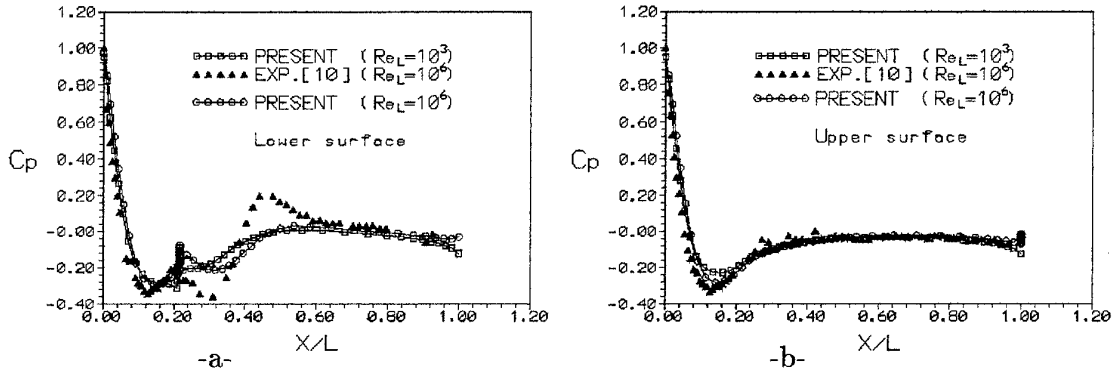

Fig.9 Surface pressure coefficient values comapred with experimental data[10] on the symmetry plane, Re=1 000 000.

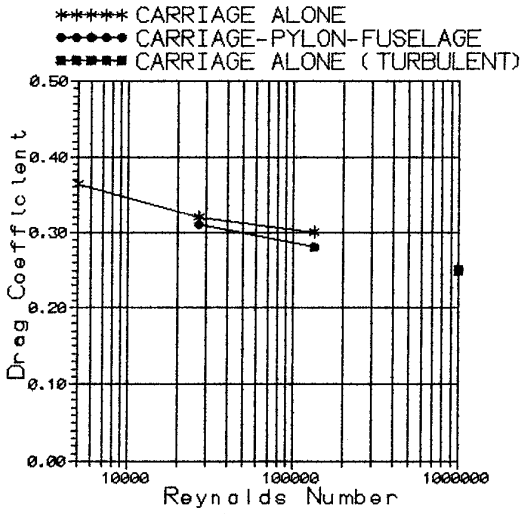

Fig.10 The variation of drag coefficient for various Re numbers.

Figure 6 shows the right halves of the cross flow velocity vector fields given on six consecutive planes in the near wake. The effect of the fusalage in terms of reducing the cross flow speed can be seen at the upper parts of each plane. The start up of a counter clockwise rotating vortex roll to the left of the center of the second plane is seen on Figure 6.b. In the following planes the vortex roll grows in size in further downstream, Figure 6. c,d,e,f. Shown on Figure 6.g is the exact locations of the planes in near wake.

The mean velocity vector field on the symmetry plane for the turbulent flow past the carriage alone is shown in Figure 7. The Reynolds number of the flow is 1 000 000. The growth in the size and intensity of the buble at the step is apparent.

The lower and the upper surface pressure plots on the symmetry plane of the carriage is shown in Figure 8.a,b with and without pylons. With pylons, the change in the pressure distribution in the vicinity of the front pylon is drastic. The pylon section is, 10% thick ellipse with a chord length of 5% L. The flow Reynolds number is 134 000 for the both cases.

The comparison of the surface pressure coefficient values ($C_p = 2(p - p_\infty)/\rho_\infty V_\infty^2$) for numerical results and the experimental data are given in plots of Figure 9.a,b. The experimental data is available only for the turbulent flow case. The agreement on the upper surface is satisfactory, Figure 9.b. For the lower surface, however, the agreement is quite good at the front, before the step, and at the region aft of 0.6L, Figure 9.a. In the recirculating region, there is a discrepancy between the calculated and the measured pressure values. On that figure, the calculated pressure values look smeared out. This smearing can be attributed to both the turbulence model and to the second order artificial viscosity intreduced for stabilizing the solutions.

Finally, shown on Figure 10 is the drag coefficients ($C_d = 2 * DRAG/\rho_\infty V_\infty^2$) versus the Reynolds number of the flow. The computed lift coefficient is insignificant for all the cases, as expected.

For the turbulent flows about bluff bodies, drag coefficients show very little change with respect to the Reynolds numbers allowing one to use incomplete similarity[11]. Since the carriage studied here is a bluff body, it is sufficient to solve the flow for one turbulent Reynolds number and apply the incomplete similarity rule for the higher Reynolds numbers.
The computations are performed on a computer equipped with i860 processor. The average computation time per time step per grid point takes approximately 0.008 seconds CPU time. Each study is carried up to the time levels where the carriage has traveled about one length which takes about 1000 time steps.

CONCLUSIONS

Flows about complex shapes are studied numerically for high Reynolds numbers using a special code developed to demand the least memory on the vector processors. The comparison between the numerical results and the experimental data shows, in general, reasonable agreement. In the large recirculating flow regions however, the pressure values are smeared because of low order approximations and artificial viscosity. Therefore, the near future studies must utilize both the high order approximations and fourth order artificial viscosity.

REFERENCES

[1] A. Mizukami and M. Tsuchiya, *A Finite Element Method for the Three-Dimensional Non-Steady Navier-Stokes Equations*, Int.J.Num Meth.in Fluids, vol.4, pp.349-357, 1984.

[2] Ü. Gülçat, *An Explicit FEM for 3-D General Viscous Flow Studies Based on E-B-E Solution Algorithms*, to appear in the International CFD Journal, 1995.

[3] B.S. Baldwin and H. Lomax, *Thin Layer Approximation and Algebraic Model for Separated Turbulent Flows*, AIAA Paper No. 78-257, 1978.

[4] A.R. Aslan, F.O. Edis, Ü. Gülçat and E. Gürgey, *Prediction of General Viscous Flows Using a Finite Element Method*, Proceedings of the 8th International Conference on Numerical Methods in Laminar and Turbulent Flows, Swansea, U.K., July 18-23, 1993.

[5] Gürgey, E., Aslan, A.R., Edis, F.O. and Gülçat, Ü., *3D Finite Element Computation of Unsteady General Viscous Flow*, Proc. of 8^{th} International Conference on Finite Elements in Fluids, New Trends and Applications, Barcelona, Spain, pp.184-193, 1993.

[6] U. Ghia, K. Ghia and C.A. Shin, Journal of Computational Physics, vol. 48, pp.485, 1982.

[7] Gülçat Ü. and Aslan A.R., *Drag and Partial Lift Prediction of a Helicopter Fuselage with a Canard Using CFD*, Paper presented at the ECCOMAS 94 Conference in Stuttgart, Germany, 5-8 September 1994.

[8] B.A. Finlayson, *The Method of Weighted Residuals and Variational Principles*, Academic Press, 1972.

[9] W.G. Stuart, *Northrop F-5 Case Study in Aircraft Design, AIAA Professional Study Series*, September 1978.

[10] Özcan O., Ünal M.F., Aslan A.R., Bozkurt Y. and Aydın N.H., *Aerodynamic Characteristics of An External Store Carriage: Part A*, AIAA paper 93-3507.

[11] R.W. Fox and A.T. McDonald, *Introduction to Fluid Mechanics*, Fourth Edition, John Wiley and Sons, Inc., New York, 1992.

DEVELOPMENT OF NUFA AND ITS APPLICATION WITHIN A HYBRID STORE LOAD PREDICTION METHOD.

by

S.McDougall and A.J.Press
Aerodynamics and Vulnerability Research Dept.,
Sowerby Research Centre,
British Aerospace (Operations) Ltd.,
P.O. Box 5,
Filton,
Bristol BS12 7QW.
U.K.

SUMMARY

The NUFA semi-empirical prediction program was originally developed to estimate the aerodynamic loads experienced by configurations immersed in a non-uniform flowfield such as those found in close proximity to a parent aircraft. The code is used throughout BAe Defence Ltd. for the prediction of isolated weapon aerodynamic loads and the determination of carriage/trajectory characteristics both in a stand-alone mode and integrated into trajectory calculation suites. A recent new release of the program incorporates a number of developments aimed at extending the range of configurations which can be modelled, improving the accuracy of existing calculation techniques and improving the user/program interface. Additionally, development work is currently being carried out to enable the modelling of stores with bodies of arbitrary cross-section with the aim of allowing the program to estimate the loads experienced on modern configurations developed for improved low observability and submunition dispensing purposes. An outline description of the new capabilities which have been incorporated into the current release version of the program and those which are still undergoing development is given within this paper.

The code has undergone extensive validation studies for the estimation of free-air store characteristics and the determination of carriage/grid loads within a hybrid load prediction scheme. The hybrid scheme requires the flowfield in which the store is immersed to be input to NUFA. The flexibility of the scheme is such that the flowfield may be obtained from any source, either experiment or theoretical method. Examples of the use of the hybrid scheme are presented, demonstrating the flexibility, relatively low cost and ease of use of the technique.

NUFA and ABACUS are UK Registered Trade Marks belonging to BAe plc.

LIST OF SYMBOLS

C_m	Pitching moment coefficient
C_n	Yawing moment coefficient
C_N	Panel normal force coefficient
C_Y	Side force coefficient
C_Z	Normal force coefficient
d	Body diameter
k_{BW}	Deflected wing on body interference factor
k_{WB}	Body on deflected wing interference factor
K_{BW}	Wing on body interference factor
K_{WB}	Body on wing interference factor
NP	Number of individual panels in a lifting surface set
r	Body radius
S	Wing gross semi-span
V_Y	Flowfield velocity component in the Y-direction (sidewash)
V_Z	Flowfield velocity component in the Z-direction (upwash)
α	Angle of attack
α_{eq}	Equivalent angle of attack
β	Sideslip
δ_j	Angle of deflection of the j'th panel
$\Delta\alpha_V$	Change in local angle of attack due to vortex interference effects
$\Delta\alpha_\delta$	Change in local angle of attack due to fin deflection
Λ_{ij}	Control effectiveness parameter for the i'th panel due to the deflection of the j'th panel

Subscripts

c	At the panel control point
i	Effect on the i'th panel
Y	Y-direction
Z	Z-direction
α	Effect due to angle of attack
β	Effect due to sideslip

1. INTRODUCTION

The Sowerby Research Centre NUFA semi-empirical aerodynamic prediction program has been developed to estimate the aerodynamic characteristics of typical store

Paper presented at the AGARD FDP Symposium on "Aerodynamics of Store Integration and Separation", held in Ankara, Turkey from 24-27 April 1995, and published in CP-570.

configurations (missiles, bombs, fuel tanks, etc.) immersed in an arbitrary flowfield. This flowfield may be either uniform or non-uniform in nature. Uniform flow can be defined simply as a total incidence angle and roll angle while non-uniform flows are defined as a series of velocity components and a dynamic pressure ratio at various longitudinal locations. The non-uniform flowfield may, in principle, be supplied from any source including experiment. However, in general it is predicted using a 3D panel or Euler method.

NUFA was originally developed from the ABACUS prediction program (Reference 1) and uses a similar technique for the determination of aerodynamic loads, i.e. the traditional component build-up approach. Lifting surface and body loads are determined in isolation and then summed using various interference terms to obtain final loads and moments. The basic calculation techniques used have been described previously in References 2 and 3. Version 1.0 of the program was released in 1991. The program was able to model axisymmetric bodies with two sets of monoplane or cruciform lifting surfaces for incidences up to 90 degrees and Mach numbers up to 5.0. Square cross-section body alone calculations could be performed at subsonic Mach numbers. The code was written, documented and released under strict Quality Assurance procedures.

This paper will give an overview of the recent developments carried out to the NUFA program at the Sowerby Research Centre and illustrate some particular applications of the code to the prediction of carriage and grid loads. The developments carried out to the program are separated into two main categories: those which primarily extend the range of geometries capable of being modelled by the code and those which are aimed at improving the accuracy of the predictions. A third category of development exists: those modifications which improve user friendliness and ease code maintenance and support, but these will only be briefly described. Some code developments have already been fully integrated into the program and are available in the latest release of the code, Version 2.0. Other developments are still currently being investigated and will be incorporated in a future release.

All developments carried out to the program must attempt to maintain the code's essential simplicity in terms of user input, it's minimal CPU requirements (and hence cost-effectiveness) and it's user friendliness. Typical run-times for a single flowfield case must be maintained at the current level, i.e. the order of seconds on a typical basic workstation. The code is developed, released and maintained under a strict configuration management system and has been widely distributed to the Military Aircraft, Dynamics and Royal Ordnance Divisions of British Aerospace Defence Ltd. where it is used for the determination of both isolated and grid/carriage loads for a wide variety of configurations. It has been fully coupled into a number of store trajectory suites for the calculation of loads and moments at each successive timestep. The code has, throughout its development history, been actively supported by the Defence Research Agency (DRA) at Bedford.

Extensive validation studies have been carried out, applying NUFA to a wide variety of configurations, ranging from missiles and fuel tanks to mortar bombs. The results of these validation studies have been incorporated into a comprehensive validation file. This extensive document has been widely distributed within BAe and the information is considered extremely valuable for end-users in assisting with the assessment of how well the program can be expected to perform under particular flow conditions for specific types of configuration. Considerable validation has also been carried out concerning the code's abilities in predicting both store carriage and grid loads, and a selection of the results from these studies will be presented.

2. NUFA DEVELOPMENTS

The recent developments to the NUFA code can be categorised as follows:

- Geometry modelling extensions
- Improvements to prediction accuracy
- User and maintenance oriented developments

The developments within each of these categories are detailed below.

2.1. Geometry Modelling Extensions

The following developments have been incorporated into Version 2.0 of NUFA:

- An ability to model up to five sets of lifting surface. This allows, for example, configurations composed of body, canard, wing and tail to be modelled.

- Each lifting surface set may be composed of up to 14 equi-spaced panels.

- Square cross-section bodies may now be defined with monoplane or cruciform lifting surfaces. The horizontal set of panels may be offset in the vertical direction.

Figure 1 illustrates some typical configurations which can be modelled with NUFA Version 2.0.

The traditional technique used for the determination of wing/body and body/wing interference terms is Slender Body Theory (SBT) as described by Nielsen (Reference

4). This technique, albeit with a number of modifications, has been utilized within NUFA for axisymmetric bodies with lifting surfaces. To allow the addition of lifting surfaces to non-circular cross-section configurations required a modification to this method.

Following the technique outlined by Warsop (Reference 5), the problem of determining an effective angle of incidence for a wing attached to a body at an arbitrary roll angle can be effectively split into two separate problems consisting of pure incidence and pure sideslip. The two solutions are combined using the laws of superposition to give the final solution at an arbitrary roll angle. Body on wing interference factors are determined for each panel in a lifting surface set for a pure incidence and sideslip ($K_{WB\alpha}$ and $K_{WB\beta}$ respectively). These interference factors can be used, together with the local flowfield incidence and sideslip angles at the panel control point, the interference due to vortex effects ($\Delta\alpha_v$) and panel deflections ($\Delta\alpha_\delta$) to determine an effective panel local incidence. Hence, the equivalent angle of attack for the ith panel is:

$$\alpha_{eq_i} = K_{WB_{\alpha i}}\alpha_{c_i} + K_{WB_{\beta i}}\beta_{c_i} + \Delta\alpha_{v_i} + \Delta\alpha_{\delta_i} \qquad (1)$$

This equivalent angle of attack can be used to determine the panel normal force coefficient. The process is repeated for each individual panel in each lifting surface set.

The determination of the panel to body carryover is a little more problematic. Since NUFA may be employed with non-uniform flowfields, where each panel will in general experience different flow conditions, it is necessary that the wing on body interference effects be determined for each individual panel. The technique employed (from Reference 5) assumes that "*the carryover load developed by each panel is directly proportional to the load on the panel (including the body on panel interference)*". Four components of panel to body carryover loading are generated for the general case of a fin positioned on an arbitrary cross-section body, i.e. Y and Z components due to both incidence and sideslip. Therefore, four wing on body interference terms are required for each individual panel ($K_{BW\alpha Y}$,$K_{BW\alpha Z}$, $K_{BW\beta Y}$ and $K_{BW\beta Z}$). Each of these interference factors are used together with the panel load, including body to panel carryover, to determine each component of wing to body carryover, e.g. the Z component of load due to the ith panel is:

$$C_{Z_{BW\alpha i}} = K_{BW\alpha Z_i} C_{N_i} \qquad (2)$$

These components are then used to determine the carryover load on the body in the Y and Z directions from the entire lifting surface set due to incidence and sideslip. For example, the Z component of body carryover load due to incidence is:

$$C_{Z_{BW\alpha}} = \sum_{i=1}^{NP} \left(K_{BW\alpha Z_i} C_{N_i} \right) \qquad (3)$$

These components of wing to body carryover load are then apportioned to each individual panel according to the magnitude of the total load on that panel.

The values of the various interference factors described above have been determined using a 2-D panel method (Reference 6) and incorporated into NUFA Version 2.0 for a limited set of configurations. Hence, for square (with arbitrary corner rounding) cross-section bodies with cruciform or monoplane lifting surfaces, with or without a vertical offset for the horizontal lifting surfaces (see Figure 1 for an example), the interference factors can be determined internally within the program.

A number of developments have recently been carried out to Version 2.0 of the program to extend the modelling of configurations of non-circular cross-section which are becoming increasingly popular for low observability and submunition dispensing configurations. The body geometry is defined as a series of sections each of which has a specified profile shape (which can be different in plan and side elevations). Body width, height and cross-sectional shape are defined at the upstream and downstream extremities of each section. Body profile shape may be defined as tangent-ogive, conical, secant-ogive, ellipsoidal and other specific shapes or as a user defined polynomial. Cross-sectional shapes can be circular, rectangular (with corner rounding), elliptical or more arbitrary in shape. Arbitrary cross-sectional shapes are defined as a series of straight lines and circular arcs. The program performs an interpolation from the sectional data input by the user to determine the intermediate body cross-sectional shapes. Figure 2 illustrates a simple example of a configuration built with two body sections using a combination of the various forms of cross-sectional shape definition and a step change in body width. For more simple cross-sectional shapes the program is able to determine appropriate lift curve slope and cross-flow drag/lift coefficient values, however, in general the user is expected to define these values at various body stations.

The 2-D panel method mentioned previously is a simple and efficient tool for the determination of linear lift curve slopes and the definition of arbitrary cross-sectional shapes within NUFA has been designed to be compatible with the panel method input format. Experimental crossflow drag/lift coefficient data for a wide variety of cross-sectional shapes has been assembled in tabular format and will be inserted into the program userguide.

A 2-D discrete vortex code has been developed at SRC and is available to assist users in the definition of these coefficients. NUFA will utilize the user input data to perform a modified Slender Body Theory/crossflow analogy calculation to determine the body load distribution. Additionally, a buoyancy loading calculation is performed to determine body loads due to the flow gradients encountered in a non-uniform flowfield.

The lifting surface calculation uses the modified equivalent angle of attack method described above. The user is required to define the appropriate interference terms but again the 2-D panel method can be used as a tool to provide this information. The interference effects due to panel deflections ($\Delta\alpha_\delta$ in equation 1) have previously been calculated within NUFA using the traditional Slender Body Theory approach of utilizing factors k_{WB} and k_{BW}. NUFA has recently been modified to use the "control effectiveness parameter" approach described in Reference 7. This technique has the advantage that it can be easily extended to bodies of arbitrary cross-section. The basis of the method is the use of an array of control effectiveness parameters which define the effect of the deflection of each individual panel on itself and on all the other panels in the lifting surface set. If Λ_{ij} is the control effectiveness parameter for the effect on the ith panel of the deflection (δ_j) of the jth panel, then the equivalent angle of attack induced on the ith panel by the deflection of all the fins is

$$\Delta\alpha_{\delta_i}=\sum_{j=1}^{NP}\Lambda_{ij}\delta_j$$

The technique can be conveniently described in matrix form. If a lifting surface set has N individual fins, then if **S** is an N element array of equivalent angle of attack increments due to fin deflections, Λ is the NxN element array of control effectiveness parameters and **D** is the N element array of panel deflections then

$$S=\Lambda\, D$$

where
$$\Lambda = \begin{pmatrix} \Lambda_{11} & \Lambda_{12} & \cdots & \Lambda_{1N} \\ \Lambda_{21} & \Lambda_{22} & \cdots & \Lambda_{2N} \\ \cdots & \cdots & \cdots & \cdots \\ \cdots & \cdots & \cdots & \cdots \\ \Lambda_{N1} & \Lambda_{N2} & \cdots & \Lambda_{NN} \end{pmatrix} \qquad D = \begin{pmatrix} \delta_1 \\ \delta_2 \\ \cdots \\ \cdots \\ \delta_N \end{pmatrix}$$

The control effectiveness parameters are known for circular bodies with cruciform lifting surfaces (Reference 7). For non-circular bodies these parameters can be determined using the 2-D panel method (Reference 6) to model the wing/body crossflow plane at the maximum span position (this will give results equivalent to SBT). Results for a circular body with a monoplane lifting surface of varying span have been determined using the panel method. The accuracy of the panel method can be demonstrated by comparing the Slender Body Theory value of k_{BW} and the panel method calculated value of $\Lambda_{11}+\Lambda_{12}$. These values should be equivalent for this monoplane configuration and the comparison is shown in Figure 3. It can be seen that the comparison is very good with a maximum error of about 4% for very small span lifting surfaces. This error is probably due to numerical inaccuracies in the panel code as a result of the very small panels which have to be used to model these small-span configurations.

NUFA has been set up to read these control effectiveness parameters from the input dataset and hence the code should be able to model deflected fins on arbitrary cross-section bodies given the appropriate user input.

It can be appreciated from the above description of the arbitrary body capability that considerable reliance is placed on the 2-D panel method for the determination of the appropriate user input parameters. It is the intention to consider the permanent inclusion of the panel method into NUFA during the next phase of the development. This has already been carried out with the SRC ASTAC code (which is used to determine the aerodynamic characteristics of aircraft configurations) and has proved to be both rapid and reliable in operation. The parameters determined by the panel method would only have to be determined once at program start-up since they are equivalent to SBT values and would be applicable for all flow conditions. It should be emphasised that the development of this arbitrary modelling capability is still in it's early stages and the method is currently undergoing validation/evaluation studies.

2.2 Improvements to Prediction Accuracy

A number of modifications to the NUFA code have been incorporated in an attempt to improve prediction accuracy.

At subsonic Mach numbers NUFA uses a modified Slender Body Theory approach to predict the loading distribution due to the nose of a configuration, which is able to account for the carryover of load from the nose to the body. This technique has been extended, under a BAe/DRA shared funded contract, to transonic and supersonic Mach numbers using a time marching and a space marching Euler code to provide the values for the various required parameters. This technique has been recently improved, under funding from BAe Defence (Dynamics) Ltd., and will be incorporated into the next release of the code. The technique will produce

predictions up to a Mach number of 5 and could be extended to higher Mach numbers if required.

A technique, termed the shock reflection model, has been incorporated into Version 2.0 of NUFA. This model is used to determine an incremental loading on an axisymmetrc body in a non-uniform supersonic flowfield due to the reflected influence of the store off of a plane surface (e.g. off the lower surface of the aircraft wing) back onto itself. The effect is illustrated in Figure 4. The technique is of value when calculating store loads and moments in or near the carriage position at supersonic Mach numbers. It is of particular value when using Euler generated flowfields since the traditional ghosting technique, as used with panel methods for incorporating the effects on the flowfield due to the store's own presence, cannot be utilized. The technique also allows the use of the basic aircraft flowfield for the calculation of loads throughout an entire trajectory range. The method uses the imaging technique of Reference 8, utilizing a distribution of supersonic, linearly varying line sources/sinks and doublets along the store axis to model volume and upwash/sidewash effects respectively. A store image is created to account for the presence of a reflection plane and the program determines an incremental body load distribution due to that image. This technique has demonstrated encouraging results and some of these are presented in Section 3.

A series of store/pylon interference models have been incorporated into NUFA Version 2.0 under funding from BAe Defence (MAD) Ltd. The techniques can be used to explicitly determine the incremental loads and moments experienced on a store in the carriage position due to the presence of the pylon. It had previously been found that the accuracy of the flowfield discretisation technique was limited in areas of very high flow gradients which are particularly prevalent around the pylon foot. This deficiency tended to lead to a poor prediction of store lateral forces and moments (at subsonic speeds this has been found to be a problem when the store is within half a calibre of the foot of the pylon). A variety of techniques, all generally based on Slender Body Theory, have been implemented to explicitly account for the presence of the pylon. It should be noted that the direct effect of the pylon should be removed from the flowfield, i.e. both the store and pylon should be 'ghosted' from the solution. Somewhat limited validation of these techniques has taken place but Figure 5 illustrates some results obtained to date. Where the store is released using an ERU mechanism the inability to accurately discretise the flowfield may not be a significant problem since the prediction of the store trajectory is often started from the end of stroke position. It is anticipated that the incorporation of the store-pylon interference model will improve the accuracy for those cases where the trajectory must start from the installed location.

In addition to the modifications described above, various more minor developments have been incorporated into NUFA Version 2.0:-

- A viscous body and trailing vortex core model has been implemented within the code. The core model gives a smoothly varying, physically realistic velocity distribution through each vortex and prevents "close approach" problems which can occur when a potential vortex passes very close to a particular control point.

- The user is now able to specify the flowfield velocity components at lifting surface control points allowing more realistic individual panel loads to be determined.

- A new technique for the improved prediction of body boattail loads has been developed and incorporated into the program.

2.3. User and Maintenance Oriented Developments

A number of modifications have been carried out to the code aimed at improving the program/user interface and simplifying code maintenance. The program will now write a geometry plotting output file during execution. This file, written in a format commonly used throughout BAe, can be utilized to view the defined geometry, providing the user with increased confidence in the specified input data. The configurations shown in Figures 1 and 2 have been plotted using this capability.

A number of further modifications have been carried out to the code enabling it to be simply and efficiently coupled into a store trajectory program with a "clean" interface. This means that the NUFA subroutines can be compiled into a stand alone version of the program or directly coupled into a trajectory suite without any internal modifications. This greatly simplifies future code updates and satisfies strict Quality Assurance procedures. Other minor modifications, such as suppressing all program output and providing a flip-out fins capability, have improved the code's interface with trajectory calculation suites.

A comprehensive userguide, effective problem reporting system and prompt user support provided by SRC assist all users in the effective exploitation of the capabilities inherent within the code.

3. HYBRID STORE LOAD PREDICTION

To predict store loads, NUFA requires, as input, the flowfield in which the store is immersed. By supplying an aircraft flowfield, store grid loads (including carriage loads) and trajectories may be predicted. The flowfield

can be obtained from any source, including experiment, simple prediction methods and CFD codes. The use of the semi-empirical code together with a flowfield generated by another means is termed a hybrid scheme. The hybrid scheme enables the ease of use, low cost (in terms of both human and computer resources) and fast turnaround of the semi-empirical code to be exploited to the full. Since the aircraft flowfield can be obtained from a wide range of methods, the hybrid scheme provides an extremely flexible technique for predicting store loads and trajectories. When a CFD code is used to predict the flowfield, its accuracy for this purpose is combined with the advantages of the semi-empirical code. Allowing the project engineer to choose from a range of methods for the prediction of the flowfield ensures that the method is always fit for purpose, whilst enabling the engineer to consistently undertake predictions within the same flexible framework. The hybrid scheme is, however, constrained by the limitations of the semi-empirical method, although as described previously, SRC are undertaking developments to the NUFA code to overcome some of these weaknesses. Nevertheless, some limitations will remain, for example, the code is unable to predict the surface pressure distribution, which may be required for stressing purposes. The hybrid scheme is therefore designed to provide a flexible tool for use by engineers, complementing both experimental techniques and numerically intensive methods.

The NUFA code has been incorporated within a number of BAe Defence Ltd. trajectory codes including the Military Aircraft Division STARS and the Dynamics Division HATS codes. The latter code was developed by SRC under funding from BAe Defence (Dynamics Division) Ltd. Use of NUFA within these codes enables full advantage of the hybrid scheme to be exploited. Where the NUFA code is used for predicting isolated weapon loads in concept or project studies, the application of the code within a trajectory method ensures that commonality in the prediction of the aerodynamic loads is maintained.

The ability of a trajectory code to accurately predict store dispersion will, in part, be determined by its ability to predict accurate static aerodynamic loads on the store. It is therefore generally advisable to evaluate the accuracy of any trajectory method by comparing predicted grid loads with experimental data, where it is available. The accuracy of the predicted grid loads is in turn determined by the ability of the method to predict both accurate isolated weapon loads and aircraft flowfields. Before undertaking the prediction of a store trajectory these elements should also be checked. A number of examples of the hybrid scheme's ability to predict accurate store grid loads will therefore be presented. These will also provide some indication of the advantages of the method, including its flexibility, accuracy and potential to provide users with predictions at relatively low cost. In each case, where suitable experimental data has been available, comparisons of predicted isolated weapon loads and aircraft flowfields have also been undertaken. NUFA has been used together with a 3-D subsonic panel method and a number of Euler codes to predict store grid loads. An example of each will be presented, including some initial predictions of submunition loads.

The first study which included the use of an Euler code within the hybrid scheme made use of the experimental data from Reference 9. This data was used to evaluate the use of a structured multiblock Euler code and its application within a hybrid scheme to predict the aerodynamic loads on a body alone configuration. The experimental data included isolated store loads, underwing flowfield data and store grid loads. The store grid loads were measured at a variety of heights below fuselage-wing and fuselage-wing-pylon configurations. Test data were available at Mach numbers of 1.5 and 2.0 at 0° and 5° incidence. The aircraft configuration is shown in Figure 6. The store was a simple tangent-ogive/circular cylinder configuration.

The BAe WMS Euler code (Reference 10) which was used for the study was developed specifically for the prediction of weapon aerodynamics. Because of this, the mesh generation software was not optimised for modelling aircraft-store configurations, however this initial study provided useful information about the use of the NUFA code with Euler methods. The study was jointly funded by BAe SRC and the DRA.

The isolated body loads were predicted using both NUFA and the WMS Euler code. Load distributions were compared between 2.5° and 10° of incidence at Mach 2.0. A typical result is presented in Figure 7. NUFA Version 1.1a was used for this study and it is evident that the load distribution on the nose of the configuration is over-predicted. Also, the carryover from the nose onto the body is not represented. Development of an improved supersonic body model, as described earlier, is almost complete and will be incorporated within the next release of the code. The accuracy which could be expected from this model is demonstrated in Figure 8 for the same configuration as that in Figure 7. The comparison with the experimental data has been significantly improved. Returning to Figure 7, the load distribution is relatively well predicted by the Euler code, although it is evident from the loads on the aft part of the body that the non-linear effects due to body separations are not predicted. This discrepancy increases with incidence, as would be expected.

An example of the flowfield comparisons is presented in

Figures 9. The sidewash and upwash distributions along an axial traverse 1.37 inches below the wing mean chord plane are presented for both the pylon on and off configurations at Mach 2.0, α=5°. The leading edge shock is predicted slightly too far aft and tends to be smeared. In general the flowfield is fairly well predicted for the pylon off configuration. With the addition of the pylon the discontinuities in both the sidewash and upwash distributions are not well predicted, although there does appear to be some scatter in the experimental data. The wing leading edge shock was poorly represented by the WMS code when the pylon was modelled. This was probably largely due to the mesh quality, and emphasises the need to ensure good mesh density and quality in regions where flowfield data is to be extracted for grid load or trajectory calculations. From Figure 9 it is clear that the velocity gradients around the pylon foot are very high. As indicated in Section 2.2, due to the discretisation method used within NUFA, the accuracy of the predicted loads in the presence of these very high gradients may be degraded. This was confirmed by the store load comparisons although use of a store-pylon interference model could be expected to improve the comparison with experimental data at the installed position.

The Euler code was used to both predict the store grid loads and to provide flowfield for input to NUFA. Comparison of the load distributions on the store located below the fuselage-wing configuration highlighted the need for a correction to be incorporated within NUFA to account for the reflection of the store nose shock off the wing lower surface. The effect of the shock reflection model (described in Section 2.2), at M1.5, α=5°, on the predicted load distribution at a height of 2.87 inches below the wing is indicated in Figure 10. Inclusion of the shock reflection model improved the predicted load distribution. The overshoots in the NUFA load distribution at axial stations less than 0.4 are caused by the use of Slender Body Theory, as highlighted by the load distribution comparisons for the isolated body.

Store grid loads are presented in Figures 11(a) to 11(d) for the normal force, pitching moment, side force and yawing moment at M2.0, α=5°. The distance of the store below the installed position was varied from 0 to 4.5 inches (equivalent to 6 calibres). The normal force and pitching moment are well predicted by NUFA, although the discrepancy in pitching moment increases as the store approaches the wing lower surface. The apparent differences between the predicted and experimental data between 3 and 4.5 inches is due to the lack of predicted data points. The quality of the predicted side force and yawing moment is not as good.

It is notable that there is a close correlation between the loads predicted by the Euler code and those by NUFA. To produce the predicted loads from the Euler method presented in Figure 11 required the code to be executed seven times: each time the store was moved and remeshing required. For each position the code took approximately 10 hours of CPU time on a Cray 2. The NUFA predictions were undertaken using the flowfield data extracted from a single execution of the WMS code. The CPU time required by the semi-empirical code is negligible; a few seconds on a workstation. The flowfield data for the predictions presented in Figure 11 were provided for the fuselage-wing configuration, there being no need to model the store using the Euler code. This greatly simplified the modelling. Execution of the Euler code for the flowfield calculation required approximately 6 hours of CPU time, resulting in a saving of up to 64 hours of CPU time and a considerable amount of labour. The output from the WMS code for the fuselage-wing configuration could, in fact, be used to provide an estimate of the store loads at any position within the flowfield of the aircraft. Also, any number of store configurations could be analysed, providing potentially massive savings in computing and labour costs.

The hybrid scheme has also been applied at transonic Mach numbers to the more complex aircraft-store configuration shown in Figure 12. The loads on a missile at various locations beneath the M165 combat aircraft research model were measured in the ARA transonic wind tunnel under funding from SRC. The M165 model, which was loaned by the MoD, has a twisted, cambered, swept wing with a number of leading and trailing edge control surfaces, although none of the control surfaces were deployed during the tests. A mid-span pylon was manufactured for these tests and loads on the missile were measured both with and without the pylon present. As well as measuring five components of load on the missile, the underwing flowfield, store isolated loads and wing surface pressures were acquired. Tests were undertaken at Mach numbers of 0.7 and 1.2 at a number of angles of incidence. Following the normal procedure, the predicted isolated store loads were compared with experimental data. This was followed by a comparison of the flowfield data. The experimental flowfield data were compared with results from both multiblock structured Euler and unstructured Euler codes.

For this missile configuration no 'tuning' was required to match the experimental isolated loads, although at the lower Mach number it was evident that the interference of the body and wing trailing vortices on the tail was being over-predicted. This problem has now been overcome with the introduction of a vortex core model. A comparison of predicted and experimental store loads for the missile at 6 locations below the M165 clean aircraft are shown in Figures 13(a) to 13(d). Loads were actually measured at 24 locations, corresponding to 4

axial lines of 6 points as shown in Figure 14. The results presented in Figure 13 are for the uppermost line, with the axial position at x=0.0 corresponding to the installed position, had the pylon been present. The lines are inclined at an angle of 3.75° to the wing reference plane. The comparison of the flowfield data indicated that for the particular flow conditions presented here (M0.7, α=0°, 4°, 9° and 12°), the actual and nominal five hole probe traverses may have been at a slightly different orientation, with a difference of at most 0.4° in the incidence and sideslip planes. Although it has not yet been undertaken, the wing pressures should give some indication of the difference between the nominal and actual aircraft incidence angles. From Figure 13 it can be seen that the normal force, side force, pitching moment and yawing moment are well predicted by the hybrid scheme throughout the incidence range investigated. The results are particularly pleasing since the structured grid for the M165 configuration was not optimised to provide flowfield data beneath the wing. The lack of optimisation of the grid for the purpose for which it was to be put was more clearly shown in the supersonic results, although, even for the higher Mach number the trends in the variation of the missile loads were reasonably well predicted as shown by the side force results presented in Figure 15, again for the uppermost axial line. Here results are presented at 0°, 3° and 6° incidence.

With the introduction of a pylon, significant changes can be expected in the grid loads around the pylon foot. The five hole probe data clearly showed, as was seen in the previous test case, that the presence of the pylon introduces significant non-uniformities in the flowfield, with extremely high velocity gradients around the pylon foot. The flowfield comparisons for these flow conditions indicated that the difference between the nominal and actual probe traverses was, as before, of the order of 0.4°. A comparison of the predicted and experimental missile loads with the pylon fitted are shown in Figures 16(a) to 16(d), for the second highest axial traverse. Data are presented for the lower Mach number at 0°, 4° and 9° incidence. Clearly the trends are well predicted, although the magnitude of the side force and yawing moment tend to be over-predicted, the discrepancies decreasing with increasing distance from the pylon.

The hybrid scheme has also been applied to the prediction of the loads on a Terminally Guided Submunition (TGSM). Comparisons with the measured data have only been completed recently and some initial results are presented. The work was funded by the MoD through the Defence Research Agency, WX8 Division. No flowfield data was measured during the tests and it was therefore only possible. for this particular configuration, to compare the isolated TGSM loads before undertaking predictions of the grid loads. The tests were undertaken at a low subsonic Mach number (Reference 11) and therefore the BAe SPARV 3-Dimensional panel method was used to predict the flowfield in which the TGSM was immersed. No dummy submunitions were used during the testing and thus the only interference during the tests was between the TGSM and the dispenser. The tests were undertaken to ascertain, amongst other things, the effect of varying incidence and yaw angles, opening various bays, moving the longitudinal position of the dispenser wing, adding a canard to the dispenser and the effect of varying the TGSM attitude relative to the dispenser. The dispenser had six bays; a forward and rear set each having three bays.

Isolated TGSM loads were measured in the DRA 8'x6' wind tunnel. Data were obtained on various build standards of the model: body alone, body-strake and body-strake-tail. The configurations with strakes would present a challenge to any prediction method due to their very low aspect ratio and the interaction of the vortices from the strakes with the tail surfaces. A comparison of the isolated loads for the three configurations are shown in Figure 17. The 'tuned' NUFA loads are presented together with the experimental data. Version 2.0 of NUFA was used for this study. The loads are well predicted by the semi-empirical code, including the loads on the body alone, which, it is worth noting, had a hemispherical nose.

The loads on the TGSM (body-strake-tail) at a range of y stations were predicted with the submunition pitch and yaw attitude varying relative to the dispenser. At the closest position to the dispenser (y/D=2), which was configured with all bays covers on, the submunition was just outside the top rear bay. Various views of a panel model showing the geometry of one of the configurations is shown in Figure 18. Predicted grid loads were obtained using a 'clean' dispenser (i.e. no TGSM was modelled by SPARV). SPARV predicted flowfields were input to NUFA to obtain predictions of the grid loads. Comparisons of the predicted and experimental grid loads at an angle of incidence of 5° are shown in Figures 19(a) to 19(d) for the TGSM pitch attitude relative to the dispenser varying by +/-5°. Results are presented for two different dispenser boattail models. Use of the second model clearly improves the comparisons with the experimental data, particularly for the side force and yawing moment. The effect of varying lateral position is very well predicted. The variation with pitch attitude is well predicted for the normal force and pitching moment. The trend with pitch attitude is not as well predicted for the lateral characteristics, although the relative scale of the graphs should be noted.

The effect of yaw attitude was not predicted as accurately

and further work is required to refine the panel model used to generate the flowfield data used within NUFA.

The effect of opening a bay was briefly investigated. Data were obtained for a store emerging from the bottom forward bay. The dispenser was configured as a body alone. Only the bay from which the submunition was being traversed was opened. The experimental and predicted submunition loads are presented in Figure 20 for a dispenser and submunition pitch angle of 5°. The removal of the bay cover has a significant effect on the submunition loads, primarily on the lateral characteristics. The effect of removing the bay cover was well predicted by the hybrid scheme. With the bay cover removed the side force and yawing moment are under-predicted. Although the initial results have been very encouraging they have highlighted the need for further work, including improved modelling of the effect of the open bay on the flowfield characteristics.

4. CONCLUSIONS

The NUFA semi-empirical code continues to be developed since it provides project engineers with a low cost, flexible and easy to use method for predicting both isolated weapon aerodynamics and store loads. When incorporated within a hybrid store trajectory prediction method, engineers are able to combine these advantages with the accuracy of CFD codes for predicting aircraft/dispenser flowfields. Although CFD codes may be used as a prime source of flowfield data, the flexibility of the scheme is such that the flowfield data may be obtained from a variety of sources, including simple prediction methods and experiment. The hybrid scheme has been designed to complement both experimental techniques (wind tunnel and flight test) and complex, relatively high cost prediction methods. Engineers are therefore able to choose from a range of methods, enabling the most appropriate technique to be applied, depending on the problem at hand, the availability of resources, the timescales and the budget.

The accuracy and versatility of the hybrid scheme has been demonstrated by a number of comparisons with experimental data. Substantial savings in both computing time and labour are possible due to the flexibility of the hybrid scheme, a single aircraft/dispenser flowfield being used to calculate any number of grid loads and trajectories for a virtually unlimited number of store configurations.

ACKNOWLEDGEMENT

This work has been carried out with the support of the Military Aircraft, Dynamics and Royal Ordnance Divisions of British Aerospace (Defence) Ltd. and the Defence Research Agency, HWA Bedford and WX8 Farnborough. The authors would like to acknowledge P.S.Barratt, G.D.Booth, F.J.Delafaille, P.C.Dexter, H.M.S.Figueiredo and G.A.Johnson from the Sowerby Research Centre Aerodynamics and Vulnerability Department all of whom have contributed to the NUFA and hybrid scheme development and validation work presented in this paper.

REFERENCES

[1] P.G.C.Herring. A computer program which evaluates the longitudinal aerodynamic characteristics of typical weapon configurations. AGARD-CP-336, Missile Aerodynamics, Paper 26, September 1982.

[2] S.A.Bizon. NUFA - A technique for predicting characteristics of store configurations in a non-uniform flowfield. AGARD-CP-389 Paper No.14, October 1985.

[3] S.McDougall, A.J.Press and P.S.Barratt. NUFA: A semi-empirical method for the prediction of isolated weapon aerodynamics. AGARD-CP-493, Missile Aerodynamics, Paper 9, 23-26th April 1990.

[4] J.N.Nielsen. *Missile Aerodynamics*. McGraw-Hill Book Co., New York, 1960.

[5] C.Warsop. Application of interference terms for arbitrary configurations. BAe SRC unpublished notes, February 1992.

[6] D.Isaacs. A two-dimensional panel method for calculating Slender Body Theory loading (or loading for minimum vortex drag) on a body of arbitrary cross-section. RAE Technical Report 81003, January 1981.

[7] J.N.Nielsen, M.J.Hemsch and C.A.Smith. A preliminary method for calculating the aerodynamic characteristics of cruciform missiles to high angles of attack including the effects of roll angle and control deflections. Office of Naval Research CR215-226-4F, November 1977.

[8] F.K.Goodwin, M.F.E.Dillenius, J.Mullen. Prediction of supersonic store separation characteristics including fuselage and stores of noncircular cross-section. Volume 1- theoretical methods and comparisons with experiment. AFWAL-TR-80-3032, November 1980.

[9] M.F.E.Dillenius, F.K.Goodwin and J.N.Nielsen. Prediction of supersonic store separation characteristics. Volume 1 - Theoretical methods and comparisons with experiment. AFFDL-TR-76-41, Vol.1., May 1976.

[10] P.A.Shepherd and G.R.Tod. Development and application of a Weapons Multiblock Suite. AGARD CP 437, Validation of Computational Fluid Dynamics, Paper No.23, May 1988.

[11] A.J.Kearse and M.J.Blackburn (HEL). Aerodynamic interactions between submunitions and dispensers. Unpublished RAE Report.

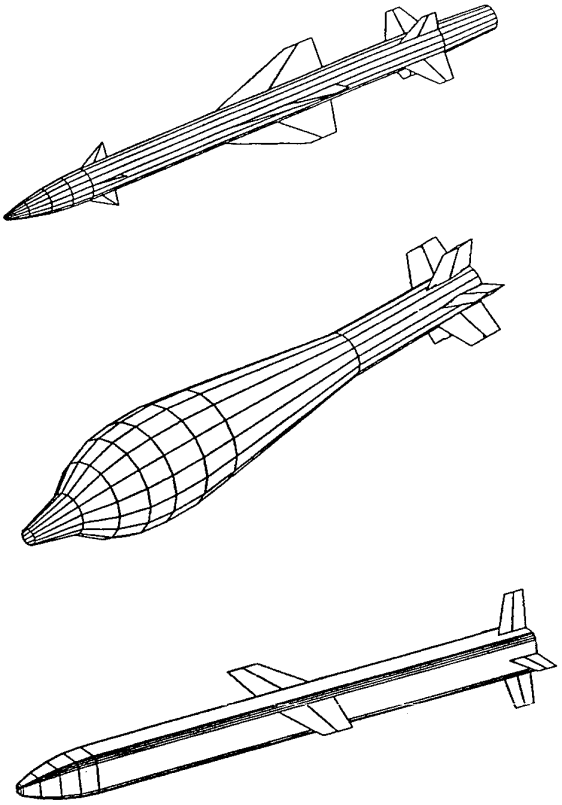

Figure 1 : Typical NUFA Version 2.0 Geometries

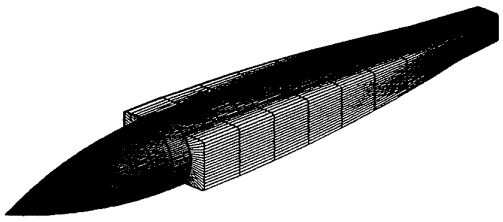

Figure 2 : Example Arbitrary Body Geometry

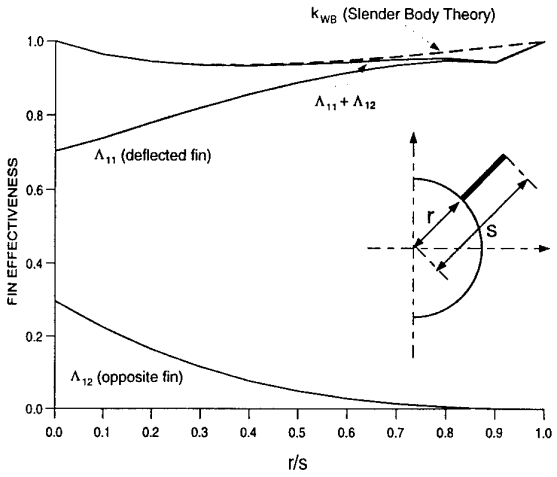

Figure 3 : Circular Body / Monoplane Fin Control Effectiveness Parameters

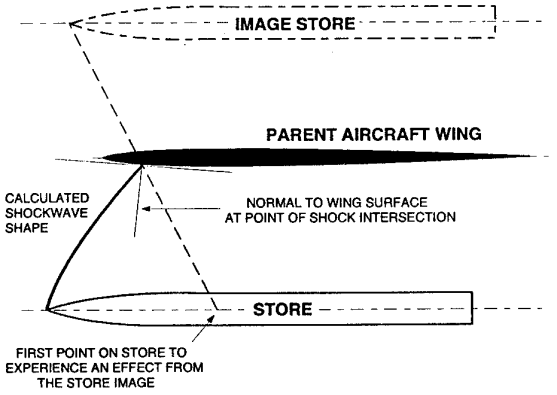

Figure 4 : Shock Reflection Model

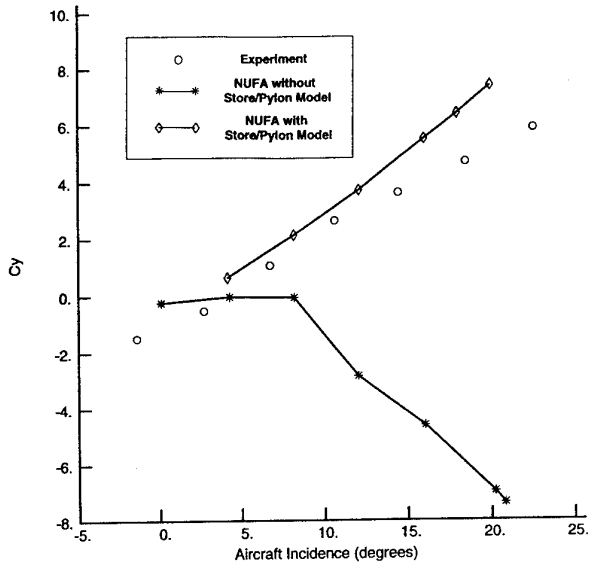

Figure 5a : Effect of the Store/Pylon Interference Model. Missile A on Inboard Wing Pylon of Tornado (Wing at 45° Sweep)

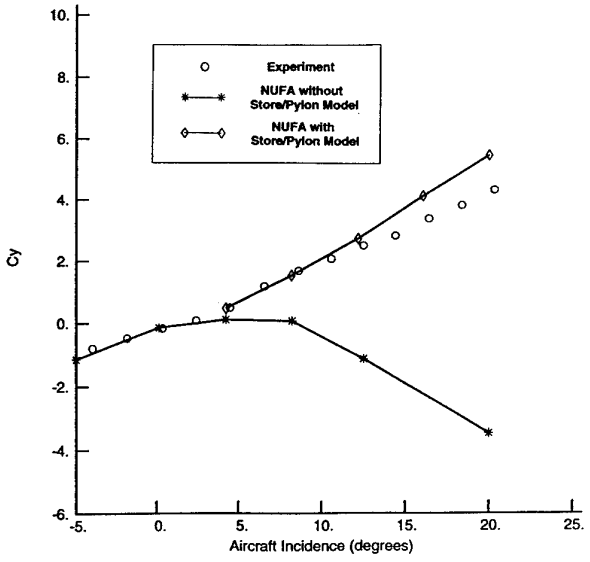

Figure 5b : Effect of the Store/Pylon Interference Model. Missile B on Inboard Wing Pylon of Tornado (Wing at 45° Sweep)

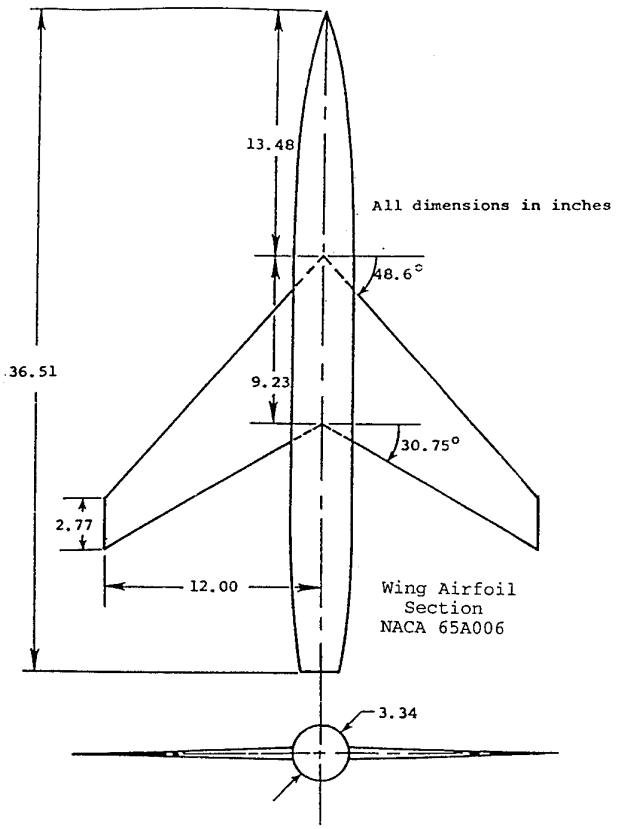

Figure 6 : Aircraft Geometry (extracted from Reference 9)

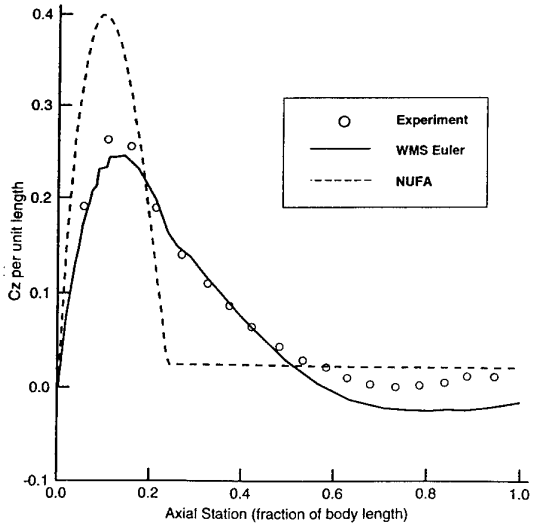

Figure 7 : Comparison of Predicted and Experimental Isolated Body Load Distribution

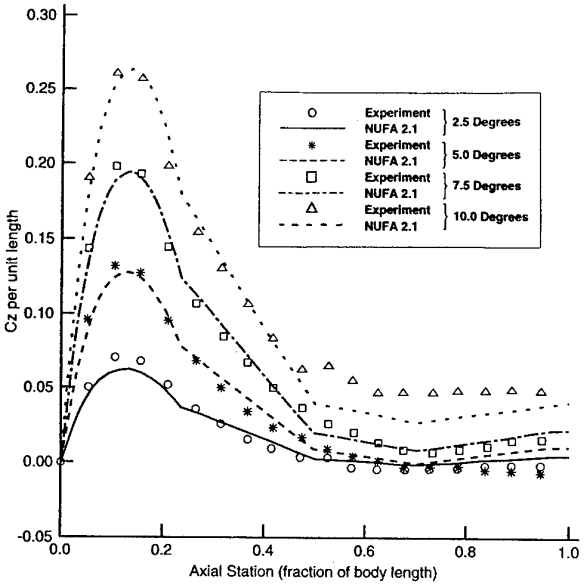

Figure 8 : Comparison of Experimental and Updated NUFA Isolated Body Load Distributions

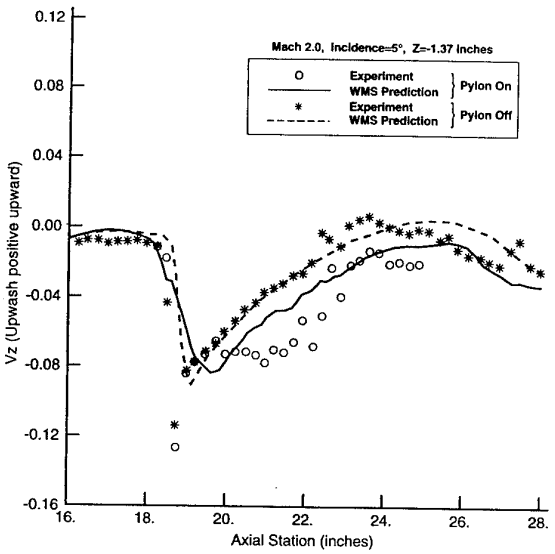

Figure 9 : Comparison of Predicted and Experimental Flowfield Distributions.
(b) Upwash Distribution for Wing/Body and Wing/Body/Pylon

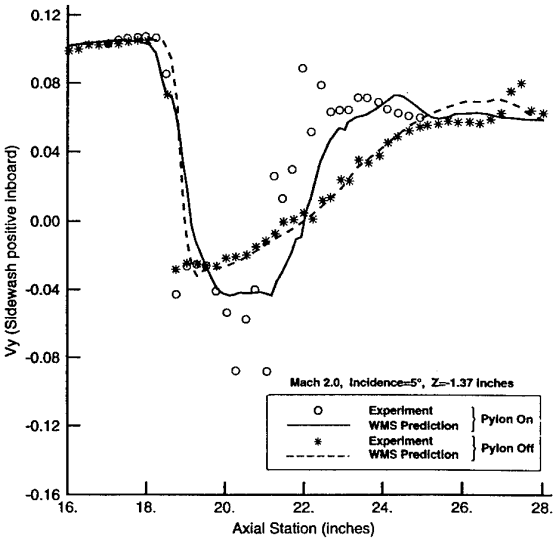

Figure 9 : Comparison of Predicted and Experimental Flowfield Distributions.
(a) Sidewash Distribution for Wing/Body and Wing/Body/Pylon

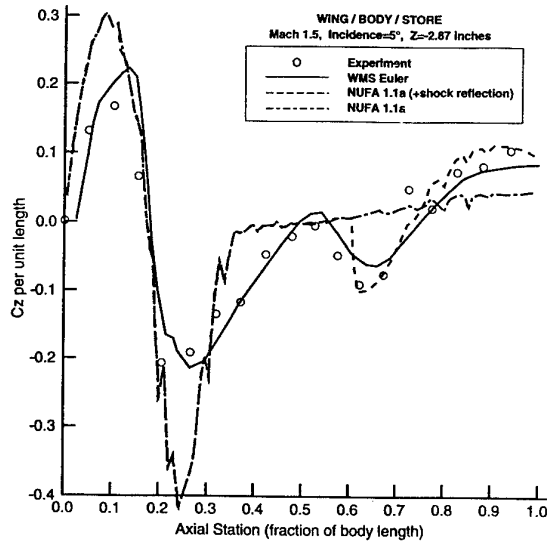

Figure 10: Comparison of Predicted and Experimental Load Distributions.
(a) Normal Force Distribution

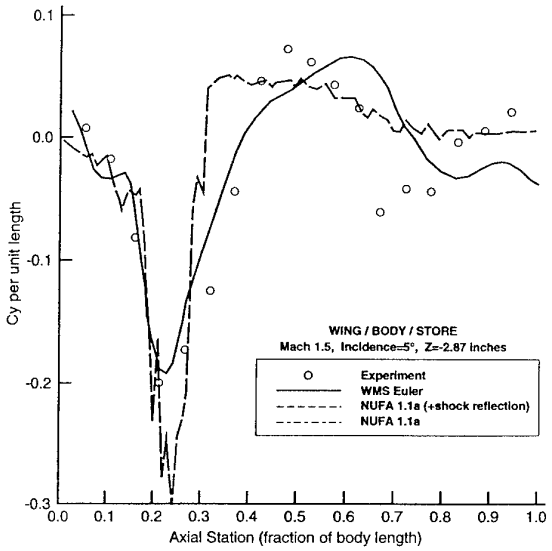

Figure 10: Comparison of Predicted and Experimental Load Distributions.
(b) Side Force Distribution

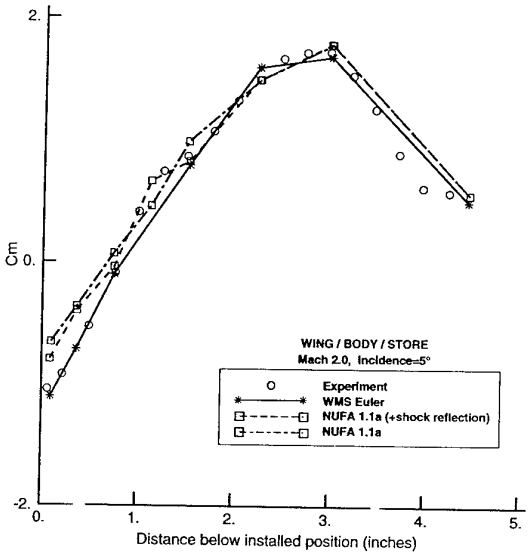

Figure 11: Comparison of Predicted and Experimental Grid Loads.
(b) Pitching Moment

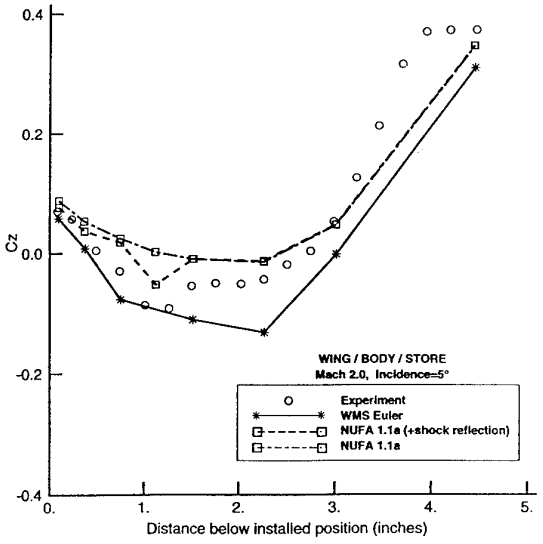

Figure 11: Comparison of Predicted and Experimental Grid Loads.
(a) Normal Force

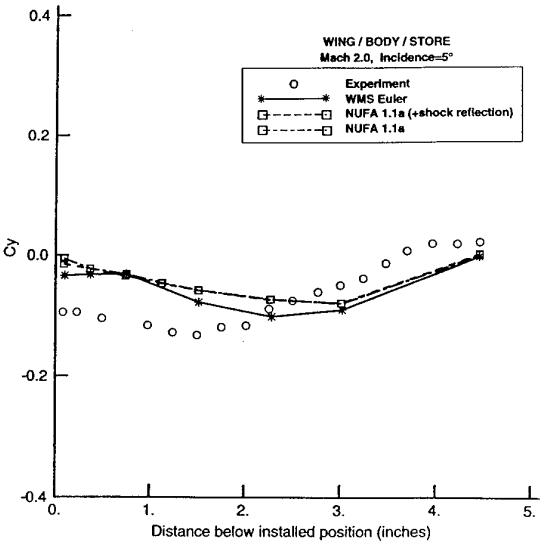

Figure 11: Comparison of Predicted and Experimental Grid Loads.
(c) Side Force

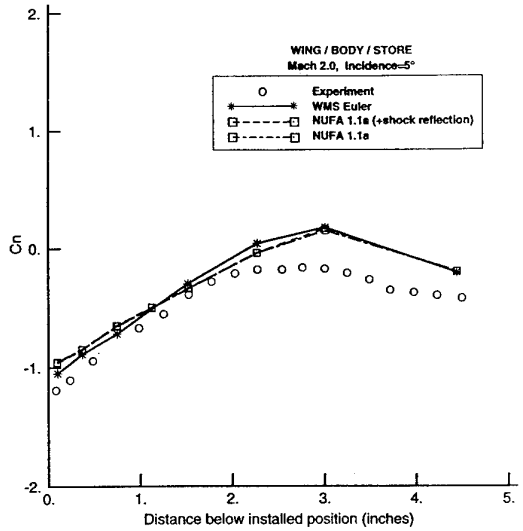

Figure 11: Comparison of Predicted and Experimental Grid Loads.
(d) Yawing Moment

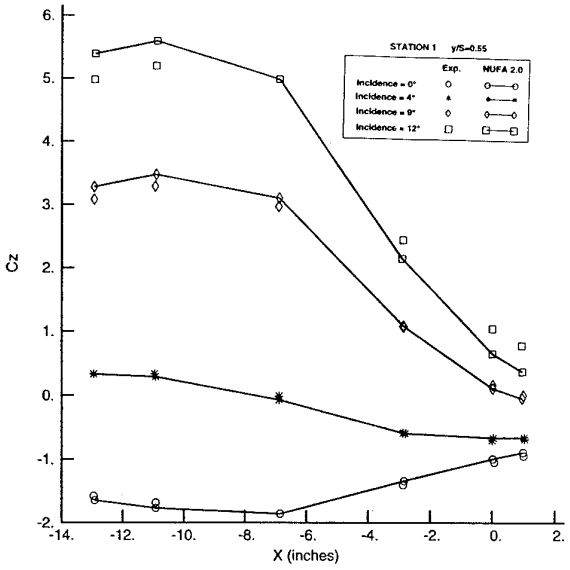

Figure 13: Comparison of NUFA and Experimental Grid Loads Beneath Model M165 at Mach 0.7
(a) Normal Force Coefficient

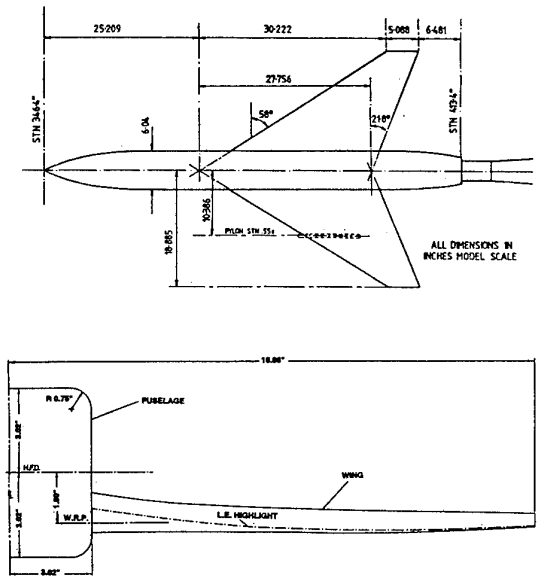

Figure 12 : Geometry of Model M165.

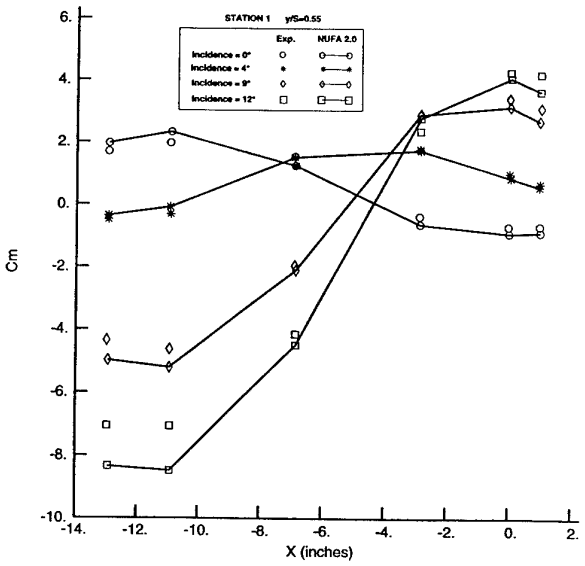

Figure 13 : Comparison of NUFA and Experimental Grid Loads Beneath Model M165 at Mach 0.7
(b) Pitching Moment Coefficient

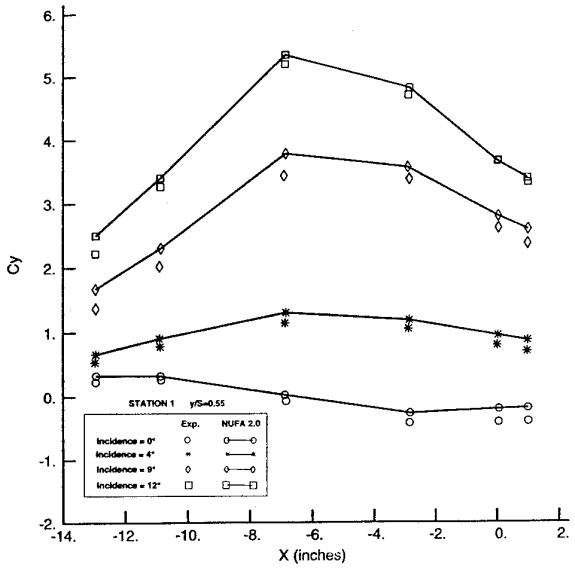

Figure 13 : Comparison of NUFA and Experimental Grid Loads Beneath Model M165 at Mach 0.7
(c) Side Force Coefficient

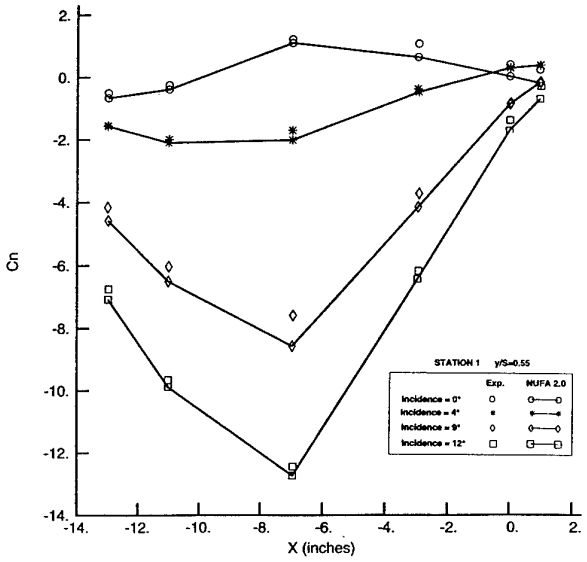

Figure 13 : Comparison of NUFA and Experimental Grid Loads Beneath Model M165 at Mach 0.7
(d) Yawing Moment Coefficient

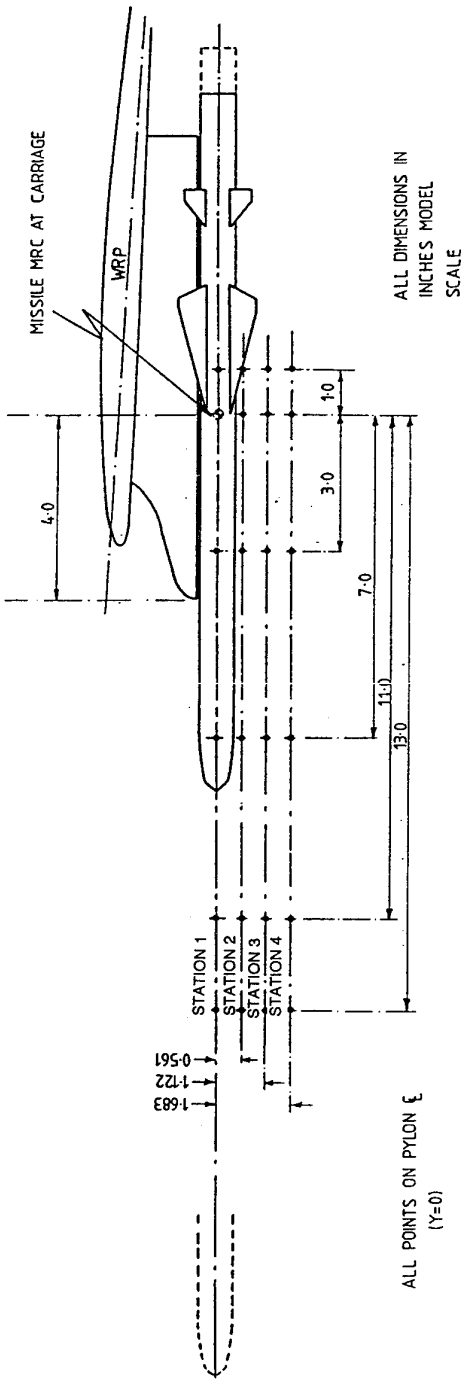

Figure 14 : Grid Load Measurement Locations.

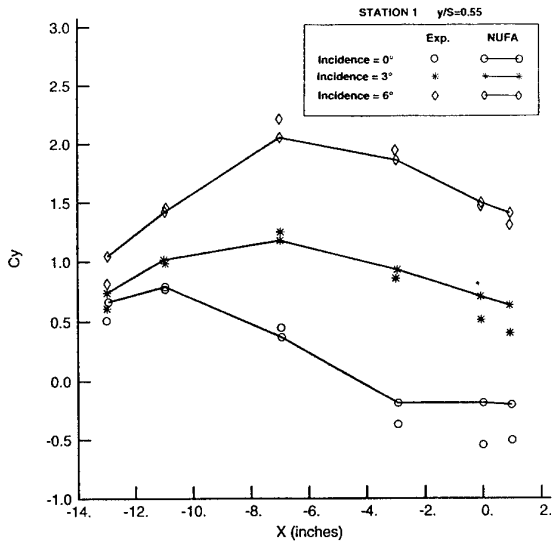

Figure 15: Comparison of Predicted and Experimental Side Force at Grid Points Beneath Model M165 at Mach 1.2.

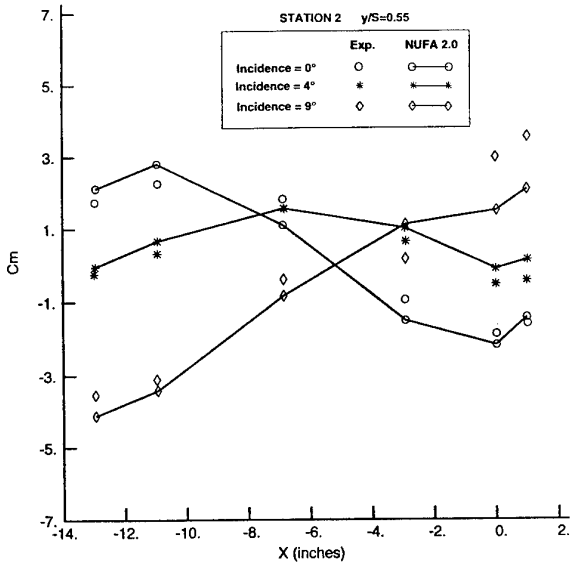

Figure 16 : Comparison of NUFA and Experimental Grid Loads Beneath Model M165 with Pylon at Mach 0.7
(b) Pitching Moment Coefficient

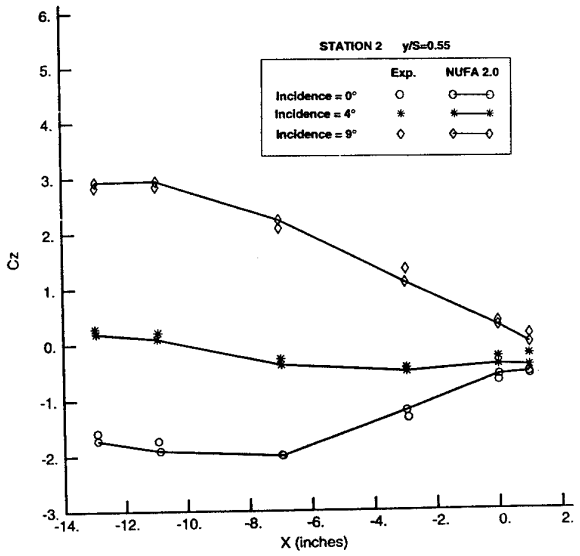

Figure 16 : Comparison of NUFA and Experimental Grid Loads Beneath Model M165 with Pylon at Mach 0.7
(a) Normal Force Coefficient

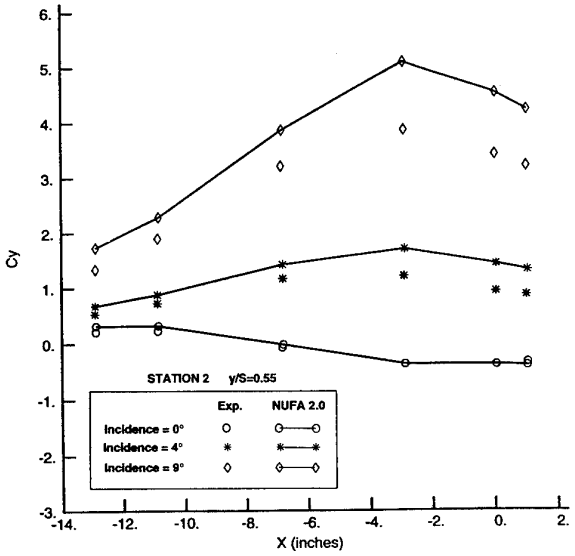

Figure 16 : Comparison of NUFA and Experimental Grid Loads Beneath Model M165 with Pylon at Mach 0.7
(c) Side Force Coefficient

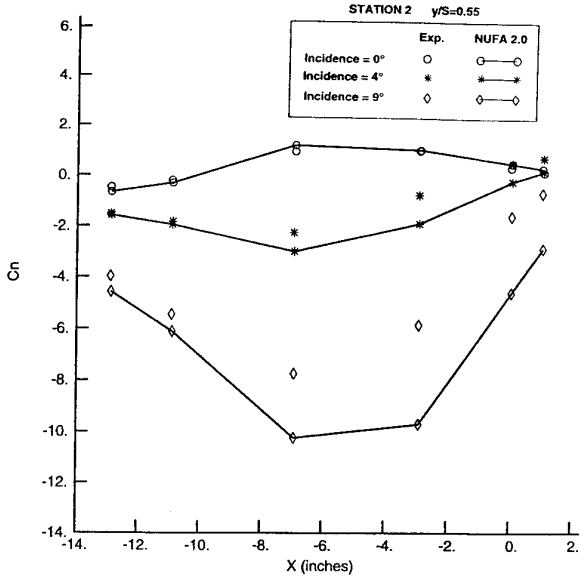

Figure 16 : Comparison of NUFA and Experimental Grid Loads Beneath Model M165 with Pylon at Mach 0.7
(d) Yawing Moment Coefficient

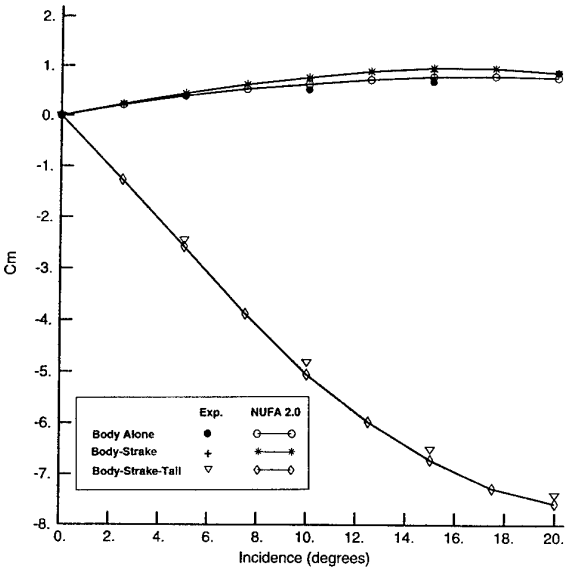

Figure 17 : Comparison of NUFA and Experimental TGSM Loads
(a) Pitching Moment Coefficient

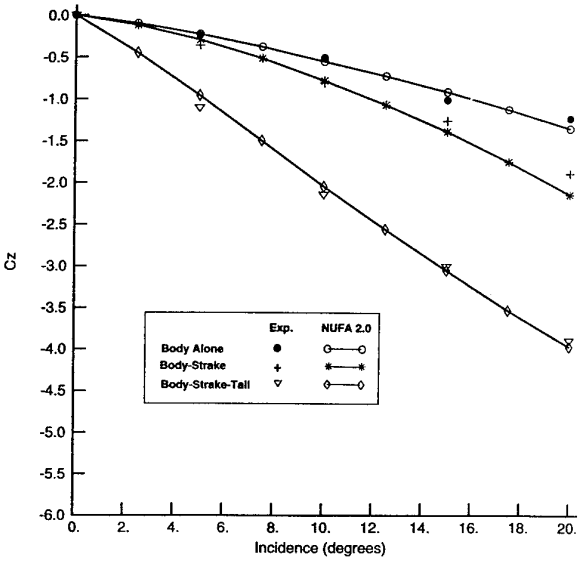

Figure 17 : Comparison of NUFA and Experimental TGSM Loads
(a) Normal Force Coefficient

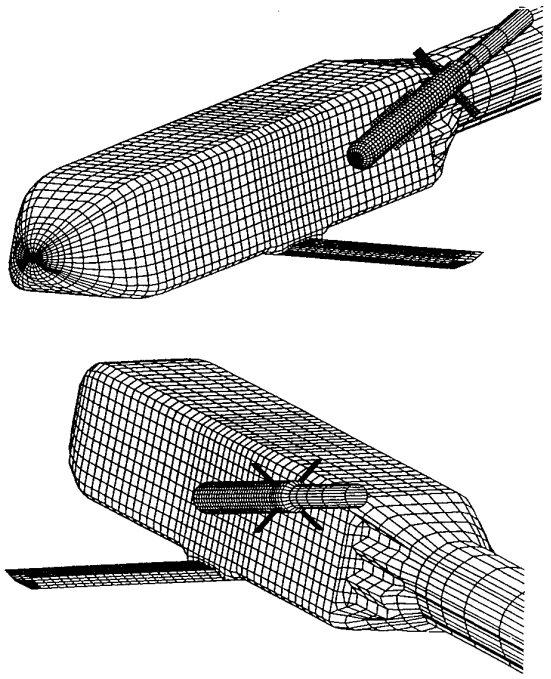

Figure 18 : Dispenser Geometry for Traverse from Bay 3R.

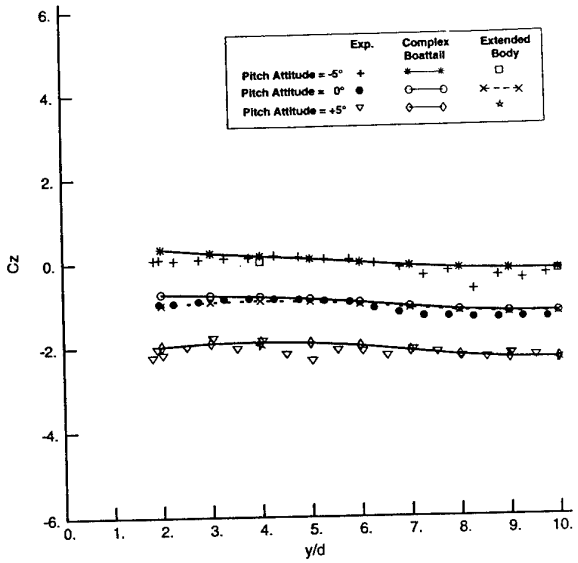

Figure 19 : Comparison of NUFA and Experimental Grid Loads. Traverse from Bay 3R. All Bay Covers On. Variation in TGSM Pitch Attitude by ±5°
(a) Normal Force Coefficient

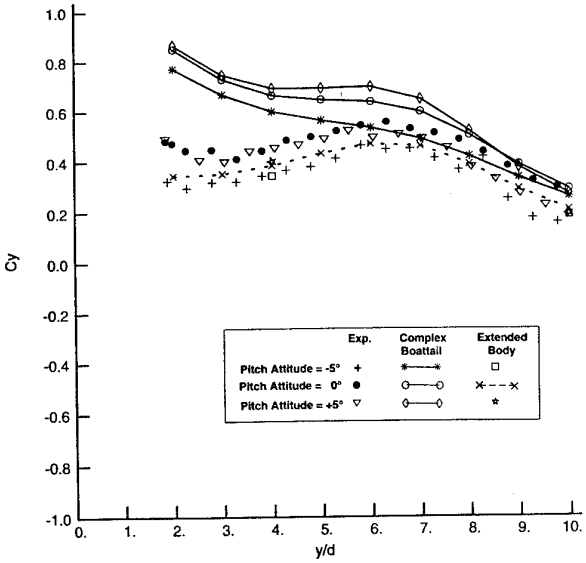

Figure 19 : Comparison of NUFA and Experimental Grid Loads. Traverse from Bay 3R. All Bay Covers On. Variation in TGSM Pitch Attitude by ±5°
(c) Side Force Coefficient

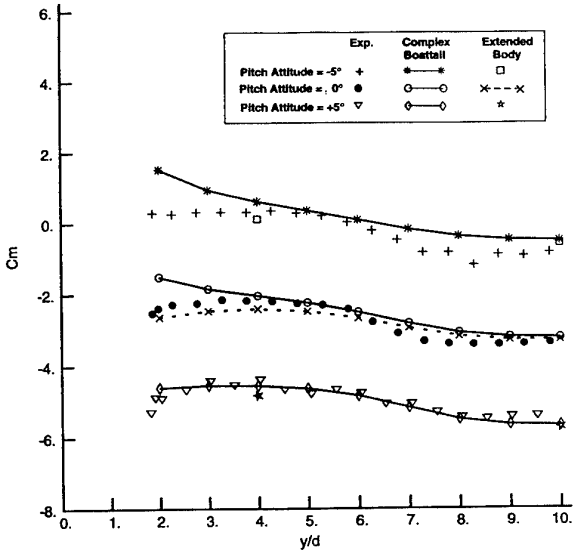

Figure 19 : Comparison of NUFA and Experimental Grid Loads. Traverse from Bay 3R. All Bay Covers On. Variation in TGSM Pitch Attitude by ±5°
(b) Pitching Moment Coefficient

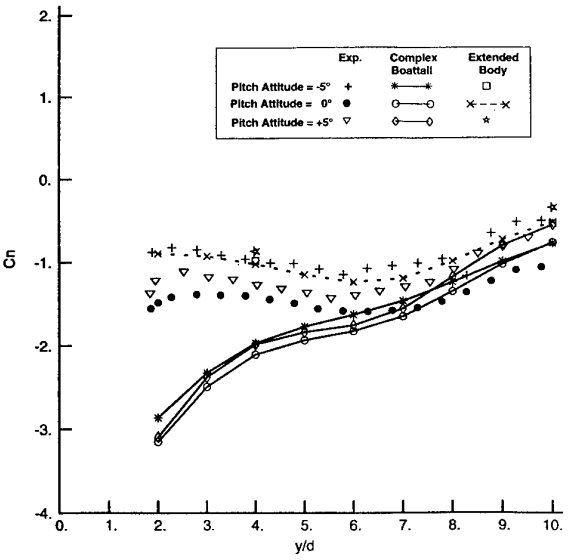

Figure 19 : Comparison of NUFA and Experimental Grid Loads. Traverse from Bay 3R. All Bay Covers On. Variation in TGSM Pitch Attitude by ±5°
(d) Yawing Moment Coefficient

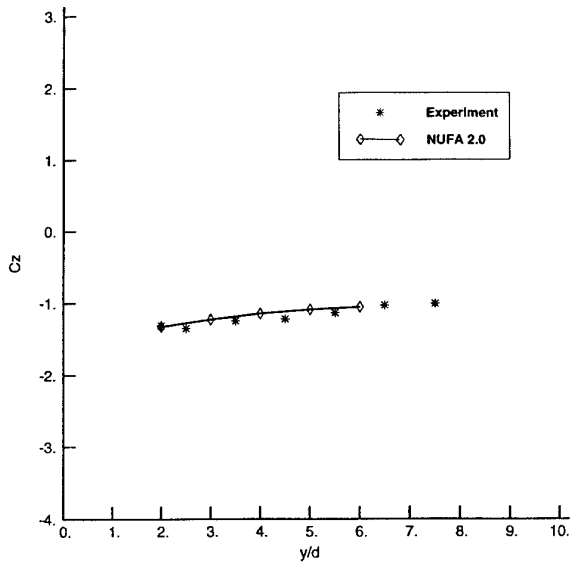

Figure 20 : Comparison of NUFA and Experimental Grid Loads. Traverse from Bay 1F. Bay 1F Cover Off.
(a) Normal Force Coefficient

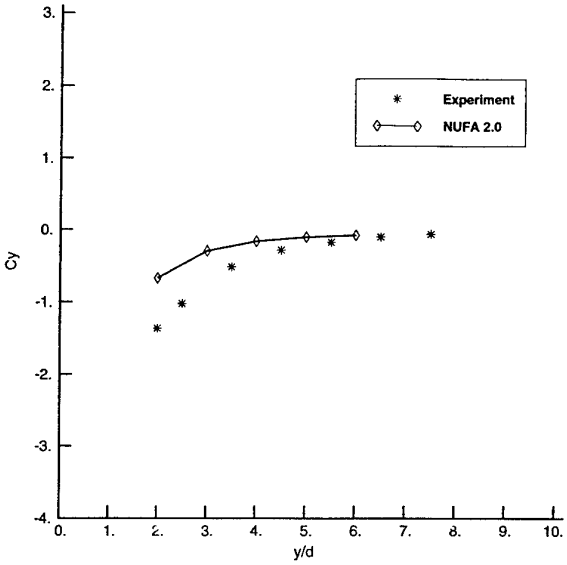

Figure 20 : Comparison of NUFA and Experimental Grid Loads. Traverse from Bay 1F. Bay 1F Cover Off.
(c) Side Force Coefficient

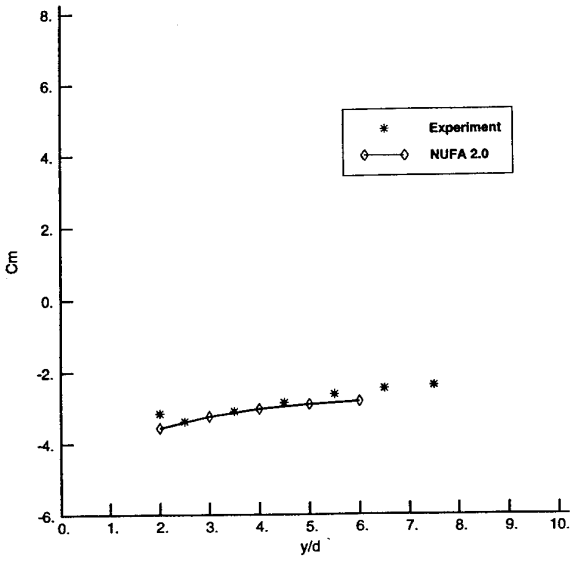

Figure 20 : Comparison of NUFA and Experimental Grid Loads. Traverse from Bay 1F. Bay 1F Cover Off.
(b) Pitching Moment Coefficient

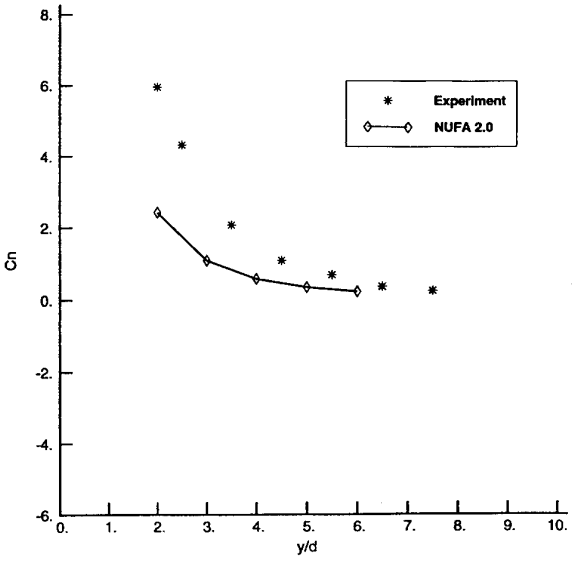

Figure 20 : Comparison of NUFA and Experimental Grid Loads. Traverse from Bay 1F. Bay 1F Cover Off.
(d) Yawing Moment Coefficient

ENGINEERING-LEVEL METHODS FOR CARRIAGE LOADS, HIGH ALPHA LAUNCH FROM PITCHING AIRCRAFT, AND SUBMUNITION AERODYNAMICS

Marnix F. E. Dillenius, Stanley C. Perkins, Jr.,
Daniel J. Lesieutre

Nielsen Engineering & Research, Inc.
526 Clyde Ave
Mountain View, CA 94043-2212 USA

SUMMARY

Recent applications are presented of engineering-level methods to describe or predict store carriage and separation problems. The examples described in this paper are concerned with estimating aerodynamic loads acting on the tail fins of a wing-tip mounted missile, predicting trajectory characteristics of a stable and a less stable missile rail-launched from a pitching aircraft at high angle of attack, and predicting aerodynamic aspects of submunitions in the vicinity of a dispenser. In most cases, comparisons with experimental data are shown. The engineering-level approaches are capable of handling parametric studies involving store component loads and store separation from a maneuvering aircraft, and the methodology can predict submunition aerodynamics quickly. The particular store separation problems described herein are not easily accomplished with the more accurate CFD approaches especially for cases involving maneuvering parent aircraft.

LIST OF SYMBOLS

CFD	Computational Fluid Dynamics
CG	center of gravity of submunition
C_N	normal-force coefficient, positive up; normal force/$q_\infty S_{ref}$
C_m	pitching-moment coefficient about CG location, positive nose up; pitching moment/$q_\infty S_{ref} l_{ref}$
D_d	maximum diameter of dispenser
l_{ref}	reference length, submunition maximum diameter
M_∞	freestream Mach number
q_∞	freestream dynamic pressure
r	radial distance from dispenser centerline
S_{ref}	reference area, submunition base area
t	time
x,y,z	coordinates of store CG in parent aircraft system relative to carriage position; x positive forward, y positive starboard, z positive down
X_S,Z_S	nondimensional location of submunition CG relative to dispenser nose tip and centerline, respectively; XSMC/D_d, ZSMC/D_d; positive aft and down, respectively
XSMC, ZSMC	dimensional location of submunition CG relative to dispenser nose tip and centerline, respectively; positive aft and down, respectively
α_s	submunition angle of attack relative to dispenser centerline, positive for submunition nose towards dispenser centerline
Ψ,Θ,Φ	Euler yaw, pitch, and roll angles in parent aircraft system relative to carriage position; Ψ positive nose to starboard, Θ positive nose up, Φ positive right wing down.

1. INTRODUCTION

Recently, development of relatively simple to use and fast-running engineering-level methods for store separation analyses has come essentially to a halt with the exception of code maintenance and extensions/modifications of existing methods. At the same time, CFD-based methods for store separation analyses have made considerable progress. However, because of the specialized skills and computer resources required, and because of the particular flow conditions associated with missile launch and dispense, CFD-based methods are not yet widely used in the areas of store launch from maneuvering aircraft, or in parametric studies of store separation characteristics including submunition aerodynamics. It is clear, however, that CFD-based methods should be used in the transonic and the very high Mach number speed ranges. CFD based methods should be employed to calibrate and check the engineering-level methods whenever possible. (The reverse is also true.)

Paper presented at the AGARD FDP Symposium on "Aerodynamics of Store Integration and Separation", held in Ankara, Turkey from 24-27 April 1995, and published in CP-570.

In addition to the above, wind tunnel and/or flight tests are expensive, and flow conditions associated with a maneuvering parent aircraft can not be easily modeled and/or simulated. Therefore, engineering-level methods are still very useful to provide a first order answer to very complex problems in store separation.

Provided engineering-level methods contain models of dominant and sometimes nonlinear aerodynamic phenomena, they can be successfully applied to the problem of providing estimates of aerodynamic loads acting on the components of a missile attached to a maneuvering aircraft. The analysis of the trajectory characteristics of missiles rail-launched from a pitching aircraft can be performed quickly by engineering-level methods. Submunition aerodynamics during dispense from closed and open bays can be analyzed with a fair degree of accuracy by such methods.

In what follows, references are made to computer programs developed over the years at Nielsen Engineering & Research (NEAR). In particular, the missile aerodynamics prediction programs SUBDL (Ref. 1), SUPDL (Ref. 2), and the store separation codes SUBSTR (Ref. 1) and HASLSB (Ref. 3) are applied singly or in combination to a variety of store separation problems in the areas of tail fin loads of a wing-tip mounted missile, and the launch characteristics of a stable and less stable missile airframe from a pitching aircraft at high angle of attack. The above-mentioned computer codes have been extended and modified under contract to NAWC, China Lake, to provide timely aerodynamic support. In connection with submunition aerodynamics, reference will be made to submunition dispense codes based on NEAR supersonic store separation programs (Refs. 4, 8).

2. TECHNICAL APPROACH

The SUBDL (Ref.1) and SUPDL (Ref. 2) missile aerodynamics prediction codes are based on fast-running subsonic and supersonic panel methods, respectively, for modeling the fin sections including fin-body interference, and subsonic point or supersonic line singularities are employed to model the axisymmetric bodies. In these codes, body and fin flow separation vortices are tracked aft along the configuration and their nonlinear effects are included in the aerodynamic load analysis. Simple fin stall models are incorporated. Detailed descriptions applicable to the SUBDL and SUPDL codes are available in Refs. 1 and 2. Application of these codes to the calculation of aerodynamic loads acting on the tail fins of a wing-tip mounted missile is described in this paper.

The subsonic store separation code SUBSTR (Ref. 1) employs subsonic paneling and other singularity methods to model volume and lift of the fuselage, wing and pylon components of the parent aircraft. The aerodynamic loads acting on the launched store are calculated by modified slender body theory and include forward fin on tail fin wake interference as well as effects of damping due to translational and rotational motion. Information about an earlier version of SUBSTR can be found in Ref. 1. The latest version of SUBSTR, designated HASLSB (Ref. 3), includes effects of the launching aircraft pitching up at user-specified g load. The SUBSTR code can also be used to compute flow fields for use in the detailed aerodynamics codes SUBDL mentioned above. An example of the combined use of these programs is given in this paper.

Computer programs applicable to the prediction of aerodynamic characteristics of submunitions in close proximity to a dispenser in supersonic flow are designated NEAR/MICOM Dispense Code and Modified 1986 NEAR Supersonic Store Separation Program (Refs. 4,8). In both programs, the dispenser interference flow field is calculated from supersonic linearly varying source/sink and doublet distributions which represent the volume and angle of attack effects, respectively. The calculated dispenser flow field contains a nonlinear correction to account for the presence of the bow shock. In addition, an equivalent streamline technique is employed to approximate the aerodynamic effects of dispensers with open cavity bays. Low and intermediate level methods are employed in the two different codes for obtaining the loads on the submunition. In the low level method contained in one program (NEAR/MICOM Dispense Code, Refs. 4,8), submissile aerodynamic forces and moments are calculated using slender body theory with the submunition in the presence of the dispenser flow field. In the intermediate level method contained in the other program (Modified 1986 NEAR Supersonic Store Separation Program, Refs. 4,8), the submunition is modeled by line singularities or by panel methods, and surface pressure distributions are integrated to obtain loads. Effects of reflected shocks are included in the latter method. In both programs, the submunition fin forces and moments are calculated on the basis of slender body theory including reverse flow theorems, or using panel methods. Additional details regarding the flow models can be found in Reference 4.

3. SELECTED RESULTS

In the next section, examples are presented involving various aspects of store carriage and trajectory problems, including submunition aerodynamics. Geometrical characteristics affecting the flow models and/or specific flow phenomena included in the engineering level methods are pointed out.

3.1 Fin Loads on Wing-Tip Mounted Missile

A drawing of the F/A-18 aircraft with a Sidewinder missile on the wing tip launching rail is shown head-on

in the upper portion of Figure 1. Until recently, the structural analysis of the launch rail lacked the effects of aerodynamic forces. In order to provide estimates of the aerodynamic loads including those acting on the large tail fins, the store separation code SUBSTR (Ref. 1) was employed to provide flow field data, and the SUBDL (Ref. 1) missile aerodynamics code was used to calculate distributions of aerodynamic loads on the missile components. In this process, it became clear that the F/A-18 wing deformation in torque and dihedral had a large effect on the missile aerodynamic loads. A schematic of the simplified aircraft model is shown in the lower portion of Figure 1 which shows the wing dihedral angle included in the calculations. The dihedral and the nose-down attitude of the missile on the wing tip are functions of the g-load experienced by the F/A-18 aircraft. These data are available from the aircraft manufacturer. This information should be included in the geometric description for use in engineering level and especially in CFD-based approaches.

An example is shown in Figure 2 of calculated aerodynamic tail fin loads compared with flight test data. The flight test data consisted of tail fin loads deduced from strain gage data. The strain gage response was calibrated with point loading tests in the laboratory. Therefore, the effect of actual aerodynamic force distribution was not accounted for. In any event, the strain gage data was used to test the prediction to first approximation.

The flight conditions associated with the data in Figure 2 included the following. The F/A-18 aircraft was in level flight at 2.2 deg angle of attack, Mach 0.84, and at 10256 ft altitude. From this condition, the aircraft executed a 3.4 g pull-up maneuver to 4.6 deg angle of attack. In actual fact, the aircraft flew at 90 deg roll angle in a horizontal circle at the specified g load. Figure 2(a) shows the peak or maximum aerodynamic loads (in lbs) acting on the tail fins of the instrumented wing-tip mounted missile. The loads at the start of the maneuver are indicated in Figure 2(b). The difference between the two results is shown in Figure 2(c). The corresponding flight test values shown in Figure 3(d) were determined from strip charts containing the strain gage response starting at 2.2 deg angle of attack and stopping at 4.6 deg. Three of the four fins were instrumented with a strain gage on both sides of the fin surface near the one-half root chord location. The outboard fins appear to be influenced by the vortical flow field near the wing tip included in the wing vortex lattice model. The prediction for the outboard fins aerodynamic loads is well within engineering level accuracy. CFD methods can be applied to this problem but will require considerable effort to set up the grid and computer resources to perform these calculations.

3.2 High Angle of Attack Missile Launch

An application of the engineering-level store separation analysis code HASLSB (Ref. 3) is shown in Figure 3. The figure shows trajectory characteristics of two different canard-tail missiles rail-launched from the wing tip of the launching aircraft. The launching aircraft is in a 2g pull-up maneuver and at 45 deg angle of attack. One missile configuration is very stable, and the other configuration is much less stable. Neither missile was guided in the calculations.

The wing vortex lattice wing model in HALSB (Ref. 3) includes a stall model based on section lift considerations. The store aerodynamic load calculation includes cross flow drag. In addition, special care was taken in the equations of motion for the missile to assure that it does not separate from the rail on the wing tip of the pitching aircraft after motor ignition (t=0) until the missile base clears the rail.

The plots at the top of Figure 3 are instantaneous pictures taken from the animated display program MBSGX (Ref. 5) at real times 0.15, 0.51, and 0.92 secs. The aircraft pitches up 7.11 deg during this time. The missiles are labeled stable and less stable. The fins are not shown. The lower portion of Figure 3 show the translational and angular orientation angles relative to the aircraft as a function of real time. The stable configuration tends to feather into the wind and oscillate in pitch. The less stable configuration exhibits much less initial pitch down motion. Specifically, the stable configuration cycled to a maximum pitch down angle of 45 deg relative to the aircraft at 0.7 secs. Up to 1 sec in real time, the less stable configuration pitched down in a monotonic fashion to 30 deg relative to the parent aircraft.

Many parametric calculations such as the example described above can be performed quickly with engineering level methods. The graphical displays serve to enhance greatly the understanding of the trajectory characteristics.

3.3 Submunition Aerodynamics

The next section contains descriptions of selected comparisons between measured and predicted aerodynamic forces and moments acting on submunitions in the vicinity of a dispenser missile. The experimental data consist of submunition forces and moments as a function of submunition horizontal and vertical position, and submunition angle of attack relative to the dispenser. The data base is called MICOM SUBMIS submunition data. A summarized description of the SUBMIS data base is given in Reference 6. The predictions obtained with the referenced codes include the nonlinear effects of shocks present in the flow field. The shock locations are

obtained from the linear body solutions on the basis of a local Mach number and Prandtl-Meyer considerations (Ref. 7). Further details of the engineering level submunition aerodynamics prediction methodology can be found in References 4 and 8.

3.3.1 *Closed Bay Dispenser*

A sketch of a submunition designated S2T1 in the vicinity of the closed bay dispenser designated D1 is shown in Figure 4. The submunition and dispenser both have circular cross section bodies. The simulated dispenser shock shape and free-stream Mach cone for $M_\infty = 1.81$ are also shown in Figure 4. Additionally, the reflected submunition shocks, as determined by the Modified 1986 NEAR Supersonic Store Separation Program (Refs. 4,8), are shown for two vertical positions of the submunition CG below the dispenser centerline.

The data shown in Figures 5 and 6 were obtained by carrying out a vertical traverse of the submunition with the submunition CG at a given axial position relative to the dispenser nose. In Figure 5, the submunition CG is located 0.7187 ft. aft of the dispenser nose and the free-stream Mach number is 1.81. In Figure 6, the submunition CG is located 5.5 dispenser diameters aft of the dispenser nose and the free-stream Mach number is 3.0. In both figures, the dispenser angle of attack is 0 deg.

Comparisons shown in Figure 5 for $M_\infty = 1.81$ indicate very good agreement between data and the predicted results obtained with the NEAR/MICOM Dispense Code (Refs. 4, 8). While the predicted results exhibit a slight horizontal shift with respect to the data, and the maximum pitching-moment is underpredicted slightly, the overall trends and levels of the data are predicted very well.

Comparisons of measured and predicted results for $M_\infty = 3.0$ and submunition angles of attack equal to 0 and 5 degrees are shown in Figure 6. Predicted results from both the NEAR/MICOM and 1986 NEAR codes (Ref. 8) are shown in this figure. In general, fair agreement between theory and data is shown, with the vertical positions at which the submunition experiences maximum normal force and pitching moment better predicted by the NEAR/MICOM code, and the magnitude of these peaks better predicted by the 1986 NEAR code. Effects of angle of attack are indicated well by both codes.

3.3.2 *Open Bay Dispenser*

Models for the open bay dispenser are obtained using an inverse technique by which an equivalent cavity streamline is determined as follows. For a given Mach number, results from a vertical traverse with a body-alone submunition configuration at zero degrees angle of attack with respect to the dispenser are used to calibrate the predicted results. A manual iterative procedure is carried out to obtain a "best fit" comparison of data and theory over the entire vertical traverse, thereby arriving at a cavity streamline applicable to the dispenser at the given Mach number and dispenser angle of attack (0 deg for the cases described here).

A sketch of a modeled shape developed for the open bay dispenser at $M_\infty = 1.2$ is shown in Figure 7. The dashed lines shown in this figure are the modeled equivalent streamlines, with solid vertical lines separating the bays. These representations of the open bays were obtained by the previously descibed technique using the hemisphere-cylinder submunition S1 (body alone) at zero incidence relative to the open bay dispenser D1FCA. Predicted results were then obtained using the NEAR/MICOM code (Refs. 4,8) for the body-tail submunition S1T1 at 0, +10, and -10 deg (angle α_s) relative to the dispenser. The axial station of interest is 2.37 dispenser diameters from the dispenser nose and represents the release of the submunition from the front bay.

Comparisons for $\alpha_s = 0$ deg, shown in Figure 8(a), indicate excellent agreement between measured and predicted results. For $\alpha_s = +10$ deg, shown in Figure 8(b), predicted normal force variation with vertical coordinate agrees very well with data. The trends exhibited by the pitching moment data are also predicted well; however, the predicted magnitude of the pitching moments is much larger than that seen in the data. The comparisons for $\alpha_s = -10$ deg, shown in Figure 8(c), are very similar to those for $\alpha_s = +10$ deg. For this case, the predicted and measured pitching-moment coefficients appear to differ by a constant amount over the entire vertical traverse.

The submunition aerodynamics examples show that engineering-level methods can provide good estimates as long as the presence of the shocks is included.

4. CONCLUSIONS

Examples of applications of engineering level methods to various store carriage and separation problems indicate that the methods are capable of predicting complicated characteristics fairly well provided important nonlinear flow phenomena are included in the flow models. These phenomena include vortical flows, effects of shocks, and effects of stall. Another important aspect is the fact that engineering level methods lend themselves to the treatment of store separation from maneuvering aircraft. Finally, OP4ause the engineering level methods are relatively easy to use and run fast on modern work stations, many kinds of parametric studies can be accomplished in a short time. CFD-based methods should be used to check and/or used to define important flow phenomena present in store separation problems; eventually the CFD-based methods will be

used routinely to handle examples described in this paper.

REFERENCES

1. Lesieutre, D. J., Dillenius, M. F. E., and Whittaker, C. H.,"Program SUBSAL and Modified Subsonic Store Separation Program for Calculating NASTRAN Forces Acting on Missiles Attached to Subsonic Aircraft", NAWCWPNS TM 7319, May 1992.

2. Dillenius, M. F. E., Perkins, S. C., Jr., and Lesieutre, D. J., "Modified NWCDM-NSTRN and Supersonic Store Separation Programs for Calculating NASTRAN Forces Acting on Missiles Attached to Supersonic Aircraft", NWC TP 6834, September 1987.

3. Dillenius, M. F. E., Whittaker, C. H., Lesieutre, T. O., and Lesieutre, D. J., "High Angle-of-Attack Missile Launch Computer Analysis Code", NEAR TR 456, February 1993.

4. Perkins, S. C., Jr., Dillenius, M. F. E., and Nazario, S. M. N., "Submunition Dispensing Modeling", NEAR TR 366, October 1986.

5. Hegedus, M. C., "MBSGX Multiple Body Graphical Display User's Manual", NEAR TR 488, January 1995.

6. Deep, R. A., Brazzel, C. E., and Sims, J. L., "Aerodynamics of Submunitions During Dispense", AIAA Paper 85-0105, January 1985.

7. Dillenius, M. F. E. and Allen, J. A., "Paneling Methods with Vorticity and Corrections for Nonlinear Compressibility", Tactical Missile Aerodynamics, Vol. 104 of Progress in Astronautics and Aeronautics, AIAA 1986.

8. Perkins, S. C., Jr. and Dillenius, M. F. E., "Supersonic Submunition Aerodynamics During Dispense", J.Spacecraft and Rockets, *28*, 3, May-June 1991, pp 276-284.

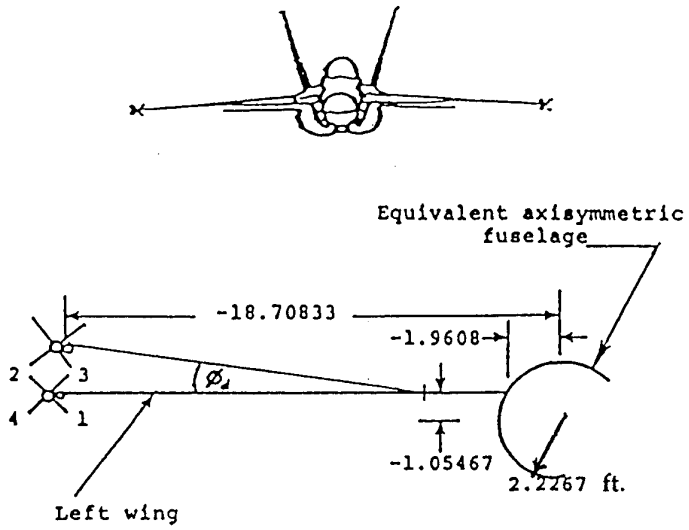

Fig. 1. - Simplified F/A-18 aircraft fuselage and wing with missiles.

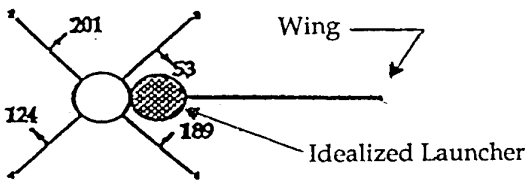

(a) FTID = 1, Predicted Peak Values

Mach Number = 0.85
Parent Aircraft Angle of Attack = 4.6°
Altitude = 9508 ft.
Includes Wing Twist/Camber/Dihedral
Missile Angle of Attack = 0.29°
g-load = 3.4g

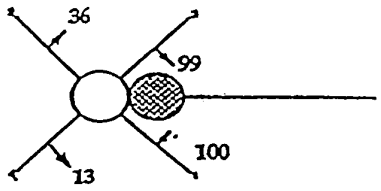

(b) FTID = 1, Predicted Values at Start of Maneuver

Mach Number = 0.85
Parent Aircraft Angle of Attack = 2.2°
Altitude = 10256 ft.
Includes Wing Twist/Camber/Dihedral
Missile Angle of Attack = 2.17°
g-load = 1.0g

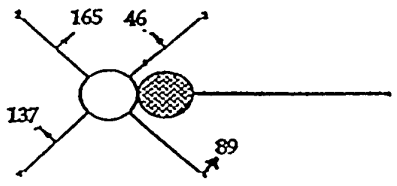

(c) FTID = 1, Predicted Change in Fin Normal Force, (a minus b)

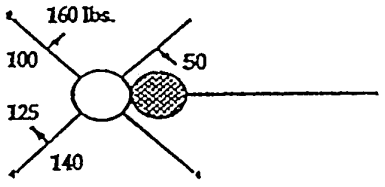

(d) FTID = 1, Strain Gauge Derived Values for Change in Fin Normal Force

Fig. 2. - Comparison of predicted tail fin loads with flight test data.

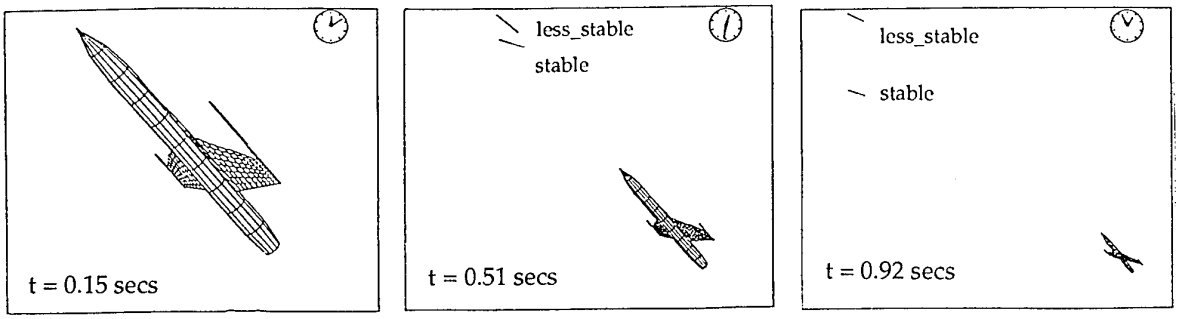

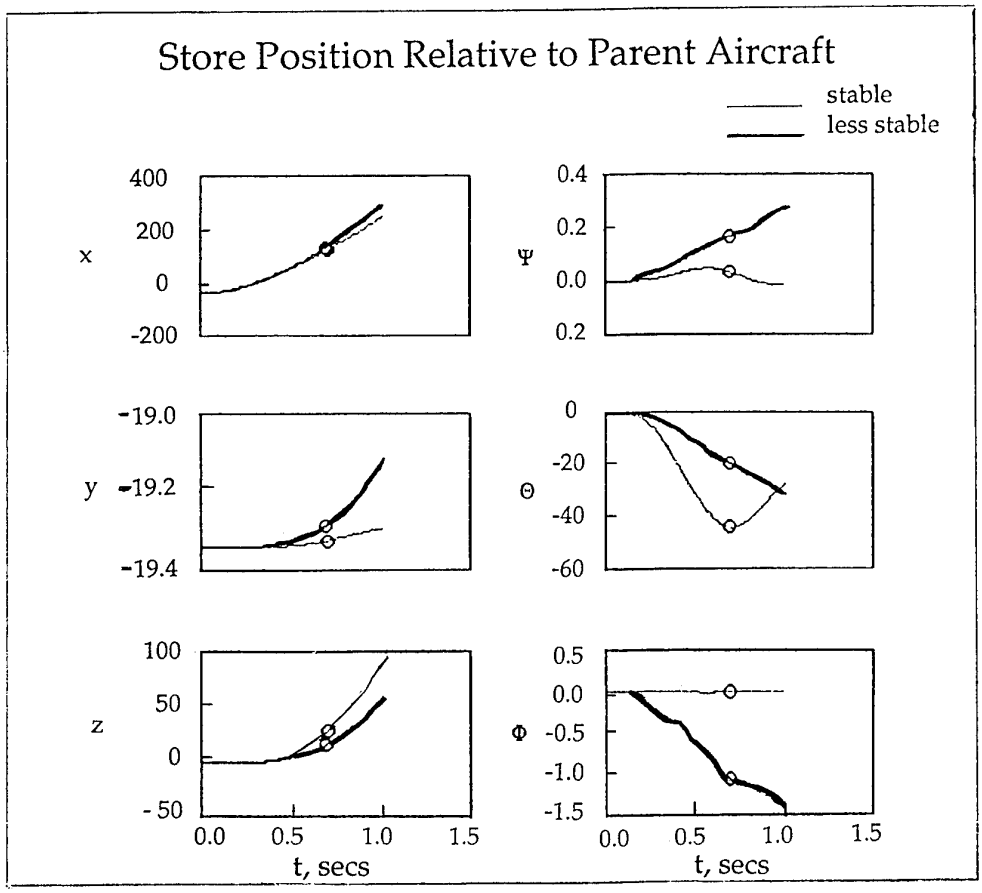

Fig. 3. - Two difference stores rail-launched from pitching aircraft, $M_\infty = 0.25$ $\alpha = 45°$, 2g pull-up, h = 20,000 ft. calculated by HASLSB.

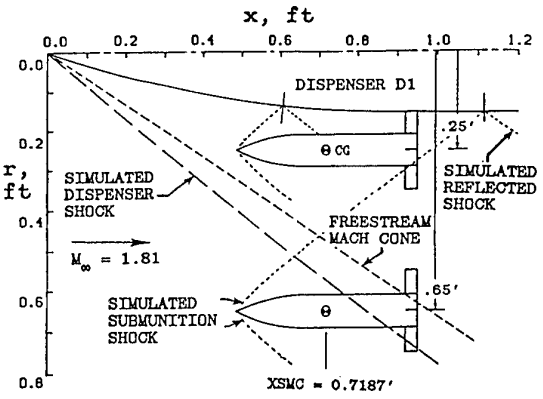

Figure 4.- Sketch showing simulated shocks and reflected shocks (as determined by the 1986 NEAR Supersonic Store Separation Program) for submunition S2T1 in vicinity of closed bay dispenser D1, $M_\infty = 1.81$.

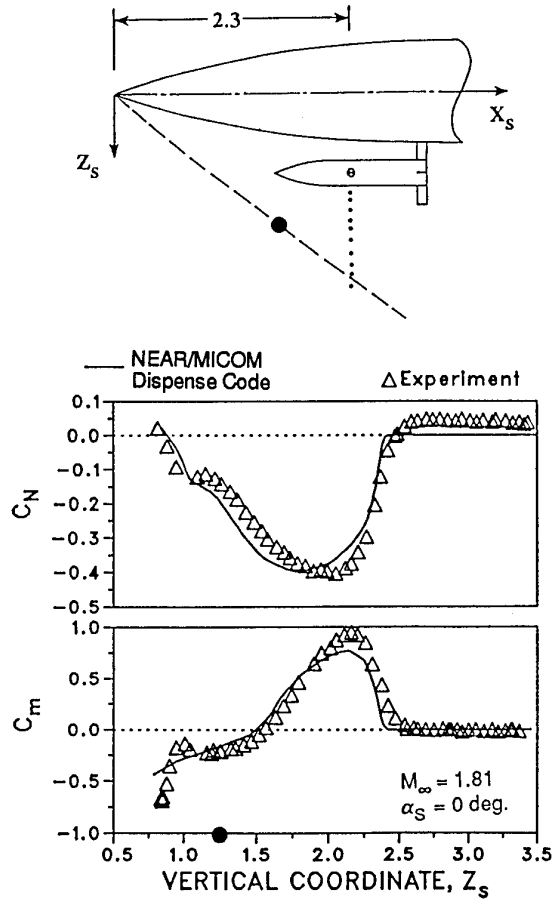

Figure 5.- Measured and predicted vertical variation of aerodynamic coefficients on submunition S2T1 in vicinity of closed bay dispenser D1; $M_\infty = 1.81$.

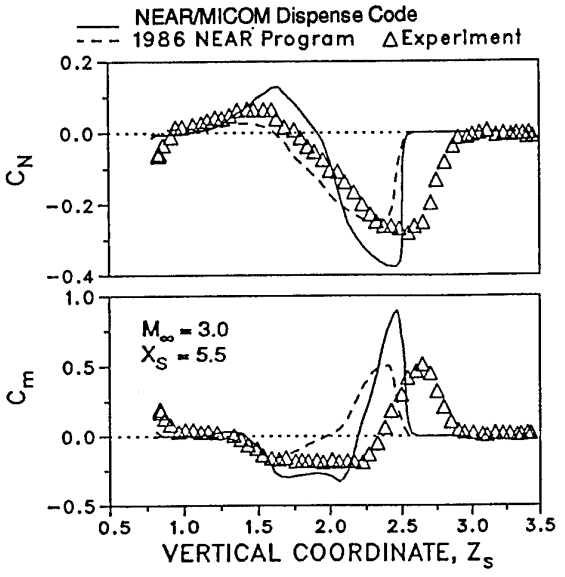

(a) $\alpha_s = 0$ deg

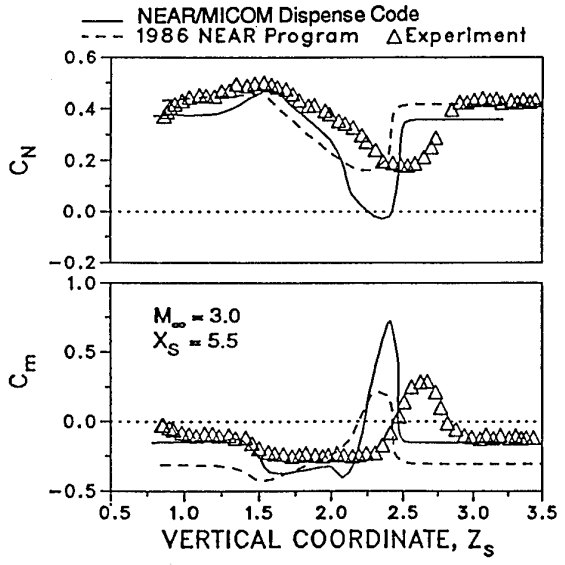

(b) $\alpha_s = 5$ deg

Figure 6.- Measured and predicted vertical variation of aerodynamic coefficients on submunition S2T1 below closed bay dispenser D1; $M_\infty = 3.0$, $X_s = 5.5$.

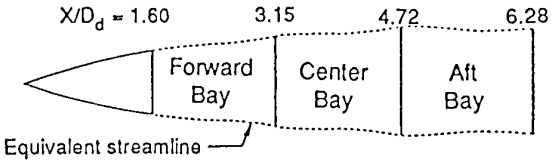

Figure 7.- Equivalent streamline representation for open bay dispenser D1FCA, $M_\infty = 1.20$.

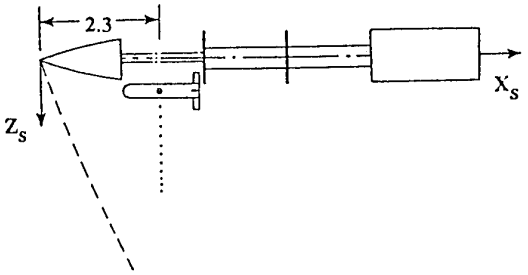

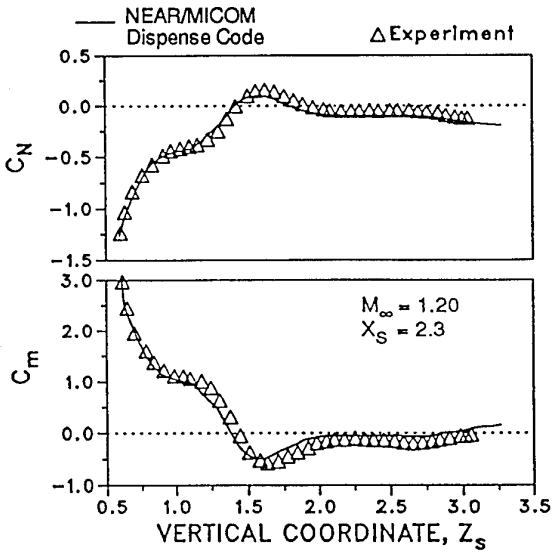

(a) $\alpha_s = 0$ deg

Figure 8.- Measured and predicted vertical variation of aerodynamic coefficients on submunition S1T1 below dispenser D1FCA; $M_\infty = 1.2$, $X_s = 2.37$.

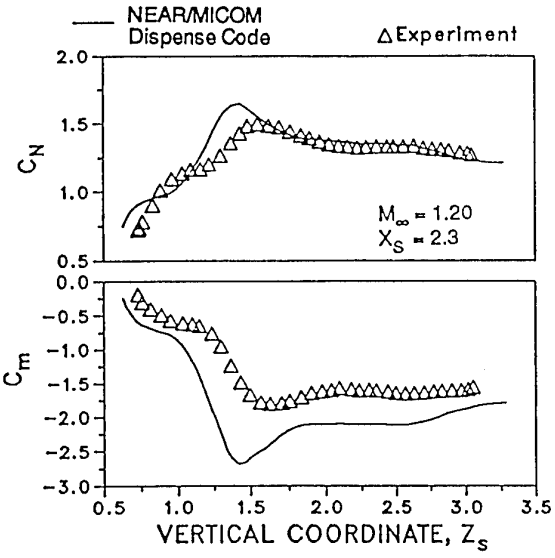

(b) $\alpha_s = 10$ deg

Figure 8.- Continued.

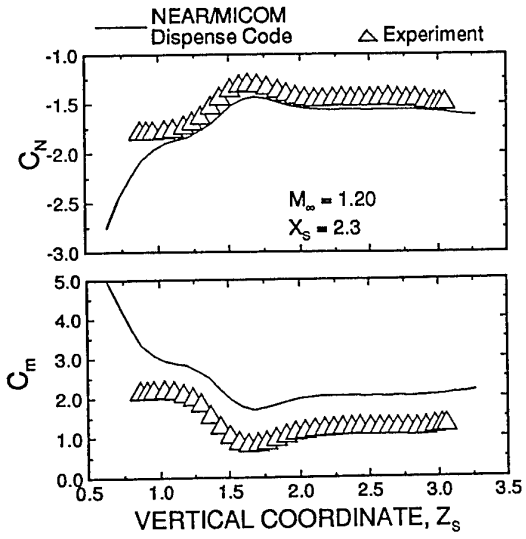

(c) $\alpha_s = -10$ deg

Figure 8.- Concluded.

CARRIAGE AND RELEASE AERODYNAMICS OF THE PEGASUS® AIR-LAUNCHED SPACE BOOSTER

Michael R. Mendenhall, Teresa O. Lesieutre,
Daniel J. Lesieutre, Marnix F. E. Dillenius

Nielsen Engineering & Research, Inc.
526 Clyde Avenue
Mountain View, CA 94043 USA

SUMMARY

Pegasus®, the air-launched space booster designed for launch from B-52 and L-1011 aircraft, was developed using computational aerodynamic methods without benefit of specific wind tunnel or flight testing. This paper describes the methods and procedures used for predicting the carriage and launch characteristics of Pegasus from both B-52 and L-1011 aircraft. Flight data from four B-52 launches and a single L-1011 launch are available to validate the prediction methods.

SYMBOLS

c	wing chord
c_n	section normal force coefficient, (dN/dy)/qc
h	altitude
M_∞	free stream Mach number
N	normal force
q	dynamic pressure
S	reference area
α	angle of attack, deg.
β	angle of sideslip, deg.
ϕ	roll angle, deg.
θ	pitch angle, deg.

INTRODUCTION

Successful carriage and the initial launch trajectory of Pegasus are critical elements of each flight and, to a large extent, can determine the success of the overall mission. Flow models and prediction methods to analyze the carriage and launch of the Pegasus configurations from the B-52 and L-1011 aircraft are required because experimental ground and flight test investigations of launch characteristics during preliminary design are impractical from both economic and scheduling considerations, particularly in light of the large range of potential release flow conditions of interest. The availability of an analytical method to predict various carriage and launch simulations permits the evaluation of a wide range of launch conditions to better understand the effects of Mach number, flow incidence angles, and altitude, as well as Pegasus configuration changes. In addition, the analytical method can be used to investigate emergency launch conditions without any danger to the carrier aircraft.

® Pegasus is a registered trademark of Orbital Sciences Corporation of Dulles, VA

Pegasus Background

Pegasus (Fig. 1) is an air-launched space booster developed privately by Orbital Sciences Corporation to provide reliable launch services at low cost for small payloads. It is carried aloft beneath the wing of a B-52 bomber or under the fuselage of a modified L-1011 commercial transport aircraft. In level flight at approximately Mach 0.8 and 40,000 feet, Pegasus is released from its carrier aircraft and allowed to free fall for five seconds before first-stage ignition.

The aerodynamic design and analysis of Pegasus was conducted without benefit of wind tunnel and flight testing using only computational aerodynamic methods.[1] All levels of codes, ranging in complexity from empirical database methods to three-dimensional Navier-Stokes codes, were used in the design. The aerodynamic methods were validated with flight test data from four successful flights of the standard configuration, and the comparisons between predicted and actual aerodynamic characteristics are reported in Ref. 2.

Six flights of the standard Pegasus configuration have been launched from the B-52 carrier aircraft. A single launch of the Pegasus XL has been conducted from the L-1011 aircraft. Pegasus XL (Fig. 1) has a longer body and is slightly heavier than the standard configuration; however, the wing and tail surfaces are identical for both vehicles.

Prediction Philosophy

The philosophy of the technical approach for the carriage and launch analysis was similar to that chosen for the aerodynamic design and analysis.[1] That is, the methods selected must be simple, fast, accurate, and reliable engineering methods which can be set up and run quickly and economically. The methods must be applicable to a wide range of launch flow conditions to cover the normal launch envelope as well as emergency drop or jettison conditions. As part of the methods evaluation and selection, the highest level of technology needed to accomplish a specific task will be used, but conversely, a higher-than-necessary level of technology will not be selected unless it is required for specific analysis goals. Based on previous experience predicting carriage and launch characteristics for store separation applications, it was anticipated that computational fluid dynamic methods would not be required for the Pegasus analyses. The predicted results were compared with other independent results to build confidence in the approach.

Paper presented at the AGARD FDP Symposium on "Aerodynamics of Store Integration and Separation", held in Ankara, Turkey from 24-27 April 1995, and published in CP-570.

Requirements

The methods used to predict carriage loads and launch characteristics of Pegasus must satisfy certain basic requirements. The main features of the methods are that they must provide accurate modeling of the nonuniform flow physics in the region of the carrier aircraft, and they must predict the aerodynamic characteristics of Pegasus in this nonuniform flow field. Because of the necessity of verifying the carrier aircraft-induced forces and moments on the various components of Pegasus, the distribution of aerodynamic loads on the wing and tail surfaces are needed.

The economic and schedule requirements dictate that the prediction method require no experiments on specific configurations; therefore, an engineering method consisting of aerodynamic theory plus generic empiricism or a purely analytical method is required. The method should have enough prior use to establish confidence in the approach and method, and an inordinate amount of validation should not be necessary. Since approximately one hundred different carriage and launch calculations were needed during the preliminary design and analysis stage, the level of technology which could be used was limited by necessity.

PREDICTION METHODS

In this section, the engineering methods for carriage and launch predictions are discussed to provide some background for the Pegasus analysis. An extensive summary and discussion of other available prediction methods are described in Refs. 3, 4 and 5.

Engineering Methods

Engineering level prediction methods for store separation are based on solutions to the linear potential equation, and analytical models usually include singularity distributions and paneling methods. Mutual interference effects between the parent aircraft and the store are treated in an approximate manner; that is, the parent aircraft has an influence on the store, but the store has no or only first order influence on the parent aircraft. Store trajectory or drop analysis is handled in a quasisteady manner in which the instantaneous flow conditions are used to predict the instantaneous forces and moments on the store.

The NEAR subsonic store separation program provides an analytical prediction method for the forces, moments, and trajectories associated with stores released from carrier aircraft.[6,7] Originally, the stores of interest were bombs, fuel tanks, and missiles; however, the techniques developed were applicable to any problem involving the powered or unpowered motion of one flight vehicle in close proximity to another.

The engineering level store separation analysis methods have been under constant use and development at NEAR since their origination. For example, prior to NASA dropping two variations of the Shuttle solid rocket boosters from the B-52 to test parachutes, the NEAR prediction method was used to verify launch safety.[8] The U. S. Navy sponsored a study to predict the loads on missile tail fins during carriage on a modern fighter aircraft.[9] Recently, the methods were used for an analytical investigation of missile carriage and launch from a maneuvering fighter aircraft at high angles of attack.[10,11]

Other Methods

The importance of analytical determination of store separation characteristics is emphasized by the number of different approaches directed to the problem. A variety of methods at all levels of technology are described in detail in Refs. 3 and 4. These methods range from semiempirical methods[12-14] to various computational fluid dynamics (CFD) methods.[15-20]

Solutions of the Euler equations provide possibly the best opportunity for practical CFD results for store carriage and separation at the current time. An excellent Euler result for the Pegasus XL in carriage on the L-1011 aircraft is available.[17] These results are compared with the NEAR method in Ref. 5.

Solutions of the Navier-Stokes equations include effects of the viscous phenomenon, flow separation, and the other complex fluid physics associated with carriage and launch of stores, and the potential for time-accurate computations exists. However, these calculations require significant labor for grid generation and state-of-the-art computer resources for a carriage result. Time-accurate results are beyond the practical reach of most organizations, particularly for preliminary design studies.

TECHNICAL APPROACH

The forces and moments acting on the Pegasus vehicle in close proximity to the carrier aircraft, B-52 or L-1011, is a complex problem in aerodynamic interference. The approach taken for the carriage and launch analysis is to make a first-order estimate of the primary or gross interference. The success of the prediction method is in proportion to the degree to which the primary interference effects include all the significant effects and the secondary interference effects are negligible. During the development and validation of the original store separation method,[6,7] it was shown that the effect of secondary interference on the store is small.

The approach of the NEAR method is as follows. First, with the carrier aircraft represented as accurately as possible by singularity distributions, the three-dimensional velocity field in which Pegasus is operating is calculated. This is accomplished by removing Pegasus from the field and predicting the perturbation velocity field from the aircraft components at a number of field points which represent critical control points on Pegasus. Pegasus is placed back into this perturbation velocity field with the free stream velocity included. The total velocity seen by the store is the free stream plus the perturbation velocities plus any motion of the store relative to the carrier aircraft. The forces and moments on Pegasus in this complex velocity field are calculated.

Launch characteristics are calculated using a six-degree-of-freedom trajectory simulation method which includes the aerodynamic forces and moments on the store

generated in the nonuniform flow field. The equations of motion are integrated over a short time period assuming the forces and moments on Pegasus are constant. Pegasus moves to a new position, and the velocity field from the carrier aircraft is calculated at the new position. Loads are recalculated and the integration continues. The computation marches in time until Pegasus is outside the influence of the launching aircraft.

Flow Models

Pegasus was placed in the predicted nonuniform flow field associated with both the B-52 and L-1011 at various flight conditions to predict the forces and moments used for carriage loads and trajectory simulations. The flow models required for each of the carrier aircraft are described below.

B-52 Model

The longitudinal aerodynamic model of the B-52 consists of the fuselage, right wing, three pylons, two engine pods, and a pylon mounting adaptor for Pegasus. The NEAR subsonic store separation code, SUBSTR (Ref. 6), was used to conduct the aerodynamic analysis. The flow field for incompressible subcritical flow is governed by a velocity potential which satisfies Laplace's equation, and a Prandtl-Glauert correction is used to account for first order compressibility effects.

The standard Pegasus configuration is carried on a pylon some distance from the B-52 fuselage; therefore, there is no significant coupling between the noncircular shape of the B-52 fuselage and Pegasus. Consequently, the B-52 fuselage is modeled as an axisymmetric body with the actual cross sectional area distribution. The two engine pylons are modeled with panels, and each engine pod is represented by an axisymmetric body with the appropriate cross sectional area distribution. The third pylon on which Pegasus is carried includes a pylon mounting adaptor modeled as two axisymmetric bodies having equivalent area distributions as the actual adaptor.

The volume of the B-52 fuselage is modeled by a distribution of three-dimensional point sources/sinks along the body longitudinal axis. The strength of these singularities is determined by satisfying body radius and slope boundary conditions at points on the body surface. Fuselage angle-of-attack effects are modeled by two-dimensional doublets in the crossflow planes. With the source/sink and doublet distributions, perturbation velocities can be calculated at any point in the flow field due to the B-52 fuselage. This same flow model has been successfully used and validated for missile bodies and fighter forebodies.[21]

The aerodynamic modeling of the B-52 wing and pylons is accomplished with source panels and horseshoe vortex-lattice panels. The source panels are used to model the wing and pylon thickness, and the horseshoe vortex-lattice panels account for lifting effects, including angle of attack, dihedral, camber, and twist. The effect of wing-body interference is modeled by imaging the horseshoe vortex-lattice inside the axisymmetric fuselage. The effects of the fuselage body volume and angle of attack are included in the wing and pylon boundary conditions.

L-1011 Model

The L-1011 analysis presented a number of flow problems which required the use of more sophisticated methods than those used for the B-52 because of the close coupling between the L-1011 and Pegasus and the resulting aerodynamic interference. The major features of the aerodynamic model of the L-1011 aircraft are the wing and noncircular fuselage. An updated version of the NEAR subsonic store separation code includes the effects of sidewash, and a conformal mapping procedure was incorporated to model the noncircular fuselage cross sections to better predict the flow field of the L-1011 aircraft. Compressibility effects are accounted for using a Goethert transformation which maintains the body cross sectional shape but stretches the axial body coordinate.[22]

The noncircular cross sectional shape of the L-1011 fuselage is an essential feature of the flow model and must be accurately represented. In each crossflow plane, a conformal transformation is determined which maps every point on or outside the noncircular body to a corresponding point on or outside an equivalent circular body.[21,22] Three-dimensional point sources/sinks are used to model body volume effects, and two-dimensional doublets account for angle-of-attack effects. The potential flow field around the equivalent circular body is determined, and this flow solution is transformed back to the noncircular body plane with an inverse conformal mapping procedure.

Details of the L-1011 wing, pylons, and engine nacelles modeling are the same as those described above for the B-52 wing. The rear engine and tail surfaces are not included in the L-1011 model because of their negligible influence on the flow field near Pegasus.

Pegasus Carriage Model

The flow models presented above for the B-52 and L-1011 aircraft produce the perturbation velocities in the flow field adjacent to the aircraft. The effect of these velocities on the forces and moments acting on Pegasus when in the vicinity of the aircraft is the primary interference on Pegasus. By summing up the perturbation velocities due to the aircraft components and by adding them to the free-stream velocity, the total velocity at any point in the flow field where Pegasus is located can be calculated.

The aerodynamic model for Pegasus XL used for predictions of the forces and moments during carriage on the L-1011 aircraft is slightly different from the model used for the trajectory simulations described in the next section. In the carriage position, the body of Pegasus is centered under the L-1011 fuselage, and the spacing between the upper surface of the Pegasus wing and the L-1011 fuselage is the order of six inches. This close coupling and the associated interference effects dictate a more accurate model to predict the carriage forces and moments on Pegasus.

A vortex lattice method is used to model the L-1011 wing and the portion of the fuselage in the wing section.[23] Vortex lattice panels are distributed on the wing and around the circumference of the fuselage in the region of the wing root chord to form an interference shell. This

shell is used to model the carryover forces between the wing and fuselage. The boundary condition applied on the lifting surfaces includes velocities due to the freestream velocity, body volume and angle of attack effects, and other interference effects.

The Pegasus body is modeled with three dimensional sources and sinks to account for volume effects. The body doublet solution models the freestream angle of attack effects and includes effects due to the perturbation velocities from the L-1011 flow model. The wing, tails, and interference shells are modeled with horseshoe vortex lattice panels. Body-on-fin interference is included, and fin-on-body lift carryover is modeled by the interference shell as described above. Flow tangency boundary conditions consider the freestream velocities and the perturbation velocities from the L-1011 flow model to produce the primary interference effects.

At high angles of attack, fin leading and side edge flow separation can occur on Pegasus, and load augmentations due to this flow separation are included. Nonlinear effects due to wing-on-tail vortical interference are modeled by discrete vortices as are the forebody flow separation vortices.

Pegasus Launch Model

The B-52 and L-1011 flow models produce a perturbation velocity field in the vicinity of the aircraft through which Pegasus must fly during the first few seconds after release from the carrier aircraft. Performing the velocity field calculation at various points on the Pegasus configuration produces the nonuniform flow field which can have significant influence on the motion of Pegasus immediately after release.

The force and moment coefficients due to buoyancy and slender body theory are calculated using methods described in Ref. 24. This calculation is performed over the portion of the store for which the flow is attached. Viscous forces become important after flow separation occurs, and if the local flow angle of attack approaching Pegasus exceeds 15°, the viscous crossflow calculation method is automatically engaged. From the axial location of the beginning of separated flow to the base of Pegasus, a viscous crossflow calculation is used in place of the slender-body calculation. A crossflow drag coefficient, defined as the section drag coefficient of a circular cylinder placed normal to the airstream, is imposed on the Pegasus body and a force integration is performed over the portion of the body in separated flow.

The remaining forces and moments are due to the lifting surfaces of Pegasus. The lift curve slope for the Pegasus wing and tail must be specified from the aerodynamic calculations.[1]

To determine the trajectory of Pegasus, the six degree of freedom equations of motion are integrated to calculate the location and angular orientation as a function of time relative to a specified initial position. At each time step in the integration of the equations of motion, the nonuniform flow field and the forces and moments acting on Pegasus are updated.

Launch Trajectory Simulation

The equations of motion for six degrees of freedom are integrated in time to predict the trajectory of Pegasus after release from the carrier aircraft. This is a direct simulation of the motion using the predicted instantaneous forces and moments acting on Pegasus; no stability derivatives are required. The equations of motion are for a rigid body with appropriate mass and inertia asymmetries. It is not required that the store center of mass lie at the origin of the axes of geometry symmetry. It is also not required that the principal axes of inertia of Pegasus coincide with the geometric axes; therefore, the inertia tensor includes products of inertia.

In the present analysis it is assumed that the carrier aircraft is flying at constant velocity, constant angle of attack, and constant flight path angle relative to the horizontal. After release, the aircraft motion is assumed unchanged, and the motion of Pegasus is calculated relative to the moving coordinate system fixed in the aircraft. The integration procedure permits a variable time step in the trajectory calculation so that a level of accuracy can be specified and maintained.

RESULTS

Comparisons of measured and predicted carriage and launch characteristics for the B-52/Pegasus configuration are presented below for the first four flights. Predicted launch characteristics of Pegasus XL from the L-1011 are presented for the first flight.

B-52 Analysis

Flight data from the first four standard Pegasus flights were obtained from onboard flight instrumentation as well as from additional research instrumentation.[25] The flight data included onboard control surface position and inertial navigation system data, ground-based radar data, and weather observations.

It is not possible to put an exact error band on the flight data; however, the uncertainties must be kept in mind when evaluating the following comparisons between measured and predicted carriage and launch characteristics.

Carriage Loads

During the analysis of carriage loads on the standard Pegasus mounted on the B-52, no flight data or other validating information was available. NASA/Dryden Flight Research Center supplied NEAR with measurements of hook loads obtained during inert Pegasus carriage tests and Flight 1 prior to launch. NASA estimates of relative accuracy of the measured flight loads is ±5,000 lb or better.

The measured hook loads at a nominal cruise flight condition include the weight of Pegasus, the weight of the pylon adapter, the preload on the hooks, and the induced aerodynamic load. Comparisons of measured and predicted loads on the B-52 for the two flights available are shown in Fig. 2. For the inert flight test, there was a shift in the static hook loads between take off and landing, but even with this uncertainty, the differences between the measured and predicted loads

are within the stated accuracy of the measurements. The agreement between measured and predicted loads for Flight 1 is very good.

Launch Characteristics

Predicted launch characteristics of the standard Pegasus after release from the B-52 are shown in Fig. 3. These results were obtained by keeping the Pegasus controls locked in a neutral position for the three seconds of the simulation shown. The general characteristics of the initial trajectory are that Pegasus pitches nose down at a low rate and rolls right wing down at a low rate.

Based on the predictions, the pitch down is caused by the small positive angle of attack experienced by Pegasus after release and its normal stability characteristics. The roll outboard with respect to the B-52 is caused by the asymmetric flow field induced by the B-52 at the Pegasus carriage position. The combination of flow around the B-52 fuselage and the swept wing induced flow field produces an upwash on the left wing of Pegasus. This produces a slightly higher lift on the left wing and causes a small rolling moment.

Trajectory data for the standard Pegasus are available for the first four launches from the B-52. The measured and predicted separation distances between Pegasus and the B-52 are shown in Fig. 4. The Pegasus controls were locked for the predictions; however, the flight vehicle has controls locked for only 0.2 seconds after release. After this time, the control system is active, and it is moving to correct the initial roll caused by B-52 interference. There are some uncertainties in the data as discussed above, but in general, the results are good.

Some of the areas of disagreement in the measured and predicted separation distances have not been explained. For example, agreement for Flight 1 is very good for the first second after release, but Flight 2 shows a difference of two to three feet in the separation distances. The measured results show an instantaneous drop of approximately two feet at about 0.1 seconds. This phenomenon cannot be explained, but the flight data are not modified in any way to remove this uncertainty.

Similarly, Flight 3 predictions are in good agreement with the flight data until about 0.3 seconds. At this time, the flight data are flat and unchanging for approximately 0.1 seconds. This causes the measured separation distance to be less than that predicted for the remainder of the simulation. Flight 4 comparisons exhibit good agreement for the first 0.5 sec.

Pegasus roll and pitch angles immediately after release are available from the first B-52 launches. The control surfaces are not locked in a neutral position at the instant of release; there is a deflection angle preset prior to release to provide an initial correction for the induced roll from the B-52. Fin deflection data indicate immediate deflections from the preset values of each of the surfaces beginning at 0.2 seconds to make attitude adjustments dictated by the autopilot.

In the predicted results for Flights 1 and 3, a preliminary effort was made to correct the fin deflections after 0.2 seconds. Based on the flight data, the fin deflections were corrected in the analysis to agree with the measurements. This was accomplished in a quasisteady manner with no attempt to model the unsteady or dynamic aerodynamic effects.

Measured and predicted pitch and roll angles of Pegasus during the first second after release are shown in Fig. 5 for the first three flights. Flight 4 data are not considered because of roughness and uncertainty in the fin deflection data. For Flight 1 shown in Fig. 5(a), the pitch and roll angle results are good until 0.5 seconds; then the predicted results diverge from the data. It appears that the simple modeling of the changing deflection angles is not successful.

Pitch and roll comparisons for Flight 2 shown in Fig. 5(b) are in poor agreement after 0.2 seconds. There was no attempt to model the changing deflection angles for this flight.

Flight 3 results are shown in Fig. 5(c). In this case, the predicted pitch angle is in very good agreement with the data, but the roll angle is in poor agreement.

Even though there is some discrepancy between the measured and predicted attitude parameters of Pegasus after release from the B-52, the differences are small, and the overall attitude angles are small. The post-release trajectory of Pegasus is benign, and any small differences between measured and predicted characteristics seems to be handled adequately by the control system.

L-1011 Analyses

The close coupling between Pegasus XL and the L-1011 is illustrated in the model shown in Fig. 6. Great care has been taken in the calculation of interference effects between the two vehicles to avoid any unrealistic influence caused by the close proximity of two singularities. It is very obvious that a large portion of the Pegasus wing is blanketed by the L-1011 fuselage which is nearly flat in the region of the wing. Notice that the Pegasus rudder fits up into a cavity in the L-1011 fuselage.

Carriage Characteristics

During the flight tests with the L-1011, several modifications to the configuration were made. Brush seals were added to close the gap between the upper surface of the Pegasus XL payload fairing and the lower surface of the L-1011 fuselage fairing. A conformal fairing was added to close the gap between the L-1011 fuselage and the Pegasus wing. Finally, brush seals closed the opening in the rudder cavity in the L-1011 fuselage. Some estimates of the magnitudes of the loads associated with these modifications are available from flight measured pressures.[26] Preliminary results indicate that the total effect of the brush seals and the conformal fairing is to increase the positive or up load on the Pegasus XL configuration during carriage flight.

Loads on the five carriage hooks between the inert Pegasus XL and the L-1011 are available from flight tests at a range of Mach numbers at two altitudes. These data have a large uncertainty and are not conclusive; however, comparison of measured and predicted flight loads are described in detail in Ref. 5.

During the carriage flight tests of the inert Pegasus XL vehicle, wing static pressure measurements were obtained at two spanwise locations, BL60 and BL90, 60 and 90 inches from the center or root chord of the wing, respectively. These data not only provide another level of comparison with the analytical results, they also provide added understanding of the character of the L-1011 interference on the Pegasus XL wing during carriage.

Pressure data at the two wing stations were integrated to form a section normal force coefficient at three flight conditions during tests of the inert Pegasus XL vehicle. These results are illustrated by the dashed lines in Fig. 7 as a function of Mach number; however, this presentation is only a convenience as angle of attack and altitude are also changing at each Mach number. Notice that the wing at the two stations has a negative or downward loading. That is, the L-1011 is pushing down on the wing even though the total configuration is at a positive angle of attack. The lower portion of Fig. 7 illustrates the repeatability of the flight data at BL90.

The predicted results from the NEAR carriage analysis method are shown at similar flight conditions. The overall trend of the predicted wing loading is the same as the data, but there are some significant differences. The important result in Fig. 7 is that both the measured and predicted wing loadings are negative in this narrow range of flight tests.

Launch Characteristics

The NEAR store separation method was applied to the Pegasus XL/L-1011 configuration to study the post-release trajectory characteristics. The predicted results for a nominal launch are shown in Fig. 8. As shown for the B-52 launches of the standard Pegasus configuration, the trend for Pegasus XL is to fall cleanly away from the L-1011 and gradually pitch nose down because of the static stability of the vehicle. The major difference between a launch from the L-1011 and one from the B-52 is the absence of roll during the L-1011 launch. Since it is released from the plane of symmetry of the L-1011, there is no asymmetry in the flow field to cause induced roll effects.

Measured and predicted separation distance between the L-1011 and Pegasus XL for the first launch are compared in Fig. 9. As before, the predicted trajectory was obtained with the control surfaces locked at launch, but the actual controls were free to move after 0.2 seconds. These results indicate that Pegasus XL is predicted to separate at a lower rate than occurred in the first launch. The reason for this difference is not clear at this time; however, it is fortunate that the predicted drop rate at launch is conservative in that Pegasus remains near the L-1011 for a longer period of time.

Predicted launch trajectory characteristics from the NEAR method and an Euler method are described in Ref. 5. The x- and z-separation distances are nearly identical for the two methods for the first two seconds after release. Even though the two prediction methods are very different, there are insignificant differences in the predicted trajectories.

The launch results described above are for design launch conditions. In the interest of safety, it was necessary to demonstrate that Pegasus XL has the potential of being launched from the L-1011 under a range of off-nominal flight conditions. Most conditions examined were inside the L-1011 flight envelope, but some specific conditions were selected outside the envelope. Nearly one hundred different launch flight conditions were investigated prior to the first operational launch.

The results of the extensive launch study were that Pegasus XL could be released from the L-1011 under a wide range of flow conditions without danger of recontact with the L-1011. This study involved emergency releases in which Pegasus was dropped with no intent of completing the mission. A launch condition in which the possibility of recontact is high is an emergency drop after a control system failure locks all three tail fins at maximum deflection for maximum roll. Possible recontact between Pegasus and the L-1011 is shown in Fig. 10.

Other launch calculations were made to expand the launch envelope for safe release without recontact. The results of this study showed that the critical flow parameter is the sideslip angle of the L-1011/Pegasus XL configuration. The possible point of recontact is the tip of the rudder as it leaves the fin cavity. Pegasus XL can be launched without recontact at sideslip angles as high as $\beta = 3°$, well outside the normal launch envelope. The predicted positions of Pegasus XL with respect to the L-1011 after a launch at maximum sideslip conditions are shown in Fig. 11. The location of the rudder inside the fin cavity at the instant of safe clearance is illustrated in the inset in Fig. 11. At larger sideslip angles there is some chance of contact of the rudder tip with the edge of the fin cavity.

CONCLUSIONS

The most important conclusion from the carriage and launch analysis was that Pegasus can be safely carried and launched from both the B-52 and L-1011 aircraft. This was predicted prior to the first B-52 and L-1011 launches, and it was demonstrated in the subsequent six B-52 launches and the single L-1011 launch.

ACKNOWLEDGEMENTS

The authors gratefully acknowledge the Orbital Sciences Corporation for the sponsorship of the technical investigation reported herein.

REFERENCES

1. Mendenhall, M. R., Lesieutre, D. J., Caruso, S. C., Dillenius, M. F. E., and Kuhn, G. D.: Aerodynamic Design of Pegasus - Concept to Flight with CFD. AIAA 91-0190, January 1991.

2. Mendenhall, M. R., Lesieutre, D. J., Whittaker, C. H., Curry, R. E., and Moulton, B.: Aerodynamic Analysis of Pegasus - Computations vs Reality. AIAA 93-0520, January 1993.

3. Dillenius, M. F. E. and Nixon, D.: Prediction Methods for Store Separation. Proceedings: NEAR Conference on Missile Aerodynamics, Nielsen Engineering & Research, Mountain View, CA, 1989.

4. Dillenius, M. F. E., Perkins, S. C., Jr., and Nixon, D.: Pylon Carriage and Separation of Stores. Tactical Missile Aerodynamics: General Topics, Vol. 141 of Progress in Astronautics and Aeronautics, ed. by M. J. Hemsch, AIAA, 1992, pp. 575-666.

5. Mendenhall, M. R., Lesieutre, T. O., Lesieutre, D. J., and Dillenius, M. F. E.: Carriage and Launch Characteristics of the Pegasus Air-Launched Space Booster. AIAA 94-1910, August 1994.

6. Dillenius, M. F. E., Goodwin, F. K., and Nielsen, J. N.: Extension of the Method for Predicting Six-Degree-of-Freedom Store Separation Trajectories at Speeds up to the Critical Speed to Include a Fuselage with Noncircular Cross Section, Vol. I - Theoretical Methods and Comparisons with Experiment, Vol. II - Users Manual for the Computer Programs. AFFDL-TR-74-130, November 1974.

7. Dillenius, M. F. E., Goodwin, F. K., and Nielsen, J. N.: Analytical Prediction of Store Separation Characteristics from Subsonic Aircraft. J. Aircraft, Vol. 12, No. 10, October 1975, pp. 812-818.

8. Goodwin, F. K. and Smith, C. A.: Theoretical Separation Characteristics of Two Conceptual Solid Rocket Booster Parachute Test Units from the B-52 Aircraft. NEAR TR 114, August 1976.

9. Dillenius, M. F. E., Lesieutre, D. J., Perkins, S. C., Jr., Jeter, E. L., and Schulz, J. C.: Methodology for Aerostructural Analysis of a Missile Attached to a Maneuvering Aircraft. AIAA 89-0480, January 1989.

10. Dillenius, M. F. E., Whittaker, C. H., Lesieutre, T. O., and Lesieutre, D. J.: High Angle-of-Attack Missile Launch Computer Analysis Code. NEAR TR 456, February 1993.

11. Dillenius, M. F. E., Lesieutre, D. J., Whittaker, C. H., and Lesieutre, T. O.: New Applications of Engineering Level Missile Aerodynamics and Store Separation Prediction Methods. AIAA 94-0028, January 1994.

12. Bamber, M. J.: Store Separation Investigation by Grid Method Using Wind Tunnel Data. DTMB Rept. 2202, Aero Report 1107, 1966.

13. Tessitore, F., Cenko, A., Meyer, R., Dyer, R., and Waskiewicz, J.: A New Approach to Weapon Separation Aerodynamics. Jour. of Aircraft, Vol. 19, No. 12, 1981, pp. 1070-1075.

14. Keen, K. S.: Improvements of Prediction Techniques for Store Loads and Trajectories. 1986 JTCG Aircraft/Stores Compatibility Symposium, Wright-Patterson AFB, OH, April 8-10, 1986.

15. Belk, D. M., Janus, J. M., and Whitfield, D. L.: Three-Dimensional Unsteady Euler Equations Solution on Dynamic Grids. AIAA Journal, Vol. 25, No. 9, 1987, pp. 1160-1161.

16. Dougherty, F. C., Benek, J. A., and Steger, J. L.: On Applications of CHIMERA Grid Schemes to Store Separation. NASA TM-88193, October 1985.

17. Sickles, W. L., Rist, M. J., Morgret, C. H., and Parthasarathy, K. N.: Separation Analysis of the Pegasus XL From an L-1011 Aircraft. AIAA 94-3454, August 1994.

18. Meakin, R. L. and Suhs, N. E.: Unsteady Aerodynamic Simulations of Multiple Bodies in Relative Motion. AIAA 89-1996, June 1989.

19. Kraft, E. M. and Belk, D.: Advances in the Use of CFD for Weapons Integration. RAE Store, Carriage, and Release Conference, Royal Aeronautical Society, London, 1990.

20. Meakin, R. L.: Computations of the Unsteady Flow About a Generic Wing/Pylon/Finned-Store Configuration. AIAA 92-4568, August 1992.

21. Mendenhall, M. R., Perkins, S. C., Jr., and Lesieutre, D. J.: Vortex Cloud Model for Body Vortex Shedding and Tracking. Tactical Missile Aerodynamics: Prediction Methodology, Vol. 142 of Progress in Astronautics and Aeronautics, ed. by M. R. Mendenhall, AIAA, 1992, pp. 225-285.

22. Mendenhall, M. R. and Lesieutre, D. J.: Prediction of Subsonic Vortex Shedding From Forebodies with Chines. NASA CR 4323, Sept. 1990.

23. Lesieutre, D. J., Dillenius, M. F. E., and Whittaker, C. H.: Program SUBSAL and Modified Store Separation Program for Calculating NASTRAN Forces Acting on Missiles Attached to Subsonic Aircraft. NEAR TR 393, Sept. 1991.

24. Goodwin, F. K., Dillenius, M. F. E., and Nielsen, J. N.: Prediction of Six-Degree-of-Freedom Store Separation Trajectories at Speeds up to the Critical Speed, Vol. I - Theoretical Methods and Comparisons with Experiment, Vol. II - Users Manual for the Computer Programs. AFFDL-TR-72-83, October 1974.

25. Curry, R. E., Mendenhall, M. R., and Moulton, B.: In-Flight Evaluation of Aerodynamic Predictions of an Air-Launched Space Booster. NASA TM 104246, 1992. Also, Paper No. 6, AGARD Conference Proceedings 514. Torino, Italy. 1992.

26. Mendenhall, M. R., Lesieutre, T. O., Lesieutre, D. J., and Dillenius, M. F. E.: Carriage and Launch Characteristics of the Pegasus Air-Launched Space Booster. NEAR TR 477, March 16, 1994.

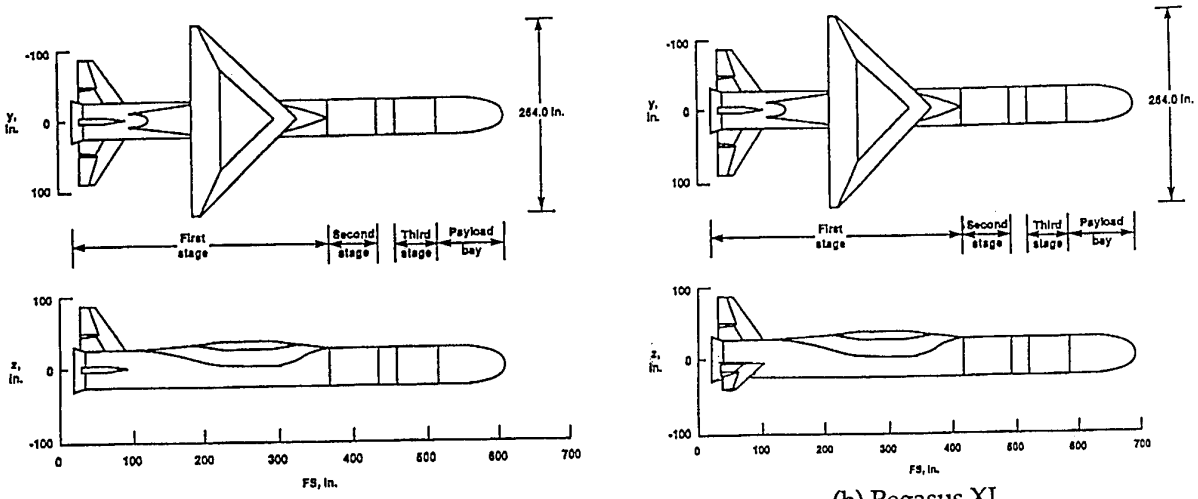

(a) Standard Pegasus

(b) Pegasus XL

Fig. 1. Pegasus configurations.

	Inert Flight $M_\infty = 0.8$ h = 33,000 ft.	Predicted	Flight 1 $M_\infty = 0.8$ h = 42,900 ft.	Predicted
Total Hook Loads:				
Pre Flight	44,935 lbs.		42,620 lbs.	
Carriage	58,578	57,663	50,094	50,592
Post Flight	49,134		-	
Aero Loads: (positive down)	9,444 to 13,643	12,728	7,474	7,972

Fig. 2. Measured and predicted carriage loads for the standard Pegasus on the B-52.

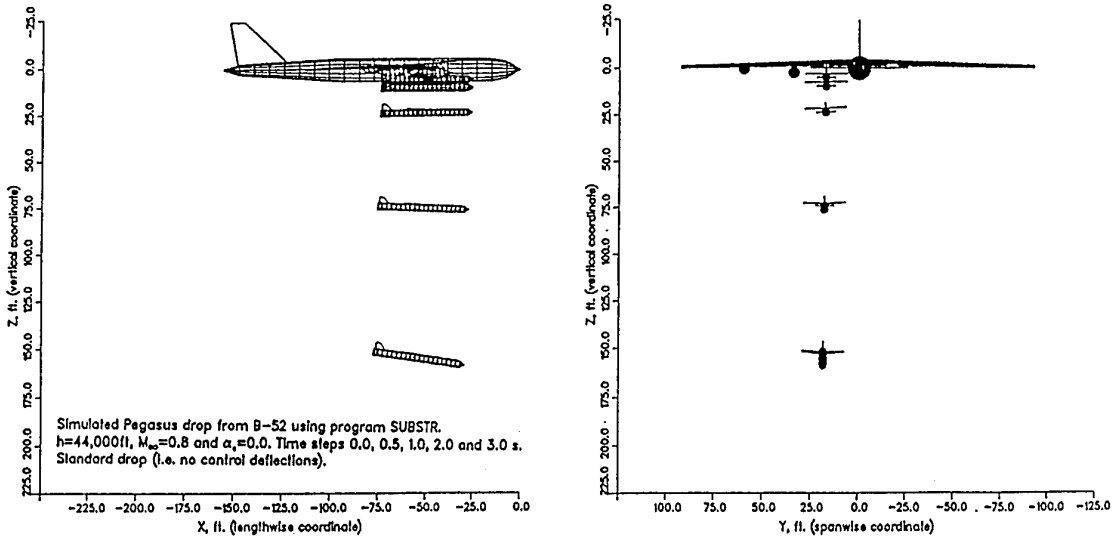

Fig. 3. Predicted launch characteristics of the standard Pegasus from the B-52.

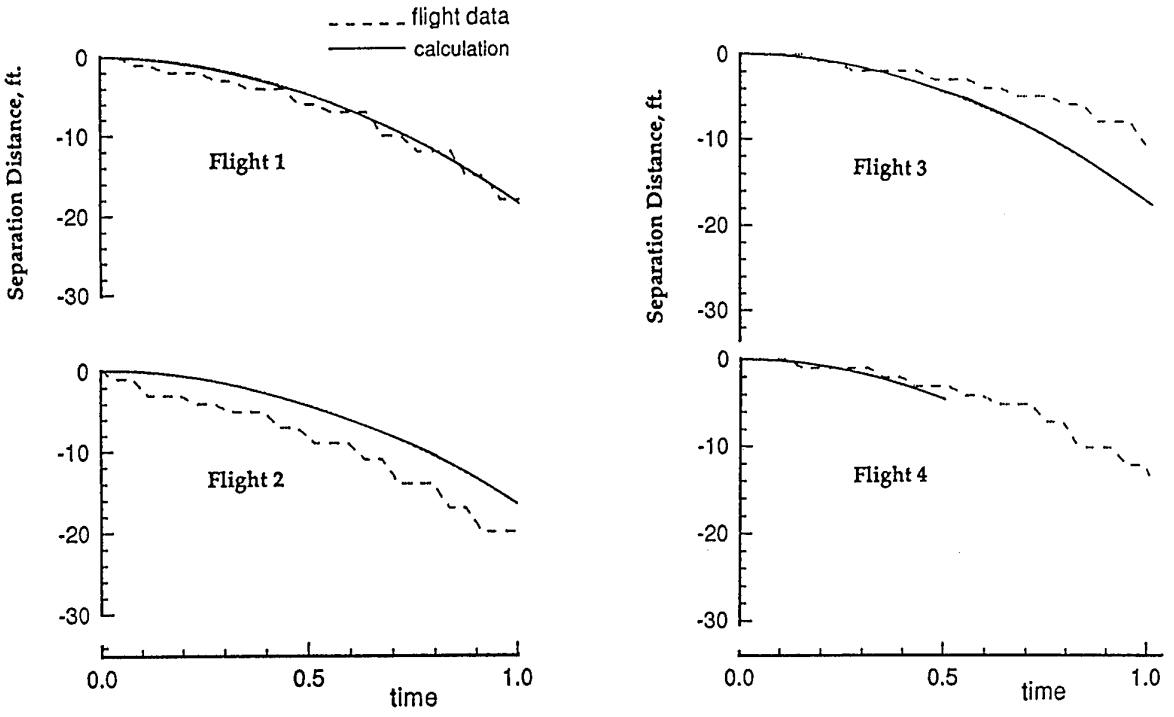

Fig. 4. Measured and predicted separation distance for standard Pegasus launches from the B-52.

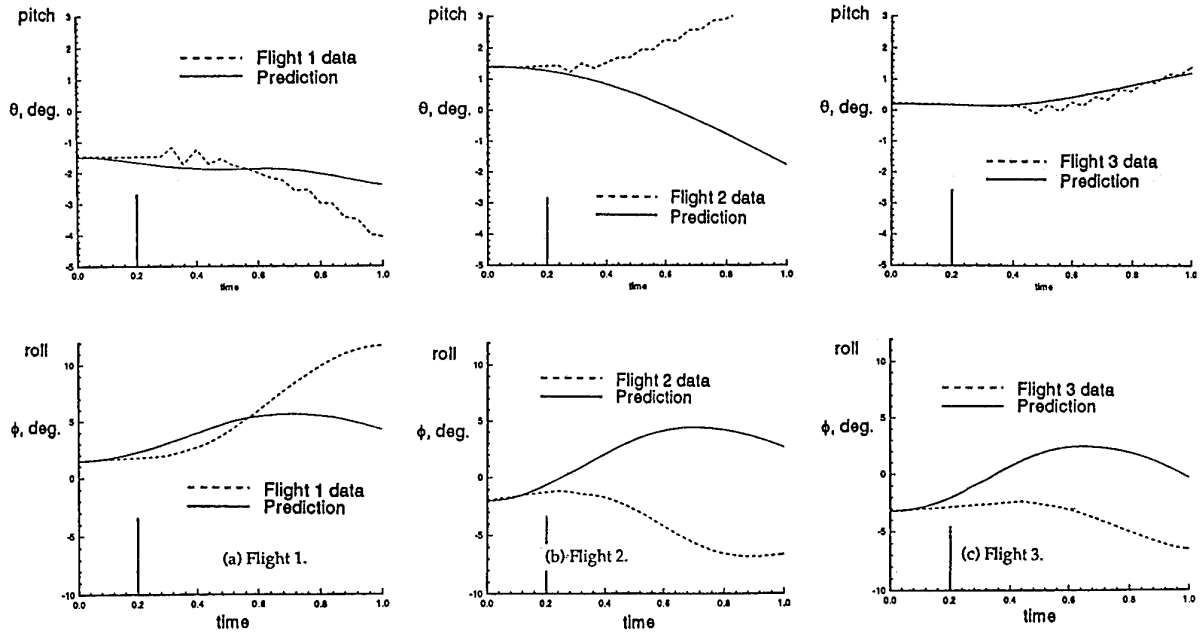

Fig. 5. Measured and predicted pitch and roll characteristics of the standard Pegasus after launch from the B-52.

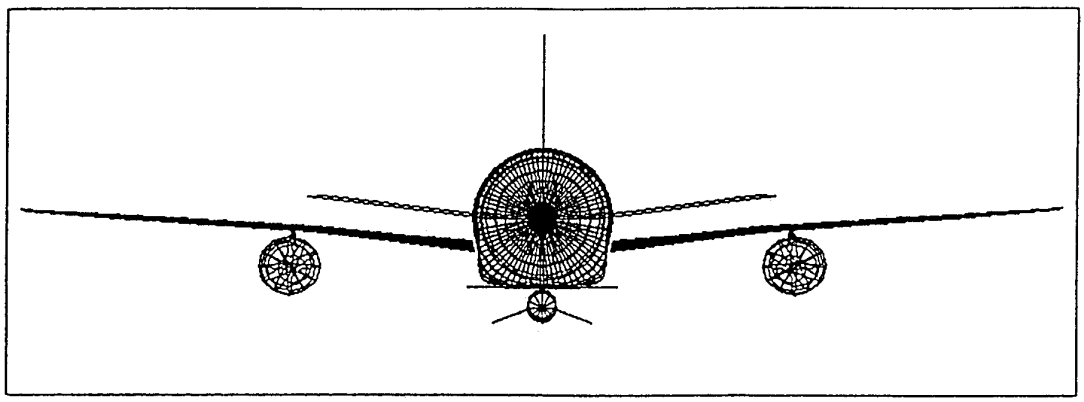

Fig. 6. NEAR analytical model of Pegasus XL and L-1011 in carriage configuration.

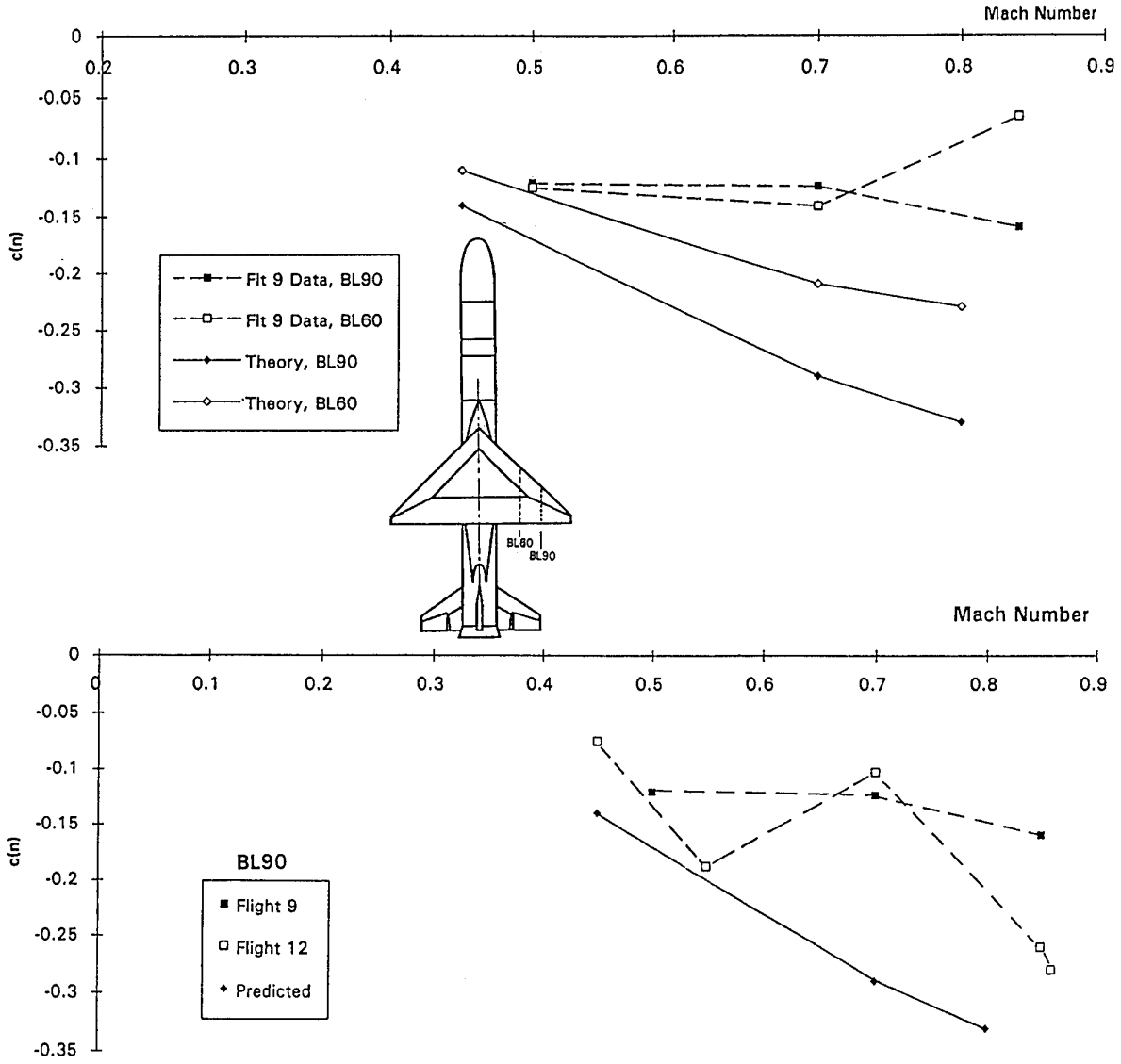

Fig. 7. Measured and predicted wing loading on the Pegasus XL during carriage by the L-1011 aircraft.

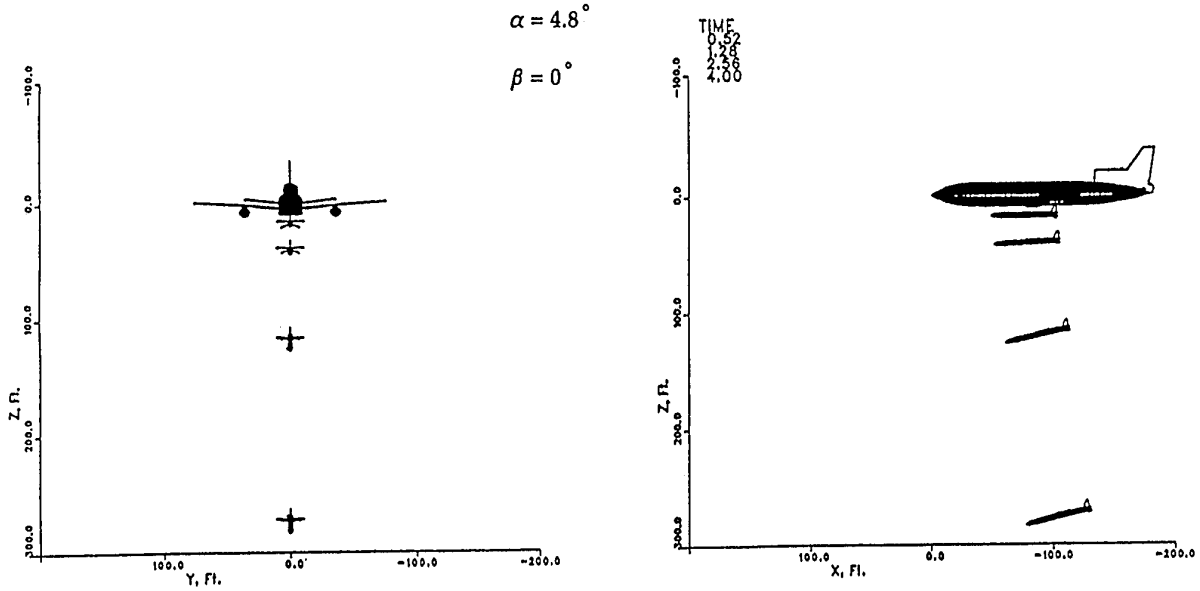

Fig. 8. Predicted Pegasus XL launch from the L-1011 aircraft.

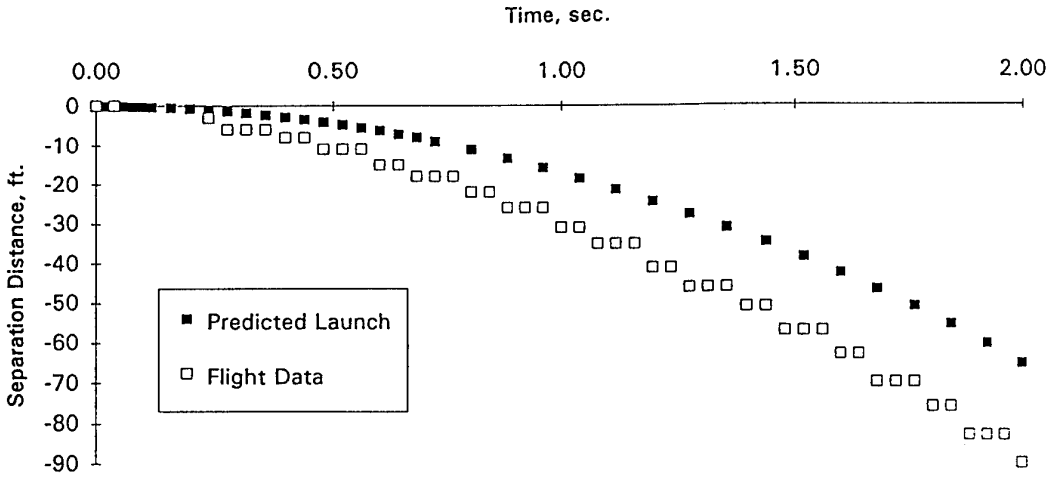

Fig. 9. Measured and predicted separation distance for the Pegasus XL launch from the L-1011.

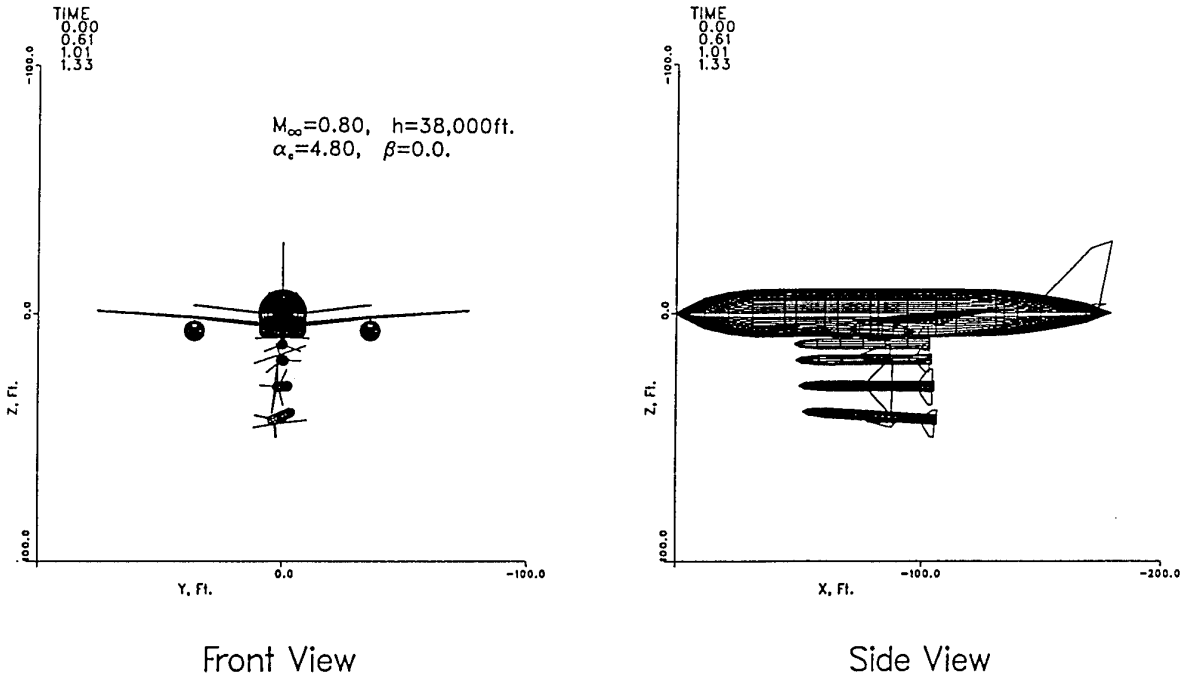

Fig. 10. Predicted emergency launch trajectory of Pegasus XL with fin deflections for maximum roll.

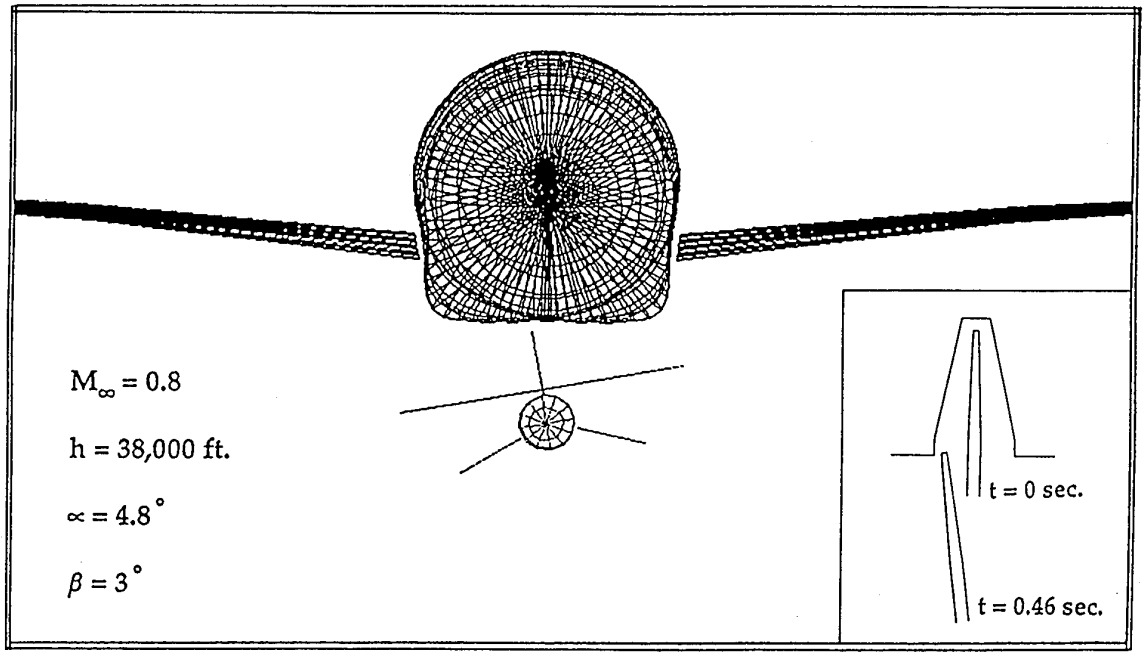

Fig. 11. Effect of sideslip angle on the Pegasus XL clearance during launch from the L-1011 aircraft.

USE OF A CAPTIVE TRAJECTORY SYSTEM IN A WIND TUNNEL

G. Lombardi
Department of Aerospace Engineering, University of Pisa
Via Diotisalvi 2, 56126 PISA, Italy

C. M. Johnston
Medium Speed Wind Tunnel, CSIR
P.O. Box 395, PRETORIA 0001, South Africa

SUMMARY

The capabilities of a six degree of freedom Captive Trajectory System (CTS) in a transonic wind tunnel are investigated, and some aspects related to its operation are singled out. The two operative modes ("position" mode and "velocity" mode) and the repeatability of the data under those conditions expected to be critical are analysed. The capabilities of the facility, are studied by means of a test campaign with a typical interference geometry, composed of a store and a wing-fuselage aircraft. The results obtained show that the CTS technique can simulate the effect of the various parameters affecting the trajectory of a released store, within the usual limitations of a wind tunnel simulation. With the CTS technique, the analysis of several different parameters proved easy and fast to carry out. Furthermore, a "grid test" performed on the same configuration underlined the importance of this application of the CTS for a better understanding of the aerodynamic behaviour of the interfering bodies, which appears to be an essential feature for correctly defining safe and efficient conditions for store release.

LIST OF SYMBOLS

b	parent model span (m)
c.g.	centre of gravity of the store
c_{ma}	parent mean aerodynamic chord (m)
C_L	lift coefficient
C_l	rolling moment coefficient
C_m	pitching moment coefficient
C_Z	normal force coefficient
C_Y	lateral force coefficient
M	Mach number
t	time from separation (s)
x	longitudinal position of store centre of gravity
y	lateral position of store centre of gravity
z	vertical position of store centre of gravity
α	parent angle of attack (deg)
ϕ	store roll angle (deg)
θ	store angle of attack (deg)
ψ	store yaw angle (deg)

1 INTRODUCTION

The carriage and release of stores from fighter aircraft are aspects of primary importance for their operative capability. Therefore, it is of the utmost interest to accurately determine both the aerodynamic loads during carriage (which are strongly dependent on the reciprocal interference effects) and the trajectory executed by the released store until the aerodynamic interference becomes negligible. A separation trajectory is defined as the time history of the c.g. position of the released body and its attitude with respect to the aircraft. The prediction of the trajectory of a released store in an aircraft flow field has always been difficult, particularly in the transonic regime. Several numerical prediction methods were developed for the subsonic regime (see, e.g., Ref. 1), and, more recently, with the advances in computer performance, attempts have also been made to solve the problem numerically also for the transonic regime (see, e.g., Ref. 2). However, the use of a wind tunnel testing technique remains essential in obtaining reliable data, although significantly longer lead times are involved.

Two different techniques are typically used in release wind tunnel tests: dynamic, or free drop, tests, and wind tunnel computer simulations. The advantages of the dynamic drop technique are that there is no danger of interference effects from the store model support system, and that the technique permits the simulation of a multiple stores release. On the other hand, because of the unsteady-state nature of the problem, it is necessary to simulate not only the applied forces, but also the inertial response of the store. This means that the inertial characteristics of the store must also be simulated in the scale model. The problem is that not always is it possible to obtain simultaneously the correct model inertia, weight and c.g. location and, in any case, a different model is required for each inertial configuration of the store. Furthermore, several store models may be required to simulate the various configurations to be tested, and each model may be complicated and expensive.

In the transonic Medium Speed Wind Tunnel (MSWT) of the Aerotek Division of the Council for Scientific and Industrial Research (CSIR) in South Africa, a wind tunnel computer technique is in use, based on the use of a Captive Trajectory System (CTS). The capabilities of this facility and some aspects related to its operation are discussed in this paper.
With the CTS it is possible to obtain information on the loads acting on the two interfering models, and on the trajectory performed by the store model as it separates from the parent model. It is evident that the experimental results are valid within the limits of the

Paper presented at the AGARD FDP Symposium on "Aerodynamics of Store Integration and Separation", held in Ankara, Turkey from 24-27 April 1995, and published in CP-570.

wind tunnel simulation. The main factors affecting the accurate prediction of the aerodynamic behaviour of the store are related to Reynolds number differences, sting support interference, wall interference, and the difficulty of representing geometric details in a small scale store model.

Because of the lack of knowledge of the damping value of the store, aerodynamic damping derivative coefficients are set as constant values in most trajectory evaluation codes. In fact, the aerodynamic damping characteristics of the store are not generally well defined even in the free stream conditions; furthermore, they may well be sensitive to position and attitude in the highly non-uniform flow field surrounding the parent aircraft. This disadvantage is related not only to experimental trajectory evaluation, but also applies to computer simulation in general. However, significant variations in the constant values of damping (up to ±50%) produce little change in trajectory motion for low amplitude angular excursions.[3]

Store release at high angles of attack can also be simulated using the CTS technique, as can the release of a store when the aircraft is performing a manoeuvre. However, the analysis of multiple store releases, which is an important problem, can not be solved using the CTS technique.

2 EXPERIMENTAL SET-UP

2.1 The Wind Tunnel

The wind tunnel tests were carried out in the Medium Speed Wind Tunnel of the CSIR, in South Africa. This is a closed circuit, variable density, transonic wind-tunnel. Its operational speed ranges from M=0.25 to M=1.5 with stagnation pressure varying from 20 kPa to 250 kPa. The Reynolds number can be changed by modifying the pressure. The test section has a 1.5m x 1.5m square cross section and is 4.5m in length. All four walls are equally longitudinally slotted ("coke bottle" type) for a total porosity of 5%.

The main flow characteristics in the test section are summarised in Table 1 (σ=root mean square). This table is derived from the complete calibration of the wind tunnel, as presented in Ref. 4. The behaviour of the wind tunnel with respect to blockage is particularly important when the CTS rig is used, because two different support systems are simultaneously inserted in the wind tunnel test section. The behaviour of the MSWT is very satisfactory in this regard, particularly in the critical condition close to Mach one. This can be seen from the analysis of the blockage in the dedicated tests described in Ref. 5.

Two different standard model supports are available in the MSWT. The Main Model Support (MMS) consists of a pitch sector fitted with a roll head. The mechanism is capable of an angle of attack range of -10° to 30° and ±180 in roll. The Side Wall Support (SWS) provides an angle of attack range of ±30°, and is typically used for half model tests.

2.2 The CTS Facility

The Captive Trajectory System rig, shown in Fig. 1 with the configuration analysed in this paper, is a six degree of freedom system used for store clearance. It can be used in conjunction with either of the other support systems in the wind-tunnel. Each degree of freedom is driven by a separate servo motor system, thus the motion controls are all independent. All the drive units are mounted externally to the wind-tunnel to reduce the blockage of the system. The angular movements occur at the "roll head" on the rig. The linear movements and angular head ranges are given, along with their positioning accuracy, in Table 2.

The rig can be driven by means of a trajectory generation code (using a PDP 11/83 dedicated computer), to generate captive trajectories in the wind-tunnel. The trajectories are generated by integrating, through an Adams-Moulton algorithm with a Runge-Kutta start at the first step, the six-degree-of-freedom equations of motion. The release conditions and physical characteristics of the store are specified in the code via a set of input constants, while the aerodynamic loads on the store are those measured by a five - or six - component strain gauge balance mounted in the store model on the CTS rig. The use of a five component balance is related to a testing procedure in which the drag is not measured during the trajectory simulation, but is imposed on the store by the code. In this way it is possible to take into account the effect of the propulsive system of the store on the drag. The drag is the force component most affected by the interference effects caused by the model support. It is then possible to use more accurate drag data, obtained by grid tests carried out with a dedicated, more precise, outfit, or on a larger scale model. This particular procedure, though more complex and expensive, can reduce the uncertainty related to interference effects in the drag evaluation.

Stability of Mach number with time	$\sigma_{Mt} \leq 0.0043$	
Stability of stagnation pressure with time	$\sigma_{P_0} \leq 0.0077$ kPa	
Stability of stagnation temperature with time	$\sigma_{T_0} \leq 0.58$ °K	
Spatial variation of Mach number	$\sigma_M \leq 0.002$ (subsonic) ;	$\sigma_M \leq 0.004$ (supersonic)
Spatial variation of flow angularity	$\sigma_\mu \leq 0.15°$ (subsonic) ;	$\sigma_\mu \leq 0.30°$ (supersonic)
Acoustic pressure coefficient fluctuation	$\Delta c_p \leq 0.01$	
Acoustic fluctuation frequency content	$[n\ F(n)]^{1/2} \leq 0.007$	
Turbulence level	$\sigma_u/U_\infty \leq 0.001$ (low Mach) ;	$\sigma_u/U_\infty \leq 0.002$ (high Mach)

Table 1 - Main flow characteristics in the wind tunnel test section

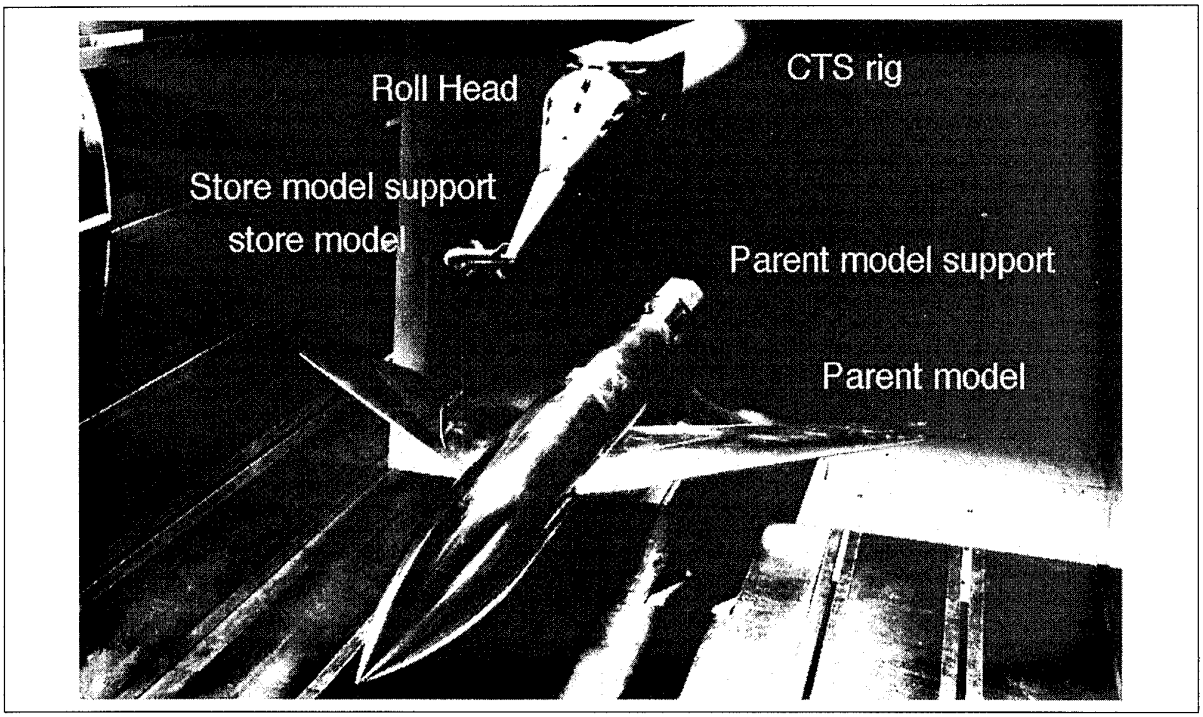

Fig. 1 - The Captive Trajectory System with the configuration analysed in this paper.

	axial (mm)	width (mm)	height (mm)	pitch (deg)	yaw (deg)	roll (deg)
RANGE	± 560	± 410	± 525	± 45	± 45	± 180
TOLERANCE						
Design	0.5	0.5	0.5	0.1	0.1	0.4
Verified	0.30	0.15	0.16	0.05	0.08	0.13

Table 2- Range and accuracy of the CTS rig

The CTS can operate in two different modes, i.e. the "position mode" and the "velocity mode". In the "position mode", the store model is positioned at the starting point of the trajectory, the aerodynamic loads are measured and the displacement that the store would undergo during a short time interval is calculated. The calculation involves the integration of the aerodynamic forces and moments acting on the store and the effects of the non-aerodynamic loads. The CTS rig moves the store model to the new position (in all the six degrees of freedom) and the process is repeated. In the "velocity mode", the trajectory is generated in the same manner except that the store model does not come to rest during the trajectory. This mode is used to minimise the test time. The main difference between the two operating modes is that in the "position mode" the store model is stationary when the balance readings are taken, while it is not in the "velocity mode". A "position mode" trajectory simulation requires about 20 minutes of wind tunnel time, a "velocity mode " about 10 minutes; in both cases the time required for model installation is the same.

Another way to use the CTS rig is in the "grid" test. In this case there is no trajectory calculation, rather the load components (or other quantities such as pressure, etc.) are measured at a predetermined set of store attitudes and positions with respect to the parent model. The "grid" tests can be used to great benefit for the general study of interference between the two bodies, as the input for an "off line" trajectory generation program, or to verify Computational Fluid Dynamics codes.

3 THE CTS CAPABILITIES

3.1 Configuration and Conventions

To verify the capabilities and the accuracy of the CTS facility described above, a test campaign on a typical interference geometry was carried out. The 1:15 scale configuration analysed was composed of a store model, defined in Fig. 2, and a NACA wing-fuselage parent

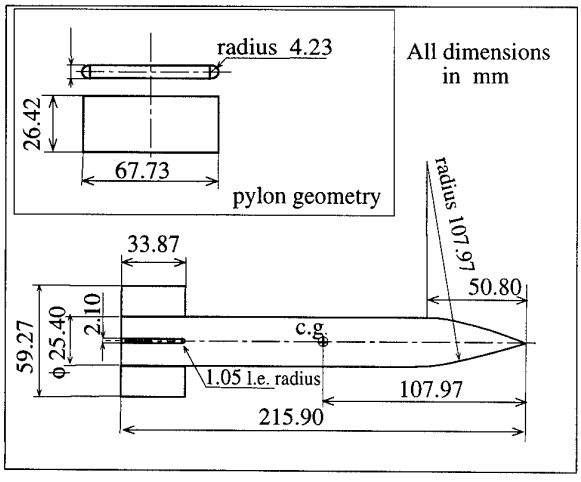

Fig. 2 - The store model and pylon geometries

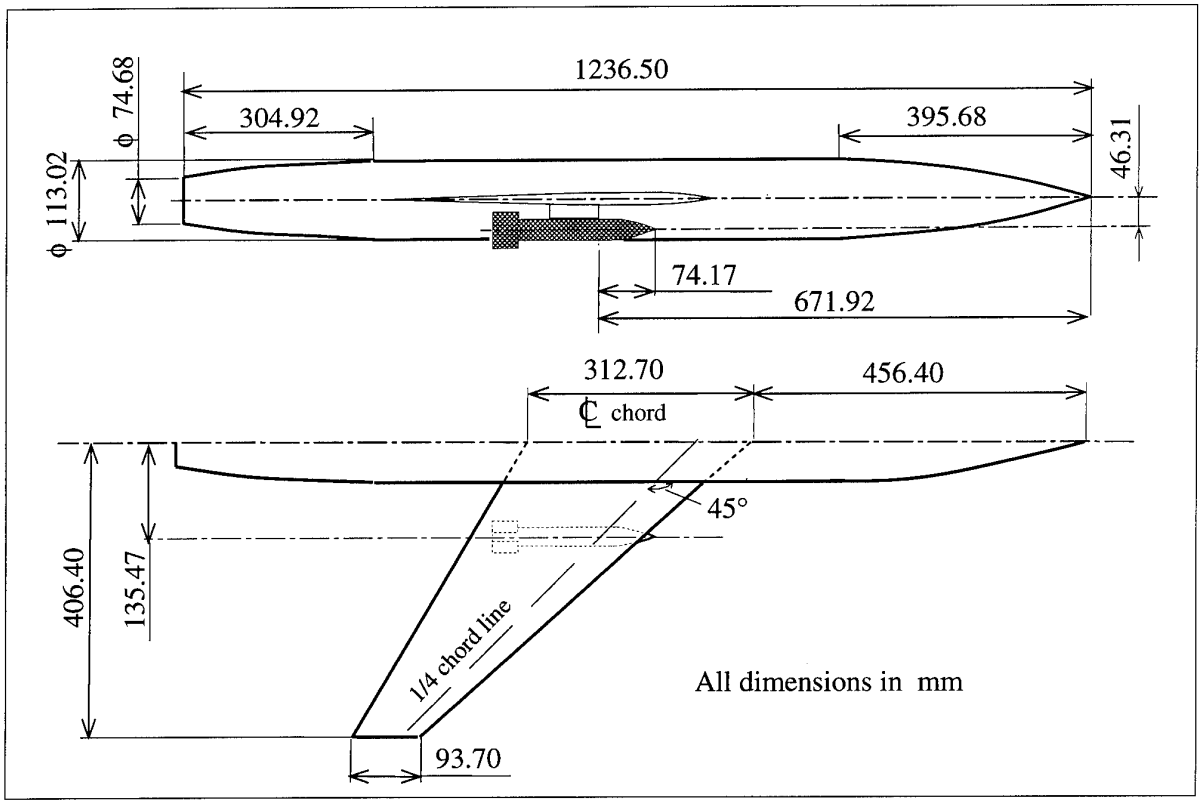

Fig. 3 - The wing-fuselage parent model with the store model in carriage position

model,[6] shown in Fig. 3. The store model had an ogive nose, a cylindrical fuselage and a set of four rectangular fins oriented, in the carriage position, at 45° to the vertical. It was mounted on the CTS rig via a six-component, internal strain gauge balance mounted on the CTS sting. The parent model was composed of an axial-symmetric fuselage and a 45° swept wing. The wing had a NACA 65A006 airfoil section, taper ratio of 0.3, aspect ratio of 4, zero twist and dihedral angles and a mean aerodynamic chord (c_{ma}) of 0.223 m. It was mounted on the MMS by means of a sting. The store model was placed with its axis of symmetry at a span station 0.194 semispans from the fuselage. The reference system is shown in Fig. 4. The origin is placed at the position assumed by the c.g. of the store model before the separation. The forces acting on the store were non-dimensionalised with the dynamic pressure and the cross sectional area of the store fuselage, while the moments (evaluated with respect to the centre of gravity of the store) were non-dimensionalised with the same quantities and the store diameter.

In all the cases discussed the parent model was kept at an angle of attack of 0°.

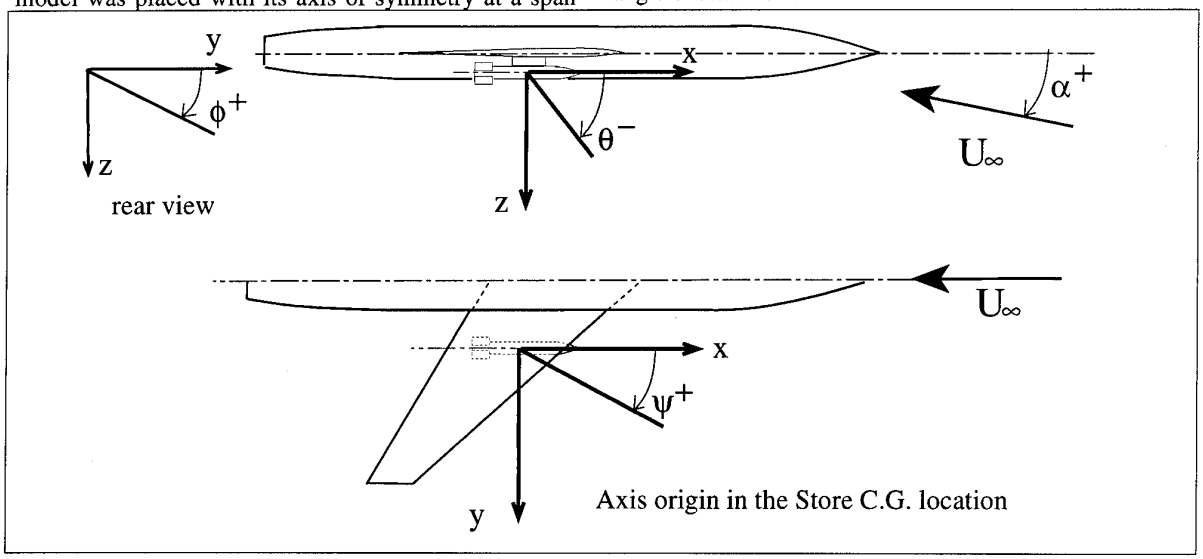

Fig. 4 - The reference system

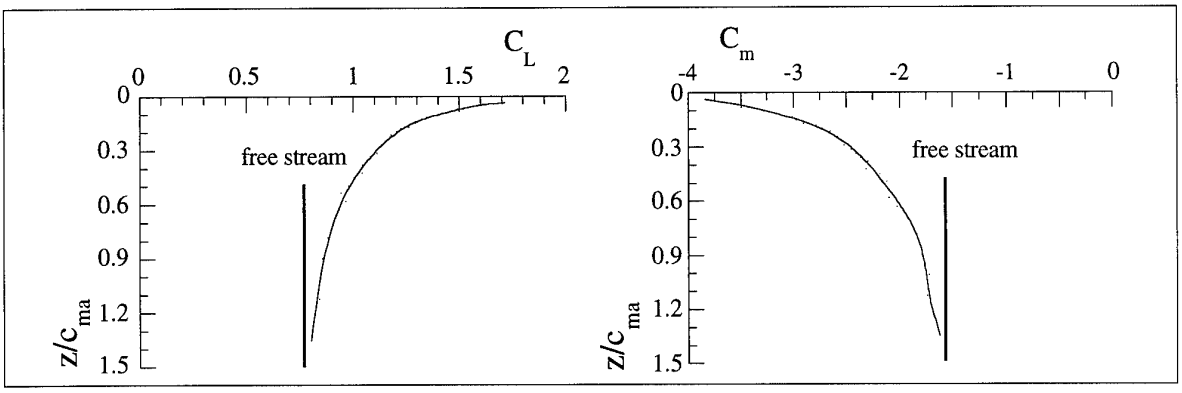

Fig. 5a - Loads acting on the store in the longitudinal plane versus vertical displacement.
M = 0.9 ; α=0; θ_{store} = 4°

3.2 Grid Tests

A grid test campaign allows a better understanding to be obtained of the interference effects felt by the store due to the presence of the parent aircraft. With a grid test it is possible to make a preliminary estimate of the store behaviour in the initial, most critical period of the separation.

The grid tests were performed in transonic conditions (Mach 0.9) with the parent model at an angle of attack of 0° and the store placed at an angle of attack of 4°.

Fig. 5a shows the longitudinal aerodynamics characteristics of the store, with varying vertical displacement from the carriage position. The increase in the normal loads, caused by the interference with the parent, is evident. At a distance of 1.5 c_{ma} from the pylon, the effects became negligible (measurements on the isolated store, performed with the same equipment, give C_L=0.795 and C_m=−1.553); these values are more than doubled in the carriage position. Of relevance is the displacement of the centre of pressure, estimated by means of the ratio $-C_m/C_L$ (fig. 5b).

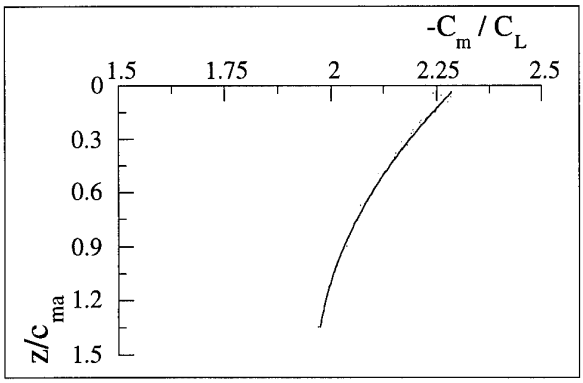

Fig. 5b - Estimation of the store lift point of application versus vertical displacement.
M = 0.9 ; α=0; θ_{store} = 4°

The forward movement of this point, with increasing distance from the carriage position can clearly be seen. This means that the store is aerodynamically more stable in the carriage position than in the isolated condition, and, during the first stage of detachment, it undergoes a decrease in its stability characteristics - in other words, the store experiences a severe nose-down pitching moment increment while in carriage, which must be balanced on release to ensure a safe separation.

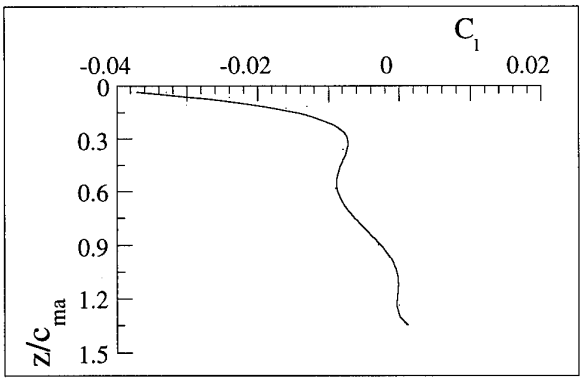

Fig. 5c- Store rolling moment versus vertical displacement.
M = 0.9 ; α=0; θ_{store} = 4°

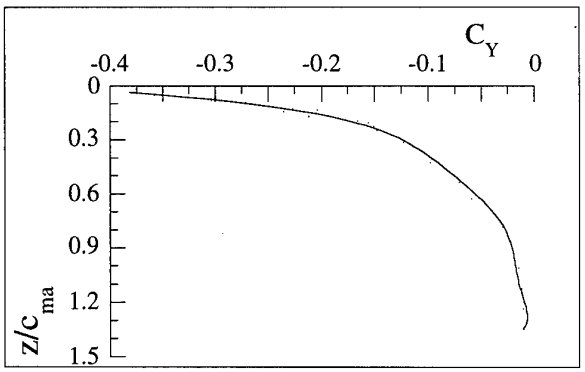

Fig. 5d - Lateral force acting on the store versus vertical displacement.
M = 0.9 ; α=0; θ_{store} = 4°

The store roll behaviour is also modified by the parent (fig. 5c). The interference with the parent introduces a non negligible rolling moment on the store, which acts in the first stage of the detachment, up to a displacement of about one c_{ma}. It is necessary to take into account the effects produced by this rolling moment on the trajectory - in fact, the attitude of the store may be significantly modified. Lateral characteristics are also markedly affected by the parent (fig. 5d). With the store close to the parent, a significant lateral force develops. In the tested conditions, the lateral force acts inboard; this happens because there is no lift acting on the parent wing. Therefore there is no significant outboard lateral component of velocity, so that the most important effect is the "buoyancy" of the parent fuselage, which increases the velocity of the flow on the inbord side of the store. When the wing is producing lift, the lateral force tends to act in the outboard direction, because of the outboard flow velocity component present on the lower surface of the wing. This behaviour was also observed in Ref. 7.

In Fig. 6, different longitudinal positions (at a vertical distance of 0.0564 c_{ma} from the carriage position) are analysed. The store lift is found to be practically independent of the longitudinal position, but a strong effect on its point of application is evident. From Fig. 6a it can be seen that there is a decrease in longitudinal stability with the rearward movement of the store. On the other hand, the lateral force (Fig. 6b) showed a significant reduction.

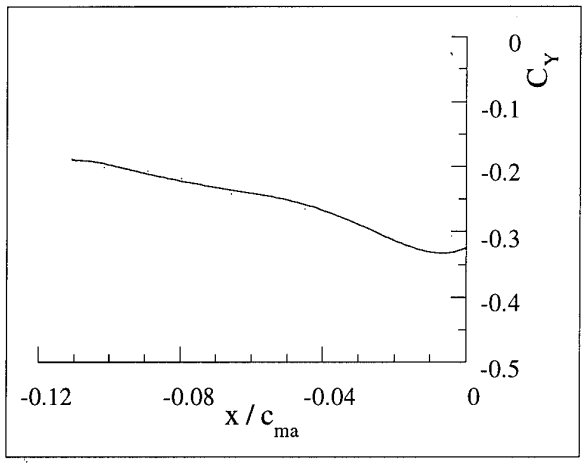

Fig. 6b - Lateral force acting on the store versus horizontal displacement.
z/c_{ma} = 0.0564; M = 0.9 ; α=0; θ_{store} = 4°

More significant are the effects of a spanwise displacement (as shown in Fig. 7), again for z/c_{ma}=0.0564. The lift tends to decrease with the distance from the pylon, with the greater reduction for inboard displacements, while its point of application shows an almost constant move closer to the c.g. when the store is moving outward (Fig. 7a). Furthermore, a significant reduction in the lateral force occurs as the store moves inboard (Fig. 7b).

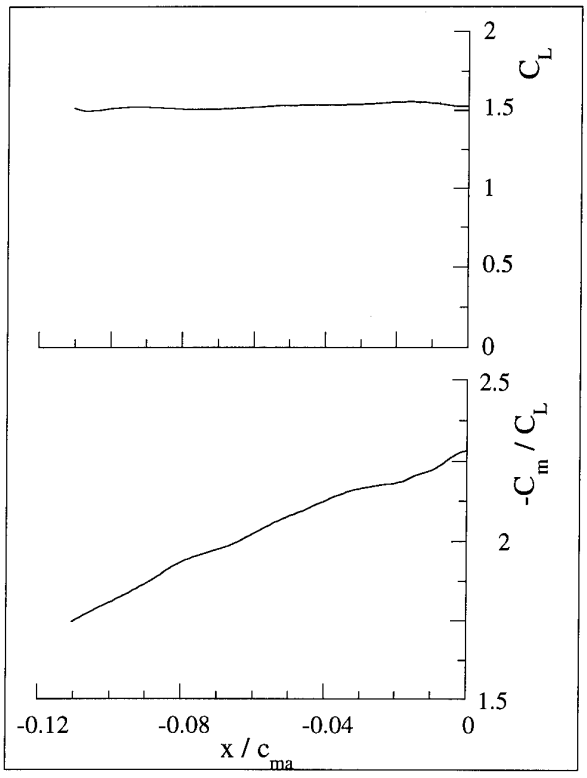

Fig. 6a - Loads acting on the store in the longitudinal plane versus horizontal displacement.
z/c_{ma} = 0.0564; M = 0.9 ; α=0; θ_{store} = 4°

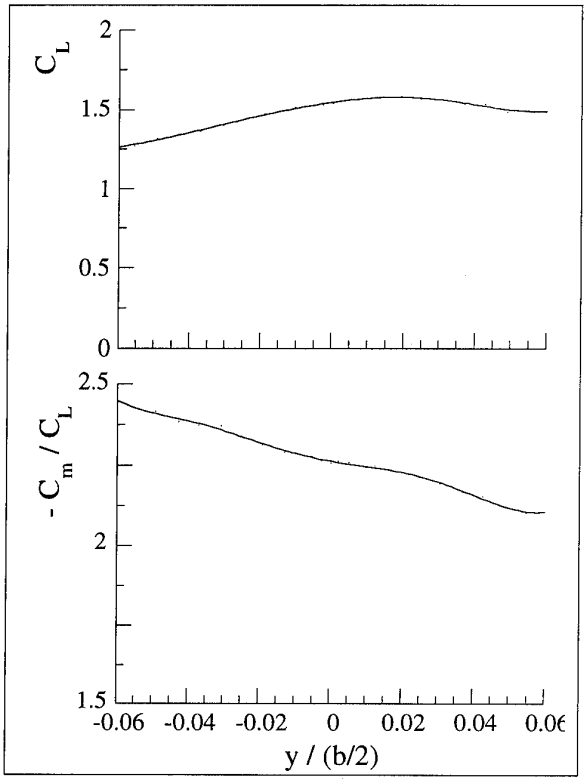

Fig. 7a - Loads acting on the store in the longitudinal plane versus spanwise displacement.
z/c_{ma} = 0.0564; M = 0.9 ; α=0; θ_{store} = 4°

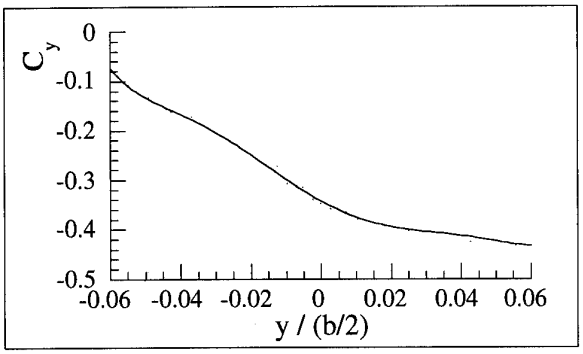

Fig. 7b - Lateral force acting on the store versus spanwise displacement.
$z/c_{ma} = 0.0564$; M = 0.9 ; α=0; $\theta_{store} = 4$

3.3 Effect of the mode of operation

In Fig. 8 the differences between "position mode" and the "velocity mode" trajectories are shown, for a Mach number of 0.7 and no initial release conditions applied to the store. The time step in the integration of the equations of motion started at a value of 0.0025 seconds and increased to 0.005 seconds after 0.01 seconds of trajectory flight time. These time steps were maintained for all the trajectories presented in this paper.

The differences appear negligible as far as the linear displacements are concerned, except for a difference in y displacement after 0.2 seconds of trajectory. More significant seem to be the differences in angular displacement, particularly in the yaw angle. In any case,

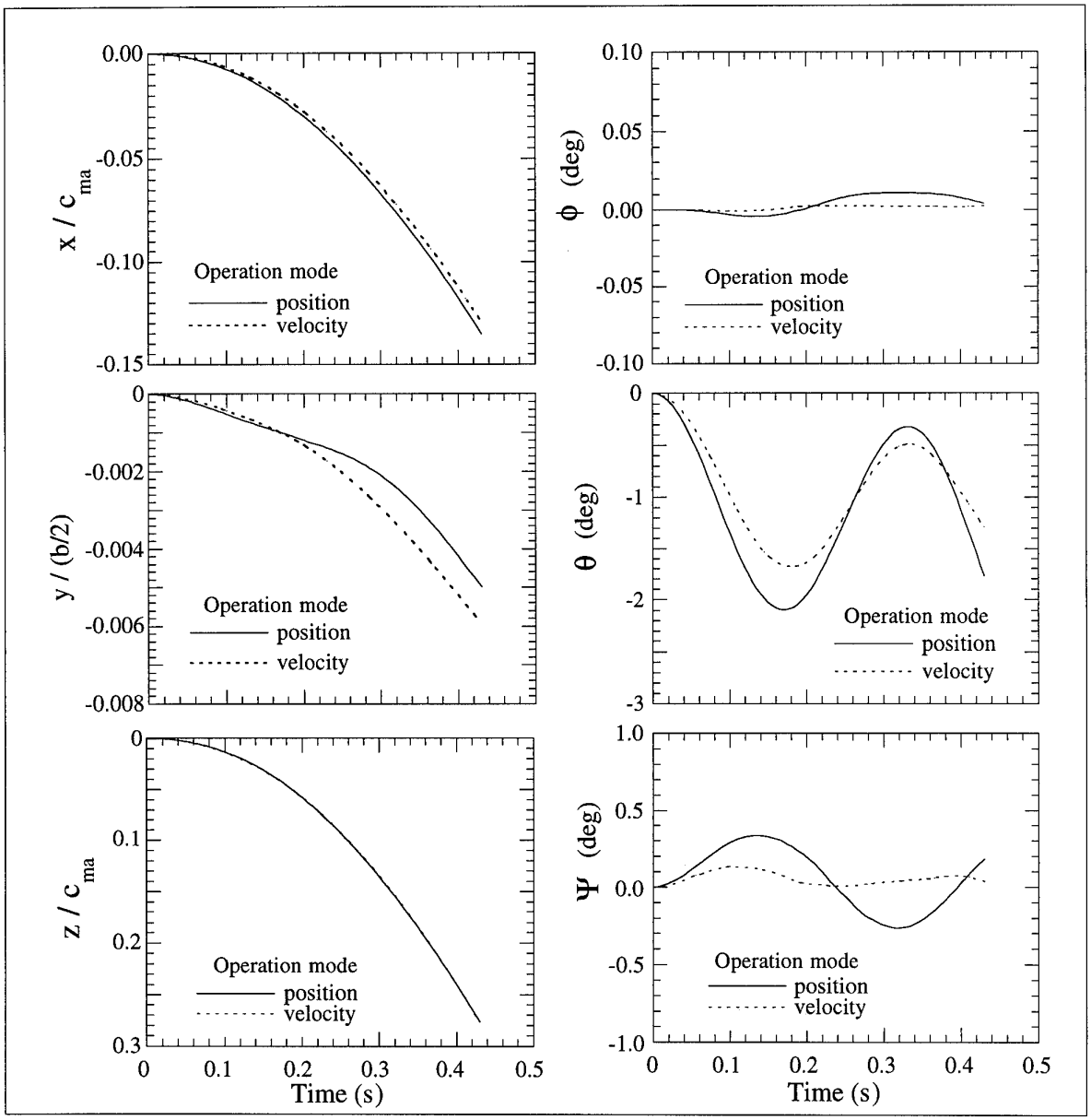

Fig. 8 - Effects of the mode of operation. M = 0.7

it can be noted that the differences in the pitch and roll angles are very small, therefore the above effects do not significantly modify the store trajectory. In conclusion, if a high accuracy is not strictly required, the "velocity mode" can be used.

3.4 Repeatability

Repeatability tests were performed for the velocity mode of operation, at a low Mach number (M=0.4). These conditions were chosen as being the most challenging for the repeatability - in fact, the aerodynamic phenomena are small and, in the velocity mode, the measurements are less accurate.

In Fig. 9 three trajectories, evaluated in the same conditions, are shown. It can be seen that the differences in longitudinal motion (i.e. the x and z displacements and pitch angle) are negligible, while some differences can be observed in the lateral motion and in roll. This dispersion is probably caused by the very high load gradients, in the lateral plane, when the store moves from the carriage position - consequently, small differences in positioning during the integration procedure could result in significant differences in their evaluation. In any case, the trajectory behaviour is well defined in all tests, and the quantitative differences are not particularly important (it should be noted that in Fig. 9 the scales are enlarged).

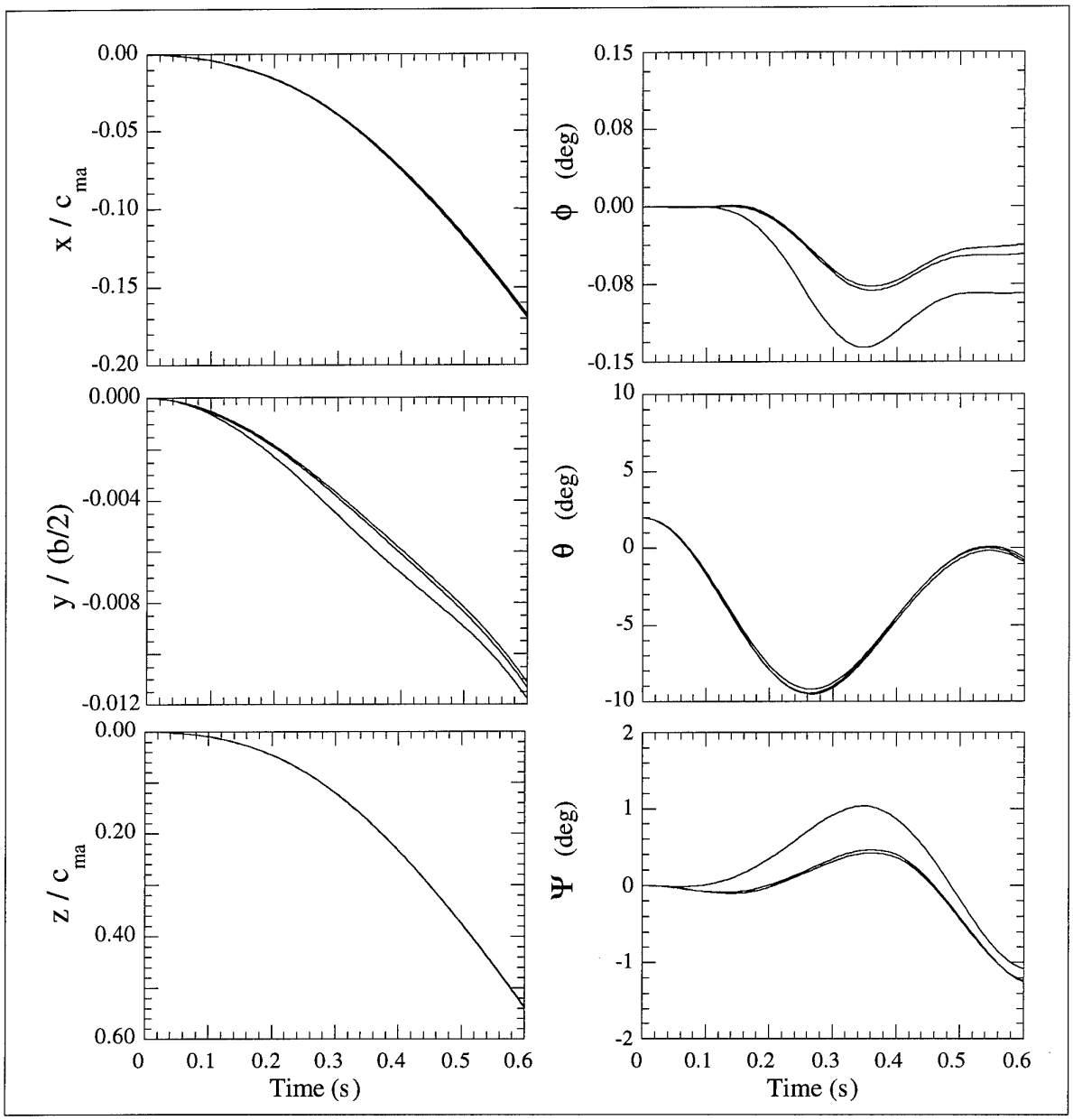

Fig. 9 - Repeatability tests. Velocity mode. M = 0.4

3.5 Examples of applications of the CTS

To illustrate the capabilities of the CTS methodology, the effects produced by different initial conditions (in the vertical velocity and the initial store attitude) were analysed.

In Fig. 10, the effects of imposing an initial downward velocity equivalent to 0.95 c_{ma} per second on the store, are shown. This condition could represent a means for reducing the problem of the physical interaction between the parent and the store, i.e. that the store does not separate from the parent model fast enough.

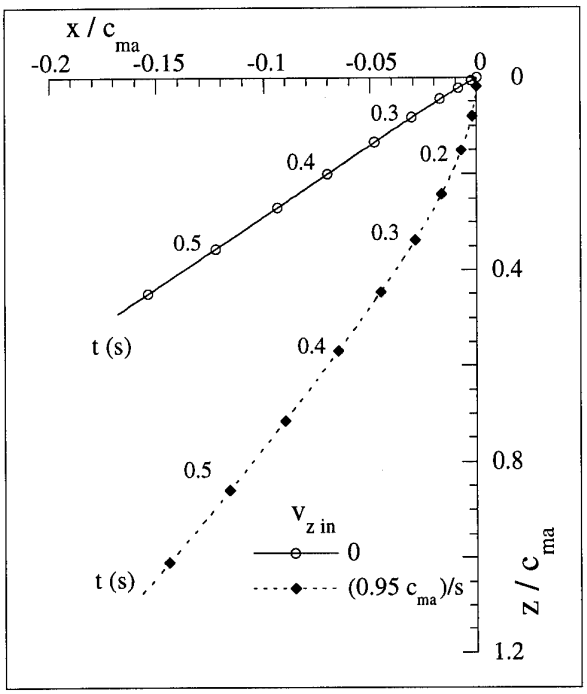

Fig. 10a - Effect of the initial vertical velocity on the trajectory in the vertical plane. M = 0.4

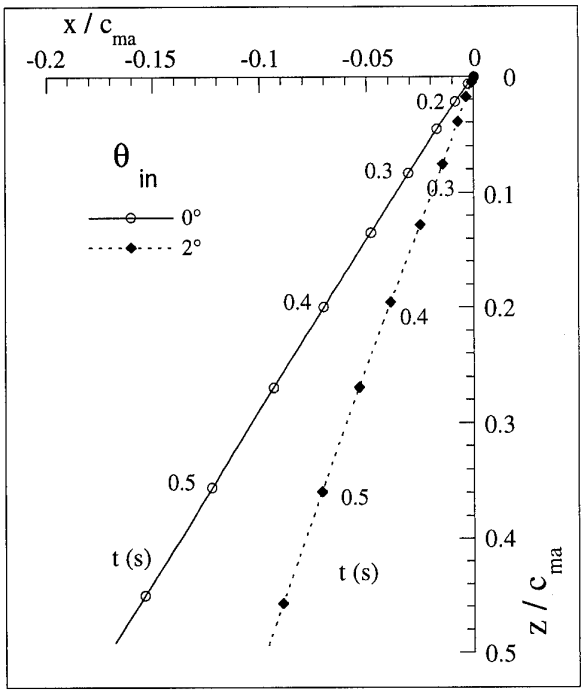

Fig. 11a - Effect of initial pitch position of the store on the trajectory in the vertical plane. M = 0.4

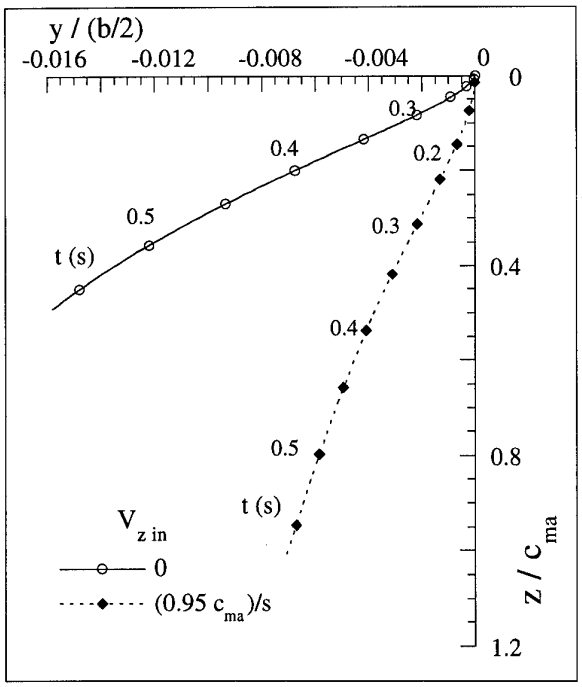

Fig. 10b - Effect of the initial vertical velocity on the trajectory in the lateral plane. M = 0.4

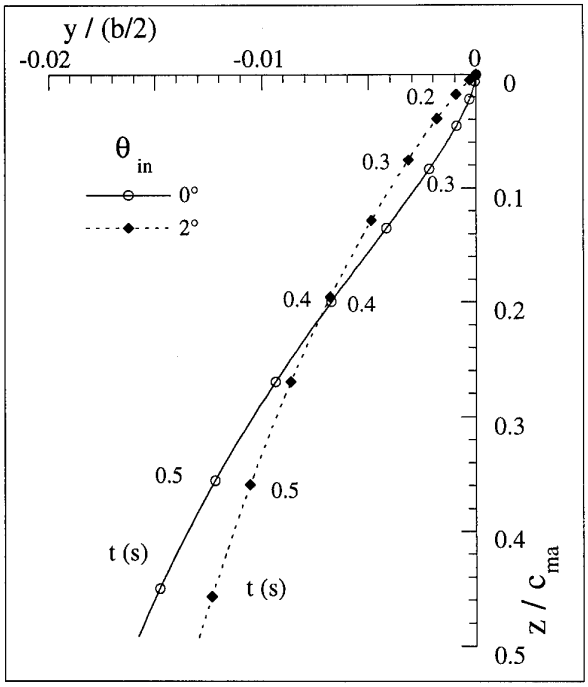

Fig. 11b - Effect of initial pitch position of the store on the trajectory in the lateral plane. M = 0.4

The marked effect of the initial velocity can easily be observed. The trajectory with an initial downward velocity is characterised by an immediate movement of the store away from the parent.

Fig. 11 shows the effects produced by an initial pitch angle of 2° (with no initial vertical velocity of the store). In this case the differences in the trajectory are less significant, but a significant amplification in the oscillation in the pitch motion is present (Fig. 11c). This can be relevant, because dynamic problems could be amplified by a motion characterised by high level of the oscillations.

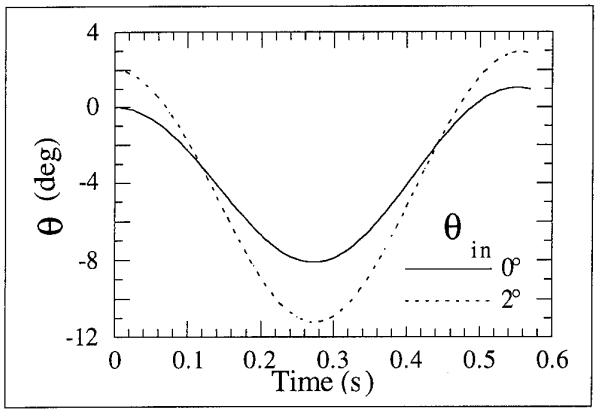

Fig. 11c - Effect of initial pitch position of the store on the pitch angle. M = 0.4

The trajectories showed in Figures 10 and 11 are a clear example of the investigations that can be performed on the store separation by means of the CTS facility.

4 CONCLUSION

To verify the capabilities of the CTS facility in the MSWT, a test campaign was carried out on a typical interference geometry, composed of a store and a wing-fuselage parent aircraft. The results obtained confirm that the CTS technique scan appropriately simulate the effect of the various parameters affecting the trajectory performed by a store well, although, obviously, within the limits of the wind tunnel simulation (i.e. allowing for Reynolds number differences, sting support interference, wall interference, etc.).

A major advantage of the CTS technique is that the analysis of several different parameters (e.g. initial store attitude, applied forces, different mass distributions, different attitudes of the parent, etc.) is easy and fast to carry out.

The differences between "position mode" and "velocity mode" trajectories appear limited; therefore, if a high level of accuracy is not strictly necessary, the "velocity mode" could be used. It should be noted, however, that this conclusion cannot be considered to be general, as the differences would depend considerably upon the gradients in the flow field, and therefore upon the specific geometry tested .

The "grid test" data underlined the importance of this experimental technique for a better understanding of the aerodynamic behaviour of interfering bodies, which is essential for an accurate definition of safe and efficient conditions for separation. Since the aerodynamic characteristics are significantly affected by the interference, and it is difficult to reliably predict these effects (especially in transonic flow), it is necessary to consider grid tests in a fairly preliminary phase of a project.

REFERENCES

1. Van den Broek, G.J., "The Use of a Panel Method in the Prediction of External Store Separation", Journal of Aircraft, Vol. 21, May 1984.

2. Lijewski, L.E., Sush, N.E., "Time-Accurate Computational Fluid Dynamics Approach to Transonic Store Separation Trajectory Prediction", Journal of Aircraft, Vol. 31, July-Aug. 1994.

3. Marshall, J.C., Summers, W.E., "An Analysis of the Relative Importance of Parameters Required for the Simulation of Store Separation Trajectories", Aircraft Store Compatibility Symposium Proceedings, Vol. 2, pp. 67-126, Dec. 1971.

4. Hurlin, R.S., Davis, M.W., "Preliminary Calibration Results for the CSIR Medium Speed Wind Tunnel", DAST Report 90/320, Nov. 1990.

5. Lombardi, G., Morelli, M., "Analysis of Some Interference Effects in a Transonic Wind Tunnel", Journal of Aircraft, in printing.

6. Goodwin, F.K., Dyer, C.L., "Data Report for an Extensive Store Separation Test Program Conducted at Supersonic speeds - Final Report for the Period June 1975 - August 1979", Technical Report AFFDL-TR-79-3130, Wright-Patterson Air Force Base, Dec. 1979.

7. McKinney, L.W., Polhamus, E.C., "A Summary of NASA Data Relative to External-Store Separation Characteristics", NASA TN D-3582, Nov. 1966.

Nouveau Système de Trajectographie Captive pour la grande soufflerie sonique S1MA de l'ONERA

J.C. Raffin (*) **J.N. Remandet (**)**
ONERA
Centre d'essais de Modane-Avrieux
(*) B.P. n°25 73500 Modane France
(**) B.P. n°72 92320 Châtillon France
D. Rondeau
DASSAULT - AVIATION
Aérodynamique expérimentale
B.P. n°12 78140 Vélizy-Villacoublay France

SOMMAIRE

L'Office National d'Etudes et de Recherches Aérospatiales (ONERA) vient de mettre en service dans la grande soufflerie S1MA un Système de Trajectographie Captive (STC) qui figure parmi les plus grands dispositifs opérationnels de ce type dans le monde.

Ce dispositif a été étudié et réalisé dans le cadre d'un contrat avec le Service Technique des Programmes Aéronautiques (STPA).

Le STC de S1MA et les premiers résultats d'essais avec vent sont présentés ci-après.

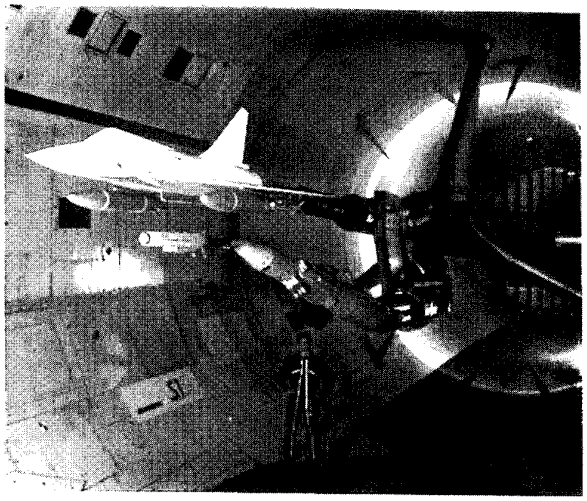

Fig. 1 - STC en veine

ABSTRACT

ONERA, the French National Establishment for Aerospace Research has just implemented at the large subsonic S1MA wind-tunnel a Captive Trajectory System (CTS) which is one of the most important devices of this type in the world.

STPA, the Technical Departement for Aeronautical Programme of the French Ministry of Defence has funded an important part of the study and manufacture of this new device.

This device and the first test results wind-on are presented here after.

1 - INTRODUCTION

L'étude en soufflerie de la séparation d'une charge sous avion peut se faire, soit par largage libre d'une maquette dynamiquement semblable, soit au moyen de mesures d'efforts dites "pesées" d'une maquette de la charge déplacée dans le champ aérodynamique d'une maquette de l'avion.

Au Centre d'Essais de Modane-Avrieux de l'ONERA, les premiers largages libres de petites maquettes dans la soufflerie S3MA datent de 1960. En 1977, le premier essai de ce type a été effectué à grande échelle (1/5) dans la soufflerie S1MA.

La première "pesée" d'engin sous avion a été réalisée à petite échelle en 1956, au moyen d'un dard animé manuellement en incidence et en translation parallèlement au dard support de l'avion.

Un système conçu et réalisé par l'ONERA a permis une première étude par la méthode de la trajectoire captive en 1977. Le dispositif mécanique comportait alors cinq motorisations pour une campagne de séparation de l'engin AS30L sous Mirage F1 dans la soufflerie S2MA. L'adjonction d'un mouvement supplémentaire en roulis a transformé le système initial en un dispositif à six degrés de liberté (voir fig. 2).

Depuis sa mise en service, ce dispositif a été régulièrement amélioré et adapté à l'évolution des besoins. les modifications ont le plus souvent porté sur les logiciels de pilotage et de restitutions des trajectoires, mais des transformations ont également concerné les asservissements, les motorisations et les débattements du dispositif. Ce système a permis l'étude de nombreuses séparations notamment pour l'armement du Mirage 2000 et du Rafale de Dassault Aviation. Il est toujours fréquemment utilisé.

Paper presented at the AGARD FDP Symposium on "Aerodynamics of Store Integration and Separation", held in Ankara, Turkey from 24-27 April 1995, and published in CP-570.

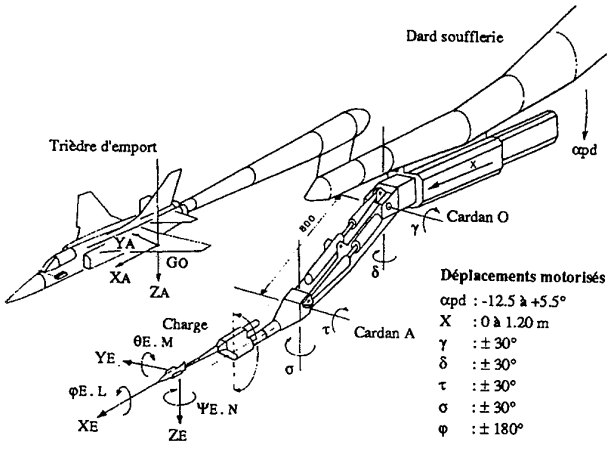

Fig. 2 - Dispositif de trajectographie captive à six degrés de liberté utilisé à S2MA depuis 1977

De nombreuses charges aéroportées actuelles comportent des éléments mobiles pilotés dès l'instant du largage. L'intégration de parties mobiles motorisées est difficile dans une maquette à l'échelle du 1/15 sur le dispositif à six degrés de liberté à S2MA. La manoeuvrabilité de certaines charges nécessite aujourd'hui d'augmenter encore les amplitudes d'animation en dérapage et en incidence.

Les essais en largage libre utilisent des maquettes particulières et coûteuses qui doivent à la fois être dynamiquement semblables au modèle et fragilisées pour ne pas endommager la soufflerie. Cette technique comporte des risques de pollution du circuit aérodynamique par les débris de maquettes, pour les études de laminarité qui s'effectuent dans la même soufflerie. Ces essais dont le nombre de maquettes limite le nombre de cas d'essais, nécessitent des corrections importantes pour être représentatifs des largages réels.

Ces raisons majeures ont conduit le STPA à proposer à l'ONERA de se doter, en accord avec les avionneurs et les missiliers, d'un Système de Trajectographie Captive (STC) de grande taille. L'étude de ce nouveau dispositif destiné aux essais dans la soufflerie S1MA a débuté en 1989. Il est conçu pour des maquettes à échelle du 1/6. Son domaine cinématique d'utilisation doit permettre des angles d'incidence et de dérapage importants, nécessaires aux simulations de largage de bombes ou de réservoirs et aux cas de panne de braquage de gouvernes.

2 - DISPOSITIF MÉCANIQUE

2.1 - Présentation

Le STC est un robot d'animation à sept axes, destiné à positionner la charge en X Y Z et l'orienter en roulis, en incidence et en dérapage par rapport à l'avion porteur, dans un large domaine de travail.

Le STC et le dard en bout duquel est fixée la maquette de l'avion sont portés simultanément par la partie mobile en roulis, dérapage et incidence du support "tripode" (fig. 3). Toute manoeuvre de cette partie mobile agit également sur les attitudes de l'avion et de la charge. Cette disposition a l'avantage de faciliter la succession des essais à des incidences différentes, tout en simplifiant les manoeuvres de ralliement du point d'emport.

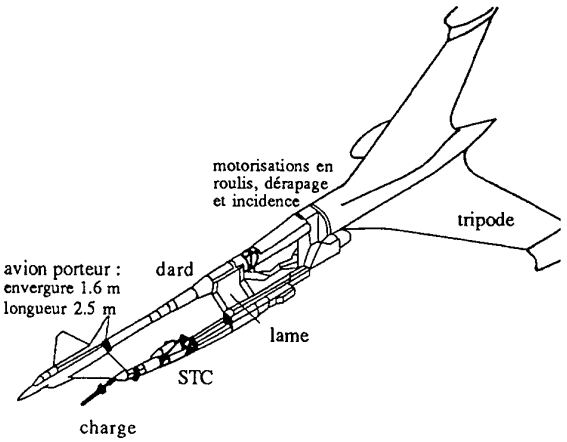

Fig. 3 - Montage du STC sur le dispositif tripode

La partie aval du STC, constituée d'une bride et d'une lame, supporte l'ensemble des éléments mobiles. L'orientation de la lame est normalement perpendiculaire au plan des ailes de l'avion (fig. 4a). Cette disposition convient pour les essais avec des charges en emport sous le fuselage ou sous l'aile gauche dont la demi-envergure n'excède pas 0.80 m. Cependant, il est possible de caler la bride du STC par pas de 22.5° en roulis, de sorte que le domaine d'animation de la charge soit mieux adapté à des points d'emport plus latéraux (fig. 4B).

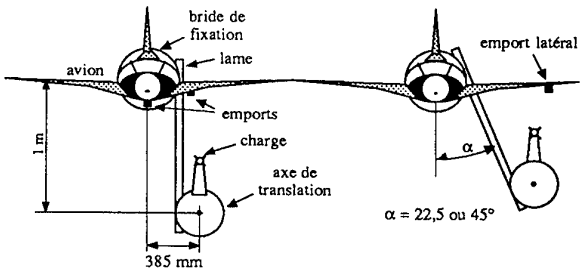

Fig. 4a Montage normal

Fig. 4B Montage avec décalage latéral

Les sept axes d'animation sont cinématiquement consécutifs (fig. 5).

De l'aval vers l'amont, les mouvements successifs sont une translation, un roulis longitudinal, une articulation transversale, un roulis longitudinal, une articulation transversale et deux roulis longitudinaux.

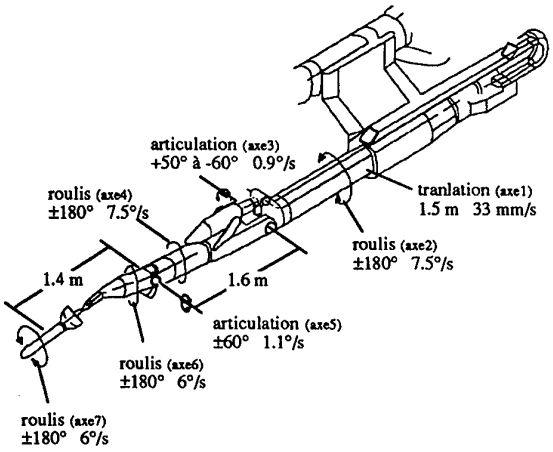

Fig. 5 - Cinématique

Le mouvement de translation (axe 1) a une amplitude de 1.50 m et une vitesse maximale de 33 mm/s. Le mécanisme utilisé comporte un coulisseau équipé de deux rails à double portée en V guidé par des systèmes précontraints à recirculation de rouleaux (fig. 6). La motorisation comporte une vis entraînée par un moto-réducteur et liée au coulisseau et la cage de recirculation d'éléments roulants fixée au fourreau porté par la lame.

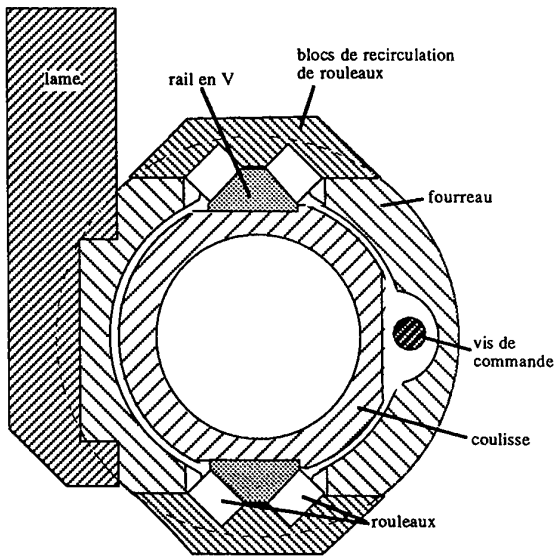

Fig. 6 - Guidage en translation

Les cinq mouvements intermédiaires entre le mouvement de translation à l'aval et le mouvement de roulis qui porte la charge, constituent une succession alternée de trois roulis (axes 2, 4 et 6) et deux articulations transversales (axes 3 et 5). Cette conception avec articulations simples a été préférée à celle du dispositif de S2MA qui comporte deux rotules. Cette technique permet les grands débattements nécessaires au domaine d'utilisation, tout en facilitant la maîtrise des jeux. Les mouvements de roulis ont une amplitude de 360° et une vitesse maximale de 450°/min pour les axes 2 et 4 et 360°/min pour l'axe 6. Les articulations transversales sont motorisées par deux vérins équipés chacun d'une vis entraînée par un moto-réducteur et d'un écrou à recirculation de billes.

Afin d'affiner au mieux la silhouette du STC, le vérin avant, d'une conception très compacte, est entièrement contenu dans le corps enveloppe. Les débattements vont de -60° vers le bas à +50° vers le haut pour l'articulation arrière et de -60° à +60° pour l'articulation avant. Les vitesses articulaires maximales sont de 50°/min pour l'axe 3 et de 66°/min pour l'axe 5.

Le mouvement le plus en amont (axe 7) est contenu dans un bras coudé à 20° et oriente la charge autour de l'axe de roulis avec un débattement maximal 360°. L'axe 7 est un élément amovible. Cette disposition ménage l'avenir et l'on peut imaginer posséder à terme une panoplie de mouvements de différentes géométries parmi lesquels on choisira le mieux adapté à l'essai envisagé.

Chacun des sept mouvements est doté d'une motorisation électrique associant un moteur de type sans balai à un résolver transmetteur de marque Sagem qui permet de piloter l'alimentation des bobinages du moteur au moyen d'une commutation électronique. Un circuit de refroidissement peut distribuer de l'air comprimé sur les enroulements des moteurs des axes 2 à 5 si nécessaire. Les motorisations des axes 2 à 7 sont couplées à un réducteur à jeu réduit de type Harmonic Drive. Un frein électrique permet de bloquer chaque axe en position lorsque le moteur n'est pas alimenté. La figure n°7 présente un exemple de la forte intégration des composants de l'axe 7. Les mécaniques des axes 3 à 6 ont un niveau d'intégration semblable.

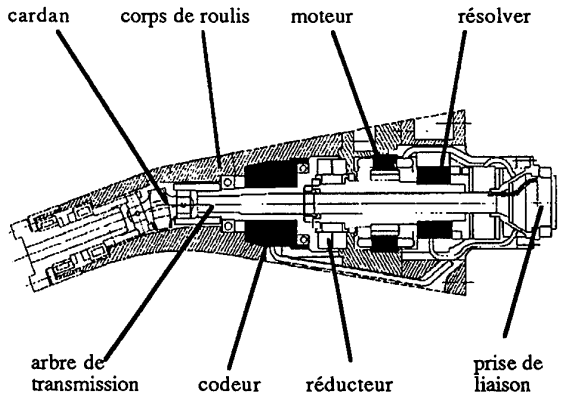

Fig. 7 - Mouvement de roulis axe 7

2.2 Domaine d'utilisation

L'axe 7, qui porte la charge, a une capacité en moment de roulis de ±100 Nm. La résultante aérodynamique sur la charge peut atteindre 2500 N pour un centre de poussée situé à 1,45 m en avant de l'articulation amont, ce qui correspond à un moment de 3625 Nm sur cette articulation. Les montages effectués avec une charge placée au-delà de 1,45 m sont possibles, mais ceux-ci obligent à limiter la valeur de la résultante aérodynamique de façon à respecter le moment limite de 3625 Nm.

Le domaine spatial d'utilisation dépend de la combinaison des axes d'animation. Le volume d'utilisation courante est un cube de 1,5 mètre de côté. Les amplitudes maximales atteintes pour les combinaisons des axes qui leur sont favorables sont d'environ 3 mètres en vertical, ±1 mètre en latéral, 2 mètres en longitudinal, ±70 degrés en incidence, ±60 degrés en dérapage. L'amplitude de ±180 degrés en roulis est possible dans tout le domaine. Le domaine [déport latéral - angle de lacet] paramétré en fonction de l'angle d'incidence et le domaine [altitude - incidence] paramétré en fonction de l'angle de lacet sont présentés fig. 8 et fig. 9. Ces domaines, qui sont établis pour une loi de conjugaison particulière des sept axes d'animation, sont assez proches des domaines extrêmes et non présentés que permet le mécanisme.

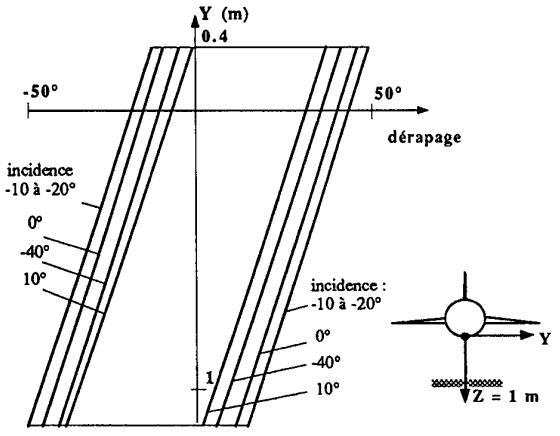

Fig. 8 - Exemple de domaine [déport latéral - angle de lacet]

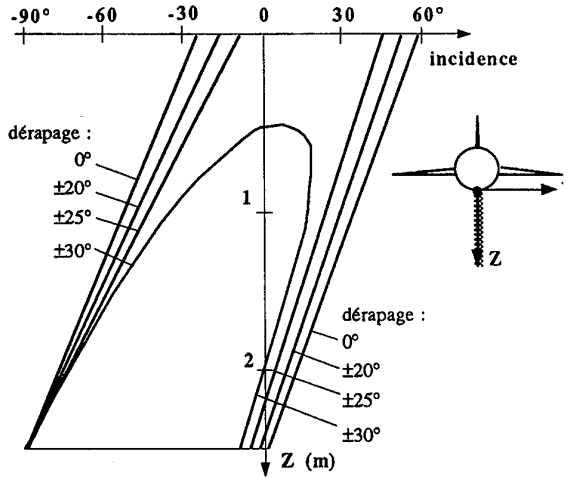

Fig. 9 - Exemple de domaine [altitude - angle d'incidence]

2.3 - Mesures de position

La position des axes est mesurée au moyen de codeurs absolus Codechamp 17 bits (fig. 10), dont la résolution est de 0,016 mm pour l'axe 1, 0,0055° pour les quatre axes de roulis et 0,0015° pour les axes 3 et 5. Une électronique, placée dans la baie du système d'animation, alimente les capteurs, acquiert les signaux, met à disposition de la chaîne de mesures de la soufflerie et du système d'animation les mesures de position mises en forme et génère les signaux logiques de fins de courses électroniques.

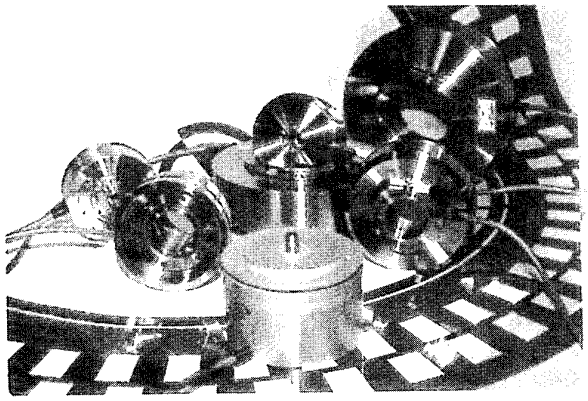

Fig. 10 - Codeurs Codechamp

2.4 - Câblages

Le câblage du STC permet le contrôle de trois éléments motorisés de la charge et la liaison avec une balance à six composantes. Les câblages cheminent nécessairement axialement en raison de la succession des quatre mouvements de roulis de grande amplitude. Cette disposition protège les câbles contre toute sollicitation mécanique due à l'écoulement externe. Une chaîne porte-câble relie l'arrière du coulisseau à la lame-support.

2.5 - Equipement de mesure des déformations

Le STC est équipé de quatre capteurs destinés à la détermination de sa déformée :

• deux ponts d'extensométrie permettent de connaître les contraintes de traction dans les tiges de vis des vérins des axes 3 et 5. Le moment développé sur les axes de basculement est ensuite aisément déduit en tenant compte des relations géométriques des systèmes de manoeuvre ;

• un inclinomètre Qflex placé à l'arrière du coulisseau du mouvement de translation indique l'angle de roulis local. La différence entre cette mesure et la mesure de roulis du dispositif d'orientation en extrémité du tripode sert à évaluer la déformée de la lame-support et du fourreau de coulisseau dans le plan transversal ;

• un second inclinomètre Qflex placé à l'extrémité amont du coulisseau indique l'angle d'incidence local. La différence entre cette mesure et la mesure d'incidence du dispositif d'orientation en extrémité du tripode sert à évaluer de la déformée de l'ensemble bride-lame-axe1 dans le plan longitudinal vertical.

2.6 - Pesée de la charge

La charge est pesée par une balance. Les balances actuellement utilisables pour des essais sur le STC sont les suivantes :

balance	X (N)	Y (N)	Z (N)	L (Nm)	M (Nm)	N (Nm)
Ø26 n°5 5 composantes		2200	3800	135	160	95
Ø26 n°6 6 composantes	600	2200	3800	48	148	72
Ø30 n°4 6 composantes	1500	6200	9000	185	350	200

Les balances Ø26 n°5 et n°6 ont été spécialement réalisées pour les essais sur le STC et la balance Ø30 n°4 a été utilisée pour l'essai de qualification du STC.

La figure n°11 montre la balance Ø26 n°6 en bout du dard support.

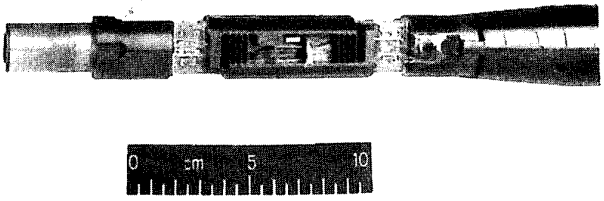

Fig. 11 - Balance Ø 26 n°6 à six composantes montée sur dard

3 - ARCHITECTURE DU SYSTÈME

Le synoptique de la figure 12 présente l'architecture matérielle du système.

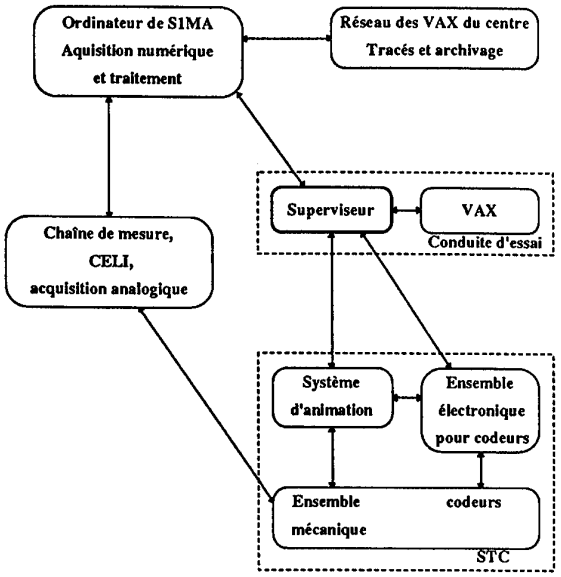

Fig. 12 - Architecture matérielle en essai

Le STC est composé de l'ensemble mécanique placé dans le circuit aérodynamique et équipé des sept codeurs de position, de la commande numérique qui réalise l'asservissement de position des axes mécaniques et de l'ensemble électronique qui alimente les codeurs, gère les signaux et met les mesures à disposition du superviseur de la conduite d'essai et de la commande numérique.

Le superviseur de la conduite d'essai effectue la gestion du déroulement de l'essai, en coordonnant et en séquençant les actions à chaque point de trajectoire :

- lancement des acquisitions analogiques (balance et inclinomètres, ...) au moyen de la chaîne CELI, associée à l'ordinateur de la soufflerie SIMA qui traite et restitue les mesures numérisées,
- acquisition et traitement des mesures fournies par les codeurs,
- calcul de la position et de l'attitude de la charge exprimées dans divers trièdres et en particulier par rapport à l'avion,
- calcul de mécanique du vol pour estimer la position et l'attitude de la charge au point suivant de la trajectoire,
- transformation inverse de coordonnées, par calcul sur le VAX du système de conduite, pour définir les consignes correspondantes dans l'espace des axes d'animation du STC,
- envoi de ces consignes au système d'animation qui asservit le STC aux positions d'axes demandées,
- gestion de l'interface homme-machine au moyen d'écrans de contrôle et de claviers de dialogue,
- transmission des résultats aux ordinateurs VAX du réseau du centre, pour effectuer les tracés de résultats, des calculs en temps différé et les archivages.

4 - SYSTÈME D'ANIMATION

4.1 - Présentation

Le système d'animation est composé d'une commande numérique et d'un ensemble de variateurs de vitesse qui alimentent chacune des sept motorisations. Placé sous le contrôle de la conduite d'essai, le système d'animation assure en permanence l'asservissement de la position de chaque mouvement. Cet asservissement est constitué de trois régulations en cascade dont la première boucle, analogique et de bande passante de l'ordre de 200 Hz, réalise la régulation du courant délivré au moteur de façon à contrôler le couple mécanique fourni par ce dernier. Une deuxième boucle, réalise l'asservissement numérique de vitesse du mouvement par un variateur de vitesse. Enfin, une boucle numérique assure l'asservissement de position de l'axe par une commande d'axes. Ces deux dernières boucles utilisent pour retour, soit les signaux issus du résolver, soit la mesure délivrée par le codeur de position absolue.

La commande numérique est constituée d'un système au standard VME regroupant la commande d'axes et une unité centrale qui lui fournit les positions finales à rallier émises par la supervision de la conduite d'essai

accompagnées d'une consigne de vitesse. A partir de cette consigne, la vitesse de chaque mouvement est ajustée dans le but d'obtenir une excursion synchrone des sept axes, La commande d'axes exécute sept asservissements simultanés et surveille en permanence les sécurités des axes : fins de course, erreur de poursuite des asservissements. Lorsqu'un fin de course ultime est atteint, un arrêt d'urgence bloque les freins des motorisations et ouvre la boucle d'asservissement. Une commande manuelle permet alors de regagner le domaine autorisé sous le contrôle de l'opérateur.

Les trajets définis par la supervision de la conduite d'essai peuvent être réalisés avec une vitesse générale programmable permettant ainsi d'exécuter des phases d'approche du porteur à vitesse réduite pour la sauvegarde des maquettes. La trajectoire suivie par le centre de la charge est élaborée en garantissant un temps de parcours. Une évolution envisageable serait le contrôle géométrique du trajet.

4.2 - Performances

Les boucles de régulation numériques ont une récurrence de 0,5 ms par axe. L'ensemble des surveillances et asservissements des sept axes est rafraîchi en moins de 10 ms.

La précision statique de positionnement est de l'ordre de ± 2 points codeur absolus (voir paragraphe 7.2).

5 - PILOTAGE

5.1 - Généralités

La position cible que doit atteindre le centre de la charge est issue du calcul de mécanique du vol. Les coordonnées et les attitudes de la cible (angles d'Euler) sont données dans le repère cartésien "STC" lié à la bride de fixation sur le dispositif d'orientation en tête du tripode. Le problème consiste à déterminer les consignes dans l'espace des axes qui correspondent aux consignes écrites dans l'espace cartésien. Cette opération s'appelle : "transformation inverse de coordonnées".

La configuration de robot à sept axes d'animation présente l'avantage de permettre l'optimisation du choix de la combinaison des axes parmi plusieurs solutions possibles. Le choix de la solution peut se faire sur un critère de forme du robot *(fluidité des lignes)* ou un critère de temps de ralliement pour réduire la durée du trajet ou bien dans le but de contourner les zones singulières, là où la pilotabilité devient insuffisante ou nulle.

5.2 - Déformations

Réaliser un positionnement précis nécessite de tenir compte des déformations du dard support de l'avion, des éléments du STC et de la balance qui pèse la charge, aussi bien pour le calcul de la position de la charge, que pour le calcul des consignes de la position cible. Le calcul des déformations est fait à chaque point de mesure de trajectoire. La prise en compte de la déformation du dard support de l'avion est faite en amont de l'appel du module de transformation inverse de coordonnées.

La détermination de la déformée du STC nécessite de connaître les caractéristiques de raideur de chacun des éléments qui le composent et les efforts qui leur sont appliqués. Les matrices de raideurs ont été établies d'après les résultats de tarage sous charges élémentaires. Le poids de chaque élément est connu. Pendant l'essai en soufflerie, les efforts appliqués sur les éléments du STC ont pour origine la pesanteur et les effets aérodynamiques. Les efforts connus sont ceux mesurés par la balance, ceux développés par les vérins des axes 3 et 5 et la pesanteur. Une formulation mathématique donne une évaluation des autres efforts aérodynamiques et un recalage est effectué à partir des efforts de vérins. Après calcul des déformées, un second recalage est fait grâce aux indications des deux inclinomètres placés sur le coulisseau du mouvement de translation.

5.3 - Transformation inverse de coordonnées

L'expression des coordonnées cartésiennes (trièdre STC) dans l'espace des axes a une représentation très fortement non linéaire du fait des axes intermédiaires 2, 3, 4, 5 et 6. Ceci rend donc la transformation inverse de coordonnées plus compliquée. La méthode utilisée consiste à progresser depuis la position initiale en direction de la position cible sur des segments de trajectoire dont la longueur est compatible avec une approche linéarisée itérative et convergente. Un jacobien (matrices des coefficients d'influence des axes d'animation sur la position et l'attitude de la charge) est établi à chaque phase de calcul. L'ajout d'une relation linéaire des variables d'axes lève l'indétermination.

La résolution par inversion de matrice donne des consignes d'axes correspondant à un point de plus en plus proche de l'extrémité du segment considéré. Une longueur de segment de 0,05 m convient généralement. Pour le dernier segment, l'itération est poursuivie jusqu'à ce que les consignes d'axes de la cible soient obtenues avec la précision convenable, alors que pour les segments précédents, une approche plus grossière est suffisante. Une itération en deux pas de calcul pour chaque segment suffit généralement pour obtenir la précision souhaitée.

5.4 - Stratégie de pilotage

L'opérateur de l'essai choisit et modifie à sa guise la stratégie de pilotage parmi les options du code de calcul :

- bloquer un axe particulier,
- appliquer une combinaison linéaire pour les axes 2, 4 et 6 avec un terme constant fixe ou recalculé en chaque point stabilisé de la trajectoire ou à l'origine de chaque segment intermédiaire,

• choix automatique, parmi les solutions trouvées, de la solution qui réalise une optimisation de forme ou qui minimise le temps de trajet.

Le programme propose à l'opérateur des options de pilotage lorsque l'un des axes atteint une butée ou lorsqu'il entre dans une zone singulière. Il est envisageable que le programme puisse calculer automatiquement une trajectoire de contournement de zone singulière pour atteindre la cible.

5.5 - Mode de fonctionnement (grilles ou trajectoires)

Ce dispositif est conçu pour permettre deux modes de fonctionnement, le mode "grille" et le mode trajectoire.

• Fonctionnement en mode grille

Cette méthode consiste à faire décrire à la charge une suite de positions ou d'attitudes prédéterminées.

La façon la plus simple est de fixer cinq paramètres parmi les trois coordonnées de position et les trois angles d'attitude de la charge. Une grille est alors obtenue par incrémentation du sixième paramètre à partir d'une valeur initiale fixée. D'autres types de grilles peuvent être réalisés, par modifications de plusieurs valeurs en même temps et également par variation continue des axes d'animation du dispositif mécanique.

Toutes ces grilles sont réalisées par paliers avec calcul et prise en compte à chaque point des déformations complètes du STC et de la ligne de dard support de l'avion. Ces grilles pourront être également réalisées en continu, l'acquisition étant faite sans arrêt du dispositif à chaque point de mesure.

• Fonctionnement en mode trajectoire

Le dispositif STC fait décrire à la maquette de la charge, une trajectoire homothétique de celle que suivrait la charge réelle dans le champ aérodynamique de l'avion en vol.

A partir des efforts appliqués à la charge dans une position donnée, le logiciel associé calcule, par résolution des équations de la mécanique du vol, la position que doit occuper la charge à l'instant suivant. Cette nouvelle position est transmise à la Commande Numérique. La charge est déplacée et une nouvelle pesée est effectuée.

La charge décrit ainsi, point par point, une "trajectoire captive". Actuellement, l'acquisition des mesures et les calculs sont faits alors que l'asservissement de position du STC reste constamment actif. Un fonctionnement en continu sans arrêt au point de mesure pendant les trajectoires est en projet et vise à réduire les temps d'essais.

6 - CALCUL DES TRAJECTOIRES

Le logiciel de calcul des trajectoires est fortement inspiré de celui utilisé avec le dispositif de trajectographie de la soufflerie S2MA. La figure 13 montre l'organigramme d'un pas de calcul.

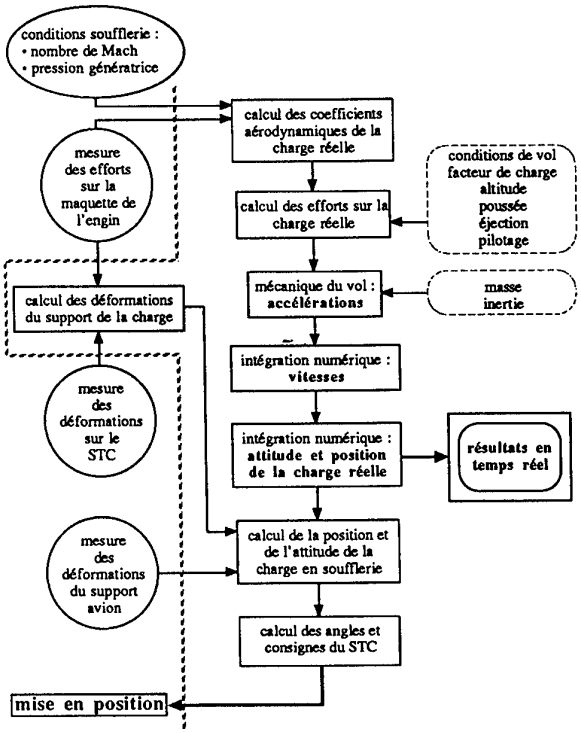

Fig. 13 - Organigramme d'un pas de calcul

En soufflerie, la représentation exacte des conditions initiales de séparation a une importance capitale pour la suite de la trajectoire. De même, la géométrie de la maquette de la charge doit être respectée précisément car les moindres défauts peuvent affecter de façon importante les trajectoires. Le logiciel permet de tenir compte des différents cas d'éjection. En plus des efforts aérodynamiques, la charge est également soumise à la poussée des éjecteurs et la poussée du propulseur. Pendant l'éjection, il faut également simuler les guidages ou les dispositifs locaux de retenue de la charge.

De même, le calcul tient compte des frottements sur les patins des éjecteurs, des glissements, de la rotation induite par les réactions transversales.

La réduction de masse de la charge liée à la combustion durant le fonctionnement de son propulseur et la variation correspondante de la position de son centre de gravité et de ses inerties sont simulés.

Bien entendu, la trajectoire de l'avion dû à son facteur de charge (ressource) intervient dans le mouvement relatif de la charge par rapport à l'avion.

Le STC permet de tester des charges de grandes tailles. La motorisation de certains éléments de la maquette est possible :

- braquage de gouvernes,
- déploiement d'ailettes ou de dérive,
- partie arrière tournante.

Ces variations de géométrie peuvent dépendre d'une loi simple, fonction d'une distance, d'un temps, où d'un calcul plus complexe prenant en compte l'intégration d'efforts ou la trajectoire elle-même. Dans le cas d'une charge pilotée, une version simplifiée de l'autopilote de la charge réelle est intégrée dans la boucle de calcul de la trajectoire.

7 - ESSAI PRÉLIMINAIRE : COMPORTEMENT VIBRATOIRE ET PERFORMANCES SOUFFLERIE

Dès la livraison du système complet sur le site, un essai préliminaire avec vent a permis de vérifier :

- le comportement vibratoire du montage,
- les performances de l'asservissement,
- le nombre de Mach possible avec le dispositif en veine.

7.1 - Comportement vibratoire

De nombreux accéléromètres ont été installés sur le dispositif mécanique et sur la maquette de la charge. Des acquisitions ont été réalisées pour plusieurs attitudes du STC, pour plusieurs nombres de Mach sans, puis avec l'avion porteur et dans les trois cas : STC en mouvement, STC asservi en position et STC non asservi.

Les résultats ont montré que les vibrations relevées sur le STC lui-même sont très faibles. Pour la maquette, les déplacements obtenus par intégration n'ont atteint que 2 mm dans les conditions extrêmes.

Dans la plupart des cas, pour le positionnement en emport, les vibrations observées visuellement ou à l'aide des capteurs optiques de proximité sont inférieures au millimètre (pour une charge de 800 mm de long et 80 mm de diamètre).

7.2 - Fonctionnement de l'asservissement

L'asservissement complet réglé en usine (gains, retards, ...) n'a nécessité que quelques retouches mineures faites sur le site avec le montage complet.

Pour chaque axe, l'asservissement assure, sans vent, une précision statique et une répétabilité de positionnement de ± 2 points codeurs absolus. Ce qui correspond pour la charge à une précision de ± 0,1 mm suivant l'axe de la charge, de ± 0,3 mm latéralement et verticalement, de 0,05° en roulis et de l'ordre de 0,01° en assiette et azimut.

Avec vent, les performances de l'asservissement sont très peu affectées par les efforts aérodynamiques et les vibrations. Les fluctuations des mesures par codeurs atteignent ± 3 points pour le mouvement de translation et les quatre mouvements de roulis et de ± 6 points pour les deux articulations d'incidence.

7.3 - Performances de la soufflerie

Veine vide, le nombre de Mach de 1 peut être atteint dans la soufflerie S1MA. L'objectif est de réaliser des essais de trajectographie jusqu'à Mach 0,93 avec ce nouveau dispositif. Au cours de l'essai préliminaire le nombre de Mach 0,92 a été atteint.

Le relevé de pressions sur les parois de la veine d'essai a permis d'améliorer la loi de section par la mise en place de remplissages. Un accordage en présence du STC a servi ensuite à déterminer les lois de corrections du nombre de Mach. Actuellement, les trajectographies peuvent être réalisées dans de bonnes conditions aérodynamiques jusqu'au nombre de Mach de 0,95.

8 - ESSAI DE QUALIFICATION DU STC

L'essai de qualification a consisté à réaliser un essai complet de trajectographie. Le type de charge a été choisi pour montrer que les résultats obtenus avec ce nouveau système sont comparables à ceux déjà réalisés sur le dispositif de trajectographie à six degrés de liberté de la soufflerie S2MA. Le constructeur possède également des résultats pour quelques cas de largages réels en vol.

Les maquettes de l'avion et de la charge sont à l'échelle 1/5,78 (pour 1/15 à S2MA). L'avion porteur est le Mirage 2000 de la société Dassault Aviation. La charge n'est pas décrite dans ce document pour des raisons de confidentialité.

8.1 - Préparation

Un emplacement spécifique a été aménagé dans le bâtiment de la soufflerie pour permettre une préparation complète dans des conditions très proches de l'essai avec vent et garantir la confidentialité.

Différentes trajectoires et grilles sont simulées et vérifiées par le calcul théorique puis par métrologie : moyen optique ou autres. Tous les tests demandés sont préparés et simulés sans vent pour détecter les contacts éventuels entre le STC et l'avion porteur et sa ligne de dard. Ces essais préalables permettent à l'opérateur de sélectionner les stratégies de pilotage les mieux adaptées aux circonstances (voir §5.4).

8.2 - Pesée en champ libre

Comme à S2MA, les essais de trajectographie débutent par quelques pesées de la charge en "champ libre" c'est-à-dire sans avion. Ces pesées ont pour objet de mesurer les effets de l'interaction du STC et de quantifier l'influence des imperfections de la maquette sur les coefficients aérodynamiques de la charge. Des termes correctifs sont déterminés d'après les références fournies par le constructeur. Ceux-ci sont fonction du nombre de Mach et de l'attitude de la charge en roulis par rapport à la partie amont du dispositif STC. Dans quelques cas plus rares, un terme supplémentaire fonction de l'incidence de la charge peut être introduit dans ces corrections.

Les termes correctifs retenus sont ajoutés aux coefficients déterminés à chaque point de pesées en grille et en trajectoire effectué en présence de l'avion porteur.

8.3 - Essais

De nombreux tests ont pu être réalisés aussi bien en mode trajectoires qu'en mode grilles. Les essais ont été effectués pour des nombres de Mach de 0,2 à 0,93. Le système a fonctionné comme prévu. En mode trajectoire, des tests ont été faits pour plusieurs vitesses conventionnelles, facteurs de charge et incidences avion. Certaines trajectoires représentent des séparations de détresse au décollage, d'autres des cas de pannes de pilotage de la charge (mise en butée intempestive de gouvernes).

9 - RÉSULTATS DE L'ESSAI DE QUALIFICATION

Le STC a naturellement été testé suivant les deux modes de fonctionnement décrits précédemment, c'est-à-dire le mode "grille" (ou boucle ouverte) et le mode "trajectoire" (ou boucle fermée). Nous nous limiterons ici à la présentation des résultats les plus significatifs obtenus en mode trajectoire.

9.1 - Fidélité des résultats

Deux trajectoires ont été réalisées deux fois, simulant les conditions de séparation suivantes :

M = 0,27	Vc = 180 kt	n = 0,5	α_{av} = 8,2°
M = 0,5	Vc = 250 kt	n = 1	α_{av} = 6,5°
M = 0,9	Vc = 560 kt	n = 1	α_{av} = 1,4°

avec :
M : nombre de Mach,
Vc : vitesse conventionnelle en noeuds,
n : facteur de charge de l'avion,
α_{av} : incidence de l'avion.

Les résultats sont présentés en annexe sur la figure 14.

Cette figure montre l'évolution des coordonnées X et Z du centre de gravité de la charge en fonction du temps, par rapport au point d'emport dans le trièdre avion ; les grandeurs sont ramenées à l'échelle avion (vol).

On constate que la fidélité est parfaite en X et très honorable en Z puisque la dispersion maximale, observée dans les conditions de pression dynamique faible, n'excède pas 15 cm au bout de 1,5 seconde.

La figure 14 montre également l'évolution des attitudes en tangage (THETA) et lacet (PSI) en fonction du temps de la charge par rapport au trièdre avion. Les écarts observés sont très inférieurs au degré : par exemple 0,3° en THETA à M = 0,5 au bout de 1,5 seconde.

La fidélité des mesures est donc excellente.

9.2 - Comparaisons avec les résultats obtenus à S2MA et en vol

Les courbes suivantes :

• trajectoire du centre de gravité de la charge dans le trièdre avion : X = f(Z)

• attitudes de la charge par rapport à l'avion en tangage et lacet : THETA et PSI = f(temps)

sont présentées pour quatre conditions de séparation :

M = 0,5	Vc = 250 kt	n = 1	α_{av} = 6,5° → figure 15
M = 0,9	Vc = 560 kt	n = 1	α_{av} = 1,4° → figure 16
M = 0,92	Vc = 590 kt	n = 0,5	α_{av} = 0,8° → figure 17
M = 0,92	Vc = 590 kt	n = 2	α_{av} = 2,4° → figure 18

Ces comparaisons montrent qu'entre S1MA et S2MA, les trajectoires du centre de gravité de la charge sont très voisines : identiques à M = 0,5, très proches à M = 0,9, légèrement plus dispersées, mais tout à fait acceptables à M = 0,92.

La comparaison avec les séparations réelles en vol indique des écarts dans le sens d'un recul de la charge plus important en vol qu'en soufflerie, liés à une incertitude sur la valeur de la traînée en soufflerie.

On remarquera néanmoins que, lorsqu'un écart existe entre S1MA et S2MA, S1MA est plus proche du vol.

Les évolutions des courbes de tangage présentent de bonnes similitudes entre S1MA et S2MA, les valeurs extrêmes sont du même ordre de grandeur : par exemple, à M = 0,92, n = 2 on note THETA mini = - 15,9° à S1MA et - 16,2° à S2MA, malgré des écarts ponctuels plus importants (figure 18).

Contrairement à ce que l'on a constaté sur les trajectoires du centre de gravité, les comparaisons avec les résultats de vol ne montrent pas, sur ce paramètre, d'écarts à caractère systématique : à M = 0,9, n = 1 (figure 16), le vol est plus proche de S2MA, par contre à M = 0,92, n = 0,5 ou 2 (figures 17 et 18), S1MA est plutôt meilleure que S2MA.

En ce qui concerne les attitudes en lacet, les évolutions se caractérisent par des oscillations dont les amplitudes sont légèrement supérieures à S1MA mais "en phase" entre les deux souffleries.

Les oscillations en vol sont pratiquement en phase avec celles observées en soufflerie avec par contre, des amplitudes un peu plus faibles.

En conclusion, on peut dire que, malgré quelques écarts locaux, les évolutions en attitude entre les résultats de S1MA, de S2MA et en vol, sont bien de la même "famille" et les comparaisons tout à fait satisfaisantes.

9.3 - Trajectoires de "détresse"

Ces séparations interviennent dans le cas où, dans la phase décollage, l'avion est victime de graves ennuis qui l'obligent à se délester au maximum pour assurer sa sécurité. Ces essais sont donc simulés à l'altitude Z = 0, faible Vc ; pour bien mettre en évidence l'effet de la Vc, nous avons simulé deux essais à Z = 0, n = 0,5, Vc = 140 et 180 kt à la même incidence avion de 8,2°.

La figure 19 montre que, si la trajectoire du centre de gravité est peu affectée par la différence de Vc, l'évolution des attitudes est sensiblement différente, montrant ainsi la nécessité de nombreuses simulations pour couvrir ce type de séparations.

Avant la mise en service du STC, ce type d'essai était réalisé dans d'autres installations, en utilisant la technique des "largages libres" conduisant à fabriquer de nombreuses maquettes de charge. Dorénavant, les séparations en détresse des charges stables pourront être étudiées au moyen du STC, ce qui représentera pour les constructeurs une amélioration sensible des coûts et des délais.

10 - CONCLUSION

Le nouveau Système de Trajectoire Captive mis en service dans la soufflerie S1MA de l'ONERA à Modane Avrieux permet la réalisation d'étude de séparation pour des maquettes à grande échelle jusqu'au nombre de Mach de 0,95.

Ce système est aujourd'hui opérationnel et les essais avec vent ont montré des résultats très proches de ceux obtenus avec le dispositif ONERA de la soufflerie S2MA et de ceux obtenus au cours d'essais de séparations en vol.

L'ONERA est aujourd'hui doté d'un des plus grands dispositifs en service dans le monde pour l'étude de trajectographies des charges actuelles dont le pilotage précoce est simulé en soufflerie par des maquettes équipées d'éléments motorisés.

Les représentants du constructeur Dassault-Aviation jugent que les résultats de l'essai de qualification du STC de S1MA sont très satisfaisants et autorisent les essais industriels. En effet, en plus de la qualité des résultats obtenus, compte tenu des difficultés liées à la mise en service de ce moyen d'essai hautement sophistiqué, l'essai de qualification s'est déroulé avec un minimum de problèmes.

11 - REMERCIEMENTS

Le projet de réalisation du STC a été mené par la direction des Grands Moyens d'Essais (GME) de l'ONERA. Le suivi du projet a été réalisé par M. REMANDET, la conception mécanique par M. PACAUD, la conception du système d'animation par M. TOBELI et les conceptions et réalisations des logiciels de la conduite d'essais par M. RAFFIN qui assure la responsabilité des essais avec vent. Diverses compétences du Centre de Modane-Avrieux ont été mises à contribution pour l'aboutissement de ce projet.

La société GIAT Industries a eu à sa charge la fabrication mécanique, l'étude du système d'animation, sa réalisation et sa mise au point.

ANNEXE

Liste des "figures résultats" concernant l'essai de qualification du STC de S1MA.

1 - Fidélité des résultats à M = 0,27 / 0,5 / 0,9 :

courbes X et Z = f(temps)
courbes THETA et PSI = f(temps) fig. 14

2 - Comparaisons avec les résultats obtenus à S2MA et en le vol :

Courbes : X = f(Z)
THETA et PSI = f(temps)

M = 0,5 Vc : 250 kt n = 1 α_{av} = 6,5° fig. 15
M = 0,9 Vc : 560 kt n = 1 α_{av} = 1,4° fig. 16
M = 0,92 Vc : 590 kt n = 0,5 α_{av} = 0,8° fig. 17
M = 0,92 Vc : 590 kt n = 2 α_{av} = 2,4° fig. 18

3 - Séparations en "détresse" :

courbes : X = f(Z)
THETA et PSI = f(temps)

n = 0,5 - α_{av} = 8,2°
M = 0,2 (140 ft)
M = 0,27 (180 ft) fig. 19

ONERA

DASSAULT AVIATION

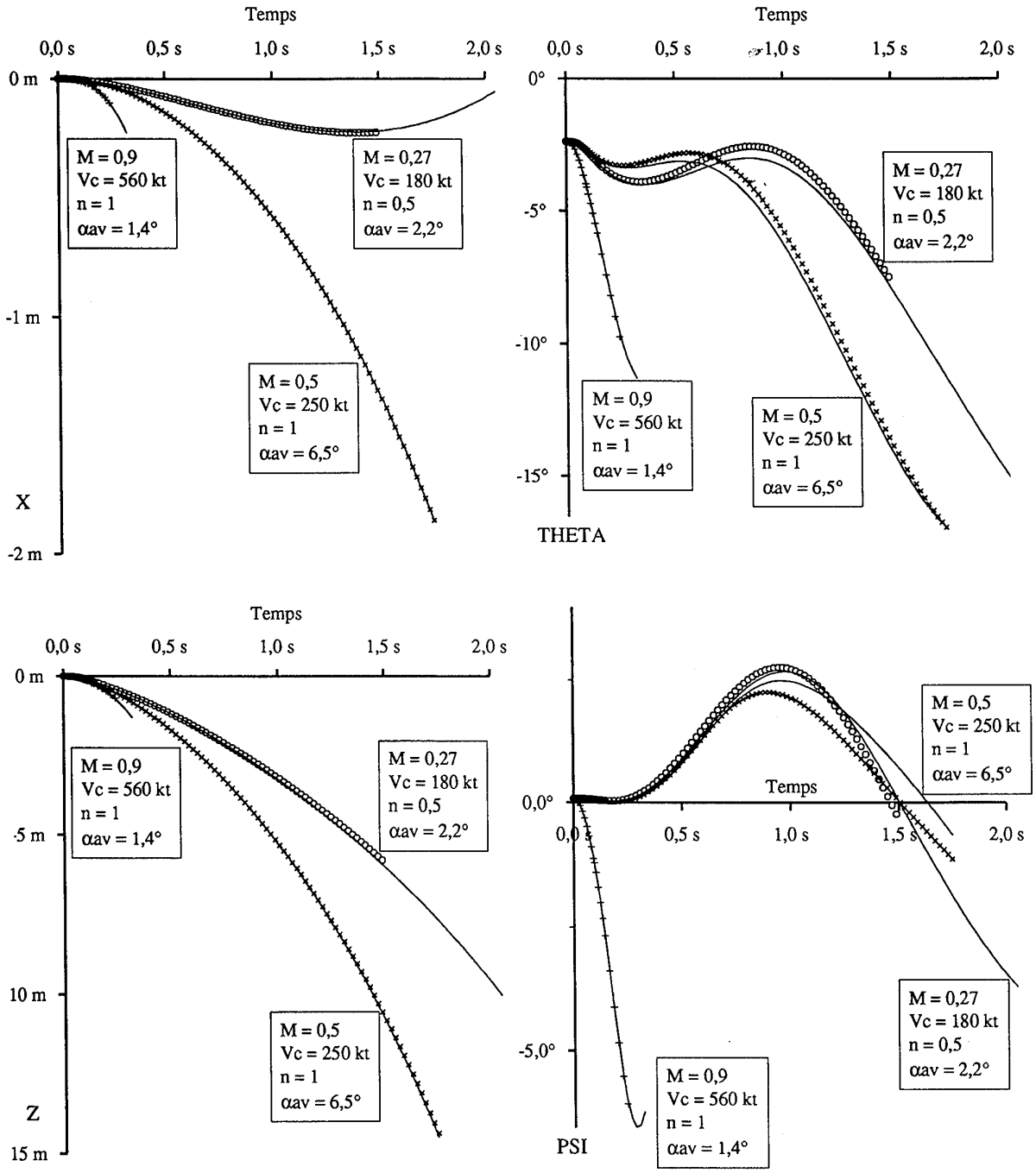

Fig. 14 - Fidélité des résultats

ONERA

DASSAULT AVIATION

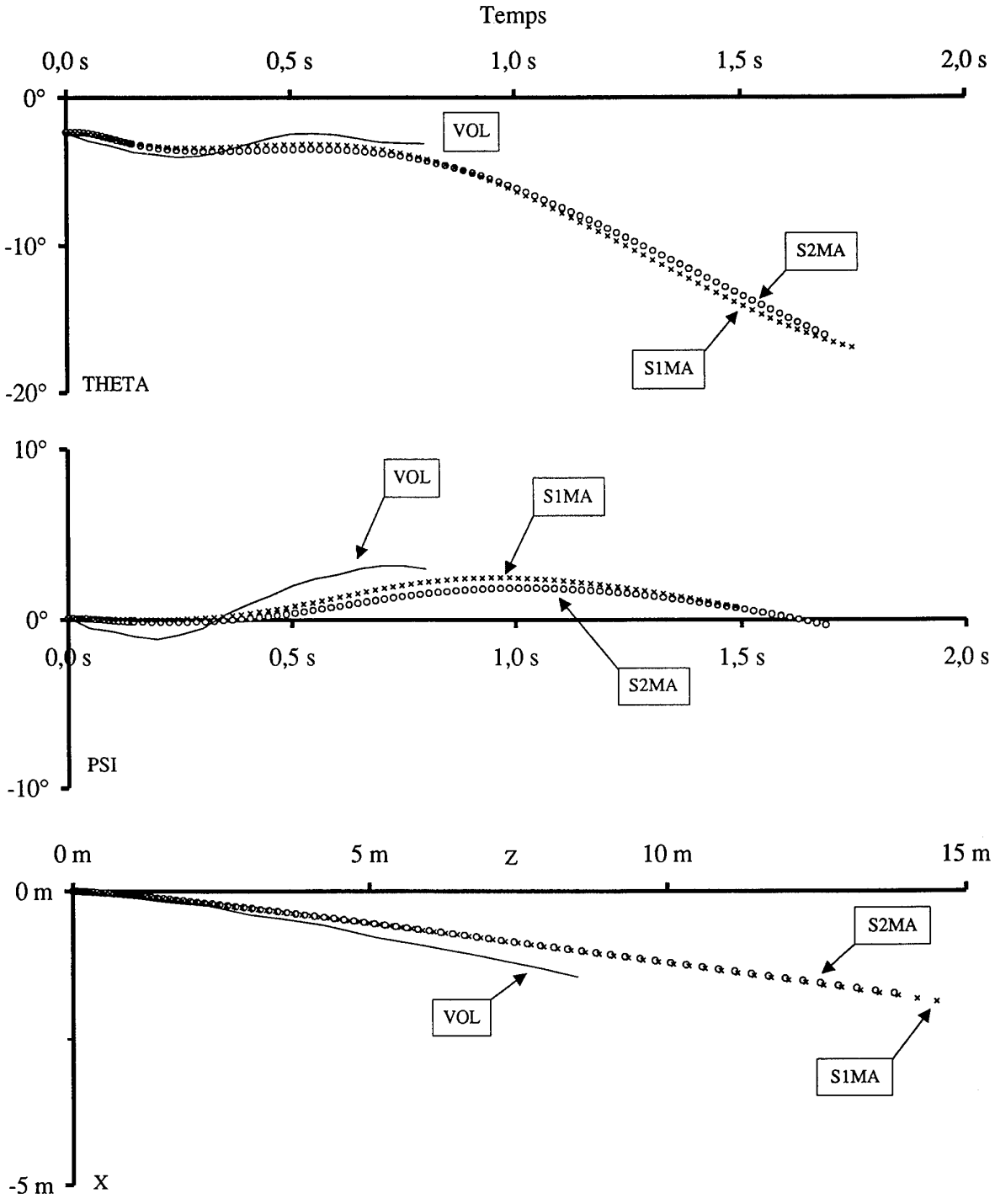

Fig. 15 - Comparaison entre S1MA, S2MA et le vol : M = 0,5 Vc = 250 kt n = 1 αav = 6,5°

ONERA

DASSAULT AVIATION

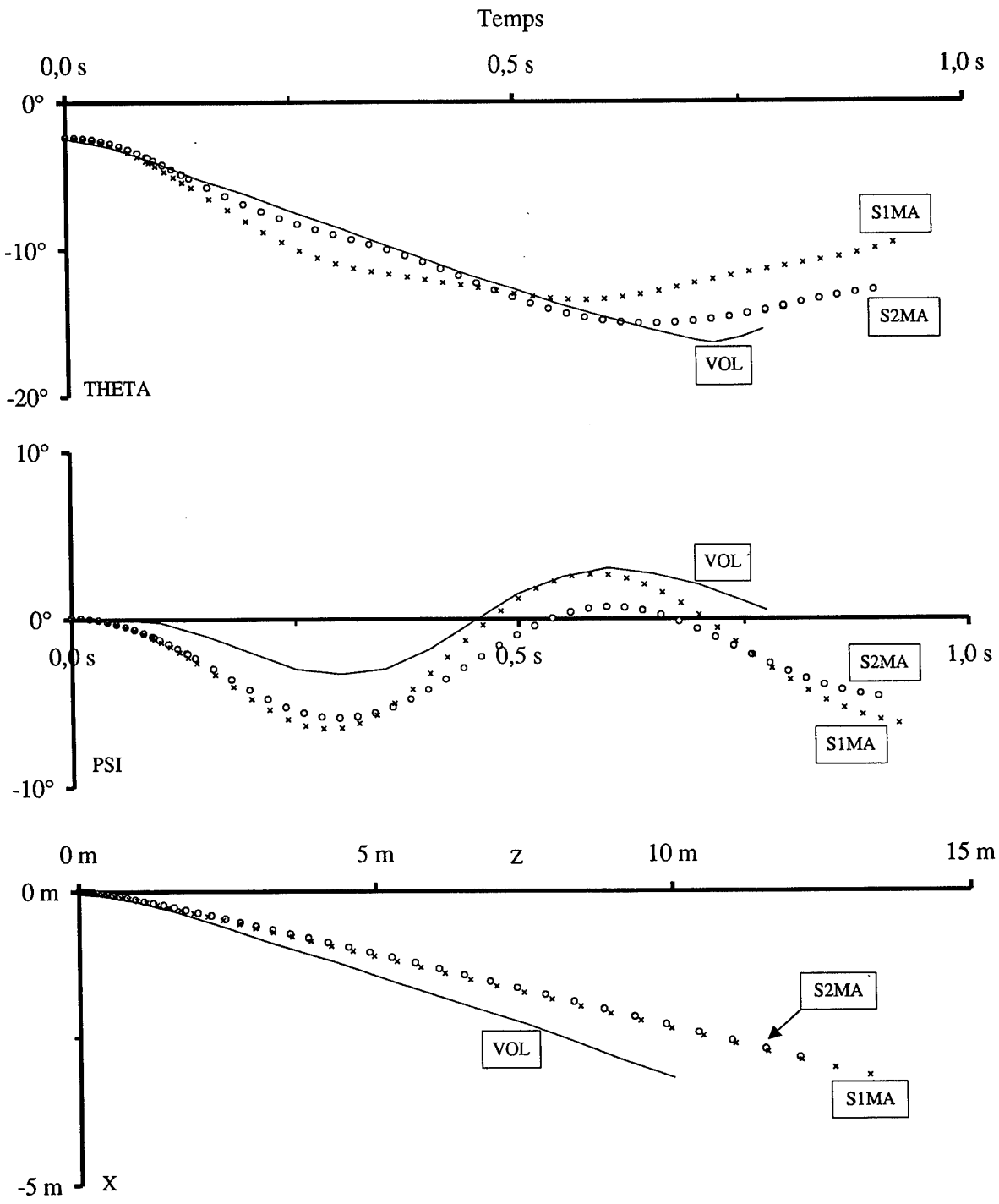

Fig. 16 - Comparaison entre S1MA, S2MA et le vol : M = 0,9 Vc = 560 kt n = 1 αav = 1,4°

ONERA DASSAULT AVIATION

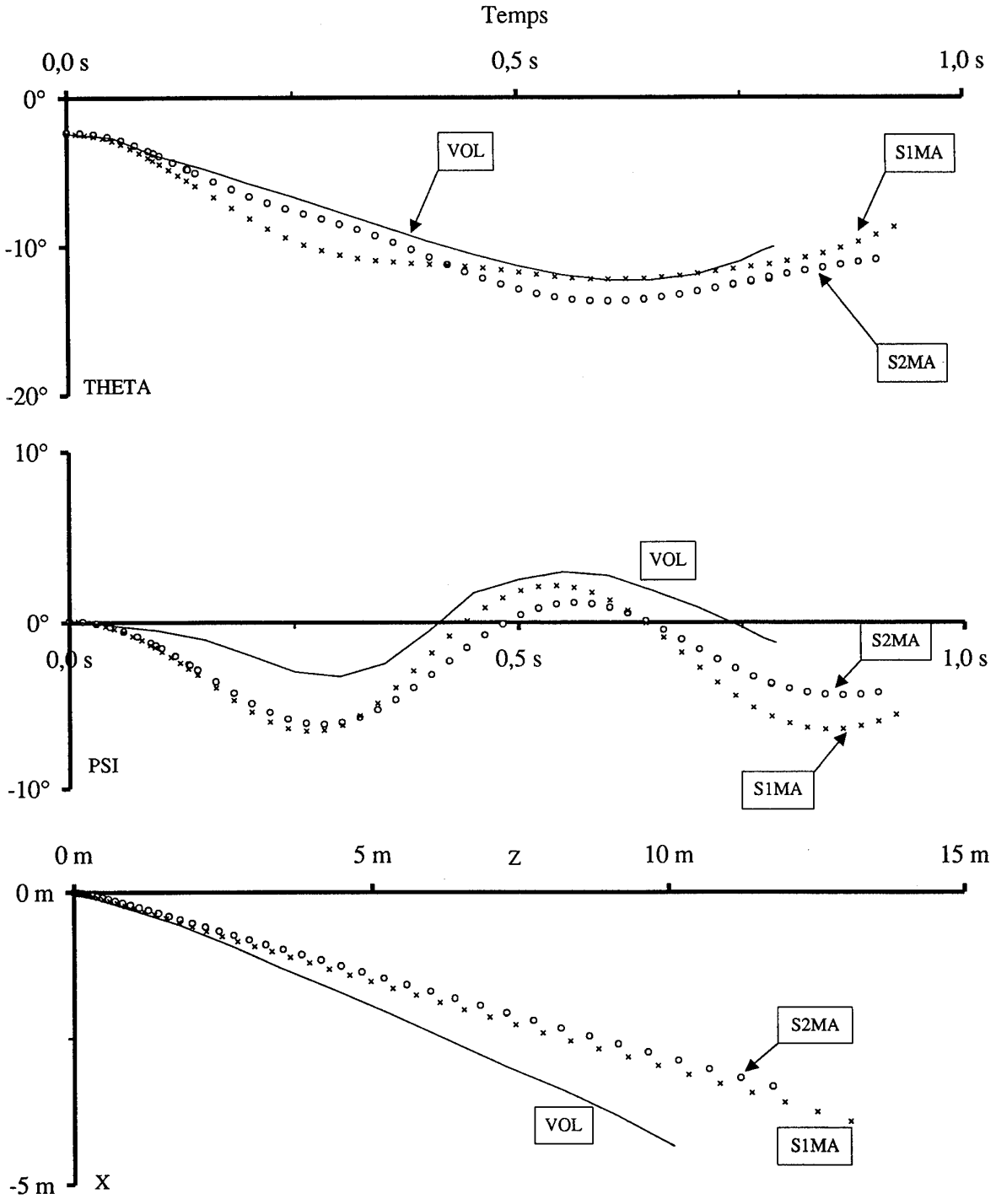

Fig. 17 - Comparaison entre S1MA, S2MA et le vol : M = 0,92 Vc = 590 kt n = 0,5 αav = 0,8°

ONERA

DASSAULT AVIATION

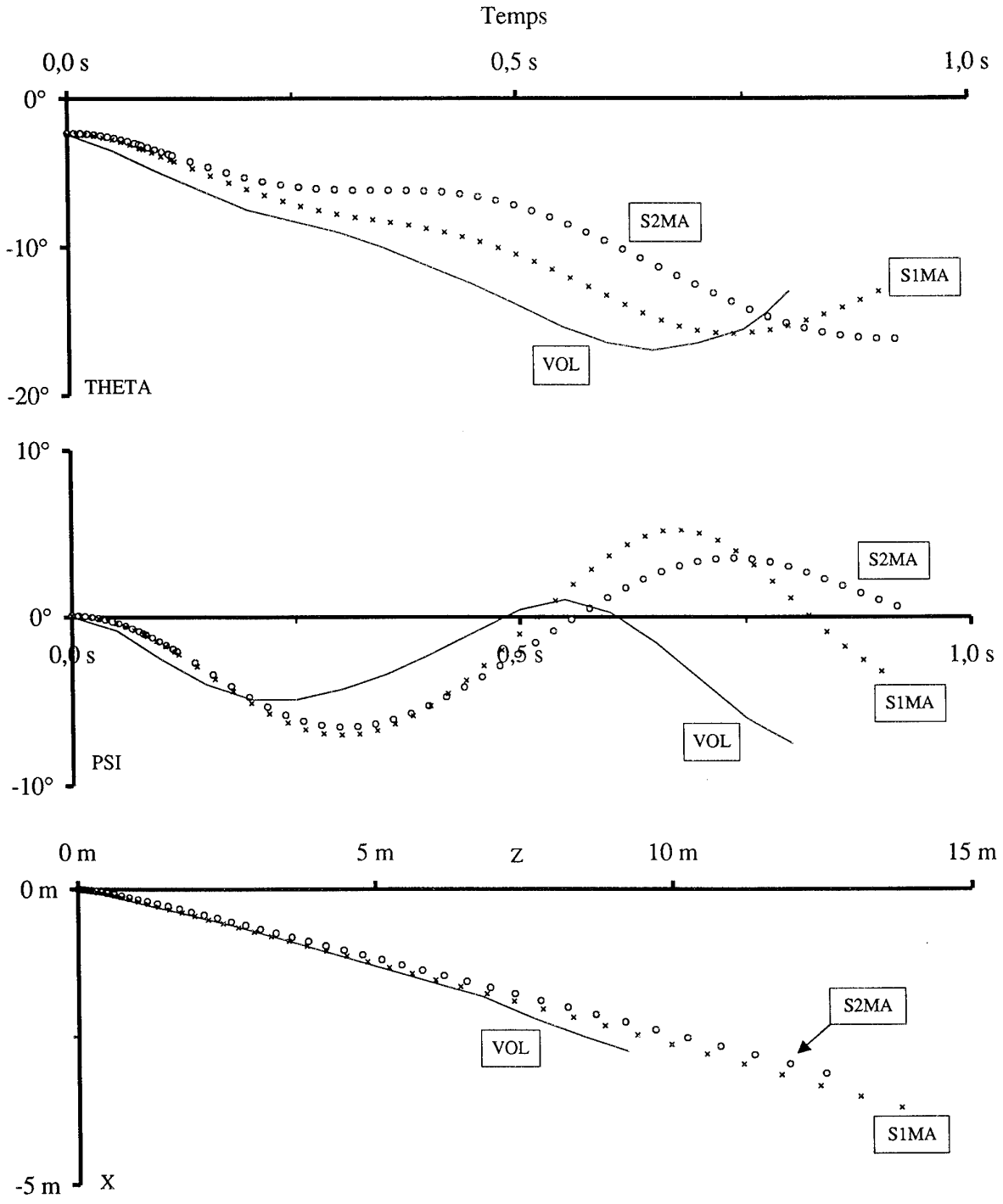

Fig. 18 - Comparaison entre S1MA, S2MA et le vol : M = 0,92 Vc = 590 kt n = 2 αav = 2,4°

ONERA

DASSAULT
AVIATION

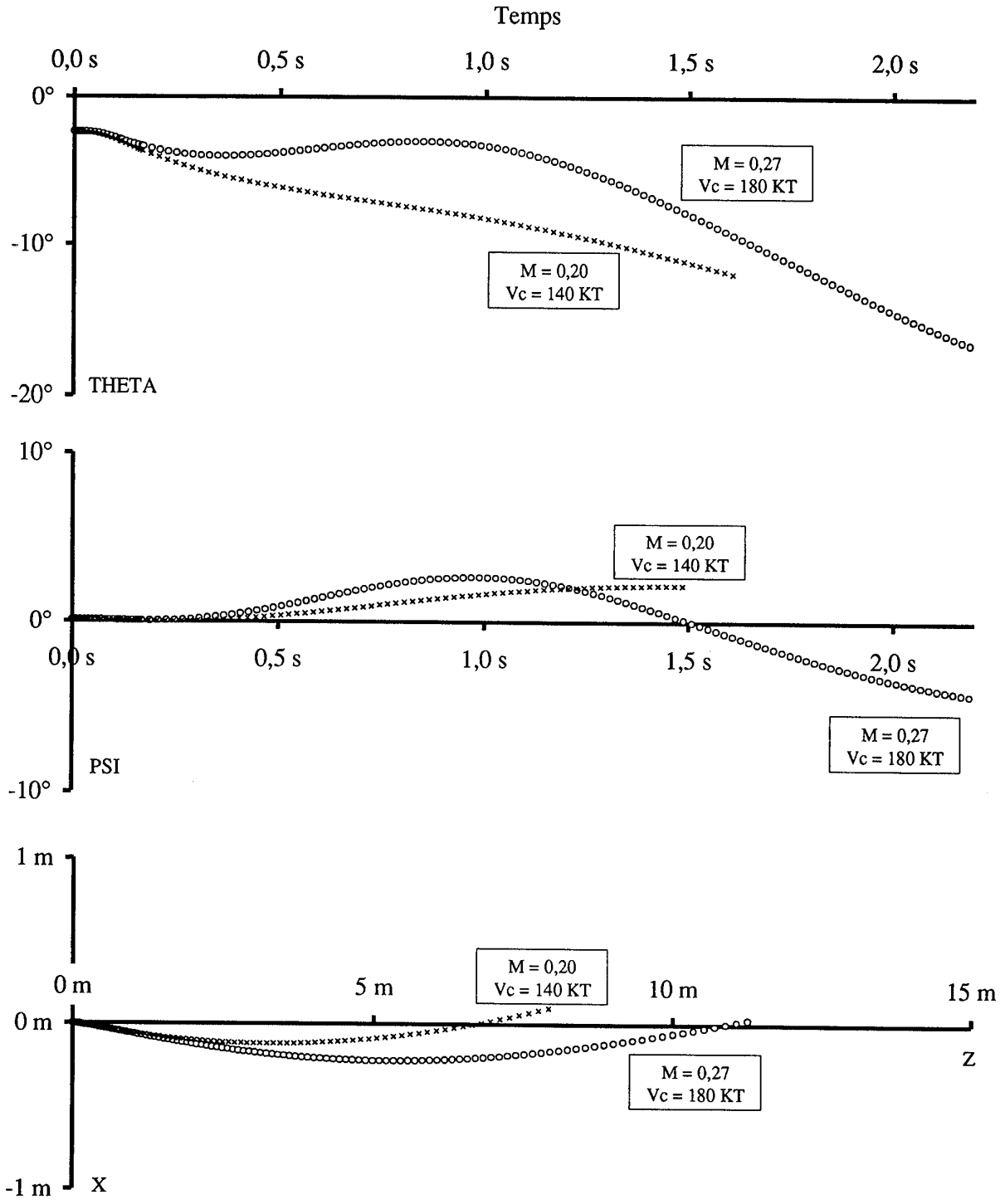

Fig. 19 - Trajectoire de détresse, influence de la vitesse conventionnelle : $n = 0,5$ $\alpha_{av} = 8,2°$

EXPERIMENTAL TECHNIQUES FOR MODELLING STORE CARRIAGE AND RELEASE AT SMALL SCALES

by
V.H.A. Bettridge
Gp.Ldr. Methods Devt., Aerodynamics Technology Dept.
Military Aircraft Division, British Aerospace PLC
N. Humberside HU15 1EQ
United Kingdom

SUMMARY

This paper will discuss wind-tunnel testing aspects of store trajectory modelling and store carriage load evaluation, at small scale, in the British Aerospace, Military Aircraft Division,(M.A.D.) wind-tunnel facilities.

There is discussion of the enhancements, developed within the department, of the 'light model' scaling technique for free store wind-tunnel releases, and of the recent re-appraisal of strain gauge balance design philosophy and the use of newer concepts in strain measurement in small, stiff, balance structures, which is building on our expertise in this field.

INTRODUCTION

Two of the most technically demanding aspects of wind-tunnel testing lie in the precise determination of installed store loads, and in the accurate dynamic simulation of store trajectories in the release phase. The common objective in further improving the data available from these ground-based techniques being to provide the aerodynamicist with the best possible means to evaluate airframe loads and store clearance margins, over a range of aerodynamic conditions and carriage configurations, and with sufficient confidence that full-scale flight trials can be reduced to a minimum.

In order to provide the required improvements in accuracy, a programme of work has been established within M.A.D. wind-tunnel facilities to improve the process of balance design and calibration, and investigate the use of semi-conductor strain gauges in the necessarily small-scale models appropriate to the Division's 1.2m. High Speed Wind Tunnel. Work has also been carried out in developing the capabilities of the free-store trajectory visualisation technique which utilises so-called 'Light Model' scaling, at very small scales.

STRAIN GAUGE BALANCE DEVELOPMENT - A NEW APPROACH

IMPROVEMENTS TO THE DESIGN PROCESS

Wind-tunnel strain gauge balances have hitherto been designed using the Engineer's Theory of Bending to determine the sizing and distribution of flexures in the balance structure to satisfy simultaneously the conflicting requirements for sufficient strain gauge output, appropriate sharing of stress between the balance components, overall stiffness to avoid model fouling, etc. This process is iterative and very time-consuming, and in order to reduce the time taken for design whilst ensuring a 'best-compromise' structure, a programme of work has been initiated to investigate the benefits of Finite Element Modelling. Here the structure is built up from a large number of elements, where each element is analysed for its role in the overall design, and the structural solution for the whole assembly of elements is derived from computation. The method will determine stress paths in the structure, and also thermal paths where a temperature gradient exists - this will have enormous potential when considering balances for use at cryogenic temperatures - as well as providing a theoretical 'calibration' for the balance under a range of loads which will reduce the empirical calibration time by around 50%.

SEMI-CONDUCTOR STRAIN GAUGES

It is well known that semi-conductor strain gauges offer much higher output per unit stress than conventional foil gauges, thus creating the possibility of stiffer balance structures at smaller scales, for equivalent output, with attendant reduction in deflection and lower risk of model fouling. The designer is thus free to choose from a much wider range of output/stiffness options than would be the case with conventional gauges. However, past use of semi-conductor gauges has been restricted to applications where temperature change effects have been of secondary importance compared with the requirement for high output

Paper presented at the AGARD FDP Symposium on "Aerodynamics of Store Integration and Separation", held in Ankara, Turkey from 24-27 April 1995, and published in CP-570.

– e.g. flutter and vibration, because the semi–conductor devices have defeated all attempts to achieve satisfactory and reliable temperature compensation over the normal range of wind–tunnel operating conditions.

SEMI–CONDUCTOR DEVICES TODAY

Recent advances in semi–conductor technology for devices such as pressure transducers have led to crystals having far tighter limits in their unstrained temperature response,and hence it was felt that the incorporation of discrete semi–conductor strain gauges into balance structures was a topic that should be revisited.

The principle employed by these devices is the piezoresistance effect, which is defined as the change in electrical resistivity with applied stress. All materials exhibit this to some degree, but in certain semi–conductors the effect is very large. The characteristics of the semi–conductor material can be greatly modified by the quantity and type of electrically active impurities present in the crystal structure, which are deliberately added during crystal growth – a process known as 'doping'. The gauges are then allocated a code letter to denote the doping level, and hence their range of defined characteristics.

In choosing gauges for our application, consideration was given to ways of minimising the electrical compensation which must be provided in all practical strain–gauge circuits, by means of the addition of discrete resistors,to cancel apparent strain arising purely from changes in temperature. Semi–conductor gauges exhibit an apparent change in strain, because the crystal gauge factor changes with temperature. We found that by selecting gauges where the factor changes with temperature at the same rate as the elastic modulus for steel changes, their output remained proportional to stress regardless of the temperature, thus eliminating the need for gauge factor compensation.

Since members of the team were used to handling conventional strain–gauges and had access to the usual range of equipment, we decided to begin the investigation by using the 'encapsulated' type of gauge, where the crystal is supplied sandwiched between thin layers of epoxy–impregnated glass cloth. This gives far greater ruggedness than the alternative 'bare'crystal gauge until expertise has been built up.

A SINGLE COMPONENT "BALANCE"

An experiment was set up to investigate the behaviour of semi–conductor gauges in a Wheatstone bridge circuit. The bridge, which can be made up using from 1 to 4 strain gauges, is the most popular circuit for use with all types of strain gauges, owing to the fact that it converts the strain–induced resistance change of the gauge to a change in voltage, which can be measured more directly with conventional instruments.

A single component test beam was instrumented as shown in figure 1. Tag strips were sited close to each gauge position to facilitate resistor insertion, in appropriate arms of the bridge.These resistors are required to compensate for the inevitable change in null output with temperature for any real circuit of this type, arising from the inability to perfectly match gauges, or the manner in which they are mounted.

The test piece was ground, the central area vapour blasted, and the gauge positions chemically cleaned before the application of the gauges, since the smallest foreign body becoming trapped between the gauge and the substrate would have a strongly adverse effect on the gauge behaviour.

Excitation was set at 5.000 volts since consideration of the bridge current at this level indicated a figure of 50 milliwatts power dissipation per gauge – the manufacturer's upper limit for acceptable zero–strain stability. The specimen was placed in a temperature–programme controlled oven which was capable of cycling the temperature over a specified range for any period. It has been established practice with any new gauge installation to allow the cycle to operate two or three times before measurements are made to allow the system to stabilise. It was found that several more cycles of temperature were required for the semi–conductor bridge to settle, at the chosen power level.

The values and placing of the compensation resistors, described above, for semi–conductor strain–gauge bridge circuits, are determined from standard "case" tables depending on whether the sign of the unstrained output is positive or negative , and whether the change in output with temperature is positive or negative going. Knowledge of the bridge resistance, and of the current in the bridge, is required at the temperature extremes. Compensation for the circuit will require the addition of a series resistor to one of the arms, a shunt resistor across one of the gauges, or both. It was found that only very high quality, high stability resistors were suitable for use.

After some further trimming of the resistor values, the test piece was calibrated with a series of dead weight loadings whilst still in the oven. Loading programmes were carried out at three selected temperatures.

Considering the data led to three interesting conclusions:–

1. The system linearity was commensurate with the

published figures for the 'L' type crystals chosen

2. The conventional strain gauge output equation was verified for this type of gauge

3. The use of 'L' type gauges on steel did indeed eliminate the need for gauge factor compensation.

This work indicated that we now have a potential capability hitherto not available to us, and which could be exploited to our advantage, in the consideration of very small, reliable balances.

LOOKING TO THE FUTURE

The anticipated benefits of the Finite Element approach to balance design will include a better optimised structural solution owing to the large number of iterations that can be performed in a computational method, and a much faster convergence to that solution which will reduce the design phase for the balance, currently some 6 weeks, to perhaps 2 weeks. The method will also lend itself to the production of a theoretical 'calibration' of the final design, which, whilst not replacing the conventional method, will reduce the number of loadings required, and hence the time required for calibration, from some six weeks for a six component balance, to perhaps around three weeks.

The successful outcome of the semi-conductor work has led on to the use of this type of strain gauge for a full ix-component overall forces balance, which we believe is a world first ,and their incorporation in very small balance structures to provide component measurement where the use of conventional gauges would have resulted in insufficient output – for example, axial force measurement on a small stiff cantilever. The most recent six-component design is shown in figure 2, and here only the axial force system is gauged with semi-conductors – the balance is of the order of 10mm. diameter.

Further work is about to begin on providing balances for Sidewinder missiles at 1:21 scale; this leads to a balance of approximately 5mm. diameter, and in turn to thoughts of materials, for example Tungsten, having much greater inherent stiffness than the usual maraging steels, because at this size, the problem changes from one of ultimate material strength to one of balance deflections giving rise to model fouling.

THE LIGHT MODEL SCALING TECHNIQUE

The best way of simulating the release of stores from combat aircraft in the wind tunnel is a problem that has exercised the minds of aerodynamicists and wind tunnel engineers for decades. The Aerodynamic Technology department at British Aerospace M.A.D. has used the so-called 'Light Model' scaling technique. Here the model store is made to full scale density, which greatly simplifies model manufacture, but owing to the absence of a scaled gravitational field, and in the presence of correctly scaled aerodynamic forces, the vertical separation characteristic between store and parent aircraft will be pessimistic. To overcome this effect, the relative acceleration between the aircraft model and the store must be correctly scaled, whereas, in unmodified 'light model' scaling, and for a typically 1:30 scale model, as used in the relatively confined space of the Division's facilities, there would be a 29g deficiency in this parameter.

THE ACCELERATED MODEL RIG

The solution to this problem of the vertical separation error lay in the development and utilisation of an actuation system, capable of accelerating the parent aircraft model upwards at the instant of store separation, with pre-calibrated magnitude governed by the scale being used. The device developed at British Aerospace was known as the Accelerated Model Rig (A.M.R.) which was designed specifically for the use of typically 1:30 scale models, and was therefore required to accelerate an approximately 3Kg. model upwards at 29g. for a period of 0.020 seconds (equivalent to 0.6 seconds at full scale), being sufficient time to investigate the effects of store/aircraft flowfield interaction. Figure 3 shows the rig mounted on the roof of the now closed BAe. 0.68m.x 0.68m. High Speed Wind Tunnel, and figure 4 is an in-tunnel view of a Hawk model attached to the rig's accelerating strut. Although now out of commission, this rig provided much development of expertise in the techniques associated with accurate small-scale modelling, some description of which is worthy of inclusion here.

The accelerated model technique compensates for the displacement deficiency of the store relative to the aircraft, but there is still a small residual induced incidence deficiency arising from the store having an incorrect vertical component of velocity. This can be itself reduced to insignificance by the use of a tiny offset in the miniature ejector release unit line of action, to correct the initial store pitch rate.

E.R.U's

Ejector Release Units as fitted to British military aircraft generally comprise two rams, which are made to bear down on the top surface of the store to be released by the action of a gas generation cartridge exploding and feeding gas to the ram cylinders, via settable throttles. Differential sizing of the throttles will result in an initial pitch characteristic being imparted to the store during the ram stroke. The unit also incorporates positive hook latching of the store to the pylon, which is automatically released by the action of the rams.

The model ejector release units have been developed to fully simulate the action of 'in-service ' devices (e.g.ERU119, ERU120, MACE etc.), including ram force, stroke length and pitch offset. Two main designs have been used over the past few years, which both rely on pneumatic tubing feeding high pressure air to the gun , the mechanism being held 'safe' by a small stainless steel bolt, ground locally to form an electrical fuse. When conditions for release have been achieved in the wind-tunnel, the 'burn-bolt' is electrically fused by the discharge of a pair of large capacitors, allowing the applied compressed air to operate the ram.

The original design used the compressed air to force a miniature piston down a cylinder, the free end of the piston bearing onto a flat faced stud counterbored into the store body. Pitch correction could be achieved by previously calculated position in relation to the store centre of gravity, and moving the ram assembly, within its own housing in the pylon, to match the stud position. The burn-bolt was connected directly between store and pylon, and formed the primary means of reacting the aerodynamic loads until release.

Modifications and improvements to this design have realised a miniature gun, shown in figure 5, having an actuating 'foot', which is made to bear on a very small reaction pin in the store body, positioned in the same way as the larger stud. The alteration of the required pitch characteristic is now much more easily achieved by simply moving the reaction pin on the store (assuming the required movement is within the confines of the length of the ejector foot). Another benefit of this design is the simultaneous unlatching of a pair of small catches, during store ejection, via direct contact with the ejecting foot, which were previously engaged in mating cut-outs in the store body top. The catches provide positive latching of the store to the pylon and counteract the aerodynamic loads until the point of release. This allows the burn bolt to be housed within the foot actuation mechanism, where any small variation in the fusing characteristic will have no effect on the store trajectory.

The ejection units are calibrated before each trials series according to 'pit-drop' gun performance figures supplied by the relevant E.R.U. manufacturer, which have been adjusted for predicted aerodynamic loading. These figures are used to derive the required pneumatic pressures and gun line of action offset to reproduce the end-of-stroke velocity and pitch rate conditions sought. Figure 6 shows how the airborne E.R.U. mathematical model is translated into the wind-tunnel E.R.U. simulation.

INITIATION PULSE

During wind tunnel trials, the pulse to initiate the firing sequence was derived from the control system driving a set of high-speed cine' cameras. When correct wind-tunnel conditions had been achieved, the cameras were started, and on reaching a pre-determined framing rate (usually 2000 frames per second), the release occurred, thus capturing the whole trajectory on film, for later analysis.

STOREMODELS

The model stores themselves were usually moulded from a variety of plastics to fine dimensional tolerance, and carefully prepared to ensure their principal mass characteristics were correctly scaled using internal ballast. Figure 7 shows a fuel tank made from expanded polyurethane foam, and a BL755 cluster weapon moulded in polystyrene. Lifting surfaces were also usually moulded from polystyrene and correctly scaled wherever possible, but the slenderness of some full-scale designs occasionally dictated slight over-thickness to provide sufficient strength.

Some variations in store manufacture were developed along the way, including the use of carbon fibre laminate to strengthen weak plastic areas; stores were sometimes made with densities greater than the full scale value in order to simulate release at high altitude; and common salt was used inside otherwise empty fuel tank models in an effort to simulate the effects of residual fuel sloshing around.

FLIP-OUT CONTROL SURFACES

The early aerodynamic capture of released stores is crucial to the subsequent lift characteristics, and many stores now incorporate 'flip-out' surfaces which operate early in the release phase, whilst the store is in close proximity to the aircraft.

This sequence of events was seen as the next logical development in the wind-tunnel free-store release simulation technique, and a major success for the team has been the provision of 1:30 scale models of the general proportions of the cruise-missile, equipped with flip-out

wings, which were deployed after a representative delay in the release sequence. Figure 8 shows the weapon installed on the port shoulder pylon of a 1:30 scale model Tornado, and figure 9 shows the store 'before and after' wing deployment.

The delayed wing deployment was achieved using a miniature in–store explosive protractor device to actuate the wing deployment mechanism. It was found necessary to provide a dual electronic circuit inside the store body to cater for the detonation pulse, and for the time delay from release for its initiation. The firing circuit was electrically charged via contacts between the store body and pylon, and on the instant of release, the timing circuit began its task of acting as a delay switch before redirecting the firing circuit charge to the protractor. Closely repeatable releases were performed, and the delay could be adjusted, by selection of the timing circuit resistor value, to simulate a range of full–scale deployments.

CONCLUSIONS

The improvements sought in the balance design process will lead to a marked reduction in the design cycle time for strain–gauged balances, and the successful outcome of the programme to evaluate the use of semi–conductor strain gauges has led on to the production of a number of balances incorporating these devices. Semi–conductor devices offer significant advantages over conventional foil gauges for applications where physical size limitations, coupled with the conflicting requirements of fairly stiff structures and reasonable signal output, must be reconciled. We have shown that it is possible to fully temperature compensate bridge circuits composed of semi–conductor gauges, and would encourage other potential users to conduct their own appraisal of these devices.

The wind–tunnel stores separation technique has proved to be extremely useful in looking at the release envelope for a number of store/aircraft/aerodynamic configuration combinations, especially where the release characteristics have been found to be marginal in terms of risk to the airframe. The results of this work have demonstrated that accurate results are entirely possible at very small scales given that flight trial comparisons were invariably favourable, and the technique became a tool against which other methods could be calibrated in the effort to reduce stores clearance costs.

Whilst Computational Fluid Dynamics is gradually taking over from wind–tunnel testing in the prediction of store release characteristics, there are some special areas, notably in 'flip–out' wing and fin modelling, and multiple stores release, where C.F.D. has quite a lot of ground to cover before the methods are fully developed.

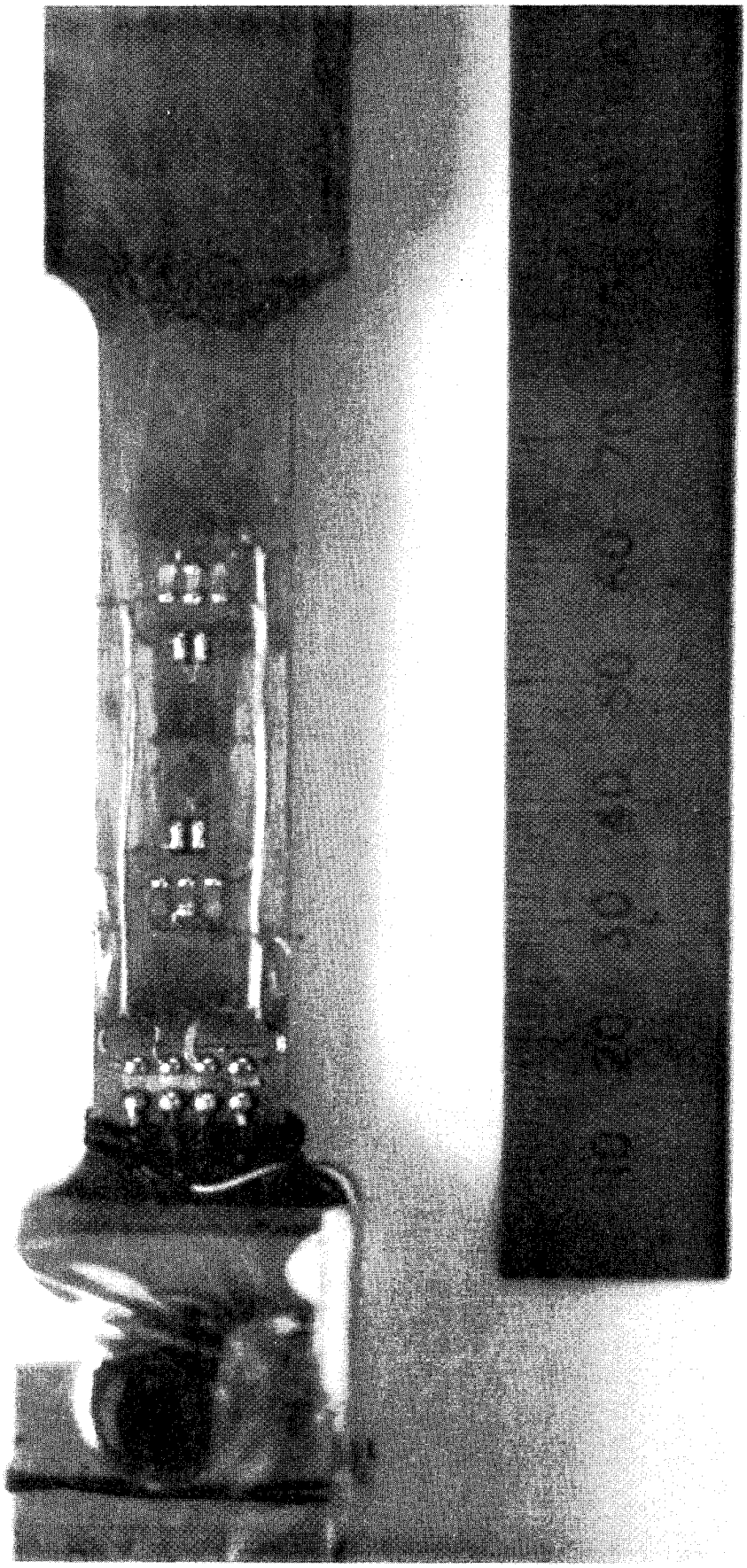

Figure 1 - Single Component Test Beam

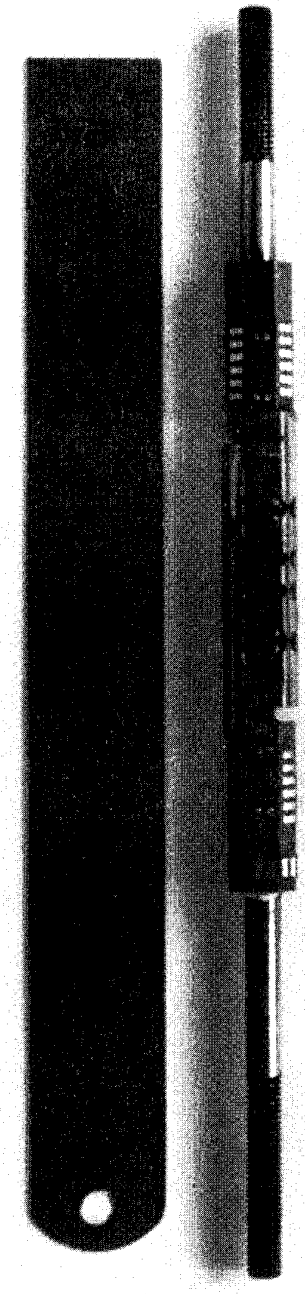

Figure 2 - 10mm Diameter 6-Component Balance

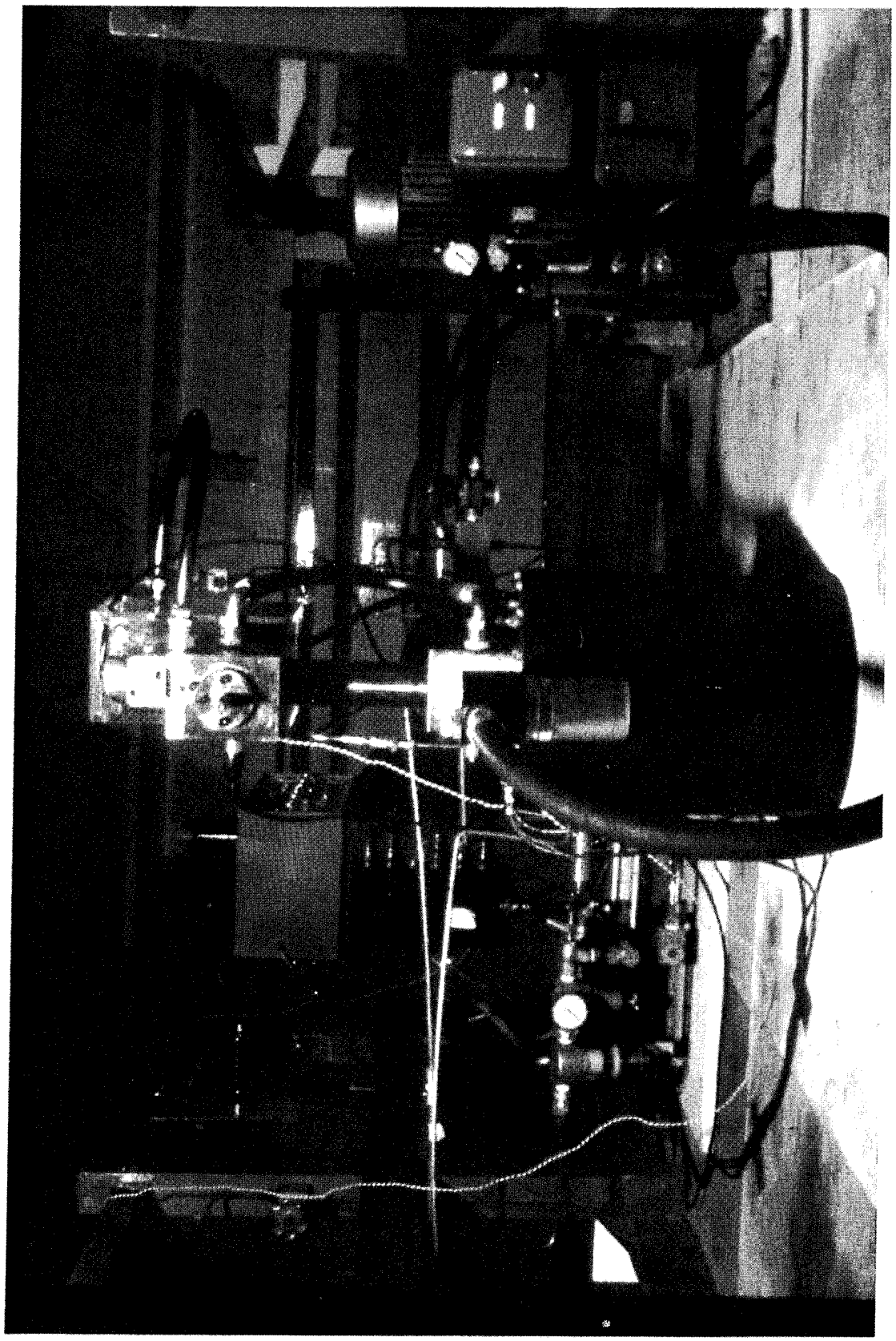

Figure 3 - The Accelerated Model Rig

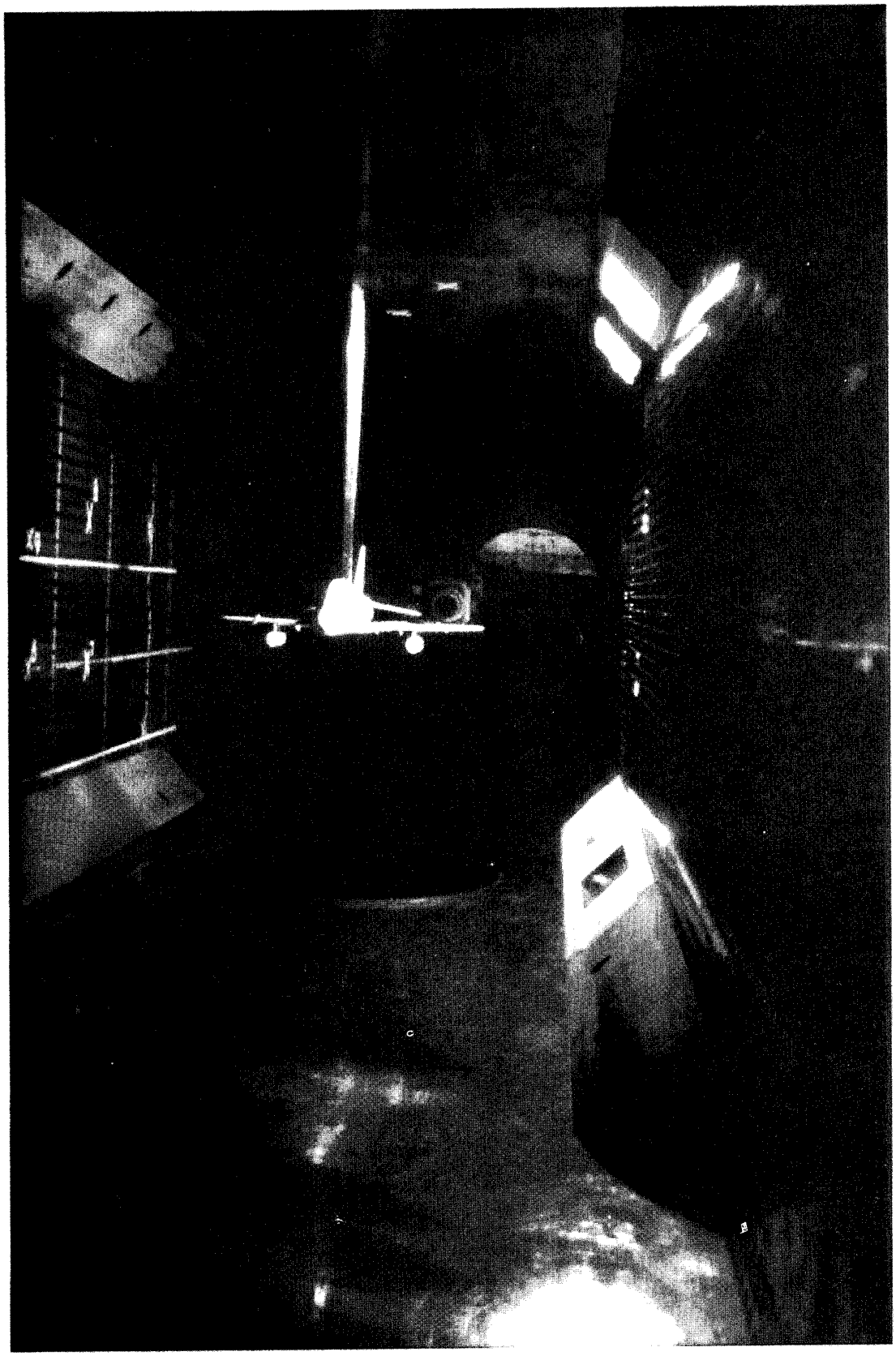

Figure 4 - Hawk Model on A.M.R. Strut

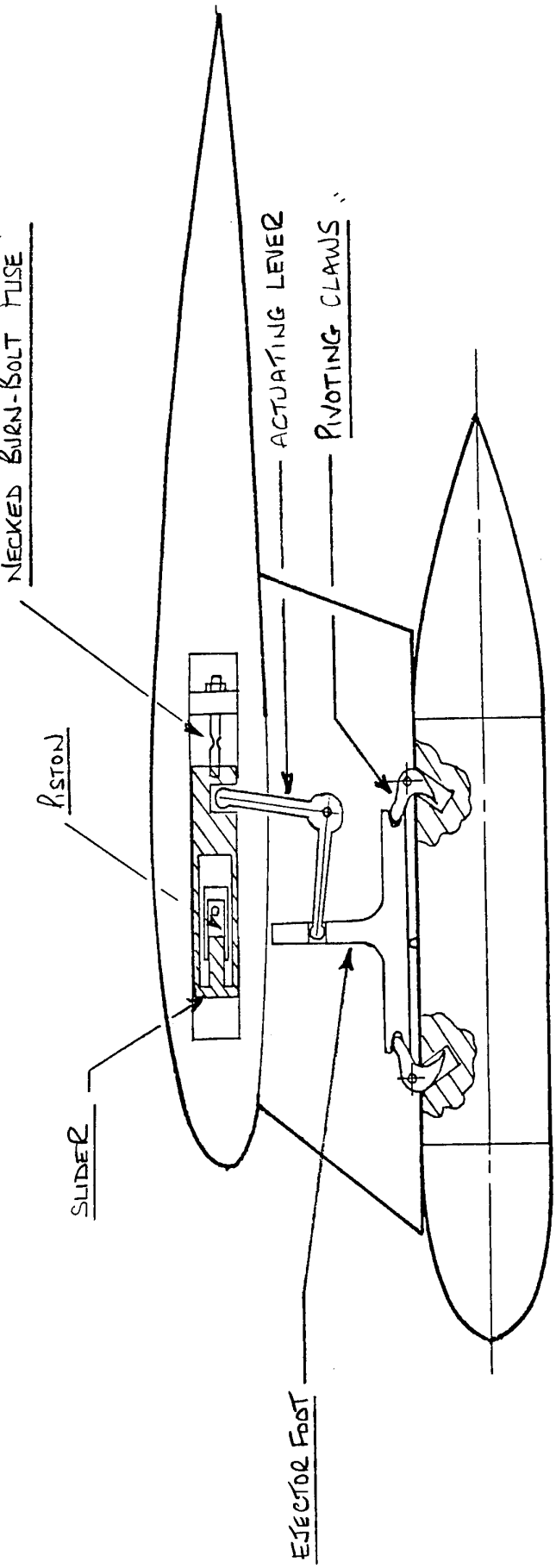

Figure 5 - Active Claw Model E.R.U.

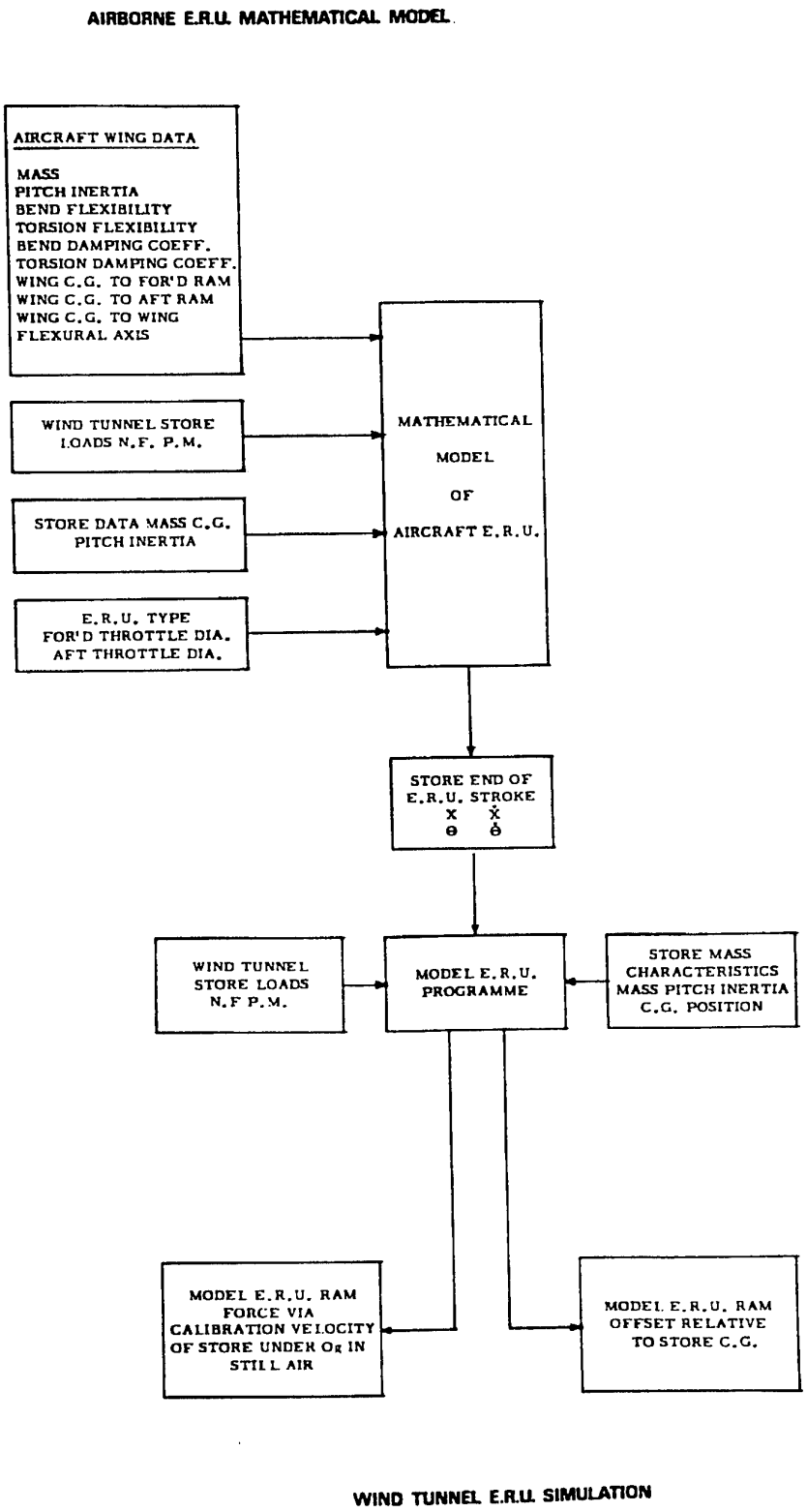

Figure 6 - Airborne E.R.U. Model to Wind-Tunnel Model Simulation

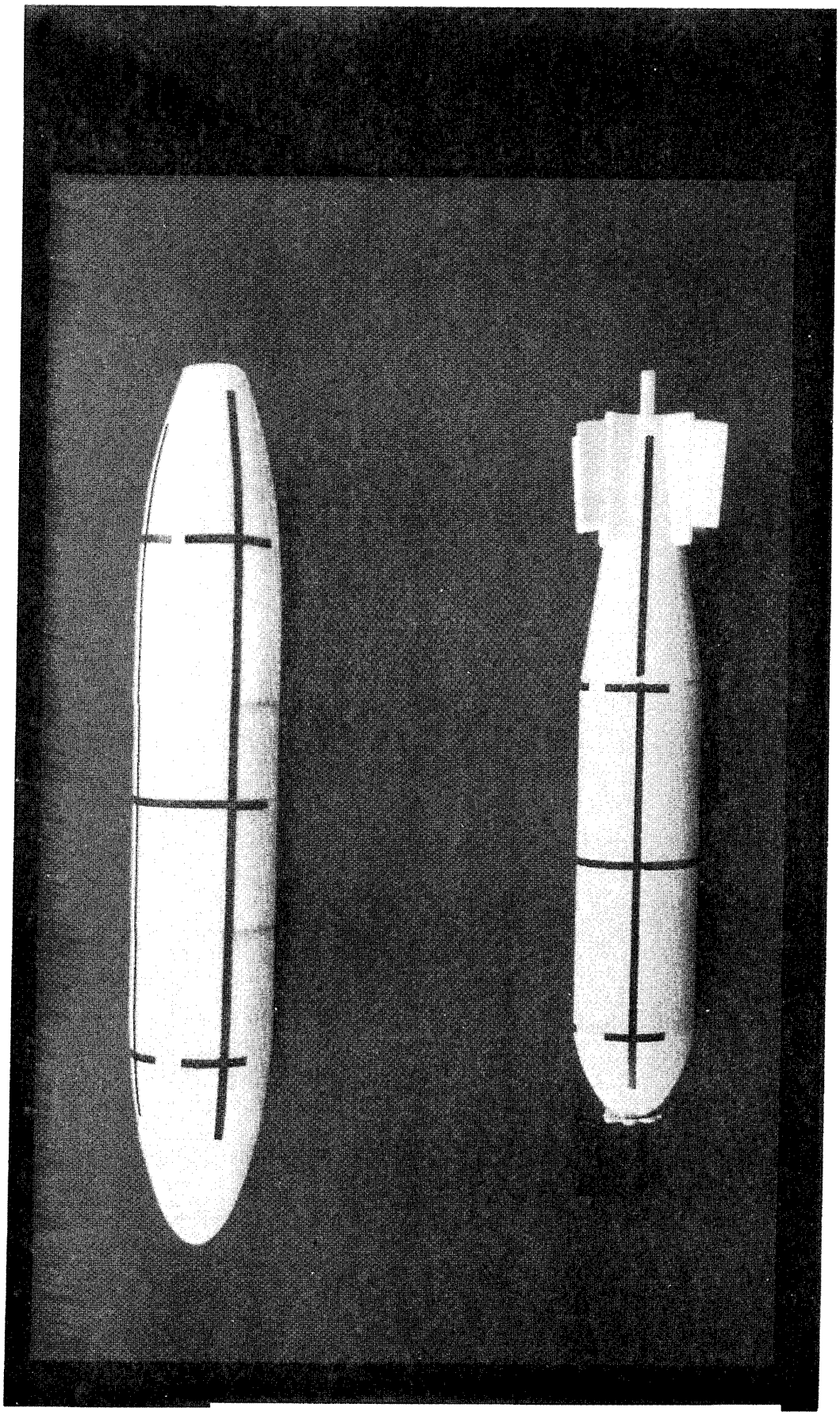

Figure 7 - Typical Moulded Store Models

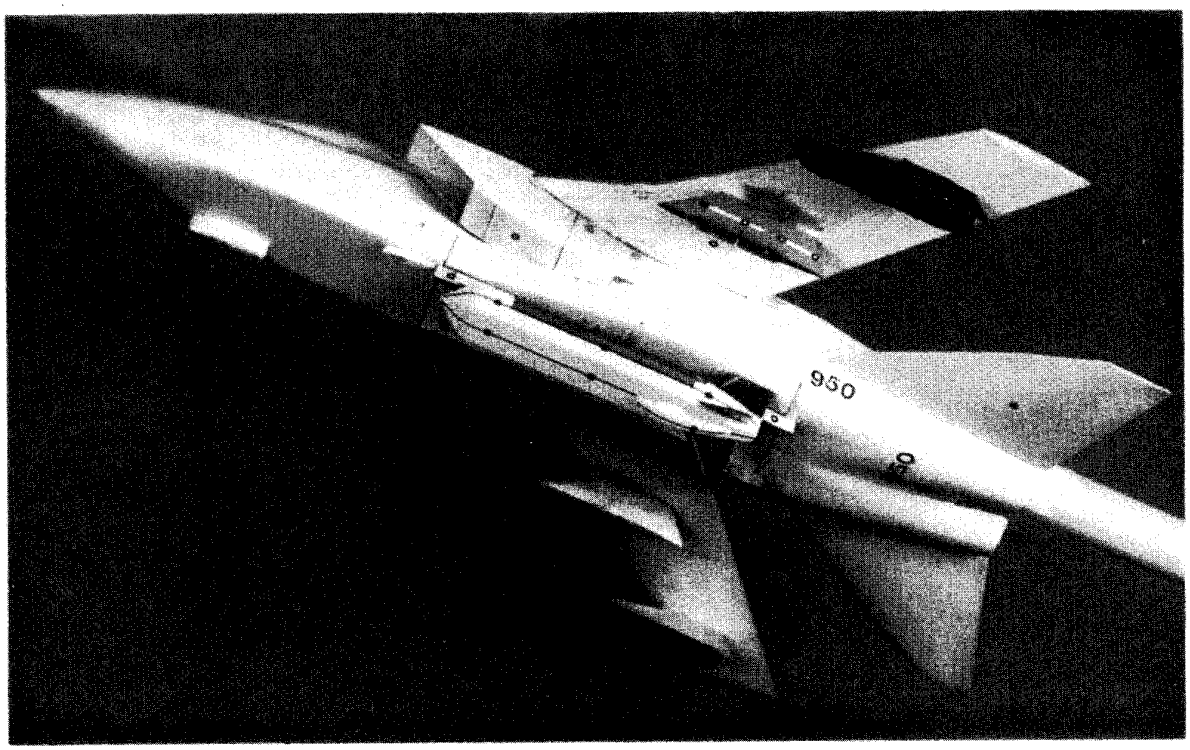

Figure 8 - Installed Store Model Having Active Wings

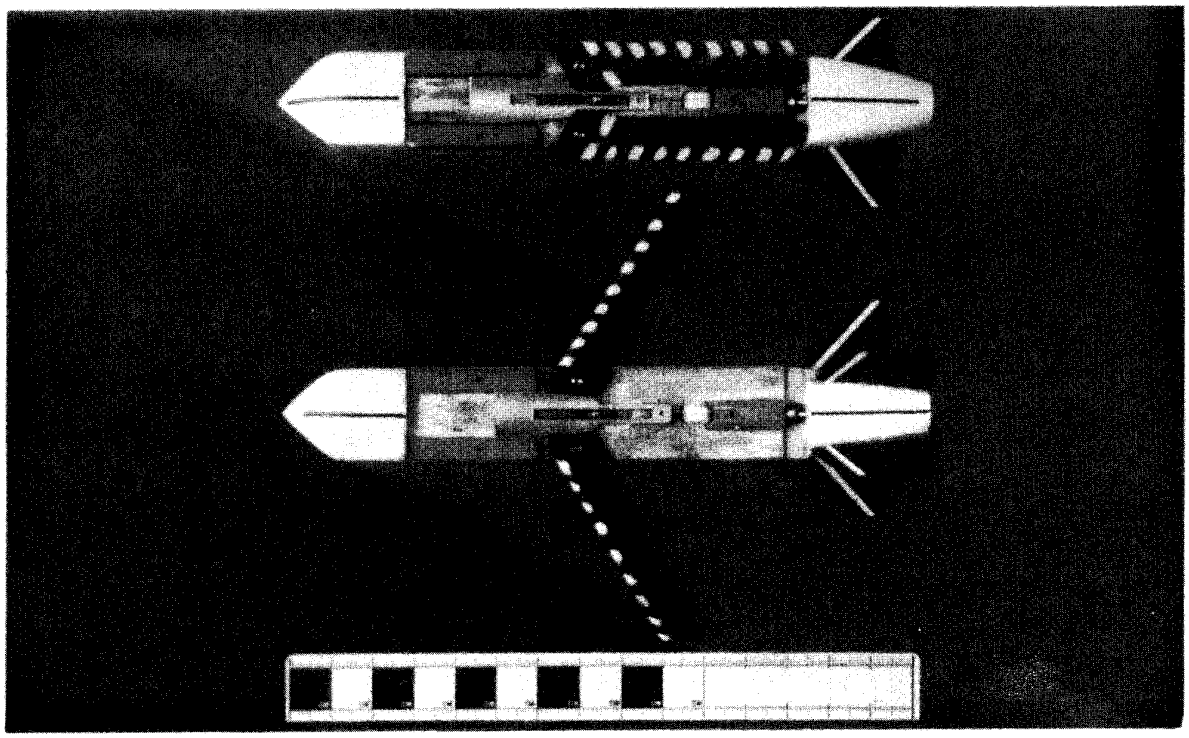

Figure 9 - Model Before and After Wing Deployment

F18 EXTERNAL STORES GRID MEASUREMENT TESTING IN THE IAR/NRC 1.5m BLOWDOWN WIND TUNNEL

James A. Thain
Research Council Officer, Institute for Aerospace Research,
High Speed Aerodynamics Laboratory, National Research Council,
Montreal Road, Ottawa, Ontario, Canada. K1A 0R6

Capt. Robert Lafrance
CF 18 Stores Certification Engineer, DFTEM 7-7-2,
National Defence Headquarters,
Ottawa, Ontario, Canada. K1A 0K2

SUMMARY

A Canadian Forces stores separation prediction capability was initiated in the late 1970s with the development of a store separation computer model supported by wind tunnel measurements. The separation of an external store from an aircraft is a complex event requiring, among other items, a detailed knowledge of the influence of the aircraft flowfield upon the store. The grid survey method, which is essentially a flowfield mapping technique, offers an accurate method for acquiring aerodynamic interference coefficients which are input to the store separation model. However, due to small model scales used for grid survey measurements, additional larger scale wind tunnel investigations are often necessary in order to ensure a faithful reproduction of the store model.

1 INTRODUCTION

The certification of external stores carriage and release cannot be obtained by flight test alone because of the prohibitive cost of testing a multitude of aircraft/store combinations and the associated risk to pilot and aircraft. It is imperative that all external stores released from an aircraft separate cleanly without interfering with the aircraft structure or other external stores. Over the past 25 years the method for determining the safe release of external stores from military aircraft has evolved into procedures which combine theoretical, analytical and experimental techniques.

The procedure generally followed in Canada to assess the relative safety/risk of the release of external stores from the CF-5 and CF-18 aircraft is by means of a Store Separation Model (SSM) which was developed at Canadair, a Division of Bombardier in Montreal (Reference 1). The SSM uses aerodynamic and gravitational forces and moments and ejection system simulation to predict the store trajectory by solving the Euler equations of motion. Accurate and reliable store trajectory predictions require a competent knowledge of the aerodynamic effects which, in some instances, govern the store trajectory and its safe release from the parent aircraft.

Under a joint Canadian Department of National Defence (DND)/National Research Council (NRC) Store Certification Technology Program which commenced in 1979 a capability was developed in the Institute for Aerospace Research (IAR) 1.5m blowdown wind tunnel, with limited funding, to conduct grid survey measurements of a variety of external stores in the flowfield of a 6% scale model of the F18 aircraft.

This paper describes the grid survey technique currently employed in the IAR 1.5m blowdown wind tunnel and includes a description of some additional wind tunnel investigations which were performed to support the grid survey results. Our future plans regarding enhancements to our experimental techniques are also discussed.

2 TEST FACILITY

The aerodynamic measurement programmes were carried out in the 1.5m x 1.5m blowdown wind tunnel. This facility has trisonic capability to a maximum Mach number of 4.25 and may be operated through a range of stagnation pressure at fixed Mach number thus allowing independent variation of Mach and Reynolds numbers. The transonic test-section, having ventilated walls, was used for the programmes being discussed. A description of the facility with performance tables is given in Reference 2.

3 GRID SURVEY RIG

3.1 General

Grid survey wind tunnel tests require a two sting rig and a simple, inexpensive system shown schematically in Figure 1, was developed for the IAR 1.5m blowdown wind tunnel (Reference 3). This rig features a sting mounted aircraft model (F18) attached to a strut which

Paper presented at the AGARD FDP Symposium on "Aerodynamics of Store Integration and Separation", held in Ankara, Turkey from 24-27 April 1995, and published in CP-570.

is suspended from the wind tunnel ceiling and a store positioning rig, or articulated sting, which is mounted on the main model mounting strut. Only the vertical and horizontal motion of the store rig are powered but store pitch, roll and lateral position, and the parent aircraft pitch angle may be adjusted manually.

Aerodynamic forces and moments on the store are measured utilising either a five or six-component internal strain gauge balance. The store position relative to the parent aircraft is determined using an optical system. The "Watsmart" optical tracking system was commissioned in 1985 and used in numerous wind tunnel entries through 1991 and in March 1993 the IAR took delivery of a new enhanced system, the OPTOTRAK/3020. Like the old system the new equipment obtains, by non-intrusive means, the X, Y, Z locations and Yaw, Pitch, Roll of both the parent aircraft model and an external store. However, unlike the old system which suffered from optical reflection deficiencies and low data rates, the new equipment has enhanced optical capabilities and the data rate, reliability and accuracy have been substantially improved.

3.2 Camera System And Installation

The OPTOTRAK system consists of four major hardware components: target markers, a camera unit, a system control unit and a computer. The camera unit is responsible for sensing the positions of the target markers while the system control unit has three functions. These are, the timing control of the Optotrak system, the processing of the camera sensing information and interfacing with the computer. The markers used with the Optotrak system consist of small Infrared Emitting Diodes (IREDs). Two types were supplied with the new camera system, one for the parent aircraft and another for the stores, however some of our older stores are equipped with older markers which still function with the new camera system.

Two Optotrak/3020 cameras were installed in the plenum chamber on the south side of the wind tunnel as shown in the schematic in Fig. 1. Each camera consists of two one-dimensional sensors mounted such that two 2048 element (pixels) linear charge-coupled device (CCD) arrays are orthogonal and at least two cameras are required to determine the 3-dimensional position of a marker (IRED). The linear CCD array accurately measures the position of the imaged line projected by the lens system from the target marker. This CCD overcomes the reflection problems encountered with the old Watsmart system by digitising the image and, by examining the brightest pixel along its neighbours the resolution of the sensor is increased to better than 1:2048. The median position of the of the image is then determined by a weighted algorithm and this technique ignores all low level interference such as ambient lighting and reflections. Unlike the original system installation, which had one camera in the wall and one in the floor, both cameras are mounted in the test section wall insert, close to the tunnel floor, and there is no glass between the cameras and the airstream. In an effort to minimise the effect of the wall cut-outs, which are large relative to the camera dimensions, on the test section flow, skirts were fitted between the cameras and the wind tunnel wall. The cameras and system control units are air cooled by means of filtered, regulated shop air.

The orientation of the cameras in the tunnel walls is such that the viewing area on the tunnel centreline, as seen by both cameras, blankets an area measuring approximately 20" x 20" which includes the parent F18 IREDs close to its upper boundary. The optical system has demonstrated an accuracy which meets or exceeds the manufacturers specifications.

3.3 F18 Parent Aircraft

The IAR 6% scale complete model of the CF18 is mounted on a 1.5 inch diameter 6-component balance, (or on a dummy balance if parent forces and moments are not required), and secured to a roof mounted sting which is attached to the tunnel ceiling at one of the five available axial locations. The axial location selected depends on the type of store and the associated trajectory programme, while ensuring that the store and parent aircraft IREDs are within the camera viewing area for a grid area of interest. Although a minimum of four diodes are needed to define a rigid body a total of ten markers were installed so that the model could be installed at a number of axial positions and still have the minimum number within the viewing area.

3.4 Articulated Sting

In order to place a store or probe adjacent to the parent F18 model, and have the facility to move it during a blowdown, an articulated sting was conceived and built for the IAR wind tunnel. The specifications required that the probe be adjustable (by pre-setting in pitch, roll, yaw and spanwise translation), in height and axial translation under power. The probe was designed to carry either a six-component force and moment measuring balance or a pressure and flow angle sensor. The articulated sting, shown in-situ in Figure 1 is mounted on a powered strut (normally used to mount sting supported models), which is housed in the diffuser section of the wind tunnel. This strut has a vertical range of 38 inches while the axial translation of the articulated sting carrier is 16 inches. Differential

indexing of the inboard and outboard arms of the mechanism allows the carrier to be placed in over 100,000 positions relative to the support strut within a radius of 24 inches from the centre of the mounting shank.

During a grid survey investigation of a missile model which was conducted in 1991, it was found that the axial travel of the articulated sting was severely limited due the drive motor stalling as the sting was being extended. Excessive aerodynamic loads on the "goose neck" sting due to its conical shape and high crank angle and a considerable amount of friction in the axial drive mechanism were thought to be the cause. A new sting, having a much reduced crank angle, was designed and constructed, and replaced the old sting for future grid survey tests. Like the old "goose-neck" the new sting has an internal bore to accommodate the balance wiring harness and a surface trough has been provided for wring to power store Infrared Emitting Diodes (IREDs.

4 TEST TECHNIQUE

4.1 General

The flow of data from the wind tunnel measuring equipment through the data processing phase for a grid survey investigation is shown schematically in Figure 2. It should be noted that the vision system data channels are correlated in time with the filtered balance data by digitally filtering the appropriate channels. The processed data is used as input to a Stores Separation Model (SSM) program, developed by Bombardier Inc., Canadair Div., Montreal (shown as Client Workstation in Figure 2). The SSM program computes the trajectory of the ejected store from the CF18 and has the capability to visually display the results.

4.2 Store Position

The set-up procedure which is performed prior to a blowdown to position a store at a known position relative to the parent aircraft is currently a time consuming, labour intensive, exercise but as we gain experience and confidence with the new vision system we feel that this time can be considerably reduced. Since we only have control of the store in the axial and vertical planes under power the store spanwise position and its attitude must be pre-set prior to a blowdown. The set-up is further complicated by the effects of aerodynamic loading on the articulated sting and the parent aircraft which initially requires some intuitive estimates for their deflections under load.

Prior to obtaining the new vision system the set-up procedure involved positioning the store at known locations relative to its carriage position on the parent aircraft; operate the vision system; and input the calculated co-ordinates in the appropriate vision system channels. During the most recent stores clearance investigation we gained a great deal of confidence with the new equipment which permitted us to revise and simplify the set-up procedure resulting in a considerable saving of time and effort. By replacing the real store with a simplified pseudo store, whose IREDs have a common reference point with those on the real store, and attaching it to the parent aircraft in the carriage position we simply use the vision system to define the carriage position. We do, however, perform a visual safety check with the real store close to the carriage position and carefully examine the vision system calculated co-ordinates. The final task in the set-up procedure is to perform the desired grid survey traverses wind-off and examine the calculated results.

4.3 External Store Investigation

Three 6% scale models of external stores, namely a Mk83 bomb, an Aim7 missile and a BL755 bomb, were tested during a lengthy test period in 1993. Grid survey measurements were conducted with these stores in the underwing flowfield of the 6% scale model of the F18 aircraft at a number of high subsonic Mach numbers for a variety of adjacent external store configurations.

The stores under investigation were mounted on the IAR 5-component (Normal and Side forces, Pitching, Yawing and Rolling moments) ARA 0.35 inch internal strain gauge balance. Each store was equipped with 6 surface IREDs located in pockets on the main store body. These markers and the associated wiring channels were covered with transparent epoxy and faired flush with the surrounding surface. The depth of the IRED pockets were designed so that only a very thin epoxy film was required to cover the marker thus eliminating any potential for refraction. The instrumentation wiring from the IREDs was routed to the surface of the sting, bridging the metric and non-metric surfaces, and soldered to the built-in wiring on the cranked sting. The x, y and z co-ordinates of these markers were accurately measured as well as those on the parent aircraft.

The Aim7 missile was tested in 1991, but the results obtained during that grid survey experiment were unsatisfactory due to the previously described problems with the articulated sting, so the current investigation was a repeat of that exercise. The modifications to the articulated sting and associated equipment detailed above, and a new approach to the test technique, helped overcome most, but not all, of the deficiencies experienced in 1991. For this investigation the parent aircraft was rolled 17 degrees in order to align the store traverses with the ejection plane (The Aim7 is ejected

at an angle of 17 degrees). This technique was employed at aircraft angles of attack of 0 and 2 degrees only and traverses performed as shown in Figure 3. At higher parent angles of attack the aircraft was set at roll 0 degrees and three vertical traverses were performed to encompass the 17 degree ejection plane.

The Mk83 and BL755 bombs were traversed in the aircraft flowfield as shown in Figure 4. On completion of the traverses a freestream datapoint was recorded with the store positioned as far upstream as possible and well below the parent aircraft.

4.4 Results

Figure 5 presents typical aerodynamic results plotted as a function of radial distance from the carriage position for the three traverses detailed in Figure 4 for a single blowdown. These data are the total static aerodynamic forces and moments acting on the ejected store and are the sum of the freestream and interference contributions. Also shown in the Figure is a single freestream datapoint which as explained earlier was obtained with the store in what was assumed to be "freestream". It was noted during the analysis of these results that the "freestream" data varied when the store was located at different lateral and radial positions particularly at Mach numbers of 0.85 and above. Isolated store freestream measurements were then obtained with the parent model removed from the test section. The results shown in Figure 6 demonstrate that the aircraft flowfield effects are significant at distances well below the parent.

By subtracting the freestream values from the total values, at the same store incidence, the interference forces and moments are obtained as a function of store attitude and position in the aircraft flowfield. Due to the small scale (6%) of the grid measurement store models it is not possible to reproduce a model which is devoid of scale effects so the isolated store aerodynamic data should be obtained from a large scale wind tunnel model. These results serve as a database in the SSM for subsequent trajectory calculations.

5 MUTUAL INTERFERENCE EFFECTS

5.1 General

A few years ago the Canadian Forces embarked on a CF18 stores certification programme for a variety of weapons released in proximity to the 480 gallon (US) external fuel tank. However, due to in-flight collisions during multiple store releases from VERs in the presence of the smaller 330 gallon external fuel tanks, the cause of these incidents had to be investigated prior to performing multiple releases of weapons adjacent to the 480 gallon tanks. The reason for the collisions was suspected to be caused by wing and VER recoil motion and/or mutual store-to-store aerodynamic interference effects. Consequently a wind tunnel investigation was conducted to determine the mutual interference aerodynamic effects for a pair of external stores.

5.2 Wind Tunnel Investigation

The wind tunnel investigation was conducted in the IAR 1.5m blowdown wind tunnel on a pair of 25% scale models of the Mk 20 Rockeye II Cluster bomb. The models were secured to 6-component balances to measure the aerodynamic forces and moments and mounted on stings as shown in Figure 7. One of the models, simulating the attached store, was secured to a pedestal at fixed angles of incidence (zero, -5 and +5 degrees) while the second model, simulating the ejected store, was mounted on the main wind tunnel support strut on a cranked sting (Figure 7). The latter was swept through an incidence range from -32 to +20 degrees at a fixed horizontal distance from the former. Interference effects were investigated for a variety of vertical separation distances as shown in Figure 8. It should be noted that the VER, shown in the figure, was not present during the investigation. The effect of extending the tail fins on the ejected store, a situation which occurs after the store has been released, was explored at some of the vertical displacements. To determine the aerodynamic interference coefficients the ejected store was tested in isolation to obtain freestream data. The tests were conducted at discrete Mach numbers in the range 0.6 to 0.95 at a unit Reynolds number of 6.5 million.

5.3 Results

Preliminary analysis of the data indicate that freestream longitudinal stability coefficients are fairly consistent but the lateral data clearly demonstrates the effect of asymmetric vortex shedding at large positive and negative angles of attack. The mutual interference effects are significant at high angles of attack when the stores are close. On completion of the analysis the appropriate data will be input to the SSM so that theoretical multiple release analysis may be performed. Consequently flight testing will be performed by the end of 1995.

6 FUTURE PLANS

6.1 Grid Survey Measurements

Our experience with the Optotrak vision system has shown that the equipment is reliable, sufficiently accurate and easy to operate, so it could be utilised to provide real time feedback of the position and attitude of the parent and store. This should provide the following significant benefits which are currently being implemented.

Collision Avoidance

The parent and the store/articulated sting are complex three dimensional objects which are manipulated in close proximity to each other in a variety of attitudes to generate the required trajectories. The possibility for human error in programming an erroneous trajectory, the elastic deflections under aerodynamic loads and a failure of the servo controlled positioning system could lead to a costly collision. A real time feedback system which can detect and avoid collisions by taking the appropriate action is currently in the design stages.

Deflection Correction

The servo systems which are currently used to position the store model do not account for deflection of the system under aerodynamic loads. In practice these deflections are estimated but this approach is labour intensive and error prone. The real time system discussed above will be designed to measure and correct for these effects.

6.2 Carriage Loads

In most grid survey investigations performed to date in the IAR blowdown test facility a store has never been closer than approximately 0.25 inches to the carriage position during a wind-on run. By implementing the above system enhancements we may be able to reduce this gap but only marginally. Even with these improvements extrapolating the store forces and moments to the carriage position can be a difficult task. A wind tunnel investigation is currently underway to determine the carriage loads for the 6% scale Mk83 bomb utilising VER mounted in-store 5-component balances as shown schematically in Figure 9. As well as obtaining carriage aerodynamic forces and moments data will be gathered at 0.15 and 0.3 inches (model scale) below the carriage position, thus overlapping with the grid survey measurements.

During the grid survey investigation of the Mk83 bomb described above the store forces and moments were adjusted theoretically to account for the support sting effects. A comparison of the above carriage aerodynamic data with the grid survey measurements should confirm the effect of the support sting.

7 CONCLUDING REMARKS

a. The new vision system performed favourably in measuring store attitude and position particularly when the new store IREDs, optimised for the Optotrak camera position, were utilised.

b. It was initially assumed that the "freestream" store measurement performed in conjunction with the grid traverses was interference free but it was found that these data varied with aircraft angle of attack and configuration. By repeating the "freestream" points with the parent aircraft removed the results clearly demonstrated a difference between true and pseudo freestream values.

c. The store set-up procedure utilising a pseudo store is fast, accurate and repeatable, and significantly reduces the possibility of human error

d. The store support sting was redesigned to reduce deflections but the lateral deflections are still high at the store which results in time consuming set-up procedures.

e. The mutual interference wind tunnel measurements and the subsequent flight testing should help the Canadian Forces understand the dynamics of stores ejected in the ripple release mode.

ACKNOWLEDGEMENTS

This work was funded by the Department of National Defence (DFTEM), and the permission of both DND and the Institute for Aerospace Research to present this data is gratefully acknowledged.

REFERENCES

1. Kohiyar, F.A., Ugolini B., "Aerodynamics of Store Separation", First Canadian Symposium on Aerodynamics, Canadian Aeronautics and Space Institute, December 1989.

2. Brown, D. "Information for users of the National research Council's 5ft. x 5ft. Blowdown wind Tunnel at the National Aeronautical Establishment.", Sept. 1977

3. Brown, D., Ellis F.A., Bureau J.L. "Measurements of Aerodynamic Forces on Aircraft External Stores in the NAE Trisonic Blowdown Wind Tunnel", First Canadian Symposium on Aerodynamics, Canadian Aeronautics and Space Institute, Dec. 1989.

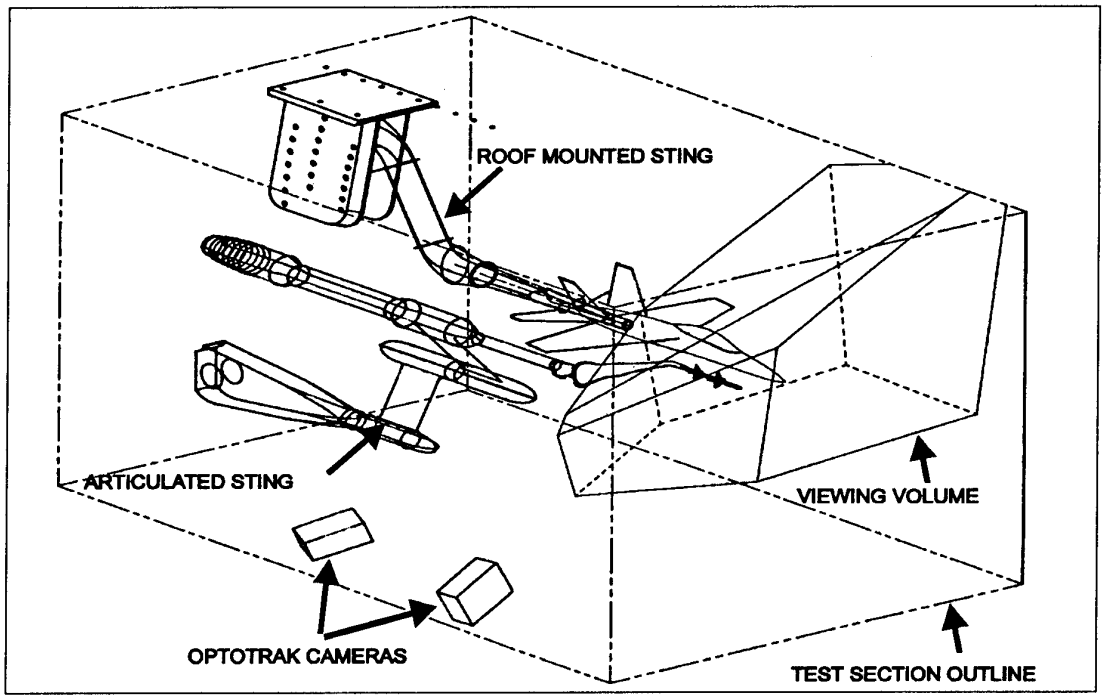

Figure 1 - GRID SURVEY RIG SCHEMATIC

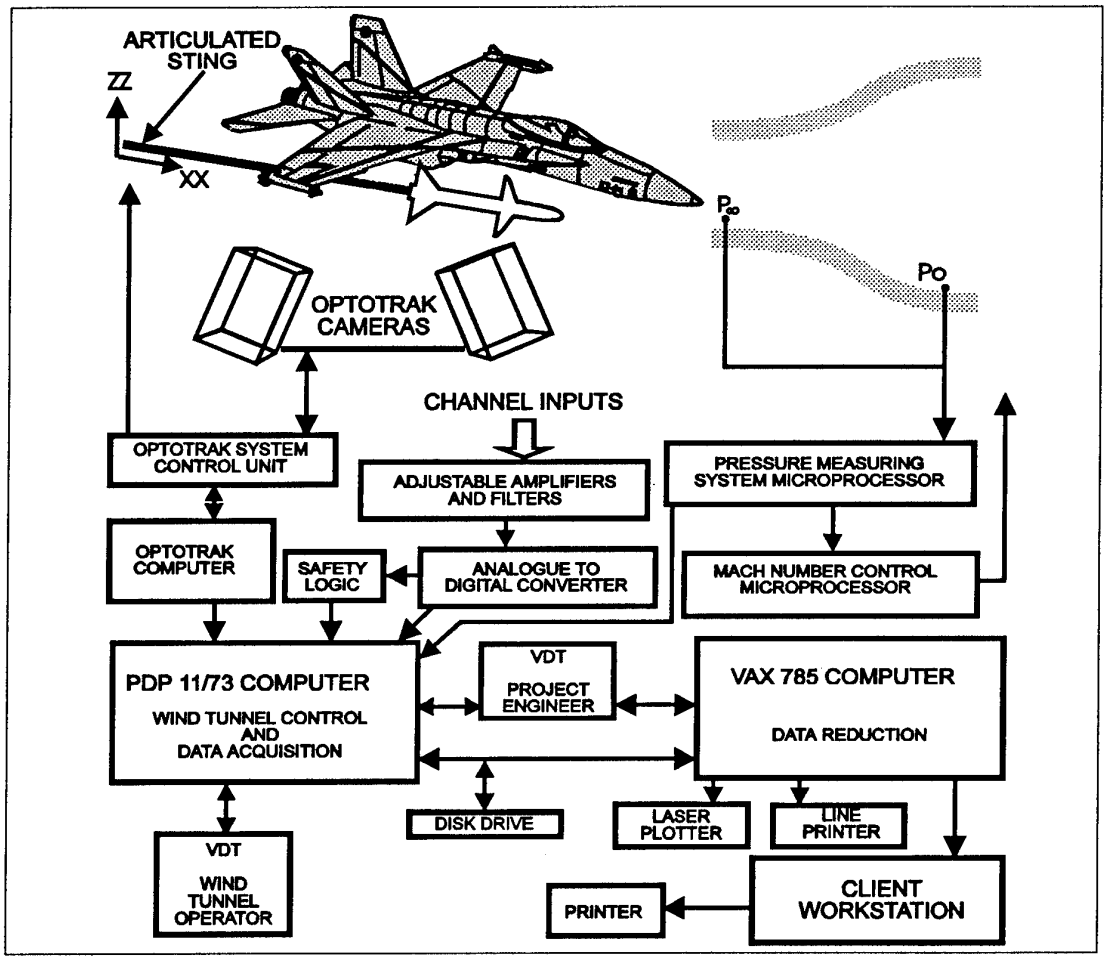

Figure 2 - DATA FLOW CHART

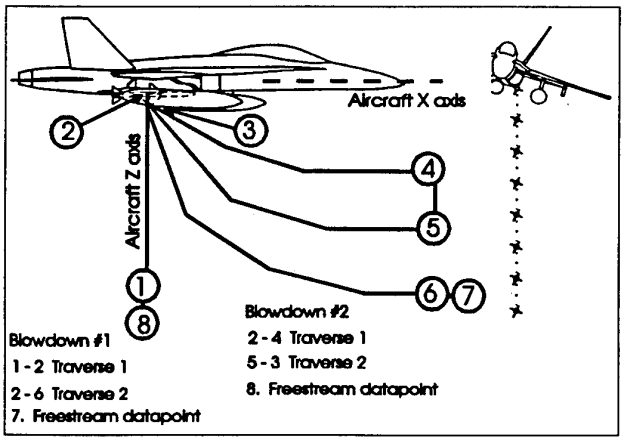

Figure 3 - MISSILE TRAVERSE PATHS

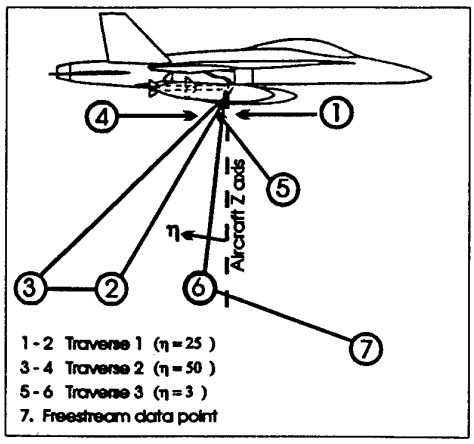

Figure 4 - BOMB TRAVERSE PATHS

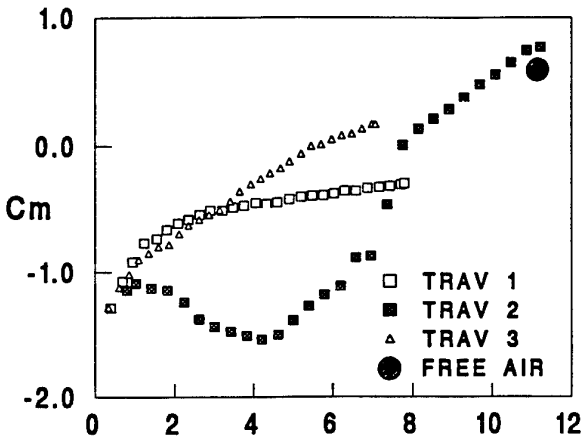

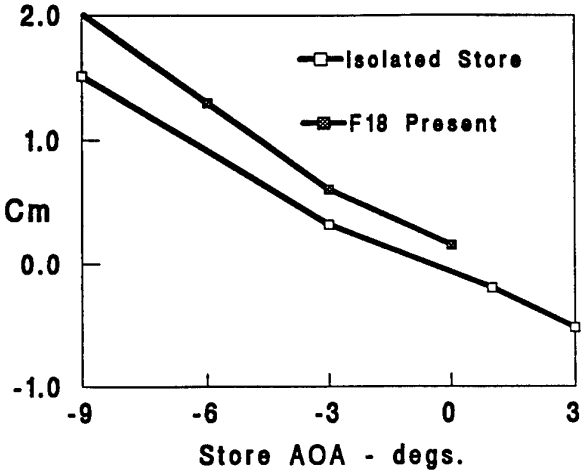

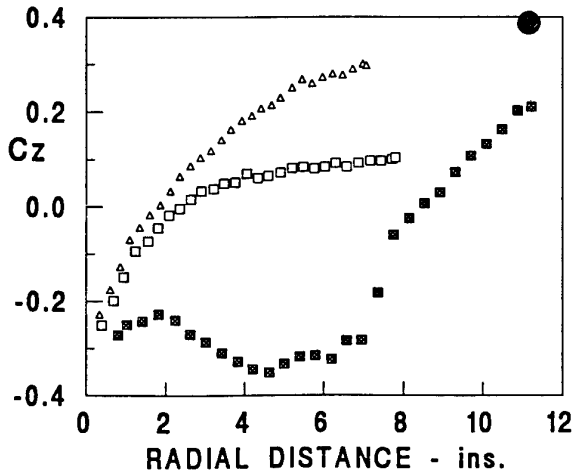

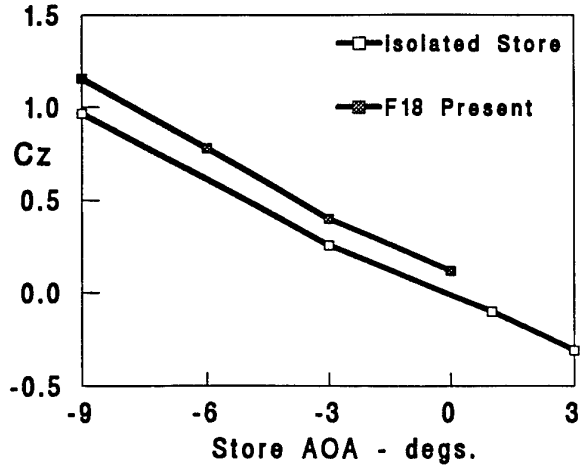

Figure 5 - TYPICAL FLOWFIELD DATA

Figure 6 - FREESTREAM DATA

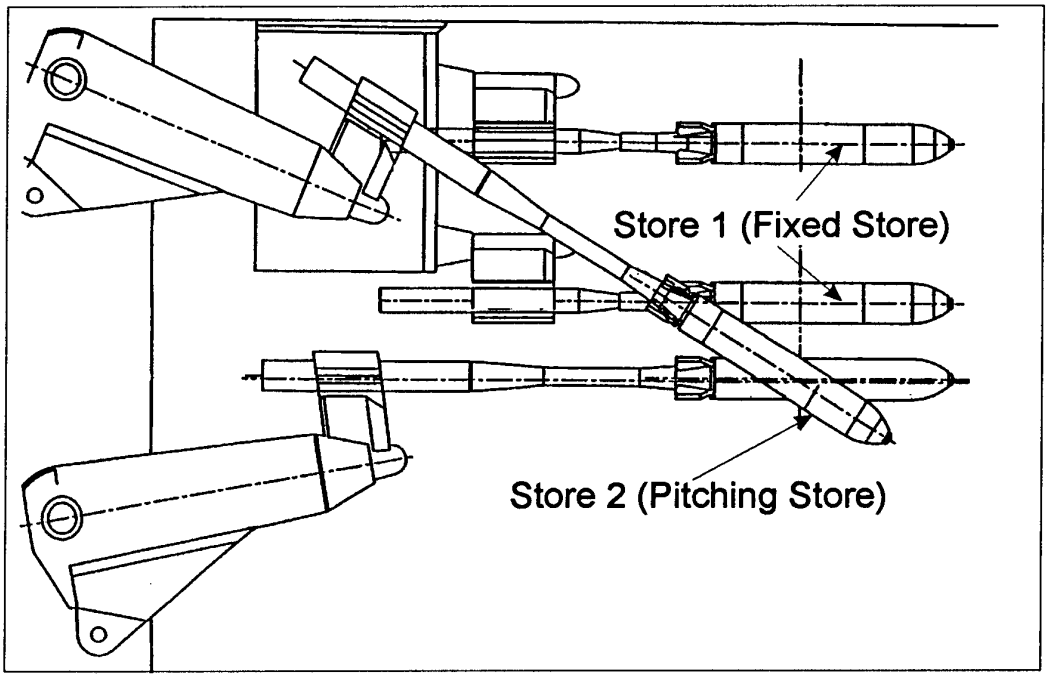

FIGURE 7 - MUTUAL INTERFERENCE TEST RIG

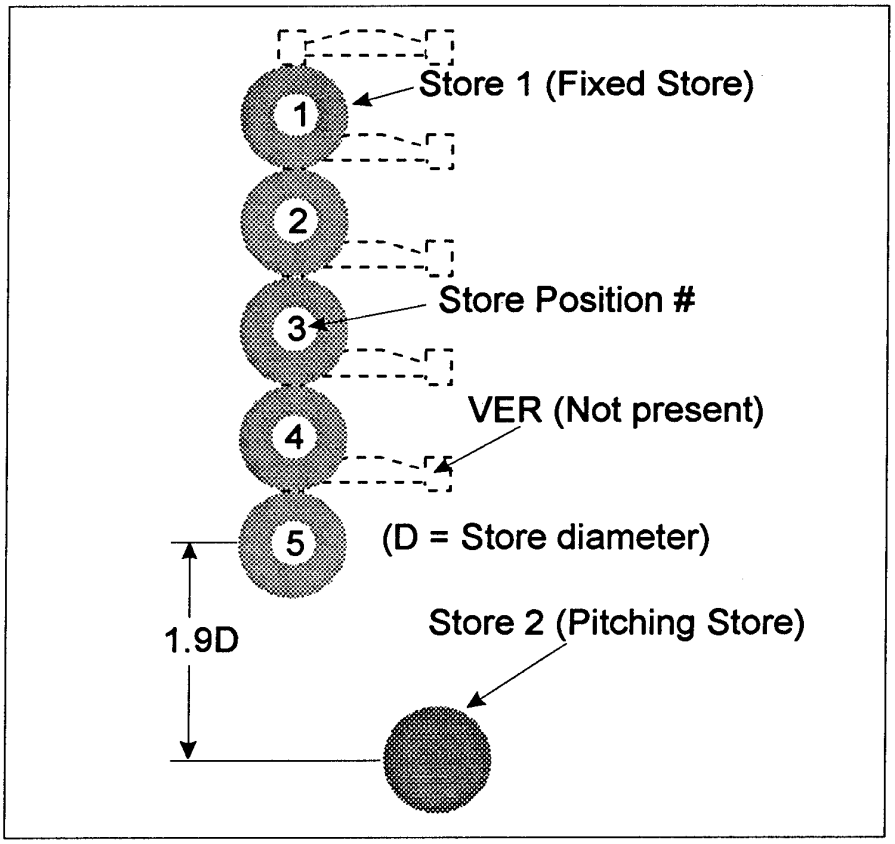

FIGURE 8 - MUTUAL INTERFERENCE TEST MATRIX

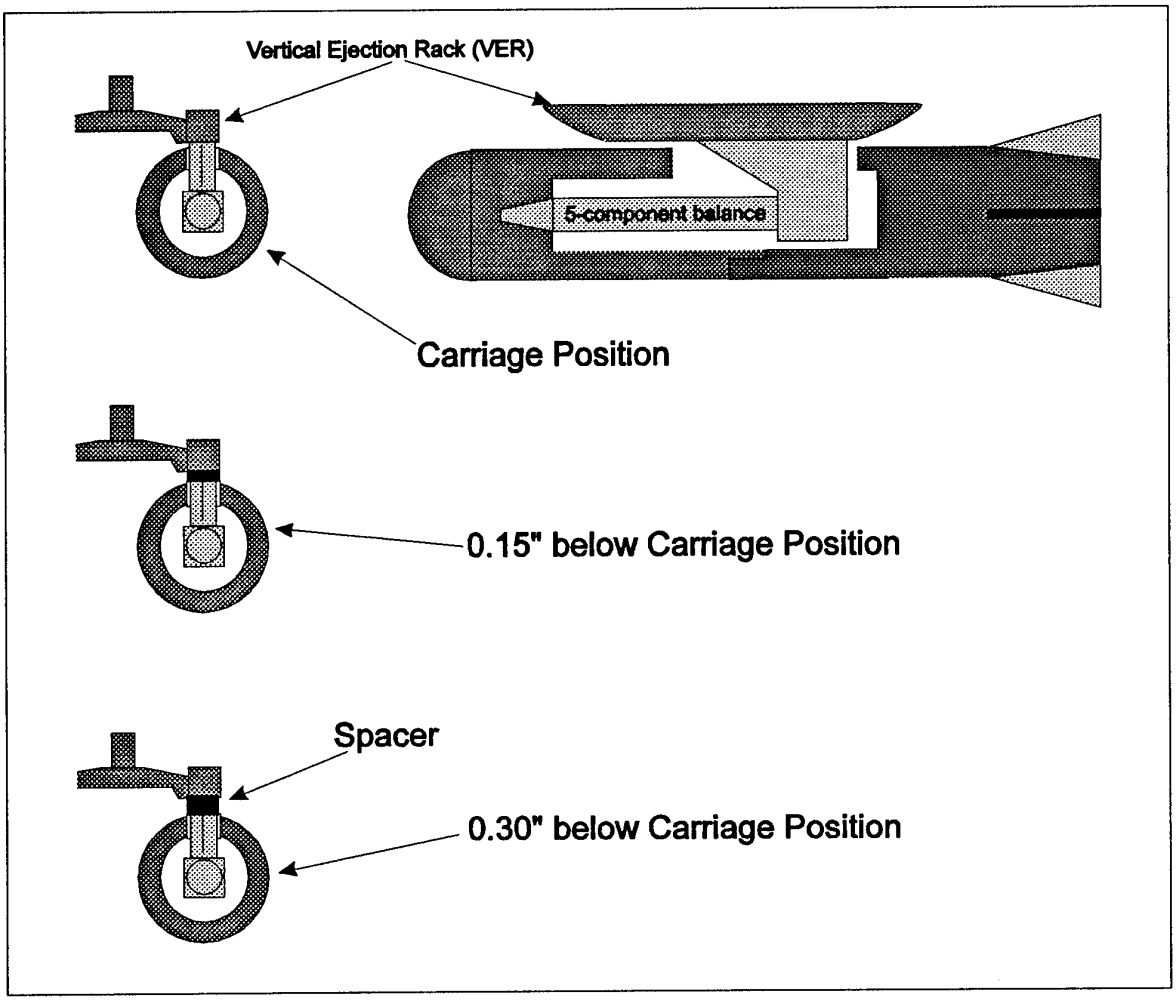

Figure 9 - CARRIAGE LOADS AND MOMENTS

Estimation of Store Interference Loads using Transonic Small Disturbance Theory and Influence Function Method

P. Piperni
K. Stokoe
Canadair Aerospace Group, Bombardier Inc.
400 Cote Vertu Road West
Dorval, Quebec, Canada H4S 1Y9

1. SUMMARY

This paper presents a method for predicting aerodynamic interference loads on stores which are ejected or launched from the CF-18 aircraft at transonic flight conditions. A transonic small disturbance theory and an influence function method were employed to estimate interference loads. Predictions for the AIM-7 sparrow missile in the presence of a 330 gallon fuel tank on the aircraft centerline and 480 gallon fuel tanks on the inboard wing pylons are compared with wind tunnel test results. Corrections for sting effects are also included.

2. LIST OF SYMBOLS

AEDC	Arnold Engineering Development Center
AIM-7	Sparrow Missile
AOA	Aircraft Angle-of-Attack
Cy	Side Force Aerodynamic Interference Coefficient (positive outboard)
Cn	Yawing Moment Aerodynamic Interference Coefficient (positive nose outboard)
Cz	Normal Force Aerodynamic Interference Coefficient (positive down)
Cm	Pitching Moment Aerodynamic Interference Coefficient (positive nose up)
CF	Canadian Forces
CFD	Computational Fluid Dynamics
CSF	Computational Surface - Fuselage
DND	Department of National Defence, Canada
EFT	External Fuel Tank
IAR	Canadian Institute for Aerospace Research, Ottawa Canada
IDL	Interference Distributed Loads
IFM	Influence Function Method
KTRAN-M	Canadair Transonic Small Disturbance Computational Fluid Dynamics Program - Military Version
NAWC	U.S. Naval Air Warfare Center
SSM	Store Separation Model
TSD	Transonic Small Disturbance

3. INTRODUCTION

Canadair has been contracted by the Canadian Department of National Defence to predict the trajectories of stores (weapons or external fuel tanks) released from CF-18 aircraft and the clearances between the released stores, the aircraft and other stores, carried or released. In order to accomplish this task, Canadair engineers have developed a store separation model which solves the six degree-of-freedom Euler equations of motion for rigid bodies using aerodynamic, ejection and gravitational loads. Accurate SSM predictions require an accurate aerodynamic data base, comprising freestream and interference coefficients. Freestream coefficients provide isolated store aerodynamic loads as functions of incidence (AOA, sideslip) and Mach number. Interference coefficients account for loads which are induced by the aircraft flowfield.

Historically, interference coefficients have been obtained from wind tunnel tests. This approach has been very time consuming and expensive, since tests are required for each combination of aircraft configuration and metric store. An alternative approach would be to use theoretical methods to predict interference coefficients for every aircraft configuration followed by validation of critical cases by wind tunnel tests.

The U.S. Naval Air Warfare Center employs a technique for evaluating interference coefficients using a map of the aircraft flowfield and store influence coefficients. Influence coefficients are obtained from a program which combines the Arnold Engineering Development Center Interference Distributed Loads program and an Influence Function Method program, referred to as IDL/IFM. Canadair obtained the IDL/IFM program from DND. Flowfield data required by IDL/IFM may be obtained from computational fluid dynamics methods.

Canadair engineers have developed a CFD program (KTRAN-M) capable of predicting aircraft flowfields for complex aircraft configurations at transonic speeds. To effectively use KTRAN-M for store separation, an external fuel tank mounted on the fuselage centerline was modelled.

4. DESCRIPTION OF KTRAN-M

The KTRAN-M program was developed at Canadair under two DND contracts (references 1 and 2) using the method described in reference 3. The version delivered to DND in 1989 could model the CF-18 aircraft (excluding the vertical tail) with under-wing stores and engine flow through effects.

KTRAN-M solves a modified version of the transonic small disturbance equation in a system of embedded grids. In this method a global grid, which encompasses the entire computational domain, is used to solve the flow equations in areas where gradients are small and is also used as a communication link between fine grid solutions. The fine grids, which are embedded in the global grid, are used to provide accurate solutions near each aircraft component. One fine grid is allocated for each component; fuselage, wing, horizontal stabilizer and for each store mounted on the aircraft. An illustration of the global grid and fine grid boundaries for the wing, horizontal tail, Mk-83 mounted on

Paper presented at the AGARD FDP Symposium on "Aerodynamics of Store Integration and Separation", held in Ankara, Turkey from 24-27 April 1995, and published in CP-570.

the wing outboard pylon, 480 gallon EFT mounted on the wing inboard pylon and 330 gallon EFT mounted on the fuselage centerline is shown in figure 1a. A front view of the CF-18 aircraft model, depicting the global, fuselage, centerline tank and wing mounted store grids, is shown in figure 1b. Also shown in this figure are the global grid points and fuselage fine grid points, as circles and dots respectively, which lie on the fuselage computational surfaces.

4.1 Computational Surfaces

Lifting surfaces, such as wings and horizontal stabilizers, are modelled by applying flow tangency conditions on equivalent planar surfaces. This technique is only accurate if the distance between the planar and lifting surfaces are small. The aircraft fuselage and store surfaces have large tangential gradients in some areas, particularly at the nose and tail. Computational surfaces are employed for these bodies, since they reduce the effect of large surface gradients in the computational domain. Computational surfaces are of constant cross-section, defined by grid points closest to the physical surface at the location of maximum width. This profile is extended longitudinally, usually to the limits of the computational domain. Boundary conditions are calculated on the computational surfaces, using slender body potential theory to correct for the separation distance between the physical and computational surfaces.

4.2 Boundary Conditions

Two types of boundary conditions, Dirichlet and Neumann, are calculated by KTRAN-M. Dirichlet boundary conditions are applied on grid perimeters. They are used to transfer information from outside the grid domain and are obtained by interpolating solutions from adjacent grids. Neumann boundary conditions are applied on computational surfaces and lifting planar surfaces. They are obtained by imposing flow tangency conditions at the physical surface.

4.3 TSD Solver

KTRAN-M uses a modified version of the transonic small disturbance equation (reference 4) and a successive line over-relaxation method to solve for the flow in each grid. The equation is in the form of the perturbation potential, which assumes isentropic and irrotational flow. The numerical scheme uses upwind differencing in supersonic zones and central differencing in subsonic zones. The solution is over-relaxed in subsonic zones only. This method is described in detail in reference 3.

To effectively use the present application, KTRAN-M required extensive modification to include a 330 gallon EFT mounted on the fuselage centerline.

CF-18 Model (Top View)

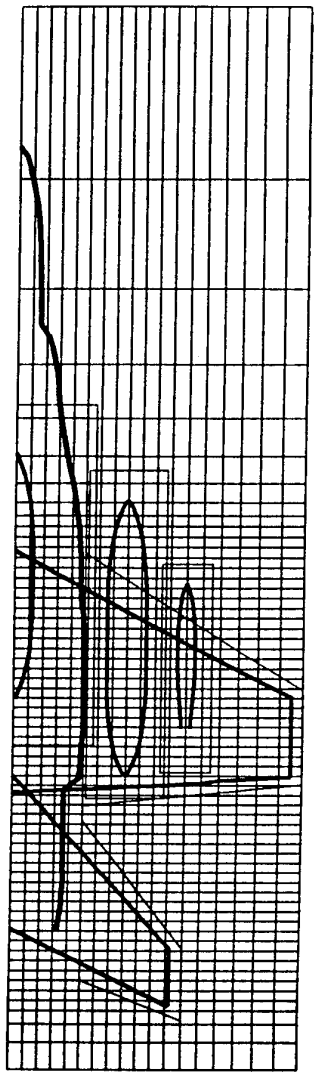

Figure 1a

CF-18 Model (Front View)

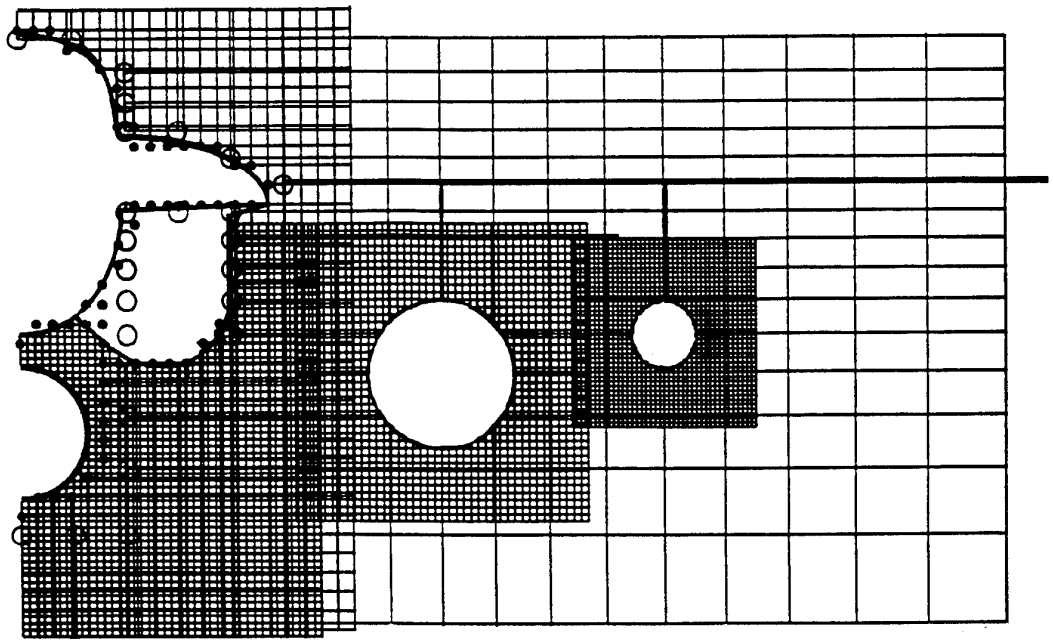

Figure 1b

5. KTRAN-M MODIFICATIONS

Two approaches were considered in order to model a fuel tank mounted on the fuselage centerline.

(1) Modify the fuselage fine grid algorithms to include the centerline store.

(2) Incorporate a fine grid, computational surface and flow solver which are dedicated to the centerline mounted store.

The first approach would have required a substantial increase of the fuselage fine grid density in order to properly resolve the flow between the fuselage and centerline store. This would have been very inefficient, since the fuselage fine grid encompasses large regions where high resolution grids are not required. Consequently, the second approach was adopted.

5.1 Grid Domains and Computational Surfaces

A Cartesian grid for the centerline store was embedded in the fuselage fine grid. Within each component fine grid, the computational domain typically extends to the grid limits. In the case of the centerline store fine grid, the grid upper boundary coincides with the fuselage lower surface, as shown in figure 1b.

For most problems, it is realistic to constrain the flow to be parallel to the unperturbed freestream at all grid points on the computational surface upstream and downstream of the store. However, this would be unrealistic for a store mounted on the fuselage centerline, due to its close proximity to the fuselage. Therefore a finite centerline store computational surface was defined.

The fuselage computational surface was originally composed of two sections, in front of the engine inlet (CSF1) and behind the engine inlet (CSF2) as outlined in figure 2. This arrangement is used to account for engine flow-through effects. Additional fuselage computational surfaces were required in order to include the centerline store. The downstream boundary of CSF1 was moved forward of the centerline store and the upstream boundary of CSF2 (re-numbered as CSF4) was moved behind the store. Two new computational surfaces, designated CSF2′ and CSF3, are situated between CSF1 and CSF4. These new surfaces have the same geometry as CSF1 and CSF4 respectively, except that they circumscribe the centerline store as outlined in figure 3. Computational surface 2′ extends from the aft face of CSF1 to the engine inlet and computational surface 3 extends from the

engine inlet to the front face of CSF4.

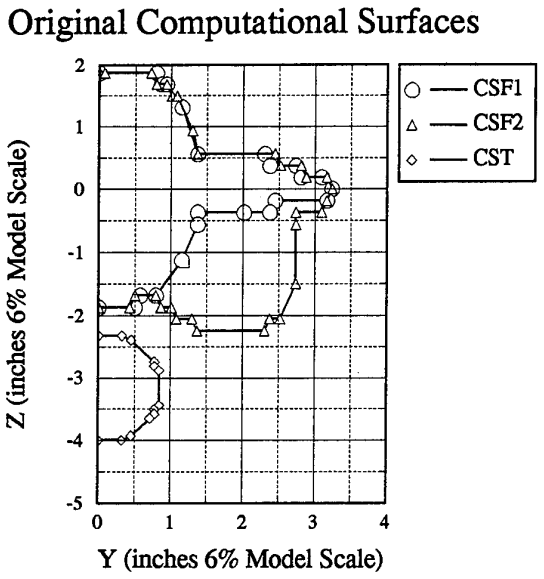

Figure 2

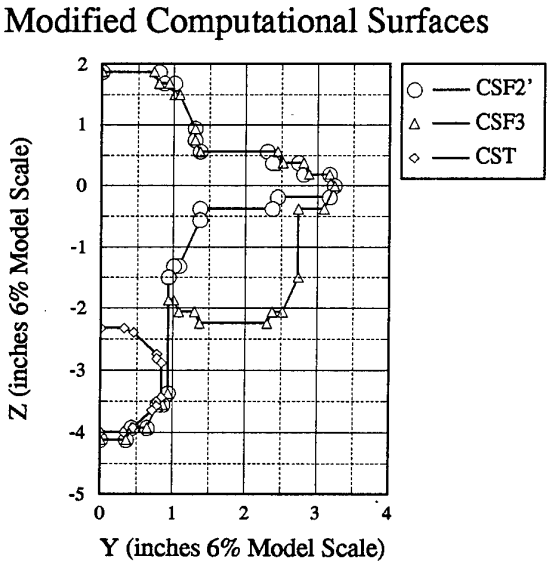

Figure 3

5.2 Application of Boundary Conditions

Neumann boundary conditions are calculated at fuselage fine grid points on fuselage computational surfaces 2′ and 3 as shown in figure 3, using fuselage and centerline store surface normals. Fuselage normals are used at all surface grid points above the engine inlet bottom. These boundary conditions are imposed for all fuselage fine grid iterations up to and including iteration ITBMAX, which is input by the user. For the first ITBMAX fine grid iterations, a solution is obtained using all aircraft component fine grid solvers except for the centerline store fine grid. This ensures that the fuselage fine grid solution at the centerline store fine grid outer perimeter has sufficiently evolved before activating the centerline store fine grid.

Once the centerline store fine grid solver is activated, Dirichlet boundary conditions are applied at all fuselage fine grid points on CSF2′ and CSF3, including the front face of CSF2′ and the rear face of CSF3. These boundary conditions are calculated by interpolating from the centerline store fine grid solution.

Neumann boundary conditions are calculated at all centerline store fine grid points on the fuselage and centerline store computational surfaces. The number of grid points on CSF2′ and CSF3 depends on grid height, grid width and grid density. The user inputs these parameters. Upper limits for this grid are constrained to coincide with the fuselage computational surface.

Boundary conditions applied at centerline store fine grid points located on the engine inlet face and on the front and rear faces of the centerline store computational surface are based on mass flow ratios. Mass flow through the engine inlet is input by the user. Mass flow at the entry and exit planes of the centerline store computational surface is calculated using the local fuselage fine grid solution.

6. DISCUSSION OF RESULTS

A KTRAN-M solution, depicted as pressure contours on the CF-18 aircraft and store surfaces, for Mach = 0.95 and AOA = 0° is shown in figure 4. In this figure regions of red indicate positive pressure and regions of blue indicate suction. This solution is realistic since it shows:

1) an increase in pressure near the engine inlet caused by inlet blockage,

2) large pressure gradients at the centerline store nose and tail

3) centerline store interference effects on the aircraft fuselage, above the store nose and tail.

Supersonic flow is indicated on the aft bodies of the external fuel tanks and fuselage surface above the centerline EFT by the favorable pressure gradient (yellow upstream to dark blue downstream), as shown in figure 4.

KTRAN-M Solution (Mach=0.95, AOA=0)

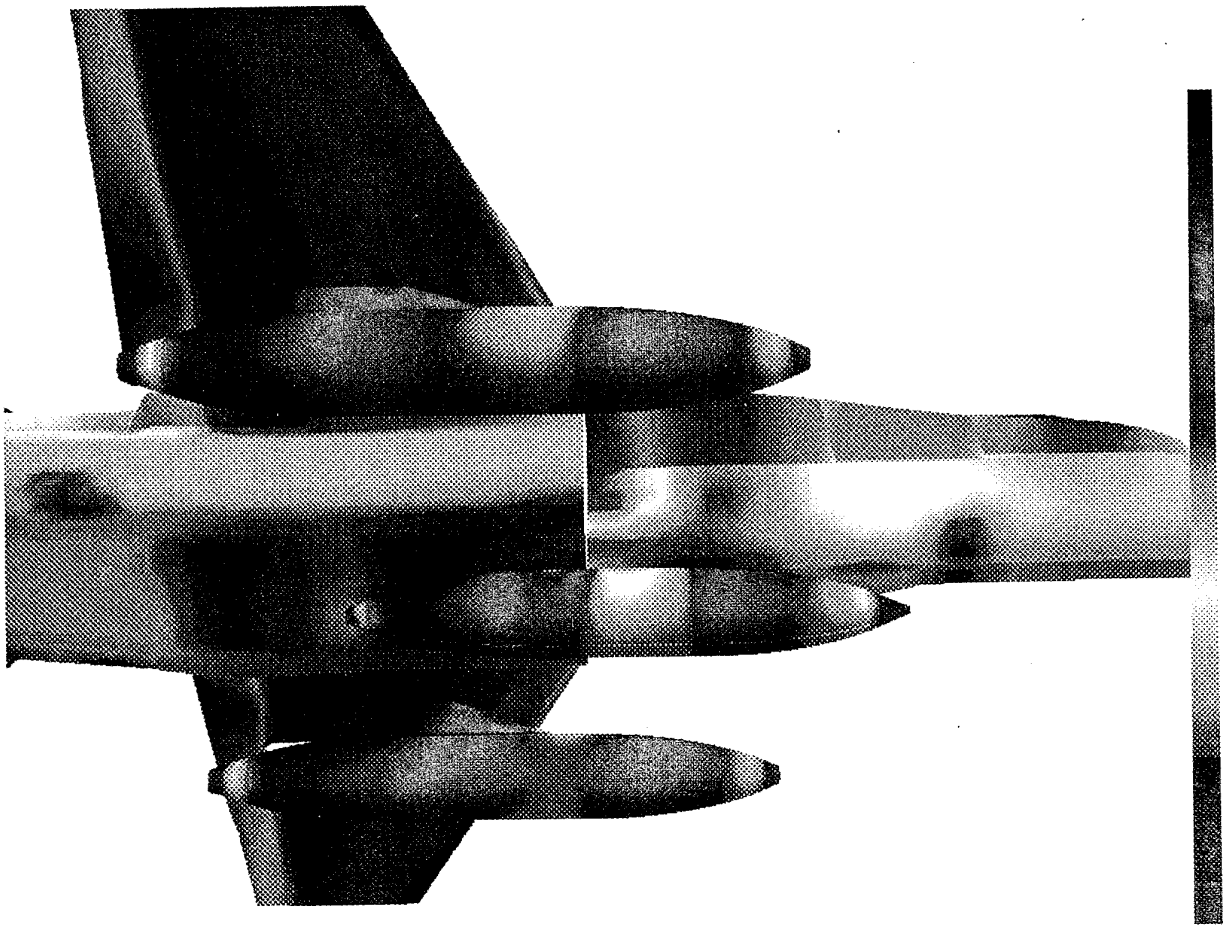

Figure 4

6.1 AIM-7 Interference Coefficients

To evaluate the KTRAN-M /(IDL/IFM) method, predictions for the AIM-7 missile ejected from the CF-18 fuselage station, with a 330 gallon EFT on the fuselage centerline and 480 gallon EFT on wing pylons, were compared with wind tunnel test results. This is a difficult problem for any theoretical method to solve, since the AIM-7 has large wings and fins which pass very close to the fuselage and external fuel tanks. Wind tunnel measurements of interference coefficients along four paths, as shown in figure 5, were obtained from tests at IAR in 1993.

The wind tunnel results included herein for comparison with theoretical predictions are for aircraft angles-of-attack of 0 and 4 degrees. The metric store was traversed along all four paths in the store ejection plane for AOA = 0°. This plane is inclined 17° with respect to the aircraft vertical axis. For AOA = 4°, these paths are in the vertical plane containing the store captive position.

A program was developed at Canadair to calculate the interference loads using IDL/IFM influence coefficients and KTRAN-M flowfield – angularity data. This program calculates interference loads for a metric store oriented in any manner relative to the parent aircraft and along any path which is described in aircraft body axes. The flow angularity data is interpolated at the centroid of each body segment and multiplied by the body segment influence coefficient. These products are then summed over the length of the body. This technique assumes that the flowfield gradient is linear across each body segment.

IDL/IFM calculates influence coefficients by estimating the loads applied to the store at multiple locations in a known non-uniform flowfield (conducted in the IDL section), and then solving a system of equations which relates influence coefficients and flowfield angularity with these loads (conducted in the IFM section). Consequently, the only unknowns are the influence coefficients. A detailed description of IDL/IFM is provided in reference 5.

Sting effects were estimated by adding an after-body to the IDL/IFM model in order to obtain body-sting influence coefficients. Interference coefficients were then calculated using influence coefficients corresponding only to the body. This technique should eliminate the influence of the metric store base pressure on interference predictions.

IAR test results for side force, normal force, pitching moment and yawing moment interference coefficients are shown in figures 6 to 8. These figures also include predictions, with and without sting effects.

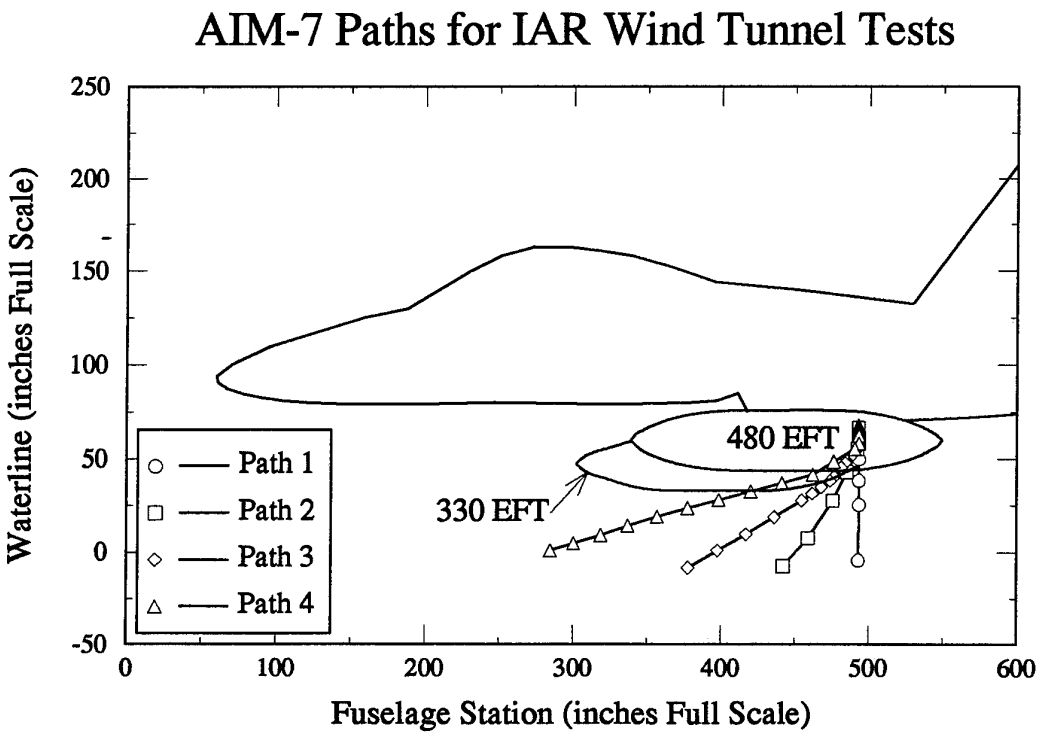

Figure 5

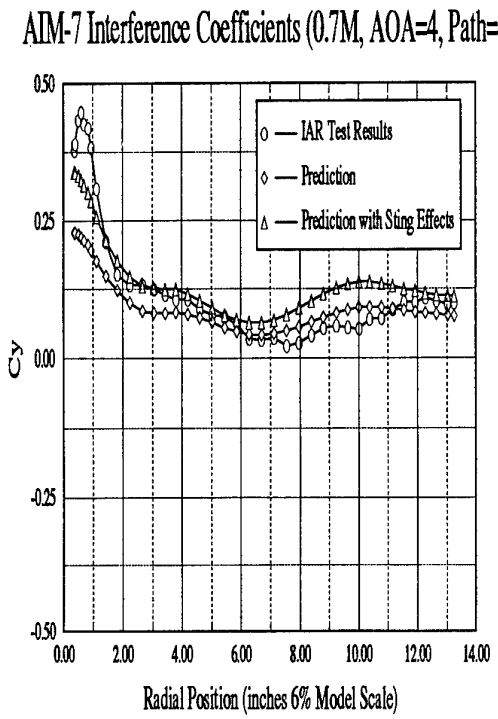

Figure 6a

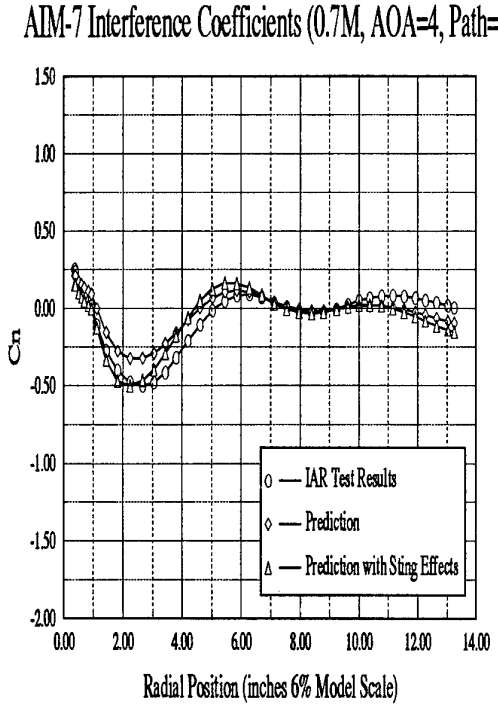

Figure 6b

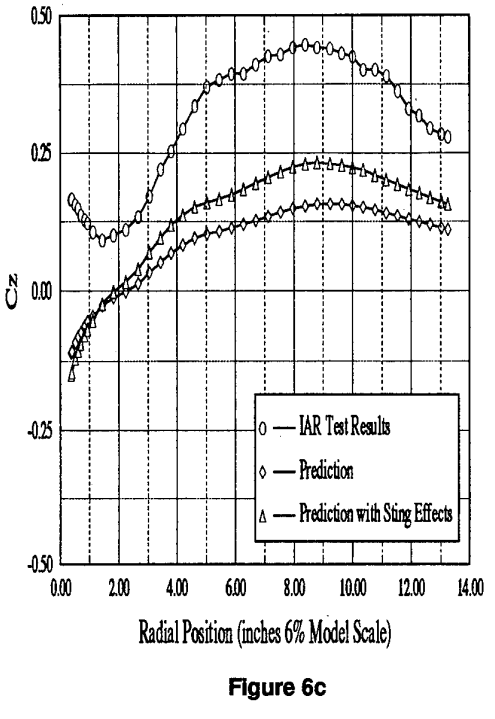

Figure 6c

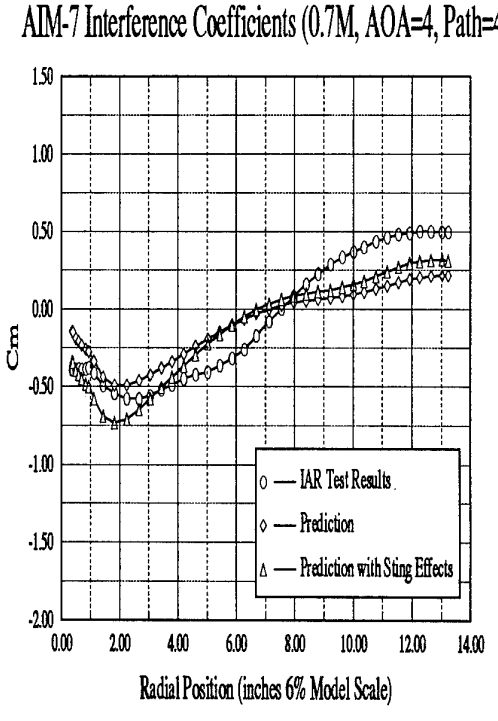

Figure 6d

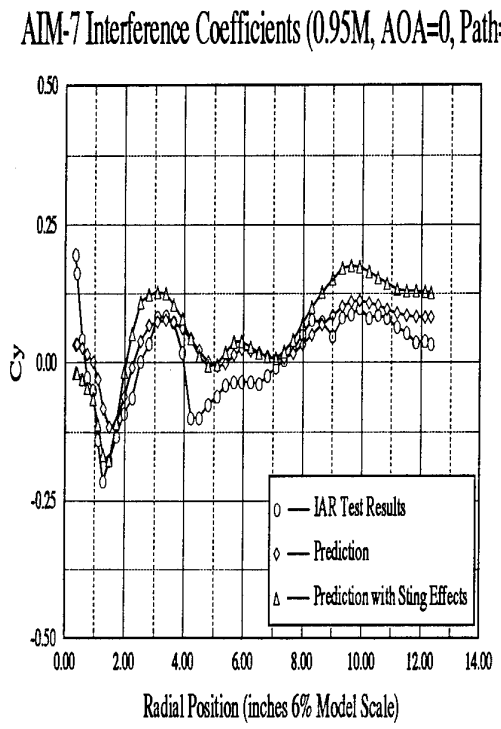

Figure 7a

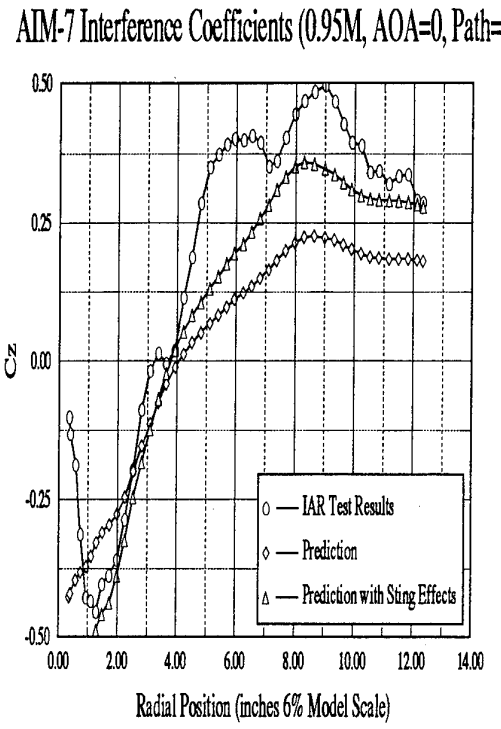

Figure 7c

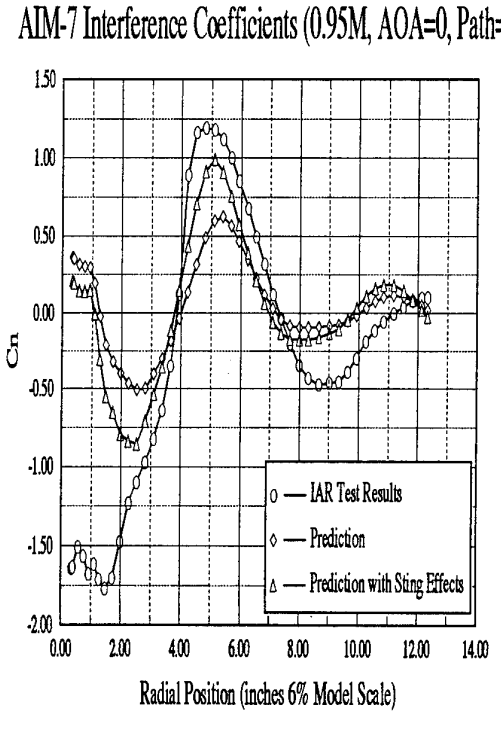

Figure 7b

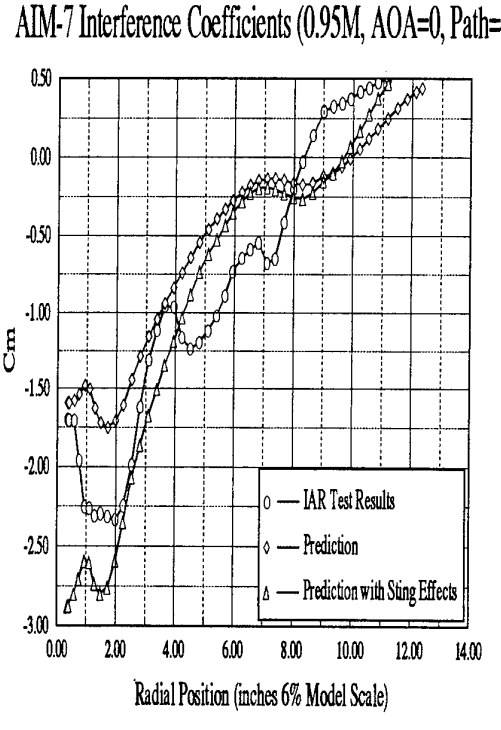

Figure 7d

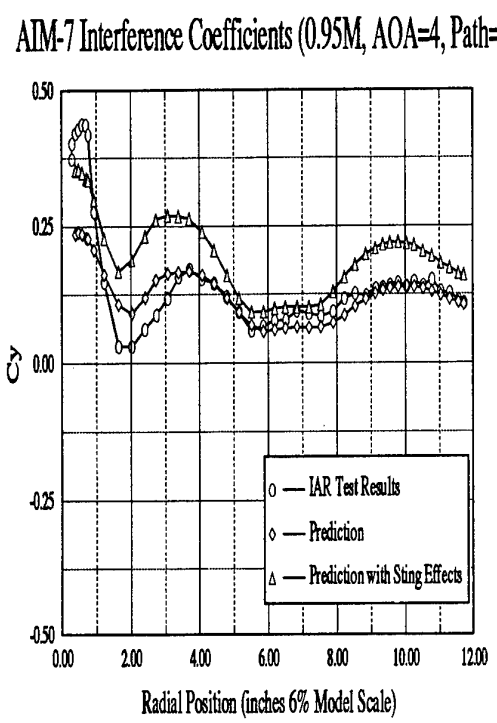

Figure 8a

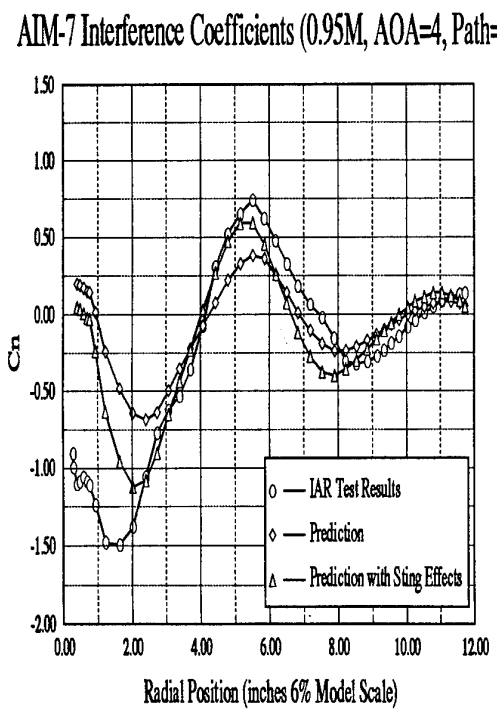

Figure 8b

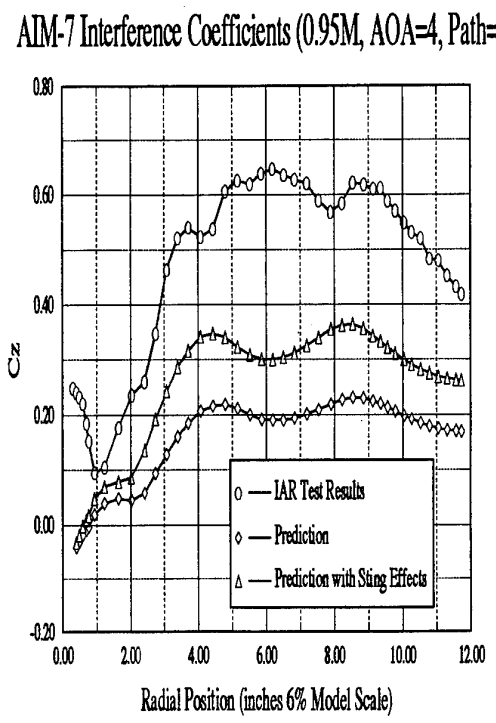

Figure 8c

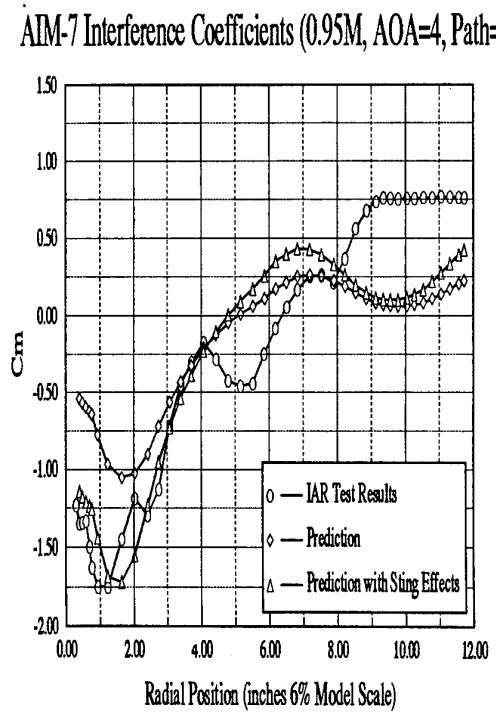

Figure 8d

Predicted normal force interference coefficients are consistently smaller than IAR test results, as shown in figures 6c, 7c and 8c. Also, predictions are significantly smaller than test results for AOA=4°, as shown in figures 6c and 8c. Side force, yawing moment and pitching moment interference predictions are in much better agreement with test results for AOA=4°, as shown in figures 6 and 8. Normal and side force interference coefficients were based on a common set of influence coefficients, since the AIM-7 is a symmetric store. Modifying influence coefficients to improve normal force correlation would therefore diminish side force correlation and modifying KTRAN-M downwash values would diminish pitching moment correlation. Some of the discrepancies between test results and predictions may be due to wind tunnel model imperfections or store/sting misalignment. The AIM-7 moment reference center is located very close to the store wing center of pressure. Therefore if the wind tunnel model's horizontal wing was deflected slightly, normal force correlation could be affected by an increase in AOA without significantly affecting pitching moment correlation. The AIM-7 wing was damaged during the first test for positive aircraft angles-of-attack. This wing was re-aligned by IAR staff, to undetermined levels of tolerance.

Inclusion of sting effects consistently increases values of the interference coefficients, which usually improves correlation with IAR test results.

Correlations between predictions and IAR test results for paths 2 and 3 are similar with correlations for path 4. Results are not included due to space limitations.

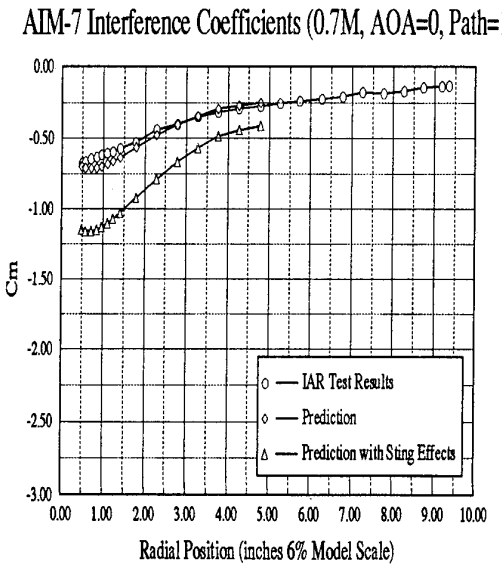

Figure 9a

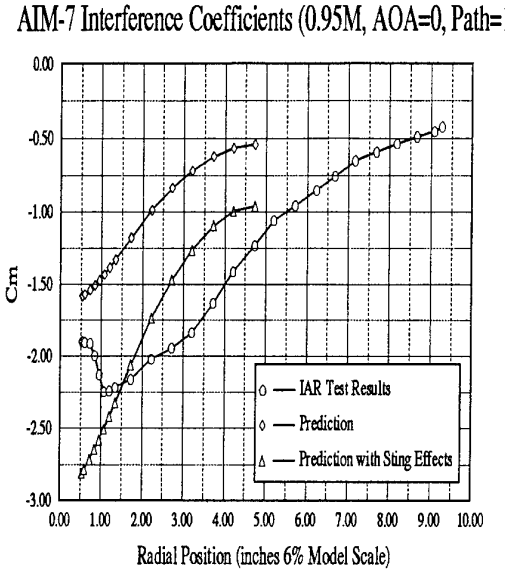

Figure 9b

Correlations between predictions with sting effects and test results are not as good for path 1, as shown in figures 9a and 9b. The technique used to include sting effects is detrimental to the correlation with IAR test results for low transonic or subsonic Mach numbers, but improves correlation for cases at high transonic Mach numbers, as shown in figures 9a and 9b respectively. The AIM-7 position along path 1 remains close to the inboard wing pylon and the tank after-bodies. Pressure recovery near the tails of bodies with substantial taper angles, such as fuel tanks, are typically over-estimated by CFD codes, which do not account for viscous effects. This can further degrade KTRAN-M predictions, since shock strength could be over-estimated and strong shocks cannot be accurately resolved. Evidence of shocks is indicated by the test results, which show a significant effect of Mach number on yawing moment and a lesser effect on side force. Predictions do not reproduce these effects. It may be necessary to include a boundary layer correction on store surfaces in order to improve correlation. Store and sting interference on the aircraft flowfield can also diminish correlation between IAR test results and predictions, since the IDL/IFM method cannot account for these effects.

7. CONCLUSIONS

Predicted interference coefficients are in reasonable agreement with IAR test results for various flow regimes. This demonstrates the viability of the overall approach. The present analytical tool should provide adequate estimates of interference coefficients for a wide variety of test conditions, thereby reducing reliance on wind tunnel test results.

It must be kept in mind that the evaluation of aerodynamic loads in transonic flow on a store ejected from an aircraft with multiple stores is a very difficult aerodynamic problem. The complexity of the flow, which typically includes strong shocks, significant viscous effects and flow separation, is challenging for any CFD method, including the most capable Euler and Navier-Stokes codes. The strength of the present method is that it combines a CFD method (KTRAN-M) with a semi-empirical tool (IDL/IFM) to produce interference loads which would be difficult to significantly improve upon with any other theoretical method. The use of a TSD method with a mesh embedding technique also avoids the generation of body fitted grids required by higher-order methods, which significantly reduces computing time.

Wind tunnel testing is still required to validate predictions for critical cases. Predictions of interference loads for stores located in the carriage position are less accurate, since the IDL/IFM method does not account for effects of the metric store on the aircraft flowfield. Critical cases also occur for metric store locations where the aircraft induced flowfield is dominated by strong shocks and viscous effects, which KTRAN-M cannot account for.

8. ACKNOWLEDGEMENTS

The authors wish to thank DND and Bombardier for their permission to present this paper.

9. REFERENCES

1) F. Kafyeke:
"An Analysis Method For Transonic Flow about Three Dimensional Configurations",
Canadair Report RAZ-000-516, February 1986

2) P. Piperni and F. Kafyeke:
"Enhancement of an Analysis Method for Transonic Flow About Realistic Aircraft Configurations",
Canadair Report RAZ-000-543, April 1989

3) C.W. Boppe:
"Transonic Flow Field Analysis for Wing-Fuselage Configurations",
NASA Contractor Report 3243, May 1980

4) H. Lomax, F.R. Bailey and W.R Balhaus,
"The Numerical Simulation of the Three-Dimensional Transonic Flow with Application to the C-141 Wing",
NASA TN D-6933, August 1973

5) K. Scott Keen:
"A Refined Implementation of the Influence Function and Incremental-Coefficient Methods for Store Trajectory Generation",
AEDC-TR-86-35, October 1986.

FLIGHT TEST TECHNIQUES FOR WEAPON/STORE RELEASE TRAJECTORY ANALYSIS

T. Donaldson
A.D. Gill
Flight Test (W27K)
British Aerospace Defence Limited
Military Aircraft Division
Warton Aerodrome, Warton, Preston
Lancashire PR4 1AX, England

1 SUMMARY

The use of store trajectory prediction techniques is an integral part of a stores release clearance programme. In support of these prediction techniques, it is necessary to produce a highly accurate measured trajectory from the flight trial demonstrations. The procedure used at Warton is based on a mathematical model and a fly - match - fly progression and this paper identifies the techniques used by British Aerospace Warton to calculate the store release trajectories. It identifies the store trajectory analysis system that is currently in use and the system enhancements, which includes an automatic tracking facility, that are being introduced. The aim of the system updgrade is to produce more accurate trajectories in reduced timescales and hence reduce the number of flights and store releases required. This will lead on to a reduction in costs and shorter trials programmes. The paper also identifies future system enhancements that can be introduced that may lead to the advent of real time store trajectory analysis.

2 INTRODUCTION

This paper defines the techniques and systems used by British Aerospace Warton Flight Test department to calculate the nearfield trajectory of stores and weapons when released from an aircraft. It identifies the system that is presently in use and identifies the system enhancements that are currently being introduced and assessed.

3 REQUIREMENT FOR STORE TRAJECTORY ANALYSIS

The procedure currently used at BAe Warton for store safe separation clearance work is based on a mathematical model and a "Fly - Match - Fly" progression as shown in Figure 1.

The mathematical model is the starting point for all stores safe separation work and is based on data inputs such as aircraft flowfield, weapon carriage system characteristics, installed loads, free air aerodynamics and the release/jettison characteristics for each store. The model is used to predict the store behaviour during release and jettison throughout the required flight envelope for a particular aircraft and store combination. The factors that influence store trajectories include:

- Gravity
- Store aerodynamic forces and moments
- Aircraft flowfield
- Flowfield due to adjacent stores
- Aircraft/store mutual interference effects
- Initial release velocity and store pitch rate given by the ejector release unit(ERU)
- Store attachment flexibility
- Store physical characteristics, mass and CG
- Motor thrust characteristics for powered stores
- Physical restraints, rail hangar, hooks
- Parachute deployment characteristics for retarded stores

The aircraft flowfield has a dominant effect on the store trajectory behaviour and can be generally divided into three zones as shown in Figure 2.

Based on the mathematical model, a flight condition is defined at which a release trial is to be carried out at, and from which it will be possible to validate the store release model. In support of this, the requirement is that Flight Test produce an accurate measured trajectory from the flight trial demonstration. Accuracy is essential in order to reduce the number of flights and store releases required to a minimum and hence reduce costs and shorten trials programmes.

Paper presented at the AGARD FDP Symposium on "Aerodynamics of Store Integration and Separation", held in Ankara, Turkey from 24-27 April 1995, and published in CP-570.

4 VIDEO IMAGING STORE TRAJECTORY ANALYSIS (VISTA)

The system used by BAe Flight Test is called VISTA and has been in use since 1984. This was developed by BAe and consists of a number of pieces of hardware linked together to operate as a complete system via a PDP11/34A computer. The major elements of hardware are shown in Figure 3 and comprise:

i. 16mm manually operated Cine Film Projector and Video Camera (Telecine unit) which is used to convert the film images to video.

ii. Colour graphics processor and computer VDU which are used to give "at a glance" information regarding the stores trajectory with graphical displays of displacement in each of the six degrees of freedom against time. Manipulation of the computer generated image is achieved using a Data Tablet which allows control of the image in each of the six axis.

iii. Random access hard and floppy discs for picture and data storage.

The analysis technique is based on superimposition principles. Images recorded in flight by onboard high speed cine cameras using 16mm wet film are displayed on a TV monitor via a video processor. The Flight Test engineer controls the position and attitude of a computer generated outline image of the store which is produced based on the the camera lens type fitted and the relative positions of the camera selected and the store position. The operator places the computer generated outline over the store image and by analysis of several camera views, in conjunction with the computer generated store image, this allows a progressive build up of the store positional data culminating in a three dimensional and rotational trajectory of the store release.

5 ANALYSIS SUPPORT REQUIREMENTS

In support of the VISTA analysis there is a large amount of setting up work to be done prior to the flight trial as detailed below.

i. An accurate 3D model of the store to be released must be input into the computer.

ii. The position of the aircraft reference markers which are identified as fixed points from an analysis point of view, and camera positions within the relevant pods must be input into the system.

iii. A synchronised camera system should be used where possible such that each film frame from different cameras views the store at the same instant in time. It is possible to use non-synchronous cameras, but a procedure to identify the time differences between different frames on the cameras is required.

iv. Corrections for the camera lens should be incorporated within the computer.

6 VISTA OPERATION

Once the film has been processed and having established the frame rates for each camera, the general philosophy for VISTA is to build up a trajectory in three dimensions by use of a logical sequence of camera views and superimposing the outline of the computer generated store image upon them. Certain camera views will provide better opportunity for analysis of specific parameters than others, and individual cameras will view the store over different timeslices.

VISTA offers three levels of operation for performing an analysis:

Level 1:

This allows analysis of a single camera view and superimposition of the store image throughout the viewed trajectory.

Level 2:

This allows the display of two camera views of the same time frame to be viewed sequentially, allowing the operator to modify the store outline on one camera view and select the second view on the other camera to see how the outline is positioned over the image from that frame.

Level 3:

This allows the display of two camera views simultaneously allowing the operator to visually assess the effects of store manipulation on both the current camera view and a previously stored camera view. This facility is invaluable for determination of lateral store movement and its coupled effect on vertical movement. Similarly the pitch/yaw interplay can be more accurately determined. To carry out Level 3 analysis, it is essential that the frames being analysed are matched in time.

Due to the advantages that Level 3 analysis offers over Level 2, it has been found that in practice only Level 1 and Level 3 are used for full analysis.

A normal analysis would generally consist of starting in Level 1 and selecting a camera which has a good view of the store to be released/fired when in its installed position on the aircraft. At least three aircraft reference markers should be in view and a good overlay of these markers should be obtained throughout the camera analysis. This allows for any wing bending or camera pod movement and is achieved by manipulation of the camera orientation and focal length using the data tablet. Once this has been achieved, a good fit of the store outline in the installed position should automatically follow. The film is then progressed using a suitable frame increment, which is selected dependant on the store/weapon type being released, by matching the overlay of aircraft reference markers and store outline respectively. This continues until the store passes out of view or is too small to match, and the analysed trajectory is saved.

A second camera is then chosen and using the trajectory from the previous camera it is possible to confirm the trajectory trend. Adjustments can be made to improve the overall fit and the modified trajectory is saved. This method can continue, using each available camera, or it is possible to return to the original camera and start a more detailed analysis using Level 3, storing the pictures onto disc. The second and subsequent cameras are selected to allow comparison and manipulation of the store outline on the two camera views.

Throughout the analysis, confirmation of a smooth consistent trajectory is obtained via displays of each parameter on the VDU. This is useful for identifying any obvious errors that may occur in positioning the store outline and identifying any Y/Z displacement errors or pitch/yaw attitude errors.

On completion, data is stored onto disc and the trajectory analysis is passed over to the design department for them to validate their mathematical model. The cycle then continues as they determine the next flight condition for a release trial.

7 PROBLEMS WITH VISTA

The problems for VISTA and the technique used for analysis is that it is costly and time consuming, but it is reliable and reasonably accurate. The main error associated with this technique can be put down to the interpretation of the store position and orientation by the analyst. The main costs associated with this system can be attributed to two factors:-

i. The time taken to acquire and process the imagery.

ii. The time taken to match a model of the store to multiple frames of imagery and different camera views to calculate the trajectory.

To improve on the errors associated with the engineers interpretation of the store position and orientation and reduce analysis time, an automatic tracker has been and is still being developed by the British Aerospace Sowerby Research Centre and is a major part of the upgrade that the system is currently undergoing as an upgrade to the VISTA system.

8 VISTA UPGRADE

Sowerby Research centre were originally approached to identify a replacement for the VISTA system taking advantages of the latest image processing and analysis techniques.

The requirement for the new system was to act as an assistant to the Flight Test Engineer automatically tracking the stores under his supervision. The original objective was that the tracking system should operate in real time but for this to be possible, the aircraft would have to transmit high speed video image data back to the ground for analysis. However, it was recognised that this is not likely in the near future and therefore the new system uses digitised cine film as at present.

The aim of the automatic system is to free the Engineer from the drudgery of manual tracking whilst considerably speeding up the trajectory analysis. The automatic system will enable the data to be analysed in more detail since every frame can be measured instead of a representative sample as at present.

The framework upon which SRC worked in order to produce the system was:

i. All 6 parameters of position and orientation of the store relative to the aircraft must be found ie. Pitch, Roll, Yaw, X, Y and Z.

ii. Camera positions are known and calibrated as is the starting position of the store.

iii. Predicted models of the store trajectory exist.

iv. Tracking should be automatic as far as possible with little operator intervention beyond a monitoring role. However, in order to make tracking easier the operator may alter various parameters at the start of a run(such as

designating features on the store). In the event of a failure of the automatic mode the operator should have the capability of correcting the problem and continuing the run.

v. The processing time to locate the store in the image should be approximately 1 to 2 seconds per frame.

9 ARTIP (AUTOMATIC REAL TIME IMAGE PROCESSING)

The new system that has been developed as an update to VISTA has been named ARTIP and a layout of this system is shown in Figure 4.

The aim of the new system is to track a store throughout a complete release sequence. This is achieved by identifying the best fit between a computer generated image of the store and the image data supplied by the onboard cameras. At each frame, the software uses a prediction of the current store position with respect to the aircraft to calculate the projection of visible features on the store within the image data using edge detection techniques. Once these features have been located in the film image, the software adjusts the predicted store position until the computer generated image projections fit the detected features.

10 ANALYSIS SUPPORT REQUIREMENTS

The support requirements are the same as those required for the standard VISTA analysis with the addition of the following:

Predicted Store Position:

The system requires an accurate estimate of the store position for the first three time frames to be analysed which is stored within a data file. After the first three frames, predictions of store position are calculated taking into account the previous store positions. It has not been decided how this information would be provided, though there are 3 main possibilities:

i. Use the aerodynamic pre-flight predictions

ii. Use some form of equation to define predicted position dependant on the store type to be released

iii. Manually position the store outline over the store image for the first three time frames and then the system would use these values to calculate the predicted store position.

Store Markings:

To aid the automatic tracker, it will be necessary to mark up the store with areas of high contrast such that edges are well defined. This will include identifying specific schemes to highlight motion in specific orientations eg. Bands on the nose and fins to identify roll. This information is input into a data file for use by the automatic tracking routine.

11 SYSTEM OPERATION

As with VISTA, the cine film will have to be processed and the frame rates established for each camera. Analysis is then carried out by analysing two cameras at a time which can view the store over a similar time period. Ideally, for best analysis, the cameras should provide orthagonal views of the store to be released. Once the relevant cameras and frames have been selected, the system offers two modes of operation.

Semi - Automatic:

In this mode, the initial predicted position is displayed for the store. The operator can then manually adjust the position of the store outline if required. Once complete, the next time frame is selected and the model moves to the new predicted position. This procedure then continues for each time frame to be analysed thus reducing the time required to manipulate the computer generated image over the store position.

Automatic:

In this mode, feature detection and model fitting proceed with no user involvement necessary. This continues through all the time frames to be analysed.

12 SYSTEM OUTPUTS

The output from the system consists of the calculated trajectory of the store relative to the aircraft along with graphs showing predicted and calculated plots over the trajectory for each of the six degrees of freedom. A set of graphics illustrating the estimated store position overlaid on each of the camera images is also available if required.

With both VISTA and ARTIP, the calculated trajectories are automatically converted into the axis convention required by the design department for them to use and update their original model.

13 FUTURE IMPROVEMENTS

Telemetry Data:

A large number of new test vehicles developed for release trials of weapons such as AMRAAM and ASRAAM are now fitted with telemetry packs which are operational during the release and can provide acceleration data. This information can then be integrated to calculate displacement. It is foreseen that this data can be fed directly into the ARTIP system and when the cine film has been processed and is available, the image frames can be run through automatically using this data. The operator can then make manual modifications to the store outline to refine the position if required.

High Speed Video:

When high speed video becomes available in a suitable package for fitment in aircraft camera pods, the ability to transmit this image back to the ground will make the possibility of real time analysis a reality. ARTIP could be used in the automatic tracker mode for stores without telemetry and if the store does have telemetry, then this information could be used as described above. This capability will be the major breakthrough in the advent of real time store trajectory analysis.

FIGURE 1: 'FLY-MATCH-FLY' FLIGHT TRIALS PHILOSOPHY

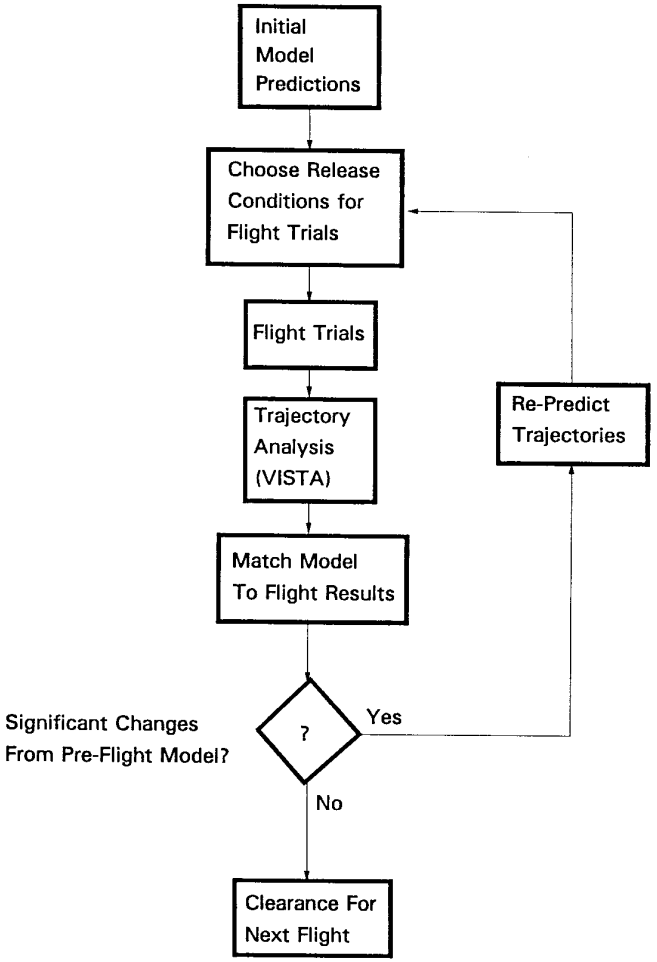

FIGURE 2: AIRCRAFT FLOW FIELD ZONES

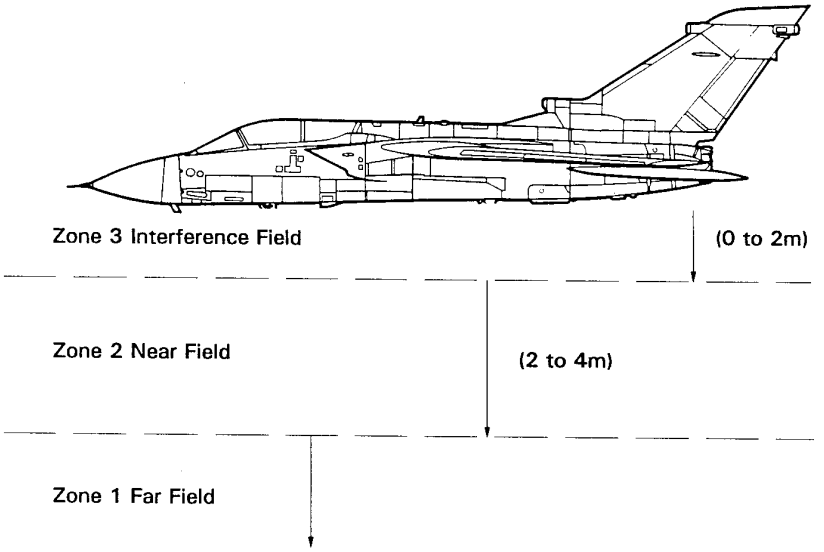

Zone 1 - Far Field
In this zone the flow is completely free stream.
It is not influenced by the presence of the aircraft.

Zone 2 - Near Field
In this zone the flowfield is influenced by the presence of the aircraft. Flow direction, local Mach Number and dynamic pressure are all assumed to be influenced by the presence of the aircraft.

Zone 3 - Interference Field
In this zone, the flowfield is affected by both the presence of the aircraft and the presence of the store due to mutual interference between them.

FIGURE 3: VISTA SYSTEM SCHEMATIC

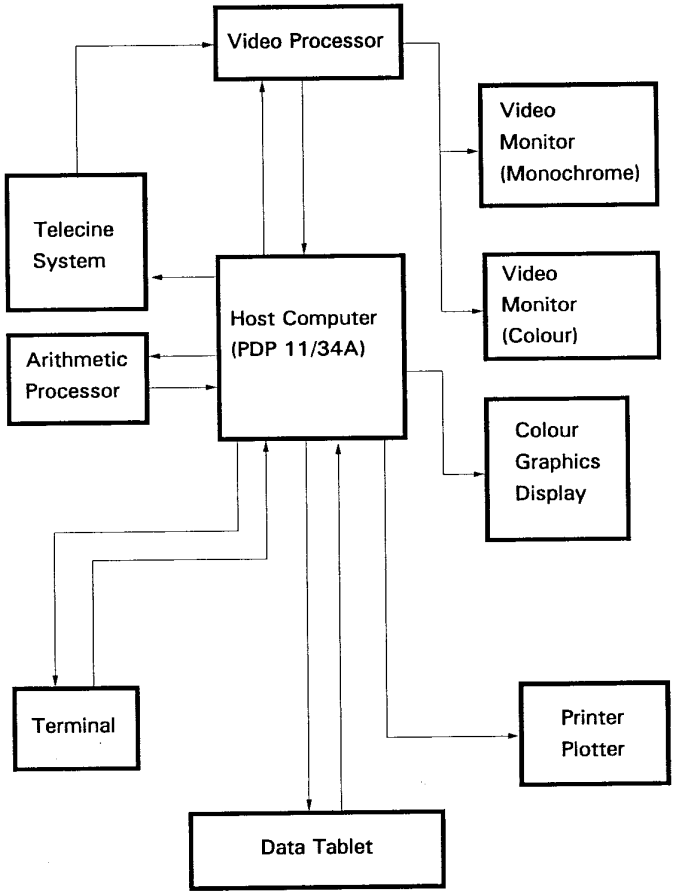

FIGURE 4: ARTIP SYSTEM SCHEMATIC

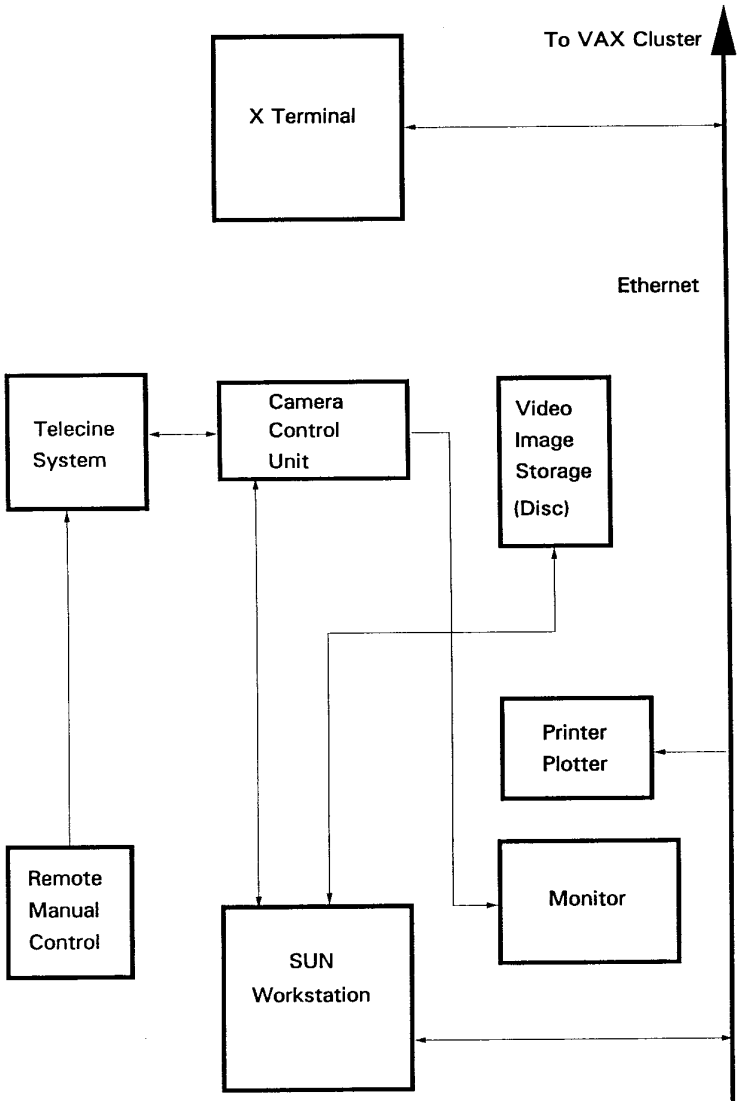

Navier-Stokes Solutions Of Turbulent Transonic Cavity Flows

J.L. Tracey
B.E Richards
Department of Aerospace Engineering
University of Glasgow
Glasgow, G12 8QQ, UK

Abstract. A code has been developed to model the flow over cavities. An implicit, finite volume technique is used to solve the two and three dimensional Navier-Stokes equations. Turbulence is modelled using the Baldwin-Lomax model with the Degani-Schiff modification. Solutions are presented for two test cases, the results of which are compared with experimental data and Rossiter's model.

1 Introduction

Cavities occur in aerospace applications such as undercarriage wheel wells or as storage areas on aircraft. Experimental studies [1] [2] have shown the flow within the cavity can be complex and have identified different types of flow which can occur depending on the geometry and freestream flow.

Motivated by the development of the next generation of military aircraft the analysis of cavity flows is receiving attention. The incorporation of stealth technology and the constant aim of decreasing drag has resulted in increasing importance being attached to the housing of missiles within the aircraft body. Internal storage has the effect of reducing the aircraft cross sectional area and in turn its succeptibility to detection by radar. The resulting decrease in cross sectional area also reduces the drag.

Cavity flows can be seen, under certain conditions, to exhibit characteristics which are undesirable. For instance, the flow over a shallow cavity will result in a large pressure differential between the front and rear of the cavity which will result in a moment acting on the store housed within. This moment may be large enough to affect and inhibit the launch of a missile. Under certain conditions deep cavities experience self-sustaining pressure oscillations which may be of such a strength as to cause structural damage or damage to sensitive electrical equipment that may be stored within the cavity.

The high cost of wind-tunnel testing coupled with the ongoing development and increasing use of computational fluid dynamics(CFD) has made necessary and possible the application of CFD to the solution of cavity flows [3] [4] [5] [6] [7] [8] [9]. The presence of a transonic, separated, highly unsteady and three-dimensional flow results in a challenging CFD problem which is computationally time-consuming and expensive to solve. The adequate resolution of the unsteady flow features is computationally intensive. In addition the transonic flow regime necessitates the use of a sophisticated and time consuming solution algorithm. Typically the flows of interest are at high Reynolds number so that a large number of grid points are needed in order to resolve the boundary layer. The resulting small cell sizes limit the maximum allowable time step, further increasing the computational overhead. The turbulent nature of the flow at these Reynolds numbers adds to the complexity of the problem and a turbulence model needs to be used to resolve the turbulent quantities of the flow.

This paper describes the various types of cavity flows as well as the method used to solve the flowfield. Results are presented for the flow over deep and shallow cavities.

2 Classification Of Cavity Flows

The flow over a cavity is characterised by a shear layer separating the relatively high speed external flow from the low speed flow in the cavity. Three types of cavity flow have been identified and can be characterised by the length to depth (L/D) ratio of the cavity.

The first of these flows occurs for $L/D < 10$ (Fig.1) and is termed open flow. In this case the shear layer bridges the cavity opening and reattaches downstream of the cavity trailing edge. The pressure remains slightly above the freestream value along most of the length of the floor but rises towards the rear of the cavity as the shear layer impinges on the rear

Paper presented at the AGARD FDP Symposium on "Aerodynamics of Store Integration and Separation", held in Ankara, Turkey from 24-27 April 1995, and published in CP-570.

face. When L/D>13 (Fig.3) the shear layer separates as the flow expands on entering the cavity before reattaching on the cavity floor. The flow separates once again before leaving the cavity and reattaching downstream. This type of flow is termed closed cavity flow. The expansion around the front face creates a low pressure region. A pressure plateau slightly above freestream occurs over the impingement region while the pressure rises sharply towards the rear of the cavity as the shear layer impinges on the rear face. Intermediate cavity flow occurs when 10<L/D<13 and the flow periodically exhibits characteristics of both the open and closed types (Fig.2).

In the case of the deep cavity self-sustaining pressure oscillations can occur. These fluctuations become increasingly random as the length to depth ratio increases. Various analytical studies [10] [11] [12] have attempted to describe the mechanism by which these oscillations occur and to predict their frequencies. Rossiter proposed a model for the prediction of the frequencies of oscillation based on the shedding of vortices from the front cavity lip. This was adapted by Heller, Holmes and Covert [13] to account for the different speed of sound in the cavity. Rossiter's adapted formula is shown below:-

$$f=\frac{U_\infty}{L}\frac{m-\alpha}{\beta+\frac{1}{k_v}} \qquad (1)$$

where:-

$$\beta=\frac{M_\infty}{(1+\frac{(\gamma-1)}{2}M_\infty^2)^{\frac{1}{2}}}$$

and α and k_v are constants that have the empirically derived values of 0.25 and 0.57 respectively.

3 Mathematical Formulation

The modelling of the cavity flowfield requires the solution of the Navier-Stokes equations. Simplifications to this set of equations such as the thin layer approximation are not appropriate due to the presence of multiple walls. The conservation laws are Reynolds-Averaged and expressed in integral form as shown:-

$$\frac{\partial}{\partial t}\int_\Omega \mathbf{Q}d\Omega+\int_S(\mathbf{H}.\mathbf{n})dS=0 \qquad (2)$$

where, in two dimensions, S represents the surface of a cell of area Ω with normal $\mathbf{n}$, and $\mathbf{Q}$ is the vector of conserved variables:

$$\mathbf{Q}=(\rho,\ \rho u,\ \rho v,\ E_t)^{\mathrm{T}}$$

where ρ represents the density and u and v are the velocity components. The flux tensor $\mathbf{H}$ can be expressed in terms of the Cartesian fluxes:-

$$\mathbf{H}=(\mathbf{E}^i-\mathbf{E}^v)\mathbf{i}+(\mathbf{F}^i-\mathbf{F}^v)\mathbf{j} \qquad (3)$$

where the superscripts i and v refer to the inviscid and viscous fluxes respectively. These fluxes are expressed as:-

$$\mathbf{E}^i=[\rho u,\ \rho u^2+p,\ \rho uv,\ (E_t+p)u]^{\mathrm{T}}$$

$$\mathbf{F}^i=[\rho v,\ \rho uv,\ \rho v^2+p,\ (E_t+p)v]^{\mathrm{T}}$$

$$\mathbf{E}^v=[0,\ \tau_{xx},\ \tau_{xy},\ u\tau_{xx}+v\tau_{xy}-q_x]^{\mathrm{T}}$$

$$\mathbf{F}^v=[0,\ \tau_{xy},\ \tau_{yy},\ u\tau_{xy}+v\tau_{yy}-q_y]^{\mathrm{T}}$$

where E_t, τ and q represent the energy, shear stress and heat conduction terms which can be expressed as follows:-

$$E_t=\frac{p}{(\gamma-1)}+\frac{1}{2}\rho(u^2+v^2)$$

$$\tau_{xx}=\frac{2}{3}\mu(2\frac{\partial u}{\partial x}-\frac{\partial v}{\partial y})$$

$$\tau_{yy}=\frac{2}{3}\mu(2\frac{\partial v}{\partial y}-\frac{\partial u}{\partial x})$$

$$\tau_{xy}=\mu(\frac{\partial u}{\partial y}+\frac{\partial v}{\partial x})$$

$$q_x=-k\frac{\partial T}{\partial x},\ q_y=-k\frac{\partial T}{\partial y}$$

The finite volume method discretises the integral form of the Navier-Stokes equations and as a result the quantities of mass, momentum and energy will remain conserved at the discrete level. This important property of the method allows the accurate resolution of flow discontinuities such as shock waves. The finite volume discretisation of (2) can be written as:-

$$\frac{\partial}{\partial t}(\Omega_{i,j}\mathbf{Q}_{i,j})+\overline{\mathbf{E}}_{i+\frac{1}{2}j}-\overline{\mathbf{E}}_{i-\frac{1}{2}j}+\overline{\mathbf{F}}_{ij+\frac{1}{2}}-\overline{\mathbf{F}}_{ij-\frac{1}{2}}=0 \qquad (4)$$

where $\overline{\mathbf{E}}_{i+\frac{1}{2}j}$,$\overline{\mathbf{E}}_{i-\frac{1}{2}j}$,$\overline{\mathbf{F}}_{ij+\frac{1}{2}}$,$\overline{\mathbf{F}}_{ij-\frac{1}{2}}$ refer to the values of the flux functions evaluated at the cell interfaces.

The algorithm calculates cell-centred values, interpreted as cell averages, for the flow variables. Fluxes are evaluated at the cell interfaces with the dependent variables extrapolated onto the interface using the MUSCL extrapolation [14] with a limiter to avoid spurious oscillations in the solution around discontinuities. The inviscid fluxes are evaluated at each cell interface using Osher's approximate Riemann solver while the viscous fluxes are calculated using central differences.

3.1 Time-Stepping Scheme

Both explicit and implicit time-stepping schemes have been incorporated in the code. Although the implicit algorithm requires more memory and is more complicated to program than the explicit scheme, the implicit method has been used in the current calculations. This is due to the fact that stability considerations require a far smaller time step to be used with the explicit method. Although the explicit scheme requires less cpu time per iteration the larger time steps possible using the implicit method mean that far fewer iterations are needed to obtain the unsteady solution. In this respect the implicit scheme is, on average, three times faster than the explicit method. The memory rquirements for each version are 16Mb

and 1.9Mb for the implicit and explicit methods respectively on a grid with approximately 8100 points. The code employs the implicit ADI scheme to update the conserved flow variables at each time step. One implicit step can be written as:-

$$(\mathrm{I}+\Delta t\frac{\partial \mathrm{R}_x^n}{\partial \mathrm{Q}})(\mathrm{I}+\Delta t\frac{\partial \mathrm{R}_y^n}{\partial \mathrm{Q}})\Delta \mathrm{Q}=\Delta t(\mathrm{R}_x^n+\mathrm{R}_y^n) \qquad (5)$$

In the above equation we have adopted the notation that the discrete nonlinear system to be solved is written as $\mathbf{R}(\mathbf{Q}) = 0$ where the elements of $\mathbf{R}$ consist of the cell based residuals arising from the spatial discretisation of the Navier-Stokes equations and $\mathbf{Q}$ is the vector of the cell based conserved flow quantities. $\partial \mathbf{R}_x^n / \partial \mathbf{Q}$ and $\partial \mathbf{R}_x^n / \partial \mathbf{Q}$ are the Jacobian matrices with respect to the conserved variables $\mathbf{Q}$ and:-

$$\Delta \mathbf{Q}=\mathbf{Q}^{n+1}-\mathbf{Q}^n$$

where n+1 and n refer to the updated and previous time steps respectively.

3.2 Boundary and Initial Conditions

At solid surfaces the no-slip boundary condition is specified, while the adiabatic condition is applied to the temperature.

$$u_{wall}=v_{wall}=0, \frac{\partial T}{\partial \mathrm{n}}=0$$

Characteristic boundary conditions are used for the inflow, outflow and farfield boundaries.

The unsteady computation is started from an approximate solution obtained from a steady cavity code which has also been developed. This solution takes 30mins to obtain on a Silicon Graphics Indy workstation with a R4400 processor and ensures that the unsteady computation is started from a solution with the boundary layer upstream of the cavity fully developed. The following initial conditions are set for the steady computation. In the freestream:-

$$u=U_\infty, v=0, T=T_\infty, p=p_\infty$$

and in the cavity static conditions are assumed:-

$$u=v=0, T=T_{wall}, p=p_\infty$$

These initial conditions are set in order to approximate, as closely as possible, the conditions above and in the cavity.

3.3 Turbulence Modelling

Turbulent effects are taken into account using the Baldwin-Lomax algebraic turbulence model [15]. Although developed and used successfully for attached or mildly separated flows the simplicity and speed of the model makes it an attractive proposition for the current study. Without modification, however, the model computes erroneously high values for the turbulent viscosity in the cavity which significantly affects the solution. The presence, in the cavity, of a large vortical structure is a source of error in the turbulent viscosity which can be eliminated by incorporating the Degani-Schiff [16] modification. This will not eliminate all the errors associated with the turbulence model as there is no capability within the model to account for turbulent history effects.

4 Test Cases

The following test cases are presented. The test cases were chosen to validate the code against experimental data of both open and closed cavity flow types. The experimental data for each test case was obtained by Tracy and Plentovich [17]. The computational grid used in the 2D computation for test case 1 is shown in Fig(4). For both the test cases the cavity length is 0.28575m, with a depth of 0.0649m and 0.0143m for case 1 and 2 respectively. Both the test cases employ 113x41 grid points in the freestream and 85x41 points in the cavity. This ensures that the boundary layer upstream of the cavity opening was resolved with at least 15 grid points. The value of y^+ in the cell adjacent to the solid surface was between 1 and 5. This was considered adequate to resolve the laminar sublayer. The values of Reynolds' numbers in Table 1 are based on the cavity length.

case	L/D	M_∞	Reynold's no.
1	4.4	0.9	2.81×10^7
2	20	0.6	2.81×10^7

Table 1. *Test cases*

5 Results and Discussion

5.1 Case 1

Case 1 is flow over an open cavity. The unsteady solution was allowed to progress for 0.011secs, corresponding to seven characteristic times. This was sufficient to allow the initial transients to decay. The characteristic time is defined as the time taken for a fluid particle to travel the length of the cavity(L) at freestream velocity. The computational data was then stored for the purpose of analysis.

The computed time-averaged pressure coefficient along the cavity floor is compared with experimental data and displayed in Fig(5). The computed values show qualitative agreement with the pressure rise towards the rear face being picked up. The data shows a large difference from the experimental values at $x/L = 0.6$. The solution obtained from the steady code is also displayed. The large difference between this solution and the time-averaged experimental data illustrates the unsteady character of this problem.

For the purposes of the unsteady analysis computed pressure data was recorded over a time of 8ms at each of the 85 points along the cavity floor. In this time the data was seen to vary greatly. Fig(6) shows the spread of values on the cavity floor by displaying the time-averaged value along the cavity floor together with the maximum and minimum values recorded at each point. This result in conjunction with the lack of agreement obtained from the *steady* state solution shows the unsteady nature of this test case.

Individual values of pressure were computed at x / L = 0.3 and a Fast Fourier Transform(FFT) was carried out on the time history pressure data in order to determine the dominant frequencies of oscillation. For this purpose 13000 data samples were taken in a sample time of 0.020855secs. This corresponds to a resolution of 48Hz. The results of the FFT carried out on the computed time pressure history can be seen in Fig(7). The values of frequency derived from Rossiter's model and the experimental data can be seen in Table(2). As can be seen from Fig(7) the code predicts the first two frequencies with values of 155Hz and 430Hz. The code also predicts some additional frequencies, such as 290Hz, which were not predicted by Rossiter's method or evident in the experimental data.

method	mode 1(Hz)	mode 2(Hz)	mode 3(Hz)
experiment	170	435	695
Rossiter	182	427	666

Table 2. *Oscillatory frequencies derived by experiment and Rossiter's formula*

Fig(12) shows the computed streamlines in the cavity at three time instants. They correctly show the shear layer bridging the cavity opening and a number of vortices in the cavity. Fig(12a) shows a vortex at x/L =0.2 which has been shed from the front of the cavity. 0.0008secs later this vortex has travelled downstream and can be seen at x / L = 0.3 in Fig(12b). At time t=0.0016secs the vortex is centred at x / L = 0.5 as shown in Fig(12c). The appearance of these vortices travelling downstream in the cavity seems to indicate the method has captured the periodic vortex shedding from the front lip.

In total this computation took 27.5hours on a Silicon Graphics Indy workstation with a R4400 processor.

5.2 Case 2

Case 2 is the flow over a closed cavity. In this case the flow should approach a steady state solution. As for case 1 the starting solution for the unsteady calculation was obtained from the steady code. The unsteady computation was allowed to progress for five characteristic times before data was stored for analysis.

The pressure coefficient along the cavity floor was obtained by averaging over 5.85ms, equivalent to one characteristic time. Fig(8) shows the comparison of pressure coefficient along the floor with the experimental data. The computed results show qualitative agreement with the experimental values in that the pressure coefficient is negative towards the front of the cavity and rises towards the rear. The computation fails, however, to resolve the pressure plateau over the centre part of the cavity floor and significant differences occur between the experimental and computed values at the front of the cavity. Also included is the solution obtained from the steady code.

The spread of computed values of pressure coefficient along the cavity floor obtained from the unsteady calculation is shown in Fig(9). These are displayed by plotting the time-averaged pressure coefficient along with the maximum and minimum values computed at each of the points along the cavity floor. As in case 1 there is a large spread of values. This was not expected for case 2 and may indicate the importance of modelling the third dimension for a shallow cavity.

The pressure at x/L = 0.3 was computed 72,000 times over 0.042secs. This is equivalent to a resolution of 23.8Hz. The FFT analysis of this computed pressure time history is shown in Fig(10). No dominant frquencies are observed which was expected for a shallow cavity.

As was stated above the large variation in time of the pressure along the cavity floor was not expected. As a result it was thought necessary to model the flow using the 3D Navier-Stokes equations. A code was developed by which this could be achieved and case 2 used as a test case.

Due to memory restrictions the computation was carried out on a relatively course grid which had 55x31x41 points in the freestream and 35x25x21 points in the cavity. A converged solution was obtained in 37 hours on an IBM RS6000 Model 320H.

The values of pressure coefficient along the cavity floor obtained at three instants during the steady 3D computation are shown in Fig(11). As can be seen from this diagram the 3D steady solution is in better agreement with the time-averaged experimental data than is the solution obtained from the 2D computation Fig(8). The 3D version resolves the pressure plateau over the centre section of the cavity which was not achieved with the 2D code. At the front area of the cavity the steady solution predicts the negative pressure coefficient while the large rise in pressure at the rear face is also picked up. The only poor part of the solution occurs for $0.85 < x / L < 0.95$ where the code underestimates the pressure. This is also the area in which the solution varies the most. As a result it would be necessary to carry out an unsteady 3D calculation

in order to resolve the time-averaged pressure coefficient in this region of the cavity.

Fig(13) shows the computed streamlines at three spanwise positions ($\frac{z}{w}$ = 0.5, 0.25,0.1, where w is the width of the cavity) in the cavity as computed by the steady 3D code. The cavity height has been magnified by a factor of two for clarity. It can be seen that the shear layer has separated at the entrance to the cavity before reattaching on the cavity floor as expected. The flow separates once again before leaving the cavity. The three-dimensional affects are illustrated by the differences in the solution at each of the spanwise positions.

6 Conclusions

The two test cases represent the two extremes of cavity flow, case 1 being of the open type and case 2 a closed flow. The characteristics of each type of flow have been captured and the results obtained from the code have been compared with the experimental data. For case 1 the computed frequencies have been compared with Rossiter's model for the prediction of the oscillatory frequencies of an open cavity.

The differences between the computed and experimental results can be explained as follows. Firstly, in the computational analysis, the data used for the time-averaging of the pressure values along the cavity floor was obtained by sampling twelve times in the course of one characteristic time. This is significantly less than the time over which the data was sampled for the experimental analysis. For the purpose of the FFT, data was sampled at one point on the cavity floor. Although an implicit time stepping scheme was used, the restriction on the maximum time step was such that a resolution of 48Hz for case 1 and 23.8Hz for case 2 could be achieved in the computed FFT values. This compares with a resolution of 3Hz in the experimental values.

The turbulence model is also a source of error. Although modifications were made to the Baldwin-Lomax model to account for the separated flow in the cavity no account is taken of the turbulent history effects which will be important in this type of flow.

The flow in a cavity is strongly three dimensional and errors in the results have been introduced as a result of modelling the flow using the two-dimensional Navier-Stokes equations. A three-dimensional model has been developed and initial validation has indicated that it is extremely time consuming when applied to the unsteady flow within cavities. The steady 3D code has been run on a shallow cavity (case 2) which is expected to exhibit a solution which on the whole does not vary significantly with time. Comparison of the results from the 2D and 3D steady codes for case 2 highlights the improved results obtained with the 3D version.

It would be beneficial to run the 3D unsteady code on a deep cavity although this would require a large amount of computing power. As a consequence of the large run times necessary for a unsteady three-dimensional computation the code is being developed for use in a parallel environment. This has been achieved, initially in two dimensions, using the Parallel Virtual Machine (PVM) message passing routines for the transfer of data between processors.

The study has shown that the code is able to capture the characteristics of the different types of cavity flow. In addition reasonable quantitive comparisons can be made with both the experimental data and Rossiter's model. The use of a three-dimensional solver and improvment in the resolution of the sampled computational data would improve the accuracy of the computation.

7 Acknowledgements

The work detailed in this paper was supported by the Defence Research Agency. The authors wish to thank Mr. Trevor Birch and Dr. John Ross of DRA(Bedford) for their assistance in producing this paper, Dr. K.J.Badcock of the Aerospace Engineering Dept. at Glasgow University for guidance in developing the code and DRA Bedford for supplying the experimental data.

REFERENCES

[1] Krishnamurty K. Acoustic radiation from two-dimensional rectangular cutouts in aerodynamic surfaces. *N.A.C.A TN-3487*, 1955.

[2] Roshko A. Some measurements of flow in a rectangular cutout. *N.A.C.A TN-3488*, 1955.

[3] Hankey W.L Shang J.S. Numerical solution of the Navier-Stokes equations for supersonic turbulent flow over a compression ramp. *A.I.A.A Paper 75-3*, 1975.

[4] Om D. Navier-Stokes simulation for flow past an open cavity. *A.I.A.A Paper 86-2628*, 1986.

[5] Stallings R.L Baysal O. Computational and experimental investigation of cavity flowfields. *A.I.A.A Paper 87-0114*, 1987.

[6] Suhs N.E. Computations of three-dimensional cavity flow at subsonic and supersonic Mach numbers. *A.I.A.A Paper 87-1208*, 1987.

[7] Rizzetta D.P. Numerical simulation of supersonic flow over a three-dimensional cavity. *Journal of Computational Physics*, 1988.

[8] Baysal O Stallings R.L. Computational and experimental investigation of cavity flowfields. *A.I.A.A Journal*, Vol.26, January 1988.

[9] Hillier R Soltani S. An experimental and computational study of hypersonic cavity flows. *A.I.A.A Paper 94-0766*, 1994.

[10] Rossiter J.E. Wind-tunnel experiments on the flow over rectangular cavities at subsonic and transonic speeds. *R.M.No.3488,British Aeronautical Research Council*, 1964.

[11] Block P.J.W Tam C.K.W. On the tones and pressure oscillations induced by flow over rectangular cavities. *Journal of Fluid Mechanics*, 1978.

[12] Bliss D Heller H.H. The physical mechanism of flow-induced pressure fluctuations in cavities and concepts for their suppression. *A.I.A.A Paper 75-491*, March 1975.

[13] Heller H.H Holmes D.G Covert E.E. Flow-induced pressure oscillations in shallow cavities. *Journal of Sound and Vibration*, Vol.18, 1971.

[14] van Leer B. Flux-vector splitting for the Euler equations. *Lecture Notes in Physics*, 1982.

[15] Lomax H Baldwin B. Thin-layer approximation and algebraic model for separated turbulent flows. *A.I.A.A Paper 78-257*, 1978.

[16] Degani D Schiff L.B. Computation of supersonic viscous flows around pointed bodies at large incidence. *A.I.A.A Paper 83-0034*, 1983.

[17] Tracy M.B Plentovich E.B. Characterization of cavity flow fields using pressure data obtained in the Langley 0.3-meter transonic cryogenic tunnel. *NASA TN-4436*, 1993.

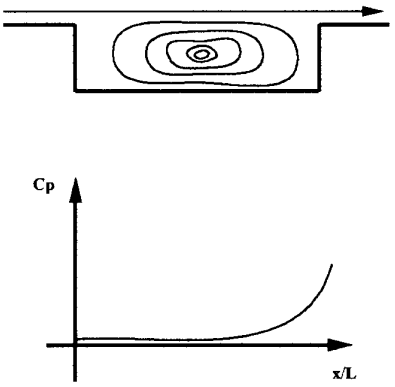

Figure 1. *Typical flowfield and pressure distribution diagrams for open cavity flow*

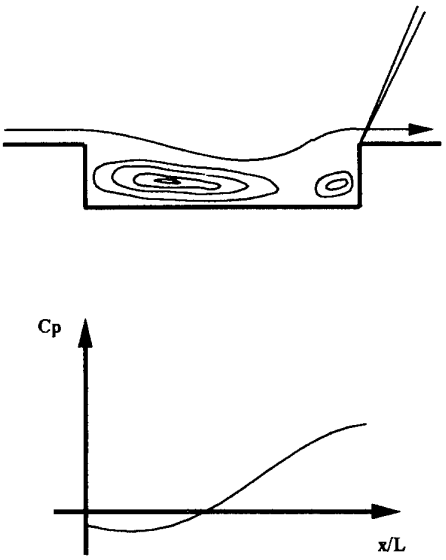

Figure 2. *Typical flowfield and pressure distribution diagrams for intermediate cavity flow*

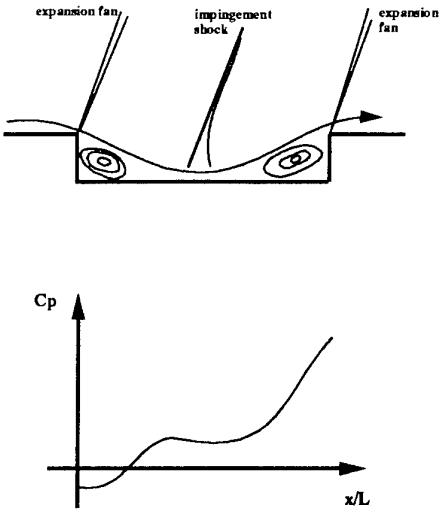

Figure 3. *Typical flowfield and pressure distribution diagrams for closed cavity flow*

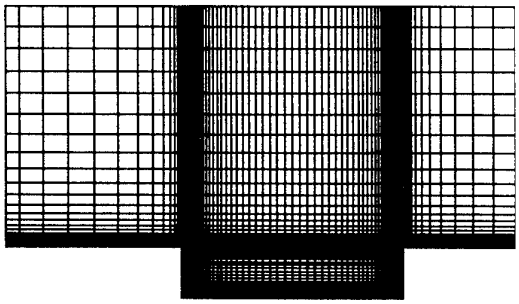

Figure 4. *Grid used for computation on deep (L/D=4.4) cavity*

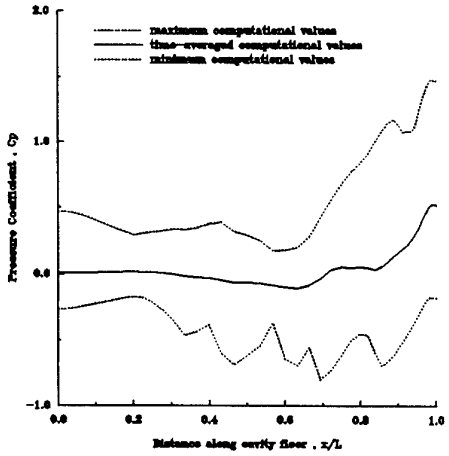

Figure 6. *Spread of cavity floor pressures for case 1*

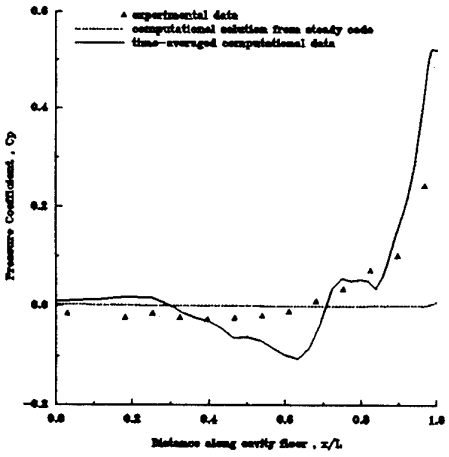

Figure 5. *Comparison of experimental time-averaged pressure coefficient along the cavity floor with the time-averaged computed values and output from the steady code for case 1*

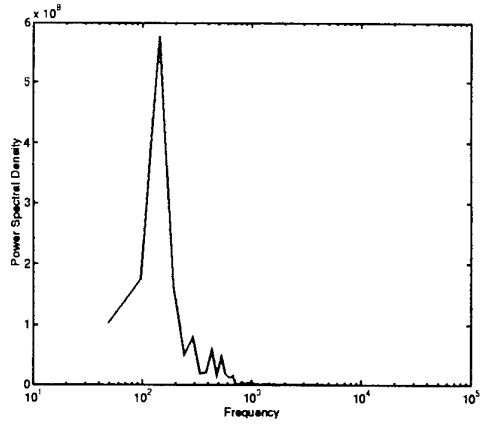

Figure 7. *FFT analysis of computed data for case 1*

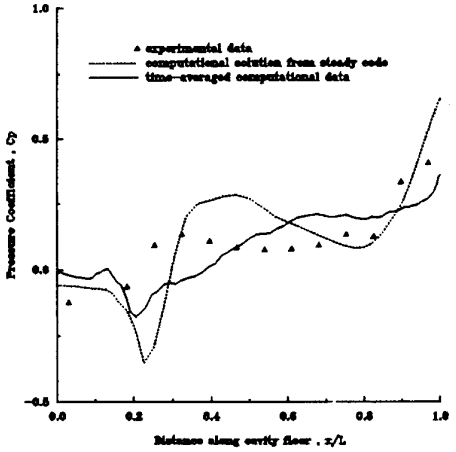

Figure 8. *Comparison of experimental time-averaged pressure coefficient along the cavity floor with the time-averaged computed values and output from the steady code for case 2*

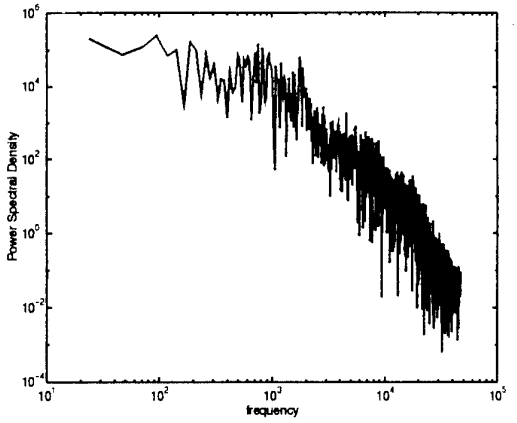

Figure 10. *FFT analysis of computed data for case 2*

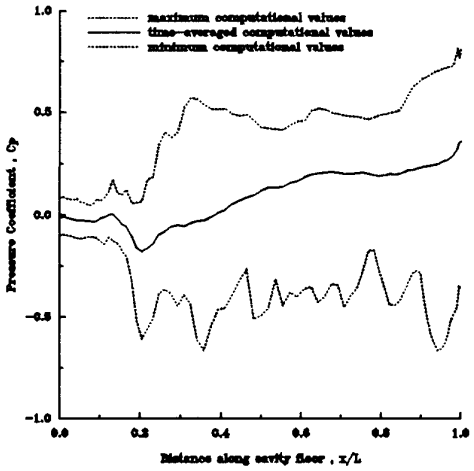

Figure 9. *Spread of cavity floor pressures for case 2*

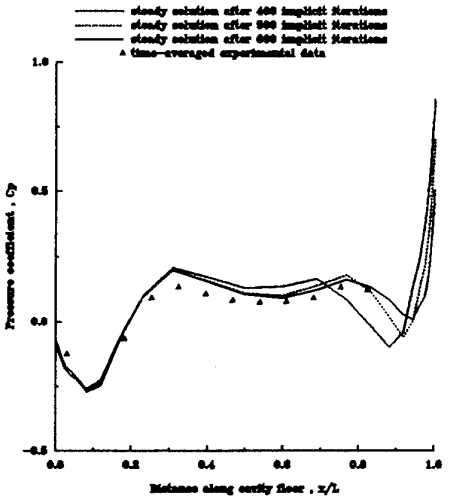

Figure 11. *Pressure coefficient along the cavity floor at three instances during the steady computation (case 2)*

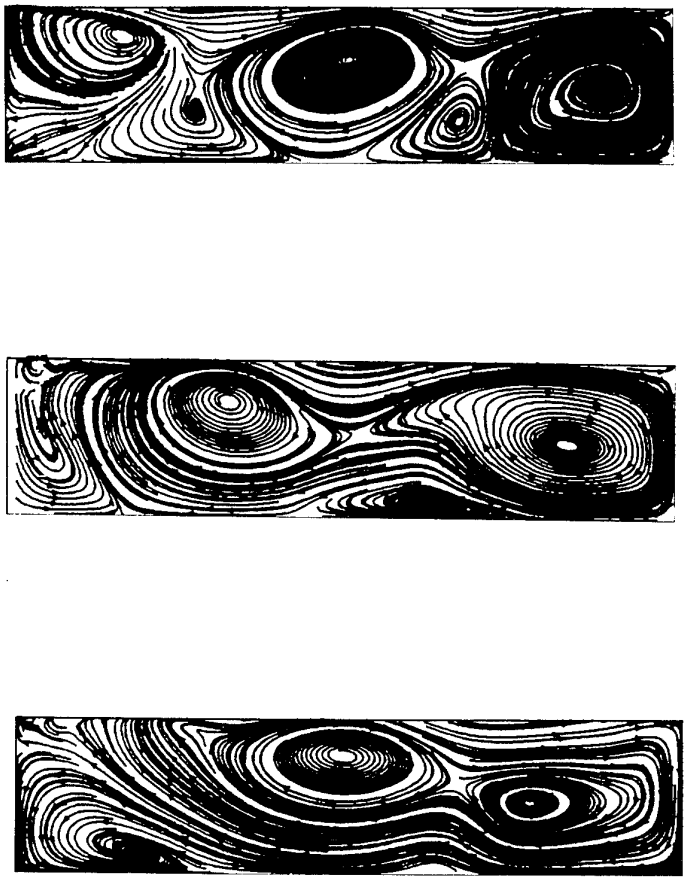

Figure 12. *Computed cavity streamlines for case 1 at times t = 0 secs(top), t = 0.0008 secs(middle) and t = 0.0016 secs(bottom)*

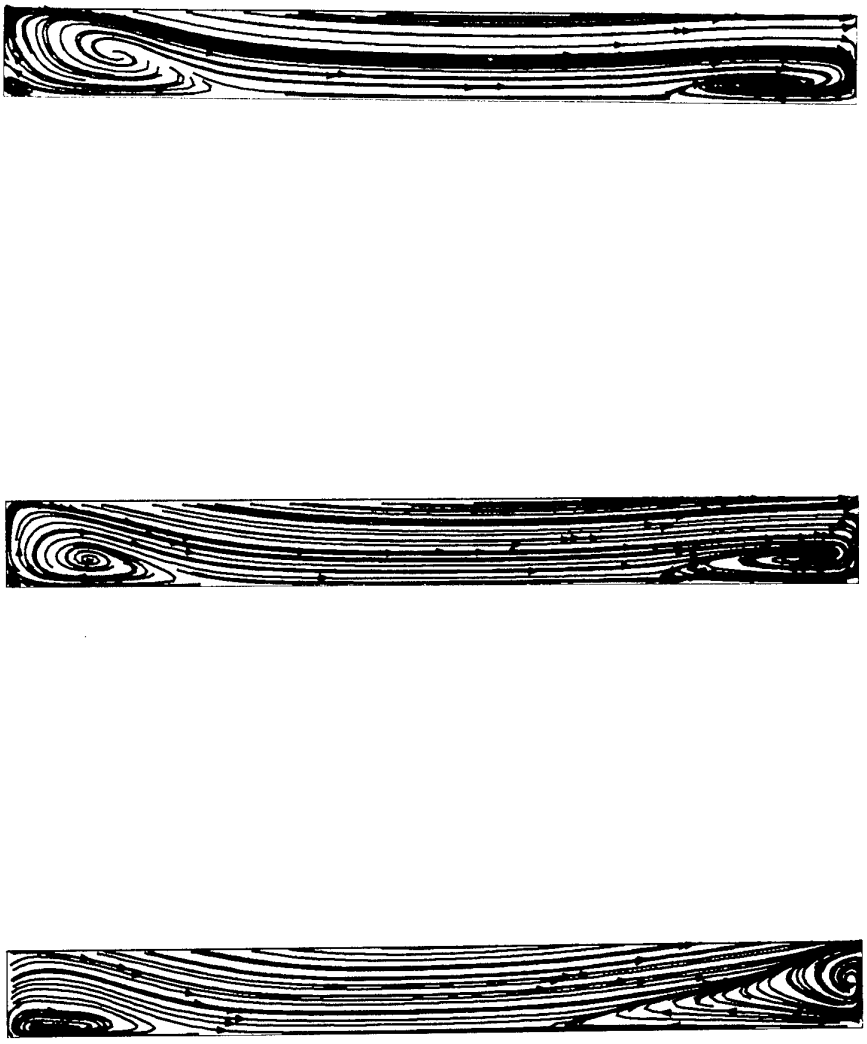

Figure 13. *Cavity streamlines at three spanwise positions for case 2 as computed by the 3D steady code, $\frac{z}{w} = 0.5$ (top), $\frac{z}{w} = 0.25$ (middle), $\frac{z}{w} = 0.1$ (bottom),*

Pressure Drag Induced by a Supersonic Flow over Cavities

Xin Zhang
Department of Aeronautics and Astronautics
University of Southampton
Southampton SO17 1BJ, England

1. SUMMARY

Pressure distribution and pressure drag due to a supersonic flow over a dual cavity geometry were studied at Mach 1.5 and 2.5. The study was performed numerically and results compared with an earlier experiment. The mass-averaged Navier-Stokes equations were solved using a finite-volume scheme. The inviscid cell interface fluxes were estimated using Roe's approximate Riemann solver with a second-order extension. Turbulence was modeled using a two-equation k-ω model with compressibility corrections. Two test configurations were selected: (1) a length to depth ratio $L/D = 1$ cavity followed by another $L/D = 1$ cavity separated by a distance of $1D$, and (2) an $L/D = 3$ cavity followed by an $L/D = 1$ cavity separated by a distance of $3D$. The pressure and drag of the individual cavity was compared with those of a single cavity of same L/D. It was found that the pressure field around the $L/D = 1$ was substantially modified by a preceding $L/D = 3$ cavity.

1. INTRODUCTION

A cavity or a cavity cascade exposed to an external stream is likely to produce a highly complex flow field. Under certain conditions, the flow could be unsteady. If the external flow is either transonic or supersonic, a shock wave system forms above the cavity, which could introduce changes in the structure performance and the acoustic field. Many applications can be found for this type of flow. An example is the flow around an internal store bay during the store release process. The induced pressure variations could cause several adverse effects, including (i) a high pressure field near the downstream corner causing the store to experience nose-up pitching moments; (ii) pressure drag increase; (iii) structure fatigue due to the pressure fluctuation; and (iv) far field noise radiation. It is necessary to develop predictive methods including numerical ones.

An important parameter in defining the pressure field is the length to depth ratio (L/D) Experimental evidence[1-3] suggests that the time-averaged flow field can be divided into "open"($L/D < 10 \sim 13$) and "closed"($L/D \geq 10 \sim 13$), depending on the shear layer attachment position (either on the downstream face or on the floor). The type of flow could be influenced by the width and yaw angle[2-3], and to a less extent by the Mach number and the Reynolds number. Under the "closed" condition, the flow is normally steady. In contrast, the "open" cavity quite often experiences large pressure fluctuations[4-6]. Here the added complexity is the momentum exchange near the trailing edge, often resulting in an increased level of the pressure drag. To study the unsteady flow requires both wind tunnel tests and numerical analysis.

There have been a number of computational efforts. Earlier attempts[7-9] followed basically the same strategy, employing finite-difference schemes and zero-equation turbulence models. Recent efforts generally used two-equation models (k-ϵ[10] and k-ω[11]. Although the two-equation models do not introduce new physics into the simulation, they are of the so-called "complete form" and avoid the ad hoc application of the zero-equation models inside and after the cavity. It is still debatable whether the unsteady environment can be faithfully reproduced. The exact unsteady behaviours are not the subject of the present paper and will be addressed in a future study. The available experimental evidences[6], though, do suggest that the internal environment is dominated by large vortices. These are driven by the turbulent shear layer. If the turbulent mix-

Paper presented at the AGARD FDP Symposium on "Aerodynamics of Store Integration and Separation", held in Ankara, Turkey from 24-27 April 1995, and published in CP-570.

ing and entrainment can be modeled correctly, it is possible that the time-averaged pressure field can be predicted. This is the strategy adopted in the current study(for details the reader is referred to the section on computation).

In the current study, we investigated the time-averaged pressure distribution over dual cavity geometries, and the interaction between the cavities. The test cases selected were also used to validate the numerical model.

2. TEST FLOW CASES

We selected two types of two-dimensional dual cavity geometries with the depth of the cavity D fixed at 15mm[12]: type A–an $L/D = 1$ cavity followed by an $L/D = 1$ cavity at a separation distance of 15mm; type B–an $L/D = 3$ cavity followed by an $L/D = 1$ cavity at a separation distance of 45mm. A schematic is given in Fig. 1. The main reason for the selection was the two types of oscillation represented by the two geometries[12]. Two Mach numbers ($M_\infty = 1.5$ and 2.5) were selected. The Reynolds number based on the depth of the cavity was 4.5×10^5. At M_∞=1.5, the freestream air temperature T_∞ was 200K and static pressure p_∞ 53801.7 psia. The oncoming boundary layer had a thickness δ of 5mm, a displacement thickness δ^* of 0.929mm, and a momentum thickness θ of 0.417mm. The skin friction coefficient C_f was 2.05×10^{-3}. At M_∞=2.5, the respective values were 128.9K, 12390.7 psia, 5mm, 0.328mm, 1.29mm and 1.79×10^{-3}. In the computation, the freestream values of the turbulent kinetic energy level k were $1.258\text{m}^2/\text{s}^2$ at M_∞=1.5, and $1.912\text{m}^2/\text{s}^2$ at M_∞=2.5.

3. COMPUTATIONAL ANALYSIS

The computational analysis solved the governing equations for the conservation of mass, momentum and energy of a viscous flow written in cartesian form[11]. Turbulence was modeled using the Wilcox k-ω model[13–14]. The model equations were modified for the effects of compressibilities[14].

We believe that the unsteady shocks are important in defining the pressure field and for the far-field acoustic radiation. This aspect of the flow was often neglected in the past and was addressed in this study through a strategy of employing a Riemann solver and a structured grid of uniform cell size. The Roe flux difference split approximate Riemann solver[15] was used to evaluate the inviscid fluxes on the cell surfaces. A second order extension was implemented[16–17]. The integration was performed by the Hancock's two-step finite-volume scheme. Implementation of the k-ω equations into the scheme followed the same procedures described by Roe[16] and will not be repeated here. To preserve monotonicity the min-mod flux limiter was used. The viscous stress and heat fluxes were calculated from the application of Gauss theorem. Central difference was used to calculate viscous terms at the cell vertex and at the cell face center.

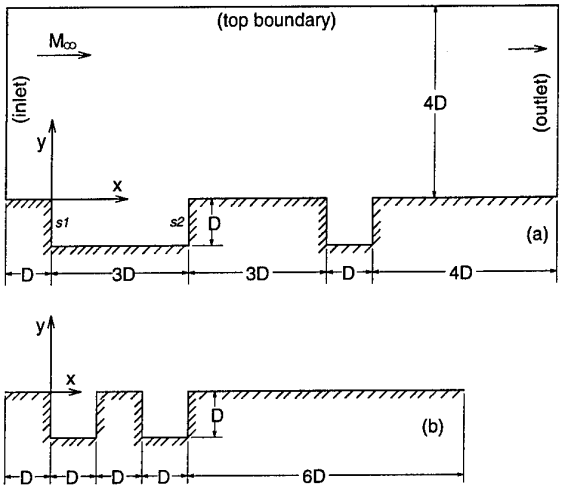

Figure 1: Schematic of the test geometry: (a) type B; (b) type A. Surface $s1$–upstream face; Surface $s2$–downstream face.

The boundary conditions were as follows: (i) along the inlet, the flow variables were fixed. The inlet profile was fully developed; (ii) the no-slip condition was applied to the solid surfaces. The surface shear stress was estimated using the Van Driest compressible law of the wall; (iii) along the top boundary, a simple wave condition was imposed; (iv) along the outlet, the conservative variables were extrapolated along the streamwise direction by assuming zero transverse components. The starting condition was the so-called 'no-flow' condition[9]. The computational domain covered was from $x/D = -1$ to 9 and $y/D = -1$ to 4 for the type A configuration, and $x/D = -1$ to 11 and $y/D = -1$ to 4 for the type B configu-

ration. The cell sizes were $\Delta x = 0.5556$mm and $\Delta y = 0.5556$mm. This followed a numerical experiment and was found to be adequate for this study[11]. A fixed time step of $\Delta t = 0.005 D/V_\infty$ was used throughout.

The pressure drag coefficient was calculated as

$$C_d = \int_{-1}^{0} \frac{p_{(s2)} - p_{(s1)}}{\rho_\infty V_\infty^2/2} d(y/D) \qquad (1)$$

4. RESULTS AND DISCUSSION

For a two-dimensional cavity flow oscillation, there are two possible sources of the unsteadiness: (1) that associated with the shear layer instabilities and longitudinal modes of oscillation; (2) that due to the pressure response to the disturbances in the shear layer spanning the cavity and transverse modes of oscillation. The longitudinal oscillation is strongly influenced by the external flow Mach number, which has a significant effect on the shear layer instabilities. At a sufficient high Mach number($M_\infty \geq 2\sqrt{2}$ for a vortex sheet), the shear layer is stable. It follows that the cavity flow will not experience the longitudinal oscillation. The shear layer though is still likely to provide some disturbances so that large pressure fluctuations could still exist.

In this study, the $L/D = 1$ cavity represents a deep cavity and the $L/D = 3$ cavity a shallow cavity. Measurements[6] showed that the $L/D = 1$ cavity flow was mainly dominated by a longitudinal mode at 25.7Hz at $M_\infty = 1.5$ and a transverse mode at 26.4Hz at $M_\infty = 2.5$. The $L/D = 3$ cavity flow was influenced by longitudinal modes at 2645Hz, 5900Hz(dominant mode), and 9155Hz at $M_\infty = 1.5$. At $M_\infty = 2.5$, the values were 3467Hz, 6787Hz and 10,010Hz(dominant mode) respectively. Current computation was able to capture the flow patterns and to predict the frequencies. While we are not claiming that our approach could resolve the time-dependent features faithfully to a high degree of accuracy. The results obtained so far suggest that the dominant physics were reproduced for the present flow conditions. Fig. 2 presents snap shoots of the density contours for the single cavity flows. A close examination of moving images obtained in the study suggests that the wave patterns in Figs. 2(a), 2(c) and 2(d) represent the longitudinal mode dominated flow oscillations and that in Fig. 2(b) represents the transverse mode dominated flow oscillation. The predicted frequencies are as follows: 25,087Hz at $L/D = 1$ and $M_\infty = 1.5$; 27,951Hz at $L/D = 1$ and $M_\infty = 2.5$; 2651Hz(1st mode) at $L/D = 3$ and $M_\infty = 1.5$; and 3408Hz(1st mode) at $L/D = 3$ and $M_\infty = 2.5$. These results are encouraging in that the weak flow oscillations at $L/D = 1$ and their mechanisms are reproduced. A main feature associated with the longitudinal cavity flow oscillation is the induced vortices by the shear layer. Their motion is coupled with the larger vortex motion inside the cavity. As they move towards to the trailing edge, the vortices grow in size. The flapping motion of the shear layer ejects the vortices out of the cavity periodically. As a result, large vortical structures exist in the wall-bounded shear layer and will exert influence on the trailing cavity flows(see Figs. 2(a) and 2(b)).

There are two possible mechanisms that may influence the cavity–cavity interaction. The first is the existence of the wall-bound shear layer and subsonic region near the wall. This will allow the trailing cavity to influence the preceding one and *vice versa*. The second mechanism is the convection of the vortical structures. Examples of the flow interaction are shown in Fig. 3. For the type A configuration(Figs. 3(a) and 3(b)), the unsteady mechanism is not altered fundamentally. However, the wave patterns above the cavity suggest that the mode is changed at both Mach numbers. It is obvious from Figs. 3(c) and 3(d) that the flow in the trailing $L/D = 1$ cavity is significantly altered by the preceding cavity in the type B configuration. The instantaneous density contours in the $L/D = 1$ cavity indicate stronger pressure fluctuations than the single cavity flow. We also notice that the flow in the $L/D = 1$ cavity at $M_\infty = 2.5$ is still influenced by a transverse mode. However, one would expect the convective vortical structures to exert a strong influence on the pressure field inside the cavity.

In order to obtain a reliable estimate of the time-averaged pressure and pressure drag, the flow was allowed to develop until a self-sustained state was reached in the computation. This required a flow running time $\geq 250 D/V_\infty$. The time was significantly longer than those in some of the earlier attempts. We found this was necessary to obtain consistent data. The long running

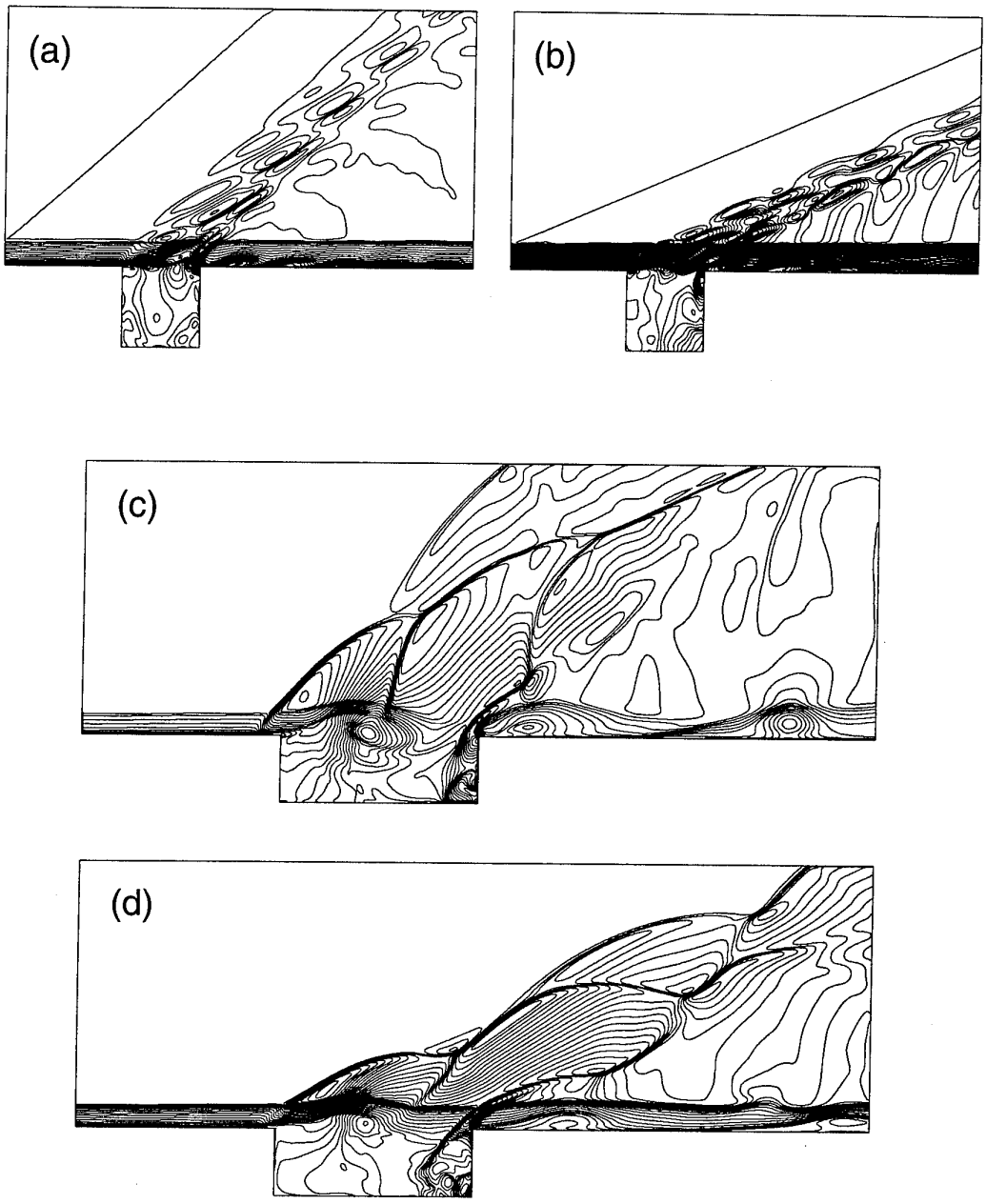

Figure 2: Instantaneous density contours: (a) $L/D = 1$, $M_\infty = 1.5$, $\Delta\rho/\rho_\infty = 0.015$; (b) $L/D = 1$, $M_\infty = 2.5$, $\Delta\rho/\rho_\infty = 0.015$; (c) $L/D = 3$, $M_\infty = 1.5$, $\Delta\rho/\rho_\infty = 0.035$; (d) $L/D = 3$, $M_\infty = 2.5$, $\Delta\rho/\rho_\infty = 0.035$;

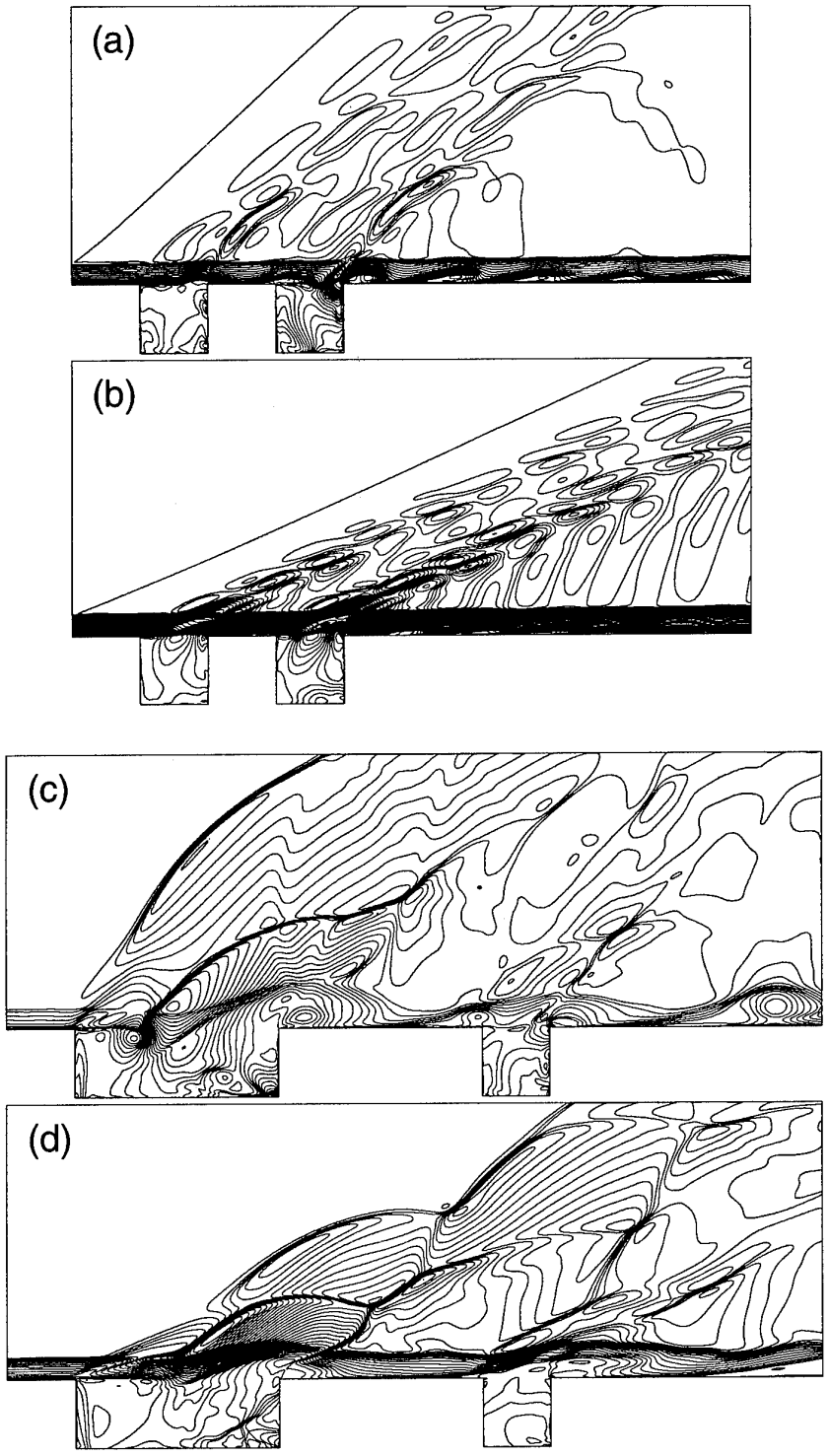

Figure 3: Instantaneous density contours: (a) type A configuration, $M_\infty = 1.5$, $\Delta\rho/\rho_\infty = 0.015$; (b) type A configuration, $M_\infty = 2.5$, $\Delta\rho/\rho_\infty = 0.015$; (c) type B configuration, $M_\infty = 1.5$, $\Delta\rho/\rho_\infty = 0.035$; (d) type B configuration, $M_\infty = 2.5$, $\Delta\rho/\rho_\infty = 0.035$;

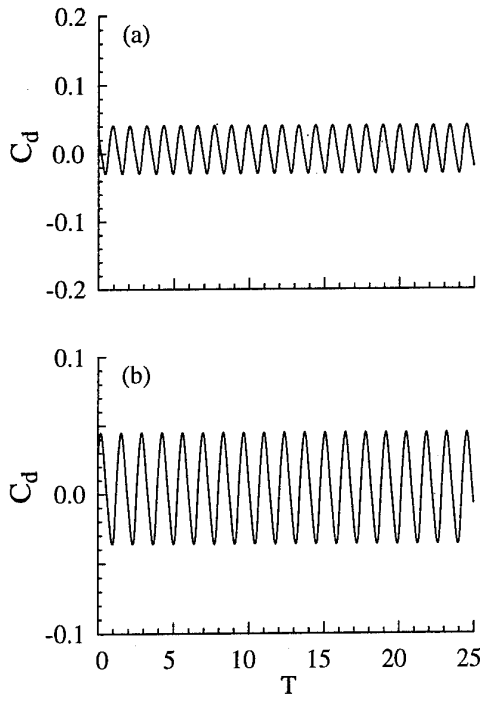

Figure 4: Pressure drag coefficient variation of a single cavity at $L/D = 1$: (a) $M_\infty = 1.5$ and (b) $M_\infty = 2.5$.

time also helped to resolve low frequency features and minimize the effects of the starting up process. The time-averaged pressure and pressure drag were monitored over a period of at least 5 oscillation cycles and the results were averaged. The calculated pressure drag coefficient results are shown in Figs. 4-6. For an $L/D = 1$ cavity, the presence of the trailing cavity is to change the dominant mode to a low frequency one. When a second cavity is added, the response is different at the two Mach numbers. For the longitudinal mode dominated flow at $M_\infty = 1.5$, the oscillation is enhanced. There is a phase shift between the oscillations. The presence of the first cavity effectively phase locks the second cavity oscillation. For the transverse mode dominated flow at $M_\infty = 2.5$, the result of the interaction is to reduce the oscillation level. This is possibly caused by the disruption to the shear layer. The effects of a preceding cavity are much more pronounced in the type B configuration. Fig. 6 shows the effects of the $L/D = 3$ cavity on the trailing $L/D = 1$ cavity. The pressure field is now influenced by the convected vortical structures which are ejected at the dominant frequency. The $L/D = 3$ single cavity results are not included as they are similar to the dual cavity ones. The averaged drag coefficients are as follows: (1) at $L/D = 1$ and $M_\infty = 1.5$, $C_d = 6.82 \times 10^{-3}$; (2) at $L/D = 1$ and $M_\infty = 2.5$, $C_d = 5.14 \times 10^{-3}$; (3) at $L/D = 3$ and $M_\infty = 1.5$, $C_d = 7.28 \times 10^{-2}$; (4) at $L/D = 3$ and $M_\infty = 2.5$, $C_d = 3.33 \times 10^{-2}$; (5) for the type A configuration at $M_\infty = 1.5$, $(C_d)_{1st} = 5.91 \times 10^{-3}$, $(C_d)_{2nd} = 8.01 \times 10^{-3}$; (6) for the type A configuration at $M_\infty = 2.5$, $(C_d)_{1st} = 2.33 \times 10^{-3}$, $(C_d)_{2nd} = 3.60 \times 10^{-3}$; (5) for the type B configuration at $M_\infty = 1.5$, $(C_d)_{1st} = 7.91 \times 10^{-2}$, $(C_d)_{2nd} = 9.81 \times 10^{-3}$; (6) for the type B configuration at $M_\infty = 2.5$, $(C_d)_{1st} = 3.98 \times 10^{-2}$, $(C_d)_{2nd} = 5.58 \times 10^{-3}$. Apart from the type A configuration at $M_\infty = 2.5$ where the pressure drag coefficient of the trailing cavity is reduced. The pressure drag coefficients of the trailing cavity are increased by the presence of the preceding cavity.

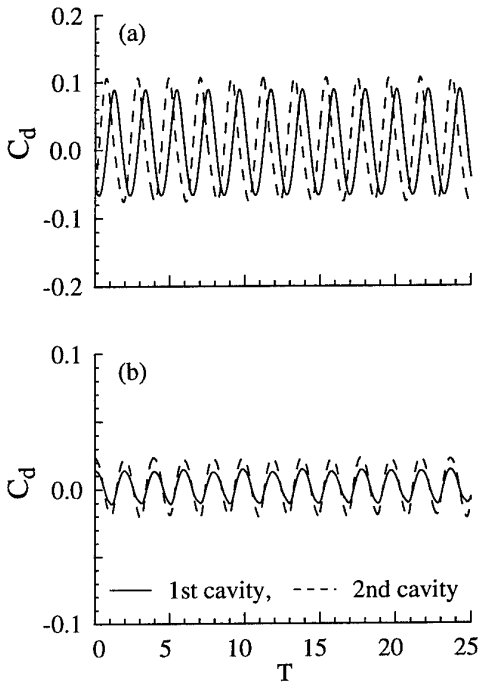

Figure 5: Pressure drag coefficient variation of a type A configuration: (a) $M_\infty = 1.5$ and (b) $M_\infty = 2.5$.

The time-averaged surface pressure distributions are presented in Figs. 7-10. These results

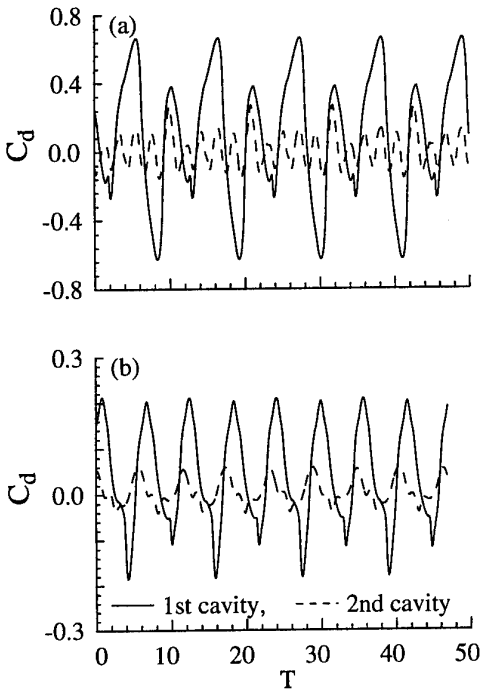

Figure 6: Pressure drag coefficient variation of a type B configuration: (a) $M_\infty = 1.5$ and (b) $M_\infty = 2.5$.

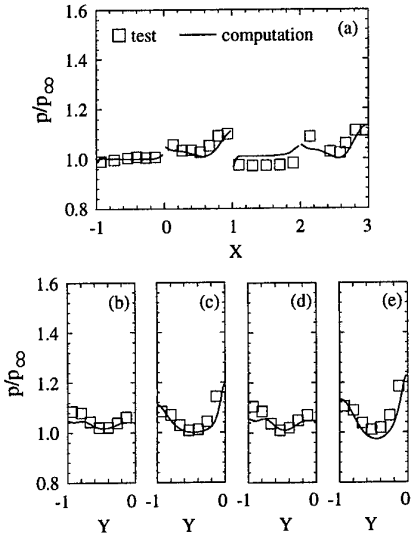

Figure 7: Averaged pressure distribution along the cavity surfaces for the type A configuration at $M_\infty = 1.5$: (a) horizontal surfaces; (b) upstream face–1st cavity; (c) downstream face–1st cavity; (c) upstream face–2nd cavity; (d) downstream face–2nd cavity.

suggest that the pressure distributions in the cavity can be predicted by the present method. The vortex dominated flow is clearly shown by the pressure distribution along the faces of the cavity. The shear layer is seen to reattach to the downstream face instead of the trailing edge of the $L/D = 3$ cavity at $M_\infty = 1.5$. The pressure between the cavities at $M_\infty = 2.5$ was not predicted well. The poor agreement reflects the turbulence model's inability in dealing with the time-dependent, separated, wall-bound shear layer. The flow inside the cavity, on the other hand, is dominated by large vortices. The present model is able to predict the turbulent mixing and flow entrainment, thus the good agreement in the cavity.

SUMMARY REMARKS

A computational analysis was carried out on flows over two dual cavity geometries at Mach 1.5 and 2.5. The mass-averaged Navier-Stokes equations were solved. Turbulence was modeled using a k-ω model. The shock waves were captured using a Riemann solver. It was found that a self-sustained oscillatory state was achieved under the computation for the present flow and geometrical conditions. For the type A configuration, the pressure drag variation was enhance compared with the single cavity flow at $M_\infty = 1.5$, where the flow was found to be dominated by a longitudinal mode. The pressure drag variation was reduced compared with the single cavity flow at $M_\infty = 2.5$, where the flow was found to be dominated by a transverse mode. The averaged pressure drag coefficient of a $L/D = 1$ cavity was increased through the presence of a preceding $L/D = 3$ cavity at both Mach numbers. The averaged pressure fields in the cavities were predicted by the present computation.

ACKNOWLEDGEMENTS

This study would not be possible without the help of his former supervisor Professor J. A. Edwards who introduced the subject to him. The author also wishes to thank Professor G. M. Lilley and Mr. A. Rona for many stimulating discussions. The approximate Riemann solver comes from the adaptive mesh refinement code of the Defence Research Agency.

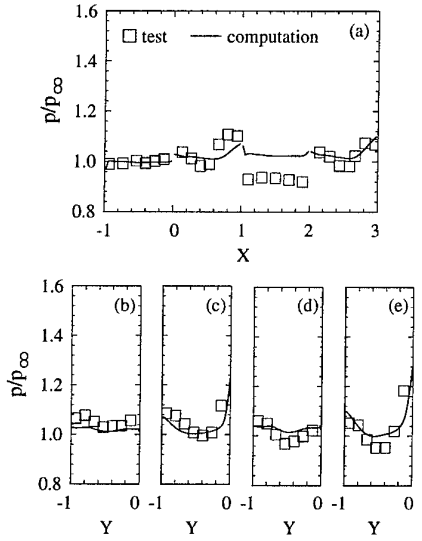

Figure 8: Averaged pressure distribution along the cavity surfaces for the type A configuration at $M_\infty = 1.5$: (a) horizontal surfaces; (b) upstream face–1st cavity; (c) downstream face–1st cavity; (c) upstream face–2nd cavity; (d) downstream face–2nd cavity.

REFERENCES

[1] Charwat, A. F., Roos, J. N., Dewey, F. C., Jr., and Hitz, J. A., "An investigation of separated flows–part I: the pressure field," *Journal of the Aerospace Science*, Vol. 28, June 1961, pp. 457-470.

[2] Plentovich, E. B., Chu, J. and Tracy, M. B., "Effects of yaw angle and Reynolds number on rectangular-box cavities at subsonic and transonic speeds," NASA TP-3099, NASA, July 1991.

[3] Plentovich, E. B., Stallings, Jr., R. L. and Tracy, M. B., "Experimental cavity pressure measurements at subsonic and transonic speeds," NASA TP-3358, NASA, Dec. 1993.

[4] Krishnamurty, K., "Acoustic radiation from two-dimensional rectangular cutouts in aerodynamic surfaces," NACA TN-3487, NACA, Aug. 1955.

[5] Rossiter, J. E., "Wind tunnel measurements on the flow over rectangular cavities at subsonic and supersonic speeds," Ministry of Aviation, Aeronautical Research Council, London, England, R&M 3438, Oct. 1964.

[6] Zhang, X. and Edwards, J. A., "An investigation of supersonic oscillatory cavity flows driven by a thick shear layer," *The Aeronautical Journal*, Vol. 94, No. 940, Dec. 1990, pp. 355-364.

[7] Hankey, W. L. and Shang, J. S., "Analysis of pressure oscillation in an open cavity," *AIAA Journal*, Vol. 18, No. 8, Aug. 1980, pp. 892-898.

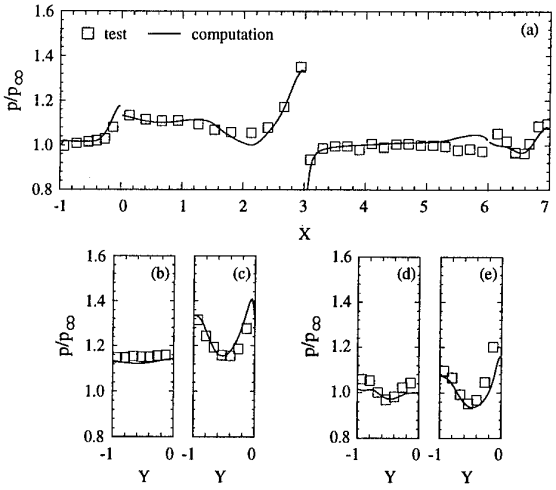

Figure 9: Averaged pressure distribution along the cavity surfaces for the type B configuration at $M_\infty = 2.5$: (a) horizontal surfaces; (b) upstream face–1st cavity; (c) downstream face–1st cavity; (c) upstream face–2nd cavity; (d) downstream face–2nd cavity.

[8] Rizzetta, D. P., "Numerical simulation of supersonic flow over a three-dimensional cavity," *AIAA Journal*, Vol. 26, No. 7, July 1988, pp. 799-807.

[9] Zhang, X. and Edwards, J. A., "Computational analysis of unsteady cavity flows driven by thick shear layers," *The Aeronautical Journal*, Vol. 92, No. 919, Nov. 1988, pp. 365–374.

[10] Shih, S. H., Hamed, A., and Yeuan, J. J., "Unsteady supersonic cavity flow simulations using coupled k-ϵ and Navier-Stokes equations," *AIAA J.*, Vol. 32, No. 10, Oct. 1994, pp. 2015-2021.

[11] Zhang, X., "Compressible cavity flow oscillation due to shear layer instabilities and pressure feedback," *AIAA J.*, Vol. 34, No. 3, Mar. 1996, *in print*.

[12] Zhang X. and Edwards, J. A., "An experimental investigation of supersonic flow over two cavities in tandem," *AIAA Journal*, Vol. 30, No. 5, May 1992, pp. 1182-1190.

[13] Wilcox, D. C., "Reassessment of the scale de-

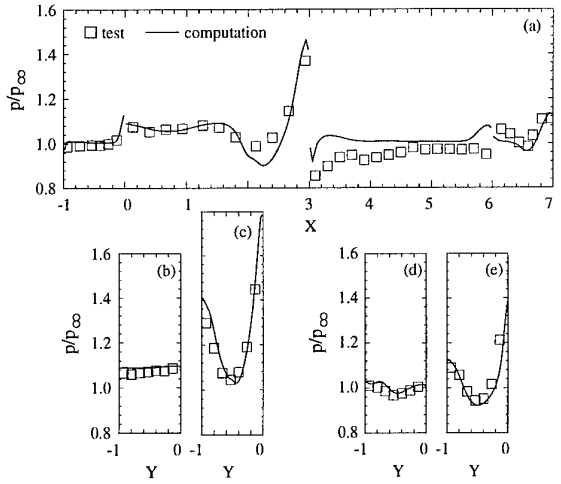

Figure 10: Averaged pressure distribution along the cavity surfaces for the type B configuration at $M_\infty = 2.5$: (a) horizontal surfaces; (b) upstream face–1st cavity; (c) downstream face–1st cavity; (c) upstream face–2nd cavity; (d) downstream face–2nd cavity.

termining equation for advanced turbulence models," *AIAA Journal*, Vol. 26, No. 11, Nov. 1988, pp. 1299-1310.

[14] Wilcox, D. C., "Dilatation-dissipation corrections for advanced turbulence models," *AIAA Journal*, Vol. 30, No. 11, Nov. 1992, pp. 2639-2646.

[15] Roe, P., "Approximate Riemann solvers, parameter vectors, and difference schemes," *Journal of Computational Physics*, Vol. 43, No. 2, Oct. 1981, pp. 357-372.

[16] Roe, P., "Characteristic-based schemes for the Euler equations," *Annual Review of Fluid Mechanics*, Vol. 18, 1986, pp. 337-365.

[17] Quirk, J. J., "An adaptive grid algorithm for computational shock hydrodynamics," PhD Thesis, Cranfield Institute of Technology, Jan. 1991.

Computational Approach to Weapons Bay Flow Field and Carriage Loads Predictions*

N. E. Suhs
Micro Craft Technology/AEDC Operations
Arnold Engineering Development Center
Arnold Air Force Base, TN, 37389-9010, USA

SUMMARY

A computational capability has been developed for predicting the flow field in a three-dimensional weapons bay (or cavity). Computations have been performed for an empty bay and for a store placed within the weapons bay. The chimera overset grid methodology, a domain decomposition strategy, is used to simplify mesh generation. An implicit Navier-Stokes code with a thin-layer approximation is used to compute the weapons bay flow field at free-stream Mach numbers of 0.6, 0.95, and 1.20. The computational results are compared to experimental results for time-averaged pressure coefficients, overall sound pressure levels, and the frequency spectrum of the sound pressure levels on the bay walls. In addition, loads on a store placed within the bay are computed.

LIST OF SYMBOLS

C_m coefficient of pitching moment about an axis through the center of gravity of the store which is parallel to the Y axis, pitching moment/qSD, positive counterclockwise looking in from the +Y direction (nose down into the bay, see Fig. 5)

$\overline{C}_m$ pitching moment (C_m) obtained from time-averaged computational results

$\overline{C}_m s$ the sum of $\overline{C}_m$ plus/minus the standard deviation of the time history of the calculated pitching moment about $\overline{C}_m$

C_N coefficient of normal force in the XZ plane, normal force/qS, positive in the +Z direction (see Fig. 5)

$\overline{C}_N$ coefficient of normal (C_N) force obtained from time-averaged computational results

$\overline{C}_N s$ the sum of $\overline{C}_N$ plus/minus the standard deviation of the time history of the calculated pitching moment about $\overline{C}_N$

C_p pressure coefficient

$\overline{C}_p$ pressure coefficient obtained from time-averaged computational results

$C_p e$ pressure coefficient obtained from the experimental data

$\overline{C}_p s$ the sum of $\overline{C}_p$ plus/minus the standard deviation of the time history of the calculated pressure coefficients about $\overline{C}_p$

D maximum diameter of the store

H bay height

L bay length

M_∞ free-stream Mach number

SPL sound pressure level

T_{avg} time interval for computing time averages

t_c characteristic time, i.e., the time required for the free-stream flow to traverse the length of the weapons bay

P_{ref} standard reference pressure (2.90075 psi)

P_{rms} root-mean-square of the pressure fluctuations about the average, in psi

q dynamic pressure in the free stream

S area of maximum cross section of the store

W width of the bay

X,Y,Z rectangular coordinate system (see Fig. 5), positive Z is into the bay

Z_s Z location of the store centerline

$\overline{\Delta C}_p$ difference in C_p of the free-stream side minus the bay side of the store [see Eq. (3)]

1. INTRODUCTION

Wind tunnel testing and analysis of weapons bay (or cavity) configurations to evaluate the separation of stores are continuing activities at the Arnold Engineering Development Center (AEDC).[1,2] A complementary computational fluid dynamics (CFD) approach to the

*The research reported herein was performed by the Arnold Engineering Development Center (AEDC), Air Force Materiel Command. Work and analysis for this research were done by personnel of Micro Craft Technology/AEDC Operations, technical services contractor for the AEDC aerospace flight dynamics facilities. Further reproduction is authorized to satisfy needs of the U. S. Government.

Paper presented at the AGARD FDP Symposium on "Aerodynamics of Store Integration and Separation", held in Ankara, Turkey from 24-27 April 1995, and published in CP-570.

testing programs is also under investigation at the AEDC.[3-5] The primary objective of the current CFD effort is to develop capabilities for computational support of internal store separation testing. Specifically, computational capabilities to predict the flow field of the weapons bay and the loads on stores within the bays have been targeted. The subject of this paper is the description of the methodology used to perform the computations and results with comparisons to wind tunnel data.

Weapons bays or cavity flows are unsteady with large velocity and pressure fluctuations inside the cavity forced by the external flow.[6-9] Cavity flow fields can be categorized into at least three types: open, closed, and transitional,[10] all forced by the external stream (Fig. 1). A boundary layer develops over the body surface upstream of the cavity, separates from the leading edge of the cavity, and becomes a free shear layer. The shear layer typically oscillates in and out of the cavity, developing a highly vortical flow in the cavity. As shown in Fig. 1a for open cavity flow (length-to-height (L/H) ratio less than about 9), the shear layer spans the cavity and stagnates on the aft wall. For closed cavity flow (L/H greater than about 13), the flow attaches to the bottom wall of the cavity as depicted in Fig. 1b. Cavities with an L/H between about 9 and 13 are considered to be transitional, where either type of flow may occur, depending on the external flow conditions. These L/H ranges for open, closed, and transitional cavities are not precise and are used only as a general guideline in categorizing cavity flow fields.

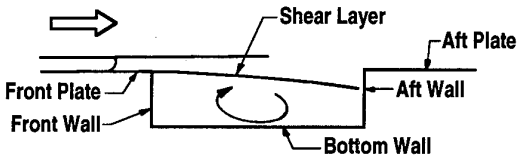

a. Open cavity flow

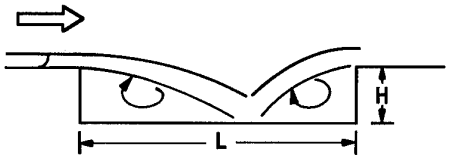

b. Closed cavity flow

Fig. 1. Flow in a cavity.

Several numerical studies which solve the Navier-Stokes equations for two-dimensional[11-16] and three-dimensional[3-5, 17-22] cavity flows have been made over the past several years. The numerical predictions reported in these studies were typically for open cavity flow, and were compared with experimentally obtained pressure coefficients and, for a few cases, the overall sound pressure levels and the frequency spectra of the sound pressure levels. The comparisons of the computed pressure coefficients with the experimentally derived pressure coefficients in the preceding numerical studies typically showed good agreement at supersonic Mach numbers and worse agreement at the subsonic and transonic Mach numbers. Typically, comparisons of computations and experiments for the frequency spectra of the sound pressure level were not conclusive. The time interval used to evaluate the frequency spectra from the computations was significantly shorter than that for the experimental results, thus giving poor frequency resolution. The exception to this was the computations performed by Rizzetta[18] for a rectangular cavity at a free-stream Mach number of 1.5. Rizzetta used a computational time interval that gave good frequency resolution for comparisons with experimental data.

The approach of using the complete Navier-Stokes formulation was followed in all the above numerical studies[11-22] with the exception of the studies by Suhs.[3-5] The approach of Refs. 3 - 5 used the thin-layer approximation to the viscous terms, which is less computationally intensive. The computations presented in this paper demonstrate the ability to apply the thin-layer approximation to compute open cavity flow (L/H = 4.5) for a three-dimensional empty weapons bay at free-stream Mach numbers (M_∞) of 0.60, 0.95, and 1.20. The results are compared with experimental pressure data for locations on the bay walls. The computations were performed for a time interval that allowed for the resolution of the frequencies. Additionally, computations of the weapons bays with a store mounted on a sting were performed. A description of the experimental data is outlined, followed by a description of the numerical procedure used to perform representative computations. Comparisons of the computations with the experimental data are then presented and analyzed.

2. EXPERIMENTAL DATA DESCRIPTION

Data used for comparisons were recorded during the Weapons Internal Carriage Separation Program (WICS), which was sponsored by Wright Laboratory/ Armament Directorate, formerly the Air Force Armament Laboratory.[1-2] The basic configuration tested, shown in Fig. 2, was a generic flat plate and weapons bay. The store, shown in Fig. 3, is an ogive-cylinder-ogive mounted on a bent sting that allows for the insertion of the store into the bay. Measurements were taken at M_∞ from 0.6 to 5.0 in AEDC Aerodynamic Wind Tunnels 4T and A. Typical instrumentation locations for the generic flat plate and weapons bay are shown in Fig. 2.

Two basic types of instrumentation were installed on the flat plate, bay, and store: static-pressure orifices (connected to Electronically Scanned Pressure (ESP) modules) and flush-mounted differential-pressure transducers.[1-2] A total of 95 static-pressure orifices and 33 differential-pressure transducers were installed on the

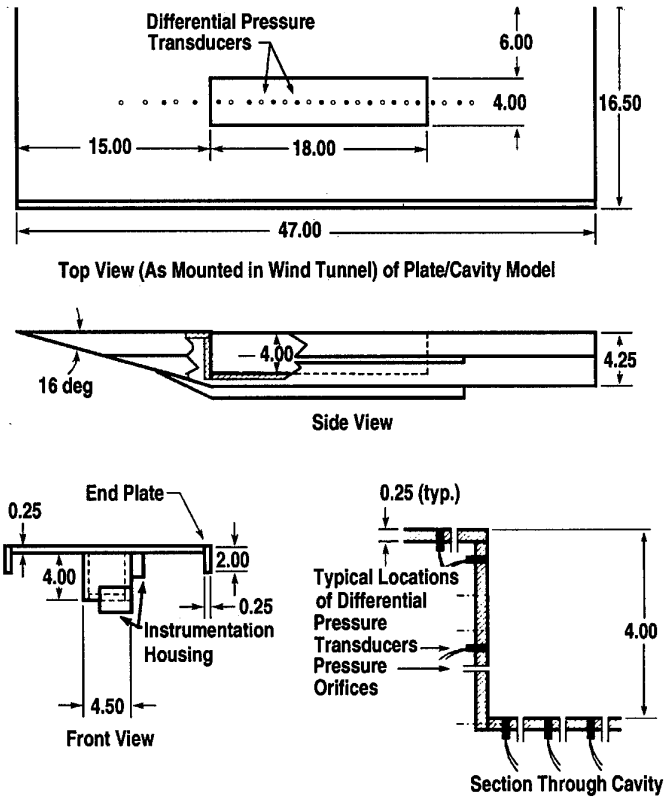

Fig. 2. Dimensions of the WICS flat — plate/bay model.

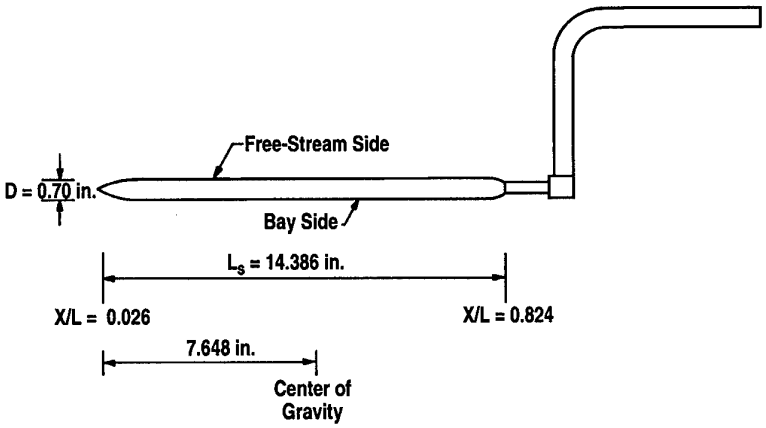

Fig. 3. Store mounted on the bent sting.

flat plate and weapons bay model, and 38 static-pressure and 6 differential-pressure transducers were installed on the store model. The static-pressure orifices were scanned at a rate of 15 Hz, and the differential-pressure transducers were scanned at a rate of 10,000 Hz.

3. NUMERICAL PROCEDURE

Several factors were taken into account in determining the numerical approach to use in the present study. First, the cavity flow field has been shown experimentally to be unsteady; hence, the numerical flow solver must be time-accurate. Second, because of the large flow gradients present, the free shear layer that crosses the cavity opening should be spatially resolved. Finally, cavity flow problems become even more complex with the addition of doors, acoustic suppression devices (spoilers, fences, rakes, vortex generators), and stores. Domain decomposition is a convenient methodology for treating such complex configurations. Thus, the chimera overset grid methodology[23 - 25] was chosen as the numerical approach for solving three-dimensional cavity flow.

The chimera methodology allows the computational domain to be divided into simpler overlapping regions for which grids are more easily constructed. The chimera methodology is composed of two codes. The first, PEGSUS,[25] uses individually generated grids as input and defines the communication and interpolation data among interacting grids. The second, XMERA, uses as input the composite mesh, interpolation data created by PEGSUS, and flow conditions to compute the flow field. The XMERA code is a three-dimensional implicit Navier-Stokes code based on the Pulliam-Steger implementation of the Beam and Warming algorithm,[26] with a thin-layer approximation to the viscous terms in one direction (normal to the flat plate and the bottom wall of the cavity, Fig. 1). The algorithm is first-order accurate in time and uses the Baldwin-Lomax turbulence model.[27] The turbulence model is used only on the flat plate and not within the bay. A trial computation using a modified version of the Baldwin-Lomax turbulence model for the shear layer gave results that differed insignificantly from the computation without a turbulence model for the shear layer.

3.1 Computational Meshes

The meshes for computing the flow field were generated to obtain good resolution for regions with high flow gradients and sized to fit in the available computer memory. Several meshes were developed and combined into the configurations required for the computations. To decrease the computational time required for each solution, the domain was reduced by one-half by assuming a lateral plane of symmetry. Representative trial computations for the entire domain showed that the flow in an empty bay was symmetric.

Two overlapping meshes were developed and combined to create the flat-plate/bay configuration. One mesh defines the flat-plate region including inflow, outflow, and symmetry planes. The weapons bay mesh defined the total bay and extended 0.25 bay depths above the opening of the bay so that most of the fluctuating shear layer is resolved within the bay mesh. Each

region was discretized with a stretched Cartesian mesh. The points in both meshes were clustered near walls and in the vicinity of the shear layer, as illustrated in Fig. 4a for the symmetry plane. Exponential and hyperbolic-tangent stretching functions[28] were used to distribute the mesh points in the flat-plate and bay meshes. The exponential stretching function was used for placing points where a specific spacing is needed at only one end point, e.g., from the flat plate to the far-field boundary. The hyperbolic-tangent stretching function was used when a specific spacing was needed at both ends of a line, e.g., from the front wall to the aft wall and from the bottom wall to the opening of the bay.

The store and sting were represented with separate body-conforming meshes. The store and sting meshes were generated separately. The mesh points on the body and symmetry plane surfaces were obtained by using both exponential and hyperbolic-tangent stretching functions. The interior mesh points were obtained by using transfinite interpolation.[28] The symmetry plane of the store and sting meshes is shown in Fig. 4b.

The store/sting meshes were combined with the weapons bay meshes using the chimera overset grid methodology.[23-25] In Fig. 4c, the symmetry plane of the flat plate and bay meshes is shown with the store/sting embedded. The points excluded from the meshes are points that are not part of the solution because of the embedded store/sting.

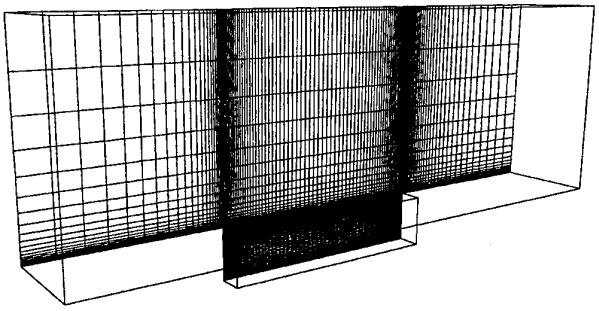

a. Symmetry plane of empty weapons bay configuration

b.Symmetry plane of stone/sting configuration

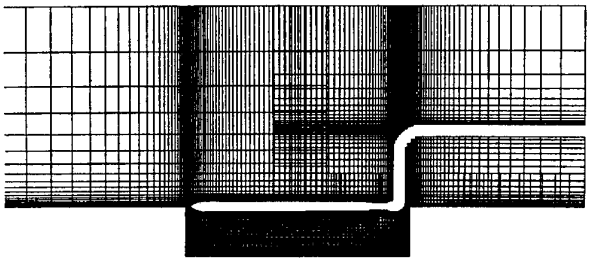

c. Symmetry plane of weapons bay with store/sting embedded

Fig. 4. Computation meshes.

3.2 Boundary/Initial Conditions

Figure 5 illustrates the location of the surfaces on which boundary conditions are specified. The Y = 0 plane is the plane of symmetry and the side plane coincides with the side edge of the flat plate. The inflow boundary condition used when $M_\infty > 1.0$ was set by placing the inflow plane one cavity depth upstream of the leading edge of the cavity, with the inflow velocity profile set to that of a turbulent boundary layer which begins at the leading edge of the flat plate. The velocity profile was based on the 1/7th power law, and the density and energy terms were computed from the X-distribution of the experimental static pressure with an assumed zero normal pressure gradient through the boundary layer. This inflow boundary condition is appropriate for free-stream Mach numbers greater than 1.0 and is used for the examples in this paper. The inflow boundary condition used for subsonic free-stream flow required the inflow plane to be located about one bay length upstream of the flat plate leading edge. The boundary layer was then allowed to develop along the plate. All points on the inflow plane were set to free-stream conditions. The no-slip condition was imposed on the solid surfaces of the plate and bay. This is the correct condition for the flat plate and for the bottom wall since the thin-layer viscous terms are included normal to these surfaces. For the weapons bay front, aft, and side walls, the no-slip condition was used as a matter of convenience to avoid double-valued points at the edges and corners. The use of the no-slip conditions (as opposed to the normally used inviscid tangential flow condition) was justified because a computation with thin-layer approximations for all surfaces showed no significant changes in the computed flow. Symmetry conditions were enforced on the side surface (see Fig. 5) of the meshes exterior to the bay and on the symmetry plane of the bay. The boundary conditions for the upper surface (see Fig. 5) were set to free-stream conditions, except for the value of the Z-component of momentum which was evaluated by zeroth-order extrapolation. The conditions on the

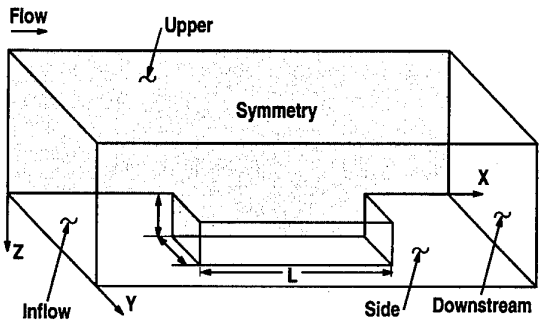

Fig. 5. Diagram of the surfaces requiring boundary conditions.

downstream outflow surface (see Fig. 5) depended on whether the local flow was subsonic or supersonic. If the flow was locally subsonic, all flow variables except the total energy were set by zeroth-order extrapolation. The total energy was calculated assuming free-stream pressure and the extrapolated values of density and momentum. If the flow was locally supersonic, all values, including the total energy, were set by zeroth-order extrapolation.

Inviscid slip conditions were imposed on the solid surfaces of the store and sting. This condition was used to keep the run time to a minimum for these calculations (i.e., if the no-slip condition were used and the viscous terms were resolved near these surfaces, finer mesh spacing would be required which would greatly increase the run time). A test case, with the viscous terms and no-slip conditions imposed on the store and sting, showed only small changes in the results from those with the slip boundary conditions.

The computational flow domain was initialized by setting the flow velocity in the weapons bay to zero and by using the boundary-layer profile prescribed at the inflow surface to define the initial condition across the entire exterior mesh. It was found that the thickness of the initial boundary layer should be as realistic as possible since an inaccurate distribution could have a significant effect on the decay of the initial-condition transients. If the initial boundary-layer thickness is too large, a significant number of additional time steps are required before the starting transients disappear.

4. RESULTS AND ANALYSIS

Two sets of computations were performed as a demonstration of this capability. First, computations for an empty weapons bay were performed at M_∞ = 0.60, 0.95, and 1.20. The second set of computations was performed for the same weapons bay, but with a store mounted on a sting placed within the weapons bay at M_∞ = 0.60, 0.95, and 1.20. For all cases a Reynolds number of 2.6 x 10^6/ft was used. The bay was 18 in. long and 4 in. deep, giving an L/H of 4.5. The results for the empty bay presented here are comparisons of computations with experimental data on the bay walls for static-pressure coefficient (C_p), overall sound pressure level (OASPL), and the frequency spectrum of the sound pressure level (SPL). The results for the store/sting in the bay are comparisons of computations with experimental data on the store for C_p. In addition, loads on the store are given, although no data comparisons are available. Before reviewing these comparisons, the methodology used to reduce the computational, as well as the experimental data, must be examined so that the relationships between the two are well understood.

4.1 Analysis Techniques

Three parameters are used to represent the pressure on the bay walls, namely C_p, OASPL, and the frequency spectrum of the SPL. The experimental pressure coefficient (C_pe) was obtained by scanning each orifice at a rate of 15 samples/sec (once every 66 msec). The most recent 15 values were averaged to give the recorded value of pressure at each location following the steady-state flow ESP sampling techniques. Because of the low number of samples and the low sampling rate, the experimental results show a variability in C_pe that is not within the normal error band of the experiment.[1] The magnitude of the variations increase as the free-stream Mach number decreases, as cited by Dix[1] and Plentovich.[29] Plentovich[29] has also shown that the variations in C_pe decrease by increasing the number of samples.

Since bay flow is unsteady, the time-averaged pressure coefficient ($\overline{C}_p$) for the computations is obtained by integrating over a time interval (T_{avg}). T_{avg} is chosen to be of sufficient length so that the average is independent of time. It is convenient to express time in units of the characteristic time (t_c), which is the time required for the flow to traverse the length of the cavity at the free-stream velocity. At the test conditions associated with a M_∞ = 0.60, 0.95, and 1.20, t_c is 0.00225, 0.00149, and 0.00123 sec, respectively. Experience has shown that to ensure that the starting transients have decayed, solutions must be calculated for $5t_c$ prior to beginning the interval, T_{avg}, used in the determination of $\overline{C}_p$. $\overline{C}_p$ is determined in the same way as for earlier computations,[3-5] i.e., for $T_{avg} = 6t_c$. Use of a larger value for T_{avg} resulted in small changes in $\overline{C}_p$ that were within the variations seen for C_pe in Fig. 6. In comparison to C_pe, which was averaged from 15 values recorded at a rate of 15 samples/sec, the $\overline{C}_p$ determined for the computations was averaged for 1,200 samples ($6t_c$) at a recording rate of 162,600 samples/sec.

The OASPL is computed in a manner similar to that used for computing $\overline{C}_p$. The OASPL in decibels (dB) is defined as:

$$OASPL = 180 + 20 \log[P_{rms}/P_{ref}] \qquad (1)$$

where P_{rms} is the root-mean-square of the pressure fluctuations about the average in pounds per square inch (psi) and P_{ref} is equal to 2.90075 psi (a standard reference pressure). P_{rms} is defined as:

$$P_{rms} = (S(P_{avg} - P)2 / N)^{0.5} \qquad (2)$$

where P is the pressure at each time step, P_{avg} is the averaged pressure used to compute $\overline{C}_p$, and N is the number of time steps. The OASPL was computed in the same way as for $\overline{C}_p$, i.e., for $T_{avg} = 6t_c$. A small variation, typically less than 1 dB, in OASPL was observed when a larger value of T_{avg} was used.

The experimental values for OASPL were obtained from over 25,000 samples recorded by differential-pressure transducers at a rate of 10,000 samples/sec. The recording rates for the computations and experimental results were much closer for the OASPL than for C_p. The recording rates for OASPL differed by a factor of 16, while the rates for the pressure coefficients

differed by a factor of 10,840. Therefore, the comparisons for the OASPL are considered more definitive.

The frequency spectrum of the SPL was determined by analyzing the time history of the pressures in the weapons bay using conventional fast Fourier transform techniques. The computational results were analyzed in a similar manner to that used for the experimental data. A recording rate of 10,000 samples/sec and sample size of 1,024 was used for both the computations and the experiment, with the data for both being analyzed by the same computer program. This recording rate and sample size are equivalent to $83.25t_c$. The only difference in the analysis methods was that 25 experimental ensembles (independent groups of 1,024 samples) were averaged to get the final frequency spectrum, while 15 ensembles were averaged for the computations. The fifteen ensembles obtained from the computations also differed in that they were not independent groups of samples like the experimental data. Instead, these 15 ensembles were obtained from over $98t_c$ of computational results which were grouped in overlapping ensembles spaced by $1t_c$.

Loads on the store were found by integration of the computed pressure. Both the coefficient of the normal force (C_N) and the coefficient of the pitching moment (C_m) were computed as time-averaged values for $6t_c$. The area of integration includes the total store surface, but excludes the base of the store.

4.2 Empty Weapons Bay

Results for the empty weapons bay are shown in Fig. 6 for $M_\infty = 0.60$, 0.95, and 1.20. In Figs. 6a, 6c, and 6e, C_p distributions are shown along the centerlines of the front, bottom, and aft walls of the cavity. The computations are represented by the solid and dashed lines. The solid line is $\overline{C}_p$ while the dashed lines are $\overline{C}_p$s, which are the sum of $\overline{C}_p$ plus and minus the standard deviation of the time history of the calculated pressure coefficients. The experimental data C_pe are shown for repeat data points. The OASPL for the computations and the experimental data at locations along the centerlines of the front, bottom, and aft cavity walls are shown in Figs. 6b, 6d, and 6f.

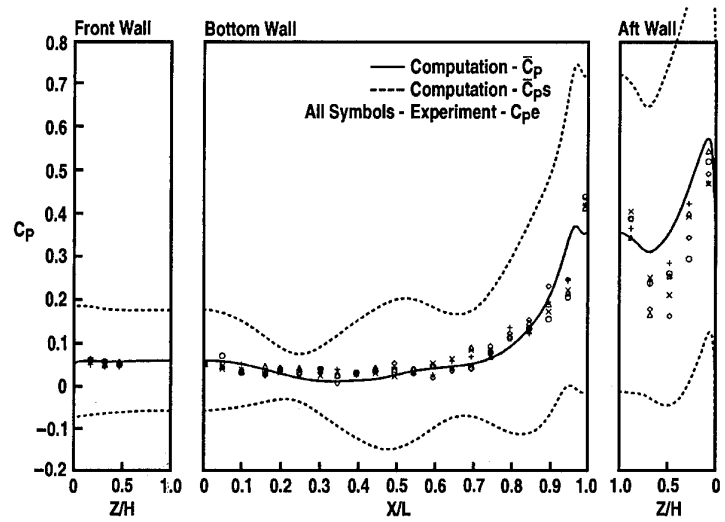

a. C_p on centerline, $M_\infty = 0.60$

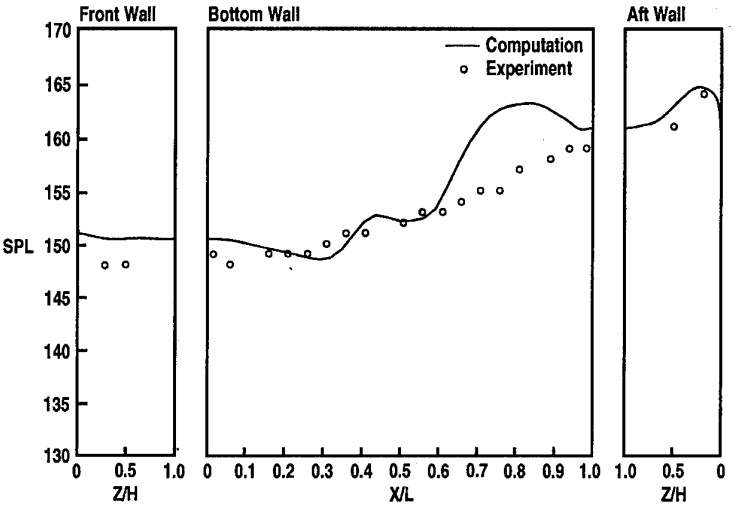

b. OASPL on centerline, $M_\infty = 0.60$

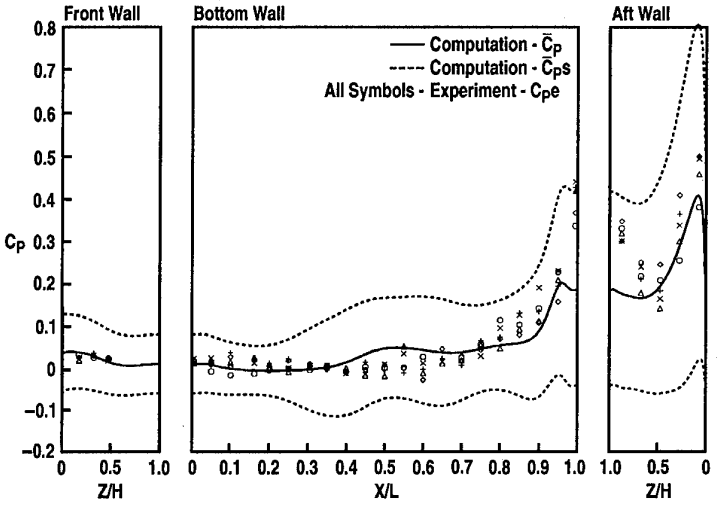

c. C_p on centerline, $M_\infty = 0.95$

Fig. 6. Comparison of computations and measurements on the walls of the empty weapons bay.

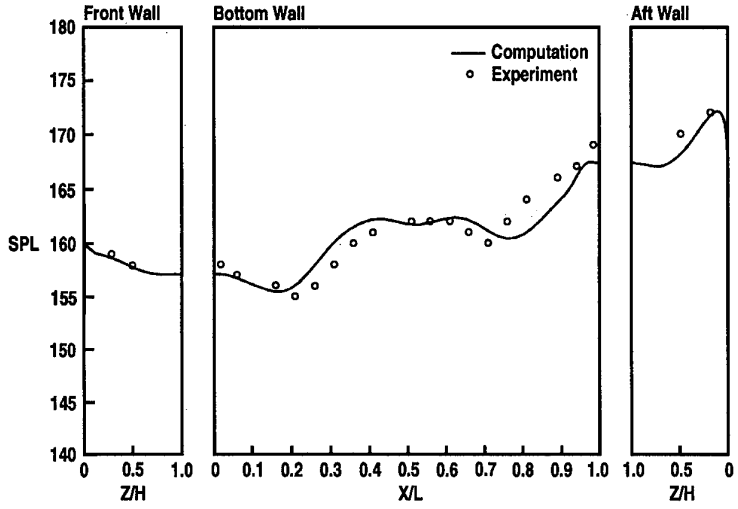

d. OASPL on centerline, $M_\infty = 0.95$

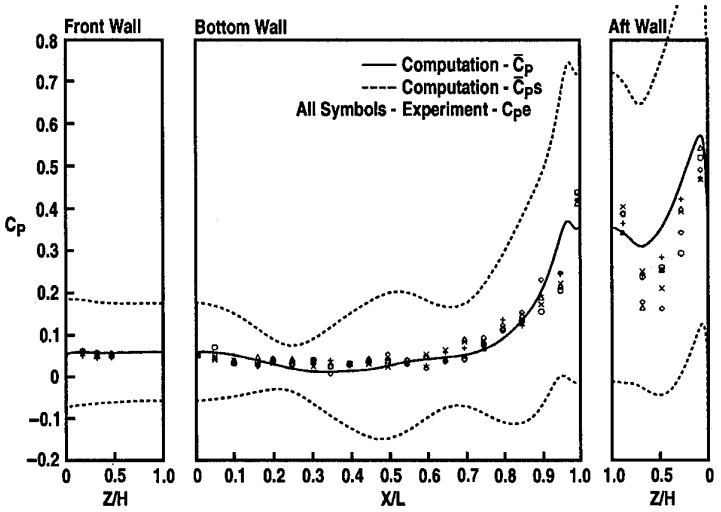

e.C_p on the centerline, $M_\infty = 1.20$

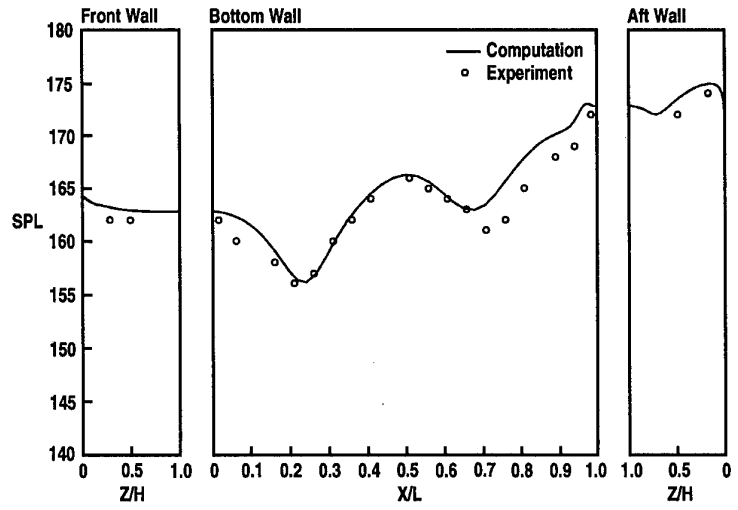

f. OASPL on the centerline, $M_\infty = 1.20$

Fig. 6. Concluded.

Shown in Fig. 6a are the C_p distribution comparisons of the computations to the experimental data for the empty bay at $M_\infty = 0.60$. The spread of experimental data is bounded by the computational results C_ps. On the other hand, as shown in Fig. 6b, the agreement was not as good for the OASPL, especially for 0.65 <X/L <1.0 on the bottom wall of the bay.

In Figs. 6c and 6d, comparisons for an empty bay at $M_\infty = 0.95$ are made. The computed and experimental data C_p distributions along the centerlines of the front, bottom, and aft walls of the bay agree well, as is shown in Fig. 6c. Depicted in Fig. 6d is the comparison of the computation and the experimental data for the OASPL. Very good agreement between the computations and experimental data is apparent as both the amplitude and trends are predicted by the computation.

In Figs. 6e and 6f comparisons for the empty bay at $M_\infty = 1.20$ are illustrated. Similar to the results obtained at $M_\infty = 0.95$, the comparisons of computations with experimental data are satisfactory for the pressure coefficients shown in Fig. 6e and for the OASPL shown in Fig. 6f.

Computations and experimental data are in good agreement when considering the results for all three Mach numbers. The variations in C_pe in the aft half of the bay indicate large fluctuations in pressure. In all cases, the variations in the experimental results are greater in the same regions where there are large variations in computed pressure coefficients. The computed OASPL at locations along the centerlines of the front, bottom, and aft bay walls agrees well with the data levels and follows the trends remarkably well. This is particularly encouraging, since the sampling rates for the experimental and computational results are closer. Note that the experimental data shows the variations in the C_p ($\bar{C}_p$s minus $\bar{C}_p$) to decrease as M_∞ increases.

In Fig. 7 a frequency spectrum is shown for an empty bay at $M_\infty = 1.20$. The spectrum is for a point on the aft wall of the bay, Z/H=0.18 from the top edge. The solid line represents the experi-

mental data while the dashed line represents the computational results. Experimental data and the computations compare very well at the low frequencies, capturing the first two modes at 225 and 518 Hz. As the frequency increases, the agreement between computations and experimental data is less satisfactory. This disagreement possibly occurs from numerical modeling effects.

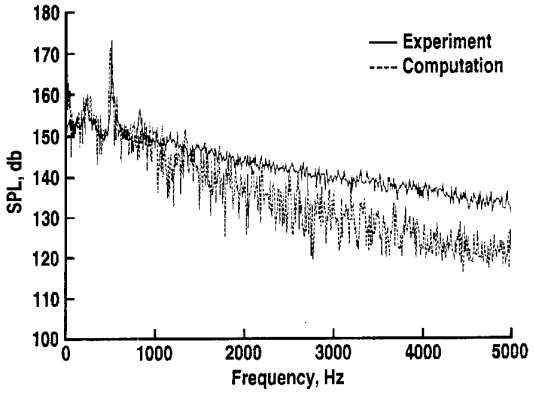

Fig. 7. Frequency spectra of SPL on the aft wall of the empty weapons bay, $M_\infty = 1.20$.

Both computational and experimental pressures along the walls of the weapons bay indicate large pressure fluctuations within the bay. In Fig. 8, Mach number contours for the symmetry plane illustrate the fluctuations that occur during a short time within the empty bay at $M_\infty = 1.20$. Three different times separated by $3t_c$ (approximately 0.0037 sec) are shown. As can be seen in Fig. 8, the flow velocities change quite dramatically, particularly in the aft region of the bay. The local Mach number ranges from zero to about one-half of the free-stream Mach number. In some cases, the flow near the bottom wall of the weapons bay is in the opposite direction to that of the free stream. Finally, note that the shear layer changes as it stagnates on the aft wall or the flat plate downstream of the bay opening.

4.3 Store/Sting in the Weapons Bay

Computations were performed for the store/sting in the weapons bay with the store located at Z_s/H = 0.75, 0.0, and –0.30 for $M_\infty = 1.20$. Additionally, computations were made with the store located at Z_s/H = 0.0 for $M_\infty = 0.60$ and 0.95. Depicted in Fig. 9 are the three locations of the store used for the computations. For all computations the store nose is located at X/L = 0.026.

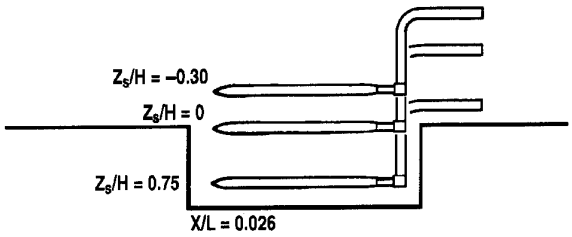

Fig. 9. Store/sting locations within the cavity.

The results for the store/sting in the weapons bay are depicted as C_p distributions on the free-stream and the bay sides of the store, as well as the difference in C_p between the two sides. The C_p distributions, $\overline{C}_p$ and $\overline{C}_p$s, were computed in an identical manner to the values in Fig. 6 for the empty bay walls. One difference in the presented results is that only one value of C_pe is available at each sensor location, unlike the empty bay

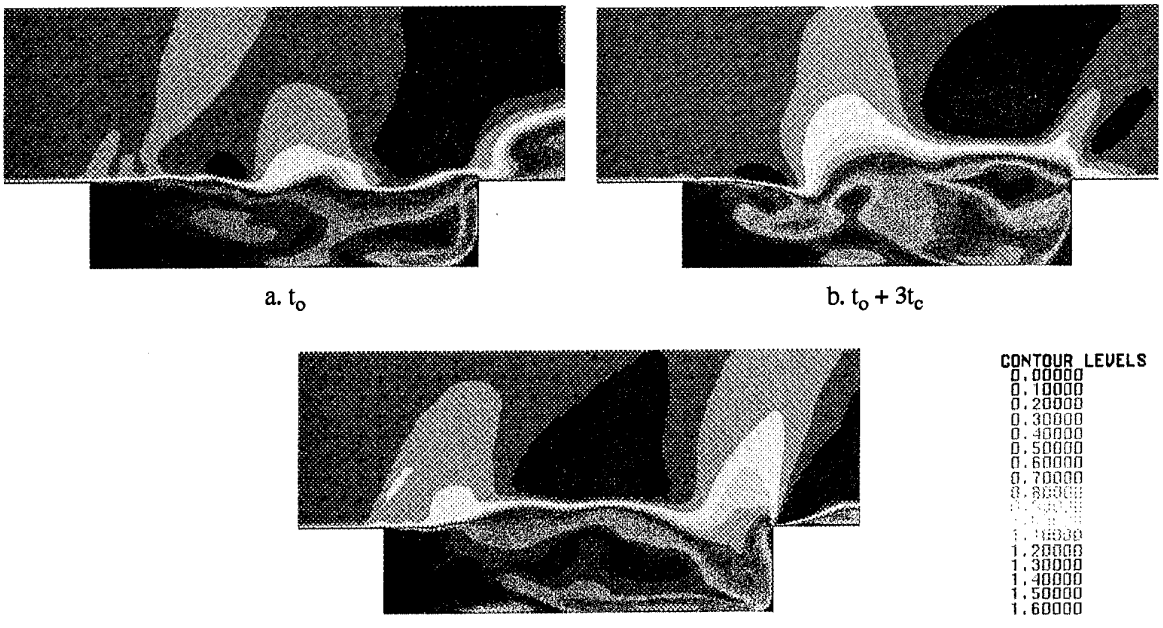

a. t_o

b. $t_o + 3t_c$

c. $t_o + 6t_c$

Fig. 8. Mach number contours in the symmetry plane of the empty weapons bay, $M_\infty = 1.20$.

results which have 5 to 13 measured values available on the bay walls. The difference in C_p between the free-stream and bay sides is defined as

$$\Delta\overline{C}_p = \overline{C}_{p,\text{free-stream side}} - \overline{C}_{p,\text{bay side}} \qquad (3)$$

The $\Delta\overline{C}_p$ distribution along the length of the store is illustrated to give a relative indication of the loads in the Z direction that would be experienced by the store. For all store results, X/L relates the position of the store in the bay, where X is the axial distance of a point on the store measured from the front wall of the bay and L is the length of the bay. Thus, the store nose is at X/L = 0.026 and the boattail of the store intersects the sting at X/L = 0.824.

Comparisons of the computations with the experimental data are depicted in Fig. 10 for the store/sting at different locations at M_∞ = 1.20. Comparisons of the computed and measured C_p distributions on the free-stream and bay sides of the store are shown in Figs. 10a and 10b, respectively, for the store placed deep within the bay at Z_s/H = 0.75. The agreement on the store is unsatisfactory in the aft region of the bay. To investigate the overall effect that the poor agreement has on computing store loads, $\Delta\overline{C}_p$ is shown in Fig. 10c. The computed $\Delta\overline{C}_p$ distribution gives a relative indication of the store loads in the Z direction. As can be inferred, the loads on the store would be predicted with relatively small errors.

In Figs. 10d and 10e, the comparisons of C_p distributions are illustrated for the free-stream and bay sides of the store. Similar to the computations at Z_s/H = 0.75 (Figs. 10a and 10b), the computed C_p increases along the aft portion of the store and does not compare well to the experimental data. Depicted in Fig. 10f is the $\Delta\overline{C}_p$ distribution for the store. The front portion of the store compares well, while the aft portion shows some divergence from the data.

The comparisons for C_p along the free-steam and bay sides of the store located outside of the bay at Z_s/H = –0.30 are shown in Figs. 10g and 10h. The agreement is very good. At this location the store is farther from the influence of the bay, and there is improved comparison between the computations and the experimental data. Finally, the $\Delta\overline{C}_p$ distribution for the store is shown in Fig. 10i. It is unsatisfactory near the nose (X/L = 0.2), which is in marked contrast to Figs. 10c and 10f.

The computational results generally display an increasing $\overline{C}_p$ with X, which implies a decreasing velocity (see Figs. 10a, 10b, 10d, and 10e). On the other hand, the experimental results display a decreasing C_pe with X, implying an increasing velocity. The incorrect trend of decreasing velocity for the computations is typically the result of inadequate spatial resolution which artificially diffuses the shear layer. Large oscillations of the shear layer cause it to move into regions with much coarser mesh resolution. Thus, the differences observed between the measured and computed C_p may be caused by inadaquate spatial resolution of the shear layer.

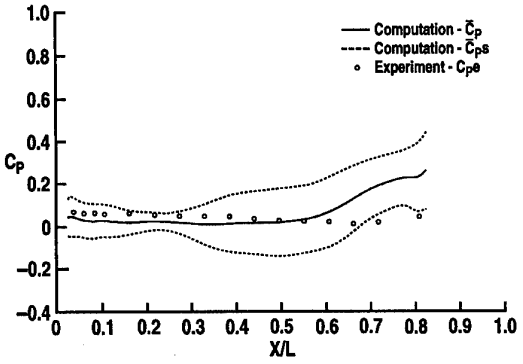

a. C_p on free-stream side, Z_s/H = 0.75

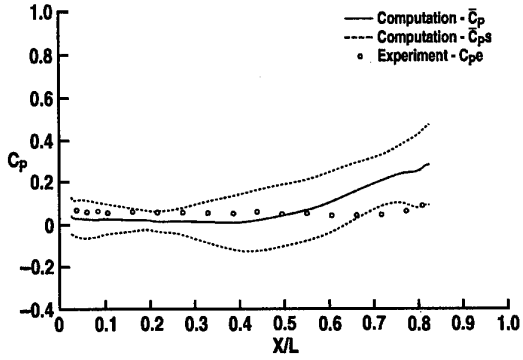

b. C_p on bay side, Z_s/H = 0.75

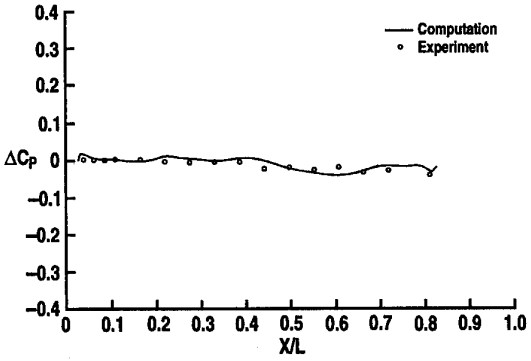

c. $\Delta\overline{C}_p$, Z_s/H = 0.75

Fig. 10. Comparisons of computations and measurements on the store/sting in the cavity.

Additional illustration of the load variations versus store position in the weapons bay is shown in Fig. 11. Both C_N (Fig. 11a) and C_m (Fig. 11b) for the store at three positions, Z_s/H = 0.75, 0.0 and –0.30, are depicted. In Fig. 11a the calculated results are represented by the time-averaged value $\overline{C}_N$ (the symbol) and the sum of $\overline{C}_N$ plus/minus the standard deviation of the time history of the calculated normal coefficient about $\overline{C}_N$ ($\overline{C}_N$s, error bar). The C_N results show little difference in the variations from one location in the bay to the next. On the other hand, C_m, which is depicted as

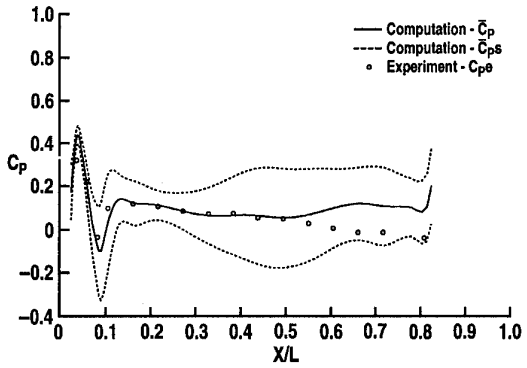

d. C_p on free-stream side, $Z_s/H = 0$

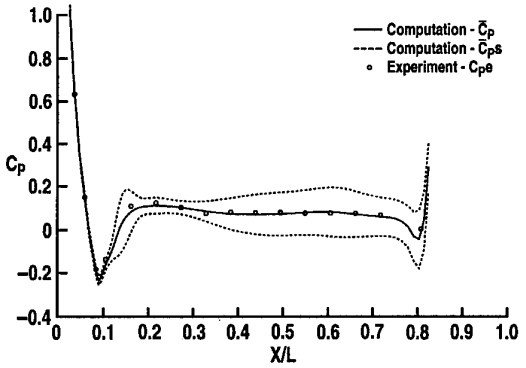

g. C_p on free-stream side, $Z_s/H = 0.30$

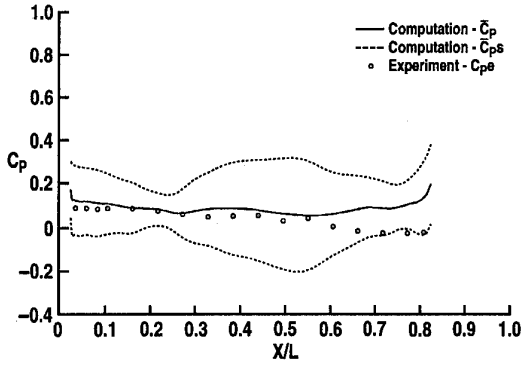

e. C_p on bay side, $Z_s/H = 0$

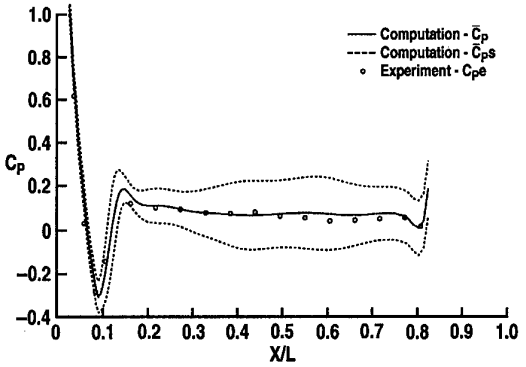

h. C_p on bay side, $Z_s/H = 0.30$

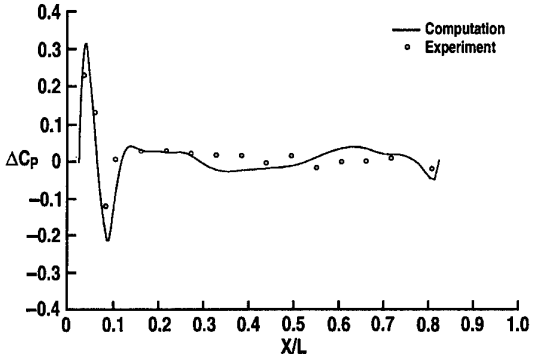

f. $\overline{\Delta C}_p$, $Z_s/H = 0$

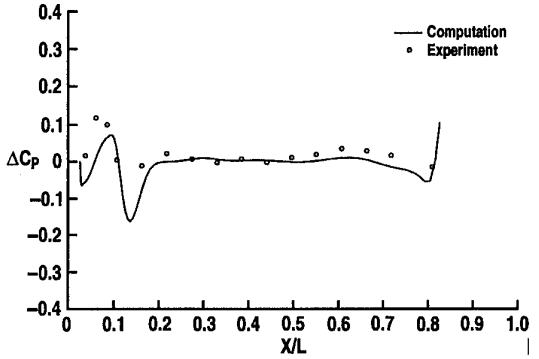

i. $\overline{\Delta C}_p$, $Z_s/H = 0.30$

Fig. 10. Concluded.

$\overline{C}_m$ and $\overline{C}_m$s in a similar manner as C_N in Fig. 11b, is seen to have the largest variations (i.e., a larger standard deviation) at $Z_s/H = 0.0$ with lesser variations at $Z_s/H = -0.30$ and 0.75.

C_N and C_m for the store at $Z_s/H = 0.0$ for M_∞ = 0.60, 0.95 and 1.20 are depicted in Fig. 12. Similar to Fig. 11, $\overline{C}_N$, $\overline{C}_N$s, $\overline{C}_m$ and $\overline{C}_m$s are shown. A definite trend in the variations of these values can be seen. As the Mach number increases, the variations of C_N (Fig. 12a) and particularly C_m (Fig. 12b) increase. This increase in variations is similar to what is seen for the computed C_p values on the empty bay wall, see Fig. 6.

The variations that are observed for the loads on the store are quite significant for each configuration examined. These variations in some cases were greater in value than the time-averaged value of the loads. The effects of these variations, i.e., the unsteadiness on store separation, are yet to be determined.

5. CONCLUSIONS

An implicit Navier-Stokes code with a thin-layer approximation has been used to compute the flow for a three-dimensional rectangular weapons bay and a store/sting located in the bay at a free-stream Mach numbers of 0.60, 0.95, and 1.20. The principal conclusions that can be drawn from this study are:

1. The empty bay computations show overall good agreement with the experimental data at all Mach numbers. On particular note, at Mach 1.20, the first and

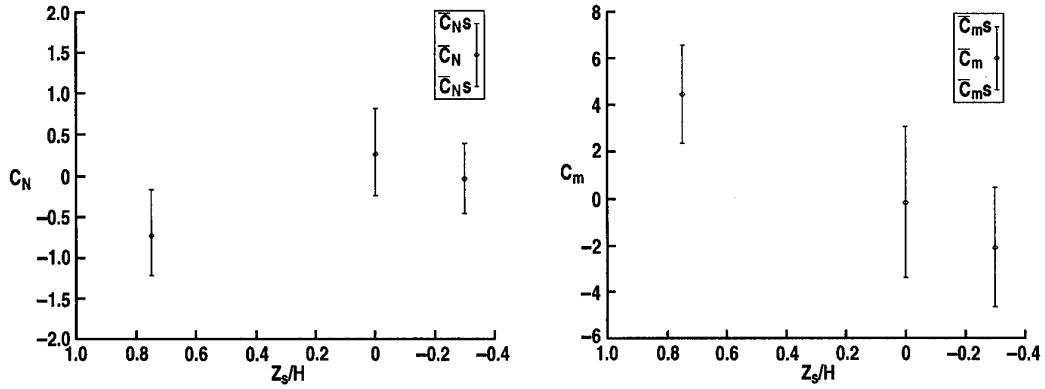

a. C_N b. C_m

Fig. 11. Loads on the store in the weapons bay, variations in location, $M_\infty = 1.20$

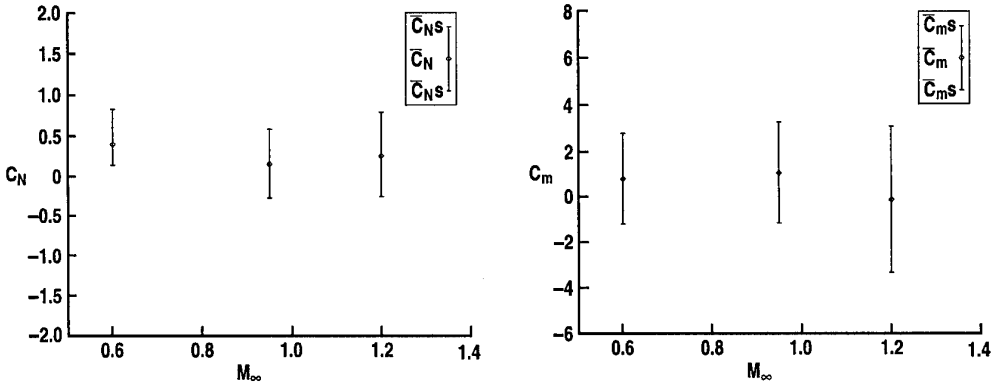

a. C_N b. C_m

Fig. 12. Loads on the store in the weapons bay, variation in Mach number, $Z_s/H = 0$.

second frequency modes of the sound pressure levels are predicted by the computations.

2. The flow within the empty bay was observed to be highly unsteady with the shear layer moving in and out of the cavity. Very low-amplitude velocities were measured and computed in the front region of the cavity, while highly varying velocity amplitudes occurred in the aft region of the cavity.

3. The computational pressure coefficients and overall sound pressure levels of the empty bay need only be integrated over 6 characteristic times to obtain satisfactory agreement with the experimental data. This integration time indicates that the quality of the computation can be evaluated after executing the computation for only a relatively short interval of only 11 time characteristics.

4. The level of agreement between computations and experimental data for the store/sting in the bay varied with the position of the store. When the store was positioned at the plane of the bay opening ($Z_s/H = 0.0$), poor agreement was observed on the aft portion of the store for all computed Mach numbers. It is believed that the poor agreement between the computations and the measurements for the aft region of the bay with the store present indicates that this region needs more resolution to avoid excessive dissipation of the streamwise velocity component. However, the computed difference in pressure across the store agreed well with the data. When the store was positioned deep within the bay ($Z_s/H = 0.75$) at $M_\infty = 1.20$, the agreement between computed and experimental data on the aft portion of the store decreased. However, the computed difference in pressure across the store agreed well with measurement and was similar to what was seen for the store at the plane of the cavity opening. Finally, when the store is positioned outside of the weapons bay at $Z_s/H = -0.30$ for $M_\infty = 1.20$, the agreement between computations and experimental data was found to be good, probably because the store was outside the shear layer.

REFERENCES

1. Dix, R. E. and Butler, C. "Cavity Aeroacoustics." *Proceedings of Store Carriage, Integration and Release Conference*, Bath, U. K., The Royal Aeronautical Society, April 1990.

2. Bauer, R. C. and Dix, R.E. "Engineering Model of Unsteady Flow in a Cavity." AEDC-TR-91-17 (AD-A243636), December 1991.

3. Suhs, N.E. "Computations of Three Dimensional Cavity Flow at Subsonic and Supersonic Mach Numbers." AIAA-87-1208, June 1987.

4. Suhs, N. E. "Transonic Flow Calculations for a Cavity With and Without a Store." AEDC-TR-92-4 (AD-A255954), September 1992.

5. Suhs, N. E. "Unsteady Flow Computations for a Three-Dimensional Cavity With and Without an Acoustic Suppression Device." AIAA-93-3402, August 1993.

6. Rossiter, J. E. "Wind Tunnel Experiments on the Flow over Rectangular Cavities at Subsonic and Transonic Speeds." British A.R.C., R & M No. 3438, 1966.

7. Heller, H. H. and Bliss, D. B. "Aerodynamically Induced Pressure Oscillations in Cavities - Physical Mechanisms and Suppression Concepts." AFFDL-TR-74-133, February 1975.

8. Kaufman, L. G. II, Maciulaitis, A., and Clark, R. L. "Mach 0.6 to 3.0 Flows Over Rectangular Cavities." AFWAL-TR-82-3112, May 1983.

9. Komerath, N. M., Ahuja, K. K., and Chambers, F. W. "Prediction and Measurement of Flows over Cavities - A Survey." AIAA-87-0166, January 1987.

10. Stallings, R. L., Jr. and Wilcox, F. J., Jr. "Experimental Cavity Pressure Distributions at Supersonic Speeds." NASA TP-2683, June 1987.

11. Hankey, W. L. and Shang, J. S. "Analyses of Pressure Oscillations in an Open Cavity." *AIAA Journal*, Vol. 18, No. 8, August 1980, pp. 892-898.

12. Baysal, O. and Stallings, R. L., Jr. "Computational and Experimental Investigations of Cavity Flow Fields." AIAA-87-0144, January 1987.

13. Venkatapathy, E., Lombard, C. K., and Nagaraj, N. "Numerical Simulation of Compressible Flow Around Complex Two-Dimensional Cavities." AIAA-87-0166, January 1987.

14. Dougherty, N. S., Holt, J. B., Nesman, T. E., and Farr, R. A. "Time-Accurate Navier-Stokes Computations of Self-Excited Two-Dimensional Unsteady Cavity Flows." AIAA-90-0691, January 1990.

15. Baysal, O., Yen, G. W., and Fouladi, K. "Navier-Stokes Computations of Cavity Aeroacoustics with Suppression Devices." DGLR/AIAA 14th Aeroacoustics Conference, Eurogress Center, Aachen, Germany, May 11-14, 1992.

16. Jeng, Y. N. and Wu, T. J., "Numerical Study of a Supersonic Open Cavity Flow with Geometric Modification on Aft Bulkhead." AIAA-92-2627CP, June 1992.

17. Gorski, J. J., Ota, D. K., and Chakravarthy, S. R. "Calculation of Three-Dimensional Cavity Flow Fields." AIAA-87-0117, January 1987.

18. Rizzetta, D. P. "Numerical Simulation of Supersonic Flow Over a Three-Dimensional Cavity." AIAA-87-1288, June 1987.

19. Baysal, O., Srinivasan, S., and Stallings, R. L., Jr. "Unsteady Viscous Calculations of Supersonic Flows Past Deep and Shallow Three-Dimensional Cavities." AIAA-88-0101, January 1988.

20. Baysal, O. and Srinivasan, S. "Navier-Stokes Calculations of Transonic Flow Past Cavities." NASA CR-4210, January 1989.

21. Tu, Y. "Unsteady Navier-Stokes Simulations of Supersonic Flow Over a Three-Dimensional Cavity." AIAA-92-2632CP, June 1992.

22. Atwood, C. A. "Navier-Stokes Simulations of Unsteady Transonic Phenomena." NASA Technical Memorandum 103962, August 1992.

23. Benek, J. A., Steger, J. L., Dougherty, F. C., and Buning, P. G. "Chimera: A Grid-Embedding Technique." AEDC-TR-85-64 (AD-A167466), December 1985.

24. Benek, J.A., Donegan, T.L., and Suhs, N.E. "Extended Chimera Grid Embedding Scheme with Application to Viscous Flows." AIAA-87-1126CP, June 1987.

25. Suhs, N. E. and Tramel, R. W. "PEGSUS 4.0 User's Manual." AEDC-TR-91-8 (AD-A280608), October 1991.

26. Pulliam, T. H. and Steger, J. L. "On Implicit Finite-Difference Simulations of Three-Dimensional Flow." *AIAA Journal*, Vol. 18, No. 2, February 1980, pp.159-167.

27. Baldwin, B. S. and Lomax, H. "Thin Layer Approximation and Algebraic Model for Separated Turbulent Flows." AIAA-78-257, January 1978.

28. Thompson, J. F., Warsi, Z. U. A., and Mastin, C. W. *Numerical Grid Generation: Foundation and Applications*. North-Holland, New York, 1985, pp. 305-310.

29. Plentovich, E. B. "Three Dimensional Cavity Flow Fields at Subsonic and Transonic Speeds." NASA TM-4209, September 1990.

THE IMPLICATIONS OF STORES CARRIAGE AND RELEASE FOR AIRCRAFT FLIGHT CONTROL SYSTEM DESIGN

D.A.Allen and K.F.Hulme
Aerodynamics Department, W310P
British Aerospace Defence Limited,
Military Aircraft Division,
Warton, Lancashire, PR4 1AX, UK

SUMMARY

Against a backdrop of a review of the capabilities and limitations of a modern digital aircraft flight control system, this paper considers the implications of the carriage and release of a wide range of stores for modern high performance military aircraft.

At the heart of any flight control system design is consideration of the characteristics of the vehicle and its operating environment. It is in consideration of these aspects that the major impact of external (and internal) stores carriage and release occurs. The relevant vehicle characteristics are described by its aerodynamic, inertial, and structural properties which are all complex in their own right but are also substantially affected by stores carriage. Releasing stores from the vehicle will excite both rigid body and flexible modes of the vehicle due to rapidly changing the vehicle's mass, inertial and aerodynamic characteristics.

Despite the rapid technological advances in flight control system design, the underlying physical limits remain, and will continue to do so! A clear recognition of these limitations and their implications is essential, particularly at the concept and early design stages of a project.

This paper addresses the major issues involved and the interaction between stores integration and flight control system design for modern fighter aircraft.

LIST OF SYMBOLS AND ABBREVIATIONS

C_{Lmax}	maximum lift coefficient
Cl_β	dihedral derivative
Cm_q	pitch damping derivative
Cm_α	pitch stiffness derivative
Cm_δ	control power derivative
$C_{N\alpha}$	coefficient of n_z per α
Cn_β	directional stiffness derivative
$Cn_{\beta dyn}$	dynamic Cn_β
dB	decibel
FCC	Flight Control Computer
FCS	Flight Control System
g	acceleration due to gravity
Hz	cycles per second
i_a	non-dimensional inertia about body x axis
i_c	non-dimensional inertia about body z axis
K_α	incidence feedback gain
ms	milli-second
M	aircraft mass
n_z	normal acceleration
q	pitch rate
s	Laplace operator
S	reference area
t_d	time to double-amplitude
V	free stream velocity
α	angle of incidence
β	angle of sideslip
σ	(unstable) root position
ρ	density of air

1. INTRODUCTION

McRuer (Reference 1) observed that the traditional process of systems integration is to make individually designed subsystems work together on an aircraft; that is, to ensure compatibility and minimize adverse interactions. The logical goal for the future must therefore be to carry out multi-disciplinary optimization of the highly interactive systems in order to maximize aircraft performance. Interdisciplinary understanding is essential to achieve an overall cost-effective balanced design for such integrated and dynamically interacting systems.

The purpose of this paper is to review the capabilities and limitations of a modern digital flight control system and examine the implications of the carriage and release of a wide range of stores. It is hoped that this paper will therefore contribute to wider interdisciplinary understanding. The effect of stores on the aircraft physical properties and their implications are described and examined from an FCS view-point. Examples of FCS design which require extensive interdisciplinary understanding chosen for this paper are the flight control system of a highly unstable combat aircraft, and some of the issues relating to flight at moderate/high incidence.

2. PITCH AXIS FCS OF AN UNSTABLE COMBAT AIRCRAFT

A fundamental part of the FCS design process is consideration of the characteristics of the vehicle and its operating environment, including the effects of stores carriage and release. The designer of the weapon system configuration and the flight control system must take due account of these interactions from day one. This section indicates, that for a highly unstable airframe, the carriage of a wide range of stores can directly affect the level of FCS design effort.

Paper presented at the AGARD FDP Symposium on "Aerodynamics of Store Integration and Separation", held in Ankara, Turkey from 24-27 April 1995, and published in CP-570.

2.1 Maximum Levels of Instability

To enable a modern fighter aircraft to have optimized lift/drag characteristics and hence exhibit maximum performance, static stability margins have been relaxed. Many of today's combat aircraft have significant static instability over large parts of their flight envelope and require stability augmentation by means of a closed-loop controller. It is perhaps worthwhile at this point to reflect on the different definitions of stability and to identify the most useful definition from the FCS engineer's view-point.

Measures of instability may include negative manoeuvre margin or positive Cm_α. Both these measures do not convey the speed at which the aircraft would depart in pitch if uncontrolled - this is a function of further parameters including the aircraft chord, pitch inertia and flight condition. The single measure of instability which provides most information for the FCS engineer is the unstable 'short period' root position, σ. This can be used to derive the time to double-amplitude, t_d, by the following expression:

$$t_d = \log_e 2 / \sigma$$

There is, of course, a limit to the instability which can be adequately controlled by the FCS and thus a limit to the extent to which the lift/drag characteristics may be optimized by reduction of static stability. The limiting instability is governed by the available hardware technology within the FCS, and the need to provide a robust control system to meet applicable airworthiness clearance criteria.

The FCS hardware necessary for correct functioning of the system introduces lags and time delays into the closed-loop control system. The hardware includes sensors, actuators, and digital computing elements such as anti-aliasing filters, asynchronous delays and computer transport delays. Additional lags are also usually present due to the structural mode filters required to attenuate flexible resonances, which may be superimposed on the rigid body motion feedback signals (FCS-structural coupling is described further in Section 2.5).

Figure 1 shows the individual contributions to the total phase lag from the hardware elements and structural notch filters within a typical flight control system. As noted above, this contributes to there being an upper limit to the level of aircraft instability which may be adequately controlled by the FCS. Based on appropriate requirements for robustness, the maximum controllable instability may be established. It is shown in Figure 2 that a root position of approximately 3.9 (t_d = 180 ms) is typically the maximum instability that may be controlled whilst meeting production aircraft criteria such as those defined in Reference 2. Less stringent criteria would lead to higher levels of instability being tolerable. For example, the X-29A is more unstable, with a time to double-amplitude as low as 120 ms (Reference 3). However, the FCS for this aircraft was designed to meet relaxed stability margins appropriate only to a carefully controlled flight test environment.

A further constraint on maximum instability levels due to hardware considerations occurs at low airspeed, when the aerodynamic control surfaces are potentially required to move through large angles. Actuator rate-limiting, which should be avoided to retain control of the aircraft, is another factor which must be considered for a balanced design. Figure 3 shows schematically how system phase lag and actuator rate-limits influence the overall aircraft instability levels.

2.2 Pitch Static Stability Augmentation

As this section describes the FCS features for non-FCS specialists, the following account is more descriptive than mathematical and avoids debate on different flight control law algorithm design techniques. Physical characteristics are described whilst avoiding, as far as possible, any complex mathematical formulae or abstract ideas.

Simple proportional incidence, α, may be used as a feedback parameter to augment Cm_α and hence provide static stability. However, alternative feedback parameters may be scaled to provide the same effect. The following approximate relationships show how normal acceleration, n_z, and pitch rate, q, may be used as feedback states in place of α to give the same effect:

$$\frac{\alpha}{n_z} = \frac{M.g}{{}^1/_2 \rho V^2 S C_{N\alpha}}$$

$$\frac{\alpha}{q} = \frac{\tau_1}{1 + \tau_1 s}$$

where $$\tau_1 = \frac{M.V}{{}^1/_2 \rho V^2 S C_{N\alpha}}$$

This flexibility allows potential interchange of α, n_z, and q feedback states throughout the flight envelope, to match the manoeuvre demand characteristics required and avoid transients when changing from one manoeuvre demand type to another. It is clear from the above expressions that appropriate scheduling of the feedback parameters is required for n_z and q to provide an 'incidence equivalent' feedback for stability augmentation. Mass, including the contribution from internal or external stores, and airspeed scheduling is required for the basic relationships. Additionally, further stores scheduling may be required if external carriage of different stores affects the $C_{N\alpha}$ term or significantly alters the control power characteristics of the aircraft.

2.3 Manoeuvre Demand and Carefree Handling Features

An integral term within a control law can be used to ensure that the steady-state response of the aircraft is equal to the n_z, α or q response, as demanded by the pilot's pitch stick position. Experience within BAe during the Experimental Aircraft Programme (Reference 4) showed that a q-demand system is desirable at medium to high speeds and low angles of incidence. At low airspeed and high incidences, an α demand system provides good flying qualities and also

enables departure limits to be easily applied to the pilot's demands via stick scaling. At high airspeed and high g-levels, an n_z-demand system provides good flying qualities and a mechanism to introduce n_z limiting to prevent over-stressing of the airframe.

Figure 4 shows a schematic of the main features of a pitch-axis flight control system of a typical unstable aircraft. In addition to the stability and manoeuvre demand features described above, a pitch rate feedback term is shown for augmenting pitch damping (Cm_q) and command path filters are shown, to enable optimum shaping of the response characteristics to provide good handling qualities. For clarity, notch filters necessary to prevent excitation of the aircraft flexible modes are not shown. Gust alleviation and autopilot functions are also not shown.

The FCS structure shown in Figure 4 utilizes several non-linear functions matched to the aerodynamic characteristics of the aircraft. These functions are determined by several factors including variations in:

* Cm_α and Cm_q with incidence, Mach number and airspeed;
* control power, Cm_δ, with flight condition;
* Cm_α, Cm_q and Cm_δ with external stores configuration;
* mass and inertia characteristics from the design database.

Clearly, external stores carriage will directly contribute to changes in aerodynamic characteristics, whereas internal carriage may only affect the aerodynamic characteristics whilst any bay doors are open. However, it is clear that in general, consideration of stores carriage may be a significant factor in the design of the aircraft FCS.

2.4 Effect of Stores Characteristics on FCS Gains

Figure 5 shows indicative variations of unstable 'short period' root position and control power with external stores for a highly unstable modern combat aircraft. The FCS designer for such an aircraft could possibly select 'average' feedback gains which provide adequate stability over the whole range of stores configurations. However, for an unstable airframe the closed-loop controller is conditionally stable. i.e. a reduced gain margin will result if the feedback gain is too high or too low. 'Average' gains may therefore not be a viable option for an extremely unstable aircraft. Hence the FCS feedback gains may require scheduling with external stores configuration to account for the effect the stores have on the aerodynamic characteristics of the aircraft.

If scheduling of the FCS feedback gains is used to directly affect the closed-loop stability of the aircraft, the scheduling signals must be of high integrity to ensure the feedback gains are appropriate for the stores being carried. Clearly, the gains must reflect the stores on the airframe at the time. The scheduling must therefore be based on the presence of the stores, rather than the store release signal, in order to accommodate some failure tolerance in respect of store hang-fires. It is noted that if the stores scheduling system is fail/safe (provides reliable indications of stores scheduling failure) the FCS may be able to revert to a back-up mode if the stores scheduling system fails. This may provide a safe condition although possibly with degraded handling qualities and/or a reduced flight envelope.

The provision of carefree handling (also known as automatic boundary control) by the introduction of appropriate manoeuvre limiting in the command path of the FCS can substantially reduce pilot workload and enhance the capability of the aircraft. This provides the pilot with the flexibility to use full-stick deflection for manoeuvres at all points in the flight envelope without risk of departure or over-stressing the airframe. In a balanced weapon system design, the carriage of internal or external stores may affect the aircraft's cleared envelope in terms of n_z and/or α. Thus, to provide carefree handling, the command path limiting must adequately reflect the appropriate boundaries in effect with the stores fitted to the aircraft. The command path functions may therefore also be scheduled with stores configuration. Note that some stores configurations may affect the gains in the feedback paths and not necessarily the gains in the command paths and vice-versa.

For an aircraft whose FCS gains are scheduled with stores configuration, the store release phase is of particular interest for FCS design engineers. As the store is released, the gains change from one value to another, directly resulting in control surface deflections and hence a transient change in the forces and moments acting on the aircraft. The changes in mass, inertia and aerodynamic characteristics resulting from the store release also contribute to a transient change in the forces and moments acting on the aircraft. The FCS design engineers must ensure that by design, the two transient effects on the airframe resulting from the store release cancel out, leaving only small residual transients. Simulation and flight testing is therefore required to evaluate any transient behaviour of the aircraft caused by the FCS during store release.

The scheduling of FCS gains with stores configuration affects the size of the FCS design and assessment task. Instead of designing gains for the clean aircraft, the FCS design engineer must provide sets of gains appropriate to carriage of different stores. To minimize this task, the external stores configurations may be grouped into 'key' configurations, with each being representative of several other stores configurations with broadly similar aerodynamic characteristics. However, the number of key configurations is a significant factor in establishing the effort required to design and clear the FCS for flight.

It is noted that scheduling of FCS gains with stores carriage only becomes necessary if the airframe instability levels are close to the limits. Inevitably there is a trade-off between performance and cost/timescales to provide an overall balanced design.

2.5 Stores Carriage and the Effect on FCS-Structural Coupling

Aircraft, like any flexible structure, exhibit many modes of vibration, each having an associated resonant frequency and mode shape. Figure 6 shows the exaggerated motion of a typical symmetric fuselage bending mode, which may have a resonant frequency of around 15Hz. Note that the FCS motion sensors are located to minimize the sensitivity to

such resonances. However, the aircraft will typically have many flexible modes and it is not possible to locate the sensors in an area which is isolated from the effects of all the resonances. Note also that many of the flexible modes will vary significantly in frequency and amplitude of response with any external or internal stores carried.

FCS-structural coupling is a phenomenon associated with the introduction of a closed-loop controller into a flexible airframe. The FCS motion sensors detect not only the rigid body motion of the aircraft, but also the superimposed higher frequency oscillations due to the resonances, or 'flexible modes' of the structure. The high frequency component of the sensor output usually requires attenuation to avoid driving the aircraft's flying control surfaces and further exciting the flexible modes (Reference 5).

Commonly, the structural coupling solution is to introduce electrical analogue or digital filters, for example notch (band-stop) filters, into the feedback paths. The major constraints on filter design are the need to meet specified stability requirements for the flexible modes, and the need to minimize additional phase lag introduced by the filters at 'rigid aircraft' control frequencies. The effect of stores carriage on the flexible modes of the airframe results in changes to the modal frequencies and amplitudes, as shown schematically in Figure 7. Consequently, a 'narrow' notch filter cannot accommodate the variation in modal characteristics. A wider notch is therefore required to reliably attenuate the high frequency signals associated with the flexible modes. Unfortunately the wider notch has more phase lag at the lower aircraft control frequencies than a narrow notch and can reduce the maximum instability which may be controlled, whilst meeting appropriate criteria for stability margins. In extreme circumstances, required instability levels may lead to 'narrow' notches being specified with the notch centre-frequency being scheduled with stores configuration.

The carriage of a wide range of stores can therefore lead to a complex design problem: to provide an adequate structural coupling solution without too severe a phase penalty at aircraft control frequencies. This is further exaggerated for highly unstable aircraft, since the closed-loop incidence feedback gain, K_α, shown on Figure 4 is a function of unaugmented instability levels. The rigid body modes of such highly unstable aircraft require high FCS gains for adequate stability augmentation, yet the need to attenuate the flexible modes leads to a conflicting requirement for the design of the FCS gains. Additionally, phase advance filters in the feedback paths improve control at the rigid aircraft frequencies by reducing overall phase lag. However, these introduce additional gain at the higher frequencies, which adds to the structural coupling problem. Interdisciplinary understanding is therefore required to provide an overall solution which uses both phase advance and structural mode filtering to give a balanced design.

BAe have, on previous fly-by-wire aircraft, incorporated a conservative approach to FCS-structural coupling stability margins. An overall gain margin of 9dB has been specified at structural frequencies, thus ignoring any phase information. Experience gained during the Experimental Aircraft Programme (Reference 4) has shown that the aerodynamic and structural models used to design the notch filters are sufficiently accurate to provide reliable phase information at the lower flexible aircraft frequencies. Relaxed stability margins for FCS-structural coupling can therefore be used, which allow reduced gain margins, provided there is adequate phase margin, up to a maximum closed-loop phase lag of 900°. The two different approaches are shown on Figure 8. The relaxed stability margins, known as 'phase stabilization', provides the following significant benefits:

* Although notch filters may still be required, they are shallower and scheduling of the filters with stores configuration is not necessary;

* The shallower notches result in reduced phase lag at rigid body frequencies, thus easing the aircraft control solution.

3. FLIGHT AT MODERATE AND HIGH INCIDENCE

The above section has concentrated on the pitch axis FCS for an unstable combat aircraft. Many of the issues described, including levels of instability and FCS-structural coupling, apply equally to the lateral/directional axes. These axes present additional design challenges and further opportunities to review where stores carriage can have implications on the aircraft FCS design.

The incidence available for aircraft manoeuvring may be limited by various phenomena, including:

* Lack of control power;
* Lateral instability at high incidence such as wing-rock arising from zero or negative dutch roll damping;
* Yaw-off arising from a reduction in directional stiffness.

The carriage of a wide range of stores can contribute to each of the above phenomena. For example, asymmetric store release can introduce rolling moments due to both store mass and aerodynamic characteristics. The amount of control deflection required to balance the aircraft may increase with load factor to counteract inertia loads caused by the mass contribution to asymmetry. The control to balance the asymmetry may also increase with incidence, depending on the asymmetric aerodynamic characteristics. In conditions where control power is a limiting factor, the FCS can only provide limited augmentation. Provided there is enough control power, a closed-loop control system may be designed to improve the high-incidence lateral handling characteristics of the aircraft.

3.1 Design of a High Incidence Lateral FCS

This example addresses the lateral departure characteristics of a strike/fighter aircraft at high incidence (typically around C_{Lmax}). Figure 9 shows the incidence limits of the unaugmented aircraft for different stores configurations, based on a margin from the onset of lateral departure. The departure mechanism for the aircraft considered in this section is wing-rock for the 'clean' aircraft and light stores configurations, and yaw-off for 'heavy stores' configurations.

The influence of stores carriage on the aircraft lateral departure mechanism is probably best described by considering the simplified equation for $Cn_{\beta dyn}$:

$$Cn_{\beta dyn} = Cn_{\beta} - Cl_{\beta}.i_c/i_a.\sin\alpha$$

It is evident that the greatly increased roll inertia, i_a, due to the heavy stores considerably reduces the Cl_{β} contribution to $Cn_{\beta dyn}$ (Cl_{β} is usually negative). This causes $Cn_{\beta dyn}$ to become negative at a much lower incidence than for light stores configurations with lower roll inertias, but with similar directional stiffness, Cn_{β}. The $Cn_{\beta dyn}$ characteristics are shown diagrammatically in Figure 10.

A closed-loop controller may be designed to augment Cn_{β} by using sideslip feedback to rudder to make Cn_{β} more positive and alleviate the loss of stiffness of the basic aircraft at high incidence. When the aircraft considered in this section was fitted with a high incidence FCS such as the one described, flight testing confirmed that the aircraft was provided with much improved incidence limits.

The above discussion has highlighted that the carriage of stores, and the effect this has on aircraft roll inertia, can significantly influence the lateral departure characteristics and hence the design of the aircraft flight control system.

3.2 Controlled Post-Stall Manoeuvring

Recent experimental programmes demonstrating post-stall manoeuvring in combat scenarios (for example the X-31 and F-16 MATV) offer enhanced weapon firing opportunities at the expense of energy loss and consequently, increased vulnerability. Whilst the operational effectiveness of this capability is still under debate, the technology is available. Through the use of alternative controls such as thrust vectoring, aircraft may be controlled at incidences well beyond those at which conventional aerodynamic surfaces cease to remain effective. Clearly the carriage of a wide range of stores in these regimes of flight will have similar implications on the FCS design as those described earlier.

It is noted that whilst a great deal of effort has been applied to the development and demonstration of highly agile airframes, there has been comparatively little development of combined airframe and weapon agility. Indeed, McKay noted that there is currently a mismatch between the weapons and airframe capability (Reference 6). The tactical advantages of post-stall manoeuvring may thus be reduced once the perceived mismatch between airframe and weapon agility has been resolved. Whilst it is recognized that fundamental research programmes are required to explore new technologies, it is considered by the authors that this is possibly an area where the research is concentrating too tightly on airframe aspects without consideration of the trade-offs necessary during the design of complete weapons systems.

This section is included to emphasise the need for fully integrated research programmes which respect appropriate trade-offs and provide answers applicable to the design of a complete weapons system.

4. SYSTEM INTEGRATION ISSUES

The application of an integrated systems approach to design is gaining momentum and providing diverse benefits, which not only offer direct systems performance improvements and possible cost savings, but also enhance the weapons system performance by reducing space and mass requirements, and enable advanced configurations to be designed which would otherwise be non-viable. Whilst current applications have tended to be limited to single integration, for example flight control system and powerplant control system integration in ASTOVL research programmes (Reference 7), the implementation of a total vehicle management system is clearly on the horizon. A vehicle management system may integrate the functionality of several, traditionally separate, airframe systems, including perhaps the FCS and stores management system together with the navigation system.

It is therefore imperative that engineers and technologists from widely differing fields understand how their respective disciplines interact. In such complex design situations, satisfactory design trade-offs will only be achieved if the multi-disciplinary influences are fully and widely understood.

5. CONCLUSIONS

This paper has reviewed some of the capabilities and limitations of modern flight control systems. The impact of stores carriage and release on the aircraft flight control system has been described by reviewing the stores effects on aircraft aerodynamic, inertial, and structural properties.

It has been shown that for highly unstable aircraft, the FCS gains may need to be scheduled with external stores configuration, to account for aerodynamic interaction between the stores and aircraft. The scheduling of FCS gains with stores configuration affects the size and cost of the FCS design task and can act as a significant factor in establishing the effort required to design and clear the FCS for flight. It has also been shown that hardware elements lead to an upper limit to the maximum static instability which may be adequately controlled.

FCS-structural coupling has been described. It has been shown that the carriage of a wide range of stores can lead to a complex design problem in order to provide an adequate structural coupling solution, without imposing too severe a phase penalty at rigid aircraft control frequencies. This may be alleviated to some extent by the use of phase stabilization.

It has also been shown that the carriage of a wide range of stores can result in different lateral departure characteristics at high incidence. Provided there is enough control power, a closed-loop control system may be designed to improve the high-incidence lateral handling characteristics of the basic aircraft. Additionally, it is recommended that future studies of post-stall technologies respect weapon limitations and provide information necessary for a balanced weapon system design.

The concept of further systems integration was briefly reviewed. It is noted that wider understanding and appreciation of other disciplines is required to ensure

appropriate trade-offs are made during the overall weapon system specification and subsequent design. It is hoped that by describing the implications that stores carriage and release has on the design of the aircraft flight control system, this paper has contributed to there being a wider understanding between disciplines.

ACKNOWLEDGEMENT

The authors wish to thank their colleagues within British Aerospace, especially Mr H.T.Widger and Mr C.Fielding, for the help and advice received in the preparation of this paper.

REFERENCES

1 McRuer,D.T. 'Interdisciplinary Interactions and Dynamic Systems Integration', International Journal of Control, Vol. 59, No. 1, January 1994, pp. 3-12

2 Mil-F-9490D General Specification For Flight Control Systems Design, Installation and Test of Piloted Aircraft

3 Clarke,R. Burken,J.J. Bosworth,J.T. Bauer,J.E. 'X-29 Flight Control System: Lessons Learned', International Journal of Control, Vol. 59, No. 1, January 1994, pp. 199-219

4 McCuish,A. 'Experimental Aircraft Programme (EAP) Flight Control System Design and Test', AGARD Conference Proceedings 560, Paper 22, January 1995

5 Caldwell,B.D. 'The FCS-Structural Coupling Problem and its Solution', AGARD Conference Proceedings 560, Paper 16, January 1995

6 McKay,K. 'Operational Agility - An overview of AGARD Working Group 19', AGARD Conference Proceedings 548, Paper 20, March 1994

7 Fielding,C. 'Design of Integrated Flight and Powerplant Control Systems', AGARD Conference Proceedings 548, Paper 4, March 1994

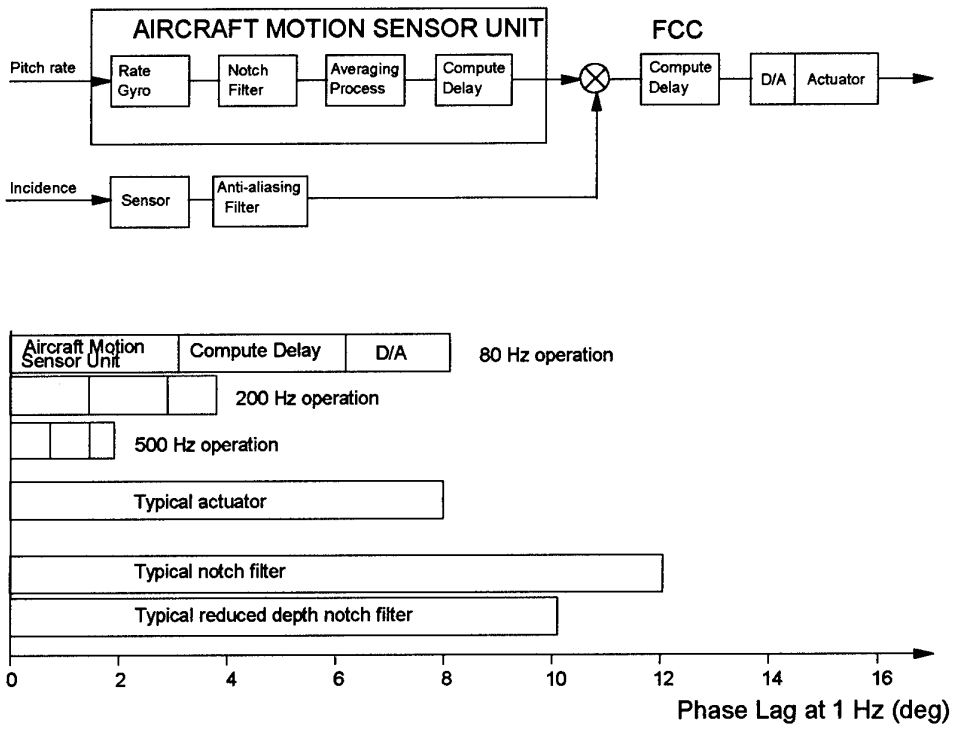

Figure 1 - Hardware Contribution to Control System Phase Lag

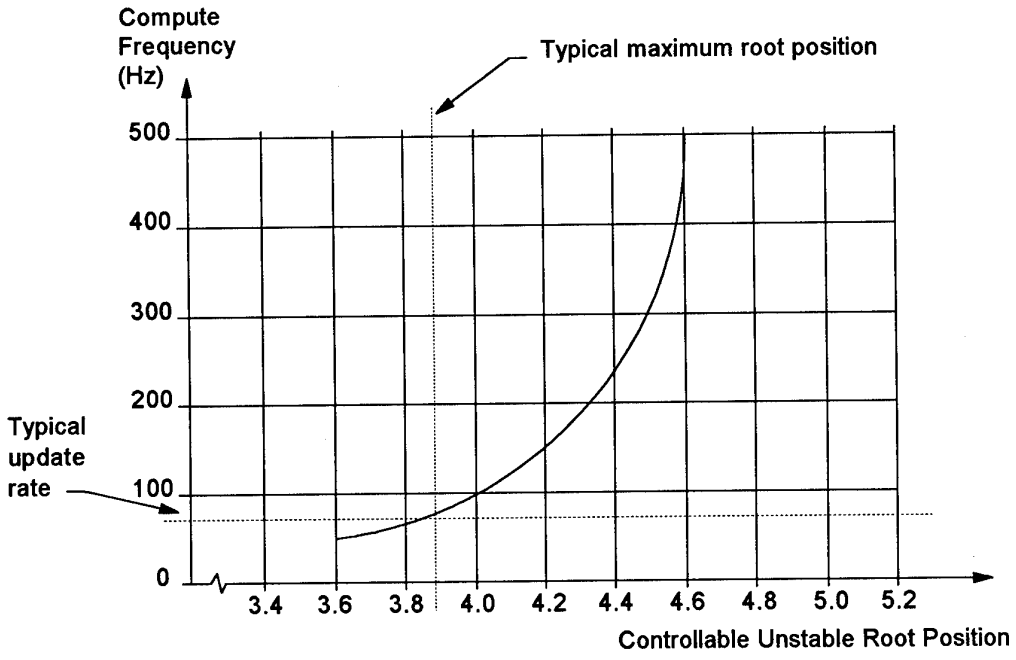

Figure 2 - Maximum Level of Controllable Static Instability

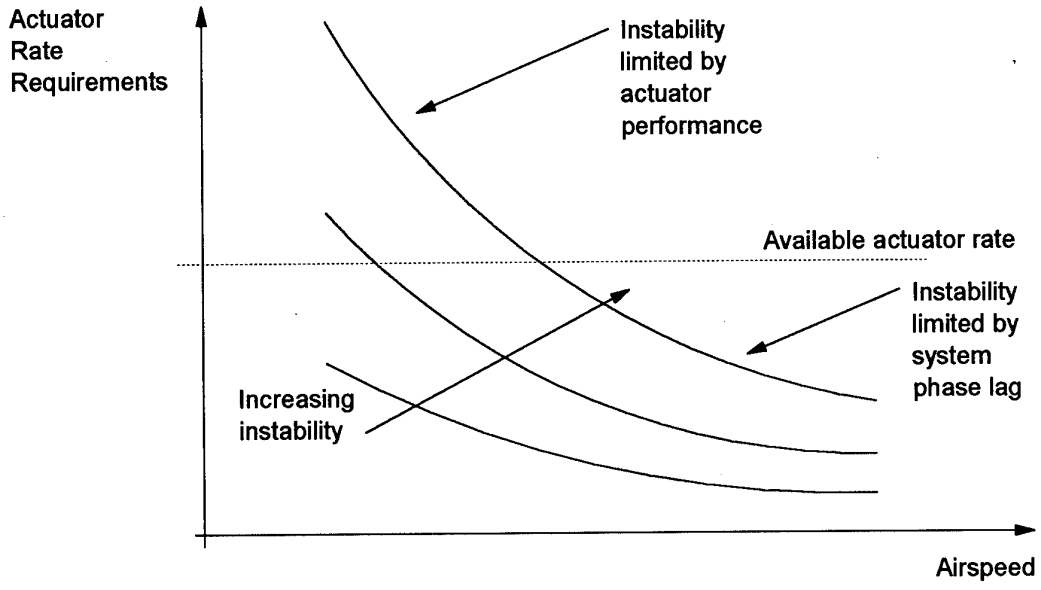

Figure 3 - Influences of Instability on Actutor Rate Requirements

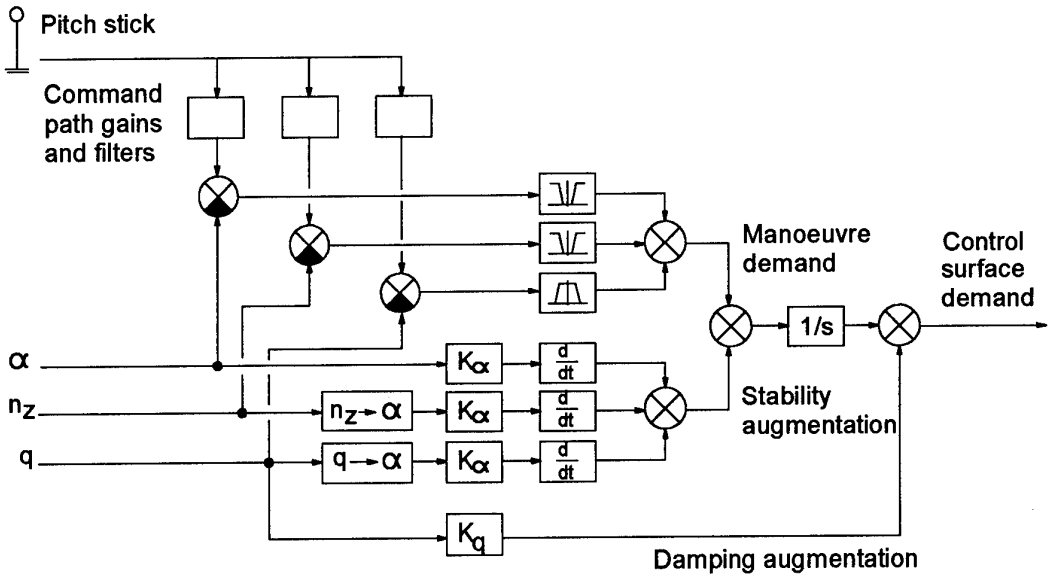

Figure 4 - Simplified Typical Pitch Flight Control System

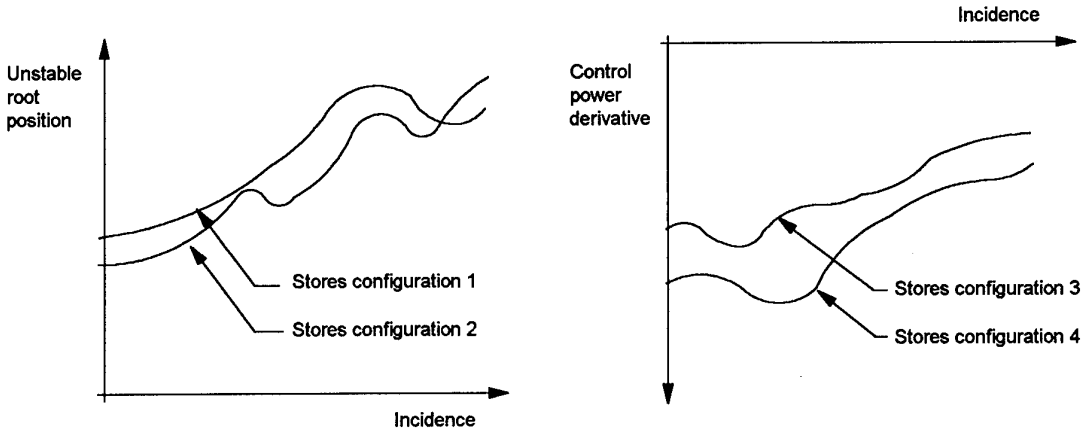

Figure 5 - Effect of Stores Carriage on Aircraft Characteristics

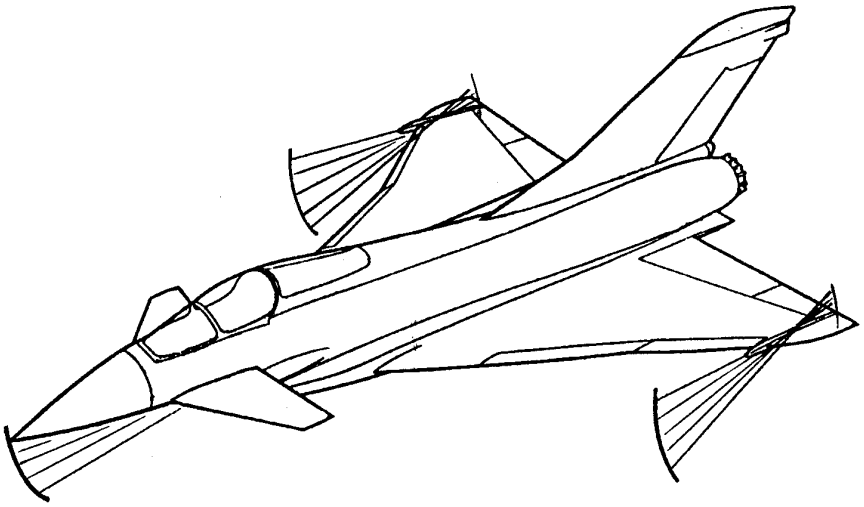

Figure 6 - Typical Fuselage Bending Mode
(Exaggerated Motion)

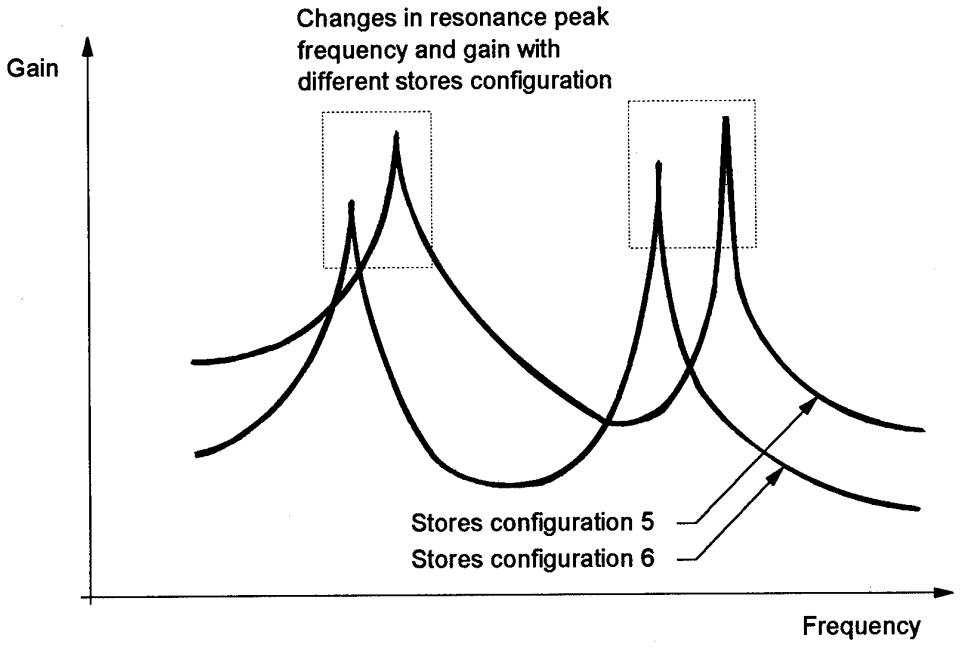

Figure 7 - Effect of Stores Configurations on Flexible Mode Characteristics

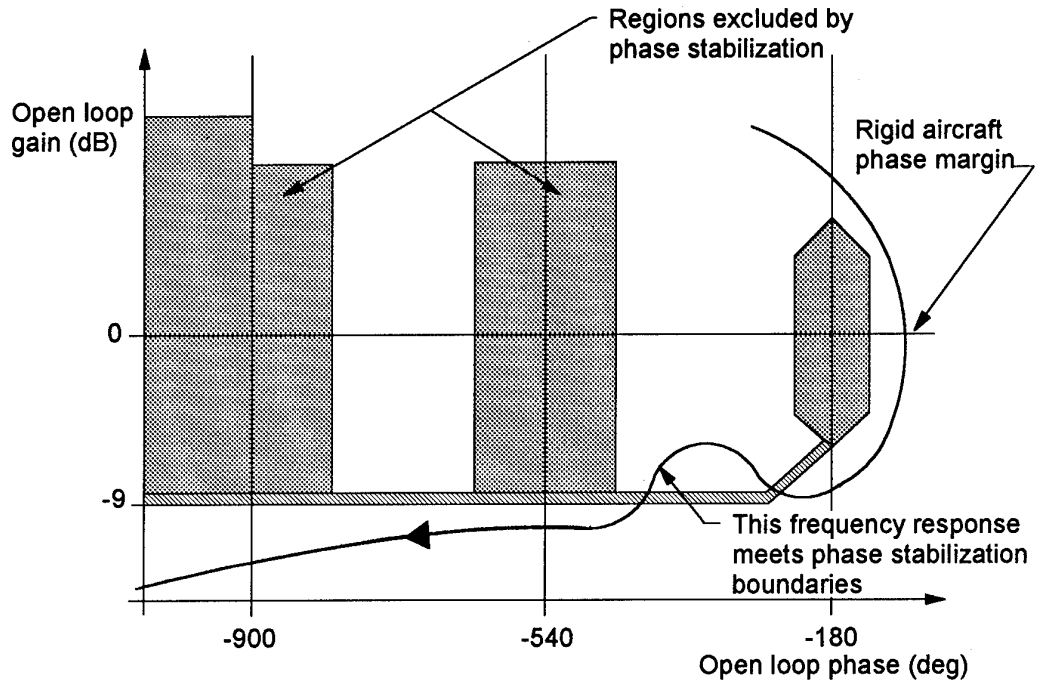

Figure 8 - FCS-Structural Coupling Stability Margins

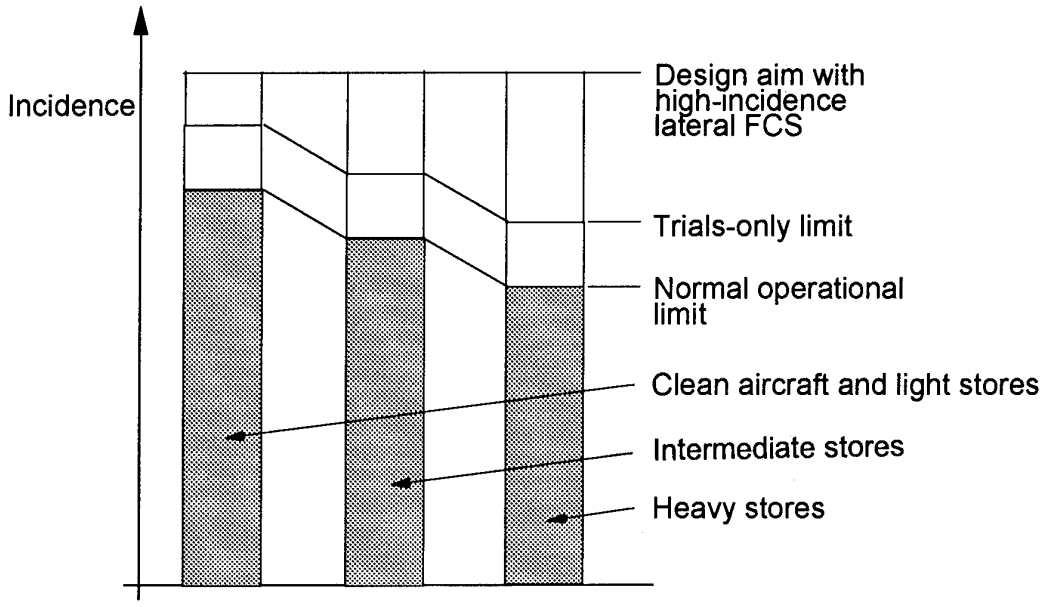

Figure 9 - Incidence Limits With Different Stores Configurations

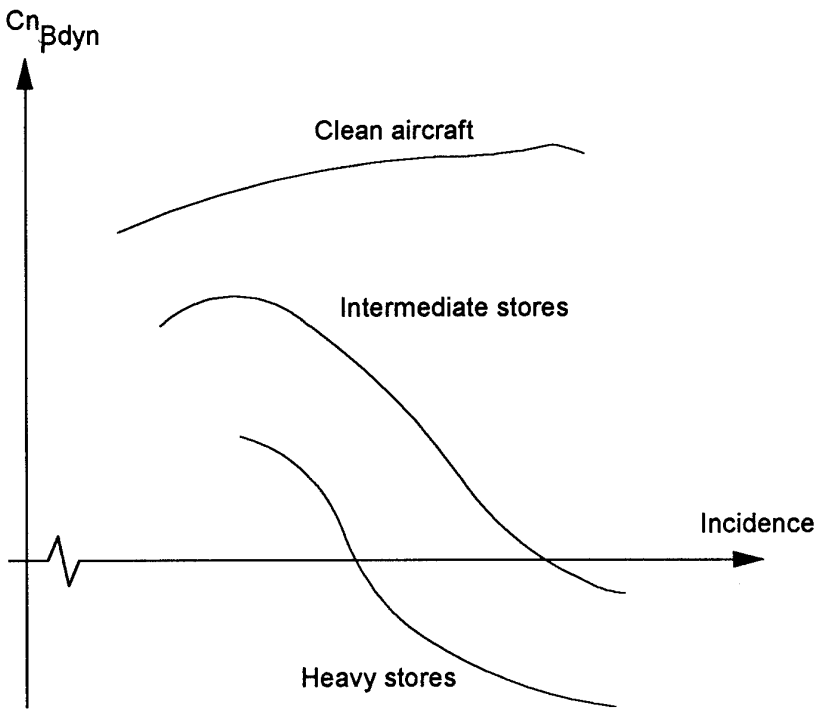

Figure 10 - $Cn_{\beta dyn}$ Characteristics

UNSTEADY SUBSONIC AERODYNAMICS FOR MANEUVERING WING/FUSELAGE/PYLON/STORE CONFIGURATION AND STORE SEPARATION INCLUDING WAKE EFFECTS

C. Ruhi Kaykayoglu

Istanbul University
Faculty of Engineering
Mechanical Engineering Department
Avcılar, 34850, Istanbul, TURKEY

Murat Yalcınel

Turkish Air Force Academy
Yesilyurt, Istanbul, TURKEY

SUMMARY

A Computational Fluid Dynamics (CFD) technique based on a Vortex Lattice Method (VLM) is presented for treating the unsteady, low speed aerodynamics of a Wing/Fuselage/Pylon/Store(W/F/P/S) combination in an incompressible flow. The main emphasis is placed on a practical, cost-effective engineering solution of the complex problem with a reasonable computational efficiency allowing the computer code to run on small personal computers. The computational model presented in this study enables the calculation of the unsteady aerodynamic forces acting on a wing system undergoing a time dependent three dimensional motion. An unsteady, wing following and wake shedding procedure provides the transient wake shapes. Computed flow field simulations are presented for various unsteady and angle of attack conditions, involving pylon/store locations at various spanwise locations under the wing. The external store separation under the influence of the unsteady wake rollup behind the wing system is modeled by considering the full mutual interaction between the store and the W/F/P configuration. The results show that the method is capable of simulating the important features of the unsteady forces and wake development behind the W/F/P/S configuration.

1. INTRODUCTION

The modeling of the unsteady wake rollup behind a maneuvering Wing/Fuselage/Pylon/Store (W/F/P/S) combination and the store separation requires advanced computational techniques. A grid based approach seems to be computationally expensive requiring a grid update during the history of the flow field. On the other hand, the VLM (Vortex Lattice Method) approach is one of the most efficient tools for complex geometries as it uses only a surface grid which is relatively easy to generate (1,2,3). The VLM is basically one of many panel methods used by today's Aerodynamicist. In the present study, the VLM model of the three dimensional flow field was used to treat arbitrary maneuvers of a trapezoidal wing with and without an underwing store. A time dependent wing following and wake shedding procedure has provided the transient wake shapes and wing loading without utilizing the iterative wake relaxation procedure. A computer code, so called TRNVLM, enables the user to orchestrate the input motions of a variety of unsteady conditions.

An underwing installations affect the performance characteristics of the wing. They are frequently a source of considerable adverse aerodynamic interference giving large increases in drag, variations in aerodynamic stability derivatives and change in flutter boundaries (4,5,6,7,8). An understanding of the wing-store interaction is central to determining the unsteady airloads, the safe store release and the sound generation characteristics.

Separation effects occur when a store is released from an aircraft and its motion is temporarily influenced by the disturbed flow between the aircraft and the store. Separation effects testing involves releasing stores from an aircraft, one at a time, under controlled test conditions. A scenario which shows negligible separation effects under one set of delivery conditions may show large separation effects at different release conditions. The total number of external stores needed for store testing reaches upto a three digits store amount for complete store characterization (4,8).

On the other hand, computer aided experiments will help the store designer to cut certain amount of possibilities before doing the full set of planned experiments. This study aims at providing a new computer aided analysis procedure that can be used to reduce the number of experiments for the store certification after the calibration and the validation of the computer code with various store testing studies.

The scope of this paper is twofold: 1) The development of a numerical procedure based on the Vortex Lattice Method (VLM) to treat time dependent aerodynamic conditions of W/F/P/S configuration which moves along a prescribed path of motion, 2) The application of a simple computational approach to study unsteady store separation from an underwing pylon. Although the basic W/F/P/S configuration to be considered in this study is simple compared to more realistic arrangements, it will provide a first step to future where more realistic geometries including boundary layer effects will be used.

2. NUMERICAL SIMULATION METHODS

There are various theoretical and experimental methods to study the nonlinear aerodynamic characteristics of the wing and other aircraft components. However, the complexity of the flow require approximate models with reasonable engineering accuracy. Recent advances in techniques for exact solutions of the Euler equations and the full Navier Stokes equations require expensive computation time (9,10,11,12). The grid generation procedures still require very large programming efforts. The combined fluid dynamic problem of an external store carriage/ release and three dimensional wing leading/trailing

Paper presented at the AGARD FDP Symposium on "Aerodynamics of Store Integration and Separation", held in Ankara, Turkey from 24-27 April 1995, and published in CP-570.

edge separations is highly complex and a challenge to the numerical predictor.

For a maneuvering aircraft, the instantaneous state of the flow field depends on the time history of the aircraft motion. Detailed solution of the complete nonlinear fluid dynamics equations (Navier Stokes Equations) along time dependent flight paths requires the computational grid to cover large wake histories. Furthermore, during the store release, the grid update procedure at new store stations need extensive programming efforts and computing time. On the other hand, the use of simplified fluid dynamic equations while retaining the three dimensional nature of the aircraft geometry and its flight path is a realistic engineering approach for the problem associated with the carriage and the release of stores from an aircraft (13,14,15).

The simulation of unsteady aerodynamics and the resulting wake dynamics due to a maneuvering aircraft is very complex and it is a very dificult task for today's Aerodynamicist. The presence of external stores complicates the overall flow field over the wing. During the complex maneuvering phases of the wing, the aerodynamic loads on the store are also modified.

In this research investigation, a computational method based on the vortex ring element representation of the body surface was used to solve three dimensional unsteady flow field equations based on a Laplace Equation formulation. This method is based on the general Vortex Lattice Method (VLM) formulation (1,2). The VLM has not been developed yet to become a full surface panel method for complex configurations. However, wide applications cited in the literature makes the method an effective and practical engineering alternative to classical panel methods (1,2,3,14). Authors have aimed at developing an engineering code based on the Vortex Lattice Method ready to be used for practical applications. The present code is named as TRNVLM (TuRkey Nonlinear Vortex Lattice Method) in which the main emphasis is placed towards maneuvering solid bodies along the prescribed paths and the store separation modeling during the path of the body motion. The TRNVLM computer code is written in FORTRAN language and it is open to structural modifications. Currently it is running on a 80486 type PC computer with a minimum required 8 Mb RAM total memory.

3. BRIEF DESCRIPTION OF THE FLUID DYNAMICS MODEL

The following brief description is aimed at explaining the important steps of the numerical formulation. More details on the principals of the formulation can be obtained in the text book by Katz and Plotkin (14, pages 422-431). The motion history of the W/F/P/S coordinate system (x,y,z) is assumed to be known and orchestrated in an inertial frame of reference (X,Y,Z). The relative motion of the origin of the W/F/P/S fixed frame reference is given by $R_0(x,y,z;t)$ and the instantaneous rotation angles are given by $\Theta_0(\phi,\theta,\psi;t)$ (See Fig.1) .

It is assumed that the flow is incompressible, inviscid and irrotational over the entire flow field apart from

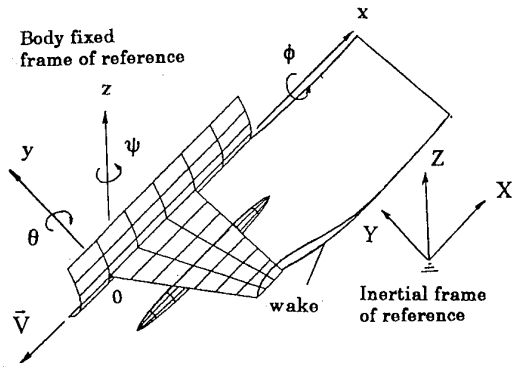

Figure 1. Research geometry and frames of references to describe the motion of the W/F/P/S configuration.

the solid boundaries and its wakes. A disturbance velocity potential $\Phi(X,Y,Z)$ can be defined in the inertial frame and the continuity equation becomes

$$\nabla^2\Phi = 0 \qquad (1)$$

The first boundary condition requiring zero normal velocity across the body's solid boundary is

$$\left(\nabla\Phi + \vec{V}\right)\cdot\vec{n} = 0 \qquad (2)$$

where $\vec{V}$ is the kinematic velocity of the W/F/P/S surface due to the motion as viewed in the body frame of reference, and $\vec{n}$ is the normal vector to the surface in terms of the body surface coordinates. If we let $\vec{V}_0$ be the kinematic velocity of the (x,y,z) system's origin and $\vec{\Omega}$ be the rate of rotation of the body frame of reference, the boundary condition which requires zero normal velocity at each control point on the body is satisfied by the equation,

$$\left(\nabla\Phi - \vec{V}_0 - \vec{v}_{rel} - \vec{\Omega}\times\vec{r}\right)_i \cdot \vec{n}_i = 0 \qquad (3)$$

where $\vec{r}(x,y,z)$ is the position vector in body (x,y,z) coordinates and $\vec{v}_{rel}$ is the velocity due to an additional relative motion with respect to (x,y,z) system. This last velocity vector is needed during the application of the store separation from the wing to satisfy the boundary condition on the store surface.

The second boundary condition for Eq. (1) requires that the W/F/P/S induced disturbance will decay far from the body. Hence,

$$\lim_{\vec{r}\to\infty}\nabla\Phi = 0 \qquad (4)$$

For the unsteady flow, the use of the Kelvin condition supply an additional condition that can be used to determine the streamwise strengths of the vorticity shed into the wake. The overall circulation, Γ, around a fluid curve enclosing the body and the wake is conserved,

$$\frac{d\Gamma}{dt} = 0 \quad \text{(for any t)} \qquad (5)$$

The solution of Eq. (1) with the above boundary conditions can be obtained by using Green's theorem which states that a general solution consists of a doublet and source distribution over the body surface and the wakes (14). However, as noted by Katz (2,14), for the lifting problem solution, the vortex distribution, which can be defined by doublets, is sufficient. In the present study, every surface is treated as a lifting surface and they were divided into panels. Then a vortex ring was placed on each panel (See Figure 2).

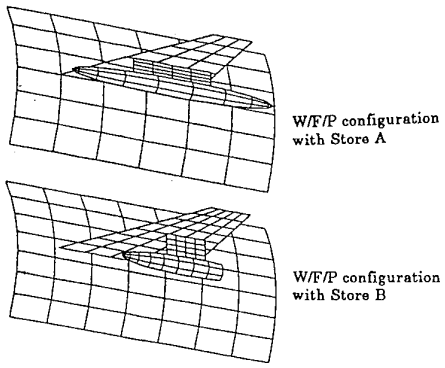

Figure 2. Example of a vortex lattice system on a W/F/P/S system

The zero thickness wing lifting surface is divided into NxM (NxM=NW) vortex rings with streamwise panelling. Each vortex ring of an unknown strength, $\Gamma_{w,j}$,(j=1,NW) is bound to the 1/4 of the panel chord thus satisfying the Kutta condition. Similar to the wing surface paneling, fuselage is divided into NNxMM (NNxMM=NF) vortex rings with, $\Gamma_{f,j}$ (j=1,NF) vortex strengths, pylon is divided into NNNxMMM (NNNxMMM=NP) vortex rings with, $\Gamma_{p,j}$, (j=1,NP) vortex strenghts. Finally, the external store surface is divided into NNNNxMMMM (NNNNxMMMM=NS) with, $\Gamma_{s,j}$ (j=1,NS) vortex strengths. Nxxx and Mxxx values represent the number of panels in the spanwise and chordwise directions respectively. Two different store geometries are studied in this investigation. The W/F/P and Store A combination is used basically to study unsteady wake characteristics. On the other hand, the W/F/P and store B combination is used both in the investigation of the transient wing/store force characteristics and the store release analysis. The lattice model of the configuration with Store B consists of 261 vortex rings, with NW=100, NF=64, NP=25 and NS=72 (See Figure 2).

The complete solution of the problem in terms of the unknown bound circulation strengths, $\Gamma_{w,j},\Gamma_{f,j},\Gamma_{p,j}$ and $\Gamma_{s,j}$, is carried out by satifying Eq.3. The induced velocity, $\left(\partial\Phi/\partial z\right)_{i,j}$, due to W/F/P/S ring vortices, the wing trailing edge wake and the wing tip wake elements is given at each control point by (14),

$$\left(\frac{\partial\Phi}{\partial z}\right)_{i,j} = [WFPS]\begin{bmatrix}\Gamma_1\\ \cdot\\ \cdot\\ \Gamma_{NW}\\ \cdot\\ \Gamma_{NF}\\ \cdot\\ \Gamma_{NP}\\ \cdot\\ \Gamma_{NS}\end{bmatrix} + [TEWI]\begin{bmatrix}1\\ \cdot\\ \cdot\\ \cdot\\ \cdot\\ \Gamma_{tew,n}\end{bmatrix} + [TIPI]\begin{bmatrix}1\\ \cdot\\ \cdot\\ \cdot\\ \cdot\\ \Gamma_{tew,m}\end{bmatrix} \qquad (6)$$

The influence matrix coefficients [WFPS][TEWI] and[TIPI] in this equation represent the influence of a unit singularity distribution on a panel acting at the control point of another panel. The influence coefficient matrices are obtained by using the Biot-Savart law. If the W/F/P/S geometry is unchanging with time, [WFPS]remains constant, although [TEWI]and[TIPI] are varied due to wake evolution. In the case, where we study store separation, a relative motion between the store and the other bodies is important. Hence, the coefficients representing the influence of the store on other bodies must be updated at any moment, t. The kinematic velocity $W_{i,j}$, at each control point, is due to W/F/P/S instantaneous velocities, $\bar{V}$ and rotations, $\bar{\Omega}$. Then the final condition that satisfies Eq. 3 will be,

$$W_{i,j} + \left(\frac{\partial\Phi}{\partial z}\right)_{i,j} = 0 \qquad (7)$$

This equation yields a set of n (n=NW+NF+NP+NS) linear algebraic equations for n bound body vortex strengths. An indirect method, the Gauss Seidel iterative technique is used to solve the unknown intensities of the vortex ring elements.

Vortex Wake Modelling

The unsteady wake roll up behind a maneuvering W/F/P/S configuration is studied by properly accounting the local flow separation from the wing tip and trailing edges. The VLM approach is one of the most efficient tools among the typical and widespread singularity methods for the modeling of the unsteady wake structure. The ability of the method is well demonstrated in the literature (1,2).

A lagrangian type wake shedding procedure is used. The modeling of the wake, which is shed from the wing tip and the trailing edge, is achieved by releasing vortex ring segments at each time interval from the corresponding edges. The vortex ring segments released at each time step, Δt, build the continuous wake structure behind the wing. The instantaneous wake deformation is simulated by calculating the velocities at each ring corner point. Then, based on an explicit single step Euler scheme, the vortex rings are moved. A very simple vortex core model (core radius equals to 0.001*CR) is used for the wake rollup procedure.

The modeling of the flow separation from the bluff store geometry was neglected and left for the future study. However, the kinematic velocity of the W/F/P/S system defines the direction of the vortex filaments of the F/P/S trailing edge horseshoe vortices, representing the vorticity field shed from the fuselage, pylon and the store trailing edges.

Unsteady Aerodynamic Loads

The calculation of aerodynamic loads on the store during carriage and release requires complicated aerodynamic strategies. In the present investigation this task involves the following sources of effects; a) unsteady interference of the wing/store system, b) the disturbance on the store caused by the unsteady wake rollup, c) unsteady effects including store and wing rotations during release and maneuvering. To evaluate these interference effects, two computation tasks were carried out simultaneously, 1) the continues mutual interference evaluated by unsteady aerodynamics including wakes, 2) the resulting store motion by flight mechanics.

After the solution of the vortex circulation strengths, the unsteady surface pressures are computed by using the Bernoulli's equation. The pressure coefficients are given by the following relation (14),

$$c_p = \frac{p - p_{ref}}{\frac{1}{2}\rho v_{ref}^2} = -\frac{(\nabla\Phi)^2}{v_{ref}^2} + \frac{2}{v_{ref}^2}\left[\vec{V} + \vec{v}_{rel} + \vec{\Omega}\times\vec{r}\right]\cdot\nabla\Phi - \frac{2}{v_{ref}^2}\frac{\partial\Phi}{\partial t} \tag{8}$$

where p_{ref} is the far field pressure and v_{ref} is the kinematic velocity defined as

$$\vec{v}_{ref} = \vec{V} + \vec{\Omega}\times\vec{r} + \vec{v}_{rel} \tag{9}$$

The contribution of a vortex ring element with an area of ΔA_k to the aerodynamic load, ΔF_k is given by

$$\Delta\vec{F}_k = -c_{p_k}\left(1/2\rho v_{ref}^2\right)_k \Delta A_k \vec{n}_k \tag{10}$$

The resulting three dimensional forces and moment coefficients are obtained by integrating each panel normal force, ΔF_k, along the body surface (14).

Store Separation Analysis

The store separation prediction techniques in use throughout NATO countries have already been discussed in the literature (4,6,8). These techniques may be discussed under three main categories: theoretical, empirical and analogy. The present study uses the theoretical approach. The theoretical store separation predictions utilize flow equations which can be either coupled or uncoupled to the equations of the store motion. By coupling the flow equations to the equations of motion, we can solve for the new altitude of the store at a specified interval of time and then use this new aircraft/store physical relationship to calculate a new flow field. In the present study, both the equations of flow and the equations of the motion are solved together.

Meto and Kaykayoglu (16) have previously investigated the separation characteristics of a store after release from an aircraft by using a flow grid method combined with a classical panel method. The similar approach was also applied by Von der Broek (17). The computer code developed by Meto and Kaykayoglu applies panel singularity distribution over the surface of the F-4 type aircraft. The isolated store, after separation from the aircraft, moves through the nonuniform flow field consisting of the free stream plus the perturbation flow field created by the aircraft. The nonuniform flow field is defined at the mesh points of a three dimensional orthogonal grid covering the separation region of interest. Hence, the presence of the store has no direct influence on the perturbation flow field. The computer code numerically integrates the six degree of freedom (6 DOF) equations of the store motion for a specified small time interval, Δt^*, to arrive at a new store position in the flow grid system. Figure 3 shows two store separation scenarios studied so as to understand the effect of store spanwise location on the store trajectory characteristics.

The separation prediction of an external store from the W/F/P system requires the evaluation of unsteady aerodynamic forces and moments on the store. These parameters depend upon the nonuniform flowfield around the W/F/P and the store motion itself. Deslandes (18) have outlined the concepts about the evaluation of aerodynamic loads on the external stores which is related to the aerodynamic coupling of four

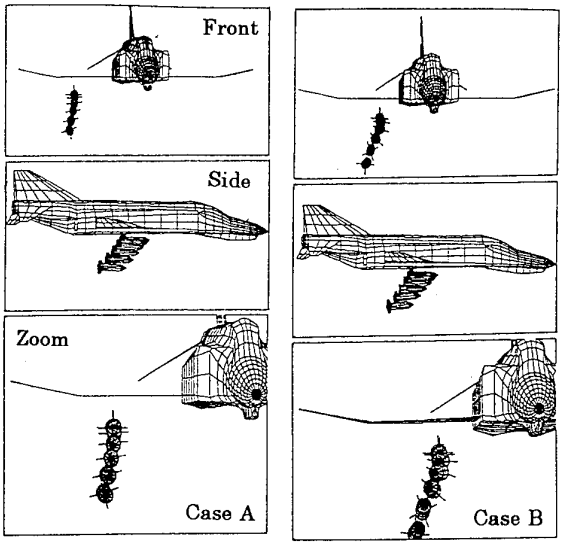

Figure 3. Store separation analyses by using a combined panel method/flow grid technique (16).

main effects. Due to the first order effects present in the method used by Meto and Kaykayoglu, authors of the present paper has preferred to use a new approach which will be more realistic and accurate for the prediction of the store trajectory. This new approach enables continuous interaction between the W/F/P and the store. In the present study, we consider 1st, 2nd and some of the higher order effects to evaluate the unsteady aerodynamic loads on the external store as described by Deslandes. First order effects, which stands for the steady interference of the W/F/P and the airflow around the store, is valid during the advancement of the store over a time step which corresponds to the shedding of one row of wake vortices from the wing's trailing edge. Second order effects, which stands for the relative motion of the store and the W/F/P including instantaneous rotations are included fully in the formulation. Higher order effects due to wake rollup during unsteady maneuvers of the W/F/P combination are also taken into account.

Aerodynamic forces and moments on the store are computed and then supplied to the 6 DOF equations of motion. The force and moment data are combined with the weight, moments of inertia and center of gravity information of the store. Then the equations of motion are solved by using a second order Runge Kutta scheme to predict the store's next position relative to W/F/P system. The time interval for shedding a vortex ring into the wake is divided into 20 equal time increments and $\Delta t/20$ is used as a time step in the Runge Kutta integration scheme. The force and moment characteristics are updated at each time step. A new store position is then used in the next time step when a new row of vortex rings are released from the wing tip and trailing edges. The computer simulation procedure is very much similar to the experimental technique so called Captive Trajectory System (CTS) (4).

In the simulation procedures, aerodynamic force and moment coefficients have to be scaled to the actual flight conditions. The accelerations of the store model will be similar to the full scale flight conditions if the total forces and moments, mass, center of gravity and

moments of inertia are properly scaled to flight conditions (4). Vortex Lattice Method based computer codes are capable of simulating low speed, incompressible fluid flows if no transformation is used to introduce compressibility effects. Hence we can assume that the simulation is reasonably valid upto Mach number 0.3 (Ma=0.3). In the present investigation, we have used linear geometric and velocity scaling for the research configuration assuming Ma=0.1. Although the present store trajectory program provides reasonable store release scenario, the sensitivity of the method to many different variables should be further studied.

4. RESULTS AND DISCUSSION

Figure 4 shows the research configuration featuring W/F/P/S setup in details. The research wing has an Aspect Ratio, AR=3 and zero thickness. The geometry of several classes of wing systems can be defined by parameters like sweep, camber and twist by the geometry module of the computer code prepared. Present investigation considers a trapezoidal wing with the relevant dimensions of CR/CT=3.28, S/CR=2 and $\Lambda = 35^0$. The W/F/P/S configuration is considered to be symmetric with respect to the plane shown in Fig. 4.

As mentioned earlier, two store geometries were studied in our investigation. The store A has a symmetric ellipsoidal geometry and the store B has an ellipsoidal geometry with a tapered trailing edge. The location of the store installation under the wing is chosen with respect to the geometric center of the store measured from the origin of the body reference axis. The Store Aspect Ratio, SAR, Store Spanwise Location, SSL/CR, Store Transverse Location, STL/CR and Store Chordwise Location, SCL/CR are the main parameters used in this investigation. The pylon has a rectangular geometry. The geometry of the pylon can be defined by parameters like used in the wing system. And finally, the wing-fuselage interaction problem is handled similar to the work of Atta and Nayfeh [19].

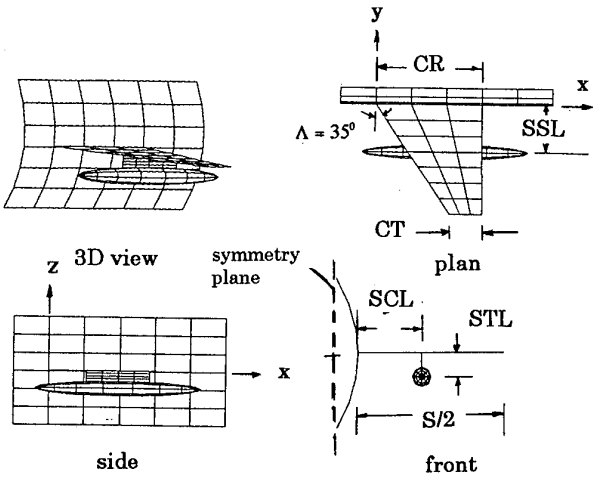

Figure 4. Geometry of the W/F/P/S combination and important parameters.

Validation of the Computer Code,TRNVLM

As means of establishing the credibility and the engineering accuracy of the computer code, TRNVLM, some basic applications of the steady and unsteady aerodynamics will be presented first.

Computer experiments have been performed to predict the lift coefficient value as a function of angle of incidence for various rectangular wings having different Aspect Ratio,AR. The variation of the lift coefficient slope with the Aspect Ratio is presented in Figure 5a. The computed results agree well with the theroetical values obtained by Graham (20). The curves shown in Figure 5b are the predictions of the transverse loads on a rectangular wing having an AR= 1. In this Figure, the experimental results of Lamar (21) and the computational results of Fang and Luo (22) are also shown. The computational results of Fang and Luo are based on a Vortex Lattice type modeling,

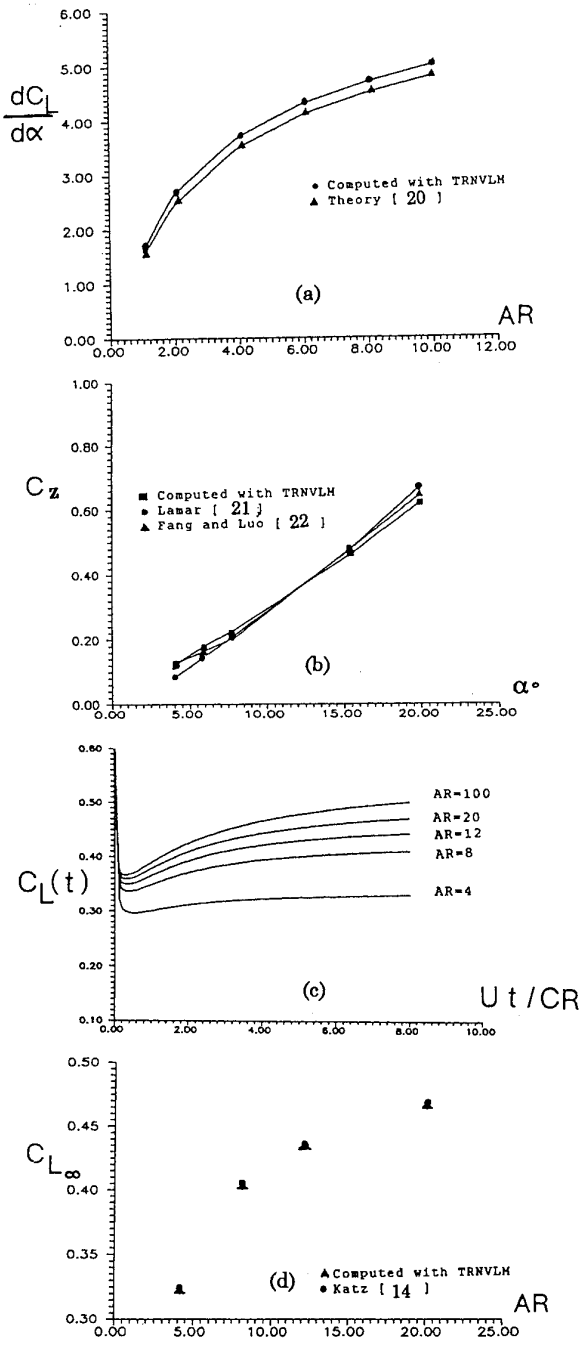

Figure 5. Validation of the computer code, TRNVLM.

too. The predictions with TRNVLM computer code are very near to both results. The transient lift coefficient variation with time for various aspect ratio rectangular wings which are suddenly set into forward flight is depicted in Figure 5c. A steady state configuration of the near wake is reached for a dimensionless time,T, approximately equal to 6. A comparison of the steady state lift coefficient predictions between the present computer code and the computational code supplied by Katz (14) is shown in Figure 5d. The agreement between two codes are remarkable.

The present computer code, TRNVLM is capable of predicting the unsteady wing loading during maneuvering flight along a three-dimensional prescribed path. The computer code, in its current state, simulates diving, climbing, pitching, heaving and rolling motions or combination of these motions where predictions by experiments and other computational techniques are limited. Furthermore, the unsteady aerodynamic problem associated with the release of a store at any instant of the maneuver can be modeled by the computer code. The examples presented in the next section serves mainly to understand the unsteady nature of both the flow field and the aerodynamic loading during the store carriage and release.

Wake Development: Effect of angle of attack

The near wake of an aircraft has major effects on the aircraft's aerodynamic characteristics, such as tail plane loads, wake induced turbulence on the approaching aircraft, wing presssures and store trajectory paths after the release. For this reason, it is essential that a computational code can model wakes accurately.

Figure 6 shows an overall plan view of the instantaneous structures of the trailing edge wakes for different angle of attacks. The shed vortex rings deform continuously under the influence of W/F/P/S configuration. The continuous spill of the flow from the lower surface of the wing combines with the upper surface flow and then forms the classical wing tip vortices at high angle of incidences. The new flow field boundary conditions imposed by the store modifies the near wake structures by creating an additional longitudinal vorticity at high angle of incidence. The clockwise rotating wing tip vortex (viewed from the rear) is augmented at higher angle of incidences. Along the wing/fuselage junction the wake is attached to the fuselage surface until it leaves the body. The similar vortex roll-up but in the counterclockwise direction takes place along the wing-fuselage junction as the wake develops in the streamwise direction. At $\alpha = 20^0$ there exists an additional secondary vortex rollup in the clockwise direction starting at about three root chord distances from the trailing edge of the wing. Such kind of a wake character also appears for the negative angle of incidence. In negative angles of attack, the secondary vortex, rotating counter clockwise forms early at about two and a half root chord distance (viewed from the rear) and then spirals into a large vortex core. Similar type of vortex formations were also observed behind a wing/ trailing edge flap combination [18].

Figures 7 through 10 show the main features of the trailing edge near wake development in details as a function of angle of attack at a nondimensional time,

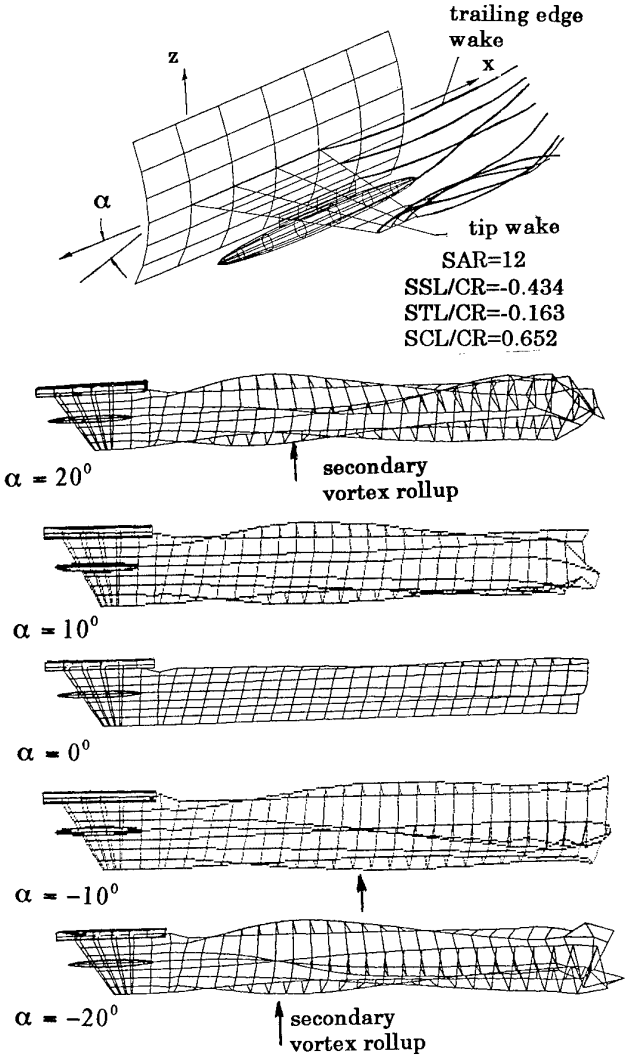

Figure 6. Computed shapes of seperated trailing edge wake structures behind the reserach configuration: effect of angle of attack.

$T = U_\infty t/CR = 8.3$. The pictures are presented at various view angles. Figure 7 shows the case for $\alpha = 0^0$ of incidence. The instantaneous wake structure is represented with the deformed shapes of the shed vortex rings. The side view of the complete wake development is shown in Fig. 7a. The transient wake development near the wing/fuselage juncture shows both a twist and also a light roll-up in the counterclockwise direction (See Figure 7b). The roll up of the trailing edge wake is viewed from the rear parallel to the wing's trailing edge in Fig.7c. The wake is deflected down by forming a bowl shape under the continuous influence of the store. The wake exhibits a strong antisymmetry thus more likely to cause an antisymmetric and downward forces on the wing.

Figures 8a-c present the wake structure for an angle of attack (climb mode) value, $\alpha = 10^0$. Figure 8a shows the side view of the streamwise vortex rings separating from the trailing edge. The distortion of the near wake due to the presence of the external store is shown from different view angle in Fig. 8b-c. There is no indication of a secondary roll up in the wake region. At a higher

positive angle of attack value, $\alpha = 20^0$, the lateral size of the wake, hence the extend of the rotational region, increases (see Figures 9a-c). The secondary rollup of the wake sheet with the influence of store complicates the wake structure. This new vortex mechanism controls the final wake shape by modifying the classical wake formation.

The direction of the wake deflection is downward for the negative values of angle of incidence (dive mode). Figure 10 shows the instantaneous wake structure from different view points. The wake sheet deflects slightly upward near the trailing edge of the wing and then deflects downwards. The upward deflected wake shape with the presence of a secondary vortex, rotating in the counterclockwise direction between the wing tip and wing/fuselage junction, is the important character of the transient wing motion during the forward dive motion.

Recently, Richason,Katz and Ashby (23) have investigated the interaction between two airplanes, large and small, flying along different paths by the use of an unsteady panel method. It was shown that the transient interaction between two airplanes causes significant changes on the time dependent forces. This is due to the unsteady nature of the bound wing vortices and the trailing edge wake developing behind them. The downwash induced by a large aircraft's wake modifies the aerodynamic loading on the smaller aircraft underneath. Hence, the interaction between two aircrafts are very much functions of the unsteady wake shapes. We believe that, the wake-aircraft interaction will be quite different under the continuous effect of an external store system on the developing trailing edge wake structure.

Unsteady Wing and External Store Loading

The transient development of the force coefficients for the wing and store geometries that were suddenly put into forward climbing motion is reported in this section. In the first part of the presentation, the wing lift coefficient variation due to the forward climb motion will be discussed. This discussion will be followed by presentation of the 3-D transient force development on the external store.

The transient lift coefficient variation for the wing suddenly set into a climb motion without an external store is presented in Figure 11. The final wake structure behind the W/F/P configuration is also presented by using streamwise vortex filaments as a function of angle of attack. During the early phases of the motion, the rate of change of the unsteady force coefficient is very large. The lift coefficient reaches its steady state value under the transient effect of the starting wing vortex and also due to the change in downwash velocities induced by the wake. The initial lift build up continues almost three root chord distance of motion for all the cases investigated in Figure 11.

Figure 12 depicts the transient lift coefficient development for the wing with an external store that is suddenly set into climb motion. In these cases, the length of the transient lift build up is a function of angle of attack. A relatively short length of transient lift development is obtained at $\alpha = 10^0$. The steady state lift value is reached after two root chord distance. The initial time length for the lift build up increases with the angle f attack.It is clear that the presence of the store modifies the initial lift variation by causing additional perturbations. The presence of the store dramatically reduces the lift values. This is primarily due to the changing wake characteristics as shown in the Figures. Of course, the change in the strengths of the wing bound vortices due to the store presence is the other major source of reason.

The cross comparison of the stady state wing lift coefficient values with and without an underwing store are presented in Figure 13 as a function of angle of attack. The variation is almost linear for the range 0 to 20 degrees. There is a negative lift value at 0 degree of incidence due to the presence of an external store. The lift coefficient values are reduced by more than 50% due to the wing-store interaction.

Understanding of the transient force development on the external store is extremely important since the characteristic values set the initial conditions for store separation. For this reason the instantaneous pressure distribution over the store surface is integrated over the subsurfaces and the normal force values are determined. By resolving the normal force components in three directions, the transient force component history is obtained(See Figure 14). Figure 15 shows the variation of the external store force coefficient in the streamwise direction as a function of angle of attack. The x-component of the store force values are found to be all positive. The streamwise x-force component decreases as the climb angle increases. The transient nature of the force variation increases with the angle of attack value. The z- directional force values are positive and reach maximum values at higher angles of attack (See Figure 15b). Figures 16a-c presents the transient moment coefficients of the external store during forward climb motion. Although steady state levels are reached in a relatively short time for the M_{cx} and M_{cy} components, M_{cz} coefficient needs longer times to reach a steady state level.

Our calculations show that the transient force build-up on the store is different than the wing's transient lift development. Since, we assume that there is no wake shedding from the store geometry, the perturbations coming from both the neighboring bodies and the developing wing wake modify the transient force and moment history.

External Store Separation

The store separation analysis consisted of calculating the aerodynamic forces and moments on the store in several locations in the vicinity of the maneuvering W/F/P configuration. The authors solve for the new altitude of the store at a specified interval of time in the store trajectory and then uses this new W/F/P/S physical relationship to calculate a new flow field. The interaction aerodynamics is updated and the process is repeated for a complete store trajectory by using the new flow field.

Figure 17 shows the transient wing normal force variation as a function of initial store position during a complete store separation scenario. The store initial position data are given in the Figure. The prescribed path of the W/F/P/S system is set to a dive mode with an angle of attack value -20 degrees. It is planned to release the store at a nondimensional time, T=2.6. The

whole configuration is assumed to continue its motion along the preset path after the store separation. As the W/F/P/S configuration set into a dive motion, a negative normal force starts to build up on the wing. Almost 99% of the steady state force level is reached by T=2.6. At this instant of time, store is released from the pylon. After the store separation, the negative force coefficient value drops sharply. Then it reaches a constant value near T=4.6. The separation effect is reflected on the transient force coefficient variation for 2 nondimensional time units. A slight change in the relative store position results in a dramatic force variations (Observe the change in the force values for the initial store position #2). In the figure, we also show the the steady state force coefficient levels. These levels indicate the steady state values corresponding to the W/F/P/S configuration with no store separation. The store which is located closer to the wing tip will result in a relatively low steady state force level on the wing. The force coefficient reaches an asymptotic level after the store separation. Although it was not shown on the Figure, two asymptotic values which corrresponding to two different initial store positions will go to the same limit value as the W/F/P motion continues. Figure 18a shows the separation scenario for the store relased from position #1. The store trajectory path is shown at four selected instants of time. The streamwise vortex filaments are also presented in the pictures. Figure 18b shows the plan view of the position of the store at $t = 2\Delta t^*$. The store pitches and also rotates around the z axis along its time dependent trajectory.

Figure 19 shows the transient normal force variation as function of initial store position during a complete store separation analysis for the climb mode. The planning of the store release scenario is similar to the case described in Figure 17. After the store separation, the transient force coefficient shows a big peak under the influence of the changes in velocity potential value. A recovery takes place in a short time duration and the force coefficient attain a fairly constant value. Figure 20a-b shows the instantaneous locations of the store after a release from the pylon. Figure 20a shows the store positions at four instants of time. The store travels a relatively long vertical distance compared to the case discussed in Figure 18. Furthermore, the rotations around the store mass center is augmented. Figure 20b shows the store position at $t = 2\Delta t^*$. The store mass center moves laterally towards the fuselage as opposed to the case observed in the Figure 18.

Figure 21 shows the transient lift coefficient variation for a W/F/P/S motion with 0(zero) angle of incidence. W/F/P/S configuration which is set into a forward sudden motion experiences negative force value under the influence of the transient wake rollup behind the wing. As soon as the store is released from the pylon (T=2.6), the force coefficient starts to level near a zero value. Hence, after the store separation, the clean wing enables the zero lift condition as expected. Figures 22a-d show the different aspects of the store separation. Figure 22a shows the instantaneous side view of the wake structure prior to store separation. The wake sheet is deflected downwards causing a negative loading on the wing. Figure 22b shows the final wake shape well after the store separation. Figure 22d shows a perspective wiew of the wake. Finally in Figure 22c, the instantaneous store positions are shown at selected times.

Roll and Pitch Motions During Steady Flight

Figure 23a shows the wake oscillation patterns behind the W/F/P/S configuration undergoing a roll motion at zero angle of incidence. The roll amplitude is 10 degrees and the whole configuration sinusoidally rolls with respect to x axis. The oscillation reduced frequency is $k = 2\pi fCR / 2U_\infty = 0.95$. The sinusoidal roll motion of the system is reflected in the wake structure. The rollup of the tip vortex sheet disappears and wake vorticity field forms crests and troughs. The wavy nature of the wake continues with a growing nature.

One of the simplest but yet an important maneuver is the oscillatory pitch motion of the system. The W/F/P/S configuration is put into a pitch mode with respect to wing apex with the same oscilation parameters chosen for the roll analysis. The final wake structure is shown in Figure 23b.

Finally, the nature of the transient force coefficient during roll motion combined with/without a store separation scenario is shown in Figure 24. The motion characteristics are as follows:oscillation reduced frequency, $k = 2\pi fCR / 2U_\infty = 1.08$, the roll angle, $\phi = 2^0$, and the angle of attack, $\alpha = 20^0$ (dive mode). The transient force coefficient oscillates with the same frequency of the roll motion. The store separation at T=2.6 slightly modifies the force values as opposed to drastic changes observed in Figures 17 and 19

5. CONCLUDING REMARKS

The topic of airframe/store compatibility is of major importance to both the aircraft and store designers. The aerodynamics problem associated with the store carriage/release are very complex. In this paper, we have aimed at presenting the capablity of a computer code, TRNVLM, for the simulation of this complex problem. The computer code offers a first look at details of the unsteady flow field due to store carriage/release that normally are not easy to obtain by experimental test techniques.

The Vortex Lattice Model enabled the calculation of the transient wing lift characteristics with and without an underwing store. Only a single store position is studied to reveal the transient nature of the aerodynamic forces and moments for the forward climb motion. The continuation of this work should include the investigation of other store positions.

The application of the VLM can be very useful in the study of store separation characteristics as long as the limitations of the methodology are kept in mind. Sample cases presented in this paper show that the post history of the wing transient forces after store separation is critical and should be studied in details.

Presently, the authors are working on the program to build a more reliable and user friendly source code for the aerodynamic solution of the store separation problem.

ACKNOWLEDGEMENT

The support of United States Air Force through European Office of Aerospace Reseach and Development is acknowledged.

REFERENCES

1. Konstadinopoulos, P., Thrasher, D.F., Mook, D.T., Nayfeh, A.H. and Watson,L., "A Vortex-Lattice Method for General, Unsteady Aerodynamics", Journal of Aircraft, 22, No.1, 1985, pp. 43-49.

2. Katz, J., "Lateral Aerodynamics of Delta Wings With Leading Edge Separation", AIAA Journal, Vol.22, No. 3, 1984, pp. 323-385.

3. Rusak. Z, Seginer, A. and Wasserstrom, E., "Convergence Characteristics of a Vortex Lattice Method for Nonlinear Configuration Aerodynamics", Journal of Aircraft, Vol. 22, No.9, 1985.

4. Arnold, R.J. and Epstein, C.S., " Store Separation Fligt Testing", AGARD Flight Test Technique Series, Vol.5, AGARD-AG-300, April 1986.

5. Triplett, W.E., "Wind Tunnel Correlation Study of Aerodynamic Modeling for F/A-18 Wing-Store Tip-Missile Flutter ", Journal of Aircraft, Vol.21, No.5, 1984.

6.-------, "Integration of Externally Carried Weapon Systems with Military Helicopters", AGARD ADVISORY REPORT No.247, April, 1990.

7. Huttsell, L.J. and Noll, T.E., "Wing Store Active Flutter Suppression-Correlation of Analyses and Wind-Tunnel Data", vol. 16, No.7, 1979.

8. Arnold, R. J. and Knight, J.B., "Weapon Delivery Analysis and Ballistic Flight Testing ", AGARDograph 300, Flight Test Techniques Series- Vol. 10., 1992.

9. Baxendale, A.J., " Application of a Multiblock CFD System to Obtaining Flowfield Predictions About Wing Body Pylon Store Configurations", Proceedings of ICAS-90,1990.

10. Luckring, M.J., " Recent Progress in Computational Vortex Flow Aerodynamics ", AGARD Conference Proceedings CP-494, 1991.

11. Nurman, E.M. and Rizzi, A., " Application of Euler Equations to Sharp-Edged Delta wings with Leading Edge Vortices", AGARD CP412, Paper no.15, 1986.

12. Hoeijmakers, H.W.M., Jacops, J.M.J.W., Berg.,J.I., " Numerical Simulation of Vortical Flow Over a Delta Wing at Subsonic and Transonic Speeds", ICAS 90-3, 1990.

13. Hoeijmakers, H.W.M., " Panel Methods for Aerodynamic Analysis and Design ", AGARD FDP Special Course on Engineering Methods in Aerodynamic Analysis and Design of Aircraft, Ankara, Turkey, May 1991.

14. Katz, J. and Plotkin,A., , Low Speed Aerodynamics, McGraw-Hill, Inc., 1991.

15. Baron,A. and Boffdossi,M., Wake Structure and Aerodynamic Behavior of High Lift Aircraft Configurations During Unsteady Maneuvers in Ground Effect ", AGARD-CP-515, 1993.

16.Meto, S. and Kaykayoglu, C.R., " Computer Simulation of an External Store Separation from a Military Aircraft with Panel Method (in Turkish)" , VII. National Mechanics Conference, Antalya, Turkey, 1991.

17. Von den Broek, G.J., " The Use of a Panel Method in the Prediction of External Store Seperation", J of Aircraft, Vol.21, no.5, 1984,pp.309-315.

18. Deslandes, R., "Evaluation of Aircraft Interference Effects on External Stores at Subsonic and Transonic Speeds", AGARD-FDP Symposium, CP-285, 1980.

19. Atta, E.H. and Nayfeh, A.H. " Nonlinear Aerodynamics of Wing-Body Combinations ", AIAA Paper 78-1206, 1978.

20. Graham, J.M.R.," A Lifting Line Theory for the Rectangular Wing in Non-Stationary Flow", The Aeronautical Quarterly, Vol XXII, 1971.

21. Lamar, J.E., NASA TR R , p.428,1974.

22. Fang, J. and Luo, S., " Compuataion of the Subsonic Nonlinear Loads on Flat Plate Wings at High Angles of Attack", Compuatational Mechanics, Balkema Press, 1991, pp 1543-1547.

23. Richason, T.F., Katz, J. and Ashby, D.L., " Unsteady Panel Method for flows with Multiple Bodies Moving Along Various Paths ", AIAA Journal, Vol.32, No.1, January 1994.

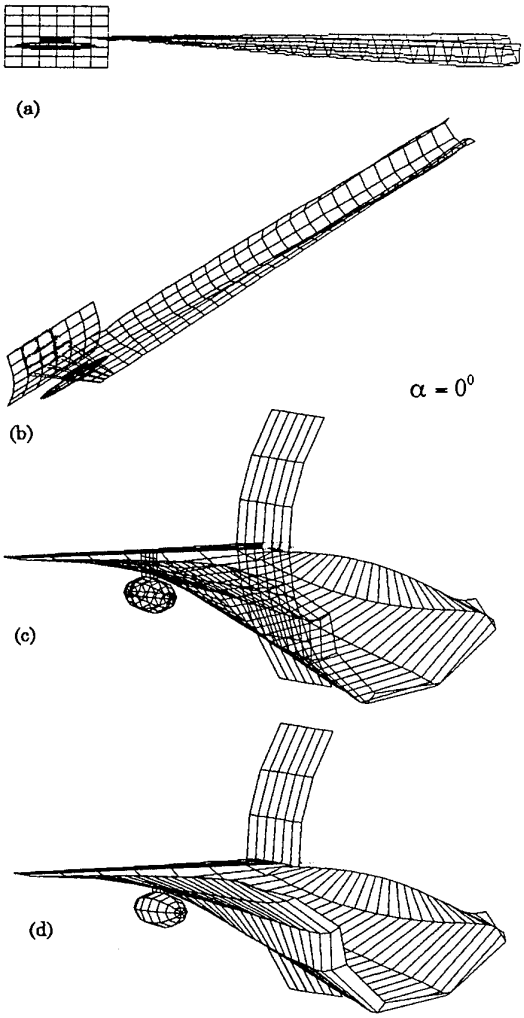

Figure 7. Computed shape of a wake structure behind the W/F/P/S configuration for $\alpha = 0^0$; a) Side view of the wake rollup. b) Perspective view of the wake evolution. c) Rear view of the wake with wire diagrams showing the vortex lattice structure. d) Rear view of the wake with hidden vortex surfaces.

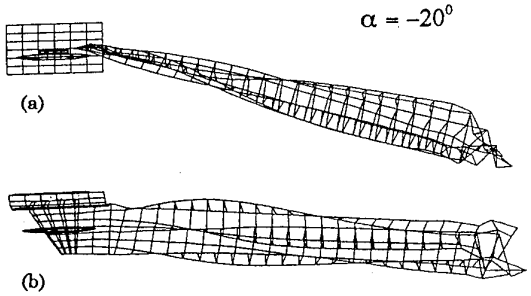

Figure 10. Computed shape of a wake structure behind the W/F/P/S configuration for $\alpha = -20^0$; a) Side view of the wake rollup. b) Plan view of the wake evolution.

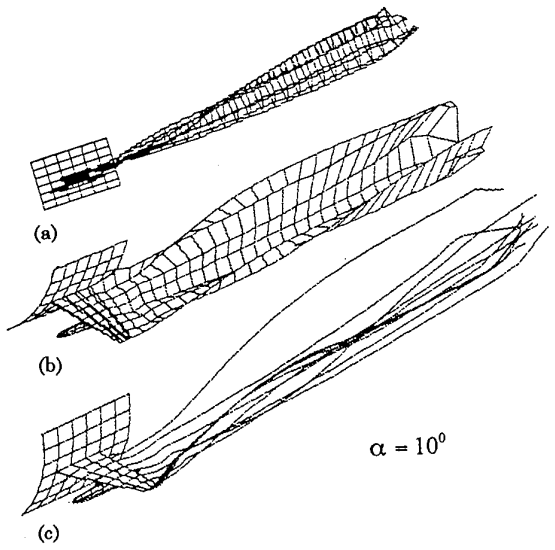

Figure 8. Computed shape of a wake structure behind the W/F/P/S configuration for $\alpha = 10^0$; a) Side view of the near wake and deformation of the wake structure. b) Perspective details of the near wake with hidden vortex surfaces. c) Representation of the wake with streamwise vortex filaments.

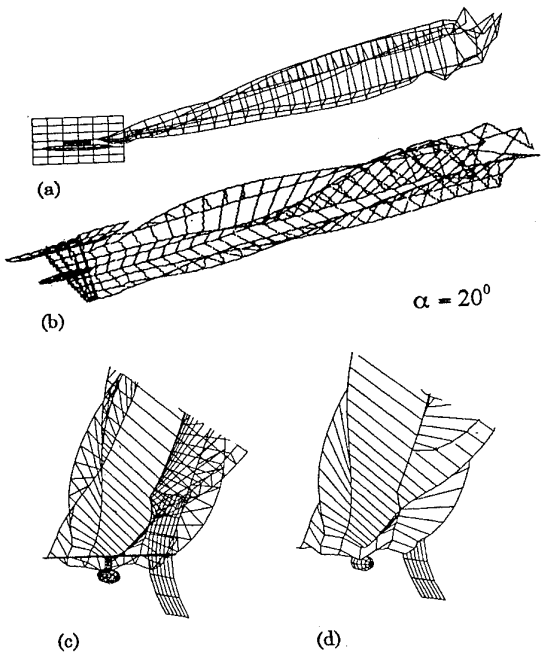

Figure 9. Computed shape of a wake structure behind the W/F/P/S configuration for $\alpha = 20^0$; a) Side view of the wake rollup. b) Perspective view of the vortex wake evolution and the formation of the secondary vortex with the influence of the external store. c),d) Details of the near wake structure.

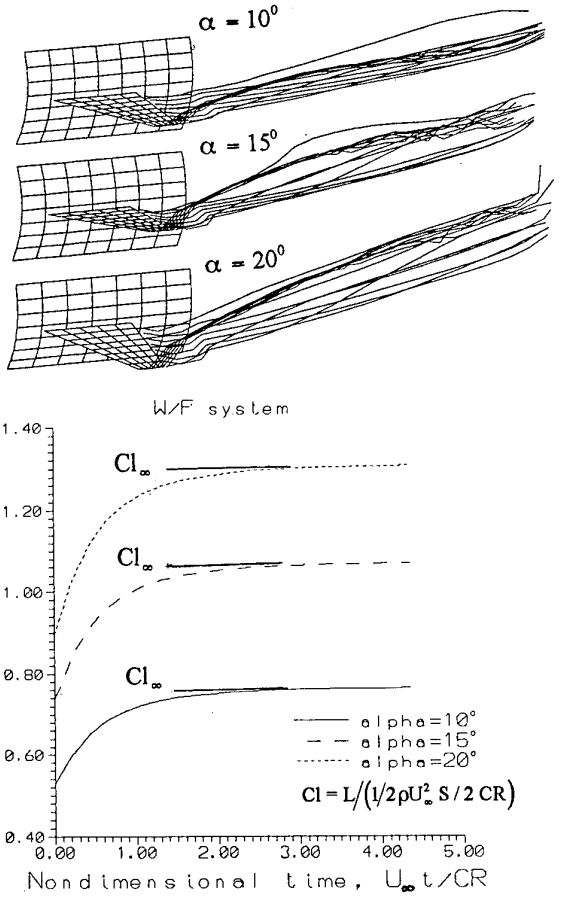

Figure 11. The transient lift coefficient of the wing after W/F configuration was suddenly set into a constant speed forward climb motion.

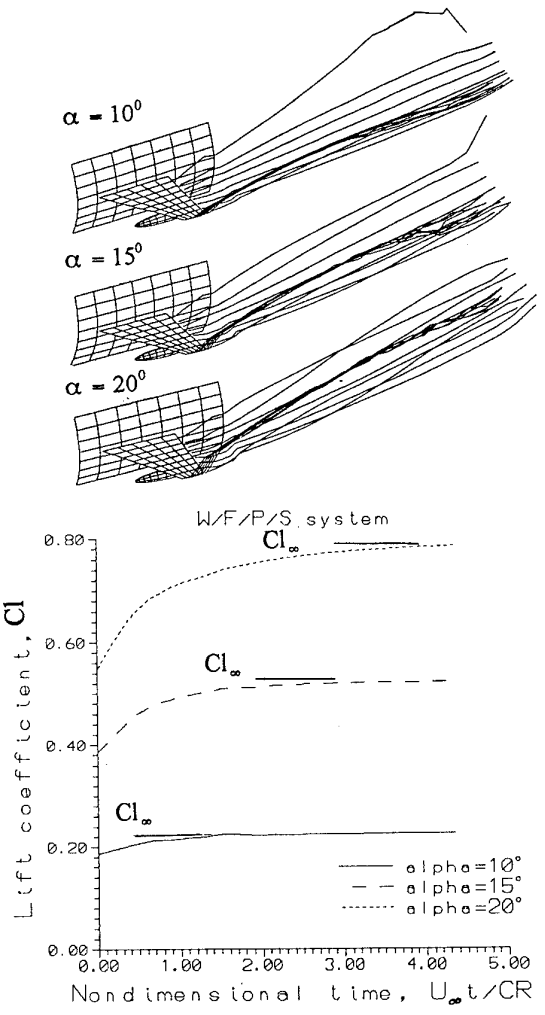

Figure 12. The transient lift coefficient of the wing after W/F/P/S configuration was suddenly set into a constant speed forward climb motion.

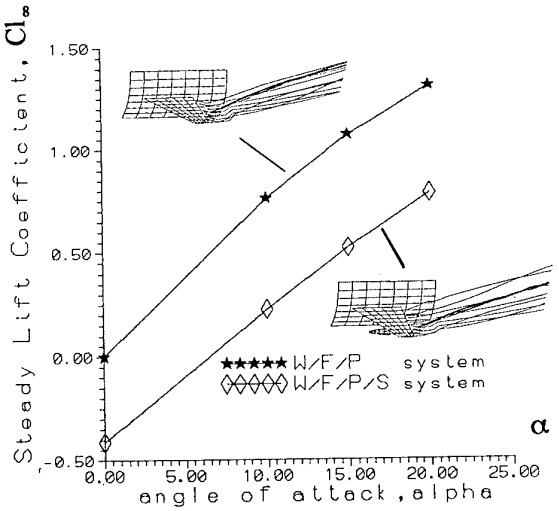

Figure 13. Effect of an external store on the steady state wing lift coefficient variation as a funtion of angle of attack.

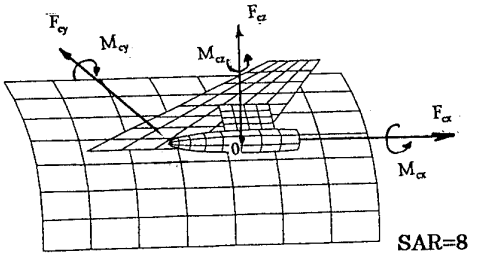

Figure 14. Underwing Store B geometry: force and moment components.

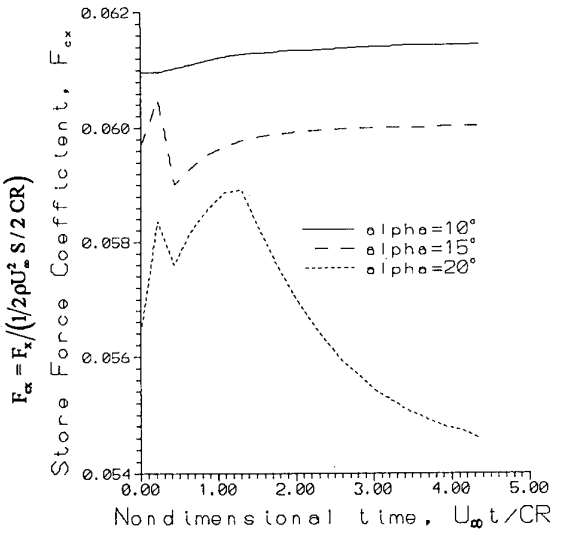

Figure 15a. The transient force coefficient, F_{cx}, of the store after W/F/P/S configuration was suddenly set into a constant speed forward climb motion.

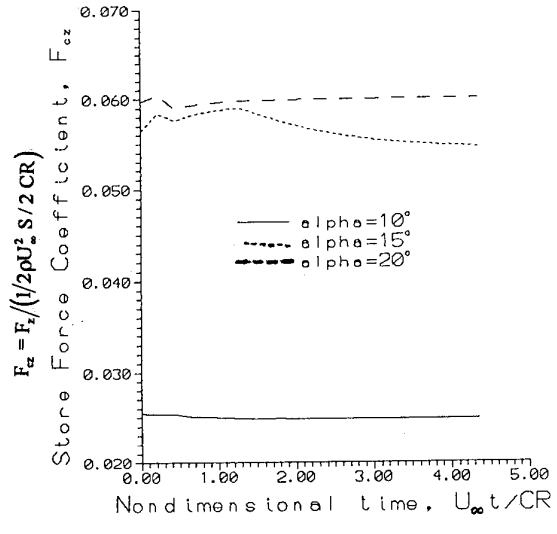

Figure 15b. The transient force coefficient, F_{cz}, of the store after W/F/P/S configuration was suddenly set into a constant speed forward climb motion.

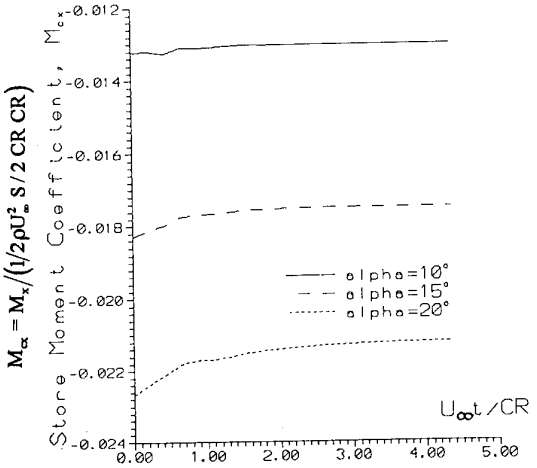

Figure 16a. The transient moment coefficient, M_{cx}, of the store after W/F/P/S configuration was suddenly set into a constant speed forward climb motion.

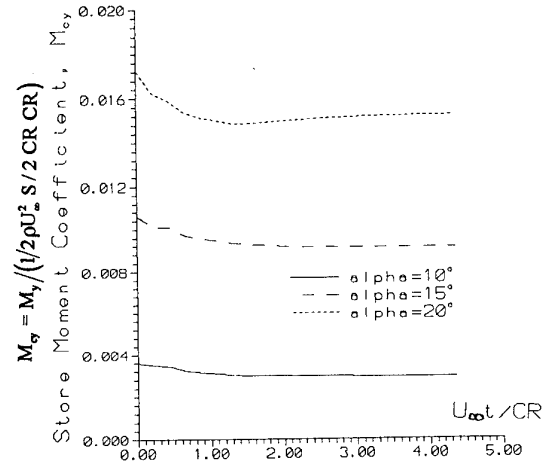

Figure 16b. The transient moment coefficient, M_{cy}, of the store after W/F/P/S configuration was suddenly set into a constant speed forward climb motion.

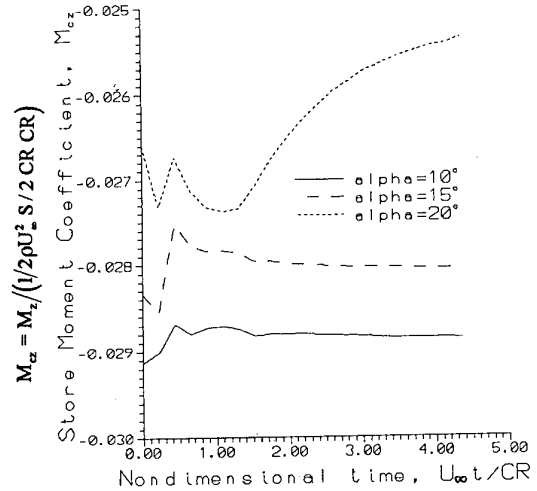

Figure 16c. The transient moment coefficient, M_{cz}, of the store after W/F/P/S was suddenly set into a constant speed forward climb motion.

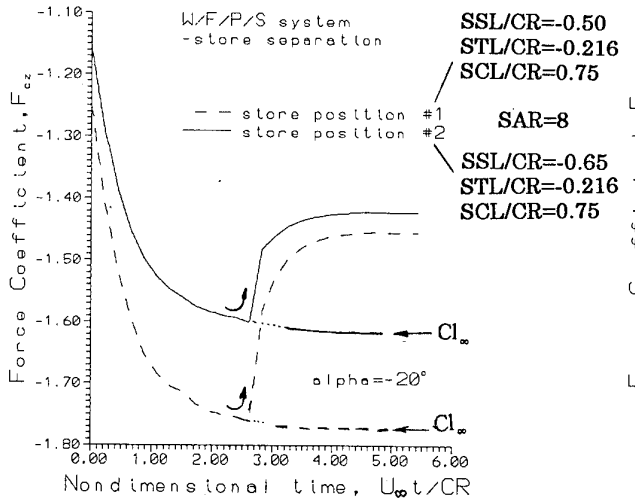

Figure 17. The transient force coefficient, F_{cz}, of the wing before and after the store separation during a constant forward dive motion: Effect of store position.

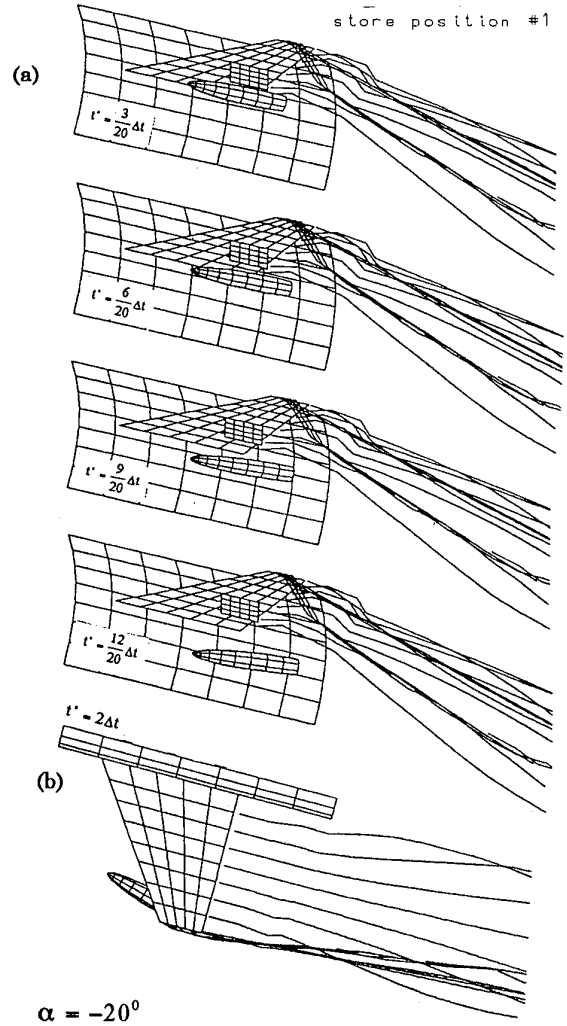

Figure 18. a)Instantaneous store positions at selected times. b) Plan view of the store position at $t^* = 2\Delta t$.

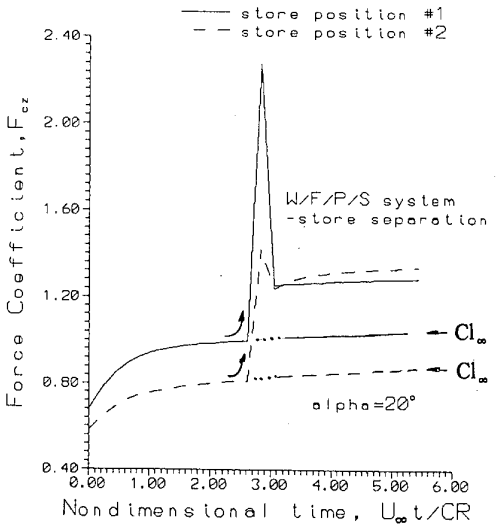

Figure 19. The transient force coefficient, F_{cz}, of the wing before and after the store separation during a constant forward climb motion: Effect of store position.

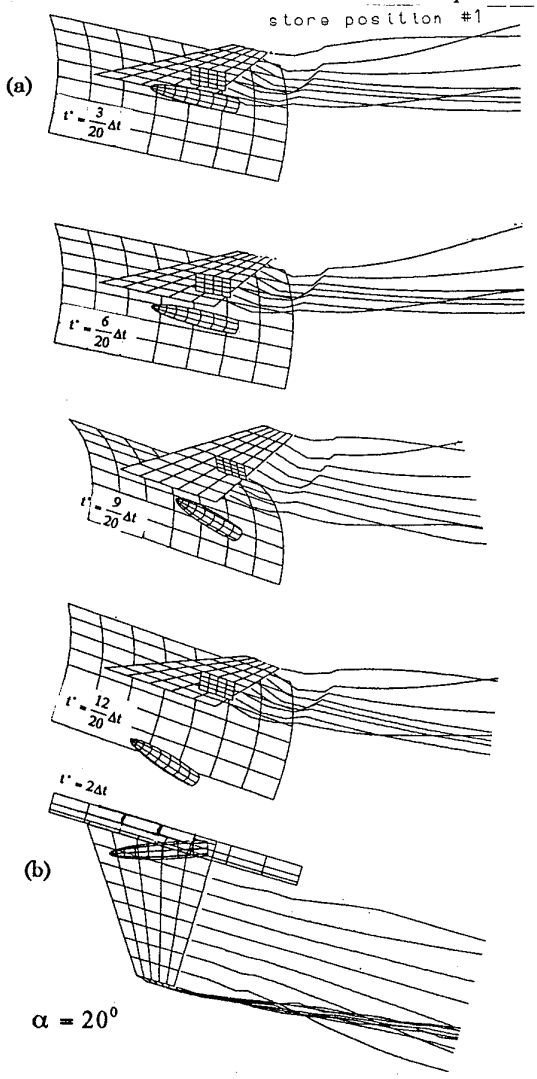

Figure 20. a)Instantaneous store positions at selected times. b) Plan view of the store position at $t^* = 2\Delta t$

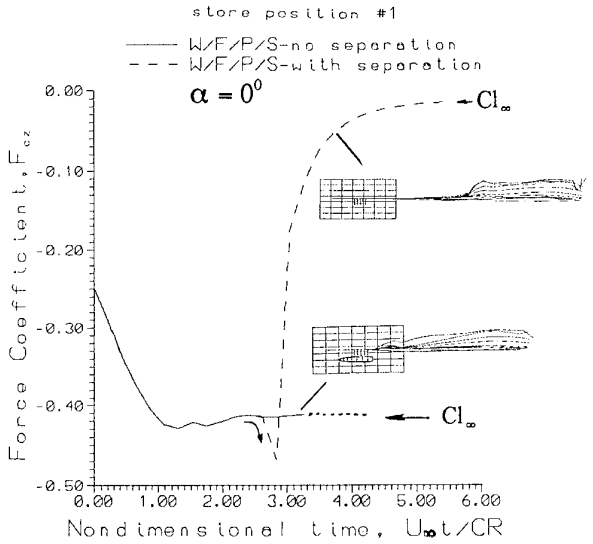

Figure 21. The transient force coefficient, F_{cz}, of the wing before and after the store separation during a constant forward zero angle of attack motion.

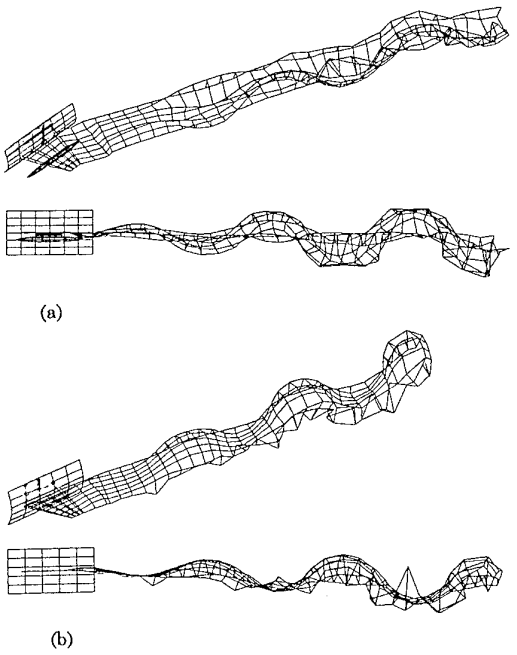

Figure 23. a) Perspective and the side view of the computed vortex wake structure behind the W/F/P/S configuration performing sinusoidal roll motion.
b) Perspective and the side view of the computed vortex wake structure behind the W/F/P/S configuration performing sinusoidal pitch motion.

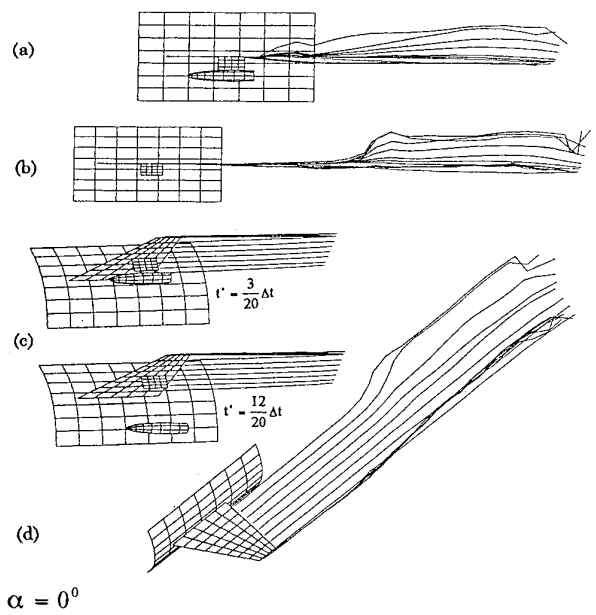

Figure 22. a)Instantaneous wake structures before the store separation. b) Instantaneous wake structures after store separation. c) Store positions. d)Perspective view of the wake showing the pre and post store separation effects.

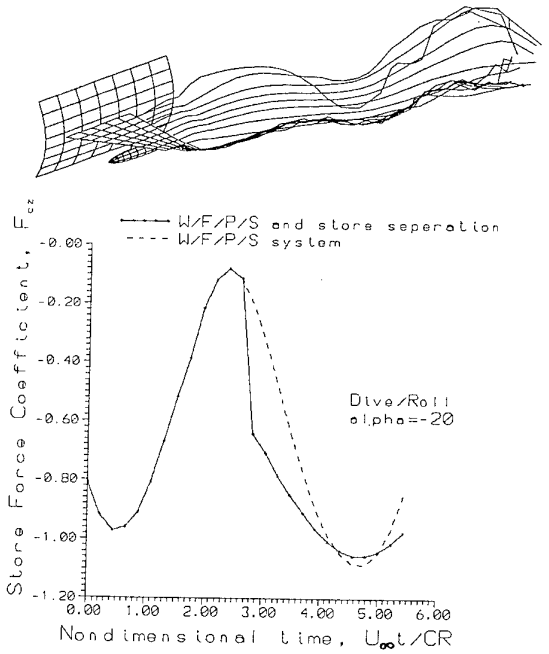

Figure 24. The transient force coefficient, F_{cz}, of the wing before and after store separation during a roll motion with forward dive motion.

PARAMETRIC IDENTIFICATION OF TRANSONIC UNSTEADY FLOW CHARACTERISTICS FOR PREDICTING FLUTTER OF FIGHTER AIRCRAFT WITH EXTERNAL STORES

Jos J. Meijer
National Aerospace Laboratory (NLR)
P.O. Box 90502, 1006 BM Amsterdam, The Netherlands
Atlee M. Cunningham, Jr.
Lockheed Fort Worth Company (LFWC), MZ 2838, Bldg 200,
Lockheed Boulevard, Fort Worth, TX 76101, USA

SUMMARY

An analysis of steady wind tunnel data, obtained for a fighter type aircraft, has indicated that shock-induced and trailing-edge separation play a dominant role in the development of Limit Cycle Oscillations (LCO) at transonic speeds. On the basis of these data a semi-empirical LCO prediction method was developed. Its preliminary version has been applied to several configurations and has correctly identified those which have encountered LCO. It has already shown the potential for application early in the design process of new aircraft to determine and understand the nonlinear aeroelastic characteristics. In the present paper this method is upgraded on the basis of results of unsteady wind tunnel force and pressure measurements obtained from on oscillating fighter type wings. In particular, an aerodynamic nonlinear state-space model embedded in the LCO prediction method will be demonstrated. The developed aerodynamic model is a semi-empirical, unsteady, nonlinear model which makes use of these experimental steady and unsteady data. Validations are presented for various fighter configurations by comparing calculated LCO results with information from flight test data.

1. INTRODUCTION

Requirements of fighter aircraft to operate with high maneuverability in the transonic speed regime increase the potential to encounter a transonic nonlinear flutter, known as limit cycle oscillations (LCO). LCO is a limited amplitude self-sustaining oscillation produced by a structural/aerodynamic interaction. The phenomenon is related to buffet but has characteristics similar to classical flutter in that it usually occurs at a single frequency. From an operational point of view, LCO results in an undesirable airframe vibration that limits the pilot's functional abilities and produces extreme discomfort and anxiety. More importantly, targeting accuracy is degraded, e.g. wing mounted missiles cannot be fired because of high levels of wing motion that prevent target lock-on.

As an example a recording is shown in figure 1 of LCO of a fighter aircraft which was encountered during flight flutter tests [1]. LCO is characterized by an almost harmonic oscillation which appears at Mach numbers ranging from 0.8 to 1.1, and at moderate angles-of-attack depending on the Mach number, but usually less then 10 deg. The flow conditions during this type of LCO are characterized by mixed attached/separated flow (Fig. 2) [2]. Lowly damped vibration modes tend to respond provided they have the proper characteristics to couple with this type of flow. This coupling frequently occurs near flutter boundaries, which implies that classical flutter predictions with linear theory may be applied as a guide for identifying lowly damped modes in the transonic speed range that might be sensitive to LCO.

Currently there are several aerodynamic computer codes available to predict the unsteady loading in subsonic, transonic, and supersonic inviscid flow. However, codes capable of dealing with the transonic speed range with regions of separated flow and shock-wave/boundary-layer interactions have not yet been developed to an acceptable level of reliability.

In response to the need to improve the accuracy of unsteady aerodynamics and flutter predictions and to reduce the time and costs of flutter clearance of the many store configurations of a fighter aircraft, an investigation was started as a cooperative effort between NLR and Lockheed Fort Worth Company (LFWC) to understand the nature of LCO experienced by fighter aircraft maneuvering at transonic speeds. This investigation has been funded by the US Air Force, The Netherlands Ministry of Defense, LFWC, and NLR.

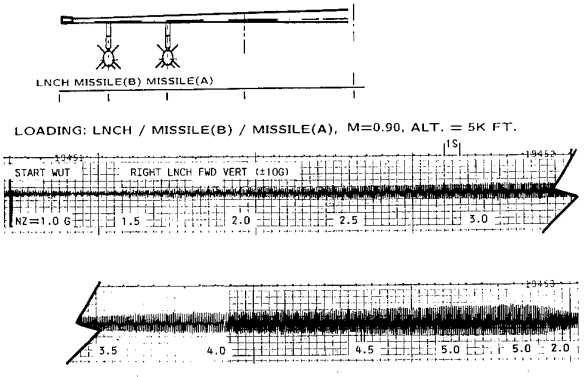

Fig. 1 Recording of accelerometer during flight flutter testing of fighter-type aircraft.

Paper presented at the AGARD FDP Symposium on "Aerodynamics of Store Integration and Separation", held in Ankara, Turkey from 24-27 April 1995, and published in CP-570.

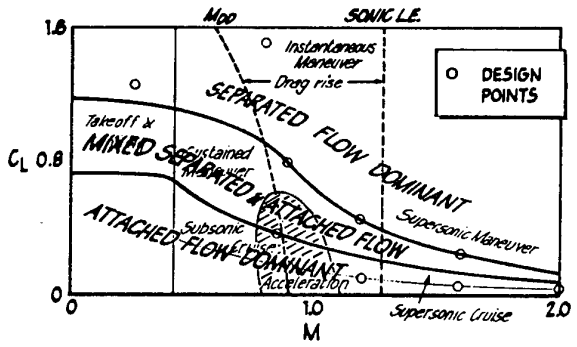

Fig. 2 Type of flow regions encountered.

The investigation existed of an extensive wind tunnel test program [3,4] with oscillating models which has been completed now, and the development of a semi-empirical method for predicting LCO characteristics of full-scale aircraft. The wind tunnel data are being used in some form in the development of this semi-empirical method.

An analysis of steady wind tunnel data, obtained for a fighter type aircraft, indicated that shock-induced and trailing-edge separation form nonlinear mechanisms which play a dominant role in the development of LCO at transonic speeds. On the basis of these data a semi-empirical prediction method was developed, which has been extended to include the use of unsteady data from the above wind tunnel test program. A preliminary version of the method was discussed in reference 5.

This paper will present the prediction method in its most recent formulation, especially the aerodynamic model which is embedded in the method. Also validations are given comparing calculated results for various fighter configurations with measured flight test data.

2. FLUTTER PREDICTION

As stated already, classical flutter predictions employing linear transonic aerodynamics may be applied as a guidance to establish LCO sensitivity. An example of such flutter predictions for a fighter aircraft is shown in figure 3 [1]. The applied aerodynamic codes were FTRAN3 [6,7] developed by NLR for oscillating three-dimensional wings in transonic attached flow, and the well-known subsonic doublet lattice method. The results in figure 3 were all computed with the doublet lattice method, except for the critical modes near 5 Hz for which also the damping curves calculated with FTRAN3 were plotted.

The results show that there exists indeed a noticeable transonic effect, although the flutter speed is hardly affected, probably because the reduced frequency is fairly high. It may be concluded that as long as the

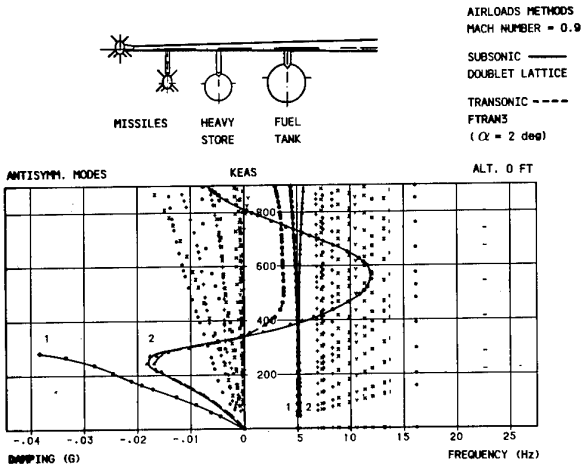

Fig. 3 Influence of transonic airloads versus subsonic airloads on calculated flutter characteristics.

the flow across the wing remains attached, conventional linear subsonic aerodynamics are sufficient.

3. NONLINEAR AERODYNAMICS

In order to identify the important nonlinearities in the aerodynamic forces that could drive LCO, steady pressure data of a full-span wind tunnel model of a fighter aircraft were analyzed at NLR which were made available by the aircraft manufacturer [8]. The objective of that test was to obtain pressure data for investigating the role of shock-induced trailing-edge separation in LCO. Pressure data were acquired on the wings, the horizontal tails and the fuselage for the following test conditions: Mach number ranging from 0.90 to 0.96, with increments of 0.01, and angle-of-attack ranging from 0 to 10 deg, with increments of 0.5 deg.

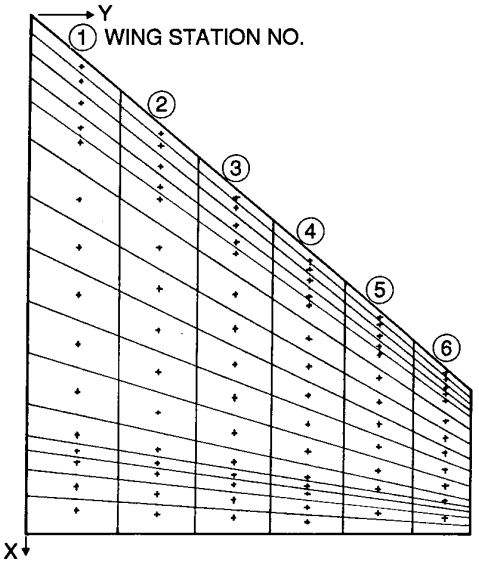

Fig. 4 Location of pressure orifices and corresponding panels on the model wing planform.

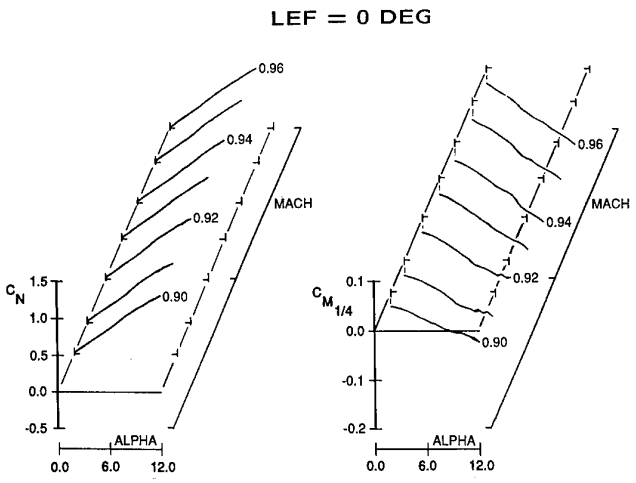

Fig. 5 Steady lift and moment coefficients at station 1 as function of Mach number and angle-of-attack at leading-edge flap setting 0 deg.

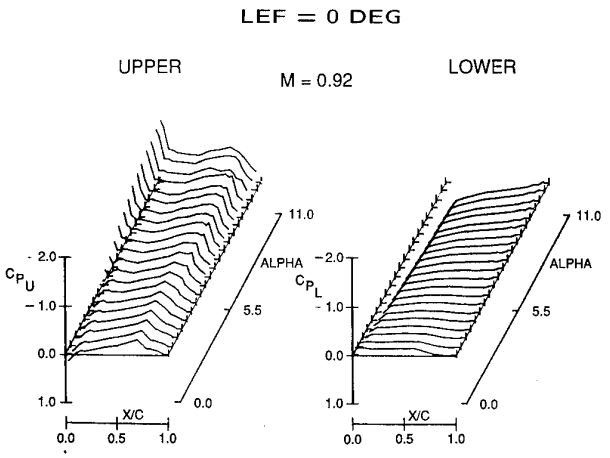

Fig. 7 Steady pressure distributions at station 1 as function of angle-of-attack and constant Mach number (M = 0.92) at leading-edge flap setting 0 deg.

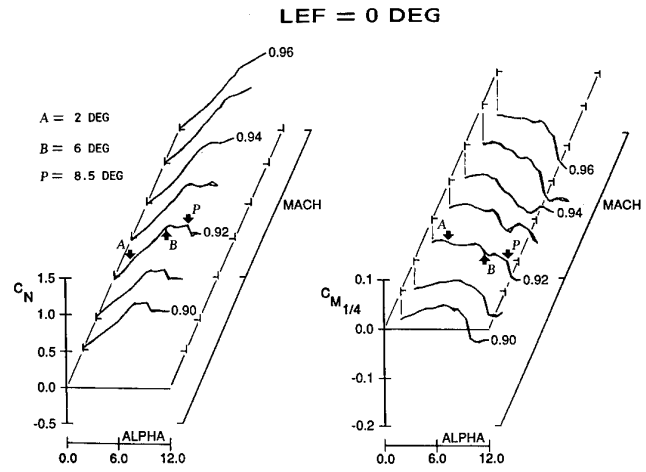

Fig. 6 Steady lift and moment coefficients at station 6 as function of Mach number and angle-of-attack at leading-edge flap setting 0 deg.

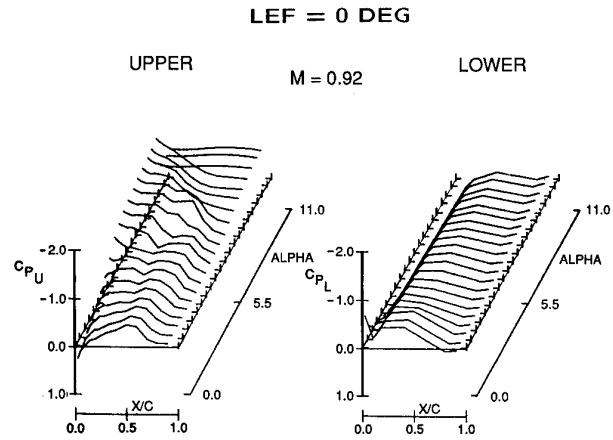

Fig. 8 Steady pressure distributions at station 6 as function of angle-of-attack and constant Mach number (M = 0.92) at leading-edge flap setting 0 deg.

During these tests different tip launchers and leading-edge flap settings were also included in the configuration matrix. The wing planform of the wind tunnel model provided with pressure orifices is shown in figure 4. Also shown is the panel distribution used in the chordwise and spanwise integration to calculate sectional and/or generalized aerodynamic forces.

Results of the NLR analysis are presented for one type of tip launcher and one leading-edge flap setting. In figures 5 and 6 the steady normal force and moment sectional coefficients are shown for stations 1 and 6 (most inboard and outboard, respectively) as function of angle-of-attack (0 to 10 deg), Mach number (0.90 to 0.96) and leading-edge flap setting of 0 deg. The coefficients for the intermediate stations show a gradual transition. It will be clear that the coefficients in station 1 do not show any irregular behavior, whereas in station 6 both the lift and moment coefficients show rapid changes in short intervals of the angles-of-attack (centered on about 5 to 7 deg) in the greater part of the Mach number interval. These rapid changes are typical of those described in reference 9 that were shown to drive LCO.

To analyze the kind of pressure distributions which lead to the rapid changes in the section aerodynamic coefficients, the pressure distributions on the upper and lower wing surface in stations 1 and 6 at Mach number 0.92 are presented in figures 7 and 8. The pressure distribution at the upper surface in station 1 shows a very gradual development with angle-of-attack, with a small upstream shift of the shock along with a slight trailing-edge flow separation at the highest angle-of-attack. At station 6 a strong upstream shift of the shock starts at about 5 to 7 deg

coupled with a rapidly developing flow separation at the trailing-edge. This occurs after a merging of the weaker nose and aft shocks into a much stronger single shock that induces the extensive separation as is discussed in detail in reference 10. The shock motion also reverses at this point which coincides with breaks in the sectional lift and pitching moment coefficients. The pressure distributions on the lower side show only very gradual developments.
For the other type of tip launcher and leading-edge flap settings the same kind of trends were observed.

4. LCO PREDICTION METHOD

The development of the LCO prediction method will be given in this section. The applied aeroelastic equations of motion, and implementation of nonlinear aerodynamics involved with transonic LCO will be discussed followed by a description of their solution procedure using a time-marching approach.

4.1 Aeroelastic Equations of Motion

An adequate description of the displacements of the unrestrained aircraft structure is obtained by taking: 1) the flexibility matrix of the free-free aircraft structure to describe the mean displacements and 2) a set of symmetric and antisymmetric natural vibration modes as generalized coordinates, completed by adding the rigid body modes. The equations for mean displacements are expressed then in matrix form as:

$$\{h_m\} = [C_{FF}]\{F_a\}, \tag{1}$$

where h_m is the vector of mean displacements, C_{FF} is the "interpolated" flexibility matrix for the aerodynamic control points which is obtained from the flexibility matrix based on the structural control points, and F_a is the vector of mean aerodynamic loading. The equations of motion are expressed in matrix form as:

$$\begin{bmatrix} M_R & 0 \\ 0 & M_E \end{bmatrix} \begin{Bmatrix} \ddot{q}_R \\ \ddot{q}_E \end{Bmatrix} + \begin{bmatrix} 0 & 0 \\ 0 & 2\zeta_E M_E \omega_E \end{bmatrix} \begin{Bmatrix} \dot{q}_R \\ \dot{q}_E \end{Bmatrix} + \begin{bmatrix} 0 & 0 \\ 0 & M_E \omega_E^2 \end{bmatrix} \begin{Bmatrix} q_R \\ q_E \end{Bmatrix} = \begin{Bmatrix} L_R \\ L_E \end{Bmatrix}, \tag{2}$$

where M is the generalized mass matrix and q is the vector of generalized coordinates. The indices R and E refer to the rigid body and elastic modes and their number is N_R and N_E , respectively. ζ and ω are the damping factor and natural frequency of each elastic mode. L_i is the generalized aerodynamic force for the i-th coordinate.
The mean aerodynamic load distribution F_a is formulated as:

$$F_a = \frac{1}{2}\rho V^2 \int_{\Delta S} C_{p_m}\langle x, y, \alpha_m\rangle dS, \tag{3}$$

in which $\frac{1}{2}\rho V^2$ is the dynamic pressure, $C_{m_p}\langle x, y, \alpha_m\rangle$ is the pressure distribution over the wing depending on the angle-of-attack distribution α_m, and ΔS is the panel area.
The generalized aerodynamic force for the i-th coordinate, L_i, is defined as:

$$L_i = \frac{1}{2}\rho V^2 \int_S \phi_i\langle x, y\rangle C_p^*\langle x, y, \alpha\langle t\rangle\rangle dS, \tag{4}$$

where $\phi_i\langle x, y\rangle$ is the natural mode shape and $C_p^*\langle x, y, \alpha\langle t\rangle\rangle$ is the differential pressure distribution over the wing,

$$C_p^*\langle x, y, \alpha\langle t\rangle\rangle = C_p\langle x, y, \alpha\langle t\rangle\rangle - C_{p_m}\langle x, y, \alpha_m\rangle, \tag{5}$$

depending on the angle-of-attack distribution α. This distribution is expressed by:

$$\alpha = \alpha_m + \Delta\alpha, \tag{6}$$

$$\alpha_m = \alpha_p + \frac{\partial}{\partial x} h_m, \tag{7}$$

$$\Delta\alpha = \sum_{N_R+N_E} \left(\frac{\partial}{\partial x} + \frac{1}{V}\frac{\partial}{\partial t}\right) \phi_j\langle x, y\rangle q_j\langle t\rangle. \tag{8}$$

α_p is the prescribed angle-of-attack, and $\Delta\alpha$ the time-dependent variation at point x, y.
Expression (5) is used to make a distinction between the mean pressure distribution resulting from nonoscillatory deflections, C_{p_m} (which, like α_m, may be a function of time), and the oscillatory pressure distribution resulting from oscillatory deflections, C_p^*. For, the oscillatory deflections are the subject of the present investigation, and may eventually lead to LCO. In the simulation process C_{p_m} is calculated by feeding C_p into a low-pass numerical filter.
The pressure distribution C_p^* in expression (4) to (5) is a time-dependent nonlinear function of α. It are these relations by which the aerodynamic peculiarities associated with shock motion, flow separation, etc. enter the equations of motion (2), weighted by an appropriate mode shape ϕ_i. The algorithm to determine C_p is discussed in section 5.

In the numerical solution of the equations of motion the aerodynamic forces F_a and L_i are discretized as follows:

$$F_a^k = \frac{1}{2}\rho V^2 \left(C_{p_m}\langle x, y, \alpha_s\rangle\right)_k \Delta S_k, \tag{9}$$

and

$$L_i = \frac{1}{2}\rho V^2 \sum_k \left(\phi_i\langle x, y\rangle C_p^*\langle x, y, \alpha\langle t\rangle\rangle\right)_k \Delta S_k, \tag{10}$$

in which ΔS_k is the k-th panel area, and $\langle C_{p_m}\rangle$ in expression (9) and the product $\langle \phi_i C_p^*\rangle$ in expression (10) are taken constant over the whole k-th panel, being evaluated at the $\langle x, y\rangle$ position of the k-th pressure orifice. Because of the nonlinear aerodynamics, these

forces have to be evaluated for both right and left wing and added correctly at each time step of the time simulation. It should be noted that in the present study only aerodynamic forces on the wing have been taken into account and those on the wing stores, fuselage and empennage surfaces have been ignored.

Before solving, the complete set of equations of motion (1) and (2), the expression (2) are brought into state space form. Writing equation (2) as:

$$[M]\{\ddot{q}\} + [C]\{\dot{q}\} + [K]\{q\} = \{L\langle q, \dot{q}\rangle\}, \qquad (11)$$

their state space form is:

$$\begin{aligned} \{\dot{s}\} &= [M]^{-1}(\{L\langle q, \dot{q}\rangle\} - [C]\{s\} - [K]\{q\}), \\ \{\dot{q}\} &= \{s\}, \end{aligned} \qquad (12)$$

and the working form is:

$$\{\dot{x}\} = [\overline{A}]\{x\} + [\overline{B}]\{u\}, \qquad (13)$$

where $\overline{A}$ and $\overline{B}$ are constant matrices that result from the change of the variables $x = [s, q]^T$ and u is the generalized force $L\langle q, \dot{q}\rangle$.

The influence of mean deformation enters the calculations through a simple iterative matrix multiplication procedure based on equation (1). If the flight conditions are hold constant and the mean deformations are within an assigned accuracy the latter are frozen.

The aeroelastic time-marching solution procedure applied to integrating equation (13) is similar to that described by Edwards et al [11]. The final result of the time integration process is the variation of the generalized coordinates q and their time derivatives as functions of time.
They can easily be reduced to quantities of practical interest, like wing tip acceleration, pilot seat acceleration, etc.

5. AERODYNAMIC STATE-SPACE MODEL

The use of unsteady aerodynamic data obtained from harmonically oscillating wind tunnel models for predicting time varying airloads for arbitrary motions is a practical means for solving aeroelastic problems where the aerodynamic characteristics are highly nonlinear.

The present unsteady aerodynamic model comprises a state-space modeling of the unsteady pressure data obtained from the wind tunnel test program with oscillating fighter type wings.

The objective of that test was to obtain unsteady pressure data for the same test conditions mentioned for the steady pressure measurements [8]. During these tests, different launchers, missiles and flap settings were included in the configuration matrix. The wing planform of the wind tunnel model (Fig. 9) and location of pressure orifices were essentially the same as

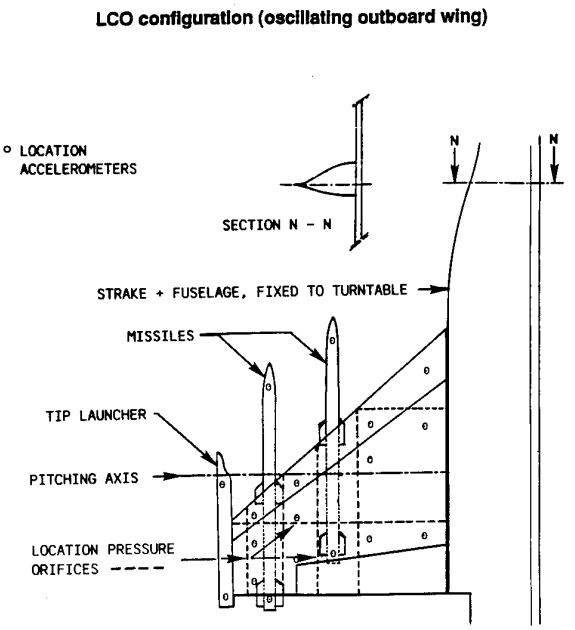

Fig. 9 Wind tunnel model of fighter type wing for LCO investigation.

shown in figure 4. In figure 10 the wing panel is shown in more detail. Support was provided through a semi-span balance beam which was in turn supported by bearings mounted on the sidewall turntable. The hydraulic actuator, also mounted on the turntable, provided the oscillatory pitching excitation of the wing panel. Model mean angle-of-attack was then controlled through positioning of the sidewall turntable indepent of the hydraulic actuator position.

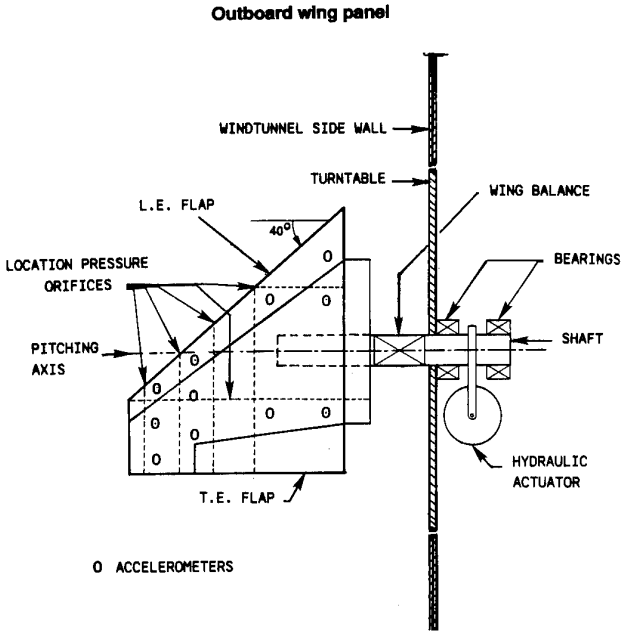

Fig. 10 Wind tunnel model of fighter type wing (Outboard Wing Panel and Support).

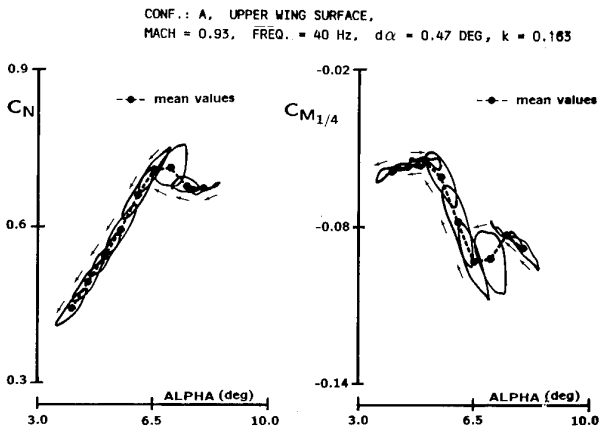

Fig. 11 Lift and moment section coefficients in WS6 as function of angle-of-attack (M = 93).

Specific requirements of the LCO wind tunnel test were to provide: (1) steady mean data for reference conditions unique to the LCO wind tunnel model geometry and test setup; (2) harmonic unsteady data with sufficient incidence and Mach number resolution; and (3) time history recordings of unsteady data.
Correlations of the steady pressure data from the semi-span test with those of the full-span test [8] showed very good agreement in spite of differences between the model and test setup. It was possible to reproduce the incidence and Mach sensitive characteristics in detail sufficiently enough to conclude that a good match between the two wind tunnel tests was achieved.

As an example hysteresis loops of integrated lift and moment coefficients are shown in figure 11 for various mean incidences and compared with the steady value curves at station 6 for Mach number 0.93. The directions in which the loops are passed are indicated. It appears that the direction of the lift coefficient loops is counterclockwise for mean incidences up to 6.5 deg and becomes clockwise for incidences from 6.5 deg on. The moment coefficients for M = 0.93 are characterized by counterclockwise loops for incidences up to 4 deg (positive damping), and by clockwise loops from 4 deg up to 8 deg (negative damping), except for the incidence at 7 deg where the orientation of the loop is changed to counterclockwise (positive damping). The moment coefficient loops appear to track clearly the slopes of the mean value curves. Negative slopes show a counterclockwise loop and positive slopes a clockwise loop. The observed trends of lift and moment coefficients are similar to the investigation presented in reference 12.
Similar hysteresis loops were found for the other wing stations and flow field conditions. On the basis of the observed unsteady trends a state-space modeling of the unsteady pressure data was chosen.

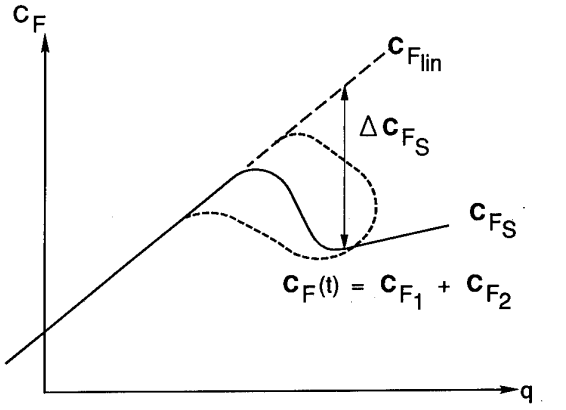

$$C_F = C_{F_1} + C_{F_2}$$

$$\dot{C}_{F_1} + a_1 C_{F_1} = f_1(q, \dot{q}, \ddot{q})$$

$$\ddot{C}_{F_2} + a_2 \dot{C}_{F_2} + a_3 C_{F_2} = f_2(q, \dot{q}, \ddot{q}, \Delta C_{F_S})$$

Fig. 12 Generalized "ONERA" unsteady aerodynamic stall model concept.

The basic model was developed by the *Office National d'Etudes et de Recherches Aerospatiales* (ONERA) for loads at rotor blade sections operating in or near stall conditions [13 to 19]. This concept has been extended by NLR to individual pressures for a three-dimensional wing as a part of the current investigation on predicting LCO characteristics of fighter aircraft.

The following subsections will first present an introductory discussion of the basic technique concept used by ONERA for fitting aerodynamic loads data. This will be followed by a condensed description of the NLR unsteady pressure model and its applications.

5.1 ONERA Unsteady Aerodynamic Model

The ONERA model is a semi-empirical, unsteady, nonlinear model which uses experimental data to predict aerodynamic forces on an oscillating airfoil which experiences dynamic stall. The model incorporates a single lag term operating on the linear part of the airfoil's steady force curve, and a two lag term operating on the nonlinear portion of the airfoil's steady force. The model was later investigated by Peters [17] who differentiated the roles of angle-of-attack due to pitch, θ and plunge, h, and by Petot & Dat [18] to reformulate the differential force equations so that they reduce to the Theodorsen formulation in the case of a flat plate in a perfect flow.
The basic principles and equations used in the dynamic stall model are illustrated in figure 12. The variations of the functions C_{F_s} and $C_F(\tau)$ are typical of two-dimensional lift near and at stall where C_{F_s} is the steady force and $C_F(\tau)$ is the dynamic force resulting from unsteady wing motion. The three equa-

tions shown in figure 12 are the generalized differential equations necessary to establish a nonlinear relationship between $C_F(\tau)$ and the displacement variable q (which is typically angle-of-attack, α). The final form of the model incorporates all terms that are needed to fit the theoretical Theodorsen coefficients in the case of a flat plate in a perfect flow [18]:

$$C_F(\tau) = C_{F_1}(\tau) + C_{F_2}(\tau), \quad (14)$$

$$C_{F_1}(\tau) = C_{F_\gamma}(\tau) + c_1 \overset{*}{\alpha} + c_2 \overset{**}{\theta} \quad (15)$$

$$\overset{*}{C}_{F_\gamma}(\tau) + a_1 C_{F_\gamma}(\tau) = a_1 \left(C_{F_{lin}}(\alpha) + b_2 \overset{*}{\theta} \right) + b_1 \left(\frac{\partial C_{F_{lin}}}{\partial \alpha} \overset{*}{\alpha} + b_2 \overset{**}{\theta} \right) \quad (16)$$

$$\overset{**}{C}_{F_2}(\tau) + a_2 \overset{*}{C}_{F_2}(\tau) + a_3 C_{F_2}(\tau) = a_3 \left[\Delta C_F(\alpha) + d_1 \frac{\partial \Delta C_F(\alpha)}{\partial \alpha} \overset{*}{\alpha} \right], \quad (17)$$

and

$$\Delta C_{F_s}(\alpha) = C_{F_s}(\alpha) - C_{F_{lin}}(\alpha), \quad (18)$$

where $\alpha = \theta + \overset{*}{h}/b$, $\overset{*}{(\,)} \equiv \partial(\,)/\partial\tau$ and $\tau = Ut/b$.
The parameters a_1, a_2, a_3 and b_1, b_2 and c_1, c_2 and d_1 must be determined empirically by parameter identification techniques. A physical meaning for these equations will be described briefly.

The first equation (14) simply states that the nonlinear function $C_F(\tau)$ is the sum of a linear part, $C_{F_1}(\tau)$, and a nonlinear part, $C_{F_2}(\tau)$. $C_{F_1}(\tau)$ is defined by the linear part of the $C_{F_s} \equiv C_{F_{lin}}$ curve (Fig. 12). The determination of $C_{F_1}(\tau)$ is obtained through the satisfaction of the conditions posed by the equations (15, 16), where $C_{F_1}(\tau)$ is further refined to include the circulatory terms (C_{F_γ}) and non-circulatory terms. These equations alone, when used in the linear region, provide a full accounting of the unsteady aerodynamic effects including time lag and flow inertia effects. These effects are analogous to the Theodorsen function in two dimensional oscillatory aerodynamics. The unknown parameters a_1, b_1 and b_2 represent a time delay, a pitch rate delay and a phase shift. c_1 and c_2 are unknown "relative mass" parameters, α is the instantaneous angle-of-attack and θ is the instantaneous pitch angle. These last two terms are determined with the expressions (6–8).

$C_{F_2}(\tau)$ (17) has to be determined when the characteristics depart from the linear variation $C_{F_{lin}}$ as shown in figure 12. Equation (17) is essentially the same as that governing a damped spring-mass system with a known nonlinear right hand side forcing function. The nonlinear feature is represented by the ΔC_{F_s} function which describes the departure of the nonlinear steady C_{F_s} curve from the linear curve, $C_{F_{lin}}$, as shown in figure 12. The unknown a_2 and a_3 parameters represent a "damping" and "stiffness" (or "frequency") respectively for the equivalent spring-mass system. Finally, the unknown parameter d_1 is another phase shift specifically for the nonlinear effects.

Additional conditions for the parameters are: $a_1 > 0$, $a_2 > 0$, $a_3 > 0$ and $4a_3 > a_2^2$. These conditions are needed to avoid instabilities and hence facilitate the fitting procedure.

Evaluation of the parameters a_1, a_2, a_3 and b_1, b_2 and c_1, c_2 and d_1 is possible using e.g. results of model tests in the wind tunnel during which the aerodynamic loads have been measured due to oscillatory motions with small-amplitude $\Delta\alpha$ about some mean angle, α_r. The values of the eight parameters are considered as constants during the small-amplitude motion, whereas C_{F_s} is variable. The measured loads are first Fourier analyzed to determine the real and imaginary components of the Fourier harmonics. The fitting procedure by which the eight parameters are evaluated takes account of these harmonics. During arbitrary wing motions e.g. LCO, the values of the parameters are not considered as constants any more. Therefore, the fitting procedure has to be repeated for a range of values α_r which is dictated by the expected arbitrary wing motions.

In this way a complete description is obtained of the unsteady loads in the time domain for any flow condition within the data base using only the eight parameters and the characteristics of C_{F_s}. Having obtained these parameters, the governing equations (14–18) can be solved to generate the unsteady aerodynamic loads for an arbitrary time history of α. The entire sequence is diagrammed in figure 13.

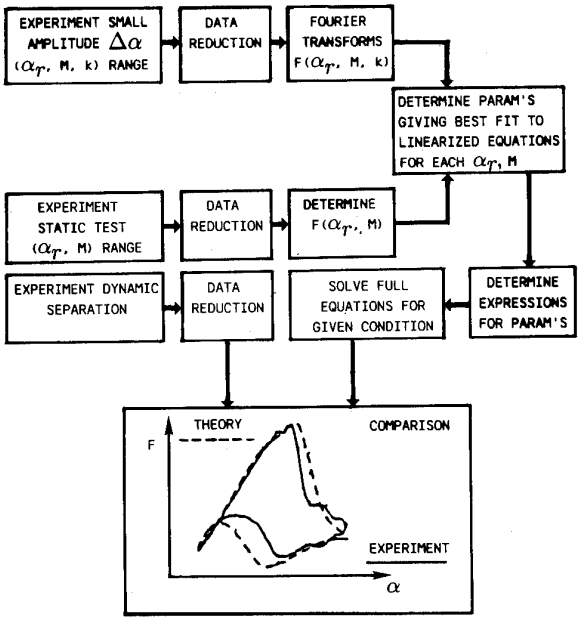

Fig. 13 Evaluation of parameters and comparison of calculated results with experimental data.

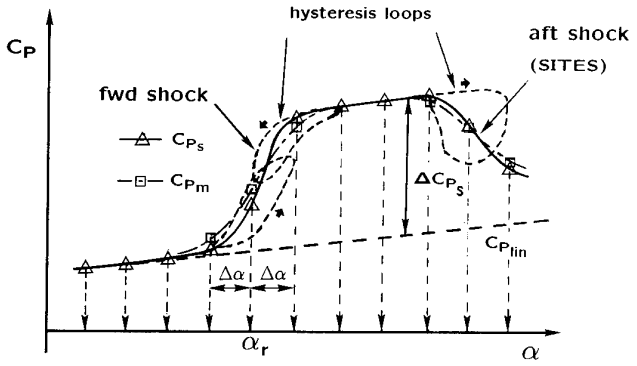

Fig. 14 "NLR" state-space pressure model concept.

5.2 NLR Unsteady Pressure Model

The NLR unsteady pressure model follows along the logic discussed above for the ONERA model for unsteady forces. The objectives of both approaches are the same where it is desired to predict nonlinear unsteady aerodynamic forces or pressures for arbitrary wing motions. A discussion of these parallels follows.

The basic principles in figure 14 and the equations (14–18) are essentially the same as those for the ONERA model, but now applied to the individual pressures over the wing area. The nonlinear variation of $C_p(\tau)$ is the sum of two parts $C_{p_1}(\tau)$ and $C_{p_2}(\tau)$, where the former is primarily governed by the slope of $C_{p_{lin}}$ and the latter by ΔC_{p_s}, the difference of C_{p_s} and $C_{p_{lin}}$. In the same way as for the ONERA model the position of $C_{p_{lin}}$ was determined originally by the linear variation of C_{p_s} with α for conditions of attached flow (small incidences) where no changes occur in flow fields such as shock passages and Shock-Induced and Trailing-Edge Separation as illustrated in figure 14. However, taking into account correctly the local nonlinear features of flow fields such as shock passages, etc. (Fig. 14) at higher incidences, the meaning of $C_{p_{lin}}$, ΔC_{p_s} and their derivatives has been redefined in the NLR pressure model. This modified approach consists of locally developed $C_{p_{lin}}$ and ΔC_{p_s} with α. So, the main difference with the ONERA model is that the complete set of equations is applied at each event, i.e. no distinction is made between linear and nonlinear portions of the C_{p_s} curves (Fig. 15). This implies that all eight unknown parameters have to be determined a priori for each reference angle-of-attack α_r and each pressure location at a given Mach number.

In section 5.1 an attempt was made to provide a physical background to the parameters in the ONERA model. This interpretation can be maintained largely in the NLR model. Thus, it might be supposed that C_{p_1}, equations (15,16), is defined mainly by the linear variation of a steady local $C_{p_{lin}}$ and five parameters,

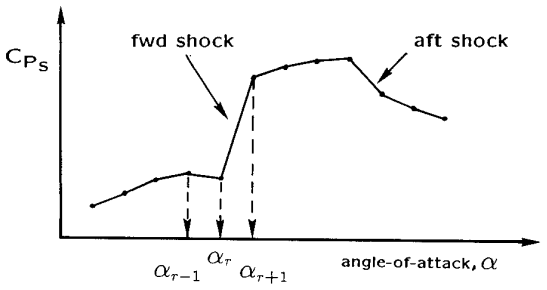

$\alpha > \alpha_r$:

$$C_{p_s}\langle\alpha\rangle = C_{p_s}\langle\alpha_r\rangle + \frac{C_{p_s}\langle\alpha_{r+1}\rangle - C_{p_s}\langle\alpha_r\rangle}{\alpha_{r+1}-\alpha_r}(\alpha-\alpha_r)$$

$$= C_{p_s}\langle\alpha_r\rangle + m_r\,(\alpha-\alpha_r)$$

$\alpha < \alpha_r$:

$$C_{p_s}\langle\alpha\rangle = C_{p_s}\langle\alpha_r\rangle + \frac{C_{p_s}\langle\alpha_r\rangle - C_{p_s}\langle\alpha_{r-1}\rangle}{\alpha_r-\alpha_{r-1}}(\alpha-\alpha_r)$$

$$= C_{p_s}\langle\alpha_r\rangle + m_{r-1}\,(\alpha-\alpha_r)$$

Fig. 15 Approximation and interpolation of measured steady pressure coefficient curve.

a_1, and b_1, b_2 and c_1, c_2. These quantities account for the time delay effects as well as flow inertia effects. In the same way C_{p_2}, equation (17), is defined by the steady local nonlinear function, ΔC_{p_s}, and three parameters, a_2, a_3 and d_1. These quantities account for such effects as flow separation and reattachment, time delay of flow transitions and shock-wave passage.

The solution procedure for evaluating the eight unknown parameters in the NLR pressure model at each reference angle-of-attack α_r and at each pressure location makes use of a parameter identification technique, in a similar way as was outlined already in section 5.1 for the ONERA model. This technique implies that

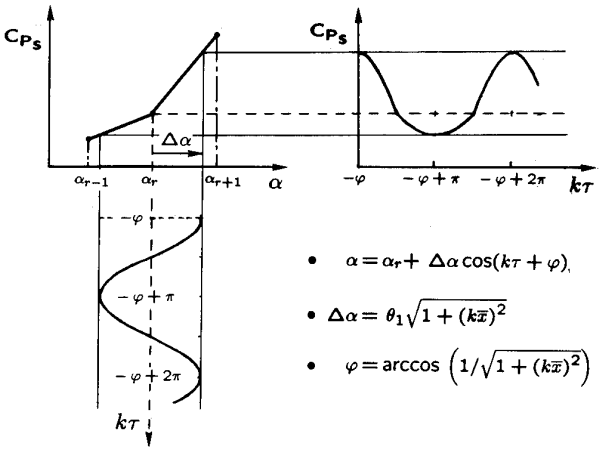

Fig. 16 Steady pressure coefficient curve to be Fourier analyzed.

use is made of results of the model test in the wind tunnel during which pressures were measured due to oscillatory motion at small amplitude about some mean angle-of-attack α_r. The technique consists of a few steps:

1. For each panel the steady pressures are approximated and interpolated as shown in figure 15.
2. Formulation of the oscillatory motion of each panel as presented in figure 16.
3. Applying Fourier analysis to C_{p_i} over the small amplitude trajectory of each panel as shown in figure 16.
4. The pressure $C_p(\tau)$ at each panel is Fourier analyzed (14–18). The Fourier components are identified with the corresponding components from the experimental data base.
5. Estimating initial values of the parameters using the above results and equations (14–18).
6. Applying a constraint optimization procedure, which searches for optimized values for these parameters, such that the pressure hysteresis loops of a set experimental values is reproduced as closely as possible.

Oscillatory data for about 0.5 deg amplitude, 40 Hz frequency, Mach number 0.93 and a reduced frequency of 0.158 from the unsteady wind tunnel test [3,4] were used to develop the parameter data base for validation purposes (see section 5.3).

The whole procedure for determining the parameters has to be repeated for each Mach number and each measured test configuration.

In the NLR unsteady aerodynamic model, time varying nonlinear C_p distributions are reconstructed for arbitrary wing motions using the above obtained parameters. The technique for reconstructing these time histories is based on a finite difference formulation of the four equations where backward differences are employed for predicting pressures at the next time step. This finite difference procedure has been implemented in the aerodynamic loads module of the LCO prediction method. The system of equations of motion is solved by the method described in reference 11.

5.3 Application of the NLR Model

The NLR model was used to recompute the unsteady pressure distributions from which the model parameters were obtained. This gave a direct evaluation of how well the method could reproduce the data which it was attempting to fit. A few typical results are shown in the figures 17 and 18 (leading-edge flap setting 0 deg), including a description of important flow characteristics to indicate how the model results correlate with various types of hysteresis loops.

The simplest case to begin with is attached flow fields where no transitions occur. This is illustrated in fig-

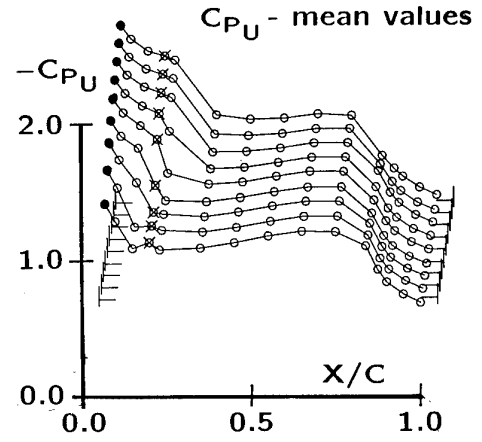

a) Mean pressure coefficients, upper wing surface, WS3.

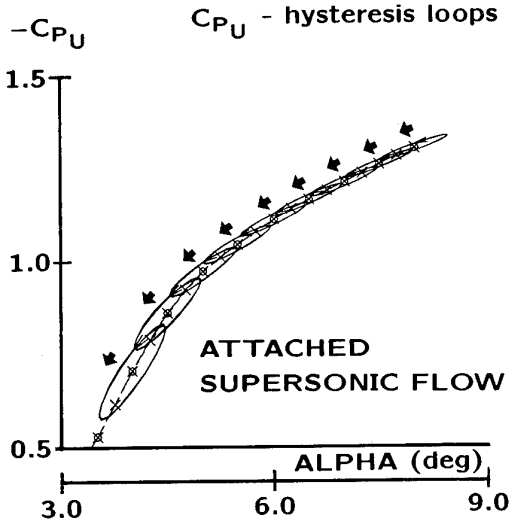

b) Pressure coefficients, upper wing surface, WS3, pt 1.

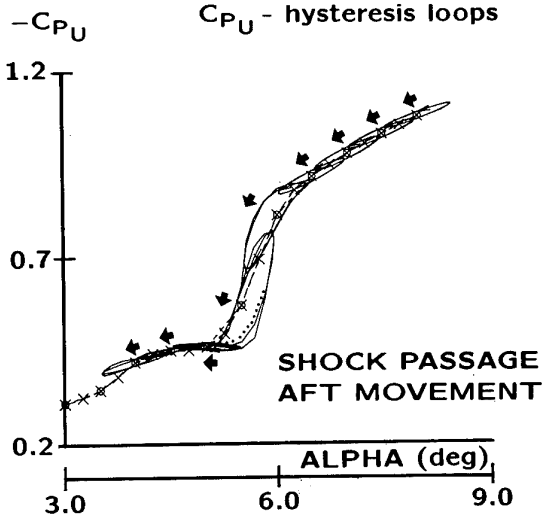

c) Pressure coefficients, upper wing surface, WS3, pt 4.

Fig. 17 Pressure coefficients, upper wing surface, WS3, pt 1 & 4, (M=0.93), comparison of calculated hysteresis loops with experimental data.

ure 17b for a forward pressure location at wing station 3 on the upper surface of the wing. With a free stream Mach number of 0.93, the flow at point 1 is continuously accelerated supersonically for all angles shown from 4 deg to 8 deg. Thus, the flow field type illustrated is attached supersonic flow where the local Mach number is always supersonic normal to the wing leading-edge. The mean (steady) chordwise pressure distributions shown in figure 17a for the incidence sweep indicate that the pressure point 1 at wing station 3 (denoted by an "•") is indeed forward of the nose shock.

The format for the unsteady pressure data portrays the hysteresis loops at a free stream Mach of 0.93 and various mean incidences about which the model is oscillating at 40 Hz with a constant amplitude of $\Delta\alpha \approx \pm 0.5$ deg. Direction of the hysteresis loops with time is indicated by arrows. Hysteresis loops for the recalculated data sets are also plotted to demonstrate how the unsteady model reproduces the measured characteristics.

When a shock develops and moves aft with increasing incidence, the characteristics shown in figure 17c between $\alpha = 5$ deg and 6.5 deg are obtained. The mean (steady) chordwise distributions (Fig. 17a) show how the nose shock develops and moves aft with incidence as indicated by the "×" symbols for a pressure point at wing station 3. The development of hysteresis loops below $\alpha = 5$ deg is typical of a local shock-induced separation bubble but is not significant in producing aerodynamic forces that are important to LCO. Those at $\alpha = 6.5$ deg and higher are typical of attached supersonic flow where the local Mach number is always supersonic normal to the wing leading-edge. The large loops near shock passage are important and are much larger than those produced at lower and higher incidences. All the loops are still counterclockwise. The outer boundary formed by the shock loops appear to form a shape that would be produced if the steady shock C_p distribution was shifted either +0.25 deg (increasing incidence or time) or -0.25 deg (decreasing incidence or time).

The comparison with recalculated loops highlights aft shock passage between $\alpha = 5.0$ deg and 6.5 deg. Some deviation is noted for the loop centered on $\alpha = 5.5$ deg, especially for increasing incidence and time. In this example, the unsteady model tries to make the loop more elliptical. On the whole, however, the match between the model and measured characteristics is excellent.

A more complicated picture arises when the transition to (or from) shock-induced trailing-edge separation (SITES) is encountered during the oscillation cycle. This characteristic is shown in figure 18b for the loop centered on about $\alpha = 7$ deg at the wing tip station 6 region. The mean (steady) chordwise pressure distributions (Fig. 18a), indicated by the symbols "•"

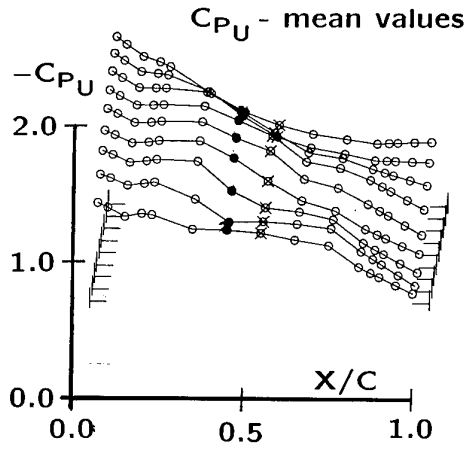

a) Mean pressure coefficients, upper wing surface, WS6.

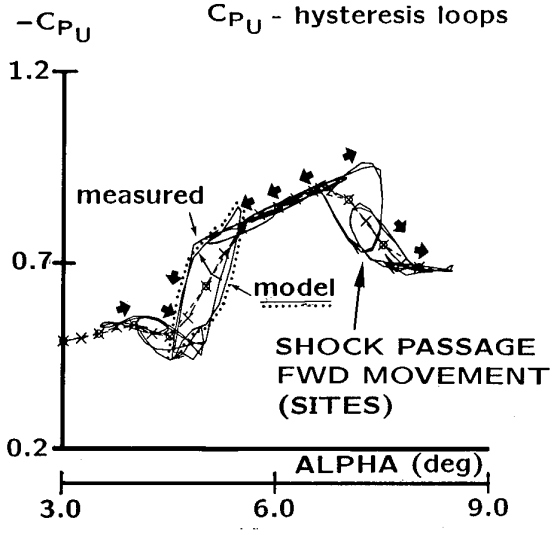

b) Pressure coefficients, upper wing surface, WS6, pt 7.

Fig. 18 Pressure coefficients, upper wing surface, WS6, pt 7, (M=0.93), comparison of calculated hysteresis loops with experimental data.

corresponding to the hysteresis loops (Fig. 18b), respectively, show how the forward shock develops, moves aft, combines with the aft shock and moves forward as the trailing-edge pressure diverges to high suction levels. The hysteresis loops at $\alpha = 4.5$ deg and 5.0 deg are characteristic of the aft shock movement noted in figure 18b. Those at $\alpha = 5.5$ deg to 6.5 deg (Fig. 18b) are typical of flows supersonic normal to the leading-edge also seen in figures 17. All of these loops are counterclockwise.

The loops at $\alpha = 7.0$ deg are typical of SITES transition and is now clockwise because the shock is moving forward. The shape of the SITES loops is also much more circular than that for shock aft passage and is indicative of much larger time lags for flow transition. Although the model reproduces the SITES transition loops at $\alpha = 7.0$ deg, it has minor trouble with the aft moving shock loops at $\alpha = 5.0$ deg and 5.5 deg, shown in figure 18b. This is not surprising since the SITES loops are nearly a circle but the aft shock passage

loops are more nonlinear. Comparing the measured and "NLR model" loops, it appears that the trends are described correctly.

The examples of figures 17 and 18 are typical of the linear and nonlinear effects that must be accounted for in unsteady aerodynamic models that are used in the prediction of transonic LCO for aircraft wings. At all other flow conditions where the flows are predominantly linear, the hysteresis loops are very elliptical and have a counterclockwise orientation.

Although the reproduction of individual pressure variations with time is important, the chordwise integral of these variations is more important for the prediction of LCO. This is true mainly because very little chordwise bending exists in the vibration modes that are typically involved in LCO. Thus, errors in the prediction at a pressure location are generally smoothed out in the integration process.

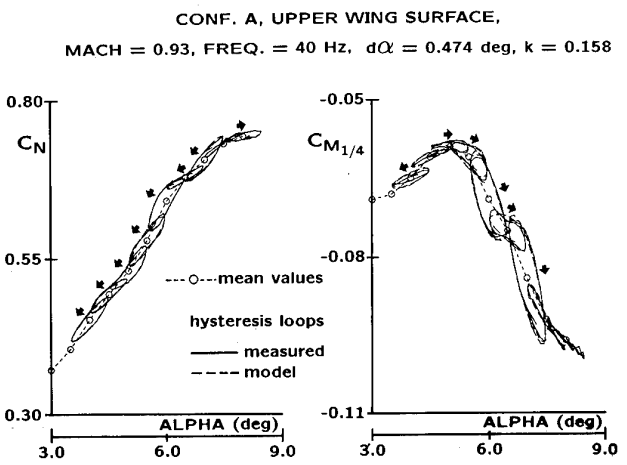

Fig. 19 Lift and moment coefficients in WS5 as function of α, (M=0.93), comparison of calculated hysteresis loops with experimental data.

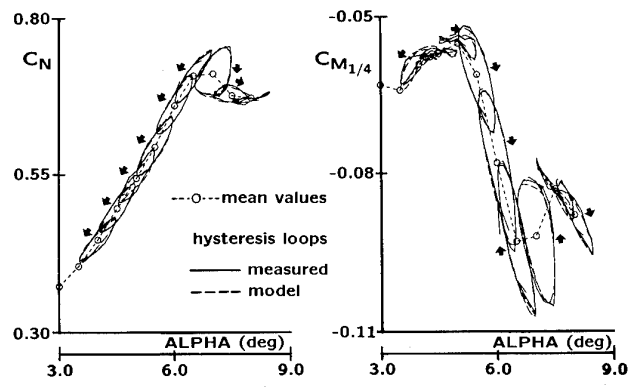

Fig. 20 Lift and moment coefficients in WS6 as function of α, (M=0.93), comparison of calculated hysteresis loops with experimental data.

Comparisons of measured section normal forces and pitching moments with those recalculated with the NLR model are carried out for the same conditions corresponding to figures 17 and 18. These results are shown for the two outer outboard chordwise pressure rows (wing stations 5 and 6) in figures 19 and 20. The same hysteresis loop format for varying mean incidence is also used in these comparisons. The measured loops are indicated by the solid lines and NLR model loops by the dashed lines.

The agreement for C_N loop predictions is excellent whereas the C_m loops show slight differences between calculated and experimental values, as was expected from the individual pressure hysteresis loops. Again deviation of loop shapes from elliptic are indicative of the local nonlinearities that are embedded in the individual pressure variations. Although the C_m loops are becoming more nonlinear in this wing station, the NLR model does quite well in following the trends. This is particularly evident for the C_m loops above $\alpha = 6.5$ deg where the flows are dominated by SITES transition. Generally, the model reproduces the measured hysteresis loops of sectional coefficients very well. Again the same observations have been established for the inner wing stations.

Thus, it has been demonstrated that the NLR unsteady aerodynamic model can reproduce the highly nonlinear features of flows which are typical of transonic LCO. The next step will be to evaluate applicability of the model to the prediction of LCO as will be discussed in the following section.

6. LCO PREDICTIONS

LCO predictions are presented for five different fighter-type aircraft configurations, e.g. A, B and a cluster of comparable configurations C, D and E, with the modified LCO calculation method that contains the NLR unsteady aerodynamic model to evaluate the applicability of the new aerodynamic force algorithm. Configuration A and B include the same underwing missiles. The difference is that configuration B is configuration A with tip missiles and external fuel tanks installed. Configuration C includes external fuel tanks, underwing (optional) and tip missiles, and different heavy stores. Finally, configuration D and E are configuration C but now equipped with multi-ejection racks equipped with three smaller stores and four smaller stores, respectively. For all configurations modal characteristics were calculated and "classical" flutter calculations were performed based on the subsonic doublet lattice method and supersonic potential gradient method [20]. For some configurations the transonic FTRAN3 method [6,7] was also applied.

Conditions for the LCO calculations are given below.

- Mach number was 0.92, altitude 5K ft, and angle-of-attack α_m=6.0 deg. This implies a sustained turn at a constant load factor.
- Natural vibration modes were considered, antisymmetric and unrestrained, with frequencies up to about 15 Hz. Structural damping was assumed uniform for all modes, g=0.02.
- Only aerodynamic forces on the wings were considered. No deflections of wing flaps and control surfaces were assumed.
- The calculated responses are (1) the normal acceleration at the front end of the tip launcher, (2) the same at the rear end and (3) the lateral acceleration at the pilot seat, all accelerations in g. In general, initial disturbances were given to the natural vibration modes which develop limit cycle oscillations.
- The simulations were carried out over a period of 20 s.

Flight test data are available for all configurations.

Generally, steady pressure data of the full-span wind tunnel model [8] were applied, augmented with the earlier determined parameters, which were used in conjunction with the aerodynamic model to reproduce the unsteady pressures.

Because the NLR model is based on steady and unsteady pressure data, realistic unsteady airloads could be generated only for the four outboard sections on the upper wing surface (see Figs. 4 and 9). For the remaining inboard sections on the upper surface and all sections on the lower surface a quasi-steady approach was applied and modified with aerodynamic damping and stiffness forces obtained from linear theory. In particular, the generalized airloads were obtained with the subsonic doublet lattice method, while the contribution of the outboard wing surface in these airloads was reduced by a factor 0.5. This approach still retains the important unsteady nonlinearities on the outboard upper surface but permits evaluation of the unsteady aerodynamic model in the prediction of LCO.
Further, the use of aerodynamic forces on the fuselage and tail surfaces [21] was neglected.
Applications of this hybrid version of the unsteady pressure model, including the latest modifications, in realistic LCO predictions will be shown in the following subsections.

6.1 Configuration A

The first example shows response calculations for configuration A. This configuration was selected because it was extensively discussed in references 21 to 24. Classical flutter calculations show an unstable antisymmetrical mode at a frequency of 7.6 Hz just above

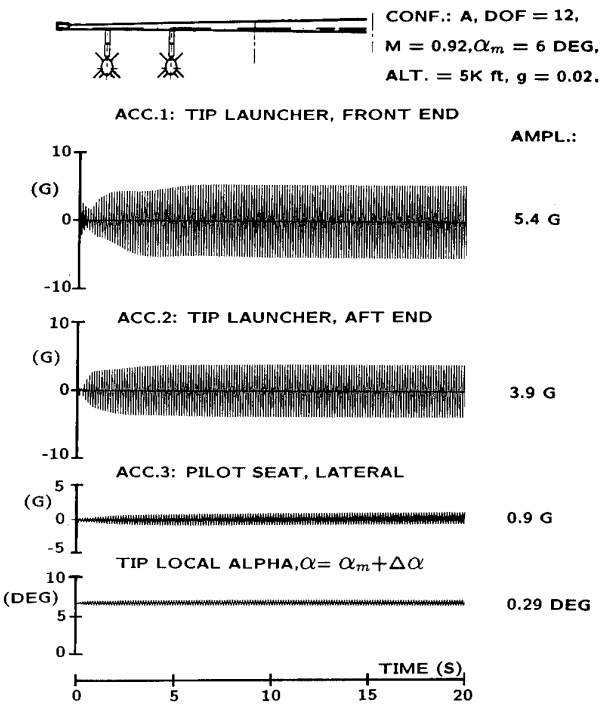

Fig. 21 Response calculation of Conf. A with state-space pressure model; 12 DOF, M = 0.92, α_m = 6 deg, alt. = 5K ft.

the desired maximum speed of 600 KEAS, neglecting structural damping. The calculations were carried out for a system with natural modes (antisymmetrical) up to 15 Hz (12 DOF). The results are presented in figure 21. The LCO response levels at the tip launcher forward location (acc.1) is ±5.4 g, at the tip launcher aft location (acc.2) ±3.9 g and ±0.9 g at the pilot seat, lateral, (acc.3) as well as ±0.29 deg oscillatory wing tip motion. As can be seen, the LCO develops uniformly and smoothly for this case. The frequency is about 7.6 Hz.
From test flight data, measured during wind-up turns, it was estimated that LCO amplitudes for the forward accelerometer on the wing tip launcher should be of the order of 3 to 5 g at the conditions used in the calculations. The conclusion is that the calculated LCO and flight test data seem to agree.

6.2 Configuration B

The loading conditions of configuration B is the same as configuration A, but now tip missiles and external fuel tanks are installed. No appropriate wind tunnel data were available for configuration B, but it is certainly justified to apply the data of configuration A, because the typical nonlinear transonic flow phenomena occur on the upper surface of the wing. Response calculations were carried out for a system with natural modes (antisymmetrical) up to 15 Hz (17 DOF). The flight conditions were kept the same as for configura-

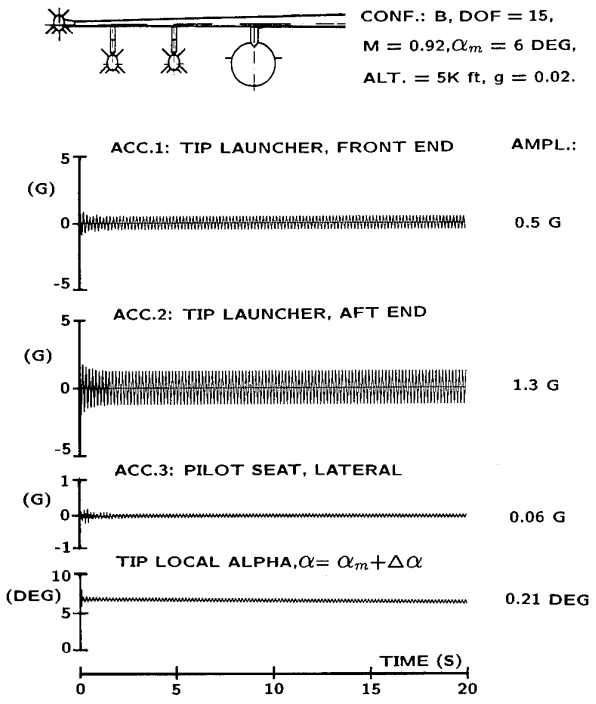

Fig. 22 Response calculation of Conf. B with state-space pressure model; 15 DOF, M = 0.92, α_m = 6 deg, alt. = 5K ft.

tion A. The results are shown in figure 22 for the responses at the tip launchers, pilot seat (lateral), and wing tip motion. It appears that an LCO develops at a frequency of about 5.8 Hz, but the amplitude levels are very low. Indeed, classical flutter calculations do not show any instability at all. In flight tests of configuration B no LCO problems were observed, so again the conclusion is that calculated LCO and flight test data correlate well.

5.3 Configuration C

LCO results are presented for configuration C, which is essentially the same as configuration A with respect to the outer wing area, but now in combination with external fuel tanks, tip missiles, and heavy stores installed. In particular, the influence of the mass properties of the different heavy stores on the LCO predictions is shown and compared with known flight test data. Classical flutter calculations already showed a severe unstable antisymmetrical mode at about 5 Hz (Fig. 3), which became even more severe at increasing mass of the heavy stores and visa versa.

Again, no appropriate wind tunnel data were available for those configurations. Therefore, the aerodynamic data of configuration A were used. The reason for applying these data was already discussed for configuration B in the same situation.

Responses were calculated for the same flight conditions as above and the four different types of heavy stores. For each case antisymmetrical natural modes up to 15 Hz (17 DOF) were applied. In figure 23 the results are presented for the case with the lighter heavy stores, referred as C.1. The following acceleration levels are found: acc.1: ±0.6 g, acc.2: ±0.9 g, and acc.3: ±0.13 g, and a wing tip motion of ±0.17 deg. The frequency is about 5.6 Hz.

The same type of calculations were repeated for the three other heavier stores. The final results for the four different types of heavy stores are presented in figure 24 as function of the heavy store mass. The bar in the lower part of figure 24 shows the four heavy store masses, indicated by C.1 to C.4. In the upper part of the figure the final response levels at the same locations of the tip launcher (acc.1, acc.2), at the pilot seat (acc.3) and the wing tip motion are shown. The results for each configuration C.1 to C.4 are indicated by different symbols.

It appears that for the first three cases C.1 to C.3 the LCO develops uniformly and smoothly with final amplitudes values shown in figure 24. The last case C.4 with the heaviest stores leads definitely to a divergent motion. Details of the calculation results are mentioned in references 25 and 26.

Available flight test data of configuration C show no LCO problem for the cases C.1 and C.2. A moderate LCO was indeed observed for the case C.3 with amplitudes for the forward accelerometer (acc.1) on the wing tip launcher of the order ±3 g at the conditions used in the calculations, but did not lead to flight restrictions.

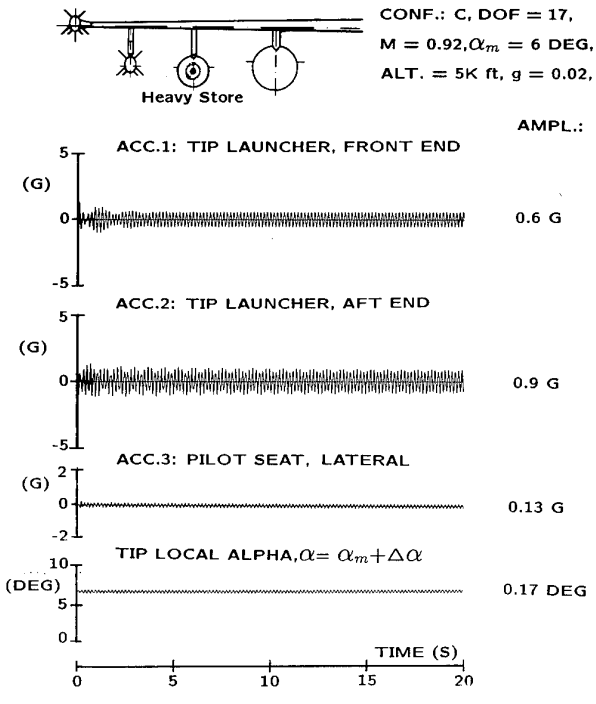

Fig. 23 Response calculation of Conf. C with state-space pressure model; 17 DOF, M = 0.92, α_m = 6 deg, alt. = 5K ft.

Configuration C.4 already experienced heavy vibration at low speed conditions and was never cleared. Again, the conclusion is that LCO predictions correlate well with the corresponding flight test data. These results lead also to the additional conclusion that the aerodynamic influence of the underwing stores play a minor role in predicting LCO.

5.4 Configurations D and E

The loadings of configurations D and E are essentially the same as configuration C, but now different multi-store racks are installed equipped with three smaller stores (loadings D.1 and D.2, slightly different mass properties of the applied stores) and two inboard or outboard smaller stores (loading E.4, maximum four stores can be carried with this rack), respectively, which corresponds to mass properties smaller than the lighter of the heavy stores of configuration C (see Fig. 24 lower bar). Classical flutter calculations showed flutter mechanisms which are the same compared to that of configuration C. The same aerodynamic data were applied as discussed for configurations B and C. LCO responses were calculated for the same flight conditions as above. Again details of the calculation results were presented in references 25 and 26. In figure 24 (left-hand side) the results are given for both configurations D and E. For configurations D again an

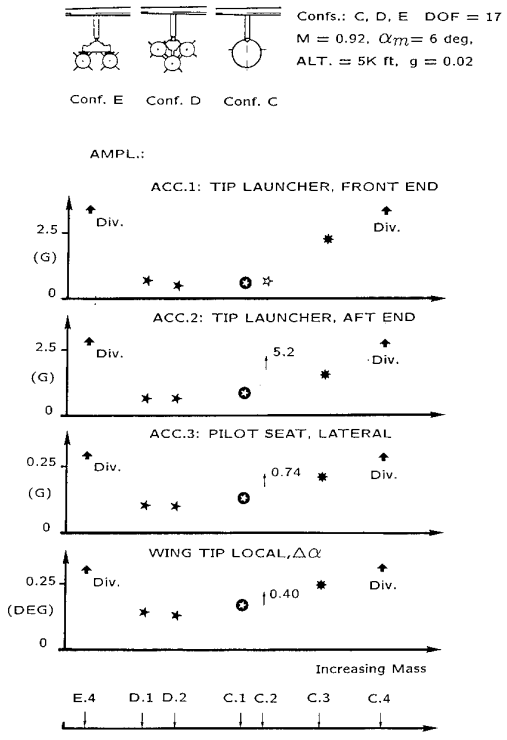

Fig. 24 Results of response calculations of confs. C, D & E with state-space pressure model; M = 0.92, α_m = 6 deg, alt. = 5K ft, as function of mid-station loading.

LCO develops uniformly and smoothly (not shown) at a frequency of about 5.5 Hz, however the response levels are low, even slightly lower than those found with configuration C.1.
In flight tests of these configurations no LCO problems were observed, which leads again to the conclusion that flight test data and calculated LCO results correlate well.
For the downloading case E.4 a slowly increasing oscillation at a frequency of about 5 Hz appeared. After a simulation time of 35 s a divergent motion occurs. From flight test data of case E.4 it is known that the downloading of configuration E is restricted up to a speed of 400 kts.
Overall, it has to be concluded (Fig. 24) that for the considered configurations C D, and E, all of the same type, the predicted LCO trends correlate well with known flight test data.

The above applications of the NLR unsteady pressure model embedded in the LCO prediction method show results which correlate correctly with flight test data. In order to apply the method in full, there is a need to extend the application of the unsteady pressure model to all known pressure orifice locations over the wing (upper and lower surface), angle-of-attack ranges, Mach number ranges and both different wing tip stores (launchers with and without missiles) and leading-edge and trailing-edge flap settings of the steady pressure data base [8]. The different ways to obtain the desired unsteady data for all mentioned steady conditions are discussed in section 7.

7. IMPROVEMENTS AND REFINEMENTS

The above description of the NLR pressure model shows that extensive use is made of steady and unsteady wind tunnel test data. It is clear that the effectiveness and reliability of the model strongly depends on the completeness of the experimental data base and the thoroughness of the evaluation of the model. These, however, have been obtained on a limited scale in the present research program. Continued research is therefore needed to enhance the confidence in the model and to establish its applicability for wide ranges of model and flow parameters. Such research may be defined in one or more of the following directions.

1. Continued pressure and load measurements in the wind tunnel.

   The aim of this test is to extend the unsteady part of the data base, which currently corresponds to a limited number of model and flow parameter values, and so to bring it in balance with the steady part of the data base, which corresponds to an extensive set of parameter values. Particularly, interest exists in collecting data for more leading-edge and trailing-edge flap deflections and denser

frequency ranges (e.g. frequency sweeps). In the test use can be made of the existing wind tunnel model (Fig. 9).

2. Development of a simplified unsteady aerodynamic model.

   In references 21 and 22 it was concluded that the LCO predictions based on steady aerodynamic data were qualitatively correct and that quantitative improvements could be obtained by introducing unsteady aerodynamic effects. Current thinking suggests that configuration and flow condition specific information can be obtained from steady pressure tests and that unsteady information can be developed that is more generic, such as transition lag times at forward shock motion and aft shock-induced trailing-edge separation (which are defined implicitly in the NLR unsteady pressure model), effects of surface motion, etc. This unsteady information is related to the different types of flow region. However, such regions can only be distinguished insufficiently on the basis of unsteady pressure measurements in the few sections of the existing wind tunnel model (Fig. 9). An effective solution is expected from the application of unsteady flow visualisation techniques and the coupling of its results with the already available results of the unsteady pressure measurements. Such an wind tunnel investigation on the same fighter type wing as used in the LCO investigation, has been started at NLR again as a cooperative effort with LWFC. The attractiveness of this approach is the use of the steady part of the data base without the need to have the full corresponding unsteady part available.

3. Application of CFD.

   For model configurations and flow conditions which have not or can not be represented in a wind tunnel test program the required aerodynamic information may be obtained from Computational Fluid Dynamics techniques, steady and unsteady. The current development of these techniques shows that they are very promising, even for the complicated types of flow including flow separation, but that they have not yet matured sufficiently. It is to be expected that in the near future these techniques may play a complementary role.

8. CONCLUSIONS

A semi-empirical method to predict LCO characteristics of fighter aircraft has been described, emphasizing the development of the NLR unsteady pressure model and its capability of producing nonlinear transonic aerodynamics that are typical of transonic LCO. Results were presented for the unsteady aerodynamic modeling and for the latest LCO predictions. In addition to the conclusions in references 5 and 21 to 24, additional conclusions from the investigations discussed in the current paper are summarized below.

1. It has been demonstrated that the NLR model can reproduce accurately the highly nonlinear features of flows which are typical of transonic LCO.

2. It seems that the NLR model is capable of producing the unsteady aerodynamic loads suitable for use in the simulation of LCO phenomena.

3. It has been shown for a number of aircraft configurations that the current LCO prediction method produces results which correlate correctly with flight test data.

ACKNOWLEDGEMENT

This investigation was funded by U.S. Air Force, Lockheed Fort Worth Company LFWC (formerly General Dynamics), The Netherlands Ministry of Defense and National Aerospace Laboratory NLR, The Netherlands. The Netherlands Ministry of Defense with monitoring of The Netherlands Agency for Aerospace Programs (NIVR) and NLR.

REFERENCES

1. Meijer, J.J., "NLR Contributions to the Flutter Certification of Aircraft with External Stores", 7th Aircraft/Stores Compatibility Symposium, Wright-Patterson AFB, Ohio, 8-10 April 1986 and at the 17th Annual Symp. of the Society of Flight Test Engineers, Washington, D.C., USA, 10-14 August 1986.

2. Bradley, R.G., "Practical Aerodynamic Problems - Military Aircraft", Transonic Aerodynamics, Edited by David Nixon, Vol. 81 Progress in Astronautics and Aeronautics, AIAA, 1982.

3. Cunningham, Jr., A.M., Boer, R.G. den, "Transonic Wind Tunnel Investigation of Limit Cycle Oscillations on Fighter Type Wings", AGARD SMP Specialist Meeting on Transonic Unsteady Aerodynamics and Aeroelasticity, San Diego, California, 9-11 October 1991.

4. Cunningham, Jr., A.M., Boer, R.G. den, "Transonic Wind Tunnel Investigation of Limit Cycle Oscillations on Fighter Type Wings – Update", 33rd AIAA, ASME, ASCE, AHS, ASC, SDM Conference, Dallas, Texas, April 13-17, 1992.

5. Meijer, J.J., Cunningham, Jr., A.M., "A Prediction Method of Transonic Limit Cycle Oscillation Characteristics of Fighter Aircraft Using Adapted Steady Wind Tunnel Data", 19th ICAS Congress, Anaheim, California, September 18-23, 1994.

6. Hounjet, M.L.H., Kolk, J.T. van der, Meijer, J.J., "Application of NLR's Numerical Simulation Methods to the Transonic Potential Flow about Oscillating Wings", AIAA-84-1564, June 1984.

7. Hounjet, M.L.H., Meijer, J.J., "Application of Time-Linearized Methods to Oscillating Wings in Transonic Flow and Flutter", AGARD CP 374, September 1984.

8. Elbers, W.K., "Wind Tunnel Data Report 1/9-Scale F-16A Pressure Model Investigation of Shock-Induced Separation for Limit Cycle Oscillation Studies (AEDC PWT-16T Test TF-695)", General Dynamics, Fort Worth Division Report 16PR4694, September 1985, (Contract No. F33657-84-C-2034).

9. Cunningham, Jr., A.M., "The Role of Shock-Induced Trailing-Edge Separation in Limit Cycle Oscillations", NASA-CP-3022, 1987.

10. Cunningham, Jr., A.M., Spragle, G.S., "A Study of the Effects of Reynolds Number and Mach Number on Constant Pressure Coefficient Jump for Shock-Induced Trailing-Edge Separation", NASA-CR-4090, August 1987.

11. Edwards, J.W., Bennett, R.M., Whitlow, Jr., W., Seidel, D.A., "Time-marching Transonic Flutter Solutions including Angle-of-attack Effects", J. Aircraft, Vol. 20, No. 11, Nov. 1983, pp. 899-906.

12. Mabey, D.G., "Physical Phenomena Associated with Unsteady Transonic Flows", Chapter 1, Unsteady Transonic Aerodynamics, edited by D.L. Nixon, AIAA Progress in Astronautics and Aeronautics Series, 1989.

13. Tran, C.T., Petot, D., "Semi-Empirical Model for the Dynamic Stall of Airfoils in View of the Application to the Calculation of Responses of a Helicopter Blade in Forward Flight", Vertica, Vol.5, 1981.

14. Dat, R., Tran, C.T., "Investigation of the Stall Flutter of an Airfoil with a Semi-Empirical Model of 2D Flow", Vertica, Vol.7, No.2, 1983.

15. Dat, R. "Development of the Basic Methods Needed to Predict the Aeroelastic Behavior of Helicopters", Rech. Aerosp. 1983-1 or Vertica Vol.8, No.3, 1984.

16. McAlister, K.W., Lambert, O., Petot, D., "Application of the Onera Model of Dynamic Stall", NASA TP2399 or AVSCOM TP84-A-3, 1984.

17. Peters, D.A., "Toward a Unified Lift Model for Use on Rotor Blade Stability Analyses", 40th Annual National Forum of the American Helicopter Society, Arlington, VA, May 16-18, 1984.

18. Petot, D., Dat, R., "Unsteady Aerodynamic Loads on an Oscillating Airfoil with Unsteady Stall", 2nd Workshop on Dynamics and Aeroelasticity Stability Modeling of Rotorcraft Systems, Florida Atlantic University, Boca Raton, Florida, November 1987.

19. Dunn, P., Dugundji, J., "Nonlinear Stall Flutter and Divergence Analysis of Cantilevered Graphite/Epoxy Wings", 31st AIAA, ASME, ASCE, AHS, ASC, SDM Conference, Long Beach, California, April 2-4, 1990.

20. Hounjet, M.H.L., "Improved potential gradient method to calculate airloads on oscillating supersonic interfering surfaces", J. Aircraft Vol.19, No.5, May 1982.

21. Meijer, J.J., Cunningham, Jr., A.M., Zwaan, R.J., "A Semi-Empirical Approach to Predict Transonic Limit Cycle Oscillation Characteristics of Fighter Aircraft", 8th Aircraft/Stores Compatibility Symp., Fort Walton Beach, Florida, 23-25 October 1990.

22. Meijer, J.J., Cunningham, Jr., A.M., "Development of a Method to Predict Transonic Limit Cycle Oscillation Characteristics of Fighter Aircraft", AGARD SMP Specialist Meeting on Transonic Unsteady Aerodynamics and Aeroelasticity, San Diego, California, 9-11 October 1991, (AGARD CP 507).

23. Meijer, J.J., Cunningham, Jr., A.M., "Development of a Method to Predict Transonic Limit Cycle Oscillation Characteristics of Fighter Aircraft – Update", 33rd AIAA, ASME, ASCE, AHS, ASC, SDM Conference/Dyn. Spec. Conference, Dallas, Texas, April 13-17, 1992.

24. Meijer, J.J., Cunningham, Jr., A.M., "Understanding and Development of a Prediction Method of Transonic Limit Cycle Oscillation Characteristics of Fighter Aircraft", 18th ICAS Congress, Beijing, China, September 21-25, 1992 and AIAA Atmospheric Flight Mechanics Conference, Hilton Head, South Carolina, August 10-12, 1992.

25. Meijer, J.J., "Applications of Aeroelastic Methods to Predict Flutter Characteristics of Fighter Aircraft in the Transonic Speed Range", 35th Israel Annual Conference on Aerospace Sciences, Tel Aviv/Haifa, Israel, February 15-16, 1995.

26. Meijer, J.J., Cunningham, Jr., A.M., "A Semi-Empirical Unsteady Nonlinear Aerodynamic Model to Predict Transonic LCO Characteristics of Fighter Aircraft", 36th AIAA, ASME, ASCE, AHS, ASC, SDM Conference, New Orleans, LA, April 10-12, 1995.

GENERAL DISCUSSION
END OF OPEN SESSION

C.D.S. Clarkson, British Aerospace Defence Ltd, U.K.
The technical Evaluator, Cliff Bore, will now lead the discussion off with a 5 to 10 minute precis of what he has seen so far.

C. Bore U.K.
Good afternoon. Thank you for the invitation. I was told yesterday I might be put on the spot today, so I haven't done a vast number of slides, you'll be glad to know. I was asked to raise some points for discussion because not everyone will be able to wait until the grand climax tomorrow afternoon. In considering ''which questions'', we have to think of what we tried to do.

We have had contributions from organizations which vary immensely in their range of experience and amount of effort that has gone in. Some people have been working 20 years with large organizations, but others have been doing University studies. I notice that the attitude of people here is (like me) that the inexperienced groups have to start somewhere and it is only right to encourage them. It is also a good idea to give them some pointers to what they might be doing to improve their efforts later on. It is in that spirit that we deal with these contributions from widely differing organizations. This doesn't mean, of course, that the experienced groups know all the answers. They wouldn't be searching and working so hard if they thought they did know all the answers.

When I started trying to prod people into looking at stores and aircraft together, 20 odd years ago, the point was that there were expensive aircraft, and much more expensive airforces, all trying to achieve objectives, but at that time stores were being developed on the basis of saying: ''these stores have got to be dropped and destroyed, so make them as cheap as possible''. What was happening was that the stores were extremely draggy things, which made very big reductions to the overall efficiencies of the airforces. In other words, the ''tail was wagging the dog'' in a bad way. Eventually, we got people to recognize that the stores and the aircraft have to work together. That is why we are here.

One way of classifying the points that we want to raise is to look at one session at a time, but remembering that we have to use all of these techniques in order to save aircraft being knocked down by the stores, and indeed, to make sure that the stores, when released, go in the right place, not in the wrong place. After all, you can have a complete, very expensive, airforce but it is of zero value if it fails to deliver its missiles on target. That really is the essence of the story.

Experience shows that serious expensive problems of store release often start from strong disturbances such as jet effluxes, vortices, shock waves, boundary layer separations, and so on. So, if we cannot predict the effects of those disturbances, we are going to miss some important effects. That is shown by experience very strongly.

When we use CFD methods, we have to try to make them predict these strong disturbances. The trouble there is that the most elaborate methods (such as Chimera plus Navier-Stokes) are expensive and time consuming. Of course, because they are time consuming it means it takes a long time to work out what to do on the aircraft. We are not only considering computer time, we are considering the delay in the design process. People don't normally point to that. It is all very well to talk about hours on the computer, but it may mean weeks of delay between seeing a problem and finding the answer. The most elaborate methods cannot be used all the time because they can be too slow and too elaborate.

So of course, the engineers tend to use the simpler, quicker methods where it is judged that they are acceptable. Can we boost simpler methods? Panel methods have been discussed and so on. Can we boost them by inserting experimental or empirical knowledge of the strong disturbances? Indeed, the paper that we have just listened to is showing something of this sort by inserting measured aerodynamic pressures back into the calculation. The general question is: ''to what degree can we make simpler methods import physical knowledge of real strong disturbances?''.

Looking at the CFD sessions we find questions such as: ''how far can we trust Euler solvers, as they can miss some viscous effects?'' and ''what are the Reynolds number effects of artificial dissipation? If it is really going to

have an effect of inserting some viscosity, it must be related to Reynolds number in some way''. No one has given an answer to that so that is a question that someone must address. Again, there are many approaches to Navier-Stokes solvers but there seem to be no criteria for knowing how accurate they are, except for the most elaborate. There is probably a need to generate rules for the fineness of the grids near the boundary layers, and other shear layers, so that the rules will make the Navier-Stokes solvers cheaper and quicker.

Not all of the schemes we have been treated to are Chimera (which was introduced to us at Athens 10 years ago). That seems to be well favoured by many people, but not everyone uses that. The questions are: ''Are the other schemes better in some way; are they more economical? What are the best overlapping grid schemes?''

Now we turn to Session 2, the engineering methods. Most of the engineering methods are so thoroughly based on long and very extensive (and expensive) work that few controversies arise. With an engineering method, it is being checked against experience all the time. There isn't a great deal of disagreement across the Atlantic between the big teams, Nielsen on one side and the British Aerospace on this side of the Atlantic. They are not in essential disagreement about what you have got to do. You have got to tie everything back to experience.

There was a younger method which raised questions about reliability of higher order panel methods in trying to predict strong disturbances. Can they be made to model boundary layer separations and wakes, and cope with stores at high angles? So can high order panel methods be trusted at this stage of the game? Maybe some more work is needed.

Session 3 - we looked at experimental techniques there. Captive trajectory rigs are still running and there are new improvements being brought in all the time. With captive trajectory rigs, the support-stings are there, which might hit the models, so people are working out anti-collision protection. The rigs can bend, so groups are working out methods of seeing where the store and the aircraft really are, instead of where they thought they were on the assumption that the rigs were rigid. Captive trajectory stings cause discrepancies if the base interference, or the wakes from the store are important.

We were treated to the latest improvements of the accelerated-model release technique which, of course, gets rid of the problems of sting mounting. I wouldn't really like to envisage a captive trajectory system for investigating release of 40 bomblets from a canister. The sight of 40 little stings criss-crossing all over the place would be formidable! So accelerated-model release has its place. I was encouraged by the new techniques being developed, notably the miniature load balances that are insensitive to temperature.

Session 4 was about cavity aspects. We have seen computer fluid dynamic results for simple cavities, and wind tunnel results for quite complex cavity/store combinations, and the experimental results are showing that indeed, the shaping of the downstream wall of the cavity can make large improvements. So a designer will ask, inevitably, what benefits we can make by making the rear wall of the cavity sloped and rounded and what effects are going to come from the opened cavity doors. Are they going to stick out or slide sideways? The effects of the doors will have to be looked at. Will little cross frames underneath the stores at the bottom of the cavity favorably interfere with the longitudinal flow recirculating down the back of the cavities? Questions of that sort maybe are not answerable here because people haven't done it yet, but it is not a bad idea to ask those questions.

Finally, we come to Session 5, Airframe Store Integration, which I hope is sufficiently fresh in your mind that I haven't got to prod your memories about that. I hope I have raised some questions to prod the discussion.

A. Boudreau, AEDC, U.S.A.

I was Chairman of the Cavity Session this morning and at the coffee break we were discussing CFD treatment of cavity flow and concluded that the CFD that we saw, the pure CFD, was on rather elementary shapes, whereas the experimental work was on quite complex configurations. Perhaps there is a challenge to the experimental and CFD community to look at some more complex shapes. As an experimentalist I was eager to jump in and say, ''why don't we try this and why don't we try that in an experiment''. We see that the environment in the cavity is quite hostile, and with the newer munitions which have electronics on board, may be very sensitive to that very hostile environment. We aerodynamicists could do a great deal, I think, to improve the aerodynamics. So, I would challenge the experimentalists to produce some more complex configurations with rounded edges, with sloping walls, etc., and then for the CFD people to try to match those.

C.D.S. Clarkson, British Aerospace Defence Ltd, U.K.
I could make one or two observations from my experience. Certainly from the Bath Conference in 1990, I was surprised here that there has been no mention of unstructured methods really. At the end of the Bath Conference that was seen as one of the ways to go with Navier-Stokes. No mention at all of unstructured methods. Very little comment on using CFD correcting for Reynolds number effect in the wind tunnels. All of our wind tunnel testing for stores is done at low Reynolds numbers. Who is to know whether that is anything like what happens in flight, especially with separations on fuel tanks and bombs. I certainly know that British Aerospace have tried to measure in-flight loads, but they have never agreed with what we saw in the wind tunnel. On the airframe side we used CFD quite a lot to correct the wind tunnel results we get at low Reynolds number for higher Reynolds number flight conditions. Similarly, with the work that Nick Sellars showed on Euler and how easy it is, if you are not careful, to fool yourself into thinking you are getting a viscous solution and then on the next solution that has a circular body it is not a viscous solution, it is an inviscid solution. How sensitive that can be to the gridding that is used. Certainly, my experience is with a lot of our younger engineers that they are very keen to get in and use the CFD without fully understanding the physics of what they are trying to model and also the physics of the method that they are trying to use. One question I would ask, there were no papers on the heavy model technique, is that technique still in use; what are peoples' experiences with it?

C. Bore, U.K.
I do have a remark on that. I hope I buried heavy model techniques 10 years ago, because I showed that they were fallacious.

C. D. S. Clarkson, British Aerospace Defence Ltd, U.K.
Finally, I must say that I was very impressed with the Arnold presentation this morning, which is very much the approach that certainly British Aerospace has sought to take to our Store Clearance work, in trying to bring together all the methods that were available into a cost effective and efficient approach to providing store clearances.

D. Lovell, DRA Farnborough, U.K.
Taking along the same line, what we haven't heard, so to speak. This Conference so far has had no papers on methods for predicting installed drag. Does that mean that people here are saying that it is a "done" thing, that they are happy with what they have? I rather doubt it. The range is going to be a very strong driver for the next airplane, so I would like to pose the question: "should we be working at CFD for very complex configurations for the aircraft with the stores on?"

J. Ross, DRA Bedford, U.K.
To answer to David's question, we are extremely active in both the experimental verification and the prediction of installed store drag. It is our view at the moment that CFD methods can do little to predict stores drag. I would greatly encourage CFD application specialists to work towards producing codes which can predict store drag increments, but the sort of tasks I am asked to do are to start on Monday and by Friday produce the installed drag increments on 6 aircraft for 15 store configurations. To do that, I am for a long time going to continue to use empirical and semi-empirical methods based on experience, because in this area, one needs to make a rapid response to operational analysis people who ask the questions. We are there to answer questions.

J. Slooff, NLR, Netherlands
Another remark on the issue of drag prediction by CFD: Before we can start hoping to predict drag for configurations with stores, we should be able to do it for the clean configurations, and that, as yet, is still an unsolved problem, I am afraid.

M. Mendenhall, Nielsen Engineering and Research, U.S.A.
I think there are a couple of points that have been made that we should emphasize. This was also a discussion during the coffee break today. That is, we really cannot lose sight of the physics. You just emphasized that yourself. I think this is a critical issue. We know from observation and experience what some of the important physics are, - the shocks, the vortices, etc., in all store separation problems. As the conversation went, as some of us older folks, who have had to work with the physics because we did not have some of the higher level computational methods available, retire and leave the industry, who is going to be around to keep emphasizing that you must always compare your CFD methods with data. I think this is a critical issue that is going to lead some of our CFD solutions down the wrong path if they don't keep looking at what is really going on. It is also interesting, from one

of the early store separation meetings that I attended 10 years ago or so, as I recall, CFD was going to solve this problem in 5 years, and we are still waiting. What has happened, and maybe this goes along with what has happened at this meeting, maybe some realism has crept into the CFD area, and it is a much tougher problem than any of us thought at the time.

C.D.S. Clarkson, British Aerospace Defence Ltd, U.K.
I would agree with that, but I was very encouraged to find that certainly CFD methods do seem to be used much more in routine design and clearance than they were 5 or 10 years ago. People are only just starting to get to grips with Chimera. People do seem to be actually using it to investigate those problems where you do have to get into the fine detail and where you have got a wealth of information available from CFD that you can use. But it has to be used in a good engineering approach.

G. Howell, Lockheed, Fort Worth, U.S.A.
We have had airplanes that were designed for many years with less than perfect methods, and I think that we all are well aware of this. I believe that in any design, there are places for the elementary methods moving from panel codes to small disturbance theory to Euler codes to Navier-Stokes. One of the things we have had missing at this Conference so far this week is a discussion of unstructured grids which I view as the technology with the most potential over the long term. I have seen some papers in the recent past that have made some extraordinary progress in this particular area. I think that we should keep those in mind as well.

C.D.S. Clarkson, British Aerospace Defence Ltd, U.K.
Certainly, as I said earlier, as a result of the Bath Conference in the early 90's, unstructured grids was seen as being one of the main players in this area, and yet we didn't really receive, although one or two mentions in people's work, there has not been much presented on unstructured grids. Certainly, at BAE we have been pursuing that approach in using unstructured grids for store carriage. Maybe Franco wants to say something about that.

F. Moretti, BAe Warton, U.K.
In the Session after lunch, I will show you some pictures of unstructured grid application. That doesn't necessarily mean that I will show you a comparison against data. We continue to use that method and think it has still got a lot of potential. The major problem at the moment is how to change the grid as the store moves down. We have seen some developments on that, but we don't have any particulars, nor do we think it is very easy to use and very simple to apply. We can throw a lot of configurations at that method. The problem still is how to get sufficient computer capacity, strong and fast enough to run all these solutions. For simple geometries we expect responses in a matter of a very few days. So, it is still something I still believe in. Unfortunately, it still is not perfect yet.

B. Simpson, Eglin AirForce Base, U.S.A.
I have a couple of comments. First, I guess about 3 years ago we ran a special session at a symposium comparing unstructured grids and the structured grids for this very case of store carriage and separation. It was very clear at that point in time that the unstructured grids was still significantly behind where the structured grids were, and the decision was made at Eglin AirForce Base to go with the structured grid, the over-unstructured grid technology. I will add though, that I think all of us certainly understand the potential there for the unstructured grid and the ultimate solution, which is often, or most often the case in the real world, it is probably going to be a hybrid solution, a combination between the two. We are working that problem. The code that I mentioned earlier that we are using at Eglin today, called the 'begger' code has been designed and is being looked at as a hybrid code application for this problem. I think that we are making progress there, but the store clearance business has to take small, slow steps because there are flight safety issues involved and they are not willing to step out on a limb with some untested technologies.

Unknown
I would like to know if anyone has been looking at the thermal effects within stores and store release. We haven't seen anybody quoting heat transfer rates and things like that. This is obviously important as the Mach number increases, i.e., ablation and things like that.

R. Deslandes, Daimler-Benz Aerospace, Germany
I didn't understand your last comments on thermal effects. I want to inject into your mind that in an Euler approach you can compute the temperatures. If you set, for instance, boundary conditions at the end of the store in the area

where the exhaust of the jet is, you can produce a good approximation of the temperature and the temperature radiation into the field. I have shown one vu-graph with the hot plume of a missile that was separating from a Tornado aircraft and you can also find it in the paper I presented. Well, it is not one hundred percent true, but however, it is a useful approximation. I doubt that you can produce a better one with a lower order method. You wouldn't be successful.

I have also some comments on what is the best method to use for store separation. The best method is always the one you have available at your company for the task. If you ask, for instance, ''what is better, Euler solutions or panel solutions?'', the answer is very simple. The Euler solution is the better one. You don't need to cheat for compressibility. The interferences are well transported through the flow field whereas in the panel method it is something like radiation by the potential. There is no transport in the panel method. Then you have the vorticity completely included in the Euler equations, and also vortex transport is included in the Euler equations. This is not included in a panel solution. You have to model the wake, as we have also seen today, and even modelling the wake you can cheat anywhere you want. It depends on the track you give to this vortex, and you will have double the lift you want to have, or half of it if you want. I think that to use Euler methods is real progress. Also the work stations today are fast enough that you can even use a Chimera approach with a fully unsteady separation computation within a reasonable time.

S. Sheard, British Aerospace Defence Ltd, U.K.
Just a final comment to respond to what Mr. Deslandes said. You sort of are saying that with panel methods you can indeed get double the lift by playing around with the wakes, but the work that Nick Sellars showed looking at four separate Euler techniques showed a similar band of scatter. I don't think you can get as consistent answers with Euler as you think.

R. Deslandes, Daimler-Benz Aerospace, Germany
I think that you were playing with separation, etc. I didn't mention separation. But, if you want, even then, I think that the Euler solution is the best available. It is worse than the Navier-Stokes solution because the Navier-Stokes solution is more complete in the formulation. However, on the next level below the Navier-Stokes I don't think that you will find something better than the Euler. That is what I think. Do you agree?

C.D.S. Clarkson, British Aerospace Defence Ltd, U.K.
I would agree with that, I think the problem is that we faced when we brought engineering methods and panel methods, that you have got to build up the same level of experience of using the method and knowing where it is right and where it is wrong, and what you need to do to correct for it. You can always correct for a method's inadequacies if you know what the inadequacies are. It is when you don't know where the inadequacies are that you have got a problem. Provided you know what they are and what physics it's modelling, then you should be able to correct them. And it is just a case of building up the right level of experience.

R. Deslandes, Daimler-Benz Aerospace, Germany
A last comment on that. I was working a very long time with the panel methods. And I was a really tricky engineer in that field. I think that it was always a bad feeling for me not to know the complete truth. This means that without any experiment I couldn't say if the trajectory I was computing with the panel method was really good or not. Well, with the Euler code I do not tune the solution any more. With the panel solution, you have to apply boundary conditions and those boundary conditions will provide you a broad variety of solutions. The Euler method always converge to one single solution or to no solution. Normally, if you make a mistake in gridding, you will have a negative density and then your square root of the sonic speed explodes. With the panel method you may have one of billions of solutions you can produce with boundary conditions. That is the great uncertainty which you have to fight with all the time if you use the panel method. On the other hand, you have good confidence with the conservative laws which are used in the Euler equations.

Unknown
Why don't you put it this way: ''panel methods is a modelling technique. Normally, it will only give you one solution. If you model correctly, namely if you impose, e.g., the Kutta condition, that will get you a unique solution of a panel method''?

R. Deslandes, Daimler-Benz Aerospace, Germany
Except that your Kutta condition means that you will have a certain flow getting out of your trailing edge. But now, you have to define the direction of this wake. Here you can cheat. If you let it go in the middle line (directly in the middle of your angle) if this is the line which you define as the line where the wake goes, you may have a completely different result as if you are using the angle of attack also in order to determine the way the wake has to leave the trailing edge. This is for me an uncertainty.

Unknown
Based on my experience, the shear of the wake has little influence on the body itself. It has a strong influence on the downstream body. If you have a panel code which allows you to model the shear, you have found out the shape of the wake has little influence upstream to the body itself.

R. Deslandes, Daimler-Benz Aerospace, Germany
I am thinking of a concrete project I was working on. It was the Sidewinder. The Sidewinder has two arrangements of wings; the front fin and the tail. Depending on the way you let your vortices or your wake come off the front fin, you could double the lift of the total configuration because they were affecting the back end. I am sorry, I cannot rely on such a method if I can tune it like this. I cannot do the work always by myself, I have to give it to other people to do it, who are not so experienced and then you fail perhaps in your analysis with such a rough tool, but you have to rely on it if you don't have anything else. If you can use, for instance, an Euler code for such a project, you are on the better side of the trajectory.

Unknown
Well, I have to agree, Euler methods give you a better answer. But time-wise there is no comparison between the panel method and the Euler code. One thing I have to emphasize here. People talk about the CPU time to run a CFD code. But, they don't talk about the engineering time required to set up the 3-D grid. That is the most expensive part. I think people spend months and months to try to set up a 3-D grid. Once you set it up you have to run it through the computer and check everything out. If something goes wrong you have to go back to change the grid. Probably today's computer speed is fast enough for a steady state Euler solution for a whole aircraft, the CPU time is only about a couple hours, but the engineering time to set up the grid takes months.

R. Deslandes, Daimler-Benz Aerospace, Germany
You need a very good grid generator. I am sorry that there is no paper on grid generation.

S. Sheard, British Aerospace Defence Ltd, U.K.
I just want to make the comment that it is our experience that the grid generation times in Euler are now approaching those for setting up panel methods. There is not going to be that much difference.

M.F.E. Dillenius, Nielsen Engineering & Research, Inc., U.S.A.
In fact, there is more to aerodynamics than panel methods, or CFD, if you want to be a classicist, and Dr. Deslandes knows about this. There are aspects of slender body theory that help you out. So, to say that I don't know what to do with the wakes in a panel method because the panel method doesn't allow wakes. Not so! That is what I was trying to make clear. You can add wake models to a panel method using elements of slender body theory and let the components that are downstream feel the wake and you can pretty reliably track these vortices using slender body theory. Sure, you have to have a slender body, that is the limitation there. So you have got to use your judgement and know what you are looking at and not just look blindly. There is plenty of room, but the lower the order of the method, the more artistry you can apply, which is what Dr. Deslandes calls ''cheating''.

C.D.S. Clarkson, British Aerospace Defence Ltd, U.K.
Which comes back to the fact that you have to know what you are trying to model and you have to know what you are trying to model it with.

M.F.E. Dillenius, Nielsen Engineering & Research Inc., U.S.A.
I have another question. My favorite topic. CAVITIES. I didn't hear anything mentioned about scaling effects. We have looked at little ones, you have applied your calculations to little ones, did they scale up to a size 100 times bigger?

C.D.S. Clarkson, British Aerospace Defence Ltd, U.K.
We were discussing this with Cliff. Our experience with Buccaneer was that the results we got in flight in the bomb bay were not the results we got in the wind tunnel. There were scaling effects that we weren't properly able to model.

M.F.E. Dillenius, Nielsen Engineering & Research Inc., U.S.A.
I didn't hear the first part, but that is O.K. I was told many times that the turbulence model near the rear wall fails when you go up in scale. As a result, the pressures on the rear wall, which are important, can be the damaging factor in a cavity, because they do not scale up.

C.D.S. Clarkson, British Aerospace Defence Ltd, U.K.
That was our problem in the 70's with Buccaneer that the acoustic field was not properly predicted in the wind tunnel, and therefore you got a more severe acoustic field in flight. With that I will close this Session. This is the end of the Open Session. I would like to thank all the authors, who did some very good presentations, all of them finishing on time. This is very good and unusual. Also the quality of the slides and presentations was very good. Thank you to the audience for the interesting questions that you raised.

GENERAL DISCUSSION
END OF SYMPOSIUM

R. Deslandes, Daimler-Benz Aerospace, Germany
I want to give you an impression I had, and I want to tell it publicly. Twenty years ago, when I started at the Aerodynamics Department of MBB-Ottobrun, I went to a VKI Symposium in Brussels. They showed me there a film about catastrophic separation and I was totally afraid. But today, I can say that it is a benefit of computational fluid dynamic methods in store separations that these catastrophic situations have disappeared completely from our field of investigation.

M. Mendenhall, Nielsen Engineering and Research Inc., U.S.A.
I don't think there is much argument here, but we have been hearing a lot about CFD methods and obviously we have heard a lot about the engineering methods people have been working on for years. I have had similar discussions at other meetings, and I am saying this as a caution. Don't believe that CFD is the only thing that we are going to need in a few years. I think every engineer in this room needs a tool box of methods. I think the engineering methods are here to stay, and they will continue to be used for some time. I think CFD methods are coming along and are obviously being used more and more. At a previous meeting I attended last year, it seemed to me that, to the exclusion of all other methods, CFD was the saviour of all of our engineering problems, and it seemed at that time that many good methods were being thrown away. The only thing that they had wrong with them was that they were probably 10 or 15 years old. Please keep that in mind. Don't throw out the good methods just because new ones are coming along.

C.D.S. Clarkson, British Aerospace Defence Ltd, U.K.
I think that we all concur with that sentiment.

Kurasori, Turkey
My comment is going to be in a parallel line with the last comment. Personally, I am working in the design group in Roketsan Industries and I am mostly interested in the conceptual design work. What you need is fast response tool boxes that you can use. One thing that I believe should be covered in such a Symposium should be some more parametric studies that help you build new design envelopes, put some constraints and borders where you want to avoid certain critical issues, during the very early phases of your design, because what you are doing in that phase of design is you have a mission need statement in your hand which has some operational and technical requirements and you try to meet those requirements with some conceptual solutions. In that case I think using CFD or going directly into the wind tunnel or flight testing, is out of the question. What you need is good parametric studies and things like this.

R. Deslandes, Daimler-Benz Aerospace, Germany
May I complete your comments by putting on some vu-graphs. I have put some items here that will be important for the future. First of all, a comment I heard two days ago. It seems that structured grids for store separation are now favored against unstructured because most of the applications were structured. The second thing which is very important for me is that quasi-unsteady or if you want, pseudo-unsteady methods are in the great majority at this Symposium. I think that Chimera codes are actually purely pseudo-unsteady in this area, and I think that the future will bring an attractive solution for improvements if Chimera codes presently in development in the different plants can find unsteady formulation. About an N-S solution, while I think they are very attractive, but they still have two big disadvantages. We have no reliable turbulence modelling and the running times are still too long for store application.

My fifth comment is on grid generation. I think that this field needs a 100% adaption to store separation problems. I think they have to become more efficient and they must be cheaper for fast solutions. Then for Chimera applications, you have to operate with smart or intelligent grids. Finally, we need an extension which is practicable on those grids for Navier-Stokes solutions. That is the future. We have seen, very nicely presented by Franco, that fuel slosh is a necessary accessory for modelling store separation. There most of the methods must introduce this improvement for the future. Finally, this means that an appropriate Euler solutions should be discussed as a focal point because there are still some misunderstandings in appropriate formulations for store separation. This is not the normal formulation you can find anywhere, it is a special one.

C.D.S. Clarkson, British Aerospace Defence Ltd, U.K.
I would agree with you. One thing I would ask about is on the unstructured grid. This morning we saw a few more papers on unstructured grids demonstrating their use at DASA, etc. I think that there are advantages in terms of gridding time, whether that outweighs or not the Chimera approach is still a question that has to be answered. Which one wins out in the future or whether both have a place is worthy of discussion.

J.W. Slooff, NLR, Netherlands
I think that there must be at least a dozen or so people who would like to react to, if not protest against, the first conclusion. I think the main reason why we have seen more structured grid applications than unstructured grid ones is that the level of proliferation, so to speak, of structured grid methods is at this point in time still somewhat larger than that of unstructured grid methods. That unstructured grid methods have a disadvantage is, of course, also true. In particular, it is not clear how accurate they are in case of viscous, that is, Navier-Stokes simulations. But, I think that it is only a matter of time.

C.D.S. Clarkson, British Aerospace Defence Ltd, U.K.
Certainly British Aerospace's experience with unstructured grids is that the limiting factor is your computer size and if you can get enough grid points, you can get equal quality to a structured grid approach for Euler solutions.

N. Malmuth, Rockwell International Science Center, U.S.A.
I sat through the Conference and I saw a very nice interplay between CFD and experimental work. One thing I found was missing was some basic theoretical activities that are possible in this area. When we look at the store problem, we look at the interaction of the store with the complete airplane. We are automatically interested in getting a result for the full-up configuration and we try to deal with the full computational complexity of that. I think there is still some room to work on some unit problems like just taking a cross-flow plane, looking at a cross-section of even a cylinder store dropped from an infinite plane, what are the time scales associated with that. Even trying to do a moving cylinder, we have got all Reynolds numbers regimes from the acceleration from zero to just dropping it in an infinite inviscid fluid and then putting a boundary on it, we have a possibility of reflection of the wakes. I think that would be a very interesting unit problem. That would give us some insight about one of the aspects that was brought up associated with the importance of unsteady effects, even though it is widely accepted that pseudo-steady is supposedly the way to go with these types of problems. I think we need some fundamental understanding and one way to get that is to work on unit problems that will enhance our insight.

C.D.S. Clarkson, British Aerospace Defence Ltd, U.K.
I think to be fair, the reason that there weren't so many fundamental papers, the Program Committee deliberately set up the Conference to be on a more practical application side of things and the call for papers reflected that. I think that is why there is so little in terms of fundamental papers this time.

P.W. Sacher, DASA, Germany
I think that that was a very valuable comment from Ronnie Deslandes, but there should be a proper balance between experiment and CFD. I know that you are a CFD man. I was very much impressed this morning during the Session by the presentation from the combined Lockheed/AEDC work, and I am always against any tendency where CFD claims to replace the experiment. Even in this complex field, I ask now for a proper balance. I have seen in at least two contributions a chart giving the impression that the experimental work is going down, the numerical work is going up, and I think that the experimental work must not disappear. There should be a proper balance. There could be much more covered by CFD, but not everything. I was really impressed this morning to see, that it seems to be a good balance in the Lockheed work and maybe in some other contributions, but some tend to overemphasize CFD. Maybe this is a little provocative, but I would not like to see somebody recommending to replace experiment completely by CFD - not yet.

M. Borsi, Alenia Aeronautica, Italy
I completely agree with the last sentence from Peter Sacher since I think that for the engineer aiming at the design and integration of new stores on an aircraft, CFD and wind tunnel experiments are two complementary tools. It is impossible to rely only upon one of them because the wind tunnel can provide data difficult to be generated by computation, it can benefit from CFD for the analysis and interpretation of results, and it supports CFD for validation aspects, while CFD-based tools can be very helpful and cost-effective for flow field estimation, store integration and release/separation simulation.

I would also like to mention another point. We know pure structured or unstructured grids, but there are new technologies, like Chimera and hybrid grids, that are trying to approach the flow simulation problem by mixing the two techniques in some way. I think that the hybrid grid technology will become very interesting for this kind of computation, since it offers the possibility to get Navier-Stokes grids, with structured-type resolution near the body and unstructured-type resolution in the flow field, with the easiness and speed of some unstructured grid generation processes.

A. Boudreau, AEDC, U.S.A.
I would also like to agree on the experimental aspects of store separation testing. What we at AEDC are calling integrated test and evaluation is in fact our future, not simply CFD. If we can't combine the best aspects of experiments, of CFD and of flight testing together in an integrated approach, we will never make progress, so they have to go forward together. I would like to make another general comment. We have emphasized in this Symposium mostly subsonic and low supersonic store separation. We need also to have one aspect of our thinking, and this is the future, and the future may be indeed a hypersonic systems, hypersonic cruise missiles and so on, and store separation from those. I would submit to you that none of us are prepared to approach that. The experimental side is very weak in this area. I know of only one CTS mechanism available for hypersonic store separation, and that is the one we have for tunnels A, B, and C at AEDC. There may be others, but I know that that one does exist. The computational aspects and challenges are mind-boggling when one thinks of all the thermal effects and so on, with hypersonic store separation. Flight testing is simply a dream at this point. So, we need to consider that future and we need not think that we are very mature in this art. It is a tremendous challenge that we have ahead of us.

J.D. Marion, Dassault Aviation, France
An additional comment concerning unstructured grids. This is an answer from the concern from Prof. Slooff and Prof. Borsi. We have some experience in this, unstructured grids, and concerning viscous effects. We think that we can take them into account with quite a good level of confidence with a grid which becomes more and more structured as we come close to the surface, so we combine structured quality in the viscous part of the flow and really unstructured grid outside where we do not need much more grid. This is one approach. The other one is, and I do also agree with Prof. Borsi, concerns the use of a hybrid scheme with hybrid grids. One part, for example, structured grid and the other part unstructured.

C. Bore, U.K.
While we are on the discussion of structured versus unstructured grids, there are two points that occur to me. Number one point, if you are doing Euler flow solvers, there is not likely to be much difference between the two. When you get to Navier-Stokes and you are interested in the boundary layer and its separation, and so on, then surely it must be necessary to have a fairly structured grid very close to the surface where all the viscous effects are happening. Number two point is that the boundary layer separation criteria need to be fed into this, and these are not only a matter of pressure gradients, they are also matters of heat transfer into the boundary layer region at the same time. I think that if anyone wants to discriminate between structured and unstructured grids, my suspicion is that you will need to look very closely at the way they resolve detailed boundary layer separation phenomena and things of that sort.

C.D.S. Clarkson, British Aerospace Defence Ltd, U.K.
We have seen some of that during the Conference.

N. Malmuth, Rockwell International Science Center, U.S.A.
I would respond to that by looking at some of the new adaptive unstructured grids that reportedly have the capability of resolving high solution curvature regions like boundary layers and other kinds of features that occur in the solution, so there is that possibility.

D. Woodward, DRA Farnborough, U.K.
Can I take you away from this perpetual argument and discussion about CFD and structured and unstructured grids and be controversial. Mr. Howell showed this morning how the release characteristics of missiles with auto pilots were fairly benign. The performance was very reasonable. If you tie that together with the idea of future weapons being smarter because you need higher accuracy, then contrary to the idea of store release being a very difficult subject, can I suggest that in future you won't have a job at all, because all of your stores will have auto pilots and you won't have any trouble in releasing them.

R. Deslandes, Daimler-Benz Aerospace, Germany
Normally, if you are utilizing an auto pilot in the vicinity of an aircraft you must be aware that the auto pilot may fail. These are failure cases you have to analyze, because some of them are allowable and have a high probability. For instance, on an AMRAAM as we have seen this morning, we have a flip-over of 30 degrees on one of the flippers and then you have to demonstrate safe separation. But you will never go into flight test to demonstrate such a case, you have to simulate it. So I think that we will not be out of a job.

D. Allen, British Aerospace Defence Ltd, U.K.
Thanks for that comment. You were controversial and it allows me to make one or two points. I think in some areas of flight control systems, be it an airplane or the weapon, there is something that can hide all the evils of the flow field around the airplane or the missile. Having studies to look at control power effectiveness and the flow field in release will be required to insure that the automatic control system can indeed provide the improvements in the trajectory that looks as if it is required in a lot of cases. Again, it is another plea to that confrontation that the flight control system isn't the answer to everybody's prayer.

C.D.S. Clarkson, British Aerospace Defence Ltd, U.K.
I think I would agree with that. Certainly, we have seen cases where the store flight control system can't cope with the non-linearities of the flow.

A.C. Roberts, British Aerospace Dynamics, Bristol, U.K.
I think that there is an intermediate case for flight control systems, which we have looked at on a number of occasions, where you have a control configuration change for launch which puts the controls into a configuration such that you get a good separation, and then full authority of the flight control system happens afterwards. So you then have the case where, if that control configuration doesn't happen, the launch doesn't happen. You have still got a problem for the jettison case, but for normal launch you can usually ensure that you are in a launch configuration prior to launch; it depends on the missile.

R. Deslandes, Daimler-Benz Aerospace, Germany
Most of the trajectories I have shown on Monday are real flight trajectories which were flight tested exactly. The first picture, which explained how long such a trajectory is in the duration, is a failure case on a Phantom where an AMRAAM was launched and was a complete auto pilot missed. The missile pitches up and these are those cases we have to take into account even if the auto pilot is degraded for the safe separation phase. You have still a high risk of malfunction and you have to take this into account.

J.W. Slooff, NLR, Netherlands
I would like to come back briefly on the so-called CFD versus experiment controversy, if you permit, Mr. Chairman. I think that there is at least one common aspect between the two. We don't know what the accuracy is, neither in the CFD case nor in the experimental case. Nobody seems to care in the CFD community, or seems to be able to afford to do a mesh-refinement study. Doing so should at least make it clear how numerically accurate the results are. To the experimental situation, for example in the case of CTS systems, the question is how accurate are the corrections for sting and wall interference and support interference and the like. If we look at test set ups with stings of a diameter of something like half of that of the store, there must be an appreciable correction. I am not sure that we can determine such corrections accurately enough (apart from questions like: "what are the scale effects for, Reynolds number effects, that we have to live with?").

C.D.S. Clarkson, British Aerospace Defence Ltd, U.K.
Certainly for me, that has always been a big bugbear in that we do all of our stores testing at low Reynolds and then we go and flight test it at high Reynolds number often on circular stores that have got separations, fuel tanks that have got separations, that are definitely Reynolds number sensitive. That is something that CFD could actually help and answer, what those Reynolds number sensitivities are.

J.W. Slooff, NLR, Netherlands
I forgot to add that as long as we are not able to answer those questions, the discussion will, as David Woodward said, be perpetual, I am afraid.

S.J. Rawley-Brooke, Armaments Trial, U.K.
As an engineer and one that is responsible for the some of the clearances, I would like to reassure all the aerodynamicists here that there is a future for them with these smart control surfaces. We test to the first failure case. If you think of the number of failures that you can actually go through on flight control systems and smart stores, and then work out the cost of actually flight trialing those, or even in the wind tunnels, then I think that there is a great future for what you are doing, provided you can give me a nice warm feeling of the accuracy of your techniques.

C.D.S. Clarkson, British Aerospace Defence Ltd, U.K.
We have got time now for one more question or comment. Does anyone have any comments to make about the computing requirements on some of these CFD methods.

N. Malmuth, Rockwell International Science Center, U.S.A.
Just to make some further comments not related to the last question, we are concentrating a lot here on the combination of CFD and experiment. I would suggest that we consider the role of **theory** in this combination. I agree with the comment regarding wall interference, particularly at the high transonic Mach numbers. It can be quite important while the stores are in the field of the parent airplane. Unit solutions, even though we have a practical emphasis in this meeting, can give us needed basic understanding of the physics of store interactions. They can be a check on CFD solutions and the experiments. Furthermore, theory, such as asymptotics, can accelerate the CFD procedures. The **triad** of theory, computation, and experiment can provide important and useful insight into the stores problem. It might be useful to think about some fundamentally oriented meeting dealing with theoretical studies of store interactions to complement the practical emphasis here.

C.D.S. Clarkson, British Aerospace Defence Ltd, U.K.
I would like to close there just before Christian gives his closing remarks as the Chairman of the Fluid Dynamics Panel. I would like to say thank you to all the authors for some very good presentations. The quality of the slides and the content was extremely good. Everyone kept to the time. Also I would like to thank the local organizers for organizing such a superb lecture room and area and doing so well with the overhead projector slides and also the translators and the man operating the video and microphone system. I would also like to thank the audience for getting well involved with questions and involved in the discussion and helping to make it such a successful conference.

C. Dujarric, ESA, France
Chris, I think that you have said the main, important things that I had to say. Ladies and Gentlemen, we have had three days of presentations and lively technical discussions. Now we will close this colloquium. I think that there was a lot of basic scientific information that will enable each of us to prepare technical recommendations for each of our respective organizations. Compiling recommendations for NATO will be more difficult, because a summary is necessary to make this specialized information understandable to the major countries. This work will be starting, on missile separation as in other areas, by the Fluid Dynamics Panel. Our Panel participates in a NATO working group organized under the initiative of AGARD. The objective of this group is to project future technological developments on military performance in the year 2020. They will provide recommendations on the future developments of military material.

The work of this week will provide us with a first class basis to give substance to the recommendations for all of us concerned with missile separation. This Symposium has been a success, due not only to the quality of the presentations, but also to the level of enthusiasm of the participants in the discussion. Excuse me for repeating the thank yous, but I would like to warmly thank the authors, the chairmen of the sessions and the persons who have participated in the discussion.

I believe that all the participants will join me in congratulating the Program Committee who defined the goals and content of this meeting, who gave it structure and controlled quality by a rigorous selection of the presentations. We, therefore, thank Mr. Chris Clarkson, Chairman of the Program Committee. We also wish to thank the members of this Program Committee, Prof. Decuypere, Dr. Chan, Mr. Jouty, Mr. Sacher, Prof. Georgantopoulos, Prof. Russo, Mr. Elsenaar, Prof. Norstrud, Mr. Monge, Prof. Ciray, Mr. Herring, Mr. Boudreau and Mr. Selegan. We thank the meeting's technical advisor/evaluator, Mr. Cliff Bore, who accomplished a particularly difficult task by making an excellent critical summary of the debates.

I believe that the high quality of the technical work should not make us forget the remarkable organizational work that we have seen, and especially the wonderful welcome we have received. In the name of the Fluid Dynamics Panel, I would like to thank the Turkish authorities, and in particular the national delegates, Colonel Batmaca and Colonel Soylerkaya, and Major Akyurek, National Coordinator, who invited us to hold our meeting at Ankara. I remind you that many organizations contributed to our delightful stay, especially TUBITAK, the Turkish Agency for Scientific and Technical Research; the Technical University of the Middle East, METU; and the Aeronautic Industries, TUSAS; the Missile Industries, ROCKETSAN; the Motorization Industries, TEI; and finally the Turkish Air Force. We thank them warmly. For all of us, I would particularly like to thank our Deputy Chairman, Prof. Ciray, who coordinated everything locally and who is the symbol of Turkish hospitality. We would also like to thank Prof. Alemdaroglu, from the FVP, who efficiently helped Prof. Ciray. These conferences would not be possible without complex logistics requiring a lot of good will, so I would like also to thank the interpreters who managed to translate, even considering the verbal enthusiasm of some of the speakers; Mrs. Celie, Mrs. Danisman and Mrs. Vioche. And we thank Mr. Abinader, our AGARD security officer, and his Turkish equivalent Lieutenant Hanifibay. Finally, we thank the technicians who kept the presentation equipment functioning, and all the people who contributed to the welcoming and the smooth running of the congress. And especially, we thank our Panel secretary, Miss Anne Marie Rivault, who was awarded the AGARD personnel medal this year for her devotion to our cause. We thank the Panel Administrator, Mr. Jack Molloy for his work with the considerable preparation for this meeting.

I remind you that, this afternoon, we will have a round table discussion on the Stealth Aircraft Aeronautics. Access to this meeting, which is classified, will be restricted to the members of the Panel and to the Speakers. The goal of this meeting is to evaluate the possibility of organizing an activity in the field of stealth aircraft.

I would like to conclude by presenting the Fluid Dynamics Panel program for 1995 and 1996. We will hold a symposium on the Progress and Future Prospects in CFD Methods and Algorithms, October 2 to October 5 1995 in Seville, Spain. I believe that this symposium will clarify certain aspects of the questions we have heard. I hope many of you will attend in Seville this Fall. In 1995, we have organized two special courses at the von Kármán Institute: the first, which just ended, on the Aero-thermodynamics of Space Capsules, and the second on Parallel Computing in CFD from May 15 to May 19 1995. In 1996, we are planning a spring conference in Norway which will cover the Characterization and Manipulation of the Wake of Lifting Bodies. In the Fall, and for the first time in AGARD's history, we will organize a symposium in Moscow. It will cover the Aerodynamics of Wind Tunnel Circuits and their Components. The Russians have a great deal of experience in this field and have promised to share their expertise. We are, therefore, on a new road to cooperation, a cooperation that could be technically very fruitful. In 1996, there will also be two special courses at the VKI, the first on Progress in Cryogenic Wind Tunnels, the second on Aerothermodynamics and Propulsion Integration for Hypersonic Vehicles. You are all invited to participate in our future programs and I hope to have the pleasure to meet you there. Thank you for your attention.

REPORT DOCUMENTATION PAGE

1. Recipient's Reference	2. Originator's Reference	3. Further Reference	4. Security Classification of Document
	AGARD-CP-570	ISBN 92-836-0022-3	UNCLASSIFIED/ UNLIMITED

5. Originator Advisory Group for Aerospace Research and Development
North Atlantic Treaty Organization
7 rue Ancelle, 92200 Neuilly-sur-Seine, France

6. Title
Aerodynamics of Store Integration and Separation

7. Presented at/sponsored by
The FDP Symposium held in Ankara, Turkey, 24-27 April 1995

8. Author(s)/Editor(s)	9. Date
Multiple	February 1996
10. Author's/Editor's Address	**11. Pages**
Multiple	302

12. Distribution Statement There are no restrictions on the distribution of this document. Information about the availability of this and other AGARD unclassified publications is given on the back cover.

13. Keywords/Descriptors

Airframes	External stores
Aerodynamics	Computational fluid dynamics
Design	Mathematical prediction
Weapon systems	Launching
Experimental data	Integrated systems
Fighter aircraft	Aerodynamic characteristics

14. Abstract

The papers prepared for the AGARD Fluid Dynamics Panel (FDP) Symposium on "Aerodynamics of Store Integration and Separation", which was held 24-27 April 1995 in Ankara, Turkey are contained in this Report. In addition, a Technical Evaluator's Report aimed at assessing the success of the Symposium in meeting its objectives, and an edited transcript of the General Discussion held at the end of the Symposium are also included.

The aim of this symposium was to bring together engineers in the fields of theoretical and experimental aerodynamics, as applied to the store integration problem, to review and discuss the state of the art in the prediction, methodology and experimental techniques currently being developed and applied to the aerodynamics of store carriage and release and to assess new design concepts.

AGARD

NATO OTAN

7 RUE ANCELLE • 92200 NEUILLY-SUR-SEINE

FRANCE

Télécopie (1)47.38.57.99 • Télex 610 176

DIFFUSION DES PUBLICATIONS

AGARD NON CLASSIFIEES

Aucun stock de publications n'a existé à AGARD. A partir de 1993, AGARD détiendra un stock limité des publications associées aux cycles de conférences et cours spéciaux ainsi que les AGARDographies et les rapports des groupes de travail, organisés et publiés à partir de 1993 inclus. Les demandes de renseignements doivent être adressées à AGARD par lettre ou par fax à l'adresse indiquée ci-dessus. *Veuillez ne pas téléphoner.* La diffusion initiale de toutes les publications de l'AGARD est effectuée auprès des pays membres de l'OTAN par l'intermédiaire des centres de distribution nationaux indiqués ci-dessous. Des exemplaires supplémentaires peuvent parfois être obtenus auprès de ces centres (à l'exception des Etats-Unis). Si vous souhaitez recevoir toutes les publications de l'AGARD, ou simplement celles qui concernent certains Panels, vous pouvez demander à être inclu sur la liste d'envoi de l'un de ces centres. Les publications de l'AGARD sont en vente auprès des agences indiquées ci-dessous, sous forme de photocopie ou de microfiche.

CENTRES DE DIFFUSION NATIONAUX

ALLEMAGNE
Fachinformationszentrum Karlsruhe
D-76344 Eggenstein-Leopoldshafen 2

BELGIQUE
Coordonnateur AGARD-VSL
Etat-major de la Force aérienne
Quartier Reine Elisabeth
Rue d'Evere, 1140 Bruxelles

CANADA
Directeur, Services d'information scientifique
Ministère de la Défense nationale
Ottawa, Ontario K1A 0K2

DANEMARK
Danish Defence Research Establishment
Ryvangs Allé 1
P.O. Box 2715
DK-2100 Copenhagen Ø

ESPAGNE
INTA (AGARD Publications)
Pintor Rosales 34
28008 Madrid

ETATS-UNIS
NASA Headquarters
Code JOB-1
Washington, D.C. 20546

FRANCE
O.N.E.R.A. (Direction)
29, Avenue de la Division Leclerc
92322 Châtillon Cedex

GRECE
Hellenic Air Force
Air War College
Scientific and Technical Library
Dekelia Air Force Base
Dekelia, Athens TGA 1010

ISLANDE
Director of Aviation
c/o Flugrad
Reykjavik

ITALIE
Aeronautica Militare
Ufficio del Delegato Nazionale all'AGARD
Aeroporto Pratica di Mare
00040 Pomezia (Roma)

LUXEMBOURG
Voir Belgique

NORVEGE
Norwegian Defence Research Establishment
Attn: Biblioteket
P.O. Box 25
N-2007 Kjeller

PAYS-BAS
Netherlands Delegation to AGARD
National Aerospace Laboratory NLR
P.O. Box 90502
1006 BM Amsterdam

PORTUGAL
Estado Maior da Força Aérea
SDFA - Centro de Documentação
Alfragide
2700 Amadora

ROYAUME-UNI
Defence Research Information Centre
Kentigern House
65 Brown Street
Glasgow G2 8EX

TURQUIE
Millî Savunma Başkanliği (MSB)
ARGE Dairesi Başkanliği (MSB)
06650 Bakanliklar-Ankara

Le centre de distribution national des Etats-Unis ne détient PAS de stocks des publications de l'AGARD.

D'éventuelles demandes de photocopies doivent être formulées directement auprès du NASA Center for AeroSpace Information (CASI) à l'adresse ci-dessous. Toute notification de changement d'adresse doit être fait également auprès de CASI.

AGENCES DE VENTE

NASA Center for
AeroSpace Information (CASI)
800 Elkridge Landing Road
Linthicum Heights, MD 21090-2934
Etats-Unis

ESA/Information Retrieval Service
European Space Agency
10, rue Mario Nikis
75015 Paris
France

The British Library
Document Supply Division
Boston Spa, Wetherby
West Yorkshire LS23 7BQ
Royaume-Uni

Les demandes de microfiches ou de photocopies de documents AGARD (y compris les demandes faites auprès du CASI) doivent comporter la dénomination AGARD, ainsi que le numéro de série d'AGARD (par exemple AGARD-AG-315). Des informations analogues, telles que le titre et la date de publication sont souhaitables. Veuiller noter qu'il y a lieu de spécifier AGARD-R-nnn et AGARD-AR-nnn lors de la commande des rapports AGARD et des rapports consultatifs AGARD respectivement. Des références bibliographiques complètes ainsi que des résumés des publications AGARD figurent dans les journaux suivants:

Scientific and Technical Aerospace Reports (STAR)
publié par la NASA Scientific and Technical
Information Division
NASA Headquarters (JTT)
Washington D.C. 20546
Etats-Unis

Government Reports Announcements and Index (GRA&I)
publié par le National Technical Information Service
Springfield
Virginia 22161
Etats-Unis
(accessible également en mode interactif dans la base de
données bibliographiques en ligne du NTIS, et sur CD-ROM)

Imprimé par le Groupe Communication Canada
45, boul. Sacré-Cœur, Hull (Québec), Canada K1A 0S7

AGARD

NATO OTAN

7 RUE ANCELLE • 92200 NEUILLY-SUR-SEINE

FRANCE

Telefax (1)47.38.57.99 • Telex 610 176

DISTRIBUTION OF UNCLASSIFIED

AGARD PUBLICATIONS

AGARD holds limited quantities of the publications that accompanied Lecture Series and Special Courses held in 1993 or later, and of AGARDographs and Working Group reports published from 1993 onward. For details, write or send a telefax to the address given above. *Please do not telephone.*

AGARD does not hold stocks of publications that accompanied earlier Lecture Series or Courses or of any other publications. Initial distribution of all AGARD publications is made to NATO nations through the National Distribution Centres listed below. Further copies are sometimes available from these centres (except in the United States). If you have a need to receive all AGARD publications, or just those relating to one or more specific AGARD Panels, they may be willing to include you (or your organisation) on their distribution list. AGARD publications may be purchased from the Sales Agencies listed below, in photocopy or microfiche form.

NATIONAL DISTRIBUTION CENTRES

BELGIUM
Coordonnateur AGARD — VSL
Etat-major de la Force aérienne
Quartier Reine Elisabeth
Rue d'Evere, 1140 Bruxelles

CANADA
Director Scientific Information Services
Dept of National Defence
Ottawa, Ontario K1A 0K2

DENMARK
Danish Defence Research Establishment
Ryvangs Allé 1
P.O. Box 2715
DK-2100 Copenhagen Ø

FRANCE
O.N.E.R.A. (Direction)
29 Avenue de la Division Leclerc
92322 Châtillon Cedex

GERMANY
Fachinformationszentrum Karlsruhe
D-76344 Eggenstein-Leopoldshafen 2

GREECE
Hellenic Air Force
Air War College
Scientific and Technical Library
Dekelia Air Force Base
Dekelia, Athens TGA 1010

ICELAND
Director of Aviation
c/o Flugrad
Reykjavik

ITALY
Aeronautica Militare
Ufficio del Delegato Nazionale all'AGARD
Aeroporto Pratica di Mare
00040 Pomezia (Roma)

LUXEMBOURG
See Belgium

NETHERLANDS
Netherlands Delegation to AGARD
National Aerospace Laboratory, NLR
P.O. Box 90502
1006 BM Amsterdam

NORWAY
Norwegian Defence Research Establishment
Attn: Biblioteket
P.O. Box 25
N-2007 Kjeller

PORTUGAL
Estado Maior da Força Aérea
SDFA - Centro de Documentação
Alfragide
2700 Amadora

SPAIN
INTA (AGARD Publications)
Pintor Rosales 34
28008 Madrid

TURKEY
Millî Savunma Başkanliği (MSB)
ARGE Dairesi Başkanliği (MSB)
06650 Bakanliklar-Ankara

UNITED KINGDOM
Defence Research Information Centre
Kentigern House
65 Brown Street
Glasgow G2 8EX

UNITED STATES
NASA Headquarters
Code JOB-1
Washington, D.C. 20546

The United States National Distribution Centre does NOT hold stocks of AGARD publications.
Applications for copies should be made direct to the NASA Center for AeroSpace Information (CASI) at the address below. Change of address requests should also go to CASI.

SALES AGENCIES

NASA Center for
AeroSpace Information (CASI)
800 Elkridge Landing Road
Linthicum Heights, MD 21090-2934
United States

ESA/Information Retrieval Service
European Space Agency
10, rue Mario Nikis
75015 Paris
France

The British Library
Document Supply Centre
Boston Spa, Wetherby
West Yorkshire LS23 7BQ
United Kingdom

Requests for microfiches or photocopies of AGARD documents (including requests to CASI) should include the word 'AGARD' and the AGARD serial number (for example AGARD-AG-315). Collateral information such as title and publication date is desirable. Note that AGARD Reports and Advisory Reports should be specified as AGARD-R-nnn and AGARD-AR-nnn, respectively. Full bibliographical references and abstracts of AGARD publications are given in the following journals:

Scientific and Technical Aerospace Reports (STAR)
published by NASA Scientific and Technical
Information Division
NASA Headquarters (JTT)
Washington D.C. 20546
United States

Government Reports Announcements and Index (GRA&I)
published by the National Technical Information Service
Springfield
Virginia 22161
United States
(also available online in the NTIS Bibliographic
Database or on CD-ROM)

Printed by Canada Communication Group
45 Sacré-Cœur Blvd., Hull (Québec), Canada K1A 0S7

ISBN 92-836-0022-3